Dongdong Gu

Laser Additive Manufacturing of High-Performance Materials

Springer

Laser Additive Manufacturing of High-Performance Materials

Dongdong Gu

Laser Additive Manufacturing of High-Performance Materials

Springer

Dongdong Gu
College of Materials Science and Technology
Nanjing University of Aeronautics and Astronautics
Nanjing
China

ISBN 978-3-662-46088-7 ISBN 978-3-662-46089-4 (eBook)
DOI 10.1007/978-3-662-46089-4

Library of Congress Control Number: 2015931634

Springer Berlin Heidelberg New York Dordrecht London
© Springer-Verlag Berlin Heidelberg 2015
This work is subject to copyright. All rights are reserved by the Publisher, whether the whole or part of the material is concerned, specifically the rights of translation, reprinting, reuse of illustrations, recitation, broadcasting, reproduction on microfilms or in any other physical way, and transmission or information storage and retrieval, electronic adaptation, computer software, or by similar or dissimilar methodology now known or hereafter developed.
The use of general descriptive names, registered names, trademarks, service marks, etc. in this publication does not imply, even in the absence of a specific statement, that such names are exempt from the relevant protective laws and regulations and therefore free for general use.
The publisher, the authors and the editors are safe to assume that the advice and information in this book are believed to be true and accurate at the date of publication. Neither the publisher nor the authors or the editors give a warranty, express or implied, with respect to the material contained herein or for any errors or omissions that may have been made.

Printed on acid-free paper

Springer–Verlag Berlin Heidelberg is part of Springer Science+Business Media (www.springer.com)

Preface

Additive manufacturing (AM), interchangeably referred to as 3D printing, has never received so much attention. Considering all of the recent spotlights in the mainstream media, one might think that AM is a new breakthrough in the advanced manufacturing industry. However, our institution, Nanjing University of Aeronautics and Astronautics (NUAA) has been working with this technology since the mid-1990s. The designations of this technology have also changed from the initial "rapid prototyping (RP)" to the present "additive manufacturing (AM)" which is regarded as a more general designation that reflects directly the unique processing philosophy of this advanced manufacturing technology. Depending on the material and objective of the final application, there are various AM processes that have been commercially available. The most common materials presently applied for AM are typically plastics, metals, and alloys such as Al-based, Ni-based, Ti-based, and Fe-based alloys. Meanwhile, more novel materials with unique properties are currently being investigated for AM and are likely to be used successfully in the near future. The most popular AM processing systems for metallic components typically use a laser to heat, melt, and consolidate powder materials. Laser-based AM technology for the fabrication of metallic components typically has two basic categories according to the different mechanisms of laser-powder interaction. One is based on the laser powder bed approach (i.e., prespreading of powder on powder bed before laser melting) and the typical processes include direct metal laser sintering (DMLS) and selective laser melting (SLM); the other is based on the laser powder feeding method (i.e., coaxial feeding of powder by nozzle with synchronous laser melting) and the typical process is laser metal deposition (LMD) or laser engineered net shaping (LENS). DMLS/SLM and LMD represent two different development directions for AM of metallic components. Parts produced by DMLS/SLM are impressive in their elaborate structures including the thin walls, sound surface finish, fine features, and small internal channels, due to the small focused laser beam size and thin powder layer thickness (generally less than 100 μm) applied during the DMLS/SLM process. Contrarily, LMD has a versatile process capability and can be applied to manufacture new components, to repair and rebuild worn or damaged components, and to prepare wear and corrosion resistant coatings. LMD demonstrates a high capability in producing the larger-sized 3D parts, since the deposition

layer thickness during LMD is in the order of millimeters. It is noted that the high deposition rate of LMD process, which is regarded as a process base for producing large components, inevitably results in the decrease in the dimensional precision of the final components after layer-by-layer deposition. LMD is accordingly a "near net shaping" AM process for the large 3D components, as relative to the "net shaping" capability of DMLS/SLM process for the relatively small 3D components.

Laser-based AM technology, due to its unconventional material incremental manufacturing philosophy combined with the highly non-equilibrium metallurgical nature of the laser process, provides a beneficial method to simultaneously develop new materials, complex 3D configurations, and unique microstructures and properties. This book describes the capabilities and characteristics of the development of new metallic material components by laser-based AM process, including nanostructured material, *in situ* composite material, particle reinforced metal matrix composites, etc. The topics and results presented in this book, similar to the laser AM technology itself, show a significant interdisciplinary feature, integrating laser technology, materials science, metallurgical engineering, and mechanical engineering. The book comprehensively covers the specific aspects of laser-based AM of new material components, in terms of materials design and preparation, process control and optimization, and theories of physical and chemical metallurgy. As a major idea highlighted in the book, the integration of "Designed Material", "Tailored Process" and "Controllable Property" presents one of the most important strategies for future sustainable research and development in laser-based AM of high-performance metallic components. We may understand the laser-based AM technology from various aspects such as process control, material design, apparatus and software, microstructure and property evaluation, etc. This book chooses a unique angle to view the research and development progress of laser-based AM technology. An interesting and important issue in AM research fields, i.e., the development of high-performance new material components by laser-based AM process, is emphasized in this book. The combination of the tailored laser-based AM process with the new materials hopefully leads to some interesting outcome, e.g., the simultaneous realization of complex shapes, unique microstructures, and high performance. We believe it is a unique book for researchers, students, practicing engineers, and manufacturing industry professionals interested in laser-based AM and laser processing of powder materials.

The book is divided into ten chapters and a quick preview of the contents is given as follows:

Chapter 1 introduces the development history of AM technology and the nomenclature principles for naming different types of AM processes. The general processing philosophy and the typical applications of AM technology are presented.

Chapter 2 reviews the current status of research and development in the three most versatile laser-based AM processes for metallic components, including laser sintering (LS), laser melting (LM), and laser metal deposition (LMD). The ever-reported metallic powder materials used for AM are classified and the associated bonding and densification mechanisms during laser-based AM are proposed. An in-depth review of the materials aspects of laser-based AM processes is presented,

including physical aspects of materials for AM, microstructural/mechanical properties of AM-processed parts, and structure/property stability of AM-fabricated parts, in order to establish the relationship between material, process, and metallurgical mechanism of various laser-based AM processes.

Chapter 3 presents the selective laser melting (SLM) AM processing of nanocrystalline TiC reinforced Ti matrix bulk-form nanocomposites. The controlled crystallization and development mechanisms of nanostructures of TiC reinforcement in SLM-processed Ti-based nanocomposites are disclosed and the underlying role of microstructural development in mechanical properties of SLM-processed nanocomposites is elucidated.

Chapter 4 presents the SLM fabrication of the *in situ* Ti–Si intermetallic-based TiC/Ti_5Si_3 and TiN/Ti_5Si_3 composite parts with novel reinforcement architecture and elevated mechanical performance. The underlying material–process–microstructure–property relationship is established to enable the successful laser-based AM of the designed *in situ* composites.

Chapter 5 proves the feasibility of the SLM process in producing the high melting point *in situ* WC cemented carbide based hardmetals. The SLM AM process demonstrates to be a unique method to produce the WC-based hardmetals parts with novel microstructural characteristics and mechanical properties.

Chapter 6 presents the SLM processing of the nanoscale TiC particle reinforced AlSi10Mg nanocomposite parts. The microstructural evolution of nanoscale reinforcement in SLM-processed parts at different SLM processing parameters is studied and the attendant densification level and mechanical properties are assessed, in order to enable the successful production of Al-based composites with nanoscale reinforcement architecture and elevated mechanical performance.

Chapter 7 deals with the SLM production of novel Al-based composites with multiple reinforcing phases starting from the SiC/AlSi10Mg composite powder having an *in situ* reaction nature. The present research attempt reveals the promising potential of SLM process in producing novel lightweight composites with unique reinforcing structures and performance.

Chapter 8 reports on the direct metal laser sintering (DMLS) AM processing of the WC particle reinforced Cu matrix composite parts. A novel design method of the graded interface between the WC reinforcing particles and the Cu matrix is applied and the formation mechanism of the graded interfacial structure during DMLS process is proposed. The control and optimization mechanisms of processing conditions and materials combinations are proposed to improve the microstructural homogeneity and resultant mechanical performance of DMLS-processed WC/Cu composites.

Chapter 9 presents the DMLS consolidation of the nano/micron W–Cu composites, which is a unique materials system due to the mutual insolubility of W and Cu. The effects of the DMLS processing parameters and the Cu-liquid content in the system on the densification behavior and microstructural characteristics of DMLS-processed W–Cu composites are disclosed. A novel W-rim/Cu-core structure and its formation mechanism during DMLS are proposed, which is regarded as a unique laser induced metallurgical phenomenon of this insoluble system.

Chapter 10 summarizes the main findings and contributions of this monograph, along with some important issues and suggestions for future sustainable development of laser-based AM technology.

This book serves as a systemic sum-up of my research work during the past 12 years on laser-based AM of high-performance new metallic materials components. As you may see, the laser-based AM research work on these materials has been carried out using the laser powder bed approach including selective laser melting (SLM) and direct metal laser sintering (DMLS). Nevertheless, the basic conclusions as presented in this book are applicable and/or transferrable to other laser-based AM processes, e.g., laser metal deposition (LMD) or laser engineered net shaping (LENS), as well as the laser-based powder processing techniques, e.g., laser cladding, laser surface alloying, laser melt injection, etc.

I gratefully appreciate your interest and the time taken to read this book entitled "Laser Additive Manufacturing of High-Performance Materials" and hope that you think it is a worthwhile work to add some unique understanding to this rapidly developing technology.

Nanjing, 2014
Prof. Dr. Dongdong Gu

Acknowledgments

First of all, I gratefully appreciate the financial support from the National Natural Science Foundation of China (Projects Nos. 51322509, 51104090, and 51054001), the Outstanding Youth Foundation of Jiangsu Province of China (Project No. BK20130035), the Program for New Century Excellent Talents in University (Project No. NCET–13–0854), the Science and Technology Support Program (The Industrial Part), Jiangsu Provincial Department of Science and Technology of China (No. BE2014009–2), the Program for Distinguished Talents of Six Domains in Jiangsu Province of China (Project No. 2013-XCL-028), the Fundamental Research Funds for the Central Universities (Projects Nos. NE2013103 and NS2010156), the Aeronautical Science Foundation of China (Project No. 2010ZE52053), the Natural Science Foundation of Jiangsu Province (Project No. BK2009374), and the Qing Lan Project, Jiangsu Provincial Department of Education, China who supported my research work on laser additive manufacturing. I am also thankful for the financial support from the Alexander von Humboldt Foundation (Sep. 2009– Aug. 2011) and the German Federal Ministry of Education and Research (BMBF) (Sep. 2013– Nov. 2013) to support my research stays at the Fraunhofer Institute for Laser Technology ILT, Aachen, Germany.

I appreciate my Ph.D. supervisors Prof. Yifu Shen and Prof. Jun Xiao who led me into this interesting research field of laser additive manufacturing. I also appreciate my German academic host, Prof. Reinhart Poprawe, and colleagues, Dr. Wilhelm Meiners, Dr. Yves-Christian Hagedorn, Dr. Konrad Wissenbach, Dr. Andreas Weisheit, Dr. Ingomar Kelbassa, and Dr. Damien Buchbinder for valuable discussions and generous assistance during my research stays at the Fraunhofer ILT. My research experience at the Fraunhofer ILT contributes a lot to the better understanding of laser-based additive manufacturing technologies. Furthermore, I wish to thank my Ph.D. and M.D. students, Mr. Chuang Li, Mr. Guangbin Meng, Mr. Donghua Dai, Mr. Guoquan Zhang, Mr. Qingbo Jia, Mr. Hongqiao Wang, Miss. Yali Li, Mr. Fei Chang, Mr. Pengpeng Yuan, Miss. Beibei He, and Miss. Sainan Cao for their diligent work for our research projects. Many of my "own" results as presented in this book actually have been achieved together with my colleagues and students.

I also gratefully acknowledge the copyright permission from the following publishers including Elsevier, Springer, Maney Publishing, IOP Publishing, AIP Publishing, The American Ceramic Society/ John Wiley and Sons, and American Society of Mechanical Engineers (ASME) for the reproduction of the author's published journal papers.

In particular, I wish to thank my wife Xiaolei Liu for her valuable encouragement and support for me in writing this book. In fact, when I planned to write this book, my daughter, Ruoyan Gu, was just born. Now I have almost finished writing the whole book and, to my greatest joy, she can call me daddy. Writing this book, just like bringing up my daughter, is really a hard task. However, thanks to this particular experience, I can have and feel a lot of achievement and happiness during this course.

This book is for my dear wife Xiaolei and lovely daughter Ruoyan!

Contents

1 Introduction 1
1.1 Development History and Nomenclature of AM Processes 1
1.1.1 Development History of AM Technology 1
1.1.2 Nomenclature of Different AM Processes 3
1.2 Basic Procedures of AM Process 4
1.3 Advantages and Application Areas of AM Technology 6
1.4 About This Book 8
References 11

2 Laser Additive Manufacturing (AM): Classification, Processing Philosophy, and Metallurgical Mechanisms 15
2.1 Classification of Laser AM Processes and Metallurgical Mechanisms 15
2.1.1 Laser Sintering (LS) 16
2.1.2 Laser Melting (LM) 20
2.1.3 Laser Metal Deposition (LMD) 23
2.2 Classes of Materials for AM and Processing Mechanisms 30
2.2.1 For LM and LMD—Pure Metals Powder 30
2.2.2 For LM and LMD—Alloys Powder 32
2.2.3 For LS and LMD—Multi-Component Metals/Alloys Powder Mixture 42
2.2.4 Metal Matrix Composites (MMCs) 48
2.3 Material/Process Considerations and Control Methods 51
2.3.1 General Physical Aspects and Design Strategies of Materials for AM 51
2.3.2 Microstructural Properties of AM-Processed Parts 54
2.3.3 Mechanical Properties and Performance Aspects of AM-Processed Parts 60
2.3.4 Structure/Property Stability of AM-Processed Parts 63
2.4 Summary 63
References 64

3 Novel Ti-Based Nanocomposites by Selective Laser Melting (SLM) Additive Manufacturing (AM): Tailored Nanostructure and Performance 73
3.1 Introduction 73
3.2 Preparation of TiC/Ti Nanocomposite Powder for SLM 75
3.3 General Introduction of Experimental Setup and Processing Procedures of SLM Work in This Book 77
3.4 General Introduction of Experimental Procedures and Methods for Microstructures and Mechanical Properties Tests in This Book 80
3.4.1 Metallographic Specimen Preparation and Examination 80
3.4.2 Characterization of Constitutional Phases, Microstructural Features, and Chemical Compositions 81
3.4.3 Mechanical Properties Testing 82
3.5 Influence of SLM Processing Parameters on Densification, Growth Mechanism, and Wear Behavior TiC/Ti Nanocomposite Parts 84
3.5.1 Influence of SLM Parameters on Constitutional Phases 84
3.5.2 Influences of SLM Parameters on Surface Morphologies and Densification 84
3.5.3 Influence of SLM Parameters on Microstructures and Formation Mechanisms 87
3.5.4 Influence of SLM Parameters on Nanoindentation and Wear Behavior 92
3.6 Influence of Nanoscale Reinforcement Content on SLM Processing of TiC/Ti Nanocomposite Parts 95
3.6.1 Influence of TiC Nanocomposites Content on Densification Behavior 95
3.6.2 Influence of TiC Nanoparticles Content on Microstructural Characteristics 97
3.6.3 Influence of TiC Nanoparticles Content on Hardness and Wear Performance 99
3.7 The Role of Nanopowder in SLM Processing of TiC/Ti Nanocomposite Parts 102
3.7.1 The Role of Nanopowder in Densification Behavior 102
3.7.2 The Role of Nanopowder in Microstructure Development 105
3.7.3 The Role of Nanopowder in Wear and Tribological Property 107
3.7.4 Influence of Nanopowder Characteristics on Densification Behavior and Microstructural Development 108
3.7.5 Relationship of Densification, Microstructure, and Wear and Tribological Performance 110
3.8 Conclusions 111
References 112

4 *In Situ* Ti–Si Intermetallic-Based Composites by Selective Laser Melting (SLM) Additive Manufacturing (AM): Designed Materials and Laser-Tailored *In Situ* Formation 115
4.1 Introduction 115
4.2 Selective Laser Melting (SLM) of *In Situ* TiC/Ti_5Si_3 Composite Parts with Novel Reinforcement Architecture and Elevated Performance 117
4.2.1 Ball Milling of SiC/Ti Powder System for SLM Process 117
4.2.2 Formation Mechanism and Microstructural Development of *In Situ* TiC Reinforcement during SLM Processing of SiC/Ti Powder System 118
4.2.3 Influence of SLM Processing Conditions on Densification, Microstructure, and Wear Behavior of *In Situ* TiC/Ti_5Si_3 Composite Parts 126
4.3 Selective Laser Melting (SLM) of *In Situ* TiN/Ti_5Si_3 Composite Parts: Densification Mechanism, Microstructural Development, and Wear Property 134
4.3.1 Ball Milling of Si_3N_4/Ti Powder System for SLM Process ... 134
4.3.2 Influence of SLM Parameters on Constitutional Phases of *In Situ* TiN/Ti_5Si_3 Composite Parts 135
4.3.3 Influence of SLM Parameters on Microstructures and Compositions of *In Situ* TiN/Ti_5Si_3 Composite Parts 138
4.3.4 Influence of SLM Parameters on Densification Behavior of *In Situ* TiN/Ti_5Si_3 Composite Parts 142
4.3.5 Influence of SLM Parameters on Microhardness and Wear Property of *In Situ* TiN/Ti_5Si_3 Composite Parts ... 145
4.4 Conclusions 148
References 149

5 *In Situ* WC-Cemented Carbide-Based Hardmetals by Selective Laser Melting (SLM) Additive Manufacturing (AM): Microstructure Characteristics and Formation Mechanisms 151
5.1 Introduction 151
5.2 Preparation of W–Ni–Graphite Powder System for SLM Process ... 152
5.3 Effect of SLM Processing Parameters on Phase Evolution of WC-Based Hardmetals Parts Using CO_2 Laser 154
5.4 Effect of SLM Processing Parameters on Microstructure and Composition Development of WC-Based Hardmetals Parts Using CO_2 Laser 156
5.5 Formation Mechanisms and Conditions of *In Situ* WC Phase during SLM Process Using CO_2 Laser 162
5.6 Relationship of Processing Conditions, Microstructures, and Microhardness of SLM-Processed WC-Based Hardmetals Parts Using CO_2 Laser 165

5.7 Crystal Growth Mechanisms of *In Situ* WC in Selective Laser Melted W–C–Ni Ternary System Using Fiber Laser 168
5.8 Conclusions 172
References 172

6 Nanoscale TiC Particle-Reinforced AlSi10Mg Bulk-Form Nanocomposites by Selective Laser Melting (SLM) Additive Manufacturing (AM): Tailored Microstructures and Enhanced Properties 175
6.1 Introduction 175
6.2 Powder Preparation and SLM Process of TiC/AlSi10Mg Nanocomposites 177
6.3 Phases Identification SLM-processed TiC/AlSi10Mg Nanocomposite Parts 177
6.4 Effect of SLM Processing Parameters on Densification Behavior of TiC/AlSi10Mg Nanocomposite Parts 179
6.5 Effect of SLM Processing Parameters on Microstructural Evolution of TiC/AlSi10Mg Nanocomposite Parts 182
6.6 Mechanical Performance of SLM-processed TiC/AlSi10Mg Nanocomposite Parts 190
6.6.1 Dimensional Accuracy of SLM-processed TiC/AlSi10Mg Nanocomposite Parts 190
6.6.2 Hardness and Wear Performance of SLM-processed TiC/AlSi10Mg Nanocomposite Parts 191
6.6.3 Tensile Properties of SLM-processed TiC/AlSi10Mg Nanocomposite Parts 195
6.7 Conclusions 198
References 198

7 Novel Aluminum Based Composites by Selective Laser Melting (SLM) Additive Manufacturing (AM): Tailored Formation of Multiple Reinforcing Phases and its Mechanisms 201
7.1 Introduction 201
7.2 Preparation and SLM Processing of SiC/AlSi10Mg Composite Powder 204
7.3 Phases Identification SLM-Processed Al-based Composite Parts from SiC/AlSi10Mg Powder System 206
7.4 Microstructures and Compositions of Al-based Composite Parts Processed by SLM of SiC/AlSi10Mg Powder 207
7.5 Densification Behavior of Al-based Composite Parts Processed by SLM of SiC/AlSi10Mg Powder 212
7.6 Hardness and Wear Performance of Al-Based Composite Parts Processed by SLM of SiC/AlSi10Mg Powder 214
7.7 Conclusions 219
References 220

8 Particle-Reinforced Cu Matrix Composites by Direct Metal Laser Sintering (DMLS) Additive Manufacturing (AM): Interface Design, Material Optimization, and Process Control 223
8.1 Introduction 223
8.2 Preparation of $(WC–Co)_p$/Cu Composite Powder System for DMLS Process 225
8.2.1 Preparation of Submicron WC–Co Composite Powder 225
8.2.2 Preparation of $(WC–Co)_p$/Cu Composite Powder System 226
8.3 Interface Design and Processing Conditions of Submicron WC–Co Particle-Reinforced Cu Matrix Composites Prepared by Direct Metal Laser Sintering (DMLS) 227
8.3.1 Interface Design and Formation Mechanism of $(WC–Co)_p$/Cu Composite System during DMLS 227
8.3.2 Influence of DMLS Processing Parameters on Microstructural and Mechanical Properties of $(WC–Co)_p$/Cu Composite Parts 235
8.4 Influence of Reinforcement Weight Fraction on Microstructure and Properties of $(WC–Co)_p$/Cu Composite Parts Prepared by DMLS 241
8.4.1 Effect of Reinforcement Content on Particle Dispersion State and Microhardness and its Distribution 241
8.4.2 Effect of Reinforcement Content on Particle–Matrix Interfacial Microstructure 242
8.4.3 Effect of Reinforcement Content on Tensile Property and Fracture Surface Morphology 244
8.4.4 Influencing Mechanisms of Reinforcement Content on Microstructural and Mechanical Properties 245
8.5 Influence of Processing Parameters on Particle Dispersion in $(WC–Co)_p$/Cu Composite Parts Prepared by DMLS 249
8.5.1 Process Map for Particle Dispersion in DMLS-processed $(WC–Co)_p$/Cu Composites 249
8.5.2 Microstructural Development of Particle Dispersion in DMLS-Processed $(WC–Co)_p$/Cu Composites 250
8.5.3 Mechanisms of Particle Dispersion in DMLS-processed $(WC–Co)_p$/Cu Composites at Different Processing Parameters 253
8.6 The Role of Rear Earth (RE) La_2O_3 Addition in DMLS Processing of Submicron $(WC–Co)_p$/Cu Composite Parts 257
8.6.1 Phase Identification of DMLS-processed $(WC–Co)_p$/Cu Composites Containing Various Contents of La_2O_3 257
8.6.2 Densification Response of DMLS-processed $(WC–Co)_p$/Cu Composites Containing Various Contents of La_2O_3 259

8.6.3 Particle Dispersion and Particle Morphology of DMLS-processed $(WC–Co)_p$/Cu Composites Containing Various Contents of La_2O_3 260
8.6.4 Etched Microstructure of Metal Matrix of DMLS-processed $(WC–Co)_p$/Cu Composites Containing Various Contents of La_2O_3 262
8.6.5 Functions of RE Element in DMLS of Particle-Reinforced MMCs 264
8.7 Conclusions 270
References 271

9 Nano/Micron W–Cu Composites by Direct Metal Laser Sintering (DMLS) Additive Manufacturing (AM): Unique Laser-Induced Metallurgical Behavior of Insoluble System 273
9.1 Introduction 273
9.2 Preparation of Nano/Micron W–Cu Composite Powder System for DMLS Process 275
9.2.1 Preparation of Nanocrystalline W–Cu Composite Powder 275
9.2.2 Preparation of Nano/Micron (W–Cu)/Cu Composite Powder System 277
9.3 Effects of Processing Parameters on Consolidation and Microstructure of Nano/Micron W–Cu Component Processed by DMLS 278
9.3.1 Mechanisms of Powder Melting and Densification during DMLS of Nano/Micron W–Cu Composite Powder 278
9.3.2 Microstructural Characteristics of Nano/Micron W–Cu Components Processed by DMLS 281
9.3.3 Process Control and its Mechanisms for DMLS of W–Cu Components 283
9.4 Influence of Cu-Liquid Content on Densification and Microstructure of Nano/Micron W–Cu Composites Prepared by DMLS 290
9.4.1 Densification and Microstructure of DMLS-Processed W–Cu Composites with Variation of Cu-Liquid Contents 290
9.4.2 The Role of Cu-Liquid Content in Densification Behavior and Microstructural Development of DMLS-Processed W–Cu Composites 294
9.4.3 Formation Mechanism of a Novel W-rim/Cu-Core Structure During DMLS of W–Cu Composite System 297
9.5 Conclusions 299
References 300

10 Summary and Prospective View 303
10.1 Summary of Main Work and Findings 303
10.2 Prospective View 306
References 308

About the Author

Prof. Dr. Dongdong Gu is currently a full professor in the College of Materials Science and Technology (CMST) and the deputy director of Institute of Additive Manufacturing (3D Printing), Nanjing University of Aeronautics and Astronautics (NUAA), PR China. He received the Ph.D. in Materials Processing Engineering from NUAA in June 2007. Then he joined the CMST of NUAA in July 2007. In March 2009 he was awarded the Alexander von Humboldt Fellowship and then had a two-year research stay in the Fraunhofer Institute for Laser Technology ILT/Chair for Laser Technology LLT, RWTH Aachen, Germany from September 2009 to August 2011. His principal research interests include laser-based additive manufacturing including selective laser melting (SLM), direct metal laser sintering (DMLS), and laser metal deposition (LMD), laser surface engineering, and laser preparation of new materials. His research is financially supported by the National Natural Science Foundation of China, the Alexander von Humboldt Foundation Germany, the German Federal Ministry of Education and Research (BMBF), the Aeronautical Science Foundation of China, the Natural Science Foundation of Jiangsu Province of China, the Ministry of Education of China, the Jiangsu Provincial Department of Science and Technology of China, etc. In recent years, Prof. Gu has co-authored two books on laser additive manufacturing published by Woodhead Publishing UK and Nova Science Publishers USA and has authored/co-authored about 100 papers in a number of internationally recognized peer-reviewed journals including *Int Mater Rev, Acta Mater, Scripta Mater, Appl Phys Lett, Metall Mater Trans A, Metall Mater Trans B, Compos Sci Technol, Mater Sci Eng A, J Phys D Appl Phys, J Am Ceram Soc, Int J Mach Tool Manuf, J Manuf Sci Eng Trans ASME, J Mater Res, J Alloys Compd, Surf Coat Technol, Appl Surf Sci, Opt Laser Technol, Mater Lett, Mater Design, J Compos Mater, Adv Eng Mater, Int J Refract Met Hard Mater, J Mater Process Technol, Mater Sci Technol,* etc., as the first author and corresponding author.

Prof. Gu is currently the editorial board member of four international journals including *Applied Surface Science* (Elsevier), *International Journal of Precision Engineering and Manufacturing* (Springer), *Lasers in Engineering* (Old City Publishing, USA), and *Additive Manufacturing* (Elsevier). He also serves as the reviewer for more than 30 international peer-review journals including *Opt Laser Technol, Int J Adv Manuf Technol, Laser Eng, Scripta Mater, Mater Sci Eng A, Mater Sci Eng B, Mater Sci Eng C, Compos Sci Technol, J Compos Mater, J Alloys Compd, Surf Coat Technol, Appl Surf Sci, J Mech Behav Biomed Mater, Mater Design, Mater Charact, Mater Lett, J Mater Res, Vacuum, J Mater Sci Technol,* etc. Prof. Gu is the committee member of the Additive Manufacturing Technology Committee, Unconventional Processing Institution of Chinese Mechanical Engineering Society (CMES) and the committee member of the Youth Work Committee, Surface Engineering Institution of CMES. He has been involved in 12 international conferences as the Academic Committee Member and/or Keynote/Invited Speaker.

Prof. Gu has been awarded the Excellent Young Scientists Fund from the National Natural Science Foundation of China (2013), the Program for New Century Excellent Talents in University from the Ministry of Education of China (2013), the Outstanding Youth Fund of Jiangsu Province from the Jiangsu Provincial Department of Science and Technology of China (2013), and the "Green Talents" from the German Federal Ministry of Education and Research (BMBF) (2012).

Chapter 1
Introduction

Abstract Different from conventional materials removal method, additive manufacturing (AM) is based on a novel material incremental manufacturing philosophy. Laser-based AM implies layer-by-layer shaping and consolidation of feedstock, typically powder materials, to arbitrary configurations, using a computer controlled laser as energy resource. The current development focus of AM is to produce complex-shaped functional metallic components, including metals, alloys, and metal matrix composites (MMCs), to meet the demanding requirements from aerospace, defense, automotive, and biomedical industries. In this chapter, the development history of AM technology is briefly introduced and the nomenclature principles for naming different types of AM processes are reviewed. The general processing philosophy of AM is addressed and the typical applications of AM technology are presented.

1.1 Development History and Nomenclature of AM Processes

1.1.1 Development History of AM Technology

The additive manufacturing (AM) serves well as a term for a class of technologies that use the computer-aided design (CAD)-based layer-by-layer manufacturing process to construct parts that are used directly as end-use products. AM is, therefore, also called solid freeform fabrication, digital manufacturing, direct manufacturing, or e-manufacturing. Recently, the term "3D printing" has been used to denominate the AM technology and is widely used in the news media, which is hopefully considered as the driver of a "third industrial revolution" since it has the potential to revolutionize the way we make almost everything [1].

Rapid prototyping (RP) and rapid manufacturing (RM) are two widely-recognized nomenclatures for the description of AM technology before the use of the nomenclature "Additive manufacturing" [2]. In the historical subsequence, a series of processes for RP was primarily established (these processes are specified in the following paragraph). Then considerable research efforts proved that some of these processes could also be used for manufacturing, especially for small runs.

© Springer-Verlag Berlin Heidelberg 2015

D. Gu, *Laser Additive Manufacturing of High-Performance Materials,*
DOI 10.1007/978-3-662-46089-4_1

Thus, “rapid prototyping” was combined with “manufacturing” to give “rapid manufacturing.” As compared to the phrases RP and RM, AM is regarded as a more general designation that directly reflects the processing strategy of this advanced manufacturing technology.

Since the first technique for AM became available in the late 1980s and was used to fabricate models and prototypes [3, 4], AM technology has experienced more than 20 years of development and is presently one of the rapidly developing advanced manufacturing techniques in the world. Different to the material removal method in conventional machining processes, AM is based on a completely contrary discipline, i.e., material incremental manufacturing (MIM) [5]. AM implies layer-by-layer shaping and consolidation of feedstock to arbitrary configurations. A wide range of feedstock can be applied for AM technology, from the low melting point polymer materials to the high melting point metals and ceramics. Meanwhile, different forms of materials, including liquid, powder, wire, etc, are feasible for AM. Based on the similar processing philosophy, the established AM techniques are versatile. The initially developed AM techniques include stereolithography apparatus (SLA) [6], laminated object manufacturing (LOM) [7], fused deposition modeling (FDM) [8], and selective laser sintering (SLS) [9, 10]. These AM processes are typically applied for the fabrication of prototypes made from low melting point polymers as communication or inspection tools. The capability of producing physical objects in a short period directly from CAD models helps to shorten the production development steps.

The layer-by-layer manufacturing technology for fusible materials was firstly established in the 1971 patent of Ciraud [11], which is considered as the precursor of 3D laser cladding processes. In the 1977 patent of Housholder [12] regarding a molding process for forming a 3D article in layers, the concept of SLS systems was proposed. Nevertheless, these primary ideas were not ready for commercialization due to the lack of powerful computers and the high price of laser systems at that time [13].

Deckard (1986) at the University of Texas in Austin developed the first deterministic turing machine (DTM) in late 1992 [14]. The as-developed process was named SLS, which further entered the market with the development the Sinterstation 2000/2500 machines and the corresponding powder materials such as DTM RapidTool, RapidSteel, and LaserForm ST. DTM Company was incorporated with 3D Systems in 2001 [15]. The EOS machine EOSINT P 350 was launched in 1994 by EOS GmbH Electro Optical Systems, which was the first European laser sintering system for manufacturing plastic prototypes. In 1995, the EOSINT M 250 direct metal laser sintering (DMLS) system for AM of metal tools for plastics injection molding was launched, which was regarded as the start of rapid tooling [16]. In 2004, EOS GmbH acquired the right to all the relevant patents of DTM, University of Texas and 3D Systems related to laser sintering [17].

In 1995, selective laser melting (SLM) started at the Fraunhofer Institute for Laser Technology ILT in Aachen, Germany [18], achieving the German patent DE 19649865 in this pioneering phase. Dr. Dieter Schwarze and Dr. Matthias Fockele from the Fockele & Schwarze (F&S) Stereolithographietechnik GmbH worked

together with the ILT researchers Dr. Wilhelm Meiners and Dr. Konrad Wissenbach on this technology. In the early 2000s, F&S entered into a commercial partnership with MCP HEK GmbH Germany. In 2007, MCP HEK Tooling GmbH was founded to promote SLM technology further. In 2008, MCP became MTT Technologies group to strengthen the approach in AM, which was renamed into SLM Solutions GmbH in 2010 [19]. Today Dr. Schwarze is with SLM Solutions GmbH and Dr. Fockele founded the Realizer GmbH [20].

Another similar and parallel development was going on at the Westinghouse Electric Corporation in a patent application in 1988 and by Sandia National Laboratories in the middle of 1990s [21]. In 1997, AeroMet was founded as a subsidiary of MTS Systems Corp. The company developed a process called laser additive manufacturing (LAM) that used a high-power laser and powdered titanium alloys [22]. The method of depositing the powder changed from "powder-in-bed" to "powder injection," which will be addressed in detail in Chap. 2. Until it shut down in December 2005, AeroMet manufactured parts for the aerospace industry as a service provider. In 1997, Optomec introduced its first commercial AM system based on the Laser Engineering Net Shaping (LENS) technology developed at Sandia National Laboratories. Optomec has now installed systems at 150 customer sites in 15 countries [23].

1.1.2 Nomenclature of Different AM Processes

At present, the production of conceptual prototypes made from polymers is no longer the current research focus of AM. Nowadays, the development of AM techniques is aiming to produce complex-shaped functional metallic components, including metals, alloys, and metal matrix composites (MMCs), that cannot be easily produced by the conventional methods, in order to meet the demanding requirements from aerospace [24, 25], automotive [26, 27], rapid tooling [28, 29], and biomedical [30, 31] industrial sectors. Actually, the components produced by AM are no longer merely used for visualization, but are also used as real production parts (i.e., end-use products) with basic mechanical properties meeting the industrial requirements. As the energy resource for AM of high melting point metallic components, the computer controlled lasers having high energy density are typically used. Most of the commercial AM machines in the market for the direct production of metallic components use high-power CO_2, Nd:YAG or fiber lasers in continuous mode. As a significant development tendency, the fiber lasers with the laser power in the range of 200–2000 W are widely used in the latest developed commercial AM machines (e.g., EOSINT M 280, ReaLizer SLM 250, SLM® 280 HL, and LENS 450) [16, 19, 20, 23]. The particular advantages of fiber lasers over other types include the high output power, high optical quality, compact size and high reliability. Furthermore, the fact that the light has been already in a fiber allows it to be easily delivered to a movable focusing element, which is important for the AM processes featured by the high flexibility.

To satisfy the demands for laser-based AM fabrication of cost-effective and end-use metallic components, three typical processes in terms of laser sintering (LS), laser melting (LM), and laser metal deposition (LMD) have been developed.[1] Throughout the world, different institutions and companies use different phrases to denominate these three most prevailing variants of AM technology, as revealed in Table 1.1.

1.2 Basic Procedures of AM Process

In general, a typical AM process is performed by means of the following basic procedures [32]:

- Create CAD model of the part to be produced

Firstly, the part to be built is modeled using a computer-aided design (CAD) software package. Normally, a solid modeling system, often called a solid modeler, is able to represent three-dimensional objects more accurately than a wire-frame model, thereby yielding better design results. The designer can use a preexisting CAD file or create one subjectively for prototyping purposes.

- Convert the CAD model to STL format

The various CAD packages use a number of different algorithms to represent solid objects. To establish consistency, the STL (stereolithography, known as the primarily developed AM technique) format has been adopted as the standard of the AM industry. The second step, therefore, is to convert the CAD file into STL format. Normally, an STL file is a triangular representation of a three-dimensional surface geometry. The surface is tessellated logically into a set of oriented triangles (facets). Each facet is described by the unit outward normal and three points listed in counterclockwise order representing the vertices of the triangle. Because the STL files use planar elements, they cannot represent curved surfaces exactly.

Increasing the number of triangles improves the approximation at the cost of the larger files size. Large and complicated files require more time to preprocess and build, so the designer must balance accuracy with manageability to produce a useful STL file. Since the STL format is universal, this process is identical for all of the AM techniques.

- Slice the STL file into thin cross-sectional layers

In the third step, a preprocessing program prepares the STL file to be built. Several programs are available, and most of them allow the user to adjust the size, location, and orientation of the model. Build orientation is important for several reasons. First, properties of prototypes vary from one coordinate direction to another. For

[1] Due to the abundant nomenclature of different AM processes, the basic phrases (i.e., LS, LM, and LMD) are used in Chaps. 1 and 2 to denominate the three most prevailing variants of AM technology for the fabrication of metallic components.

Table 1.1 Different categories and phrases of AM processes

General phrase	Two widely recognized synonymous phrases	Three typical processes	Synonyms from different institutions/companies	Reference
Additive manufacturing (AM)	Rapid prototyping (RP) & Rapid manufacturing (RM)	Laser sintering (LS)	Selective laser sintering (SLS); the University of Texas at Austin, USA	[25]
			Direct metal laser sintering (DMLS); EOS GmbH, Germany; for EOSINT M 250 machine equipped with CO_2 laser	[16]
		Laser melting (LM)	The same DMLS phrase but different processing mechanism; EOS GmbH, Germany; for EOSINT M 270/280 machine equipped with fiber laser	[16]
			Selective laser melting (SLM); widely used in Europe	[33]
			Direct metal laser re-melting (DMLR); the University of Liverpool, UK; presently merged into SLM	[34]
			Lasercusing; Sauer product GmbH, Germany	[35]
		Laser metal deposition (LMD)	Laser material deposition; Fraunhofer Institute for Laser Technology, Germany	[18,36]
			Direct metal deposition (DMD); the University of Michigan, USA	[26,27]
			Laser Engineered Net Shaping (LENS®); widely used in USA; LENS is a trademark of Sandia National Laboratory and the United States Department of Energy, USA	[37,38]
			Directed light fabrication (DLF); Los Alamos National Laboratory, USA	[39]
			Direct laser deposition (DLD); the University of Manchester, UK	[40,41]
			Direct laser fabrication; the University of Birmingham, UK	[42,43]
			Laser rapid forming (LRF); Northwestern Polytechnical University, PR China	[44,45]
			Laser melting deposition; Beihang University, PR China	[46,47]

instance, AM-processed prototypes are usually weaker and less accurate in the *Z* (vertical) direction than in the *X*–*Y* plane. Second, part orientation partially determines the amount of time required to build the model. Placing the shortest dimension in the *Z* direction reduces the number of layers, hopefully shortening the whole building time. The preprocessing software slices the STL model into a number of layers with the thickness from several micrometers to several hundred micrometers, depending on the build technique. Typically, the LS/LM process using a powder bed method requires a thinner layer thickness than the LMD process using a melt injection method. The program may also generate an auxiliary structure to support the model during the model building. Supports are useful for delicate features such as overhangs, internal cavities, and thin-walled sections. Each AM machine manufacturer supplies the proprietary or recommended preprocessing software.

- Construct the part in a layer-by-layer manner

The fourth step is the actual construction of the part using a fixed AM process. The AM machine builds one layer at a time, typically from polymer, metal, alloy, ceramic, or composite powders. The three-dimensional object is then created by layer-by-layer consolidation of the deposited material layers. Each shaped layer represents a cross-section of the sliced CAD model. Most AM machines are fairly autonomous and need little human intervention.

- Postprocessing of the part

The final step is the postprocessing, which typically involves removing the prototype from the machine and detaching any supports. Prototypes may also require minor cleaning and surface treatment. Sanding, sealing, and/or painting the part are expected to improve its appearance and durability. For the metallic parts for the practical engineering applications, postprocessing treatment such as furnace post-sintering, hot isostatic pressing (HIP), or secondary infiltration with a low-melting-point material is sometimes necessary to obtain the desired densification level and mechanical properties.

1.3 Advantages and Application Areas of AM Technology

AM technology, also widely known as RP or RM, has more than 20-year history of development and, in one sense, has started to enter mature growth stage. At present, AM has become competitive with traditional manufacturing techniques in terms of cost, speed, reliability, and accuracy. AM technology, which involves a comprehensive integration of laser technology, materials science, and mechanical engineering, is regarded as an important revolution in manufacturing industry [48]. AM is, therefore, believed by many experts that it is a “next generation” technology. The word “rapid” in RP/RM phrases is relative; it can typically produce components in a few hours, although it varies significantly depending on the type of machine being used and the size, number, and complexity of parts being produced simultaneously.

The concept "rapid" is largely reflected by its processing philosophy, i.e., the direct shaping from loose powder to bulk-form parts, without having to invest the time or resource to develop tooling for support.

Since the establishment of AM technology in the 1980s, the advantage of producing small quantities of complex-shaped parts speedily is well understood among manufacturing industry. The significant advantages and benefits of AM technology are highlighted as follows [49]:

- Production speed

Without the need for molds and dies, the AM technology allows the manufacturer to produce prototypes and parts with any complex configurations on demand.

- Design freedom

The AM technology brings the design and innovation to the forefront. AM enables the engineers to try multiple iterations simultaneously with minimal additional costs. Having the creative freedom in the production process, without time or cost penalties, is the ultimate advantage of AM over traditional manufacturing.

- Cost saving

With the aid of AM technology, companies are able to eliminate constraints and barriers so that design files can be processed digitally in one central location, and then 3D faxed to any AM operation stations on the network around the world, thereby creating global digital factories. One of the best aspects of the process is that it eliminates time and costs associated with shipping parts globally. Parts can be created at a digital factory near the manufacturing facility when and where they are needed. Additionally, AM technology allows for real-time visibility to production and receipt of parts, which further increases time and cost savings for part and original equipment manufacturer.

- Green manufacturing

Laser-based AM processes for metallic components, which use the clean, nonpollution laser as the energy resource, are environmentally friendly. Also, the versatile AM, as an enabling process that allows the right material to be deposited to the right place, is free from any waste material. When considering the mining process of steels or the retooling/remelting process required in traditional manufacturing, which generally have a large amount of energy wasted and the significantly negative impact on environment, it is easy to conclude that the AM green manufacturing has a strong relationship with the sustainable development and green growth.

Applications of AM technology have been realized in a variety of industries including aerospace, military, automotive, dental, medical, etc. The specific applications of AM technology include, but are not limited to, the following issues. The fastest-growing application for AM parts is in direct part production, rather than the simple prototyping. The production of parts using AM is expected to far surpass the current scale of prototyping using AM, which in turn has a significant impact on many industries and products. The ratio of prototypes to production parts

is typically 1:1000 or greater. In other words, for every 1000 end-use products manufactured, only one prototype is produced, although this ratio varies widely depending on the product and the industry [36]. Therefore, the opportunity for much more commercial production activity from AM tends to broaden considerably. First, the primary application of AM part production is to fabricate intricate aero- or land-based engine components in complex geometries out of hard-to-machine materials [50, 51]. AM produces shapes close enough to the final product to eliminate the need for rough machining. Second, the tooling industry applies AM to produce functional tool components, in particular the small batch or one-off parts. One of the most promising applications is to manufacture plastic injection tools and die cast tooling [24, 27]. Rapid tooling (RT) is, therefore, considered as an important subcategory of AM [52]. Thirdly, AM has found its place in medical devices manufacturing, including the specialty surgical instruments and prosthetic implants. Medical implants have to be extremely flexible to fit in a specific patient. Also, the weight of these implants is required to be as light as possible while still ensuring proper structural and mechanical characteristics. This is the reason that porous metallic parts with particular configurations are normally desired. AM technology has demonstrated to be a favorable solution [53]. Applications for the parts produced by AM technology continue to grow. An industry that was once known for rapid prototyping has extended its reach to a much broader, more diversified range of possibilities [36].

1.4 About This Book

As stated above, laser-based AM is based on an unconventional material incremental manufacturing philosophy. Combined with the highly nonequilibrium metallurgical nature of laser process, AM technology provides a beneficial method to simultaneously develop new materials, complex configurations, and unique microstructures and properties. LS/LM/LMD, being capable of processing a wide range of metals, alloys, ceramics, and MMCs, are presently regarded as the most versatile AM processes. Nevertheless, laser-based AM techniques generally involve a complex nonequilibrium physical and chemical metallurgical process, which exhibits multiple modes of heat and mass transfer [54–56], and in some instances, chemical reactions [57, 58]. The microstructural features (constitutional phase, grain size, texture, etc) and resultant mechanical properties (strength, hardness, residual stress, etc) are normally difficult to be tailored for a specific material processed with AM technology. A large amount of existent literature reveals that the complex metallurgical phenomena during AM processing is strongly material- and process-dependent and governed by both powder characteristics (e.g., chemical constituents, particle shape, particle size and its distribution, loose packing density, and powder flowability) and processing parameters (e.g., laser type, spot size, laser power, scan speed, scan line hatch spacing, and powder layer thickness) [41–44]. In this respect, significant emphasis should be laid on both design strategy of powder materials

and control methods of laser process, in order to achieve the feasible metallurgical mechanism for powder consolidation in LS/LM/LMD processes and resultant favorable microstructural and mechanical properties. Therefore, a comprehensive study of the materials design, process control, property characterization, and metallurgical theories for LS/LM/LMD of a wide variety of metallic powders is particularly necessary.

This book chooses a unique angle to view the research and development progress of laser-based AM technology. An interesting and important issue in AM research fields, i.e., the development of high-performance new materials components by laser AM process, is emphasized in this book. The capabilities and characteristics of the development of new metallic materials components by laser-based AM process are addressed, including nanostructured material, *in situ* composite material, particle reinforced metal matrix composites, etc. The topics and results presented in this book, similar as the laser-based AM technology itself, show a significant interdisciplinary feature, integrating laser technology, materials science, metallurgical engineering, and mechanical engineering. The book covers comprehensively the specific aspects of laser AM of new materials components, in terms of materials design and preparation, process control and optimization, characterization and evaluation of mechanical properties, and theories of physical and chemical metallurgy. As a key idea highlighted in this book, the integration of "Designed Material," "Tailored Process," and "Controllable Property" presents one of the most important strategies for future research and development in laser-based AM of high-performance metallic components. The contents and layout of the book are arranged as follows.

Chapter 1 starts with the introductions of the development history of AM technology and the nomenclature principles for naming different types of AM processes. The general processing philosophy of AM is addressed and the typical applications of AM technology are presented.

In Chap. 2, the current status of research and development in laser-based AM of end-use metallic components, including metals, alloys, and MMCs are reviewed, with particular emphasis on strategies of powder materials design and laser process control. The classification of currently prevailing AM processes for metallic components and the operative consolidation mechanisms are given. The ever-reported metallic materials used for AM, both commercially available and experimentally developed powders are classified, and the associated bonding and densification mechanisms during laser AM are proposed. An in-depth review of the materials aspects of laser-based AM processes, including physical aspects of materials for AM, microstructural/mechanical properties of AM-processed parts, and structure/property stability of AM-fabricated parts, is presented. The dependence of these microstructural/mechanical properties on material/process parameters is elucidated. This chapter, therefore, seeks to establish the relationship between material, process, and metallurgical mechanism of various laser-based AM processes.

In Chaps. 3–7, selective laser melting (SLM), as a newly developed powder bed-based AM process, is applied to produce the novel Ti-based nanocomposite parts, the *in situ* Ti_5Si_3 intermetallic based composite parts, the *in situ* WC cemented

carbide based hardmetals parts, the nanoparticle reinforced AlSi10Mg nanocomposites, and the Al-based composites with multiple reinforcements, respectively. The controlled crystallization and development mechanisms of nanostructures in SLM-processed Ti-based TiC/Ti nanocomposites and the underlying role of microstructural development in mechanical properties of SLM-processed nanocomposite parts are disclosed in Chap. 3. Chapter 4 presents the SLM fabrication of the *in situ* Ti–Si intermetallic-based TiC/Ti_5Si_3 and TiN/Ti_5Si_3 composite parts with novel reinforcement architecture and elevated mechanical performance, establishing a material–process–microstructure–property relationship that enables the successful laser AM of the designed *in situ* composites. In Chap. 5, the feasibility of SLM process in producing the high melting point *in situ* WC cemented carbide based hardmetals is approved, providing a unique method to process the WC-based hardmetals parts with novel microstructural and mechanical properties. Chapter 6 presents the SLM processing of the nanoscale TiC particle reinforced AlSi10Mg nanocomposite parts. The microstructural evolution of nanoscale reinforcement in SLM-processed parts at different SLM processing parameters is studied and the attendant densification level and mechanical properties are assessed, in order to enable the successful production of Al-based composites with nanoscale reinforcement architecture and elevated mechanical performance. In Chap. 7, SLM additive manufacturing of the SiC/AlSi10Mg composite powder having an *in situ* reaction nature was performed to prepare the Al-based composites with the multiple reinforcing phases. The influence of the SLM processing parameters on the constitutional phases, microstructural features, and mechanical performance (e.g., densification, microhardness, and wear property) of the SLM-processed Al-based composites was disclosed, exhibiting the promising potential of SLM process in producing novel Al-based composites with unique reinforcing phases/structures and performance.

In Chaps. 8 and 9, direct metal laser sintering (DMLS), as another kind of prevailing laser-based AM process using a powder bed method, is used to process the WC and W particle reinforced Cu matrix composite parts. In Chap. 8, the design method of the graded interface between the reinforcing particles and the metal matrix and the formation mechanism of the graded interfacial structure during DMLS process are proposed. The control and optimization mechanisms of processing conditions and materials combinations are disclosed to improve the microstructural features (especially the particle dispersion homogeneity and particle/matrix interfacial bonding ability) and resultant mechanical properties of DMLS-processed WC paticle-reinforced Cu matrix composites. In Chap. 9, DMLS process proves to be an efficient method to consolidate the nano/micron W–Cu composites, which is a unique materials system due to the mutual insolubility of W and Cu. The effects of laser processing parameters and the Cu-liquid content in the system on the densification behavior and microstructural characteristics of DMLS-processed W–Cu composites are disclosed. The formation mechanism of a novel W-rim/Cu-core structure during DMLS is proposed, revealing the unique laser induced metallurgical phenomenon of this insoluble system. Therefore, when the tailored laser-based AM process meets the new metallic materials, the simultaneous realization of complex shapes, unique microstructures, and high performance is hopefully achieved.

Chapter 10 summarizes the main findings of this book concerning laser/powder bed-based SLM and DMLS additive manufacturing of new materials components, including nanostructured material, *in situ* composite material, particle reinforced metal matrix composites, etc. Some important issues that are of particular significance for the future research and development of laser-based AM technology were also proposed.

References

1. The Economist (2012) A third industrial revolution. http://www.economist.com/node/21552901. Accessed 25 Oct 2014
2. Gibson I, Rosen DW, Stucker B (2010) Additive manufacturing technologies: rapid prototyping to direct digital manufacturing. Springer Science + Business Media, New York
3. Beaman JJ, Deckard CR (1990) Selective laser sintering with assisted powder handling. US Patent 4938816
4. Bourell DL, Marcus HL, Barlow JW, Beaman JJ, Deckard CR (1991) Multiple material systems for selective beam sintering. US Patent 5076869
5. Chua CK, Leong KF, Lim CS (2003) Rapid prototyping: principles and applications. World Scientific Publishing Company, Singapore
6. West AP, Sambu SP, Rosen DW (2001) A process planning method for improving build performance in stereolithography. Comput Aided Des 33(1):65–79
7. Park J, Tari MJ, Hahn HT (2000) Characterization of the laminated object manufacturing (LOM) process. Rapid Prototyp J 6(1):36–49
8. Gray RW, Baird DG, Bohn JH (1998) Effects of processing conditions on short TCLP fiber reinforced FDM parts. Rapid Prototyp J 4(1):14–25
9. Bourell DL, Marcus HL, Barlow JW et al (1992) Selective laser sintering of metal and ceramics. Int J Powder Metallurgy 28(4):369–381
10. Childs THC, Berzins M, Ryder GR et al (1999) Selective laser sintering of an amorphous polymer—simulations and experiments. Proc Inst Mech Eng B 213(4):333–349
11. Ciraud P (1973) Verfahren und vorrichtung zur herstellung beliebiger gegenstande aus beliebigem schmelzbarem material. German Patent DE 2263777
12. Housholder R (1981) Molding process. US Patent 4247508
13. Santos EC, Shiomi M, Osakada K et al (2006) Rapid manufacturing of metal components by laser forming. Int J Mach Tool Manuf 46(12–13):1459–1468
14. Deckard C (1989) Methods and apparatus for producing parts by selective laser sintering. US Patent 4863538
15. 3D Systems. http://www.3dsystems.com
16. EOS—e-Manufacturing Solutions. http://www.eos.info/en
17. Shellabear ON (2004) DMLS—development history and state of the art. In: Geiger M, Otto A (eds) Proceedings of the Fourth Laser Assisted Net Shape Engineering, LANE 2004, Erlangen, Germany, 2004
18. Fraunhofer ILT. http://www.ilt.fraunhofer.de/en.html
19. SLM Solutions GmbH. http://www.slm-solutions.com/en/company/
20. Realizer GmbH. http://www.realizer.com/en/
21. Arcella F (1988) Casting shapes. US Patent 4818562
22. Wohlers T, Gornet T (2011) History of additive manufacturing. Wohlers Report 2011, Wohlers Associates, Inc.
23. Optomec. http://www.optomec.com/
24. Mazumder J, Choi J, Nagarathnam K et al (1997) The direct metal deposition of H13 tool steel for 3-D components. JOM 49:55–60

25. Das S, Wohlert M, Beaman JJ et al (1998) Producing metal parts with selective laser sintering/hot isostatic pressing. JOM 50(12):17–20
26. Mazumder J, Schifferer A, Choi J (1999) Direct materials deposition: designed macro and microstructure. Mater Res Innov 3(3):118–131
27. Mazumder J, Dutta D, Kikuchi N et al (2000) Closed loop direct metal deposition: art to part. Opt Laser Eng 34(4–6):397–414
28. Levy N, Schindel R, Kruth JP (2003) Rapid manufacturing and rapid tooling with layer manufacturing (LM) technologies, state of the art and future perspectives. CIRP Ann—Manuf Technol 52(2):589–609
29. King D, Tansey T (2003) Rapid tooling: selective laser sintering injection tooling. J Mater Process Technol 132(1–3):42–48
30. Hollander DA, von Walter M, Wirtz T, et al (2006) Structural, mechanical and in vitro characterization of individually structured Ti–6Al–4V produced by direct laser forming. Biomaterials 27(7):955–963
31. España FA, Balla VK, Bose S et al (2010) Design and fabrication of CoCrMo alloy based novel structures for load bearing implants using laser engineered net shaping. Mater Sci Eng C 30(1):50–57
32. http://www.me.psu.edu/lamancusa/rapidpro/primer/chapter2.htm Accessed 20 Sep. 2012
33. Tolochko NK, Savich VV, Laoui T et al (2002) Dental root implants produced by the combined selective laser sintering/melting of titanium powders. Proc Inst Mech Eng L 216(L4):267–270
34. Morgan R, Sutcliffe CJ, O'Neill W (2004) Density analysis of direct metal laser re-melted 316 L stainless steel cubic primitives. J Mater Sci 39(4):1195–1205
35. Sauer product—Prototyping, Lasercusing. http://www.sauerproduct.com/en/index.htm
36. Kelbassa I, Wohlers T, Caffrey T (2012) Quo vadis, laser additive manufacturing? J Laser Appl 24(5):050101
37. Atwood C, Griffith M, Harwell L et al (1998) Laser engineered net shaping (LENS™): a tool for direct fabrication of metal parts. In: Proceedings of international congress on the applications of lasers and electro-optics, Orlando, FL, USA, November, 1998
38. Brooks J, Robino C, Headley T et al (1999) Microstructure and property optimization of LENS deposited H13 tool steel. In: 10th solid freeform fabrication symposium (SFF), The University of Texas at Austin, August 1999
39. Lewis GK, Schlienger E (2000) Practical considerations and capabilities for laser assisted direct metal deposition. Mater Des 21(4):417–423
40. Pinkerton AJ, Li L (2004) The behaviour of water- and gas-atomised tool steel powders in coaxial laser freeform fabrication. Thin Solid Films 453–454:600–605
41. Pinkerton AJ, Li L (2005) Multiple-layer laser deposition of steel components using gas- and water-atomised powders: the differences and the mechanisms leading to them. Appl Surf Sci 247(1–4):175–181
42. Wang F, Mei J, Wu XH (2008) Direct laser fabrication of Ti6Al4V/TiB. J Mater Process Technol 195(1–3):321–326
43 Wu X (2007) A review of laser fabrication of metallic engineering components and of materials. Mater Sci Technol 23(6):631–640
44. Liu FC, Lin X, Yang GL et al (2011) Microstructure and residual stress of laser rapid formed Inconel 718 nickel-base superalloy. Opt Laser Technol 43(1):208–213
45. Lin X, Yue TM, Yang HO et al (2006) Microstructure and phase evolution in laser rapid forming of a functionally graded Ti–Rene88DT alloy. Acta Mater 54(7):1901–1915
46. Li J, Wang HM (2010) Microstructure and mechanical properties of rapid directionally solidified Ni-base superalloy Rene'41 by laser melting deposition manufacturing. Mater Sci Eng A 527(18–19):4823–4829
47. Tian XJ, Zhang SQ, Li A et al (2010) Effect of annealing temperature on the notch impact toughness of a laser melting deposited titanium alloy Ti–4Al–1.5Mn. Mater Sci Eng A 527(7–8):1821–1827

48. Lü L, Fuh JYH, Wong YS (2001) Laser-induced materials and processes for rapid prototyping. Kluwer Academic Publishers, Norwell
49. Hanson J (2013) Top Five Benefits of Additive Manufacturing (You Never Considered). http://www.pddnet.com/articles/2013/02/top-five-benefits-additive-manufacturing-you-never-considered Accessed 20 Aug 2013
50. Dutta B, Singh V, Natu H et al (2009) Direct metal deposition. Adv Mater Process 167(3):29–31
51. Mudge RP, Wald NR (2007) Laser engineered net shaping advances additive manufacturing and repair. Weld J 86(1):44–48
52. Kruth JP, Levy G, Klocke F et al (2007) Consolidation phenomena in laser and powder-bed based layered manufacturing. CIRP Ann Manuf Technol 56(2):730–759
53. Palčič I, Balažic M, Milfelner M et al (2009) Potential of laser engineered net shaping (LENS) technology. Mater Manuf Process 24(7–8):750–753
54. Xiong YH, Hofmeister WH, Cheng Z, et al (2009) In situ thermal imaging and three-dimensional finite element modeling of tungsten carbide–cobalt during laser deposition. Acta Mater 57(18):5419–5429
55. Wang L, Felicelli S (2007) Process modeling in laser deposition of multilayer SS410 steel. Trans ASME J Manuf Sci Eng 129(6):1028–1034
56. Chen TB, Zhang YW (2006) Analysis of melting in a subcooled two-component metal powder layer with constant heat flux. Appl Therm Eng 26(7):751–765
57. Simchi A, Pohl H (2004) Direct laser sintering of iron–graphite powder mixture. Mater Sci Eng A 383(2):191–200
58. Murali K, Chatterjee AN, Saha P et al (2003) Direct selective laser sintering of iron–graphite powder mixture. J Mater Process Technol 136(1–3):179–185

Chapter 2
Laser Additive Manufacturing (AM): Classification, Processing Philosophy, and Metallurgical Mechanisms

Abstract Laser sintering (LS), laser melting (LM), and laser metal deposition (LMD) are presently regarded as the three most versatile laser-based additive manufacturing (AM) processes. Laser-based AM processes generally have a complex nonequilibrium physical and chemical metallurgical nature, which is material- and process-dependant. The influence of material characteristics and processing conditions on the metallurgical mechanisms and resultant microstructural and mechanical properties of AM-processed components needs to be clarified. This chapter starts with the definition of LS/LM/LMD processes and operative consolidation mechanisms for metallic components. Powder materials used for AM, in the categories of pure metal powder, prealloyed powder, multi-component metals, alloys, metal matrix composites (MMCs) powder, and associated densification mechanisms during AM are addressed. An in-depth review of material and process aspects of AM, including the physical aspects of materials for AM and the microstructural and mechanical properties of AM-processed components, is presented. The purpose of this chapter is to establish a general relationship among material, process, and metallurgical mechanism for laser-based AM of metallic components.

2.1 Classification of Laser AM Processes and Metallurgical Mechanisms

Although laser additive manufacturing (AM) processes share the same material additive manufacturing philosophy, each AM process has its specific characteristics in terms of useable materials, processing procedures, and applicable situations. The capability of obtaining high-performance metallic components with controllable microstructural and mechanical properties also shows a distinct difference for the various AM processes.

As revealed in Fig. 2.1, according to the different mechanisms of laser-powder interaction (i.e., pre-spreading of powder in powder bed before laser scanning vs. coaxial feeding of powder by the nozzle with synchronous laser scanning) and the various metallurgical mechanisms (i.e., partial melting vs. complete melting), the prevailing AM technology for the fabrication of metallic components typically has

© Springer-Verlag Berlin Heidelberg 2015

D. Gu, *Laser Additive Manufacturing of High-Performance Materials,*
DOI 10.1007/978-3-662-46089-4_2

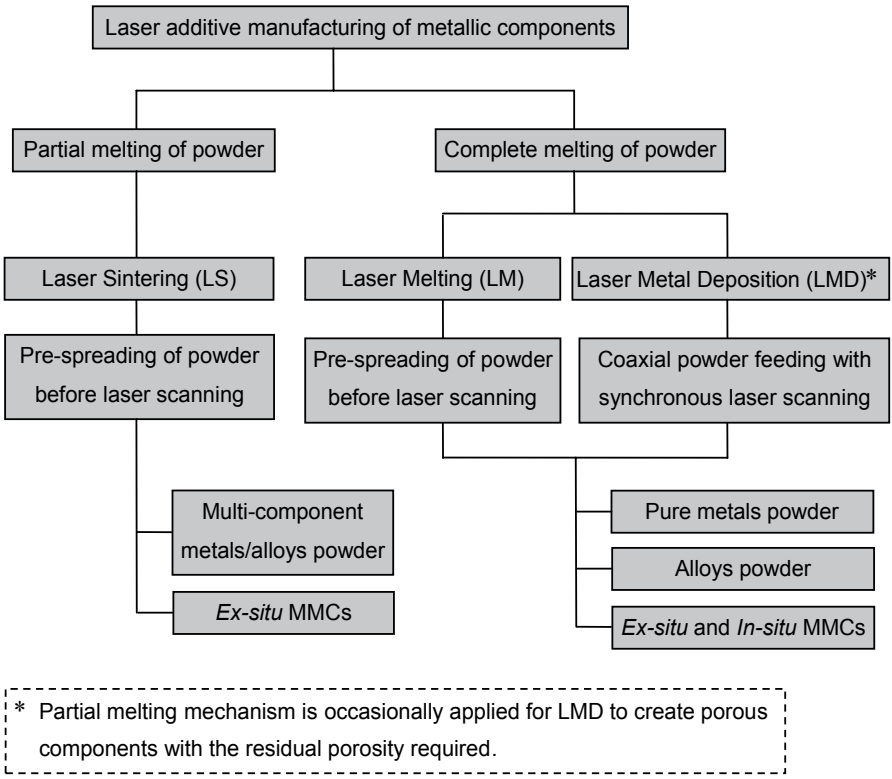

Laser additive manufacturing of metallic components
Partial melting of powder
Complete melting of powder
Laser Sintering (LS)
Laser Melting (LM)
Laser Metal Deposition (LMD)*
Pre-spreading of powder before laser scanning
Pre-spreading of powder before laser scanning
Coaxial powder feeding with synchronous laser scanning
Multi-component metals/alloys powder
Ex-situ MMCs
Pure metals powder
Alloys powder
Ex-situ and In-situ MMCs
* Partial melting mechanism is occasionally applied for LMD to create porous components with the residual porosity required.

Fig. 2.1 Classification of laser AM processes based on different mechanisms of laser-material interaction

three basic processes: laser sintering (LS), laser melting (LM), and laser metal deposition (LMD). Their deposition mode, deposition rate, processing conditions, and attendant microstructural/mechanical properties are summarized in Table 2.1 and will be addressed in detail as follows.

2.1.1 Laser Sintering (LS)

Laser sintering (LS) is a typical AM process based on the layer-by-layer powder spreading and subsequent laser sintering. As schematically shown in Fig. 2.2, the LS system normally consists of a laser, an automatic powder layering apparatus, a computer system for process control, and some accessorial mechanisms (e.g., inert gas protection system and powder bed preheating system). Different types of lasers are used, including CO_2 [1], Nd:YAG [6], fiber lasers [7], disc lasers [8], etc. The

Table 2.1 Comparisons of some representative laser-based AM processes

Process	Deposition mode	Layer thickness (μm)	Deposition rate	Dimensional accuracy (mm)	Surface roughness (μm)	Ref.
Direct metal laser sintering (DMLS)	Laser sintering	20–100	Depend on laser spot size, scan speed, and size, number, and complexity of parts	High, ±0.05	14–16	[1]
Selective laser melting (SLM)	Laser melting	20–100	ibid	High, ±0.04	9–10	[2]
Direct metal deposition (DMD)	Laser cladding	254	0.1–4.1 cm^3/min	N/A	~40	[3]
Laser engineered net shaping (LENS)	ibid	130–380	N/A	X–Y plane ±0.05; Z axis ±0.38	61–91	[4]
Directed light fabrication (DLF)	ibid	200	10 g/min (1 cm^3/min)	±0.13	~20	[5]

choice of laser has a significant influence on the consolidation of powders, mainly because:

- The laser absorptivity of materials greatly depends on the laser wavelength
- The operative metallurgical mechanism for powder densification is determined by the input laser energy density

The general processing procedures of LS are as follows:

- A substrate for part fabrication is fixed on the building platform and leveled
- The protective inert gas is fed into the sealed building chamber to reduce the interior oxygen content below a required standard
- A thin layer of the loose powder with a thickness normally below 100 μm is deposited on the substrate by the layering mechanism
- The laser beam scans the powder bed surface to form layer-wise profiles according to CAD data of the components to be built
- The above procedures including powder spreading and laser treatment are repeated and the parts are built in a layer-by-layer manner until completion

During LS, the duration of the laser beam on any powder particle depends on beam size and scan speed, and is typically between 0.5 and 25 ms [9]. Under this extremely short thermal cycle, the processing mechanism must be rapid and thus a solid-state sintering mechanism is not feasible. Melting/solidification approach is the only mechanism suitable for the rapid consolidation of powder during LS [10]. LS, as is implied in its name, is processed based on a liquid phase sintering (LPS)

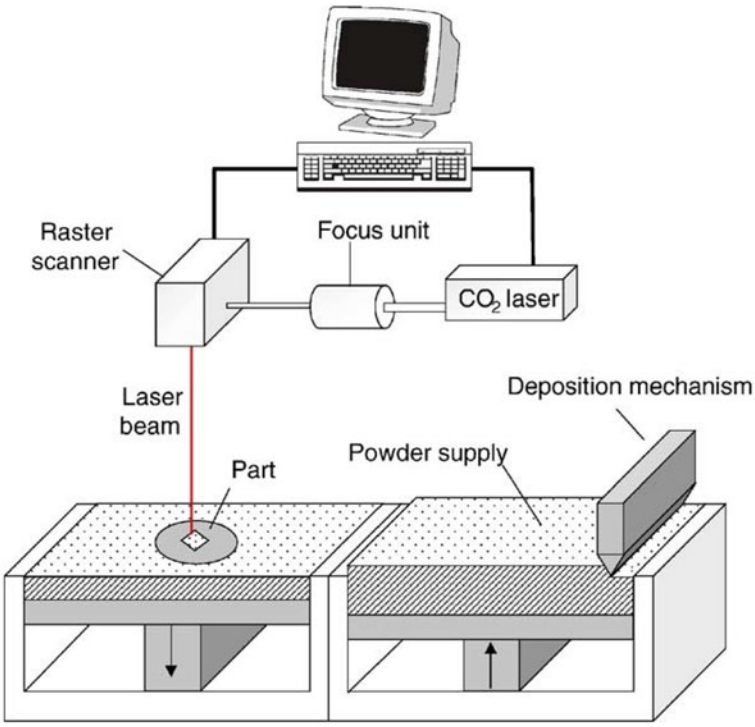


Fig. 2.2 Schematic of LS apparatus, see Ref. [13]

mechanism involving a partial melting of the powder (i.e., semi-solid consolidation mechanism). So far, LS has demonstrated the feasibility in processing multi-component metal powder and prealloyed powder [11, 12]. Powder characteristics and laser processing conditions should be carefully determined in order to realize the favorable metallurgical mechanism for powder consolidation.

The multi-component powder mixture is generally composed of a high-melting-point metallic component acting as the structural metal, a low-melting-point metallic component, taken as the binder, and a small amount of additives such as a fluxing agent or deoxidizer [14]. The operative LS temperature is carefully determined between these two different melting temperatures by adjusting laser processing parameters. The binder, thus, melts completely, while the structural metal retains its solid cores in the liquid. Densification of the solid/liquid system occurs as a result of the rearrangement of solid particles under the influence of capillary forces exerted on them by the wetting liquid. The liquid/solid wetting characteristics and the capillary force exerted on particles determine the particle rearrangement rate and resultant success of LS. LS of a multi-component Cu-based powder consisting of pure Cu powder and prealloyed SCuP powder has been performed by Zhu et al. [1, 15]. The SCuP with a lower melting point (645 °C) acts as the binder, while the Cu

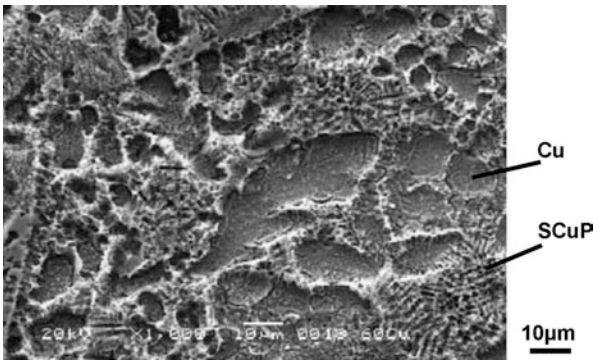


Fig. 2.3 Microstructure of LS-processed Cu–SCuP multi-component Cu-based powder, see Ref. [1]

with a higher melting point (1083 °C) acts as the structural metal (Fig. 2.3), revealing a semi-solid LPS mechanism involved in the LS process.

In contrast to pure metals with a congruent melting point, prealloyed powder exhibits a mushy zone between solidus and liquidus temperatures, within which liquid and solid phases coexist during the melting/solidification process (Fig. 2.4a). As laser processing parameters are optimized, the preferable LS temperature is in the mushy zone to produce a semi-solid system. This process, termed supersolidus liquid phase sintering (SLPS), acts as the feasible metallurgical mechanism for LS of prealloyed powders. As illustrated in Fig. 2.4b, prealloyed particles melt incongruently and become mushy once a sufficient amount of liquid is formed along grain boundaries. The liquid flows and wets solid particles and grain boundaries, leading to a rapid densification of semi-solid system by means of rearrangement of solid particles and a solution-reprecipitation process. Niu et al. [16] have demonstrated that the SLPS mechanism is operative during LS of high speed steel powder. The thick ring microstructure reprecipitated around the austenitic grain boundaries indicates the formation of liquid phase along grain boundaries within particles during SLPS (Fig. 2.4c).

It should be noted that LS of prealloyed powders through the SLPS mechanism requires a strict control of laser processing parameters to realize the incongruent melting of particles within the mushy zone. However, due to the localized, rapid nature of the thermal cycle during LS, there exists a significant difficulty in controlling the sintering temperature between solidus and liquidus, which in turn handicaps the successful operation of the SLPS mechanism. Processing problems (e.g., insufficient densification, heterogenous microstructures and properties, etc.) tend to occur in LS-processed prealloyed powders. Therefore, postprocessing treatment such as the furnace post-sintering [17], hot isostatic pressing (HIP) [18], or secondary infiltration with a low-melting-point material [19] is normally necessary to obtain sufficient mechanical properties.

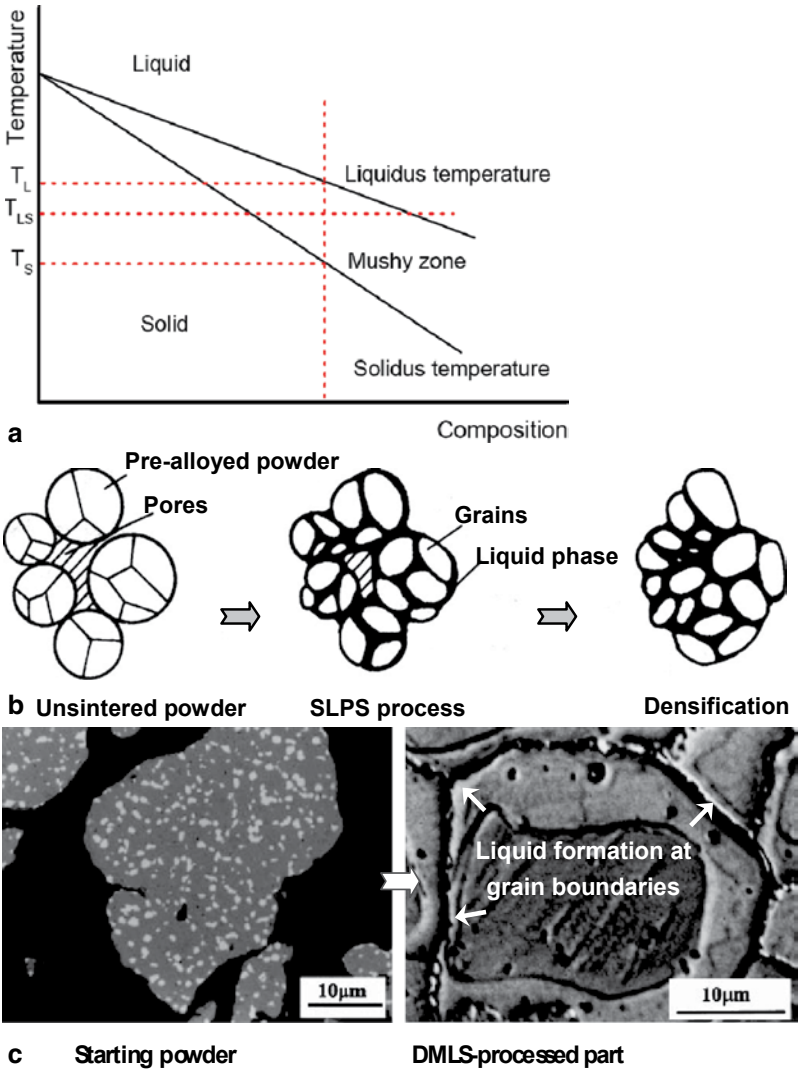


Fig. 2.4 **a** An idealized temperature-composition equilibrium phase diagram for a prealloyed binary metal system, **b** Schematic of SLPS densification of prealloyed particles, see Ref. [21], **c** Microstructural development during LS of high speed steel powder, see Ref. [16]

2.1.2 Laser Melting (LM)

Driven by the demand to produce fully dense components with mechanical properties comparable to those of bulk materials, and by the desire to avoid time-consuming postprocessing cycles, laser melting (LM) has been developed. LM shares the same processing apparatus and procedures with LS. The only difference is that

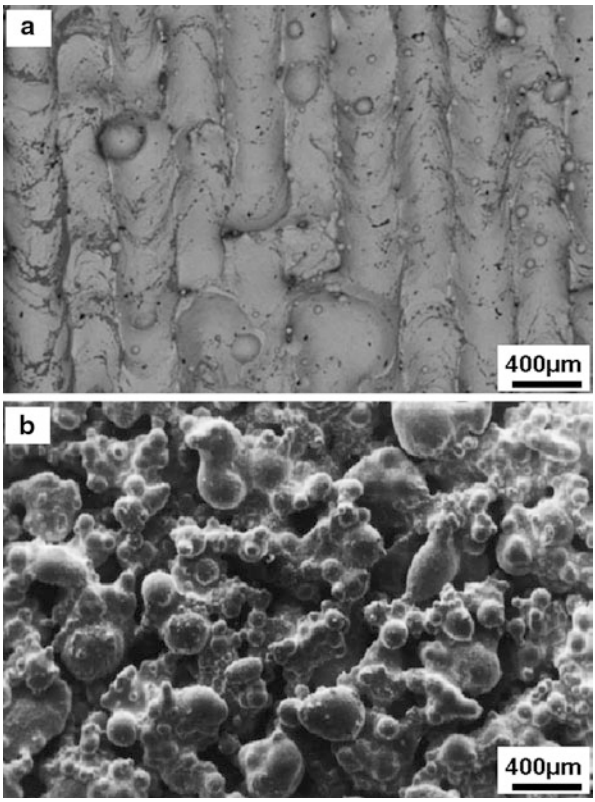


Fig. 2.5 Surface morphologies of M2 high speed steel components processed by **a** LM, see Ref. [22] and **b** LS, see Ref. [23]

LM of metallic powders is based on a complete melting/solidification mechanism. The idea of full melting is supported by the continuously improved laser processing conditions in recent years (e.g., higher laser power, smaller focused spot size, smaller layer thickness, etc.), leading to significantly improved microstructural and mechanical properties as relative to those of early time LS-processed parts [20]. LM, thus, shows better suitability to produce full dense parts approaching 99.9% density in a direct way, without post infiltration, sintering, or HIP.

Simchi [22] and Niu et al. [23] have processed M2 high speed steel using LM and LS methods, respectively. The densification rate, surface smoothness, and microstructural homogeneity of LM-processed parts under optimal processing conditions show a significant improvement upon those of LS-processed parts (Fig. 2.5).

Another major advance of LM lies in its high feasibility in processing nonferrous pure metals, e.g., Ti [24], Al [25], Cu [26], etc., which to date cannot be well processed using the LS partial melting mechanism. Early attempts to process pure metals using LS have proven to be unsuccessful, due to the considerably high viscosity and resultant balling phenomenon caused by the limited liquid formation

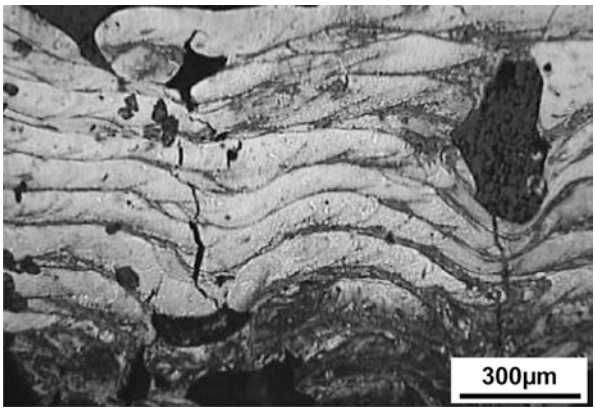


Fig. 2.6 Distortion and crack formation in LM-processed Cu–H13 powder, see Ref. [30]

[27, 28]. In contrast, the density of LM-processed pure metals is highly controllable and can be improved significantly up to 99.5 % through the full melting mechanism of LM [25, 26].

Nevertheless, LM requires a higher-energy level, which is normally realized by applying good beam quality, high laser power, and thin powder layer thickness (i.e., long building time). Consequently, LM is at significant risk for the instability of the molten pool due to the full melting mechanism used. A large degree of shrinkage tends to occur during liquid/solid transformation, accumulating considerable stresses in LM-processed parts [29]. The residual stresses arising during cooling are regarded as key factors responsible for the distortion and even delamination of the final products. Pogson et al.'s work [30] on LM of Cu–75 % H13 reveals that the incorporation of Cu into tool steel during LM produces the overheating Cu-rich region around the austenite grain boundaries, which increases the risk of cracking by hot tearing (Fig. 2.6). Furthermore, the melt instabilities may result in spheroidization of the liquid melt pool (known as balling effect) and attendant interior porosity. Therefore, proper care should be taken in the reasonable selection of both laser processing and powder depositing parameters to determine a suitable process window, in order to yield a moderate temperature field to avoid the overheating of the LM system.

It is noted that the period for rapid development of LM technology began from the year 2000. In contrast, the intensive research attempts on laser metal deposition (LMD) technology started from 1993—the production of metallic parts with favorable mechanical properties by LMD has been reported in the nineties. For instance, Mazumder et al. have reported DMD fabrication of fully dense aluminum 1100 parts as early as 1993, demonstrating to provide metal properties equivalent to a wrought process [3, 31]. Conversely, LM production of complex shaped aluminum components meeting industrial standards has been successfully performed at the Fraunhofer ILT in 2008 [25].

2.1.3 Laser Metal Deposition (LMD)

2.1.3.1 Process Overview

Although the processing strategy of LMD follows the general additive manufacturing principle, the manner of powder supply changes from prespreading in the LS/LM process to coaxial feeding in the LMD process (Fig. 2.1). The LMD powder delivery system consists of a specially designed powder feeder that delivers powder into a gas delivery system via the nozzles. The high-energy laser beam is delivered along the *z*-axis in the center of the nozzle array and focused by a lens in close proximity to the work piece. Moving the lens and powder nozzles in the *z*-direction controls the height of the focuses of both laser and powder. The work piece is moved in the *x*–*y* direction by a computer-controlled drive system under the beam/powder interaction zone to form the desired cross-sectional geometry. Consecutive layers are additively deposited, producing a three-dimensional component. With the integration of a multi-axis deposition system, multiple material delivery capability, and, in some instances, the patented closed loop control system [32, 33], LMD can coat, build, and rebuild components having complex geometries, sound material integrity and dimensional accuracy. LMD, accordingly, has a highly versatile process capability and can be applied to manufacture new components, to repair and rebuild worn or damaged components, and to prepare wear- and corrosion-resistant coatings [34].

The DMD, LENS®, and DLF (Table 2.1) are regarded as three representative processes of LMD technology. It is worth noting that the DMD technology developed by Mazumder's group at the University of Michigan is equipped with a feedback system that provides a closed loop control of dimensional accuracy during the deposition process. The feedback loop is, thus, regarded as a unique feature of DMD that differentiates from LENS® and DLF processes [35].

2.1.3.2 Constitutes of DMD System

A typical DMD system is schematically depicted in Fig. 2.7 and some of the main features are as follows [35]:

- Patented closed loop feedback control for DMD process

This unique system serves as the key tool for producing a near net-shape product. High speed sensors collect melt pool information, which is directly fed into a dedicated controller that adjusts the input processing parameters to maintain dimensional accuracy and material integrity.

- Coaxial nozzle with local shielding of melt pool

The coaxial nozzle design is based on a patent [36], and offers equal deposition rates in any direction. Inert gas blown through the nozzle helps both in powder

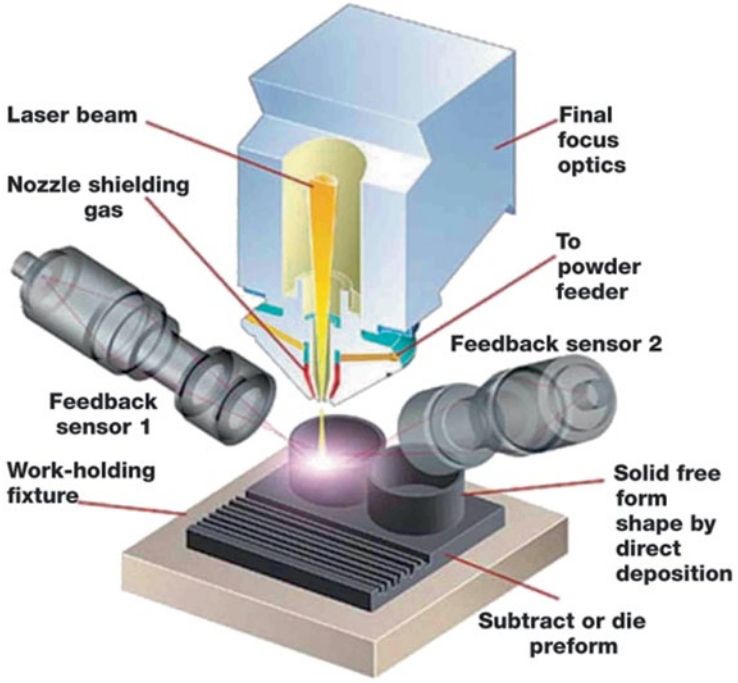


Fig. 2.7 Schematic of closed loop DMD system, see Ref. [35]

delivery and shielding the deposit from oxidation. Shielding strategy is a delicate balance between the adequate pressure to drive away the ambient air and the powder delivery without causing excessive disturbance within the molten pool.

- Six-axis computer-aided manufacturing (CAM) software for AM

Six-axis DMD CAM software for AM, which includes an integrated DMD database with process recipes as a part of the software, builds a CAM tool path directly from CAD data. Contour, surface, and volume deposition paths are provided in three dimensions, and accordingly, multi-layer deposition paths can be prepared in a single operation. Simulation and collision-detection modules are included and, thus, enable the user to detect any possible collision of the processing head and the part while creating the deposition tool path.

- DMD vision system

The DMD vision system has been developed for deposition on small objects with fine features. The system locates the coordinate position of a part in the machine and allows easy tool path generation for accurate deposition. This eliminates manual part pick-up, which is practically impossible for very small components with fine structures. Faster operation and better repeatability improve productivity considerably.

2.1.3.3 Unique Applications of LMD/DMD Technology

Similar to powder bed based LS/LM processes, LMD/DMD technology has been applied successfully in direct building near net-shape three-dimensional components, covering a broad range of industries. Besides the near net-shape part manufacturing capability, LMD/DMD, as an enabling technology that allows the right material to be added to the accurate place [35], has some unique capabilities/features that are absent in the LS/LM processes.

- Repairing and remanufacturing

Repairing of worn components is typically cost-saving as compared to purchasing new parts. Also, when a worn part is rebuilt, that component can be repaired so that it will have a longer wear life than a new part. The use of LMD/DMD technology opens new technical opportunities for repairing components previously considered nonrepairable by conventional methods [37]. The application areas best suited for LMD/DMD are turbine blades/vanes repairs [34]. The concentrated heat from the laser, typically for Nd:YAG and fiber laser beams, allows blade tip buildup with minimum distortion. The vision system and closed loop feedback system offer precision part pickup and restoration, leading to a quality product that requires minimal post grinding. Another feasible application of LMD/DMD is the repair of drive shafts [37]. Bearing, seal, and coupler surfaces on shafts, which are typically considered nonrepairable by conventional welding techniques, are perfect candidates for buildup and repair utilizing LMD/DMD. Furthermore, the LMD/DMD deposits are metallurgically bonded to the substrate, not mechanically bonded like spray or chroming processes [37].

- Cladding and hardfacing

Cladding and hardfacing are actually a form of repair buildup applied to deposit new layer(s) of material on a substrate. Multiple layers can be deposited to form shapes with complex geometry. These two variants of LMD/DMD have been used for material surface property modification and for the repair and manufacturing of multi-layer coatings [38]. Cladding and hardfacing using CO_2 lasers have proved to be highly successful. Combining the flexible LMD/DMD system with the new fiber lasers improves on this success. POM Group Inc. has developed large DMD workstations (DMD 105D) for hardfacing and repair/cladding of large dies, molds, and components [39]. The fiber laser with a shorter wavelength can achieve equivalent deposition rates with approximately 50 % of the wattage required by a CO_2 laser [37]. A favorable result is similar production rates with less stress conveyed into the part being cladded. The surface finish of the cladding may be left as-deposited or ground to finish dimension.

- Designed material

One of the unique characteristics of closed loop DMD technology is that multiple materials can be deposited in different parts of a single component with high precision. This capability can be utilized to develop a new class of optimally designed

materials, i.e., a class of artificial materials with properties and functions that do not exist in natural environments. In other words, a material system can be designed and fabricated for a chosen performance.

Mazumder's group has developed a new methodology for design, representation, and fabrication of the performance-based "Designed Material" using multiple material deposition by DMD. The methodology involves the computer integration of three key technologies, i.e., homogenization design method (HDM), heterogeneous solid modeling (HSM), and DMD [40]. The HDM is applied to determine the optimal shape and topology of a macroscale structural component and, subsequently, the HDM output is converted to a CAD model using geometric modeling techniques. This enhanced HDM can be used for material design to control Young's moduli, shear moduli, Poisson's ratios, and even thermal expansion coefficients [3]. An object with material attributes as heterogenous object and the corresponding solid model are referred to as HSM. Heterogenous objects are mainly classified into multi-material objects, which have distinct material domains, and Functionally Graded Materials (FGMs), which are a new class of composites that possess continuous material variation along with the geometry [41].

The development of FGMs by LMD/DMD is regarded as a basic strategy for "Designed Material" by tailoring the compositions and microstructures during deposition. Since LMD uses the coaxially supplied powder feedstock, it has the ability to produce FGMs by selectively depositing different elemental powders into the molten pool at specific locations in the structure during part buildup [42–44]. The adaptation of multiple powder feeders in the LMD/DMD system makes it possible. Dissimilar powder materials can be placed into separate powder hoppers. The computer control system, which is integrated into the powder feed system, enables the user to vary the deposit composition of a function of position. Shin et al. [41] have introduced an integrated design and fabrication system for heterogenous objects, especially FGMs. A variant design paradigm and a constructive representation scheme for FGMs are primarily described. A discretization-based process planning method, which converts continuous material variation into stepwise variation, is then proposed. The DMD process, which can take advantage of the proposed process planning method, is applied to prepare rectangular and circular graded parts of Cu–*x*Ni, in order to reveal how the material compositions change during deposition and, accordingly, to verify the proposed design–fabrication cycle of FGMs. Collins et al. [45] have deposited the compositionally graded binary Ti–*x*Mo alloys, from elemental Ti to Ti–25at-% Mo, within a 25 mm length part using LMD. The microstructures across the graded alloy correspond to those typically observed in α/β Ti alloys, but the microstructural scale is significantly refined. Interesting microstructure gradients are tailored across the alloy (Fig. 2.8). The ability to achieve such substantial changes in composition/microstructure across a rather limited length makes LMD a highly attractive candidate for developing novel structured FGM components with unique properties. It is widely accepted that the ability to produce near net-shape components with graded compositions from elemental powders using LMD may potentially be a feasible route for manufacturing unitized structures for high demanding aerospace applications.

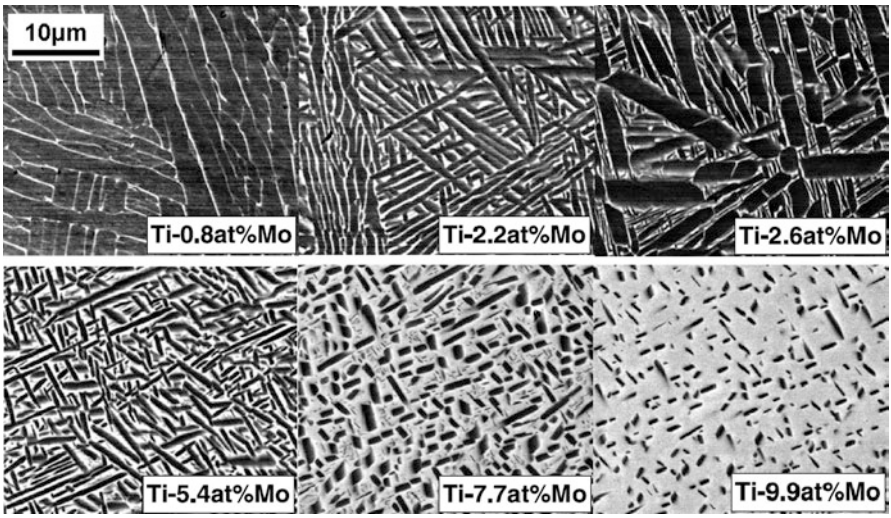


Fig. 2.8 Microstructures of LMD-processed Ti–*x*Mo graded alloy with progressively increasing Mo contents, see Ref. [45]

More importantly, the methodology for "Designed Material" has been extended from the design of compositions/microstructures of materials to the creation of microscopic structures with particular behaviors. These microscopic structures are effectively artificially designed materials and their behaviors are essentially artificial properties. Many of these properties are technologically interesting (e.g., extraordinary piezoelectricity), physically unusual (e.g., negative Poisson's Ratio), or unavailable in nature (e.g., ductile metals with negative thermal expansion) [40]. The designed materials are regarded as a revolutionary departure from the present material selection methods. One creative demonstration is first disclosed in Mazumder et al.'s research work on the homogenization DMD process using a combination of Ni and Cr. Figure 2.9 shows a structure designed by HDM and fabricated by DMD, which exhibits negative thermal expansion $dL/L \approx -0.00065$ at 150 °C and maintains such a unique property up to 300 °C [3, 40, 46].

2.1.3.4 Metallurgical Mechanisms of LMD/DMD Process

i. Molten Pool Behavior

During LMD/DMD, the laser beam creates a mobile molten pool on the substrate into which powder is injected. A continuous, stable, and precise feeding of powders into the molten pool is, thus, of primary importance. Secondly, the molten pool size has been identified as a critical parameter for maintaining optimal building conditions [47, 48]. A photograph of a single line LMD of 316 stainless steel by Hofmeister et al. [49] shows the presence of molten pool with a clear contour

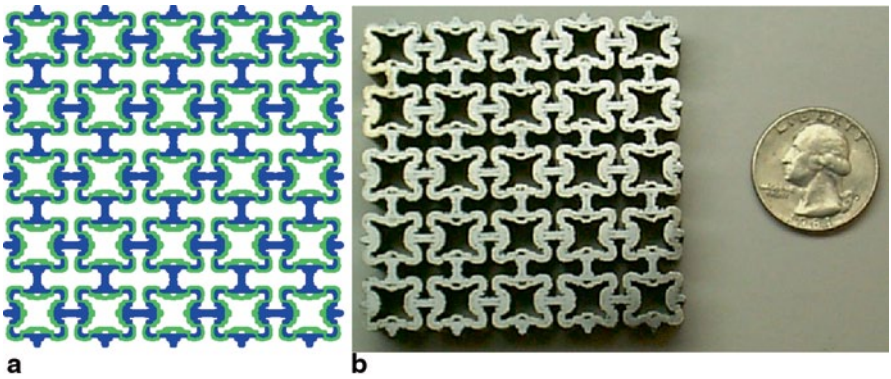


Fig. 2.9 Design (**a**) and realization (**b**) of negative coefficient of thermal expansion using DMD. (Ni—*green*, *light color*; Cr—*blue*, *dark color*), see Ref. [46]

(Fig. 2.10a). The formation of a dimensionally steady molten pool with a small heat affected zone (HAZ) and an uninterrupted solidification front is preferable. Real-time thermal imaging of molten pool size and its morphology (Fig. 2.10b) is used as a feedback mechanism to determine temperature gradient and cooling rate and to control the LMD process. The effects of laser processing parameters (e.g., laser power and scan speed) on the molten pool features have been investigated both by modeling and experiments [50–52]. For a constant scan speed, the geometry of the molten pool depends on the input heat distribution. The laser power is adjusted to make sure that the pool size is in the predefined range. Cooling of the pool is accomplished primarily by conduction of heat through the part and substrate [51]. Depending on the substrate temperature and laser energy input, cooling rates at the solid-liquid interface vary from 10^3 to 10^4 Ks^{-1} [50]. This flexibility allows the control of the final microstructures and properties of LMD-processed parts.

ii. Thermal and Kinetic History

Unlike LS/LM, LMD involves the computer-controlled three-dimensional shaping of molten materials through a deposition head, using the powder injected into a molten pool created by a focused high-power laser beam. LMD, accordingly, accommodates a wide range of materials and deposition styles. The applicable materials are primarily from the prealloyed powders of the determined compositions. In particular, high-melting-point alloys have demonstrated a unique applicability for LMD [53], due to its precision, point-by-point complete melting mechanism. Various parts have been fabricated from nickel-based alloys, titanium alloys, steels, and other specialty materials.

Nevertheless, due to the layer-by-layer additive nature of LMD, complex thermal histories are experienced repeatedly in different regions of the deposited material. The thermal histories of LMD normally involve melting and numerous reheating cycles at a relatively lower temperature [54]. Such complicated thermal behavior during LMD results in complex phase transformations and microstructural develop-

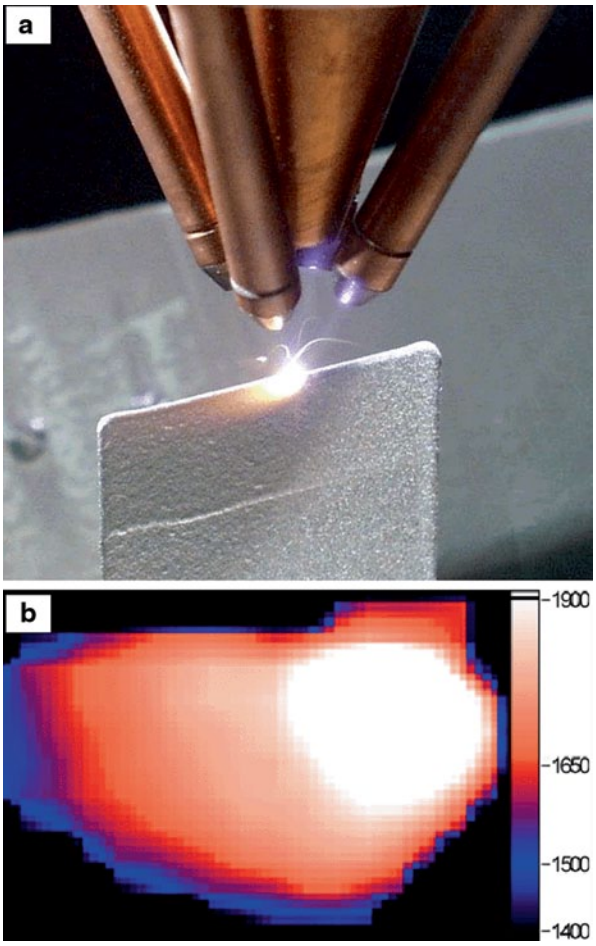


Fig. 2.10 Photograph of a single line LMD build (**a**), side view of molten pool showing temperature in Kelvin (**b**), see Ref. [49]

ments. Consequently, there are significant difficulties in tailoring the compositions/microstructures required. On the other hand, the use of a finely focused laser to form a rapidly traversing molten pool may result in considerably high solidification rate and melt instability. Complicated residual stresses tend to be locked into the parts during the building process, due to the thermal transients encountered during solidification [55, 56]. The presence of residual stresses causes deformation or, in the worst instance, crack formation in LMD-processed components. The uncontrollability of compositions/microstructures and the formation of residual stresses are regarded as two major difficulties associated with LMD.

The understanding of the origin of these defects aids in improving controllability of either the LMD process or final microstructural/mechanical properties. Actually, a series of complex physical phenomena including heat transfer, phase changes,

mass addition, and fluid flow are involved in the molten pool during LMD. Interactions between the laser beam and the coaxial powder flow are of a primary consideration, including the attenuation of beam intensity and temperature rise of powder particles before reaching the pool [57]. The temperature and velocity fields, liquid/gas interface, and energy distribution at liquid/gas interface in the pool should be monitored, in order to further control the melt pool width and length, and the resultant height and width of solidified cladding tracks [58]. Therefore, the knowledge of temperature, velocity, and composition distribution history is essential for an in-depth understanding of the process and subsequent microstructure evolution and properties.

2.2 Classes of Materials for AM and Processing Mechanisms

2.2.1 For LM and LMD—Pure Metals Powder

Pure metals that have been applied for various AM processes are listed in Table 2.2. As relative to alloys, pure metals are not the focus of AM technology, mainly due to the following two reasons. First, the relatively weak nature of pure metals, e.g., limited mechanical properties and poor antioxidization/anticorrosion capabilities, makes them less attractive as candidate materials for AM. Second, the unsuccessful early attempts to process pure metals through the partial melting mechanism by LS have lasted a long period without any significant progress before a successful application of LM [12]. For instance, the LS-processed Ti, due to the application of a partial melting mechanism, typically has a heterogenous microstructure and consists of three different regions: (1) the cores of unmelted grains, (2) the melted surface of grains, and (3) the residual pores (Fig. 2.11a) [59]. Currently, the move from LS to LM represents a major advance in AM of nonferrous pure metal components in industrial practice [60].

It is worth noting that though LMD is normally processed based on a complete melting mechanism to yield a fully dense component (Fig. 2.1), recent research efforts on LMD of pure Ti and Ta through a partial melting mechanism (Table 2.2) have demonstrated a high potential to produce complex-shaped porous implants with functionally graded porosity used for load-bearing biomedical applications [61, 62]. According to their design philosophy, complete melting of the powder is avoided by using low laser powers to partially melt the metal powder surface (Fig. 2.11b). The surface-melted powders join due to the presence of liquid metal at the particle interfaces, leaving some inter-particle residual porosity. As against solid-state sintering in the conventional powder metallurgy (PM) route of porous metals, the inherent brittleness can be eliminated. Furthermore, by changing scan speeds, the interaction time between powder particles and laser beam can be varied, creating different porous structures with various final porosities.

Table 2.2 Pure metals components produced by various AM processes

Metal	Powder characteristics	Process	Laser type	Bonding mechanism	Mechanical properties	Ref.
Ti	Spherical shape; Gaussian particle size distribution, mean size 8 μm, maximum size 30 μm	LS	Pulsed Nd:YAG laser	Partial melting in a narrow surface layer of particles	72 % theoretical density; microhardness 250–340HV; compressive yield strength 260 MPa	[59]
ibid	Spherical shape; average size 45 μm	LM	Pulsed Nd:YAG laser	Complete melting of powder	Tensile strength 300 MPa; torsional fatigue strength 100 MPa; microhardness 600–1000HV (after laser gas nitriding)	[63, 64]
ibid	Commercially pure; particle size 50–150 μm	LMD	Nd:YAG laser, 500 W	Partial melting of powder surface (avoid complete melting of powder to form desired porous structure)	Porosity 35–42vol-%; Young's modulus 2–45GPa; 0.2 % proof strength 21–463 MPa (similar to human cortical bone)	[61]
Ta	99.5 % purity; particles size 45–75 μm	ibid	ibid	ibid	Porosity 27–55vol-%; Young's modulus 1.5–20GPa; 0.2 % proof strength 100–746 MPa	[62]
Cu	–	LM	Q-switched krypton flash lamp pumped Nd:YAG laser, 90 W	Complete melting of powder	Tentative experiments on LM of Cu powder layers to produce simple 3D structures	[65]
Au	24 carat gold; mean particle size 24 μm; tap density 10.3gcm^{-3}	ibid	Continuous wave ytterbium fiber laser, 50 W	ibid	Minimum internal porosity 12.5 %; maximum microhardness 29HV	[66]

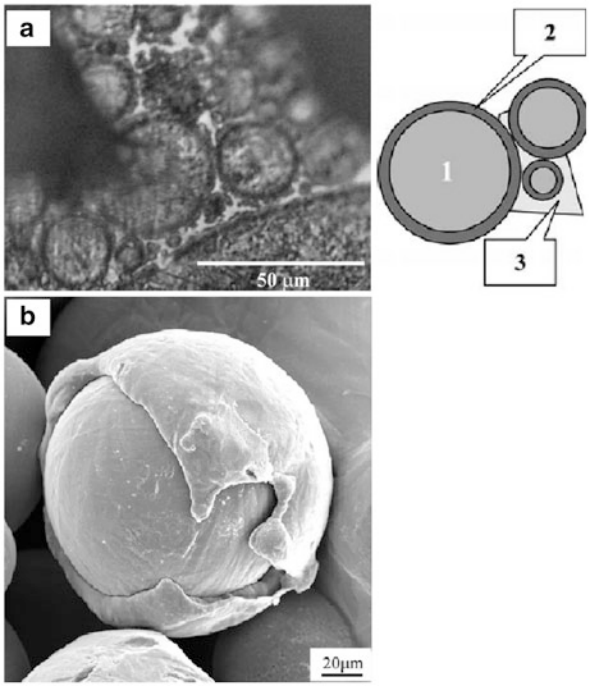


Fig. 2.11 Heterogeneous microstructure and its formation mechanism of LS-processed Ti, see Ref. [59] (**a**), partially melted particle surface of LMD-processed porous Ti, see Ref. [94] (**b**)

2.2.2 For LM and LMD—Alloys Powder

So far, a large amount of prealloyed powder has been applied for various AM processes, as reviewed in Table 2.3. A majority of research efforts have been focused on Ti-based, Ni-based, and Fe-based alloys powder, among which some material and process combinations have entered a mature phase of the practical applications. AM of Al-based alloys might be the next research focus to face the large challenge in laser processing of nonferrous alloys with high reflectivity to laser energy. Almost all the existent work on AM of prealloyed powders is based on a complete melting mechanism using LM or LMD, due to a relatively easy process controllability as compared to SLPS mechanism associated with LS (Fig. 2.4). Therefore, laser resources with high energy densities, e.g., high powered CO_2 laser, Nd:YAG laser, and fiber laser, are generally required to yield a favorable bonding mechanism (Table 2.3). Once the processing parameters are optimized to obtain fully dense parts (except for porous materials if needed), attention is focused on residual stresses and microstructures. The control of as-built microstructures is strongly influenced by the large undercooling degree during rapid solidification of the laser-generated molten pool [95]. The following sections give an overview of

Table 2.3 Alloys components produced by various AM processes

Alloy	Compositions[a]	Powder characteristics	Process[b]	Laser type	Mechanical properties	Ref.
Ti-based	Ti–6Al–4 V	Gas-atomized; Spherical shape; particle size −100+325 mesh	DMD	CO_2 laser, 6 kW	Tensile strength 1163 ± 22 MPa, yield strength 1105 ± 19 MPa, ductility ~ 4% (as-deposited); Tensile strength 1045 ± 16 MPa, yield strength 959 ± 12 MPa, ductility ~ 10.5 ± 1% (950 °C annealed)	[67]
ibid	ibid	Spherical shape; particle size 25–45 µm	LM	Ytterbium fiber laser, 200 W	Approx. 100% density; tensile strength > 1000 MPa; breaking elongation 12%	[68]
ibid	ibid	ibid	LMD	Nd:YAG laser	Tensile strength 1211 ± 31 MPa; yield strength 1100 ± 12 MPa; breaking elongation 13.0 ± 0.6% (annealed); Young's modulus 118.000 ± 2.300 MPa	[69]
ibid	Ti–25V–15Cr–2Al–0.2 C	Gas atomized; oxygen content 0.19wt-%	Ibid	CO_2 laser, 1.75 kW	Tensile strength ~ 1100 MPa/20 °C; ductility 2–4%; fatigue properties 650 MPa/450 °C, 300 MPa/550 °C, 200 MPa/650 °C	[70]
ibid	Ti–4Al–1.5Mn	Ar atomized; spherical shape; particle size 45–420 µm	Ibid	Diffusion cooled slab CO_2 laser, 5 kW	Impact toughness 599 ± 57 kJm^{-2} (as-deposited), 888 ± 33 kJm^{-2} (955 °C annealed)	[71]
Ni-based	Inconel 625 (Ni–22Cr–5Fe–3.5Nb–9Mo–0.4Al–0.4Ti–0.1 C)	Spherical shape; 95% particle size < 20 µm	LM	Continuous wave fiber laser	Ultimate tensile strength 1030 ± 50 MPa (horizontal) and 1070 ± 60 MPa (vertical); 0.2% yield strength 800 ± 20 MPa (horizontal) and 720 ± 30 MPa (vertical); Young's modulus 204.24 ± 4.12 MPa (horizontal) and 140.66 ± 8.67 MPa (vertical); elongation ~ 8–10% (both directions)	[72, 73]
ibid	Waspaloy® (Ni–13.5Co–19.5Cr–4.2Mo–2.0Fe–0.7Si–1.0Mn–1.4Al–3.0Ti–0.5Cu)	Average particle size 63 µm	Ibid	Nd:YAG pulsed laser, 550 W	Maximum 99.7% density	[74]

Table 2.3 (continued)

Alloy	Compositions[a]	Powder characteristics	Process[b]	Laser type	Mechanical properties	Ref.
ibid	Inconel 625 (64.61Ni–21.25Cr–8.45Mo–4.65Nb–1.06Fe)	Gas atomized; powder diameter 45–135 μm	DMD	CO_2 laser, 6 kW	Free from defects like crack, bonding error or porosity; as-deposited microstructure mostly consists of columnar dendrites; very high hardness 254 ± 6VHN	[75]
ibid	Inconel 718 (Ni–19Cr–18Fe–0.5Al–1Ti–3Mo–5Nb–0.042 C)	Gas atomized; spherical shape; particle size 44–150 μm	LMD	Continuous wave CO_2 laser, 5 kW	Tensile strength 845 MPa (as-deposited) and 1240 MPa (heat treated); 0.2% yield strength 590 MPa (as-deposited) and 1133 MPa (heat treated); elongation 11% and reduction in area 26% (as-deposited)	[76]
ibid	Rene88DT (Ni–17Cr–14Co–4.2W–4Mo–3.3Ti–2.2Al–0.7Nb–0.04C–0.03O–0.02 N)	Particle size 44–150 μm	ibid	ibid	Tensile strength 1400–1440 MPa; 0.2% yield strength 1010–1030 MPa; elongation 16.5–17.5% and reduction in area 17.5–18% (HIP+heat treated)	[77]
ibid	Rene41 (Ni, 18.0–20.0Cr, 10.0–12.0Co, 9.00–10.5Mo, 1.40–1.80Al, 3.00–3.50Ti, 0.06–0.12 C, 0.003–0.010B, Fe≤5.00, Zr≤0.07, Si≤0.50, Mn≤0.50, P≤0.015, S≤0.015)	Ar atomized	ibid	Continuous wave CO_2 laser, 8 kW	Tensile strength 855 MPa; yield strength 682 MPa; elongation 30.3% and reduction in area 45.8% (high-temperature tensile tests at 800 °C)	[78]
Fe-based	Stainless steel 316L (Fe–16.73Cr–13.19Ni–0.017C–0.71Si–2.69Mo–1.69Mn)	Gas atomized; spherical shape; particle size 1–56 μm, 80% < 22 μm	LM	Q-switched Nd:YAG laser, 90 W	Density > 99.5%	[79]
ibid	Stainless steel Inox 904L (Fe, 23–28Ni, 19–23Cr, 4–5Mo, 1–2Cu, Mn≤2, Si≤1, C≤0.02, P≤0.045, S≤0.035)	Spherical shape; 95% particle size < 20 μm	ibid	Continuous wave fiber laser	Successful fabrication of 20 × 20 × 5 mm object with 140 μm-thick inner compartment walls	[80]

Table 2.3 (continued)

Alloy	Compositions[a]	Powder characteristics	Process[b]	Laser type	Mechanical properties	Ref.
ibid	Tool steel H13 (Fe–0.4C–1.0Si–0.4Mn–0.03S–5.2Cr–1.5Mo–1.0V–0.3Ni)	Gas-atomized; near spherical shape; 80 % particle size < 22 μm	ibid	Nd:YAG laser, 90 W	Maximum density ~ 84 %	[81]
ibid	High speed steel M2 (Fe–0.86C–0.33Si–0.37Mn–1.25Cr–1.97V–5.23Mo–6.32 W)	Gas atomized; particle size <45 μm	LS	Continuous wave CO_2 laser	Maximum density 88.2 %; microhardness 560–1020$HV_{0.05}$	[82]
ibid	Tool Steel H13 (Fe–0.40C–0.93Si–0.35Mn–5.31Cr–0.30Mo–1.07V–0.016P–0.005S–0.006O–0.048 N)	Particle size − 70 mesh	DMD	CO_2 laser, 4.5 kW	Maximum hardness 690 Knoop; yield strength 1505 MPa; ultimate strength 1820 MPa; failure strain 6 %; reduction in area 10 %	[31, 83]
ibid	AISI 4340 high strength low alloy steel (Fe–0.42C–2.63Ni–0.90Cr–0.74Mn–0.45Mo–0.29Si)	Gas atomized; mostly spherical shape; particle size − 140/+ 325 mesh	ibid	Fiber coupled diode laser, 1 kW	Maximum porosity 4.13 %; microhardness 681–480 VHN; Microhardness decreases and amount of tempered martensite increases from the upper to the lower layers.	[84]
ibid	Stainless steel 316L (Fe, 0.08 C, 2.00Mn, 0.045P, 0.03 S, 0.75Si, 16–18Cr, 10–14Ni, 2–3Mo, 0.12Cu, 0.10 N)	Spherical shape; particle size 53–173 μm	LMD	–	Porosity 5.07vol-%; tension modulus 193.47GPa; yield stress 419.0 MPa; ultimate tensile strength 826.9 MPa; failure strain 28.95 %	[85]
ibid	Fe–15Cr–2Mn–16B–4C–2Mo–1Si–1W–1Zr (at-%)	Gas-atomized; spherical shape; particle size 10–110 μm	ibid	Continuous wave Nd:YAG laser	Microhardness ~ 900HV (9.52GPa)	[86]

Table 2.3 (continued)

Alloy	Compositions[a]	Powder characteristics	Process[b]	Laser type	Mechanical properties	Ref.
Al-based	Al–40Ti–10Si (at-%)	Mechanically alloyed partially amorphous and nanocrystalline powder	LS	Continuous wave CO_2 laser, 1.5 kW	Microhardness 745.2HV; specific wear rate 4.04×10^{-7} mm^3/Nm	[87]
ibid	Al–10Si–Mg (EOS GmbH, Germany)	–	LM	Continuous wave fiber laser	~100 % density; microhardness $150HV_{0.025}$; tensile strength 355 MPa (horizontal) and 280 MPa (vertical); 0.2 % yield strength 250 MPa	[88]
ibid	6061 Al alloy	Near spherical shape; mean particle size 50 μm	ibid	Ytterbium fiber laser	Maximum density 89.5 %	[89]
Co-based	61.78Co–29.37Cr–6.52Mo–0.23C–0.69Mn–0.68Si, Ni, Ti, Fe, S, P, N, O trace	Gas atomized; particle size −100/+325 mesh	LMD	Nd:YAG laser, 500 W	Fully dense; hardness 40HRC, equivalent to CoCrMo wrought material	[90]
ibid	Co–10.10Ni–26.41Cr–7.31W–0.81C–0.44Si	Particle size 40−100 μm	ibid	Continuous wave CO_2 laser, 5 kW	Tensile strength 946.5 MPa; elongation 27 %; microhardness 540HV	[91]
Cu-based	Hovadur® K220 (Cu–2.4Ni–0.4Cr–0.7Si)	–	LM	Continuous wave fiber laser, 1 kW	~ 99.9 % density	[92]
ibid	Cu–30Ni alloy (Cu, 29.0–33.0 Ni, 0.4–1.0 Fe, 1.0 Mn, Zn≤0.5, 0.45 C, Pb≤0.02, P≤0.02, S≤0.02)	Gas atomized; mostly spherical shape; particle size −100/+325 mesh	DMD	CO_2 laser, 5 kW	Maximum porosity 1.47 %; microhardness 115–130HVN; ultimate tensile strength 240.49 MPa; yield strength 317.16 MPa; elongation 13.9 %	[93]

[a] Unless indicated, the chemical compositions are in weight percent wt-%

[b] Besides LS process, AM of materials in Table 2.3 is based on a complete melting mechanism

four representative alloys used for AM, especially focusing on microstructural development and its mechanism.

2.2.2.1 Ti-Based Alloys

AM-processed Ti-based alloys, typically Ti–6Al–4 V, are mainly used in the aeronautical and medical fields [60, 67–69], because of their unique chemical and mechanical features and well-documented biocompatibility. A recent study by Facchini et al. [96] has disclosed the change in mechanical properties with microstructures of Ti–6Al–4 V produced by LM. Due to the formation of a unique hcp martensitic microstructure (Figs. 2.12a and c), the tensile strength of LM-manufactured parts is higher than that of hot worked parts, whereas the ductility is lower. A postprocessing heat treatment causes the transformation of the metastable martensite into a biphasic α–β matrix (Figs. 2.12b and d), resulting in an increase in ductility and a reduction in strength. The stabilization of microstructures contributes to the improvement of the ductility. This study has proved how it is possible to obtain a fully dense material and control the martensite transform in Ti–6Al–4 V alloy through the variation of LM conditions.

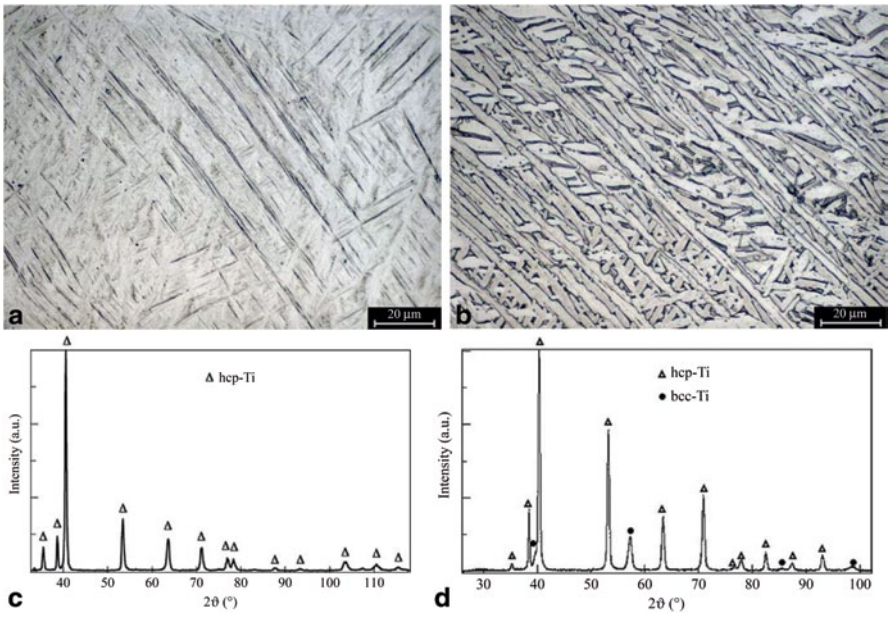


Fig. 2.12 Oriented martensite plates containing acicular hcp phase in LM-processed Ti–6Al–4 V (**a** and **c**), α–β biphasic microstructure developed in heat treated material (**b** and **d**), see Ref. [96]

2.2.2.2 Ni-Based Alloys

Ni-based superalloys, e.g., Inconel 625, 718 and Rene41, 88DT (Table 2.3), due to an improved balance of creep, damage tolerance, tensile properties, and corrosion/oxidation resistance, are normally developed for high-performance components in jet engines and gas turbines [97, 98]. As precipitate-hardened PM superalloys, Rene alloys are strengthened by the precipitation of ordered $L1_2$ intermetallic $Ni_3(Al,Ti)$ γ′ phase. The total amount of Al and Ti elements in Rene alloys is ~6wt.% [77]. Inconel alloys are Nb-modified Ni-based superalloys and their high-temperature strength is developed by solid solution strengthening or precipitation strengthening. In precipitation strengthening varieties, a fine dispersion of $D0_{22}$-ordered γ″ or $L1_2$-ordered γ′ precipitates is expected [76]. Wang et al. [78] have produced Rene41 components using LMD and found that ultra-fine directionally solidified columnar grains with a primary arm spacing of ~35 μm are formed along the deposited direction, due to the high thermal gradient and solidification cooling rate (Fig. 2.13a). The γ′ precipitate in interdendritic zones has a smaller size and a more uniform morphology than that in dendritic cores (Figs. 2.13b, c, d), due to larger supersaturation

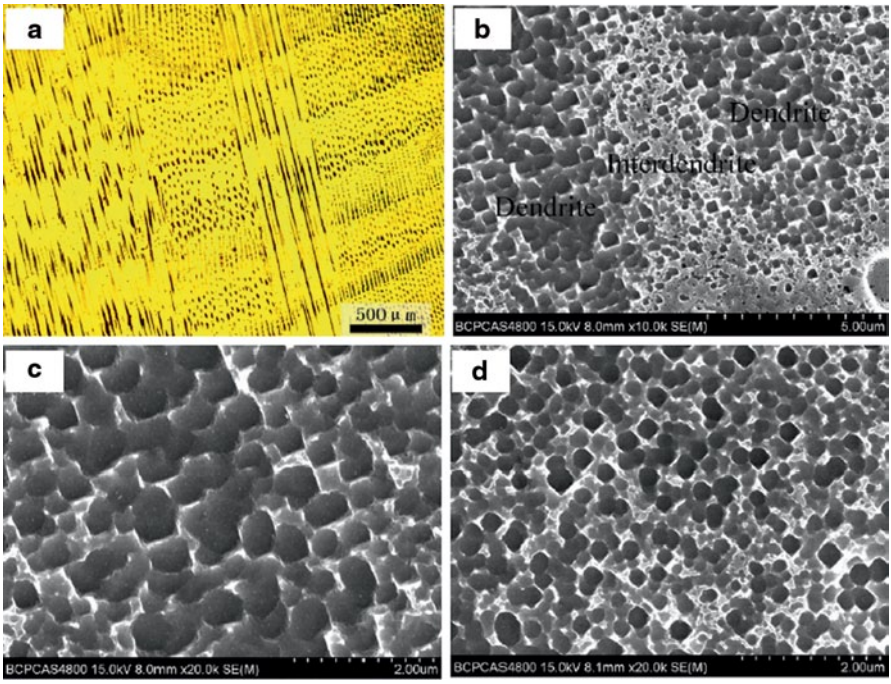


Fig. 2.13 Longitudinal microstructure of LMD-processed Rene41 (**a**), size difference of γ′ precipitate (**b**) in cellular dendritic (**c**) and interdendritic (**d**) regions, see Ref. [78]

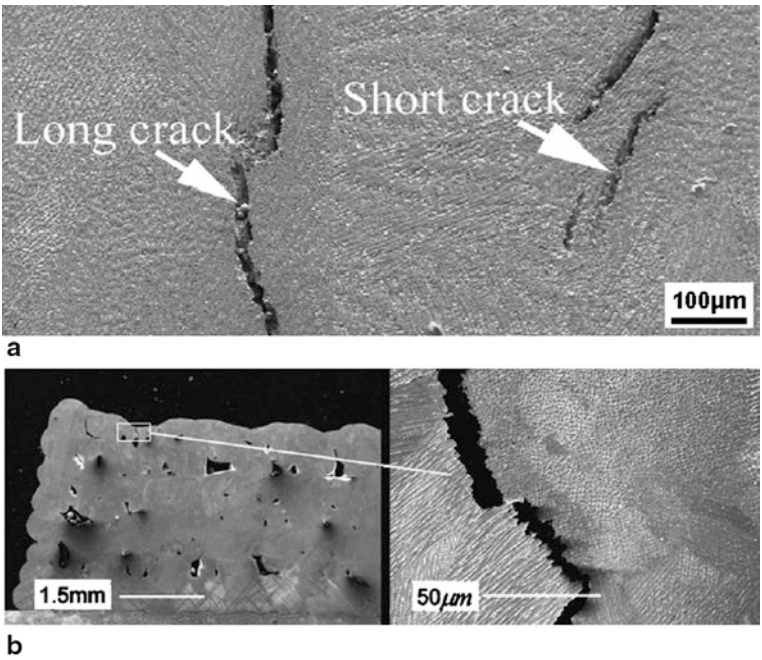


Fig. 2.14 Cracks formation in LMD-processed Rene88DT, see Ref. [77] (**a**) and LM-processed Waspaloy®, see Ref. [74] (**b**)

of elements and longer growth time of γ′ in dendrites than that located in interdendritic spaces.

However, there is a high cracking susceptivity during LM/LMD of Ni-based superalloys, because of a high amount of alloying elements and γ′/γ″-forming elements. Crack characterizations in LMD-fabricated Rene88DT (Fig. 2.14a) and LM-processed Waspaloy® (Fig. 2.14b) have been investigated by Huang et al. [77] and Mumtaz et al. [74], respectively. For LMD, cracks mainly nucleate and propagate in the overlap zone between two adjacent deposited passes. The overlapping degree has a significant effect on the size and amount of cracks. Two typical kinds of cracks, i.e., long cracks (3–10 mm) and short cracks (100–300 μm), are formed with different overlapping (Fig. 2.14a). The formation of short cracks is mainly attributed to boundary liquation cracking [99]. It is difficult to eliminate all the short cracks merely by adjusting LMD processing parameters [77]. Postprocessing steps, e.g., HIP, are required to realize a substantial improvement of mechanical properties. Comparatively, the formation of Waspaloy® parts by means of LM can be controlled by manipulating processing conditions. A definition of a feasible process window allows for the fabrication of near-fully dense (99.7%) components by LM [74].

2.2.2.3 Fe-Based Alloys

Though research reports on AM of Fe-based alloys (typically steels) are abundant (Table 2.3), it seems that the progress is not very significant. Simply in the review of densification, the obtained density of AM-processed steels generally cannot reach a full density. Therefore, AM of steels is still in the stage of pursuing the fully dense components. Nevertheless, some reports on DMD/LMD of steels have started to focus on further mechanical properties besides the densification rate [83–85]. The difficulty in AM of steels is primarily ascribed to the special chemical properties of the main elements in steels. Both the matrix element Fe and the primary alloying element Cr are very active in oxygen. A certain degree of oxidation, thus, cannot be avoided under normal powder handling and AM conditions [100]. Consequently, balling phenomena are more likely to occur during laser processing, due to a contamination layer of oxide being present on the surfaces of steel melt, severely degrading AM densification and attendant mechanical properties. On the other hand, the carbon content of steels is a critical factor in determining AM processability. Normally, AM-processed tool steels and high speed steels demonstrate a limited densification response (Table 2.3), since the high carbon content has a detrimental effect. Investigations by Wright et al. [101] reveal that as the carbon content increases, so does the thickness of the carbon layer segregated on the melt surface. Such carbon layer has the same detrimental influence as oxide layer, reducing wettability and causing the melt to spheroidize rather than flow across the underlying surface. Furthermore, the formation of complex interfacial carbides at grain boundaries increases the brittleness of AM-processed high-carbon-content steels. Childs et al.'s results [102] indicate that elevating the heat flow in the powder being treated, favors the dissolution of carbides and, accordingly, homogenizes the distribution of alloying elements. Therefore, besides the optimization of laser type and parameters, a thin powder layer thickness less than 100 μm is recommended for LM [103], in order to realize a sufficiently high volumetric energy density for both powder consolidation and elemental homogeneity.

2.2.2.4 Al-Based Alloys

Except for the research work by Mazumder et al. [3], Louvis et al. [89], and Buchbinder et al. [25, 88], very little research work has been reported on AM of Al-based alloys by LM or LMD. There are a number of difficulties in a successful LM/LMD of Al-based powders. First, the high reflectivity (>91 %) and high thermal conductivity of Al significantly increase laser power required for melting. Second, the high susceptivity of Al-based alloys to oxidation acts as a main obstacle to the effective melting. The adherent thin oxide films on molten Al reduce wettability. Oxide also causes problems when stirred into the molten pool, since the entrapped oxide generates regions of weakness within the part. Third, as to LM, it critically depends on being able to spread a thin powder layer, which is difficult because Al powders are light with poor flowability. Consequently, Al-based powders are unsuitable for

many existing powder deposition mechanisms, even though they are effective for other metallic powders of the same particle shape and size distribution.

Louvis et al. [89] have studied the oxidation mechanisms in different positions of the molten pool during LM of 6061 and Al–12Si alloys. The oxide film on the upper surface of the pool evaporates under a laser beam. Marangoni forces that stir the pool are the most likely mechanism by which these oxide films are disrupted, allowing fusion to the underlying layer. However, the oxides at the sides of the pool remain intact and, thus, create regions of weakness and porosity, as the pool fails to wet the surrounding material. Further research on LM of Al-based alloys should be primarily orientated towards new methods of controlling the oxidation process and disrupting the formed oxide films.

Recently, the Fraunhofer ILT has successfully qualified LM for Al–10Si–Mg functional prototypes (Fig. 2.15). The static and dynamic tests demonstrate that the mechanical properties of LM-processed Al–10Si–Mg specimens obtain at least the mechanical properties of serial-produced die-cast Al–10Si–Mg components according to EN 1706 specifications. Furthermore, it is found that preheating significantly increases dimensional and shape accuracy of LM-processed Al–10Si–Mg thin-wall parts [25, 88]. These inspiring results are of major importance to future industrial applications of AM technology for Al-based alloys.

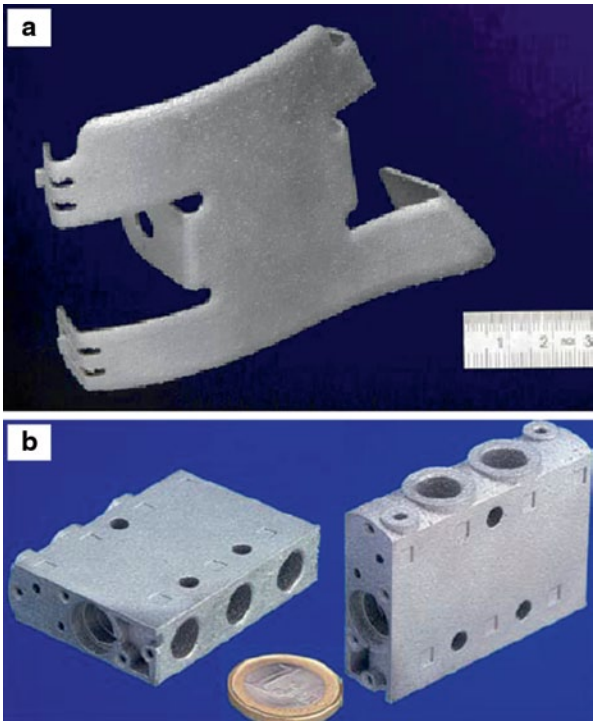


Fig. 2.15 LM-processed Al–10Si–Mg thin-wall component (**a**) and valves (**b**), see Ref. [25]

2.2.3 *For LS and LMD—Multi-Component Metals/Alloys Powder Mixture*

Multi-component metallic powders are initially designed for LS, using different binder and structural particles. As an early developed AM process for metallic materials, LS is performed based on a partial melting mechanism. The application of such a semi-solid mechanism lowers the requirements for high-powered lasers. Also, the formation of thermal stresses and resultant deformation/cracks is expected to be alleviated, due to the limited thermodynamics and shrinkage rate of a semi-solid LS system [104]. As revealed in Table 2.4, multi-component metallic powder systems can be classified under three categories:

2.2.3.1 For LS—Distinct Binder and Structural Metal With Significant Difference in Melting Points

In this category, the structural metals have a distinctly higher melting point than the metallic binder, e.g., Cu vs. SCuP (645 °C) [1]. Normally, the particle size of the binder is smaller than that of the structural metal, in order to facilitate its complete melting. Furthermore, a mixture of small-sized binder particles and relatively larger structural particles favors an improvement in the loose packing density of the whole powder system [105]. This favors a fast spreading of the molten binder by capillary forces and a rapid rearrangement of solid particles, providing a direct condition for a better densification of LS-processed components. The sufficient wetting of the structural solids by the surrounding liquid plays a crucial role in forming a sound interfacial bonding between the remaining solids and the solidified binder [10]. However, due to the considerably different melting points and/or another mismatch in chemical/physical properties, the remaining solids have a high tendency of debonding along particle boundaries, resulting in an inherent intercrystalline weakness. For instance, the fracture surface of the LS-consolidated Ni–CuSn–CuP powder system has been characterized and the large-sized brittle dimples (Fig. 2.16a) and corresponding debonded Ni particles (Fig. 2.16b) are observed [118]. The weakness caused by debonding in a fraction of areas significantly lowers the mechanical properties of LS-processed components, especially the tensile strength.

2.2.3.2 For LS—Multiple Constituents Without Significant Difference in Melting Points

As indicated in Table 2.4, Fe-based powders consisting of multiple kinds of constituents, which have the nominal chemical compositions corresponding to a certain type of steel, can be classified as the second category. Wang et al.'s work [107, 119] on LS of Fe–29Ni–8.3Cu–1.35P powder has disclosed the presence of Fe-rich ferrite α-Fe (Fig. 2.17a) and Ni-rich phase (Fig. 2.17b) in LS-processed material,

Table 2.4 Multi-component metals/alloys powder systems processed by different AM processes

Category	Materials system	Powder characteristics/considerations	Process	Bonding mechanism	Mechanical properties	Ref.
Fe-based	Fe–C–Cu–Mo–Ni	Cu binder; Ni, Mo alloying elements (~5wt-%); C decreases surface tension and viscosity of Fe base; particle size 30–45 μm	LS	Partial melting of powder	Porosity < 5vol-%; bending strength 900 MPa; microhardness 450–1000$HV_{0.025}$	[105]
ibid	Fe–(0.4, 0.8, 1.2, 1.6) C (graphite)	Water atomized/carbonyl Fe powder; mean particle size 69.4 μm/13.4 μm; fine graphite powder 2 μm	ibid	ibid	Porosity 22–34%; microhardness 137–476$HV_{0.025}$	[106]
ibid	Fe–29Ni–8.3Cu–1.35P (EOS GmbH, Germany)	Spherical Ni and Fe, irregular Cu particles; particle size Cu 32 ± 22 μm, Fe 3.6 ± 5.0 μm, Ni 6 ± 2 μm	ibid	ibid	Porosity 2.6%; microhardness 381 ± 30HV (dendritic regions), 260 ± 15HV (non-dendritic regions); roughness Ra 18.2 μm (top surface), 12.6 μm (side surface)	[107]
ibid	Fe–15Cu–15 W	Fe irregular shape, particle size 5–10 μm; Cu dendrite shape, mean size 40 μm; W prismatic shape, mean size 4.25 μm	ibid	ibid	High residual porosity; minimum surface roughness Ra 23 μm; W particles reduces part distortion	[108]
ibid	Fe–20Ni–15Cu–15Fe_3P	Spherical Fe < 50 μm, spherical Ni 5 μm, spherical Cu < 50 μm, spherical Fe_3P < 50 μm; Dissolution of P lowers surface tension and oxidation rate of melts	ibid	ibid	Density 6.29gcm^{-3}; Brinell hardness 84.72 kg/mm^2; roughness Ra 7.41 μm; bending strength 316 MPa	[109]
ibid	ibid	ibid	LM	Complete melting of powder	Relative density 91%; bending strength 630 MPa; roughness Ra 10–30 μm	[110]
ibid	Fe–0.8C–(2.5Cu, 1.0Si, 1.0Ti)	Water atomized Fe powder (0.5% oxygen) d_{50} = 58 μm, Cu d_{50} = 30 μm, Ti d_{50} < 25 μm, Si d_{50} < 8 μm	ibid	ibid	Fe–0.8 C maximum relative density 94%, minimum roughness Ra 38 μm; Cu, Ti, and Si have negative effect on surface quality and densification	[111]
ibid	Fe–4B–(9Ti)	Fe 80% < 22 μm, Fe–B 100% < 45 μm, Ti 100% < 40 μm	ibid	ibid	Fe–4B minimum roughness Ra 49 μm; mean microhardness 838.2HV; Ti increases porosity	[112]

Table 2.4 (continued)

Category	Materials system	Powder characteristics/considerations	Process	Bonding mechanism	Mechanical properties	Ref.
Cu-based	Cu–40SCuP	Electrolytic Cu, dendritic shape, mean particle size 40 μm; pre-alloyed SCuP, spherical shape, particle size 5–20 μm; P acts as flux to protect Cu oxidization	LS	Partial melting of powder	Relative density 65%; roughness Ra 14–16 μm; hardness 40 ± 7HR 15T	[1]
ibid	Cu–30CuSn–10CuP	Irregular Cu, particle size 28–75 μm; ellipsoidal CuSn 11–46 μm; spherical CuP 5–24 μm; Homogeneous powder mixture by ball mixing coarse and fine powders with a broad particle size distribution	ibid	ibid	Relative density 94.6%; fracture strength 169.2 MPa; hardness 101.7HB	[113]
Interme-tallic	Compositionally graded Ni–Al	Gas-atomized Al and water-atomized Ni; both particle sizes 45–75 μm	LMD	Complete melting of powder; *in situ* reactive alloying	Solidification and subsolidus cracking susceptibility and porosity formation	[44]
ibid	Compositionally graded Ti–Ni	From elemental Ti to Ti–23.2 at-%Ni	ibid	ibid; phase evolutions $\alpha \rightarrow \alpha+\beta \rightarrow \alpha+\beta+Ti_2Ni \rightarrow \beta/B2+Ti_2Ni$	N/A	[114]
ibid	Ti–Ni	Elemental powder blends in nominal composition of 52.04Ti–47.96Ni	ibid	ibid; formation of binary Ti_2Ni/TiNi B2 intermetallics	Microhardness Ti_2Ni phase ~600HV, TiNi phase ~244HV, Ti_2Ni/TiNi alloy ~310HV; high wear resistance	[115, 116]
ibid	γ-TiAl, Ti–47Al–2.5V–1Cr (at-%)	Ar atomized; spherical shape; Particle size 70–75 μm; oxygen content <0.06–0.1wt-%	ibid	Complete melting of pre-alloyed powder	Full density; tensile strength 600–650 MPa (longitudinal) and 550–600 MPa (transverse); ductility ~0.6% (both directions)	[117]

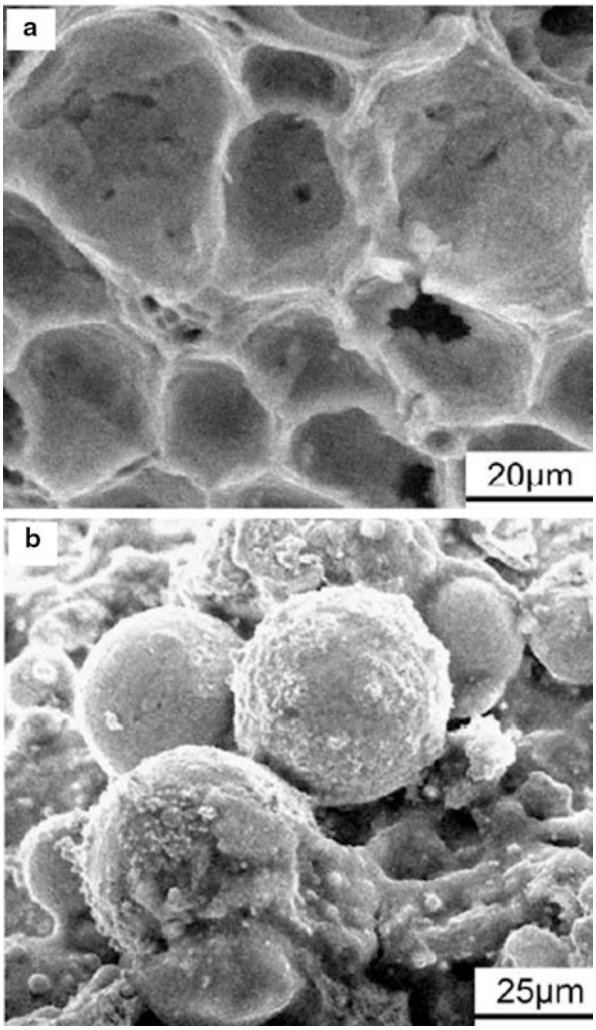


Fig. 2.16 Fracture surface of LS processed Ni–CuSn–CuP multi-component powder: **a** brittle dimples, **b** debonded solid particles, see Ref. [118]

revealing that the Fe and Ni particles are only partially melted during LS. Simchi et al.'s work [105] on LS of Fe–C–Cu–Mo–Ni powder has also revealed the formation of a heterogenous microstructure consisting of unmelted constituents (Fig. 2.17c), due to the incomplete melting and diffusion of alloying elements. Nevertheless, a general comparison reveals that almost full density is achievable for this category of materials by LS (Table 2.4), even though the constituents have not melted completely. It is noticed that LM has also been applied to process multi-component powders. Although Kruth et al.'s work [109, 110] on LM of Fe–20Ni–15Cu–15Fe_3P has proved a certain degree of enhancement of densification and bending strength

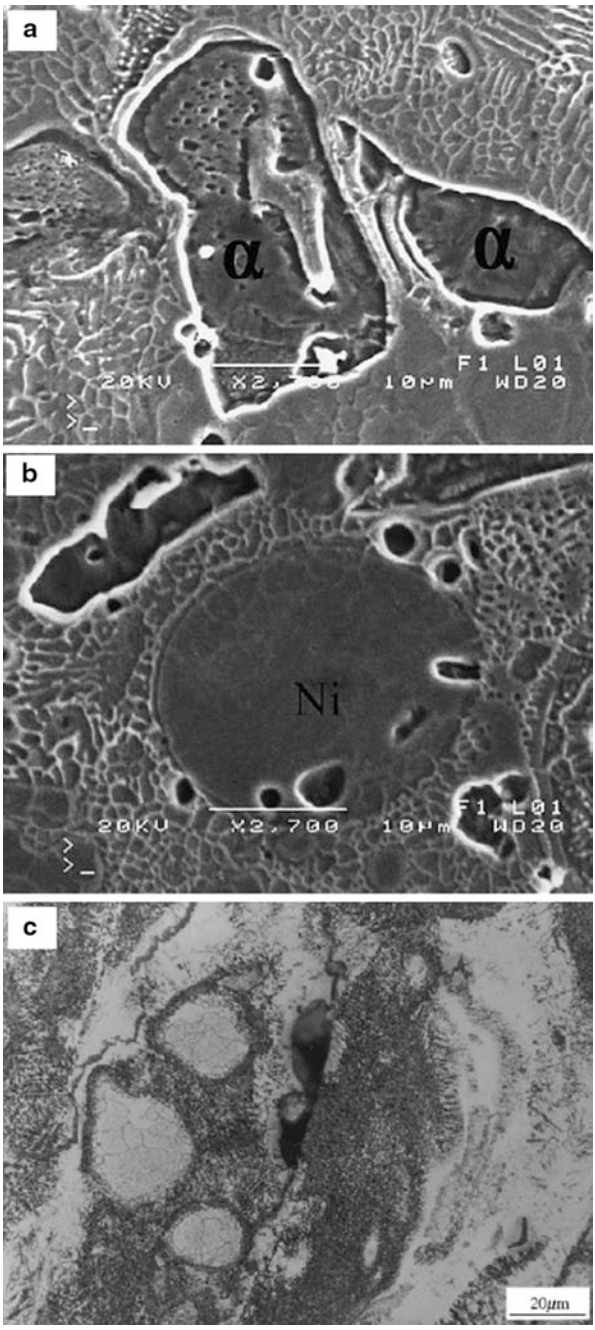


Fig. 2.17 Microstructures of LS-processed Fe–29Ni–8.3Cu–1.35P powder, see Refs. [107] and [119] (**a** and **b**), and Fe–C–Cu–Mo–Ni powder, see Ref. [105] (**c**)

as relative to LS-processed parts (Table 2.4), their work [111] on LM of Fe–0.8C–(2.5Cu, 1.0Si, 1.0Ti) and Chen et al.'s work [112] on LM of Fe–4B–(9Ti) reveal that the multiple Si, Ti, and Cu constituents have a negative effect on densification of Fe-based parts. The detrimental effect is ascribed to their high tendency to form oxides and carbides during the LM process with a significantly elevated energy input and a complete liquid formation.

2.2.3.3 For LMD—Intermetallics From Elemental Constituents

There are growing research attempts to produce intermetallics components, including compositionally graded intermetallics, via reactive *in situ* alloying from a blend of elemental powders using LMD (Table 2.4). *In situ* reactive alloying by LMD can be successfully achieved by delivering elemental powders from two (or more) powder feeders or using blown powder cladding techniques with mixed powder of pure elements. The rapid exothermic reactions, which are normally involved during liquid formation of intermetallics, ensure the homogeneity of *in situ* alloying of intermetallic compounds [120]. For multiple powder feeders, the phase formation and microstructure evolution of *in situ* alloyed intermetallics can be controlled along the deposition direction by regulating the ratio of feed rates of different powders [44]. For blended elemental powders, the chemical composition of as-deposited parts can be controlled like the premixed elemental powders by keeping the identity of the divergence angles of the elemental powder streams [121]. The *in situ* reactive formation of intermetallics by LMD has the following potential advantages [44]:

- Raw-material cost savings by eliminating the production steps required for pre-alloyed powders
- Suitability for fabricating compositionally graded structures and materials
- Decrease in laser energy requirements by using reaction-generated heat

The early research on *in situ* formation of the novel $Ni_{70}Al_{20}Cr_7Hf_3$ intermetallic alloys using laser cladding was reported by Mazumder et al. in the last eighties [122]. A 10 kW CO_2 laser with mixed powder feed has been used to produce Ni-Al-Cr-Hf alloys with an extended solid solution of Hf in a near stoichiometric Ni_3Al matrix. The laser cladding parameters, microstructure evolution, and oxidation resistance behavior have been investigated. Wang's research group has performed systematic researches on LMD fabrication of intermetallic alloys (e.g., Ti–Ni [115, 116], γ-TiAl [117], and CoTi [123]) and transition metal silicides (e.g., Ti–Ni–Si [124], Ti–Co–Si [125], Mo–Ni–Si [126], Cr–Ni–Si [127], Co–Mo–Si [128]). In particular, the microstructural development, dry sliding wear resistance, and high-temperature wear resistance of LMD-processed intermetallic components have been comprehensively studied.

2.2.4 Metal Matrix Composites (MMCs)

2.2.4.1 *Ex Situ* MMCs

Ceramics reinforced MMCs exhibit an optimum combination of ductile metallic matrix and stiffer and stronger ceramic reinforcements. As to ex situ MMCs powders, the ceramic reinforcing particles are added exteriorly into the metal matrix, each having individual particles. The MMCs powders are normally obtained by mechanically alloying a mixture of different powder components [129]. The powder particles are repeatedly fractured, cold-welded, and refractured during milling, producing MMCs powders with required characteristics for AM. In a broad sense, ex situ MMCs can be classified as multi-component systems, with the matrix metal and ceramic reinforcement acting as the binder and structural material, respectively.

AM of MMCs, as a unique method to obtain a designed composite material with comprehensive properties normally not available with a single metal or alloy, has already attracted growing interest. WC–Co is the most intensively studied MMCs for AM, including LS work by Wang et al. [130], Kumar [131], and Gläser [132], and LMD work by Xiong et al. [52, 133] and Picas et al. [134]. Gläser has disclosed that a high LS density is obtainable when applying spherical WC–Co particles, yielding a structure comparable with conventionally sintered hard metal [132]. Xiong et al. [52, 133] have fabricated bulk WC–Co MMCs using LMD, starting from the high-energy ball milled powder consisting of nanostructured WC crystallites in a Co matrix. Microstructures with alternating layers are observed, which is relevant to the thermal behavior of LMD. Variations in hardness result from the change in cooling rate along specimen height. Other preliminary researches have been performed on LS of ex situ MMCs in terms of TiC/(Fe, Ni) [135], SiC/Fe [136], SiC/Al–4.5Cu–3Mg [137], SiC/Al–7Si–0.3Mg [138], ZrB_2/Cu, TiB_2/Cu [139], and ZrB_2/Zr [140]. LMD of MMCs, e.g., (Ti,W)C/Ni [141], Ni-Coated TiC/Inconel625 [142], Ni-coated TiC/Ti–6Al–4 V [143], TiC/Ti–48Al–2Cr–2Nb [144], TiC/Ti–6Al–2Zr–1Mo–1 V [145], TiO_2/Ti [146], and Y_2O_3/Fe–Cr–Al [147], has also been reported.

Problems such as gas entrapment, particulate aggregation, and interfacial microcracks are regarded as the main obstacles to obtain full-density MMCs components with favorable microstructural homogeneity. In particular, the strength and stability of the interfacial region between ceramic reinforcement and metal matrix govern the mechanical response of MMCs. Failure that initiates by interfacial debonding is likely to occur when MMCs have weak interfaces. For example, LS-processed TiC/(Fe,Ni) MMCs subjected to the bending test show the ductile fracture of metal matrix, but brittle fracture and debonding around TiC particles (Fig. 2.18) [135]. The key factor accounting for this problem is the poor wettability between ceramics and metals. One effective strategy is to encapsulate the ceramic particles with a metal coating, in order to modify interfacial structure and promote wettability.

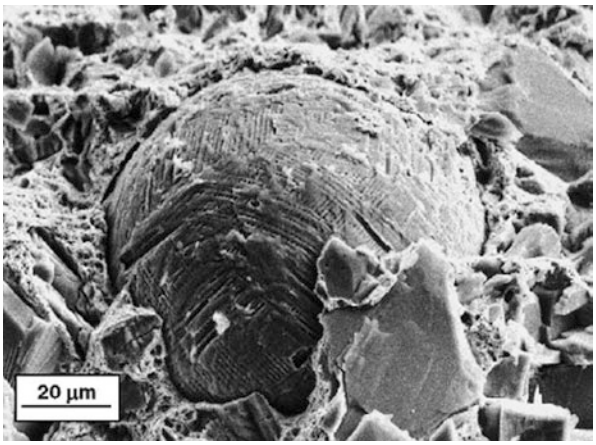


Fig. 2.18 Fracture surface of LS-processed TiC/(Fe,Ni) MMCs, see Ref. [135]

Zheng et al. [142, 143] have applied the Ni-Coated TiC to reinforce Inconel625 and Ti–6Al–4 V. This approach effectively alleviates the formation of voids or cracks at metal/ceramic interface and prevents clustering of ceramic particles in LMD-processed MMCs. Furthermore, the author's work on LS of WC reinforced Cu MMCs has revealed that the addition of a trace amount of rare earth (RE) compounds, e.g., La_2O_3 and RE–Si–Fe, can improve laser processability of MMCs. The RE elements favor microstructural refinement and improve particulate dispersion homogeneity, due to the unique metallurgical functions of RE, which will be revealed in detail in Chap. 7 of this book:

- Decreasing surface tension of the melt
- Resisting grain growth coarsening
- Increasing heterogeneous nucleation rate

2.2.4.2 *In Situ* MMCs

The development of novel *in situ* MMCs via an AM route, in which the constitutions are synthesized by chemical reactions between elements, exhibits more significant advantages. *In situ* formed ceramic reinforcement is thermodynamically stable, leading to less degradation in elevated temperature applications. Furthermore, the ceramic/metal interfaces within *in situ* MMCs are generally cleaner and more compatible, yielding stronger interfacial bonding and elevated mechanical properties of the final products [148]. AM of *in situ* MMCs components represents an important direction in AM research fields to fulfill the future demand of novel materials with unique properties.

The production of *in situ* MMCs requires a complete melting of the starting materials to form an *in situ* reaction system. Therefore, both LM and LMD have a potential applicability. The formation of *in situ* reinforcement, in a broad sense, can be regarded as a bottom-up method starting with atoms in the liquid to form the required phases. Combined with the highly non-equilibrium nature of laser processing, it provides a high possibility to create unique microstructures of *in situ* phases.

The early report on non-equilibrium DMD synthesis of *in situ* Fe–Cr–C–W composites is provided by Choi and Mazumder, offering an opportunity to produce a novel wear-resistant material. The composition and volume fraction of carbides can be controlled by controlling the preheating temperature, power density, and traverse speed. Mostly M_6C or $M_{23}C_6$ type carbides precipitate in the matrix. The diamond-shaped M_6C carbides show good tribological characteristics [149]. Zhong et al. [150] have reported on NiAl intermetallic matrix composites reinforced with TiC particles obtained by *in situ* LMD with coaxial feeding of Ni/Al + TiC powder mixture. The microstructure of LMD-processed material consists of partially melted TiC, dispersively precipitated fine TiC particles, and refined β-NiAl phase matrix. Banerjee et al. [151, 152] have applied LMD to deposit *in situ* TiB/Ti–6Al–4 V and TiB/Ti MMCs from a powder blend of Ti–6Al–4 V (or Ti) and elemental B. A unique microstructural feature of LMD-processed MMCs is the formation of highly refined nanometer-scale TiB precipitates within the grains of α-Ti. The ability to produce such an ultrafine dispersion of TiB precipitates in near-net-shape MMCs is highly beneficial from the viewpoint of applicability of these novel materials. Wang et al. [153] have also prepared TiB/Ti–6Al–4 V MMCs by LMD of pre-mixed powders of TiB_2 and Ti–6Al–4 V. The modulus, yield and ultimate strength, and wear resistance of Ti–6Al–4 V are generally increased by incorporation of TiB, but the ductility is decreased. The author has put considerable research efforts into LM fabrication of *in situ* MMCs such as TiC/Ti–Al (from Ti–Al–graphite powder) [154], WC/Ni (from W–Ni–graphite powder) [155], TiN/Ti_5Si_3 (from Ti–Si_3N_4 powder) [156], and TiC/Ti_5Si_3 (from Ti–SiC powder) [157], and the detailed results will be presented in Chaps. 4 and 5 of this book.

LMD/LM preparation of *in situ* MMCs, although it has experienced long-term development, still encounters a few challenges. The most significant one is the unpredictability and/or uncontrollability of the formation of *in situ* microstructures during processing. The non-equilibrium metallurgical process of LMD/LM makes it rather difficult to control the crystallization and growth morphology of *in situ* phases. For instance, in the author's work [154] on LM of Ti–Al–C blended powder, the morphologies of *in situ* TiC experience a successive change: a laminated shape → an octahedron shape → a truncated near-octahedron shape → a near-spherical shape, on increasing the applied laser powers (Fig. 2.19). As phase constitution and crystal structure may significantly influence the final mechanical properties of MMCs, it is highly necessary to be able to understand and control them during the LMD/LM process.

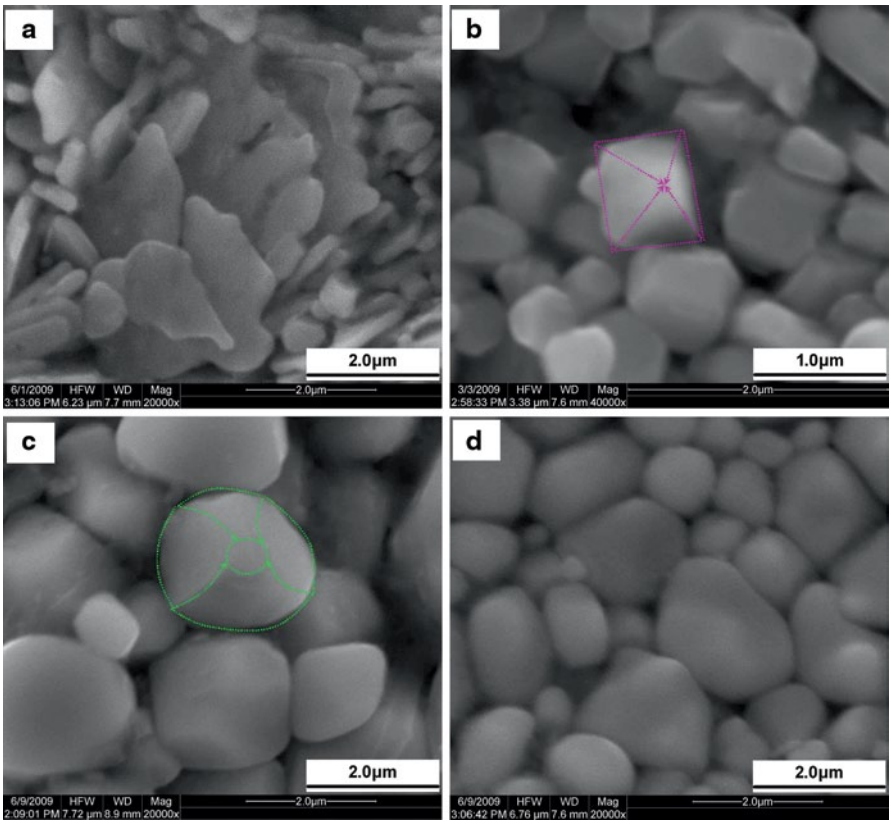


Fig. 2.19 Morphologies of *in situ* TiC reinforcement in LM-processed Ti–Al–C powder at different laser powers: **a** 700 W, **b** 800 W, **c** 875 W, **d** 900 W, see Ref. [154]

2.3 Material/Process Considerations and Control Methods

2.3.1 General Physical Aspects and Design Strategies of Materials for AM

In spite of two different AM approaches, the LS/LM and LMD/DMD processes share some common physical mechanisms. This section focuses on general physical aspects and corresponding material considerations of AM processes.

2.3.1.1 Absorptance

AM processes generally involve a direct interaction of powders with laser beams. The determination of absorptance of powders is particularly important to thermal

development, because it allows one to determine a suitable processing window free of a nonresponse of powder due to an insufficient laser energy input or a pronounced material evaporation due to an excessive energy input. The absorptance is defined as the ratio of the absorbed radiation to the incident radiation. Dissimilar as dense materials, only a fraction of the incident radiation is absorbed by the outer surface of particles. Another part of the radiation penetrates through the inter-particle voids into the depth of the loose powder layer. The absorptance of pores approaches that of a gray body [158]. The absorptance of powders has a direct influence on the optical penetration depth δ of the radiation, which is defined as the depth at which the intensity of the radiation inside the material falls to $1/e$ (~37%) of the original value. Due to the multiple reflection effect, the δ measured in powders is larger than in bulk materials [159].

To understand the absorption mechanism of powders to laser radiation, Fischer et al. [160] have considered two different energy coupling mechanisms, i.e., bulk-coupling and powder-coupling. In a first step, the energy is absorbed in a narrow layer of individual particles determined by the bulk properties of the material, leading to a high temperature of particle surfaces during interaction. After thermalization of the energy, heat flows mainly towards the center of particles until a local steady state of the temperature within the powder is obtained. Afterwards, the surrounding powder properties are responsible for further thermal development. Tolochko et al. [158] have experimentally determined the absorptance of a number of powders, with two different wavelengths of 1.06 and 10.6 μm obtained by Nd:YAG and CO_2 lasers. For metals and carbides, the absorptance of powders decreases with increasing wavelength; whereas for oxides, the absorptance increases with increasing wavelength. The changes in powder thermophysical properties, particle rearrangement, phase transitions, and melt oxidation during laser processing affect the absorptance. Also, the absorptance of powders is time- and process-dependent. Generally, the greater the absorptance of powder, the less the laser energy output required. That is why the laser radiation absorbing additives are of interest for AM-applicable powders. Simchi's work [138] has proved that the addition of 5 vol.% SiC increases the densification of Al–7Si–0.3Mg powder during LS, mainly due to a higher effective absorptance in the presence of SiC (SiC of 0.68 vs. Al of 0.06 under CO_2 laser). Nevertheless, these additives should be carefully selected to yield appropriate microstructural and mechanical properties of AM-processed powder.

2.3.1.2 Surface Tension and Wettability

The liquid-solid wetting characteristics are crucial for a successful AM process. The wetting behavior of a partially melted LS system involves the wetting between structural metal and liquid binder as well as the wetting between the molten system and the solidified preprocessed layer. For the completely melted LM/LMD systems, the second kind of wetting behavior prevails. The wetting of a solid by a liquid is

related to the surface tension of solid-liquid (γ_{sl}), solid-vapor (γ_{sv}), and liquid-vapor (γ_{lv}) interfaces. Wettability can be defined by the contact angle θ [9]:

$$\cos\theta = \frac{\gamma_{sv} - \gamma_{sl}}{\gamma_{lv}} \tag{2.1}$$

The liquid wets the solid as $\cos\theta \rightarrow 1$. Das [100] has defined a spreading coefficient

$$S = \gamma_{sv} - \gamma_{sl} - \gamma_{lv} \tag{2.2}$$

to describe the wetting behavior and, normally, a large positive S favors spreading of the liquid. Conversely, if $\gamma_{sl} > \gamma_{sv}$, $\theta > 90°$ and, accordingly, the liquid spheroidizes rather than wetting the solid substrate, so as to have minimum surface energy. Das [100] has disclosed that the contamination layer of oxide being present on the surface of melts and on the previously processed layer is a severe impediment to a sound wettability and causes defects such as balling. Essentially, the poor wettability of a molten metal with oxidation inside is due to its wetting nature similar as a metal/ceramic system. In order to mitigate oxidation, AM process must be conducted in a protective atmosphere using high purity inert gases. However, these environments alone cannot warrant a complete wetting. Due to the high reactivity at melting temperatures, most metals will easily form oxides even under very low partial pressure of oxygen [100]. A certain degree of oxidation cannot be avoided under normal AM conditions. To achieve a good wetting, reduction of surface oxides is necessary to form clean metal-metal interfaces. When choosing materials, fluxing agents or *in situ* deoxidizers can be considered. These additives are added in small quantities to the powders, either mixed or prealloyed with the matrix constituent, to aid wetting activity. In Kruth et al. [109] and Zhu et al.'s [1] work, P element is added in the form of pre-alloyed Fe_3P and SCuP to Fe-based and Cu-based powder systems, which are effective in enhancing wetting behavior and LS densification.

2.3.1.3 Viscosity

Besides the favorable wettability, it is required that the viscosity of the melt is low enough so that it can successfully spread on the previously processed layer and, in the case of LS, surround the solid structural particles. For a LS system consisting of a solid-liquid mixture, the viscosity of the molten material, μ, is expressed as [9]:

$$\mu = \mu_0 \left(1 - \frac{1 - \varphi_l}{\varphi_m}\right)^{-2} \tag{2.3}$$

where μ_0 is the base viscosity that includes temperature terms, ϕ_l the volume fraction of liquid phase, and ϕ_m is a critical volume fraction of solids above which the

mixture has essentially infinite viscosity. As to a LM or LMD system with a complete liquid formation, the dynamic viscosity of the liquid is defined by [161]:

$$\mu = \frac{16}{15}\sqrt{\frac{m}{kT}}\gamma \tag{2.4}$$

where m is the atomic mass, k is the Boltzmann constant, T is the temperature, and γ is the surface tension of the liquid. Agarwala et al.'s results [9] reveal that particle bonding during LS is controlled by μ_0. This viscosity decreases with increasing the working temperature, which in turn leads to better rheological properties of the liquid in conjunction with solid particles and, accordingly, an improved densification. With respect to viscosity, the metallic systems with a strong formation tendency of intermetallic compounds are difficult to process, because the intermetallics are generally brittle and may increase the viscosity of the melt [44]. On the other hand, the dynamic viscosity μ should be high enough to prevent balling phenomena [9]. This can be best obtained by controlling the right solid-liquid ratio during LS, or by varying the processing conditions to yield a feasible operative temperature during LM/LMD.

2.3.2 Microstructural Properties of AM-Processed Parts

2.3.2.1 Surface Morphology and Roughness

i. LS/LM—Laser Powder Bed Approach

Generally, the microstructural properties of AM-processed parts include the exterior surface microstructure and the interior grain microstructure. Balling phenomena are regarded as the typical microstructure occurring on surfaces of laser-processed parts using LS/LM from a bed of loose powder. The broadly recognized definition of balling effect is concluded as follows, by combining the previous studies by Niu et al. [162], Tolochko et al. [28], Das[100], and Simchi et al. [11]. During LS/LM, laser scanning is performed line by line and the laser energy causes melting along a row of powder particles, forming a continuous liquid scan track in a cylindrical shape. The diminishing in the surface energy of the liquid track continues until the final equilibrium state through the breaking up of the cylinder into several metallic agglomerates in spherical shape (so-called balling effect). Balling phenomena may result in the formation of discontinuous scan tracks and poor inter-line bonding property as a current layer is processed. Furthermore, during the layer-by-layer LS/LM process, balling effect is a severe impediment to a uniform deposition of the fresh powder on the previously processed layer and tends to cause porosity and even delamination induced by poor inter-layer bonding in combination with thermal stresses.

Balling effect is a complex metallurgical process that is controlled by both powder material properties and laser processing conditions. Comprehensive studies of balling effect during LS/LM of multi-component Cu-based powder and 316L stainless steel powder, including its physical nature and control methods, are presented in the author's work [163, 164]. Three kinds of balling mechanisms during LS of Cu–30CuSn–10CuP powder are disclosed [163]. Scanning the initial tracks onto a cold powder bed gives rise to the "first line scan balling" (Fig. 2.20a), due to the high thermal gradients imposed on the melt. Using a higher scan speed leads to "shrinkage-induced balling" (Fig. 2.20b), due to a significant capillary instability. "Splash-induced balling" with the formation of a large amount of micrometer-scale balls prevails at a high laser power combined with a low scan speed (Fig. 2.20c), because of the considerably low viscosity and long lifetime of liquid. The following control methods have proved feasible in decreasing balling tendency during LS/LM of 316L powder:

- Increasing the volumetric energy density
- Adding a trace amount of H_3BO_3 and KBF_4 deoxidant [164]

Recent work by Mumtaz and Hopkinson [2] has investigated LM of Inconel 625 using pulse shape control to vary the energy distribution within a single laser pulse, which is effective in attaining parts with minimum balling effect and surface roughness. High peak power tends to reduce top and side surface roughness as recoil pressures flatten out the melt pool and reduce balling formation by increasing wettability of the melt. Ramp-up energy distribution can reduce the maximum peak power required to melt material and reduce material spatter generation due to a localized preheating effect. Ramp-down energy distribution prolongs melt pool solidification, allowing more time for molten material to redistribute and, accordingly, reducing the top surface roughness of parts.

ii. LMD/DMD—Coaxial Powder Feeding Approach

The laser powder bed approach is currently the preferred technology for manufacturing small components which normally require a good surface finish [165]. In contrast, the surface roughness of the components produced by LMD/DMD approach is typically higher, due to the presence of the relatively larger molten pool induced by a larger-sized laser spot and the melt deposition mechanism applied. Control of surface and wall roughness is, therefore, an important issue for LMD/DMD components to reduce postprocessing costs. Normally, four directions with respect to the cladding should be considered for the measurements of surface roughness, i.e., the length and width directions on the top surface, and the horizontal and vertical directions on the walls [31]. As indicated in Mazumder et al.'s work on DMD of aluminum 1100 and H13 tool steel components, the roughness perpendicular to the cladding direction on the top surface is about 5% rougher than that parallel to the cladding. In contrast, the roughness in the vertical direction on the side wall was approximately 3% larger than that in the horizontal direction [3]. The directions perpendicular to the cladding direction on the top surface and in the

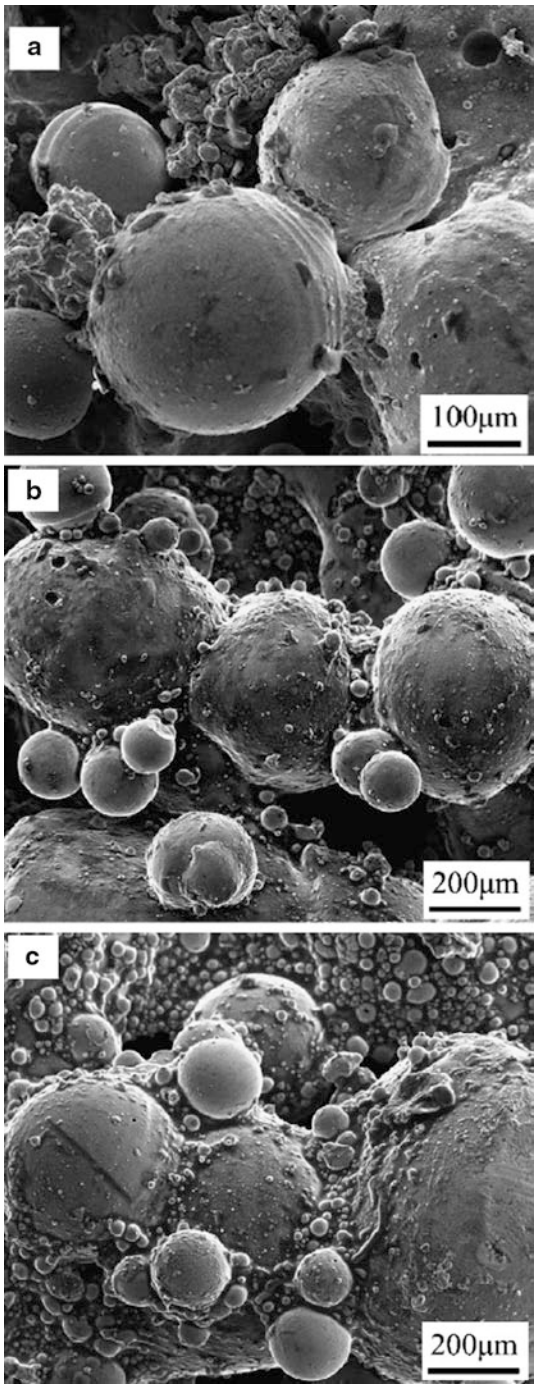


Fig. 2.20 Balling phenomena occurred during LS of Cu–30CuSn–10CuP powder: **a** First line scan balling, **b** Shrinkage-induced balling, **c** Splash-induced balling, see Ref. [163]

vertical direction on the walls, therefore, are of primary importance for determining the maximum roughness of DMD components.

Laser power, traverse speed, and powder flow rate are three important parameters influencing the roughness of DMD components. The wall roughness is directly related to layer thickness and may be increased by depositing thicker layers, due to the variation of beam diameter caused by defocusing. On the other hand, using higher deposition velocities normally makes the wall surface rougher. Mazumder et al. have proposed a sound explanation of this phenomenon [3]. At higher velocities, the cladding at the part edges normally is unable to catch as much powder as the internal cladding. Consequently, there is not sufficient time for the cladding to build to the required height, producing gaps in the cladding passes at the sample edges. In this regard, reducing the traverse speed of the deposition around the outline of the component favors a decrease in wall roughness. Furthermore, the application of three sensor systems proves to be effective in improving the height control of the DMD process and, accordingly, reduces the surface roughness average of the fabricated parts by approximately 14 % [3].

2.3.2.2 Grain Size and Structure

The key to the mechanical properties of AM-processed components is the solidification microstructure. The high-energy laser interaction gives rise to superfast heating and melting of materials, which is inevitably followed by a rapid solidification on cooling. Laser-based AM processes normally offer high heating/cooling rates (10^3–10^8 K/s) [166] at the solid-liquid interface in a small-sized molten pool (~1 mm) [167]. Furthermore, the rates of quenching that occur by conduction of heat through the substrate are fast enough to produce a rapid solidification microstructure. Therefore, as a characteristic of AM-processed materials, grain refinement is generally expected, due to an insufficient time for grain development/growth. For instance, the conventional dendritic solidification features of Fe-based materials are not well developed after AM, but show a directional cellular microstructure, due to the insufficient growth of secondary dendrite arms, e.g., LS- and LMD-processed 316L powder [164, 168] (Figs. 2.21a and b) and LM-processed Fe–Ni–Cu–Fe_3P powder [110] (Fig. 2.21c). On the other hand, either chemical concentration or temperature gradients in the molten pool may generate surface tension gradient and resultant Marangoni convection [11, 13], making the solidification a non-steady-state process. Meanwhile, rapid solidification has the kinetic limitation of crystal growth that normally follows the direction of maximum heat flow. The simultaneous but competitive action of the above two mechanisms, i.e., a non-equilibrium solidification nature vs. a localized directional growth tendency, may result in a variety of crystal orientations with a localized regularity [157]. Therefore, AM-processed metallic materials may have the inherent, more or less, anisotropic characteristics.

Recent research attempts have demonstrated that laser-based AM may be a useful strategy to consolidate a number of unconventional powders with novel microstructures (e.g., amorphous and nanostructured powders). Singh et al. [87] have applied

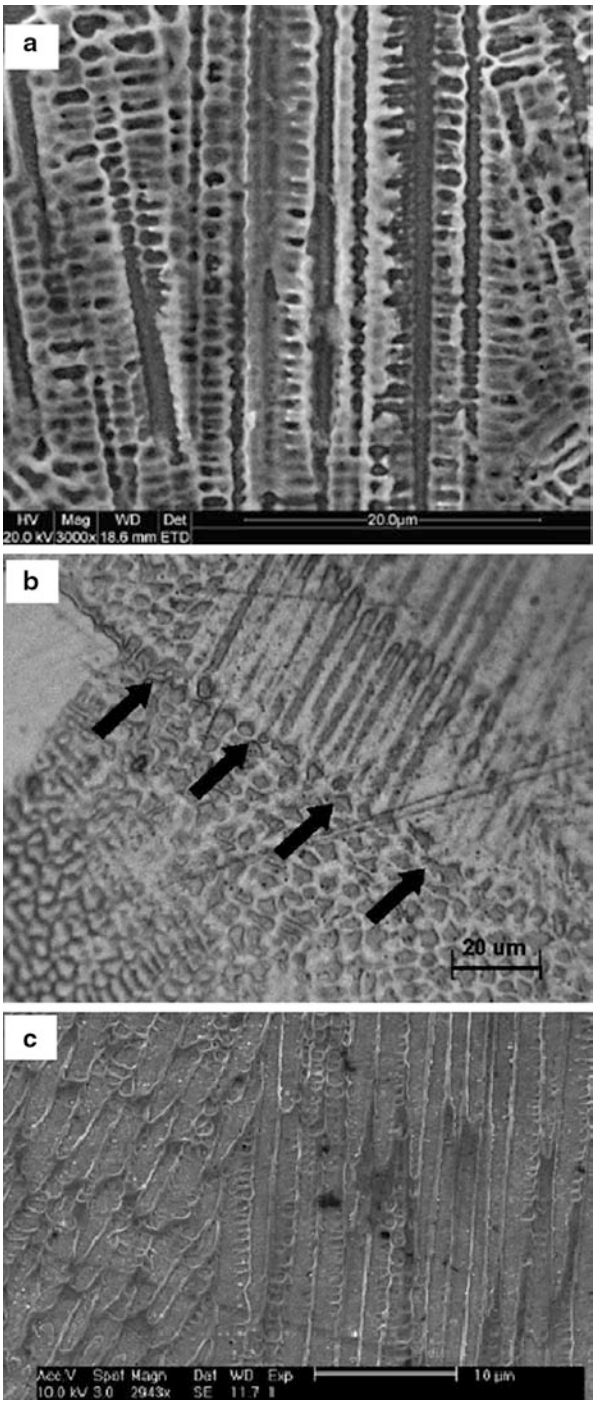


Fig. 2.21 Microstructures of LS-processed 316L, see Ref. [164] (**a**), LMD-processed 316L, see Ref. [168] (**b**), and LM-processed Fe–Ni–Cu–Fe_3P, see Ref. [110] (**c**)

LS to process mechanically alloyed $Al_{50}Ti_{40}Si_{10}$ powder with partially amorphous and nanocrystalline microstructures. Following laser irradiation, the coexistence of these two novel microstructures is well attained. The author's recent work [169] has used LM to consolidate high-energy ball-milled nanostructured TiC_p/Ti powder to prepare bulk-form TiC/Ti nanocomposites and the TiC reinforcement typically has a lamellar nanostructure with a mean thickness <100 nm. Chapter 3 in the book deals with this issue. In essence, the successful AM of these novel-structured amorphous and nanocrystalline materials is attributed to the unique non-equilibrium metallurgical nature of laser irradiation.

Another important feature that is intrinsic to AM-processed components is the microstructural difference, both in grain size and structure, between the bottom and top of a part along laser deposition direction. Hofmeister et al.'s research [167] has focused on grain size variations in LMD-processed 316 stainless steel and H13 tool steel powder. The microstructural scale at the bottom of 316 parts, where conductive cooling is highest, is 4.2–4.8 μm. Above the base ($z>4$ mm) the average increases to 5.4 μm. At the bottom of H13 parts the mean microstructural scale is 4.8–6.4 μm, and near the top ($z=20$ mm) the average is 7.4 μm. Wu et al.'s work [165] on LMD of β-Ti alloy also reveals that there is a tendency for coarsening of β grains in the re-heated region near the top of previously processed layer. Towards the top of the part, the β grains coarsen throughout the whole of each layer, as the whole region remains hot. Therefore, the occurrence of grain coarsening is due to: (i) considerable remelting of the top of previous layer; and (ii) long-term thermal accumulation. Basically, the different thermal histories of different layers of the part lead to variation of microstructures along the height direction, as the conduction, convection, and radiation conditions change.

Microstructural features of AM-processed components are significantly influenced by the processing parameters applied. Mazumder et al. have performed a comparative study on microstructures of DMD-processed H13 tool steel using two extreme processing conditions [31]. At a high specific energy combined with a high material deposition rate, the solidifying material is held at a higher temperature for a longer time and, therefore, the local temperature gradients are smaller. In this case, the grains are coarsened and mostly equiaxed, approximately 10–16 μm across. In contrast, a considerably fine microstructure is formed in the DMD part, as a lower specific energy and a smaller material addition rate are settled. A lower specific energy is realized by using a faster traverse speed in this case and, therefore, there is no sufficient time for the laser to have any annealing effect on the material. Furthermore, the profile of the molten pool becomes narrow at a higher speed and, accordingly, the local temperature gradients are enhanced throughout the whole cladding pass, producing the columnar grains within the majority of DMD part. Layer thickness is another major factor in determining the microstructures of DMD components. Its influence is dependent on other parameters, e.g., power, velocity, specific energy, and powder mass flow rate. As the specific energy is lowered, thinner layer thickness is required, because there is less energy per unit area to melt powder. The coarsening of microstructures normally occurs as the applied layer thickness increases, due to a decrease in the cooling rate [31]. Furthermore, Hofmeister et al.

[167] have confirmed that the microstructural scale of LMD parts is more sensitive to variations in z height (i.e., layer thickness) than to changes in laser power and scan speed, due to the predominance of heat conduction condition of the substrate on cooling rate and resultant microstructures.

2.3.3 Mechanical Properties and Performance Aspects of AM-Processed Parts

2.3.3.1 Densification Level

The densification level is a fundamental property that determines other mechanical behaviors of AM-processed components. As revealed in Tables 2.2–2.4, near full density components made from metals, alloys, and blended/composite powders can presently be fabricated under the optimized processing conditions, especially by LM/LMD based on a full melting mechanism. As a general rule, a proper increase in the applied laser energy density leads to higher part density, as confirmed in Kruth et al.'s work on LM of Ti–6Al–4 V [60] (Fig. 2.22). Nevertheless, for an excessive energy input, the presence of overheated liquid with a too low viscosity may aggravate balling effect and thermal stress, hence inducing porosity/cracks formation [12]. The suitable processing window for a material and process combination is normally very narrow, making it difficult to optimize the processing conditions. AM is a complicated shaping process, which follows a process routine from a "line" to a "layer" and then to a "bulk". AM starts with a single line scanning, introducing two main parameters, i.e., laser power (P) and scan speed (v). The completion of multiple scan lines produces a layer. Here, another parameter, i.e., hatch spacing (h), is involved. The layer-by-layer consolidation yields a bulk component, which requires a suitable layer thickness (d) to be determined. The individual P, v, h, and d all have great influence on densification of powder and, meanwhile, these parameters are inter-affected. In order to evaluate the combined effect of these parameters and, thus, improve the controllability of AM process, an integrated factor termed "volumetric laser energy density" (VED) is defined:

$$\mathrm{VED} = \frac{P}{vhd}(\mathrm{kJ/mm^3}) \tag{2.5}$$

The author's work on LS of Cu–CuSn–CuP powder reveals that setting VED of ~0.16–~0.23 kJ/mm^3 favors a better yield of high-density parts [170]. Simchi [22], Hopkinson et al. [171], and Hao et al. [172] have also applied the VED to integrally control energy input and melting mechanism during LS/LM of Fe-based powders, which have demonstrated efficiency in achieving a high densification response.

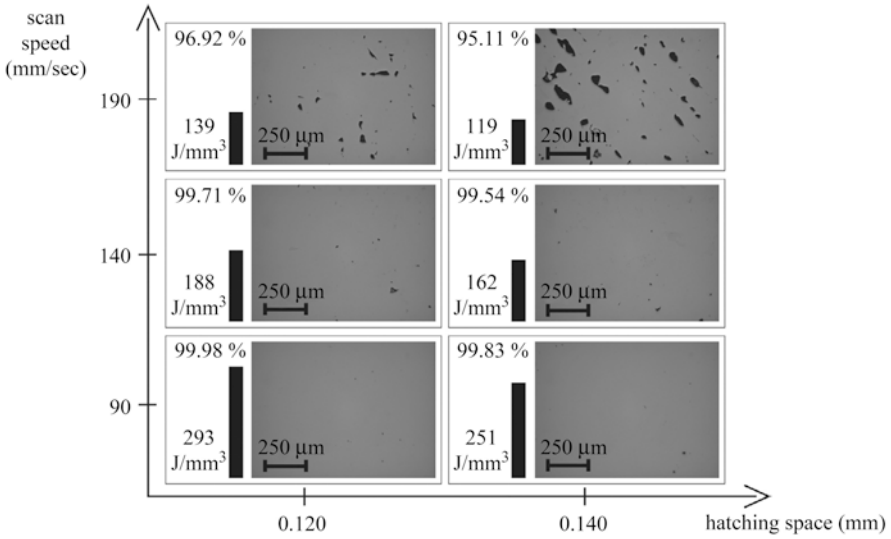


Fig. 2.22 Parameter study for part density and microstructure of LM-processed Ti–6Al–4 V, see Ref. [60]

2.3.3.2 Residual Stress and Strength

In general, residual stresses are considerably large in layer-by-layer fabricated AM parts. Theoretical and experimental studies by Kruth et al. [173] have disclosed that the residual stress profile consists of two zones of large tensile stresses at the top and bottom of a LS/LM-processed part, and a large zone of intermediate compressive stress in between. The magnitude and shape of the residual stress profile depend on: (i) the geometric height of the part; (ii) the material properties; and (iii) laser scanning strategy and processing conditions.

The elastic modulus and coefficient of thermal expansion (CTE) are two most important material properties that determine the level of residual stresses. The stresses can be controlled by using material with a low CTE [135]. Also, for MMCs parts, a reasonable selection of the ceramic reinforcement which has a similar CTE as the matrix metal is preferred [157]. Furthermore, phase transformation may be detrimental or beneficial with respect to residual stresses. Normally, the formation of brittle phases during AM may promote stress cracking, whereas some controlled phase transformations may have the potential to reduce or eliminate stresses and deformation. For instance, in carbon steels the martensitic transformation leads to a volume increase that can reach a large value of 4 % [11], so that the natural shrinkage that takes place during liquid phase processing is compensated by the material expansion after phase transformation. Nevertheless, further systematic studies are still required to quantify the role of phase transformations in stress control for AM-processed metallic components.

On the other hand, care should be taken to optimize laser processing conditions to control residual stresses. For LS/LM process, the laser scanning strategy that is being used to melt the powder has a significant influence on the residual stresses being developed. Normally, the stresses are larger perpendicular to the scan direction than along the scan direction [173]. A subdivision of the surface in smaller sectors leads to a lower stress value. A scanning geometry with short raster lines is recommended. Also, the preheating of the substrate favors a reduction of the residual stress level, due to a decreased temperature gradient [174]. For the DMD/LMD process, Mazumder et al. [83] have obtained some important understanding of stress generation and accumulation. It is found that the tool path location is a critical factor for the management of residual stress and resultant distortion. Normally, locations deposited during the last path show residual compressive stress, since they are not stress-relieved. The other locations are deposited in earlier paths and are subsequently stress-relieved, showing negligible residual stress.

Residual stress accumulation induced by rapid cooling and uncontrolled phase transformations may result in stress cracking and interlayer/interface debonding. Normally, the cracks in AM-produced components can be divided into microscopic and macroscopic cracks. The microscopic cracks are typically formed during rapid solidification, which accordingly belong to the hot cracking. Their formation is ascribed to the interruption of liquid film at grain boundaries in the solidification temperature range, due to the action of the tensile stress [99]. The macroscopic cracks are normally regarded as cold cracking. The combined influence of the low ductility of the material itself and the stress-induced part deformation accounts for their propagation. The formation of microscopic and macroscopic cracks, especially the latter, significantly lowers the dimensional accuracy, ductility, and strength of AM-fabricated components. As revealed in Table 2.3, LM/LMD-processed Ti-based parts have mechanical properties that are equivalent or superior to the wrought counterparts. However, for Ni-based and Fe-based alloys, postprocessing such as HIP and furnace annealing/strengthening is required to favor stress relief and/or microcrack healing, in order to realize a substantial improvement in the final properties. Nevertheless, Zhao et al.'s work [77] reveals that the large macroscopic cracks cannot be completely healed and eliminated through diffusion bonding during heat treatment.

2.3.3.3 Hardness and Wear Performance

Hardness is a commonly investigated mechanical property for almost all AM-processed components (Tables 2.2–2.4). In most cases, the hardness of laser-processed materials is superior to conventional PM or casting materials. On the premise of a sufficiently high densification without the formation of cracks, the remaining of a reasonable level of residual stresses in laser-processed components favors the enhancement of hardness [155]. Associated with hardness property, recent researches start to study the wear and tribology performance of AM-processed components. Kruth et al. [175] have investigated the wear behavior of prealloyed tool steel produced by LS/LM, showing that AM technique is capable of offering excellent

surface wear properties. The densification level of AM-processed parts has a fundamental influence on wear performance. Better wear resistance is obtained for fully dense components. In order to further enhance the hardness and wear property of unreinforced metals and alloys, ceramic reinforcement is introduced to prepare MMCs components using AM. In Ramesh et al.'s work [176], the microhardness and wear rate of LS-processed SiC/Fe MMCs respectively show ~1.7-fold increase and ~66.7% decrease upon the unreinforced Fe. Mazumder et al. [177] have reported the *in situ* synthesis of Fe−Cr−C−W MMCs using DMD process which leads to the development of a suitable alternate for cobalt bearing wear resistant alloys. Setting specific energy input of 9.447 kJ/cm^2 and preheating temperature at ~500 °C produces the best possible combination of wear and hardness properties and the microstructure is comprised of MC, M_7C_3 and M_6C types of carbides with ferrite matrix. The author's recent work [157] has applied LM to prepare *in situ* TiC/Ti_5Si_3 MMCs with novel reinforcement architecture. The uniformly dispersed TiC reinforcement has a unique network distribution and a near nanoscale dendritic morphology. The *in situ* TiC/Ti_5Si_3 MMCs have a considerably low friction coefficient and a reduced wear rate. The high wear resistance is attributed to the formation of adherent and strain-hardened tribolayer on the worn surface during sliding. Detailed results are presented in Chap. 4 of this book.

2.3.4 Structure/Property Stability of AM-Processed Parts

Since AM production involves a long-term line-by-line and layer-by-layer localized material deposition, the main laser processing parameters, especially the focused beam size and output laser power, will inevitably exhibit a certain fluctuation. Under the combined influence of the periodic change in laser scanning pattern, a significant thermodynamic instability may be generated in the molten pool and the melt inside. Furthermore, the protective atmosphere in the sealed processing chamber, due to the continuous release of metal vapor and/or gas impurity from the melted powder, changes significantly, particularly during the long-time AM process for large-sized components. Consequently, AM-processed metals, alloys, and MMCs parts may have the structural differences and properties instability, hence influencing their practical application reliance [178]. Nevertheless, a comprehensive understanding of material design, process control, and metallurgical mechanisms for various AM processes, as systemically presented in this review, hopefully helps to overcome the structure/property instability of AM-fabricated metallic components.

2.4 Summary

Researches on laser-based AM of metallic components, as reviewed in the present chapter, are interdisciplinary, integrating materials science, metallurgical engineering, mechanical engineering, and laser technology. Significant research and

understanding are still required in the aspects of materials preparation and characterization, process control and optimization, and theories of physical and chemical metallurgy for each AM process. The key points of this chapter are summarized as follows:

1. The current status of research and development in laser based AM of end-use metallic components, including metals, alloys, and MMCs are reviewed, with particular emphasis on strategies of powder materials design and laser process control. The classification of currently prevailing AM processes for metallic components and the operative consolidation mechanisms are clarified.
2. The ever-reported metallic materials used for AM, both commercially available and experimentally developed powders are classified, and the associated bonding and densification mechanisms during laser AM are proposed.
3. An in-depth review of the materials aspects of laser based AM processes, including physical aspects of materials for AM, microstructural/mechanical properties of AM-processed parts, and structure/property stability of AM-fabricated parts, is presented. The dependence of these microstructural/mechanical properties on material/process parameters is elucidated.
4. The comprehensive relationship among material, process, and metallurgical mechanism of various laser based AM processes is established in this chapter.

References

1. Zhu HH, Lu L, Fuh JYH (2003) Development and characterisation of direct laser sintering Cu-based metal powder. J Mater Process Technol 140:314–317
2. Mumtaz K, Hopkinson N (2009) Top surface and side roughness of Inconel 625 parts processed using selective laser melting. Rapid Prototyping J 15(2):96–103
3. Mazumder J, Dutta D, Kikuchi N, Kikuchi N (2000) Closed loop direct metal deposition: art to part. Opt Laser Eng 34(4–6):397–414
4. Griffith ML, Keicher DM, Atwood CL et al (1996) Free form fabrication of metallic components using laser engineered net shaping (LENS^{TM}). Proceeding 7th Symp. on solid freeform fabrication, The University of Texas at Austin, Austin, TX, USA
5. Milewski JO, Lewis GK, Thoma DJ et al (1998) Directed light fabrication of a solid metal hemisphere using 5-axis powder deposition. J Mater Process Technol 75(1–3):165–172
6. Fischer P, Romano V, Blatter A et al (2005) Highly precise pulsed selective laser sintering of metallic powders. Laser Phys Lett 2(1):48–55
7. Schleifenbaum H, Meiners W, Wissenbach K et al (2010) Individualized production by means of high power selective laser melting. CIRP J Manuf Sci Technol 2(3):161–169
8. Kaiser T, Albrecht GJ (2007) Industrial disk lasers for micro material processing—compact reliable systems conquer the market. Laser Techn J 4(3):54–57
9. Agarwala M, Bourell D, Beaman J et al (1995) Direct selective laser sintering of metals. Rapid Prototyping J 1(1):26–36
10. Das S, Beaman JJ, Wohlert M, et al (1998) Direct laser freeform fabrication of high performance metal components. Rapid Prototyping J 4(3):112–117
11. Simchi A, Petzoldt F, Pohl H (2001) Direct metal laser sintering: material considerations and mechanisms of particle bonding. Int J Powder Metall 37(2):49–61

12. Kruth JP, Levy G, Klocke F et al (2007) Consolidation phenomena in laser and powder-bed based layered manufacturing. CIRP Ann—Manuf Technol 56(2):730–759
13. Simchi A, Pohl H (2003) Effects of laser sintering processing parameters on the microstructure and densification of iron powder. Mater Sci Eng A 359(1/2):119–128
14. Kruth JP, Froyen L, Rombouts M et al (2003) New ferro powder for selective laser sintering of dense parts. CIRP Ann—Manuf Technol 52(1):139–142
15. Zhu HH, Lu L, Fuh JYH (2004) Influence of binder's liquid volume fraction on direct laser sintering of metallic powder. Mater Sci Eng A 371(1/2):170–177
16. Niu HJ, Chang HIT (1998) Liquid phase sintering of M3/2 high speed steel by selective laser sintering. Scr Mater 39(1):67–72
17. Agarwala M, Bourell D, Beaman J et al (1995) Post-processing of selective laser sintered metal parts. Rapid Prototyping J 1(2):36–44
18. Das S, Wohlert M, Beaman JJ et al (1999) Processing of titanium net shapes by SLS HIP. Mater Des 20(2–3):115–121
19. Kumar S, Kruth JP (2007) Effect of bronze infiltration into laser sintered metallic parts. Mater Des 28(2):400–407
20. Kruth JP, Mercelis P, Van Vaerenbergh J et al (2005) Binding mechanisms in selective laser sintering and selective laser melting. Rapid Prototyping J 11(1):26–36
21. Liu JX, Ryneson ML (2006) Blended powder solid supersolidus liquid phase sintering. U.S. Patent 7070734 B 2
22. Simchi A (2006) Direct laser sintering of metal powders: mechanism, kinetics and microstructural features. Mater Sci Eng A 428(1/2):148–158
23. Niu HJ, Chang ITH (2000) Selective laser sintering of gas atomized M2 high speed steel powder. J Mater Sci 35(1):31–38
24. Fukuda A, Takemoto M, Saito T, et al (2011) Osteoinduction of porous Ti implants with a channel structure fabricated by selective laser melting. Acta Biomater 7(5):2327–2336
25. Buchbinder D, Wissenbach K (2008) Additive manufacturing of aluminum components with minimal distortion. Fraunhofer ILT annual report, Fraunhofer ILT, Aachen, Germany
26. Becker D, Wissenbach K (2009) Additive manufacturing of copper components. Fraunhofer ILT annual report, Fraunhofer ILT, Aachen, Germany
27. Tolochko NK, Arshinov MK, Gusarov AV et al (2003) Mechanisms of selective laser sintering and heat transfer in Ti powder. Rapid Prototyping J 9(5):314–326
28. Tolochko NK, Mozzharov SE, Yadroitsev IA et al (2004) Balling processes during selective laser treatment of powders. Rapid Prototyping J 10(2):78–87
29. Shiomi M, Osakada K, Nakamura K et al (2004) Residual stress within metallic model made by selective laser melting process. CIRP Ann—Manuf Technol 53(1):195–198
30. Pogson S, Fox P, O'Neill W et al (2004) The direct metal laser remelting of copper and tool steel powders. Mater Sci Eng A 386(1/2):453–459
31. Mazumder J, Schifferer A, Choi J (1999) Direct materials deposition: designed macro and microstructure. Mater Res Innovat 3(3):118–131
32. Koch J, Mazumder J (2000) Apparatus and methods for monitoring and controlling multilayer laser cladding, U.S. Patent 6122564
33. Mazumder J, Morgan D, Skszek TW et al (2010) Direct metal deposition apparatus utilizing rapid-response diode laser source, U.S. Patent 7765022
34. Dutta B, Singh V, Natu H et al (2009) Direct metal deposition. Adv Mater Process 167(3):29–31
35. Dutta B, Palaniswamy S, Choi J et al (2011) Additive manufacturing by direct metal deposition. Adv Mater Process 169(5):33–36
36. Hammeke AW (1988) Laser spray nozzle and method, U.S. Patent 4724299
37. Mudge RP, Wald NR (2007) Laser engineered net shaping advances additive manufacturing and repair. Weld J 86(1):44–48
38. Zhong M, Liu W (2010) Laser surface cladding: the state of the art and challenges. Proc Inst Mech Eng C 224 (C5): 1041–1060
39. The POM Group Inc. http://www.pomgroup.com

40. Mazumder J (2000) A crystal ball view of direct-metal deposition. JOM 52(12):28–29
41. Shin KH, Natu H, Dutta D et al (2003) A method for the design and fabrication of heterogeneous objects. Mater Des 24(5):339–353
42. Schwendner KI, Banerjee R, Collins PC et al (2001) Direct laser deposition of alloys from elemental powder blends. Scr Mater 45(10):1123–1129
43. Banerjee R, Collins PC, Bhattacharyya D et al (2003) Microstructural evolution in laser deposited compositionally graded a/b titanium-vanadium alloys. Acta Mater 51(11):3277–3292
44. Liu WP, Dupont JN (2003) In-situ reactive processing of nickel aluminides by laser-engineered net shaping. Metall Mater Trans A 34(11):2633–2641
45. Collins PC, Banerjee R, Banerjee S et al (2003) Laser deposition of compositionally graded titanium-vanadium and titanium-molybdenum alloys. Mater Sci Eng A 352(1/2):118–128
46. Mazumder J (2009) Direct metal deposition: process control, properties and applications. THERMEC' 2009 Presentation, Berlin, Germany
47. Wang L, Felicelli S, Gooroochurn Y et al (2008) Optimization of the LENS® process for steady molten pool size. Mater Sci Eng A 474(1/2):148–156
48. Yu J, Lin X, Wang JJ et al (2010) Mechanics and energy analysis on molten pool spreading during laser solid forming. Appl Surf Sci 256(14):4612–4620
49. Hofmeister W, Wert M, Smugeresky J et al (1999) Investigating solidification with the laser-engineered net shaping (LENS™) process. JOM 51(7). http://www.tms.org/pubs/journals/JOM/9907/Hofmeister/Hofmeister-9907.html
50. Zheng B, Zhou Y, Smugeresky JE et al (2008) Thermal behavior and microstructural evolution during laser deposition with laser-engineered net shaping: part I. Numerical calculations. Metall Mater Trans A 39(9):2228–2236
51. Zheng B, Zhou Y, Smugeresky JE et al (2008) Thermal behavior and microstructure evolution during laser deposition with laser-engineered net shaping: part II. Experimental investigation and discussion. Metall Mater Trans A 39(9):2237–2245
52. Xiong YH, Smugeresky JE, Schoenung JM (2009) The influence of working distance on laser deposited WC-Co. J Mater Process Technol 209(10):4935–4941
53. Gill D Laser engineered net shaping. http://www.sandia.gov/mst/pdf/LENS.pdf
54. Griffith ML, Schlienger ME, Harwell LD et al (1999) Understanding thermal behavior in the LENS process. Mater Des 20(2/3):107–133
55. Pratt P, Felicelli SD, Wang L et al (2008) Residual stress measurement of laser-engineered net shaping AISI 410 thin plates using neutron diffraction. Metall Mater Trans A 39(13):3155–3163
56. Wang L, Felicelli SD, Pratt P (2008) Residual stresses in LENS-deposited AISI 410 stainless steel plates. Mater Sci Eng A 496(1/2):234–241
57. He X, Mazumder J (2007) Transport phenomena during direct metal deposition. J Appl Phys 101(5):053113
58. He X, Yu G, Mazumder J (2010) Temperature and composition profile during double-track laser cladding of H13 tool steel. J Phys D: Appl Phys 43(1):015502
59. Fischer P, Leber H, Romano V et al (2004) Microstructure of near-infrared pulsed laser sintered titanium samples. Appl Phys A 78(8):1219–1227
60. Vandenbroucke B, Kruth JP (2007) Selective laser melting of biocompatible metals for rapid manufacturing of medical parts. Rapid Prototyping J 13(4):196–203
61. Krishna BV, Bose S, Bandyopadhyay A (2007) Low stiffness porous Ti structures for load-bearing implants. Acta Biomater 3(6):997–1006
62. Balla VK, Bodhak S, Bose S et al (2010) Porous tantalum structures for bone implants: fabrication, mechanical and in vitro biological properties. Acta Biomater 6(8):3349–3359
63. Santos EC, Osakada K, Shiomi M et al (2004) Microstructure and mechanical properties of pure titanium models fabricated by selective laser melting. Proc Inst Mech Eng C 218(7):711–719
64. Laoui T, Santos E, Osakada K et al (2006) Properties of titanium dental implant models made by laser processing. Proc Inst Mech Eng C 220(6):857–863

65. Pogson SR, Fox P, Sutcliffe CJ et al (2003) The production of copper parts using DMLR. Rapid Prototyping J 9(5):334–343
66. Khan M, Dickens P (2010) Selective laser melting (SLM) of pure gold. Gold Bull 43(2):114–121
67. Dinda GP, Song L, Mazumder J (2008) Fabrication of Ti-6Al-4 V scaffolds by direct metal deposition. Metall Mater Trans A 39(12):2914–2922
68. Jauer L, Meiners W. Manufacturing individual titanium implants using selective laser melting. http://www.ilt.fraunhofer.de/en/publication-and-press/annual-report/2010/annual-report-2010-p111.html
69. Hollander DA, von Walter M, Wirtz T et al (2006) Structural, mechanical and in vitro characterization of individually structured Ti-6Al-4 V produced by direct laser forming. Biomaterials 27(7):955–963
70. Wu X, Sharman R, Mei J et al (2004) Microstructure and properties of a laser fabricated burn-resistant Ti alloy. Mater Des 25(2):103–109
71. Tian XJ, Zhang SQ, Li A et al (2010) Effect of annealing temperature on the notch impact toughness of a laser melting deposited titanium alloy Ti-4Al-1.5Mn. Mater Sci Eng A 527(7/8):1821–1827
72. Yadroitsev I, Thivillon L, Bertrand Ph et al (2007) Strategy of manufacturing components with designed internal structure by selective laser melting of metallic powder. Appl Surf Sci 254(4):980–983
73. Yadroitsev I, Pavlov M, Bertrand Ph et al (2009) Mechanical properties of samples fabricated by selective laser melting. Proceeding 14th Eur. Conf. on Rapid Prototyping and Manufacturing, Paris, France
74. Mumtaz KA, Erasenthiran P, Hopkinson N (2008) High density selective laser melting of Waspaloy®. J Mater Process Technol 195(1–3):77–87
75. Dinda GP, Dasgupta AK, Mazumder J (2009) Laser aided direct metal deposition of inconel 625 superalloy: microstructural evolution and thermal stability. Mater Sci Eng A 509(1/2):98–104
76. Zhao XM, Chen J, Lin X et al (2008) Study on microstructure and mechanical properties of laser rapid forming Inconel 718. Mater Sci Eng A 478(1/2):119–124
77. Zhao XM, Lin X, Chen J et al (2009) The effect of hot isostatic pressing on crack healing, microstructure, mechanical properties of Rene88DT superalloy prepared by laser solid forming. Mater Sci Eng A 504(1/2):129–134
78. Li J, Wang HM (2010) Microstructure and mechanical properties of rapid directionally solidified Ni-base superalloy Rene'41 by laser melting deposition manufacturing. Mater Sci Eng A 527(18/19):4823–4829
79. Morgan R, Sutcliffe CJ, O'Neill W (2004) Density analysis of direct metal laser re-melted 316L stainless steel cubic primitives. J Mater Sci 39(4):1195–1205
80. Yadroitsev I, Bertrand Ph, Smurov I (2007) Parametric analysis of the selective laser melting process. Appl Surf Sci 253(19):8064–8069
81. Xie JW, Fox P, O'Neill W et al (2005) Effect of direct laser re-melting processing parameters and scanning strategies on the densification of tool steels. J Mater Process Technol 170(3):516–523
82. Simchi A, Asgharzadeh H (2004) Densification and microstructural evaluation during laser sintering of M2 high speed steel powder. Mater Sci Technol 20(11):1462–1468
83. Mazumder J, Choi J, Nagarathnam K et al (1997) The direct metal deposition of H13 tool steel for 3-D components. JOM 49(5):55–60
84. Bhattacharya S, Dinda GP, Dasgupta AK et al (2011) Microstructural evolution of AISI 4340 steel during direct metal deposition process. Mater Sci Eng A 528(6):2309–2318
85. Xue Y, Pascu A, Horstemeyer MF (2010) Microporosity effects on cyclic plasticity and fatigue of LENS™-processed steel. Acta Mater 58(11):4029–4038
86. Zheng B, Zhou Y, Smugeresky JE et al (2009) Processing and behavior of Fe-based metallic glass components via laser-engineered net shaping. Metall Mater Trans A 40(5):1235–1245

87. Singh SS, Roy D, Mitra R et al (2009) Studies on laser sintering of mechanically alloyed $Al_{50}Ti_{40}Si_{10}$ composite. Mater Sci Eng A 501(1/2):242–247
88. Brandl E, Heckenberger U, Holzinger V et al (2012) Additive manufactured AlSi10Mg samples using selective laser melting (SLM): microstructure, high cycle fatigue, and fracture behavior. Mater Des 34: 159–169
89. Louvis E, Fox P, Sutcliffe CJ (2011) Selective laser melting of aluminium components. J Mater Process Technol 211(2):275–284
90. Janaki Ram GD Esplin CK Stucker BE (2008) Microstructure and wear properties of LENS® deposited medical grade CoCrMo. J Mater Sci 19(5):2105–2111
91. Xue CF, Dai Y, Tian XL (2006) Laser engineered net shaping of Co-based superalloys. Trans Nonferr Met Soc Chin 16: S1982–S1985
92. Becker D, Meiners W, Wissenbach K (2009) Additive manufacturing of copper alloys by selective laser melting. Lasers in manufacturing (LiM 2009), Munich, Germany
93. Bhattacharya S, Dinda GP, Dasgupta AK et al (2011) Microstructural evolution and mechanical, and corrosion property evaluation of Cu-30Ni alloy formed by direct metal deposition process. J Alloy Compd 509(22):6364–6373
94. Xue WC, Krishna BV, Bandyopadhyay A et al (2007) Processing and biocompatibility evaluation of laser processed porous titanium. Acta Biomater 3(6):1007–1018
95. Boccalini M, Goldenstein H (2001) Solidification of high speed steels. Int Mater Rev 46(2):92–115
96. Facchini L, Magalini E, Robotti P et al (2010) Ductility of a Ti-6Al-4 V alloy produced by selective laser melting of prealloyed powders. Rapid Prototyping J 16(6):450–459
97. Li YM, Yang H, Lin X et al (2003) The influences of processing parameters on forming characterizations during laser rapid forming. Mater Sci Eng A 360(1/2):18–25
98. Paul CP, Ganesh P, Mishra SK et al (2007) Investigating laser rapid manufacturing for Inconel-625 components. Opt Laser Technol 39(4):800–805
99. Zhong ML, Sun HQ, Liu WJ et al (2005) Boundary liquation and interface cracking characterization in laser deposition of Inconel 738 on directionally solidified Ni-based superalloy. Scr Mater 53(2):159–164
100. Das S (2003) Physical aspects of process control in selective laser sintering of metals. Adv Eng Mater 5(10):701–711
101. Wright CS, Youseffi M, Akhtar SP et al (2006) Selective laser melting of prealloyed high alloy steel powder beds. Mater Sci Forum 514–516: 516–523
102. Childs THC, Hauser C, Badrossamay M (2005) Selective laser sintering (melting) of stainless and tool steel powders: experiments and modeling. Proc Inst Mech Eng B 219(4):339–357
103. Yadroitsev I, Shishkovsky I, Bertrand P et al (2009) Manufacturing of fine-structured 3D porous filter elements by selective laser melting. Appl Surf Sci 255(10):5523–5527
104. Zhu HH, Lu L, Fuh JYH (2006) Study on shrinkage behaviour of direct laser sintering metallic powder. Proc Inst Mech Eng B 220(2):183–190
105. Simchi A, Petzoldt F, Pohl H (2003) On the development of direct metal laser sintering for rapid tooling. J Mater Process Technol 141(3):319–328
106. Simchi A, Pohl H (2004) Direct laser sintering of iron-graphite powder mixture. Mater Sci Eng A 383(2):191–200
107. Wang Y, Bergström J, Burman C (2006) Characterization of an iron-based laser sintered material. J Mater Process Technol 172(1):77–87
108. Zhu HH, Fuh JYH, Lu L (2003) Formation of Fe-Cu metal parts using direct laser sintering. Proc Inst Mech Eng C 217(1):139–147
109. Kruth JP, Kumar S, Van Vaerenbergh J (2005) Study of laser-sinterability of ferro-based powders. Rapid Prototyping J 11(5):287–292
110. Kruth JP, Froyen L, Van Vaerenbergh J et al (2004) Selective laser melting of iron-based powder. J Mater Process Technol 149(1–3):616–622
111. Rombouts M, Kruth JP, Froyen L et al (2006) Fundamentals of selective laser melting of alloyed steel powders. CIRP Ann—Manuf Technol 55(1):187–192

112. Chen XC, Xie JW, Fox P (2004) Direct laser remelting of iron with addition of boron. Mater Sci Technol 20(6):715–719
113. Gu DD, Shen YF, Fang SQ et al (2007) Metallurgical mechanisms in direct laser sintering of Cu-CuSn-CuP mixed powder. J Alloys Compd 438(1/2):184–189
114. Lin X, Yue TM, Yang HO et al (2009) Phase evolution in laser rapid forming of compositionally graded Ti-Ni alloys. J Eng Mater Technol—Trans ASME 131(4):041002
115. Gao F, Wang HM (2008) Effect of TiNi in dry sliding wear of laser melt deposited Ti2Ni/TiNi alloys. Mater Charact 59(9):1349–1354
116. Gao F, Wang HM (2008) Dry sliding wear property of a laser melting/deposited Ti2Ni/TiNi intermetallic alloy. Intermetallics 16(2):202–208
117. Qu HP, Wang HM (2007) Microstructure and mechanical properties of laser melting deposited g-TiAl intermetallic alloys. Mater Sci Eng A 466(1/2):187–194
118. Gu DD, Shen YF, Lu ZJ (2009) Microstructural characteristics and formation mechanism of direct laser-sintered Cu-based alloys reinforced with Ni particles. Mater Des 30(6):2099–2017
119. Wang Y, Bergström J, Burman C (2006) Four-point bending fatigue behaviour of an iron-based laser sintered material. Int J Fatigue 28(12):1705–1715
120. Lin X, Yue TM, Yang HO et al (2006) Microstructure and phase evolution in laser rapid forming of a functionally graded Ti-Rene88DT alloy. Acta Mater 54(7):1901–1915
121. Zhang FY, Chen J, Tan H et al (2009) Composition control for laser solid forming from blended elemental powders. Opt Laser Technol 41(5):601–607
122. Sircar S, Ribaudo C, Mazumder J (1989) Laser-clad Ni70Al20Cr7Hf3 alloys with extended solid solution of Hf: part I. Microstructure evolution. Metall Trans A 20(11):2267–2277
123. Xue Y, Wang HM (2009) Microstructure and dry sliding wear resistance of CoTi intermetallic alloy. Intermetallics 17(3):89–97
124. Dong LX, Wang HM (2008) Microstructure and corrosion properties of laser-melted deposited Ti2Ni3Si/NiTi intermetallic alloy. J Alloy Compd 465(1/2):83–89
125. Xue Y, Wang HM (2008) Microstructure and properties of Ti-Co-Si ternary intermetallic alloys. J Alloy Compd 464(1/2):138–145
126. Gui YL, Wang HM (2007) Microstructure and dry sliding wear resistance of Mo_{ss}-toughened Mo_2Ni_3Si metal silicide alloys. Int J Refract Met Hard Mater 25(5/6):433–439
127. Fang YL, Tang HB, Wang HM (2006) A wear resistant ductile metal-toughened $Cr_{13}Ni_5Si_2$ ternary metal silicide alloy. Intermetallics 14(7):750–758
128. Liu Y, Wang HM (2005) Microstructure and high-temperature sliding wear property of Co_{ss}/Co_3Mo_2Si metal silicide alloys. Mater Sci Eng A 396(1/2):240–250
129. Suryanarayana C (2001) Mechanical alloying and milling. Prog Mater Sci 46(1/2):1–184
130. Wang XC, Laoui T, Bonse J et al (2002) Direct selective laser sintering of hard metal powders: experimental study and simulation. Int J Adv Manuf Technol 19(5):351–357
131. Kumar S (2009) Manufacturing of WC-Co moulds using SLS machine. J Mater Process Technol 209(8):3840–3848
132. Gläser T (2005) Laser sintering of tungsten carbide with cobalt binder phases, Fraunhofer IPT annual report, Fraunhofer IPT, Aachen, Germany
133. Xiong YH, Smugeresky JE, Ajdelsztajn L et al (2008) Fabrication of WC-Co cermets by laser engineered net shaping. Mater Sci Eng A 493(1/2):261–266
134. Picas JA, Xiong Y, Punset M et al (2009) Microstructure and wear resistance of WC-Co by three consolidation processing techniques. Int J Refract Met Hard Mater 27(2):344–349
135. Gåård A, Krakhmalev P, Bergström J (2006) Microstructural characterization and wear behavior of (Fe,Ni)-TiC MMC prepared by DMLS. J Alloys Compd 421(1/2):166–171
136. Srinivasa CK, Ramesh CS, Prabhakar SK (2010) Blending of iron and silicon carbide powders for producing metal matrix composites by laser sintering process. Rapid Prototyping J 16(4):258–267
137. Ghosh SK, Saha P, Kishore S (2010) Influence of size and volume fraction of SiC particulates on properties of ex situ reinforced Al-4.5Cu-3Mg metal matrix composite prepared by direct metal laser sintering process. Mater Sci Eng A 527(18/19):4694–4701

138. Simchi A, Godlinski D (2008) Effect of SiC particles on the laser sintering of Al-7Si-0.3Mg alloy. Scr Mater 59(2):199–202
139. Stucker BE, Bradley WL, Eubank PT et al (1999) Manufacture and use of ZrB_2/Cu or TiB_2/Cu composite electrodes, U.S. Patent 5933701
140. Sun CN, Baldridge T, Gupta MC (2009) Fabrication of ZrB_2-Zr cermet using laser sintering technique. Mater Lett 63(28):2529–2531
141. Xiong Y, Kim M, Seo O et al (2010) (Ti,W)C-Ni cermets by laser engineered net shaping. Powder Metall 53(1):41–46
142. Zheng B, Topping T, Smugeresky JE et al (2010) The influence of Ni-coated TiC on laser-deposited IN625 metal matrix composites. Metall Mater Trans A 41(3):568–573
143. Zheng B, Smugeresky JE, Zhou Y et al (2008) Microstructure and properties of laser-deposited Ti6Al4V metal matrix composites using Ni-coated powder. Metall Mater Trans A 39(5):1196–1205
144. Liu WP, DuPont JN (2004) Fabrication of carbide-particle-reinforced titanium aluminide-matrix composites by laser-engineered net shaping. Metall Mater Trans A 35(3):1133–1140
145. Liu D, Zhang SQ, Li A et al (2010) High temperature mechanical properties of a laser melting deposited TiC/TA15 titanium matrix composite. J Alloys Compd 496(1/2):189–195
146. Balla VK, DeVasConCellos PD, Xue WC et al (2009) Fabrication of compositionally and structurally graded Ti-TiO2 structures using laser engineered net shaping (LENS). Acta Biomater 5(5):1831–1837
147. Walker JC, Berggreen KM, Jones AR et al (2009) Fabrication of Fe-Cr-Al oxide dispersion strengthened PM2000 alloy using selective laser melting. Adv Eng Mater 11(7):541–546
148. Tjong SC, Ma ZY (2000) Microstructural and mechanical characteristics of *in situ* metal matrix composites. Mater Sci Eng R 29(3/4):49–113
149. Choi J, Mazumder J (1994) Non-equilibrium synthesis of Fe-Cr-C-W alloy by laser cladding. J Mater Sci 29(17):4460–4476
150. Zhong ML, Xu XY, Liu WJ et al (2004) Laser synthesizing NiAl intermetallic and TiC reinforced NiAl intermetallic matrix composite. J Laser Appl 16(3):160–166
151. Banerjee R, Genç A, Collins PC et al (2004) Comparison of microstructural evolution in laser-deposited and arc-melted In-Situ Ti-TiB composites. Metall Mater Trans A 35(7):2143–2152
152. Banerjee R, Genç A, Hill D et al (2005) Nanoscale TiB precipitates in laser deposited Ti-matrix composites. Scr Mater 53(12):1433–1437
153. Wang F, Mei J, Wu X (2008) Direct laser fabrication of Ti6Al4V/TiB. J Mater Process Technol 195(1–3):321–326
154. Gu DD, Shen YF, Meng GB (2009) Growth morphologies and mechanisms of TiC grains during selective laser melting of Ti-Al-C composite powder. Mater Lett 63(29):2536–2538
155. Gu DD, Meiners W (2010) Microstructure characteristics and formation mechanisms of *in situ* WC cemented carbide based hardmetals prepared by selective laser melting. Mater Sci Eng A 527(29/30):7585–7592
156. Gu DD, Shen YF, Lu ZJ (2009) Preparation of TiN-Ti_5Si_3 in-situ composites by selective laser melting. Mater Lett 63(18/19):1577–1579
157. Gu DD, Hagedorn YC, Meiners W et al (2011) Selective laser melting of in-situ TiC/Ti_5Si_3 composites with novel reinforcement architecture and elevated performance. Surf Coat Technol 205(10):3285–3292
158. Tolochko NK, Laoui T, Khlopkov YV et al (2000) Absorptance of powder materials suitable for laser sintering. Rapid Prototyping J 6(3):155–161
159. Gusarov AV, Kruth JP (2005) Modelling of radiation transfer in metallic powders at laser treatment. Int J Heat Mass Trans 48(16):3423–3434
160. Fischer P, Romano V, Weber HP et al (2003) Sintering of commercially pure titanium powder with a Nd:YAG laser source. Acta Mater 51(6):1651–1662
161. Takamichi I, Roderick ILG (eds) (1993) The physical properties of liquid metals. Clarendon Press, Oxford

162. Niu HJ, Chang ITH (1999) Instability of scan tracks of selective laser sintering of high speed steel powder. Scr Mater 41(11):1229–1234
163. Gu DD, Shen YF (2007) Balling phenomena during direct laser sintering of multi-component Cu-based metal powder. J Alloy Compd 432(1/2):163–166
164. Gu DD, Shen YF (2009) Balling phenomena in direct laser sintering of stainless steel powder: metallurgical mechanisms and control methods. Mater Des 30(8):2903–2910
165. Wu X (2007) A review of laser fabrication of metallic engineering components and of materials. Mater Sci Technol 23(6):631–640
166. Das M, Balla VK, Basu D et al (2010) Laser processing of SiC-particle-reinforced coating on titanium. Scr Mater 63(4):438–441
167. Hofmeister W, Griffith M, Ensz M et al (2001) Solidification in direct metal deposition by LENS processing. JOM 53(9):30–34
168. Pinkerton AJ, Li L (2003) The effect of laser pulse width on multiple-layer 316L steel clad microstructure and surface finish. Appl Surf Sci 208–209:411–416
169. Gu DD, Meiners W, Hagedorn YC et al (2010) Bulk-form TiC_x/Ti nanocomposites with controlled nanostructure prepared by a new method: selective laser melting. J Phys D: Appl Phys 43(29):295–301
170. Gu DD, Shen YF, Yang JL et al (2006) Effects of processing parameters on direct laser sintering of multicomponent Cu based metal powder. Mater Sci Technol 22(12):1449–1455
171. Hopkinson N, Majewski CE, Zarringhalam H (2009) Quantifying the degree of particle melt in Selective Laser Sintering®. CIRP Ann—Manuf Technol 58(1):197–200
172. Hao L, Dadbakhsh S, Seaman O et al (2009) Selective laser melting of a stainless steel and hydroxyapatite composite for load-bearing implant development. J Mater Process Technol 209(17):5793–5801
173. Mercelis P, Kruth JP (2006) Residual stresses in selective laser sintering and selective laser melting. Rapid Prototyping J 12(5):254–265
174. Hagedorn YC, Wilkes J, Meiners W et al (2010) Net shaped high performance oxide ceramic parts by selective laser melting. Phys Proced 5:587–594
175. Kumar S, Kruth JP (2008) Wear performance of SLS/SLM materials. Adv Eng Mater 10(8):750–753
176. Ramesh CS, Srinivas CK, Channabasappa BH (2009) Abrasive wear behaviour of laser sintered iron-SiC composites. Wear 267(11):1777–1783
177. Choi J, Choudhuri SK, Mazumder J (2000) Role of preheating and specific energy input on the evolution of microstructure and wear properties of laser clad Fe-Cr-C-W alloys. J Mater Sci 35(13):3213–3219
178. Wang HM, Zhang SQ, Wang XM (2009) Progress and challenges of laser direct manufacturing of large titanium structural components. Chin J Lasers 36(12):3204–3209

Chapter 3
Novel Ti-Based Nanocomposites by Selective Laser Melting (SLM) Additive Manufacturing (AM): Tailored Nanostructure and Performance

Abstract Selective laser melting (SLM) additive manufacturing (AM) process was used to produce nanocrystalline TiC-reinforced Ti matrix bulk-form nanocomposites. The influences of laser energy density on densification activity, microstructural feature, nanohardness, and wear behavior of SLM-processed parts were comprehensibly studied to improve the controllability SLM process of nanomaterials. The TiC reinforcement in SLM-processed nanocomposites typically had a unique nanoscale lamellar structure, which was distinctly different from the initial particulate morphology before SLM. Reasonable physical mechanisms and conditions for the formation of TiC nanostructure reinforcing phase during SLM process were proposed. The microstructural and mechanical properties of SLM-processed TiC/Ti nanocomposite parts were sensitive to the preparation method of the starting nanocomposite powder and the content of TiC nanoparticles. The optimally processed TiC/Ti nanocomposite parts by SLM demonstrated the significantly elevated microhardness and wear performance as relative to the unreinforced Ti parts.

3.1 Introduction

Titanium (Ti) and its alloys, due to high specific strength, sufficient stiffness, and excellent corrosion resistance, have been widely used in the aeronautical, chemical, and biomedical industries [1, 2]. However, the limited wear resistance of Ti is a serious concern for the application environments where abrasive and erosion phenomena exist [3]. Considerable research attempts, accordingly, have focused on the application of various surface modification techniques to prepare ceramic particle reinforced Ti matrix composites (TMCs) coatings to improve surface properties of Ti. In particular, laser processing methods such as laser melt injection [4], laser cladding [5], and laser surface alloying [6] have demonstrated a considerable efficiency in preparing high-performance TMCs coatings. Laser processing normally offers high heating/cooling rates (10^3–10^8 K/s) for the development of nonequilibrium phases with fine-grained microstructures and novel properties [1]. Furthermore, TMCs have been realized as bulk-form components, typically through powder metallurgy (PM) [7] and casting [8] methods, and afford more significant advantages in industrial applications.

© Springer-Verlag Berlin Heidelberg 2015

D. Gu, *Laser Additive Manufacturing of High-Performance Materials,*
DOI 10.1007/978-3-662-46089-4_3

For conventional particle reinforced TMCs, either as coatings or in bulk form, the micrometer-scale ceramic particles such as SiC [9], TiB [5], and WC [10] are commonly used, varying from a few micrometers to several tens of micrometers. These relatively large-sized ceramic reinforcing particles are normally unmelted or partially melted during conventional processing. However, due to a considerably poor wettability between ceramics and metals, the interfacial bonding ability between the remaining ceramic particles and metal matrix is generally limited, especially as the larger sized ceramic particles are used. The weak ceramic/metal interfaces are prone to crack during mechanical loading, resulting in a premature failure of TMCs [11].

It is widely recognized that the ceramic particle size has a strong effect on strength, ductility, and failure mode of TMCs. Generally, decreasing the ceramic particle size can lead to a substantial improvement in mechanical properties of TMCs, e.g., the enhanced strengthening and reduced interfacial cracking [12]. Recent research attempts have ascertained that the mechanical performance of TMCs can be further enhanced by decreasing the size of ceramic particles from micrometer to nanometer level [13]. Such materials are termed as nanocomposites [14]. A nanocomposite is known as a multiphase solid material where one of the phases has at least one dimension of less than 100 nm [15]. Nanocomposites differ from conventional composites due to the particularly high surface-to-volume ratio of ceramic reinforcement. The interface between matrix and reinforcement is typically an order of magnitude greater than conventional composites [16]. Such a large amount of reinforcement surface area means that a relatively small amount of nanoscale reinforcement can have a significant effect on the integrated properties of nanocomposites. A nanoscale dispersion of ceramic phase with controlled nanostructures in TMCs tends to introduce novel behaviors that are absent in the unreinforced Ti.

To obtain desired properties of nanocomposite TMCs, especially in bulk form, the sufficiently high-densification response of TMCs is of primary importance. On the other hand, in bulk parts condensed from ultrafine nanopowders, the uncontrolled agglomeration of nanoparticles due to a considerably large van der Waals attractive force may result in microstructural inhomogeneity and even disappearance of original nanostructures. More seriously, differential stresses that develop as a result of nonuniform microstructures are directly related to the propagation of internal cracks in consolidated bodies. Therefore, following a more microscopic criterion, the nanoscale ceramic reinforcement must avoid grain coarsening during processing and, meanwhile, distribute uniformly throughout the matrix. It appears desirable to process bulk-form nanocomposites by such a method that can enhance the deagglomeration and dispersion level of the strongly interacting nanoparticles.

As presented in Chap. 2, selective laser melting (SLM), as a newly developed additive manufacturing (AM) technique, exhibits a promising potential for creating three-dimensional nanocomposite components with any complex configurations directly from nanopowders. The application of SLM in production of nanocomposite parts is expected to create new technological opportunities, because of the potential for developing novel nanocomposites with unique microstructural and mechanical properties. Since SLM is performed based on a complete melting/solidification met-

allurgical mechanism, it can be regarded, in a broad sense, as a bottom-up method starting with atoms to form nanostructures. Nevertheless, due to a complex physical nature of SLM that involves multiple modes of heat, mass, and momentum transfer induced by a dynamic laser scanning [17], the unpredictability or uncontrollability of the formation of nanostructures in SLM route remains a major challenge. Significant research efforts are required to study how the nanostructures of ceramic reinforcement are crystallized and developed during SLM. A detailed understanding of the atom-level formation mechanism that dominates during the crystallization of nanostructures is necessary. Furthermore, the underlying role of microstructural development in the variation of mechanical properties of SLM-processed nanocomposite parts should be determined.

In this chapter, the bulk-form TiC/Ti nanocomposites with unique nanostructures of reinforcement were successfully prepared by SLM. The microstructural evolutions under different powder material properties and SLM processing conditions were studied and the mechanical properties such as densification rate, microhardness, and wear resistance were assessed, with an aim to establish a relationship of material, process, microstructure, and mechanical performance of nanocomposite TMCs by SLM AM method.

3.2 Preparation of TiC/Ti Nanocomposite Powder for SLM

In the present chapter, the TiC/Ti nanocomposite powder used for SLM was prepared by the following two different methods. It is known that the flowability of the powder is of primary importance for the powder bed-based SLM process, which further requires that the powder particles have the uniform structure and size distribution. The powder preparation conditions were carefully optimized to tailor the particle morphology, particle size, and powder flowability.

- First kind of TiC/Ti nanocomposite powder—Prepared by ball milling of micron-sized TiC and Ti powders

The starting powder components included 99.7 % purity TiC powder with an irregular shape and a mean particle size of 1.5 μm (Fig. 3.1a) and 99.9 % purity Ti powder with an irregular structure and an average particle size of 45 μm (Fig. 3.1b). The TiC and Ti constituents were mixed according to a weight ratio of 15:85. Ball milling of TiC/Ti mixture was performed in a Fritsch Pulverisette 6 high-energy planetary mono-mill. The stainless steel grinding balls and the powder mixture to be ground were charged into a hardened chromium steel grinding bowl, with the ball-to-powder weight ratio of 10:1. Before the formal powder preparation, one batch of TiC/Ti powder was premilled in the grinding bowl with the grinding balls for 2 h, in order to clean the grinding media and decrease the iron or other contamination. The whole powder handling and milling process was under the protection of argon atmosphere to decrease the detrimental influence of oxygen and nitrogen. The rotation speed

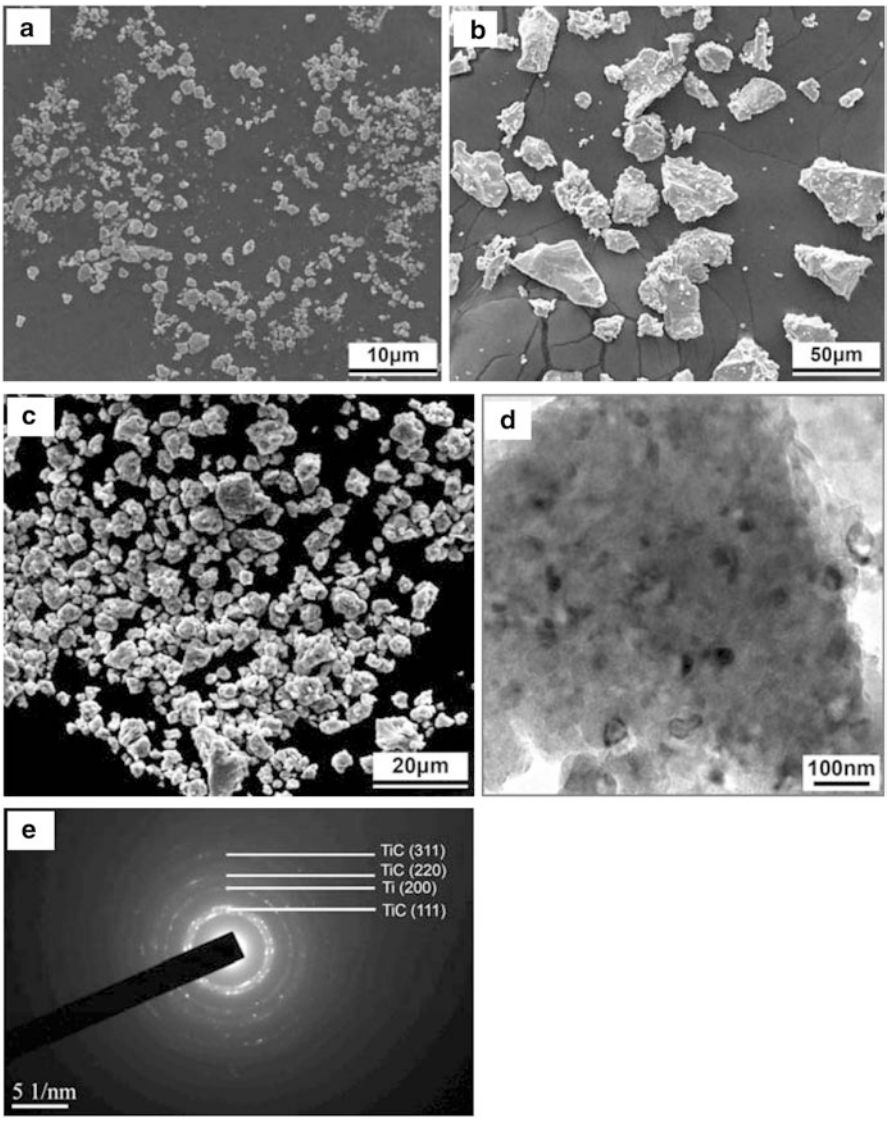


Fig. 3.1 Preparation of the 1st kind of TiC/Ti nanocomposite powder by ball milling: The starting micron-sized TiC (**a**) and Ti (**b**) powder (scanning electron microscope, SEM); (**c**) Ball-milled TiC/Ti composite powder particles (SEM); (**d**) TEM micrograph showing the dispersion of TiC nanopartilces within the interior Ti matrix; (**e**) SADP showing the existence of TiC and Ti constitution phases

of the main disc was fixed at 250 rpm and the milling time was optimized at 10 h. In order to avoid excessive temperature rise within the grinding bowl, 20 min ball milling was followed by 10 min interval. The milled TiC/Ti composite powder had a flattened and angular structure and a uniform particle size distribution, with an

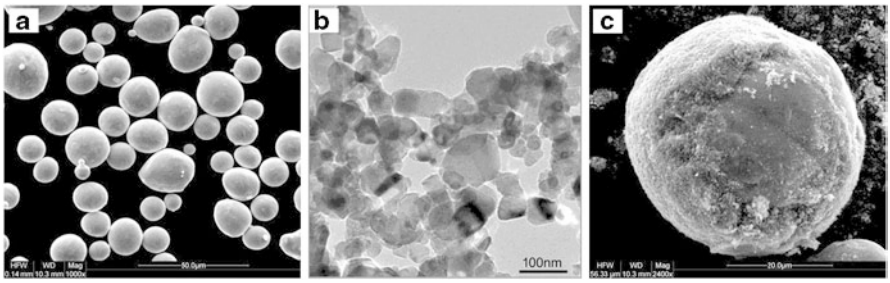


Fig. 3.2 Preparation of the 2nd kind of TiC/Ti nanocomposite powder by directly mechanical mixing: The starting micron-sized Ti powder (SEM) (**a**) and nanoscale TiC powder (TEM) (**b**); (**c**) Uniformly mixed nano-TiC/Ti nanocomposite powder (SEM)

average value of 5.8 μm (Fig. 3.1c). The selected area diffraction pattern (SADP) of the milled powder revealed the existence of TiC and Ti constitution phases (Fig. 3.1e). The bright field transmission electron microscopy (TEM) micrograph showed that the ultrafine nanoscale TiC particulates with a mean size below 50 nm were dispersed uniformly throughout the Ti matrix (Fig. 3.1d), thus confirming the formation of TiC_p/Ti nanocomposite powder after ball milling preparation.

- Second kind of TiC/Ti nanocomposite powder—Prepared by directly mechanical mixing of TiC nanopowder and micron-sized Ti powder

The 99.0 % purity TiC nanopowder with a spherical shape and a mean particle size of 50 nm (Fig. 3.2a) and the 99.7 % purity Ti powder with a spherical shape and an average particle diameter of 22.5 μm (Fig. 3.2b) were used. The TiC/Ti nanocomposite powder systems consisting of 7.5–22.5 wt.% TiC nanoparticles were mechanically mixed in a Fritsch Pulverisette 4 vario-planetary mill. The rotational speeds of supporting disc and grinding bowls were adjusted at 200 rpm and −250 rpm, respectively, and the mixing duration was settled at 4 h. The ultrafine TiC nanoparticles were dispersed uniformly around Ti particles surface after the mechanical mixing process (Fig. 3.2c). Different to the ball milling process, the powder particles did not experience the apparent deformation and structural change during the mixing process. The spherical Ti powder particles were accordingly used in this study, in order to obtain a sound flowability of the mixed TiC_p/Ti nanocomposite powder.

3.3 General Introduction of Experimental Setup and Processing Procedures of SLM Work in This Book

The SLM apparatus, as schematically depicted in Fig. 3.3a, was used to produce the specimens for microstructures and mechanical properties tests, with the typical computer-aided design (CAD) model shown in Fig. 3.3b. The SLM equipment consisted mainly of a laser as an energy source, a scanner system, an automatic powder layering mechanism, an inert argon gas protection system, and a computer system

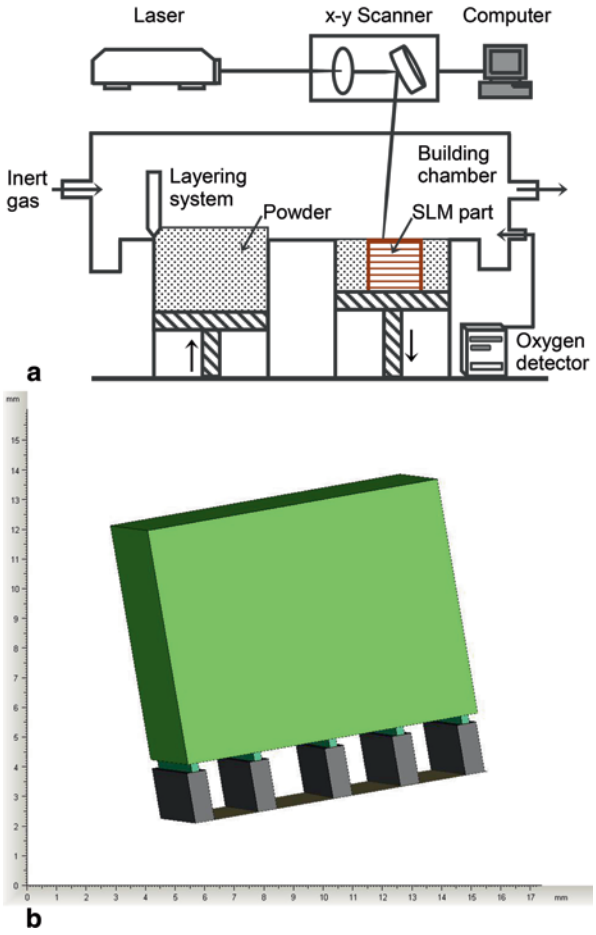


Fig. 3.3 Schematic of SLM apparatus (**a**); CAD model of parts to be built (**b**)

for process control. For the laser AM research work as presented in this book, the following three types of lasers were applied:

- A continuous-wave (CW) YLR-200 Ytterbium fiber laser ($\lambda = 1.064$ μm) with a power of ~200 W and a spot size of 70 μm;
- A CW Nd:YAG laser ($\lambda = 1.064$ μm) with a ~200 μm top-hat spot and a ~150 W power;
- A CW 2000SM Gaussian CO_2 laser ($\lambda = 10.6$ μm) with a power of ~2000 W and a spot size of 300 μm.

The real-time SLM process is illustrated in Fig. 3.4. Firstly, a polished metal substrate was fixed on the building platform and leveled. The building chamber was then sealed and the argon gas with an outlet pressure of 30 mbar was fed inside. The resultant oxygen content decreased below 10 ppm. Afterward, a thin layer of the powder with a thickness of 30–50 μm was deposited on the substrate by the layering

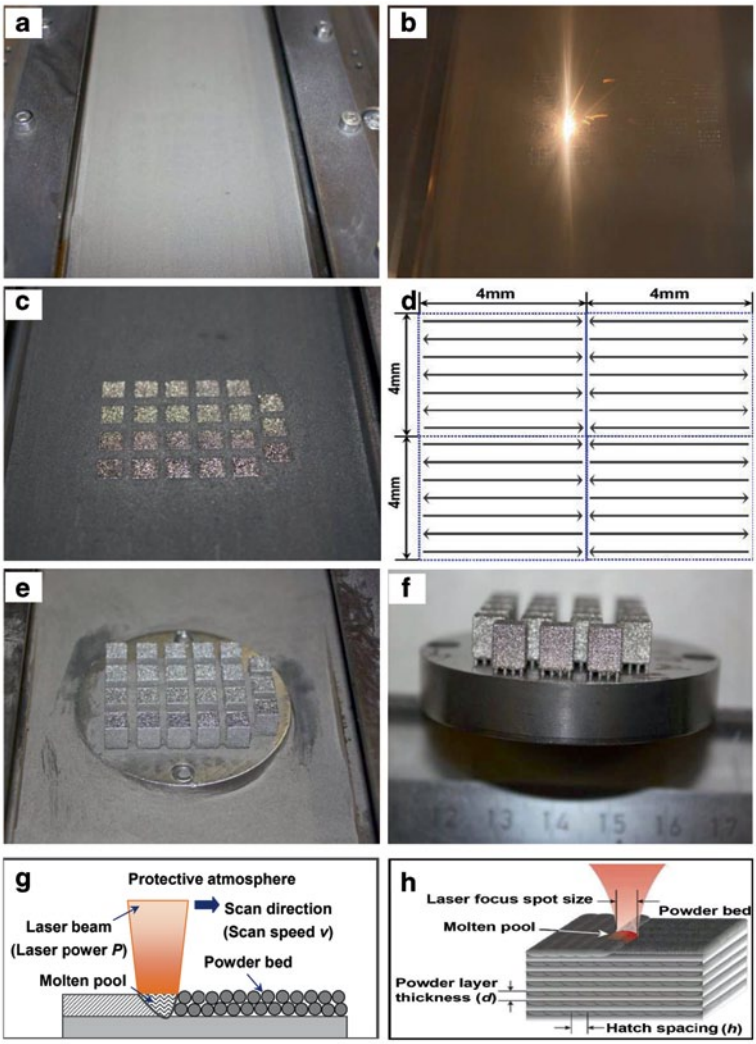


Fig. 3.4 SLM procedures for fabricating bulk-form parts: (**a**) Powder spreading on powder bed; (**b**) Interaction of laser beam with powder layer; (**c**) Surface of laser-processed layer; (**d**) Parts on powder bed after SLM; (**e**) Schematic of laser scanning pattern; (**f**) The finally completed, cleaned parts. SLM processing parameters involved in single line scanning (**g**) and multiple lines and multiple layers scanning (**h**), see Ref. [18, 19]

mechanism (Fig. 3.4a). The laser beam then scanned the powder bed surface to form a two-dimensional profile according to the CAD data of the specimens (Fig. 3.4b and c). Laser scanning of each layer was based on a sector scanning manner, as shown in Fig. 3.4d. The interior borders of each sector, 4 mm × 4 mm in dimensions, were parallel to the edges of parts. A simple linear raster scanning was performed within each sector, with a scan vector length of 4 mm and a hatching spacing of

50 μm. The above mentioned process was repeated and the specimens were built in a layer-by-layer manner until the completion (Fig. 3.4e). The number of layers that were added on the substrate was 160. The cubic specimens with dimensions of $8 \times 8 \times 8$ mm were prepared (Fig. 3.4f). During SLM process of this TiC/Ti nanocomposite powder using the fiber laser or Nd:YAG laser, the laser powers (P) of 90–140 W and the scan speeds (v) of 0.1–0.6 m/s were changed periodically by SLM control program.

SLM additive manufacturing is a complicated free-form shaping process, which follows a process routine from a "line" to a "layer" and subsequently, to a "bulk". SLM starts with a single line scanning, thus introducing two main parameters, i.e., laser power (P) and scan speed (v), as indicated in Fig. 3.4g. The completion of multiple scan lines leads to the formation of a two-dimensional layer. Here, another parameter, i.e., hatching spacing (h), is involved. The layer-by-layer bonding and consolidation yield a bulk-form component, which requires a suitable powder layer thickness (d) to be determined, as revealed in Fig. 3.4h.

In order to assess the combined effect of P and v involved in the individual line scanning, an integrated parameter, i.e., "linear laser energy density" (LED) with a unit of joule/meter (J/m), is defined to estimate the laser energy input to the powder layer being melted:

$$\mathrm{LED} = \frac{P}{v}. \tag{3.1}$$

Furthermore, the processing parameters P, v, h, and d all have influence on the densification, microstructural features, and mechanical properties of the final SLM-processed three-dimensional parts. In order to evaluate the combined effect of these parameters and, thus, control the SLM process integrally, another single factor termed "volumetric laser energy density" (VED) with a unit of joule/millimeter^3 (J/mm^3) is defined as follows:

$$\mathrm{VED} = \frac{P}{vhd}. \tag{3.2}$$

3.4 General Introduction of Experimental Procedures and Methods for Microstructures and Mechanical Properties Tests in This Book

3.4.1 Metallographic Specimen Preparation and Examination

3.4.1.1 Preparation of Metallographic Specimens of Laser-processed Parts

After the SLM process, the specimens were cut from the substrate using a spark-erosion wire cutting machine. The samples were then ground and polished according to the standard procedures for the metallographic specimen preparation and

examination. The samples were successively ground with finer and finer SiC paper as the abrasive media. After grinding the specimen, polishing was performed. The woven polishing cloths were employed to produce a scratch-free mirror finish, free from smearing or pull-outs remaining from the metallographic preparation process.

3.4.1.2 Determination of Densification Response of Laser-processed Parts

The density (ρ) of the SLM-processed specimens was defined as mass divided by volume. The mass of the specimens was measured by the analytical balance and the volume of the specimens was determined using the Archimedes' method. Archimedes' principle shows that the apparent weight of an object immersed in a liquid decreases by an amount equal to the weight of the volume of the liquid that it displaces. Since 1 ml of water has a mass almost exactly equal to 1 g if the object is immersed in water, the difference between the two masses (in grams) will equal (almost exactly) the volume (in ml) of the object weighed [20]. The experimental determination of the mass and the volume of an object allows us to calculate the density. The densification behavior and low-magnification metallographic microstructures of the samples, e.g., micropores, microcracks, defects of inclusion, etc., were further observed using an Olympus PMG3 optical microscope (OM).

3.4.2 Characterization of Constitutional Phases, Microstructural Features, and Chemical Compositions

For the microstructural characterization work on the SLM-processed samples as presented in this book, the following analytical methods were used:

3.4.2.1 X-Ray Diffractometer (XRD) Analysis

The phases of the SLM-processed specimens were identified by a D8 Advance X-ray diffractometer (XRD) with Cu K_α radiation at 40 kV and 40 mA (Bruker AXS GmbH, Karlsruhe, Germany), using a continuous scan mode. For a wide range of $2\theta°$ to be scanned, a quick scan at 4°/min was performed to give a general exhibition of diffraction peaks. If necessary, a slower scan rate of 1°/min was further used over a small range of $2\theta°$ to give a more accurate determination of diffraction peaks.

3.4.2.2 Scanning Electron Microscope (SEM), Atomic Force Microscope (AFM), and Transmission Electron Microscope (TEM) Analysis

The high-magnification microstructural features of laser-processed samples were characterized using a Quanta 200 scanning electron microscope (SEM) (FEI

Company, Hillsboro, OR, USA) in a secondary electron mode at an accelerating voltage of 20 kV, an S-4800 field-emission scanning electron microscope (FE-SEM) (Hitachi, Tokyo, Japan) in a secondary electron mode at 3 kV, or a SPI3800 atomic force microscope (AFM) (Seiko Instruments Inc., Japan). The interior crystalline microstructures of SLM-processed samples were investigated using a Tecnai G^2 20 S-TWIN transmission electron microscope (TEM) (FEI Company, Hillsboro, OR, USA). The selected area diffraction pattern (SADP) of the interior grains was studied to acquire the exact phase/crystal structures.

3.4.2.3 Energy Dispersive X-ray Spectroscope (EDX) and X-ray Photoelectron Spectroscopy (XPS) Analysis

Chemical compositions of laser-processed samples were determined by an EDAX Genesis energy dispersive X-ray spectroscope (EDX) (EDAX Inc., Mahwah, NJ, USA), using a super-ultra thin window sapphire detector. An X-ray photoelectron spectroscopy (XPS) (AXIS Ultra DLD, Kratos Analytical Ltd, Manchester, UK) was used to determine the X-ray photoelectron spectra of samples, in order to identify the exact substances/compounds in the laser-processed samples. The acquisition parameters were as follows: source type Al K_α, spot size 500 μm, pass energy 20.0 eV, and energy step size 0.10 eV. The identification of peaks was performed by reference to the standard XPS database as provided by the X-ray Photoelectron Spectroscopy Database (Version 3.5) (National Institute of Standards and Technology NIST, Gaithersburg, MD, USA).

3.4.3 Mechanical Properties Testing

For the SLM-processed materials as presented in this book, the following mechanical properties were studied:

3.4.3.1 Hardness

The Vickers hardness of laser-processed samples was determined using a MicroMet 5101 microhardness tester (Buehler GmbH, Düsseldorf, Germany) at a load of 0.1–0.3 kg and an indentation time of 15–20 s. Nanoindentation tests on the polished sections of laser-processed parts were performed using a DUH-W201S nanoindentation tester (Shimadzu Corporation, Japan) at room temperature. A loading–unloading test mode was used and a test force of 100 mN, a loading speed of 1.3239 mN/s, and a hold time of 10 s were settled, respectively. In measurements, the load and indentation depth were displayed. The raw data were then used to construct loading–unloading plots. The hardness was defined as a ratio of the peak

indentation load (F_{max}) to the projected area of hardness impression (A_c). The dynamic nanohardness (H_d) was calculated by [21]:

$$H_d = \frac{F_{max}}{A_c} = \frac{F_{max}}{26.43h_c^2} \tag{3.3}$$

where h_c was the contact depth under the maximum indentation load. The reduced elastic modulus (E_r) was calculated from the unloading curve using [21]:

$$E_r = \frac{\sqrt{\pi}}{2} \cdot \frac{S}{\sqrt{A_c}} \tag{3.4}$$

where S was the slope of the unloading curve at the maximum displacement point. The most widely used procedure of extracting information from nanoindentation tests has been developed by Oliver and Pharr [21], based on the assumption of elasticity of the material. In this study, the Oliver–Pharr method was applied to calculate h_c, S, and hence H_d and E_r.

3.4.3.2 Wear/Tribological Performance

Based on the ASTM G99 standard, the wear/tribological properties of the SLM-processed specimens were estimated by the dry sliding wear tests conducted in a HT-500 ball-on-disk tribometer (Lanzhou ZhongKe KaiHua Science & Technology Co., Ltd., China) in air at room temperature, using a test load of 230 g. The counterface material was GCr15 bearing steel ball with a diameter of 3 mm and a mean hardness of HRC 60. The friction unit was rotated at a speed of 560 rpm for 10–30 min, with the rotation radius of 2 mm. The coefficient of friction (COF) of the specimens was recorded during wear tests. The wear volume (V) of specimens was calculated by:

$$V = \frac{M_{loss}}{\rho} \tag{3.5}$$

where M_{loss} was the weight loss of the sample after wear test and ρ was the density of the sample. The wear rate (ω) was identified by:

$$\omega = \frac{V}{WL} \tag{3.6}$$

where W was the contact load applied in the test and L was the sliding distance.

3.4.3.3 Tensile Properties

The SLM-processed samples were cut using the spark-erosion wire cutting machine to prepare standard specimens for tensile tests, according to the standard GB/T228–2010. The tensile direction was parallel to the SLM-processed layers. Uniaxial tensile tests were performed at room temperature with a SANS CMT6501 universal testing machine at a strain rate of 1×10^{-4}/s (Shenzhen SANS Testing Machine Co., Ltd. China). The ultimate tensile strength and elongation were determined from the stress–strain curves.

3.5 Influence of SLM Processing Parameters on Densification, Growth Mechanism, and Wear Behavior TiC/Ti Nanocomposite Parts

In the present section, SLM processing of the directly mechanical-mixed TiC/Ti nanocomposite powder containing 15 wt.% TiC nanoparticles (Fig. 3.2) was performed using different "volumetric laser energy density" (VED) of the applied fiber laser, in order to study the influence of SLM parameters on microstructural and mechanical properties of TiC/Ti nanocomposite parts. The feasible SLM processing conditions were accordingly optimized to tailor the favorable nanostructures of reinforcement and resultant elevated wear performance of SLM-processed TiC/Ti nanocomposite parts.

3.5.1 Influence of SLM Parameters on Constitutional Phases

Typical X-ray diffractometer (XRD) patterns of SLM-processed TiC/Ti nanocomposites at various "volumetric laser energy density" (VED) are depicted in Fig. 3.5. The strong diffraction peaks corresponding to Ti (JCPDS Card No. 65-3362) and TiC (JCPDS Card No. 65-8805) were identified, revealing the general formation of TiC-reinforced TMCs at all given VED. A careful comparison of the TiC diffraction peaks at $2\theta = 36.099°$ and 41.927° showed that as the applied VED decreased from 360 J/mm^3 (Fig. 3.5a) to ≤180 J/mm^3 (Fig. 3.5b–d), the TiC diffraction peaks became significantly broadened and weak in the intensity, implying the formation of considerably refined TiC grains in SLM parts processed at the relatively lower VED.

3.5.2 Influences of SLM Parameters on Surface Morphologies and Densification

Figure 3.6 shows characteristic surface morphologies of TiC/Ti nanocomposite parts processed at various SLM conditions. At a relatively low-scan speed (v) and

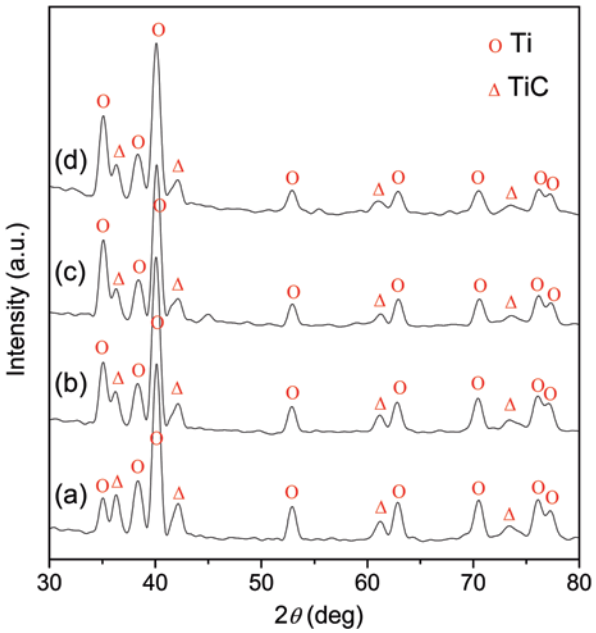


Fig. 3.5 XRD spectra of SLM-processed TiC/Ti nanocomposite parts at different "volumetric laser energy density" (VED): **a** VED = 360 J/mm^3; **b** VED = 180 J/mm^3; **c** VED = 120 J/mm^3; **d** VED = 90 J/mm^3

resultant high-volumetric laser energy density (VED), the surface was considerably smooth and dense and free of any pores (Fig. 3.6a). On decreasing the applied VED by using higher v, although the surface remained entirely dense, it became a bit of rough and a small amount of balls of tens of micrometers appeared on it (Fig. 3.6b and c). At an even lower VED combined with a higher v, large-sized balls with a mean diameter of ~200 μm were observed on the surface, producing a considerable porosity between neighboring balls and scan tracks (Fig. 3.6d).

During SLM, laser scanning is performed line by line and laser energy causes melting along a row of powder particles, forming a continuous liquid track in a cylindrical shape. The diminishing in the surface energy of the cylindrical liquid track is going on until the final equilibrium state. Due to the addition of TiC in the powder, the dissolution of ceramic in Ti liquid tends to enhance the melt viscosity significantly, hence decreasing the overall rheological performance of the composite melt. On the other hand, the dynamic viscosity (μ) of a SLM system with a complete liquid formation is temperature-dependant and can be assessed by [22]:

$$\mu = \frac{16}{15}\sqrt{\frac{m}{kT}}\gamma \tag{3.7}$$

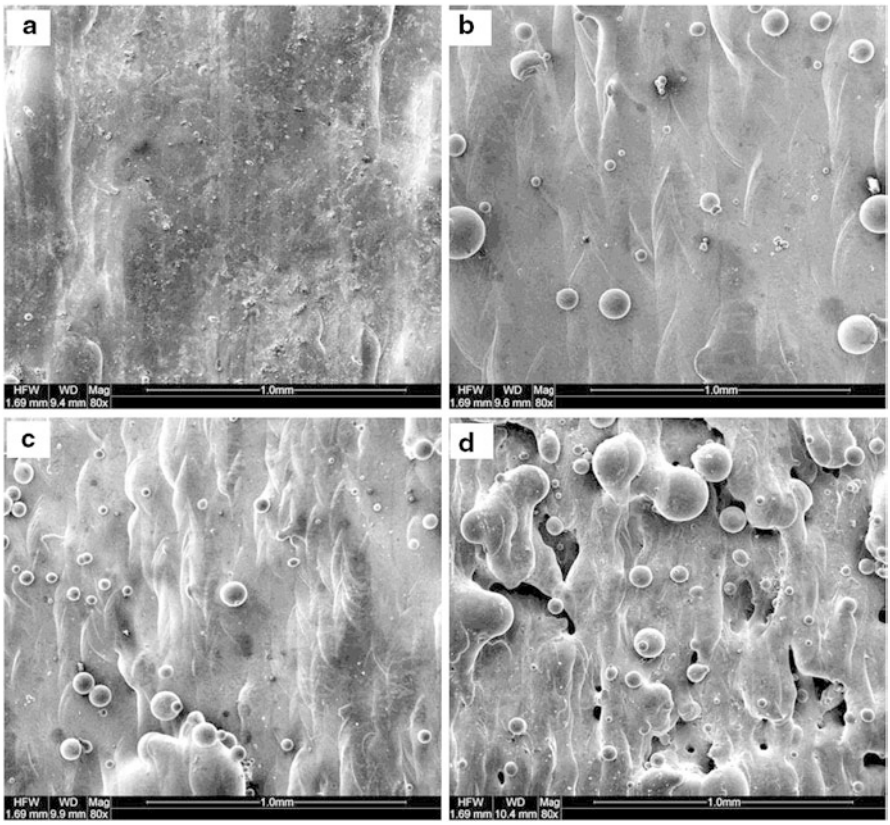


Fig. 3.6 SEM images showing characteristic surface morphologies of SLM-processed parts at different volumetric laser energy densities (VED) and scan speeds (v): **a** VED = 360 J/mm^3, v ED = 360 J**b** VED = 180 J/mm^3, v ED = 180 J**c** VED = 120 J/mm^3, v ED = 120 J**d** VED = 90 J/mm^3, v ED = 90

where m is the atomic mass, k the Boltzmann constant, T the temperature, and γ is the surface tension of the melt. As a lower VED is applied, the operating SLM temperature decreases, which in turn elevates the viscosity of the melt (Eq. 3.7). A high-melt viscosity, which is induced by both material nature and low VED, reduces the wettability and causes the melt to spheroidize rather than flowing across the underlying surface. Meanwhile, an increase in v tends to enhance the localized instability of the melt. The instable liquid track, consequently, breaks up into several agglomerates in a spherical shape to obtain the equilibrium state (Fig. 3.6d), which is termed as "balling" effect.

Laser-induced balling effect is an important factor in influencing the densification response of SLM-processed parts. Figure 3.7 illustrates the changes of relative densities and cross-sectional microstructures of TiC/Ti nanocomposite parts with the applied volumetric laser energy densities (VED). At a relatively high VED $\geq$ 120 J/mm^3, the densification levels of TiC/Ti parts remained steady and were

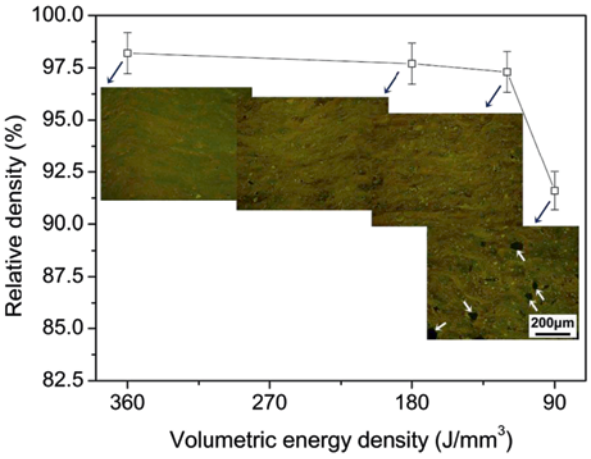


Fig. 3.7 Effect of laser energy density on densification rate of SLM-processed parts. Optical microscope (OM) micrographs of cross-sections of the corresponding parts are included

generally larger than 97%, showing dense cross-sectional microstructures free of apparent interlayer pores. However, as the applied VED decreased to 90 J/mm^3, the densification rate lowered markedly to 91.6% and the large-sized residual pores were present on the cross-section (Fig. 3.7). Such kind of interlayer pores was believed to be caused by the balling effect. Balling effect resulted in the formation of discontinuous scan tracks and large intertrack pores as a current layer was processed (Fig. 3.6d). Furthermore, during layer-by-layer SLM process, balling effect was a severe impediment to a uniform deposition of the fresh powder on the previously processed layer and tended to produce porosity induced by poor interlayer bonding (Fig. 3.7).

3.5.3 Influence of SLM Parameters on Microstructures and Formation Mechanisms

Typical microstructures of SLM-processed TiC/Ti parts at different volumetric laser energy densities (VED) were studied by field emission scanning electron microscope (FE-SEM), as provided in Figs. 3.8 and 3.9. The quantitative elemental analysis by energy dispersive X-ray spectroscope (EDX) revealed that the reinforcing phase formed under various SLM conditions were generally composed of Ti and C elements with an atomic ratio very close to 1:1. Nevertheless, the growth morphology and dispersion state of TiC-reinforcing phase were significantly influenced by the applied VED. At a relatively high VED of 360 J/mm^3, the TiC reinforcement exhibited a uniform network distribution and a dendritic morphology (Fig. 3.8a). The length of dendrite trunk and the average length of dendrite arms reached 9.2 and 1.8 μm, respectively, while the primary arm spacing 0.45 μm was within a submicron scale (Fig. 3.9a). As VED decreased to 180 J/mm^3, the microstructure of TiC reinforcement was further refined (Fig. 3.8b). High-magnification micrographs

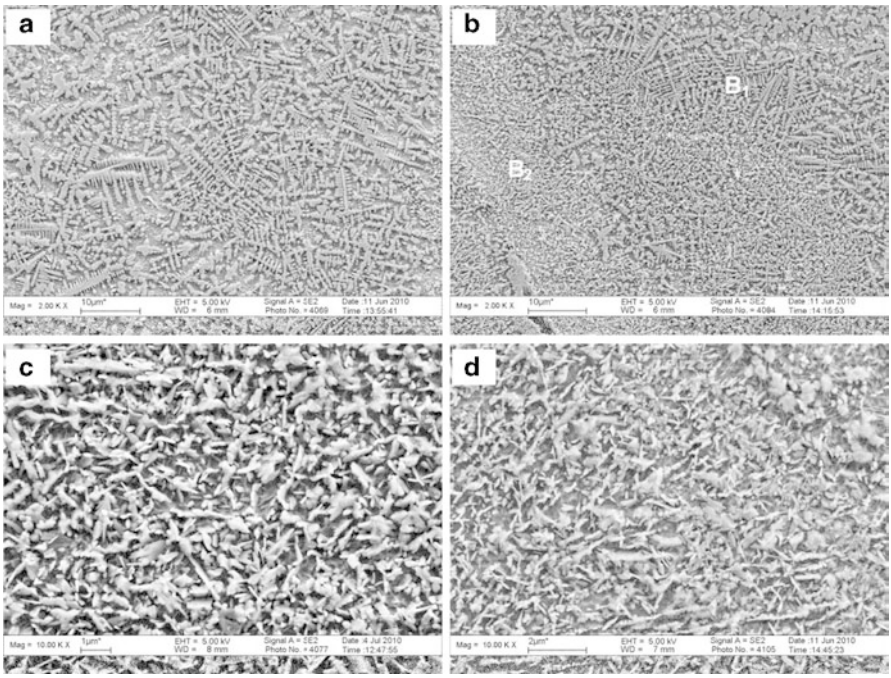


Fig. 3.8 FE-SEM images showing dispersion states of reinforcement in SLM-processed TiC/Ti nanocomposite parts at various volumetric laser energy densities (VED): **a** VED = 360 J/mm^3; **b** VED = 180 J/mm^3; **c** VED = 120 J/mm^3; **d** VED = 90 J/mm^3. In order to obtain suitable micrographs to display the dispersion of nanoscale reinforcement, figures c and d are taken at a higher magnification

revealed that the present TiC typically had two different morphologies. One was the slender dendritic structure having a reduced dendrite trunk length of 6.8 μm, a considerably refined dendrite arm length of 0.7 μm, and a primary arm spacing approaching nanoscale (B_1, Fig. 3.8b and b). The other type of structure consisted of the accumulated TiC whiskers with an average thickness of ~90 nm (B_2, Fig. 3.8b and 3.9c). It is known that nanomaterials can be defined as materials which have structured components with at least one dimension less than 100 nm [16]. Based on this definition, it was reasonable to consider that the standard nanostructured TiC reinforcement started to appear in SLM-processed structure at VED of 180 J/mm^3. Interestingly, as an even lower VED of 120 J/mm^3 was properly settled, a very homogeneous dispersion of the significantly refined TiC reinforcement was achieved (Fig. 3.8c). The TiC typically had a nanoscale lamellar structure, with the mean thickness of ~70 nm (Fig. 3.9d). The microstructural features of the nanostructured TiC reinforcement showed no apparent change as the applied VED further decreased to 90 J/mm^3, although its dispersion uniformity decreased slightly (Fig. 3.8d). It was clear that the TiC reinforcement in SLM-processed composites generally had unique microstructures distinctly different from the initial nanosized

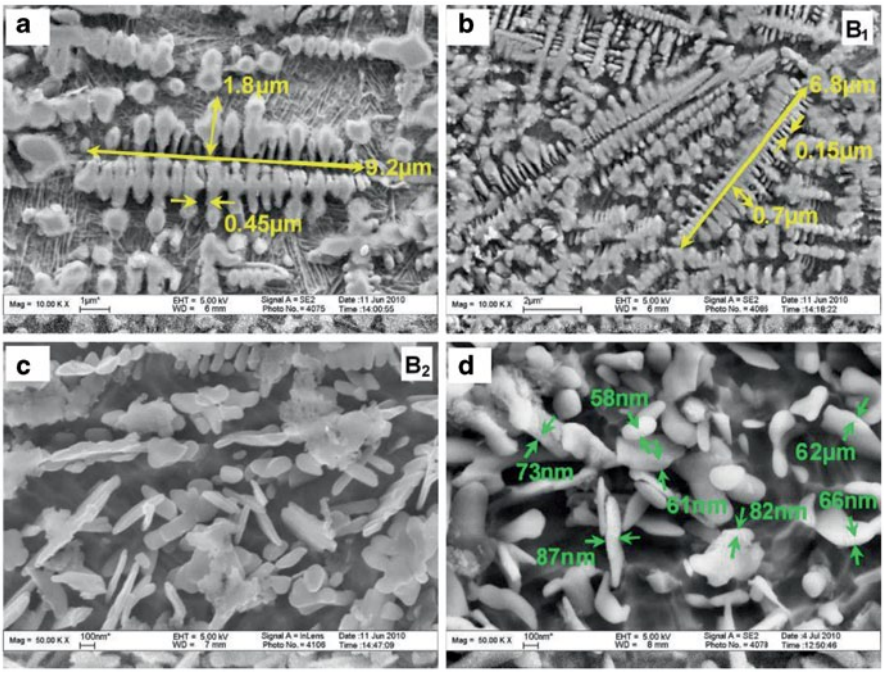


Fig. 3.9 High-magnification FE-SEM images showing characteristic morphologies of TiC reinforcement in SLM-processed parts at different laser energy densities (VED): **a** VED = 360 J/mm^3, dendritic structure; **b**, **c** VED = 180 J/mm^3, combined structures; **d** VED = 120 J/mm^3, lamellar structure

particulate morphology before SLM (Fig. 3.2b). A proper decrease in the applied VED led to a successive change from the relatively coarsened dendritic TiC to the accumulated whisker-structured TiC and, finally, to the individual nanoscale lamellar TiC (Fig. 3.9).

The mechanisms for microstructural development of TiC reinforcement with the applied VED during SLM process are disclosed as follows:

- Appropriate VED: Formation of nanoscale lamellar TiC reinforcement

SLM of powders, due to a high-energy laser source applied, is processed via a full melting/solidification mechanism. The absorbed laser energy heats up the powder particles speedily, typically in a time scale of 4×10^{-3} s [23], producing a molten pool consisting of completely dissolved TiC/Ti melts. The nanocrystalline TiC constituent (Fig. 3.2b), due to its ultrafine grain size and elevated activity, is much easy to melt and release atomic Ti and C. As the scanning laser beam moves away, the molten pool enters a rapid solidification process. In general, the TiC, as a high melting point phase, tends to form primarily through a dissolution–precipitation mechanism by means of the heterogeneous nucleation of TiC nuclei and subsequent grain growth. It is known that TiC is a typical faceted crystal and the C atoms occupy the

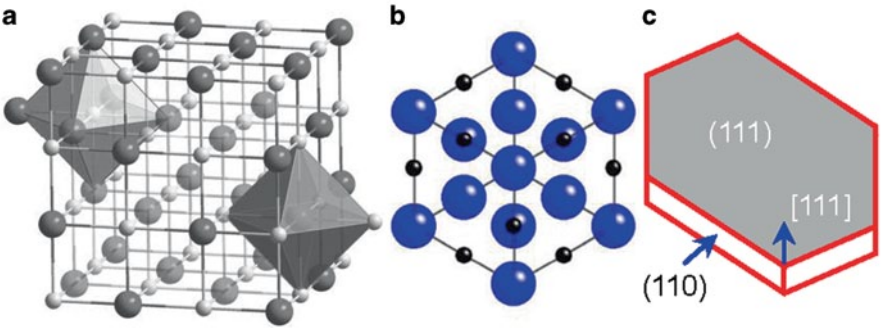


Fig. 3.10 Crystal structure of TiC (**a**); Projection of Ti–C atoms along [111] direction (**b**); Schematic of TiC lamellar crystal (**c**)

octahedral positions (Fig. 3.10a). If viewed along the direction perpendicular to the (111) plane, Ti and C atoms form a hexagonal shape (Fig. 3.10b). The hexagonal TiC nuclei precipitate from the liquid in the molten pool. As the newly arrived Ti and C atoms continue to deposit, the TiC nuclei tend to grow thicker, producing the lamellar crystals with a (111) basal plane (Fig. 3.10c). The resultant crystal shape of TiC is determined by the growth rates of different planes. The formation of lamellar TiC with a nanoscale thickness at a relatively low VED$\leq$120 J/mm^3 (Fig. 3.9d) implies that the growth rate of {110} side planes along [111] orientation is significantly restrained.

As revealed in Fig. 3.11, the unique dynamics of the molten pool induced by a nonequilibrium laser beam may account for the formation of such nanostructures. The equation for melt acceleration within the molten pool is [24]:

$$\frac{\partial v_{\mathrm{m}}}{\partial t} + v_{\mathrm{m}} \mathrm{grad} v_{\mathrm{m}} = \frac{\mathrm{grad} P_{\mathrm{eff}}}{\rho} \tag{3.8}$$

where $\partial v_{\mathrm{m}} / \partial t$ is the time derivative of melt velocity, P_{eff} is the effective pressure in the molten pool produced by the combined effect of evaporative recoil and

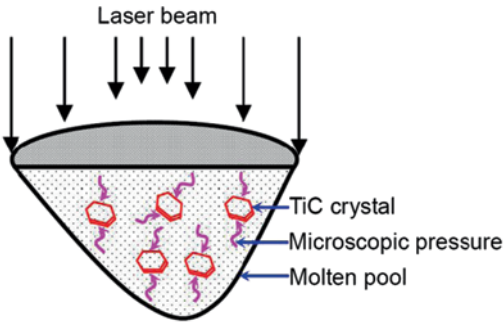


Fig. 3.11 Schematic of formation mechanism of TiC nanostructure in molten pool under laser irradiation

surface tension, and ρ is the melt density. P_{eff} is defined as the sum of recoil pressure P_{r} and surface tension pressure P_{st}, i.e., $P_{\text{eff}} = P_{\text{r}} + P_{\text{st}}$. P_{r} can be further expressed as [24]:

$$P_{\text{r}} = 0.54 B_0 (T_{\text{s}})^{-1/2} \exp\left(-\frac{U}{kT_{\text{s}}}\right) \tag{3.9}$$

where B_0 is the evaporation constant, T_{s} the surface temperature, U the latent heat of evaporation per atom, and k is Boltzman's constant. P_{st} is given by the Young–Laplace equation:

$$P_{\text{st}} = \sigma / r_{\text{m}} \tag{3.10}$$

where σ is the surface tension and r_{m} is the local radius of curvature of the melt surface. As schematically shown in Fig. 3.11, the (111) plane of lamellar TiC crystals, which are in a solid state, tends to receive a series of short pulses of nonequilibrium microscopic pressure, due to the existence of P_{eff}. The action of such pressure tends to increase the anisotropic contraction of TiC crystals along [111] orientation, preventing the thickening of {110} crystal planes and, accordingly, maintaining the desirable nanostructures after solidification (Fig. 3.9d). Furthermore, the present microscopic pressure tends to accelerate the migration of TiC crystals in a microscopic scale [25], leading to a homogeneous dispersion of nanoscale TiC reinforcing phase in finally solidified structures (Fig. 3.8c). On the other hand, the formation of nanostructured TiC reinforcement is attributed to the superfast heating, melting and solidification process induced by a short-duration, high-energy laser scanning. The laser-induced cooling rate can reach a high value up to 10^8 K/s [1]. Therefore, a further grain refinement is expected, due to an insufficient time for grain growth, well retaining the nanometric nature of TiC reinforcing phase after SLM process.

- Elevated VED: Coarsening of nanoscale TiC reinforcement

As the applied VED reached 180 J/mm^3, the SLM temperature increases and, accordingly, the Ti and C atoms in the pool become more active. More Ti and C atoms continue to deposit on the (111) plane of TiC nuclei, resulting in the morphological change of the nanoscale TiC from lamellar to the whiskered structure. Furthermore, these TiC whiskers have a tendency to stick to each other and get accumulated (Fig. 3.9c and Fig. 3.12), due to the enhanced thermodynamics within the molten pool.

- Excessive VED: Disappearance of nanostructured TiC reinforcement

The formation of the relatively coarsened TiC dendrites at an even elevated VED of 360 J/mm^3 resulted in the disappearance of nanostructure (Figs. 3.8a and 3.9a). Within the laser-induced molten pool, the local temperature gradient and chemical concentration gradient give rise to surface tension gradient and associated Maran-

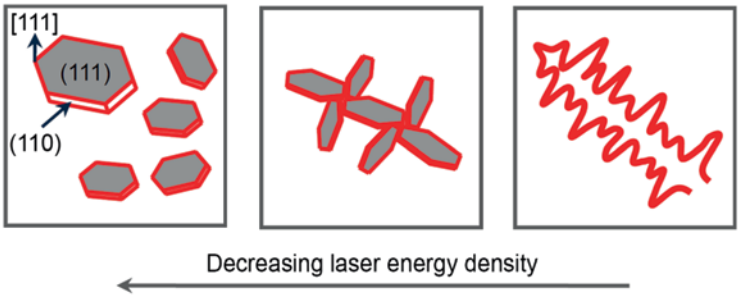


Fig. 3.12 Schematic of microstructural developments of TiC with laser energy density (VED)

goni convection. According to Arafune and Hirata's results [26], the intensity of Marangoni flow can be assessed using the dimensionless Marangoni number (M_a):

$$M_a = \frac{\Delta\sigma L}{\mu v} \tag{3.11}$$

where $\Delta\sigma$ is the surface tension difference of Marangoni flow, L the length of the free surface, μ the dynamic viscosity, and v is the kinematic viscosity. The significantly enhanced SLM temperature T in this situation results in a considerable decrease in μ (Eq. 3.7), thereby intensifying the Marangoni flow (Eq. 3.11) and resultant turbulence within the pool. Due to the instability of solid–liquid interface caused by the perturbation, the TiC precipitates tend to undergo a dendritic growth (Figs. 3.9a and 3.12). Meanwhile, because of an elevated thermalization of laser energy in this case, a large amount of heat is accumulated around the growing dendrite tips, which provides a significant internal energy and thermodynamic potential for the significant coarsening and disappearance of nanostructure of the finally developed TiC reinforcement.

3.5.4 Influence of SLM Parameters on Nanoindentation and Wear Behavior

Figure 3.13 depicts the nanoindentation load-depth curves measured on the polished sections of SLM-processed parts. The indentation depth of the pure Ti part under a maximum load (0.972 μm) was considerably larger than that of the TiC/Ti nanocomposite parts (0.204–0.292 μm). The most widely used procedure of extracting information from nanoindentation tests has been developed by Oliver and Pharr [21], based on the assumption of elasticity of the material. In this study, the Oliver–Pharr method was applied to calculate dynamic nanohardness (H_d) and elastic modulus (E_r). The maximum H_d and E_r of the TiC/Ti nanocomposites showed respectively ~22.7-fold and ~2.4-fold increase upon that of the unreinforced Ti part

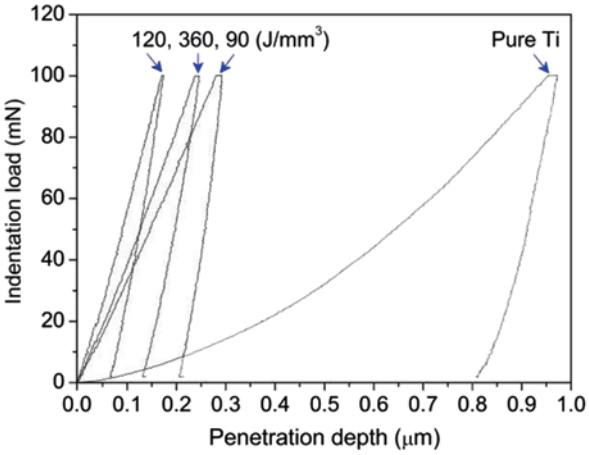


Fig. 3.13 Loading–unloading curves of nanoindentation testing of SLM-processed pure Ti and TiC/Ti nanocomposite parts at various laser energy densities

Table 3.1 Nanohardness, elastic modulus, and wear rate of SLM-processed Ti and TiC/Ti parts

Material	Pure Ti	TiC/Ti nanocomposites		
Laser energy density, VED, J/mm^3	120	90	120	360
Nanohardness, H_d, GPa	4.0	62.8	90.9	44.2
Elastic modulus, E_r, GPa	107	213	256	179
Wear rate, ω, mm^3/(Nm)	2.8×10^{-6}	3.1×10^{-7}	1.8×10^{-7}	7.0×10^{-7}

(Table 3.1), due to the incorporation of TiC reinforcement with enhanced hardness and elastic modulus. On the other hand, the applied VED significantly affected the obtainable properties and the highest H_d and E_r were achieved as a proper VED of 120 J/mm^3 was settled (Table 3.1). It indicated that only when the TiC reinforcement remained in the nanoscale structure after SLM (Fig. 3.9d) and was uniformly dispersed throughout the matrix (Fig. 3.8c), the reinforcing function of TiC could be maximized.

Figures 3.14 and 3.15 show respectively the friction coefficients and characteristic morphologies of worn surfaces of TiC/Ti nanocomposite parts processed at different volumetric laser energy densities (VED). As relative to the pure Ti, the friction coefficient of TiC/Ti nanocomposites decreased at least by half (Fig. 3.14), and the resultant wear rate lowered at least by 75 % (Table 3.1). Also, it was noted that the applied VED played a key role in influencing wear performance of TiC/Ti parts. The friction coefficient of TiC/Ti part at a high VED of 360 J/mm^3 exhibited an apparent local fluctuation, with a mean value reaching 0.6 (Fig. 3.14). The worn surface showed parallel grooves representing the abrasion wear (Fig. 3.15c). The local severe plowing of the surface during sliding resulted in a relatively high-wear rate of 7.0×10^{-7} mm^3/(N m) (Table 3.1). It might be ascribed to the formation of the relatively coarsened TiC dendrites (Figs. 3.8a and 3.9a), which tended

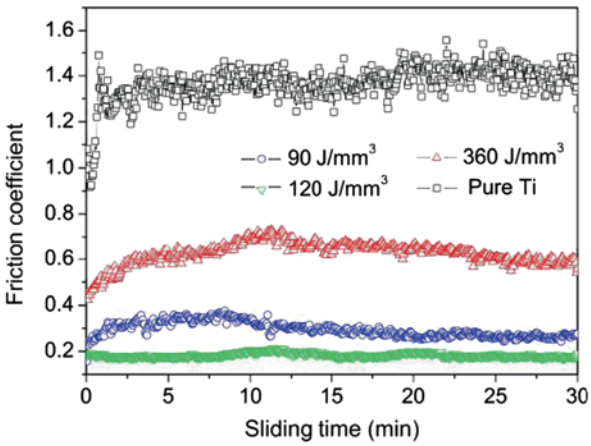


Fig. 3.14 Friction coefficients of SLM-processed Ti and TiC/Ti nanocomposite parts at different laser energy densities

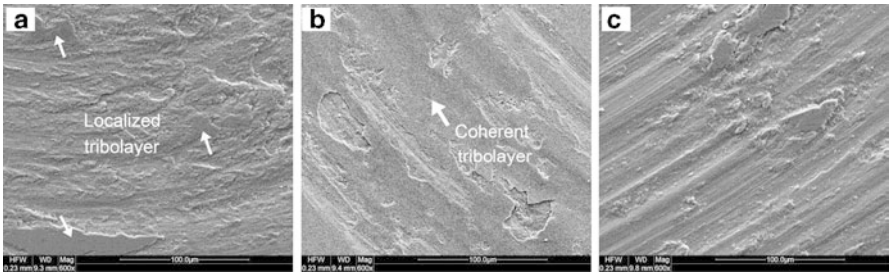


Fig. 3.15 SEM images showing typical morphologies of worn surfaces of SLM-processed TiC/Ti nanocomposite parts at: **a** VED = 90 J/mm^3; **b** VED = 120 J/mm^3; **c** VED = 360 J/mm^3

to split during serve sliding. The mean friction coefficient and wear rate of TiC/Ti nanocomposite part at 90 J/mm^3 decreased markedly to 0.3 and 3.1×10^{-7} mm^3/(N m), respectively (Fig. 3.14, Table 3.1). The localized formation of the adhesion tribolayer on the worn surface was observed in this instance (Fig. 3.15a). The TiC/Ti nanocomposite part prepared using a suitable VED of 120 J/mm^3 demonstrated the superior wear performance. A uniform distribution of friction coefficient with a considerably low average value below 0.2 was obtained (Fig. 3.14) and the wear rate, 1.8×10^{-7} mm^3/(Nm), was lowest (Table 3.1). An adherent and strain-hardened tribolayer was completely smeared on the worn surface (Fig. 3.15b). Thus, it was reasonable to consider that as the nanoscale TiC reinforcement was formed in SLM-processed nanocomposites at 90 and 120 J/mm^3 (Fig. 3.8c and d), the mechanism of material removal during sliding changed from the abrasion to the adhesion of tribolayer, which was expected to stabilize friction coefficient and reduce wear rate. Such a transition in sliding mechanisms was attributed to the following two advantages of the nanoscale reinforcement. First, the uniformly dispersed lamellar nanoscale TiC reinforcement (Fig. 3.8c and 3.9d) had considerably small interfacial stresses

with the matrix, thereby introducing less breakage in nanocomposites during sliding [12]. Second, the microhardness enhancement (Fig. 3.13, Table 3.1) helped to form the strain-hardened tribolayer (Fig. 3.15b) that prevented further wearing.

3.6 Influence of Nanoscale Reinforcement Content on SLM Processing of TiC/Ti Nanocomposite Parts

This section focuses on the influence of nanoscale reinforcement content on microstructural evolutions and mechanical properties of the directly mechanical mixed TiC/Ti nanocomposites processed by SLM, including densification, microhardness, and wear resistance. The material–microstructure–property relationship was proposed for a successful production of TiC/Ti nanocomposite parts with novel nanoscale reinforcement architecture and elevated performance.

3.6.1 Influence of TiC Nanocomposites Content on Densification Behavior

Figures 3.16 and 3.17 illustrate the effect of TiC nanoparticles addition on cross-sectional microstructures and densification behavior of SLM-processed parts. Generally, the layer-wise microstructural features were observed, due to the additive manufacturing nature of SLM. The cross-sections of SLM parts containing 7.5 and 12.5 wt.% nanoscale TiC consisted of metallurgically bonded layers, showing homogeneous microstructures without any interlayer pores (Fig. 3.16a and b). The corresponding SLM surfaces consisted of coherently bonded scan tracks and the obtained densification rates were above 98.3 % theoretical density (TD) (Fig. 3.17). As the TiC addition increased to 17.5 wt.%, the cross-section showed a heterogeneous layer-wise microstructure (Fig. 3.16c) and the SLM density decreased slightly to 97.2 % TD. A large amount of balls with diameters of 20–140 μm were formed on the surface (Fig. 3.17). It was accordingly inferred that, "balling" effect, which was a typical metallurgical defect associated with SLM, initiated in this instance. As an excessive 22.5 wt.% TiC was added, the interlayer pores with the size of ~100 μm were present on the cross-section (Fig. 3.16d) and, meanwhile, the clusters of balls and interball porosity were formed on the surface (Fig. 3.17), resulting in an apparent decrease of densification to 94.7 % TD.

SLM is processed via a complete melting metallurgical mechanism, which means that even the high-melting-point ceramic phase tends to be fully molten during SLM. The as-used TiC nanoparticles demonstrate a high tendency for complete melting due to: (i) the significantly elevated activity of nanoparticles induced by the extremely large surface area to volume ratio; (ii) the application of fiber laser having high energy density and resultant elevated SLM temperature. According to

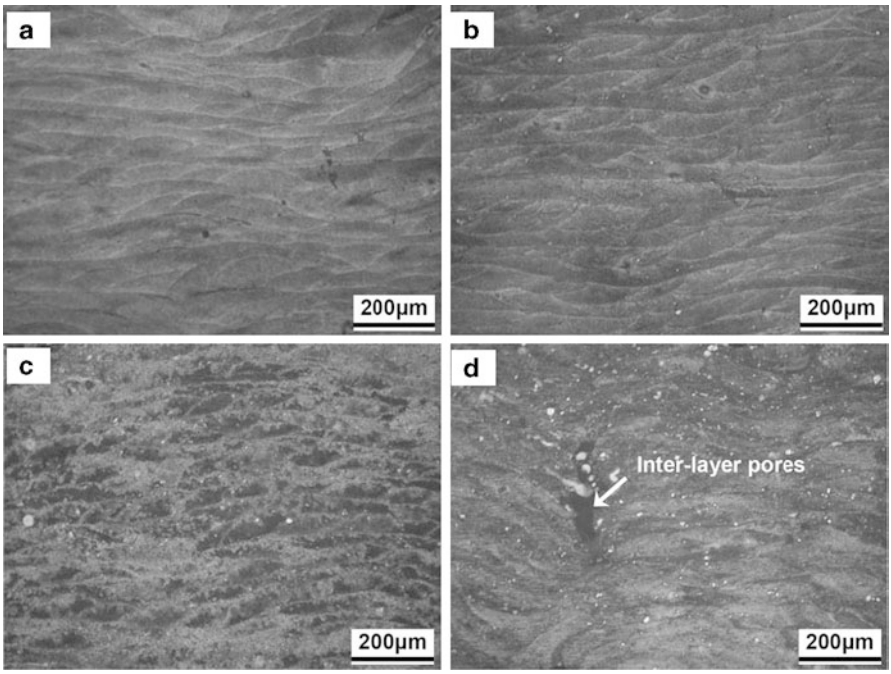


Fig. 3.16 OM micrographs showing characteristic microstructures on cross-sections of SLM-processed TiC/Ti nanocomposite parts using 7.5 wt.% (**a**), 12.5 wt.% (**b**), 17.5 wt.% (**c**), and 22.5 wt.% (**d**) TiC nanoparticles

Eq. 3.7, the dynamic viscosity of the melt (μ) is directly proportional to the liquid surface tension (γ). The γ for molten TiC is ~10–20 N/m [27], which is considerably larger than that of Ti liquid (1.588 N/m) [28]. With the dissolution of TiC in Ti liquid, the viscosity of TiC/Ti composite melt increases significantly. As a larger amount of TiC nanoparticles are melted within the molten pool, the resultant considerably high viscosity handicaps the sufficient flow of the melt, decreasing the overall rheological performance of the pool. On the other hand, during high-energy laser scanning, a steep thermal gradient is developed between the center and edge of the pool across the surface, causing the corresponding surface tension gradient and resultant Marangoni flow within the pool [29]. The Marangoni flow produces an extra force exerted on the melt. Due to the combined effect of (i) the limited rheological property of the melt caused by a high melt viscosity and (ii) the action of Marangoni force, the TiC/Ti melt containing a higher content of TiC tends to flow radially inward toward laser beam center, rather than spreading outward on the underlying surface, thereby initiating the balling effect (Fig. 3.17). Balling effect causes interball and intertrack porosity as a current layer is processed (Fig. 3.17) and severely degrades the densification of the final part due to the formation of interlayer pores (Fig. 3.16d).

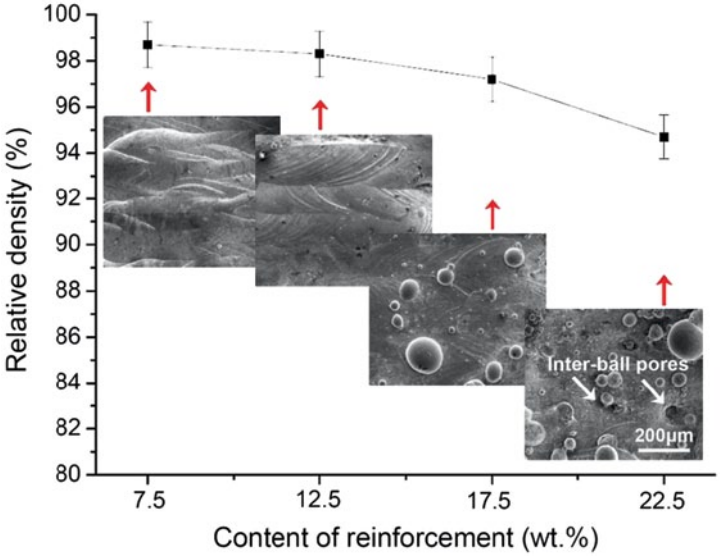


Fig. 3.17 Variations of densification rates and surface morphologies of SLM-porcessed TiC/Ti nanocomposite parts with TiC contents

3.6.2 Influence of TiC Nanoparticles Content on Microstructural Characteristics

Figures 3.18 and 3.19 illustrate the characteristic microstructures of SLM-processed TiC/Ti nanocomposites. XRD was applied to study the constitutional phases of SLM-processed samples. The three strong diffraction peaks detected for the Ti- and C-containing phase were generally located at $2\theta = 36.10°$, 41.93°, and 60.79°, which were exactly corresponding to the 2θ locations of standard peaks for stoichiometric TiC (JCPDS Card No. 65-8805). It was thus reasonable to consider that the reinforcing phase in SLM parts was the stoichiometric TiC. The TiC reinforcing phase had the entirely different microstructures from the starting particulate morphology. The contents of starting TiC nanoparticles played a key role in determining the microstructural development of TiC during SLM. At a relatively low TiC content of 7.5 wt.%, the significantly refined TiC reinforcing phase was dispersed homogeneously throughout the matrix (Fig. 3.18a), showing a lamellar structure with a mean thickness of ~93 nm (Fig. 3.19a). Nanomaterials can be defined as materials which have structured components with at least one dimension < 100 nm [16]. It was accordingly confirmed that the standard nanostructured TiC reinforcement was formed in SLM-processed part. As the TiC content increased to 12.5 wt.%, the TiC reinforcing phase remained in a nanoscale lamellar shape with a reduced average thickness of ~77 nm, showing a further refinement in its morphology (Fig. 3.19b). The distribution density of TiC within the matrix increased and its dispersion state

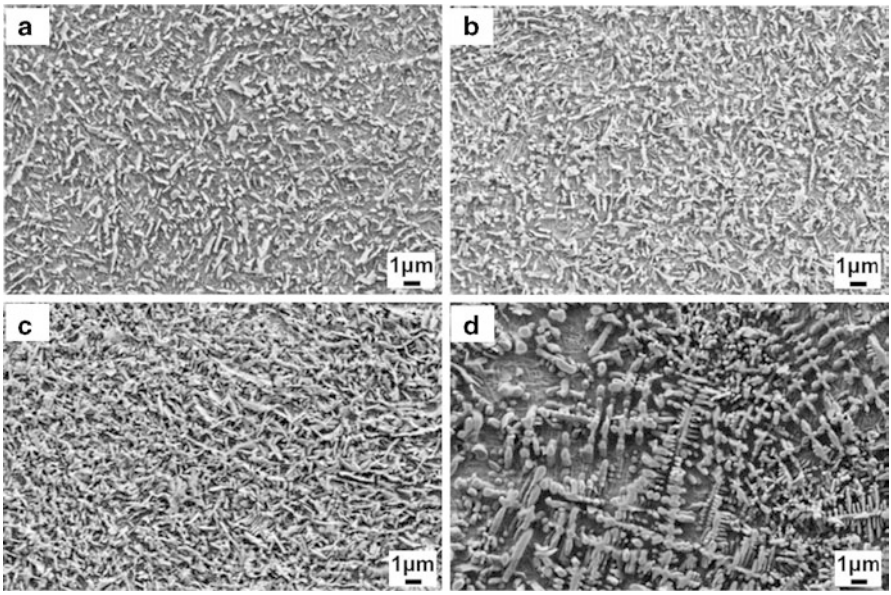


Fig. 3.18 FE-SEM images showing dispersion states of reinforcement in SLM-processed TiC/Ti nanocomposite parts using different contents of TiC nanoparticles: **a** 7.5 wt.%; **b** 12.5 wt.%; **c** 17.5 wt.%; **d** 22.5 wt.%

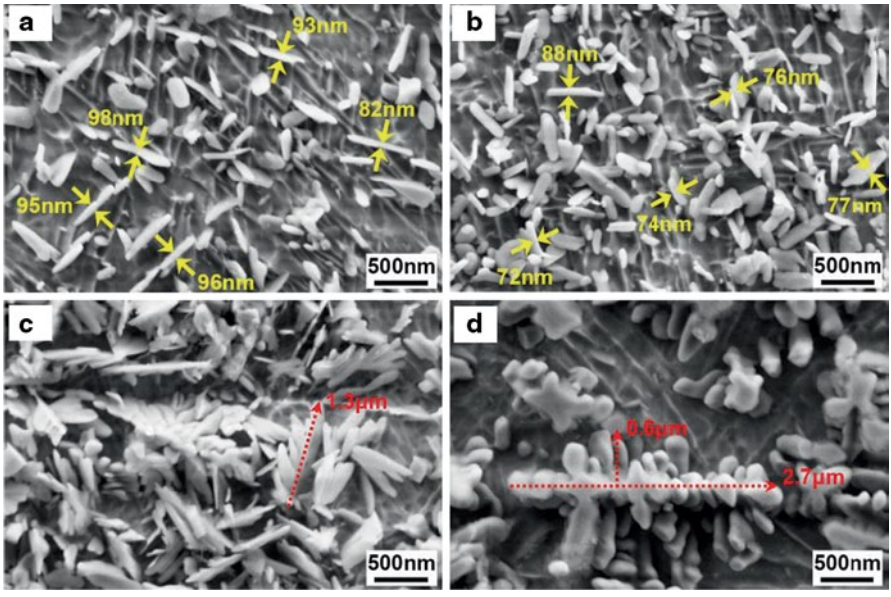


Fig. 3.19 High-magnification FE-SEM images showing typical growth morphologies of TiC reinforcement in SLM-processed TiC/Ti nanocomposite parts containing 7.5 wt.% (**a**), 12.5 wt.% (**b**), 17.5 wt.% (**c**), and 22.5 wt.% (**d**) TiC nanoparticles

was still uniform (Fig. 3.18b). With a further increase in TiC content to 17.5 wt.%, the TiC reinforcing phase was tightly clustered, exhibiting a highly dense distribution throughout the matrix (Fig. 3.18c). The TiC reinforcement had a relatively coarsened feathery morphology. The length of feather-structured TiC reached 1.3 μm and the thickness increased toward a submicron scale (Fig. 3.19c). At an even higher TiC content of 22.5 wt.%, the TiC reinforcing phase was developed into a network distribution, showing a completely different dendritic morphology (Fig. 3.18d). The average length of dendrite trunk and dendrite arms reached 2.7 μm and 0.6 μm, respectively, typically exhibiting a micron-scale structure (Fig. 3.19d). In these two situations (Fig. 3.19c and d), it was found that the nanoscale feature of TiC reinforcement was not maintained after SLM.

During SLM process with a complete liquid formation, the TiC reinforcing phase is formed via a dissolution/precipitation mechanism by means of the heterogeneous nucleation of TiC nuclei and subsequent grain growth. Due to the rapid solidification nature induced by high-energy laser melting, the effective crystal development of TiC nuclei is significantly restricted, due to an insufficient time for grain growth, hence well retaining the favorable nanoscale structure of the TiC reinforcing phase (Fig. 3.19a and b). Meanwhile, the existence of Marangoni convection within the pool induces liquid capillary force [30], which exerts on the precipitated TiC and accelerates its rearrangement in the melt, homogenizing the dispersion of nanoscale TiC reinforcement within the finally solidified matrix (Fig. 3.18a and b). As a larger content of TiC nanoparticles are melted in the pool, the solute concentration of Ti and C increases significantly. The TiC nuclei, thus, develop speedily, since a large amount of Ti and C atoms continue to gather and deposit on the precipitated nuclei. In this situation, the restrictive effect of rapid solidification nature of laser processing on TiC grain coarsening is weakened, resulting in the loss of the nanostructure of TiC after SLM (Fig. 3.19c). For an even higher TiC addition, the considerably high concentration gradient and solute diffusivity are established in the melt. As TiC crystals grow, there is a continuous accumulation of solute on the moving interface into the liquid. The lamellar TiC tends to develop side branches and undergo a dendritic growth (Fig. 3.19d).

3.6.3 Influence of TiC Nanoparticles Content on Hardness and Wear Performance

Figure 3.20 depicts the average microhardness measured on cross-sections of TiC/Ti nanocomposite parts. A maximum microhardness of $577HV_{0.2}$ was obtained as 12.5 wt.% TiC nanoparticles were added. In this case, a small-sized indentation with a clear configuration was observed, indicating a small degree of deformation during indentation. The microhardness of SLM-processed pure Ti under the same conditions was $241-287HV_{0.2}$. The incorporation of nanoscale TiC reinforcement within Ti matrix favored at least 2-fold increase in microhardness. Nevertheless, as the TiC addition increased to 22.5 wt.%, the microhardness showed an apparent

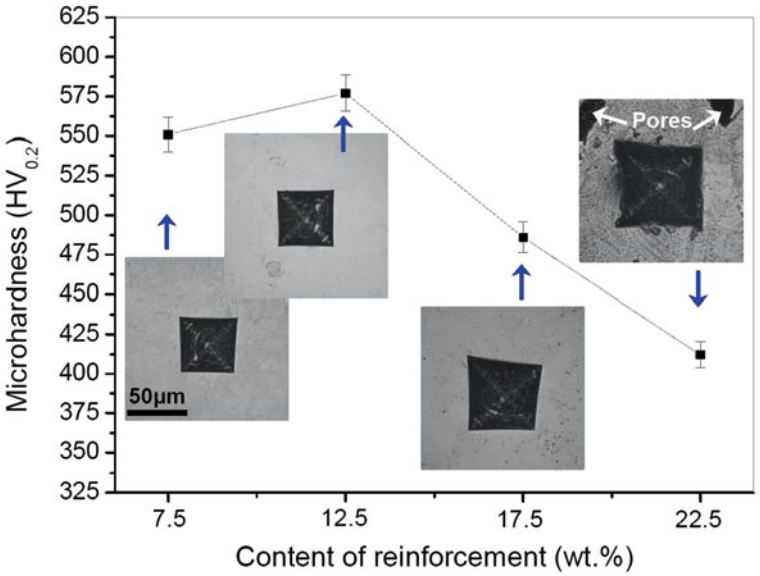


Fig. 3.20 Effect of TiC reinforcement content on microhardness and indentation morphology of SLM-processed TiC/Ti nanocomposite parts

decrease to $412HV_{0.2}$. The limited hardness was further testified by the presence of relatively large indentation with deformed and indistinct contour. Generally, the microhardness profile exhibited a similar trend as the relative density with respect to TiC content (Fig. 3.17). The limited densification due to the pore formation at 22.5 wt.% TiC was responsible for the decrease in hardness.

The influence of TiC nanoparticles addition on coefficient of friction (COF), wear rate, and worn surface morphologies of SLM-processed parts is illustrated in Fig. 3.21 and 3.22. The COFs of parts consisting of 7.5 and 12.5 wt.% TiC, with average values of 0.23 and 0.19, were considerably low, leading to the reduced wear rates of 2.6×10^{-16} and 2.3×10^{-16} $m^3/(Nm)$ (Fig. 3.21). SEM observation revealed that the worn surfaces were covered with the smooth, adherent, and strain-hardened tribolayer, indicating an adhesive wear feature (Fig. 3.22a and b). In these two cases, the uniformly dispersed lamellar nanoscale TiC reinforcement has a high tendency to adhere to each other, showing less fragmentation during sliding. Combined with the effect of microhardness enhancement (Fig. 3.20), the strain-hardened tribolayer tends to form on the worn surface, acting as a protective layer to improve wear resistance. However, the COFs of samples consisting of higher TiC contents of 17.5 and 22.5 wt.% increased sharply to 0.35 and 0.41, respectively, and the maximum wear rate showed a 3-fold increase and reached 6.5×10^{-16} $m^3/(Nm)$ (Fig. 3.21). The worn surface showed parallel grooves and irregularly shaped debris, which represented a typical abrasion wear (Fig. 3.22c and d). The decrease in wear performance was ascribed to the grain coarsening of TiC reinforcement and resultant disappearance of its nanostructure. The relatively coarsened TiC dendrites were easy to split

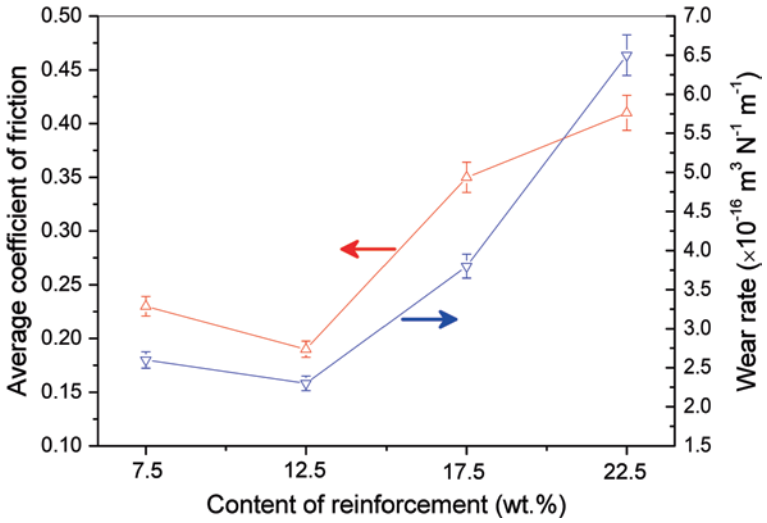


Fig. 3.21 Effect of TiC reinforcement content on average COF and wear rate of SLM-processed TiC/Ti nanocomposite parts

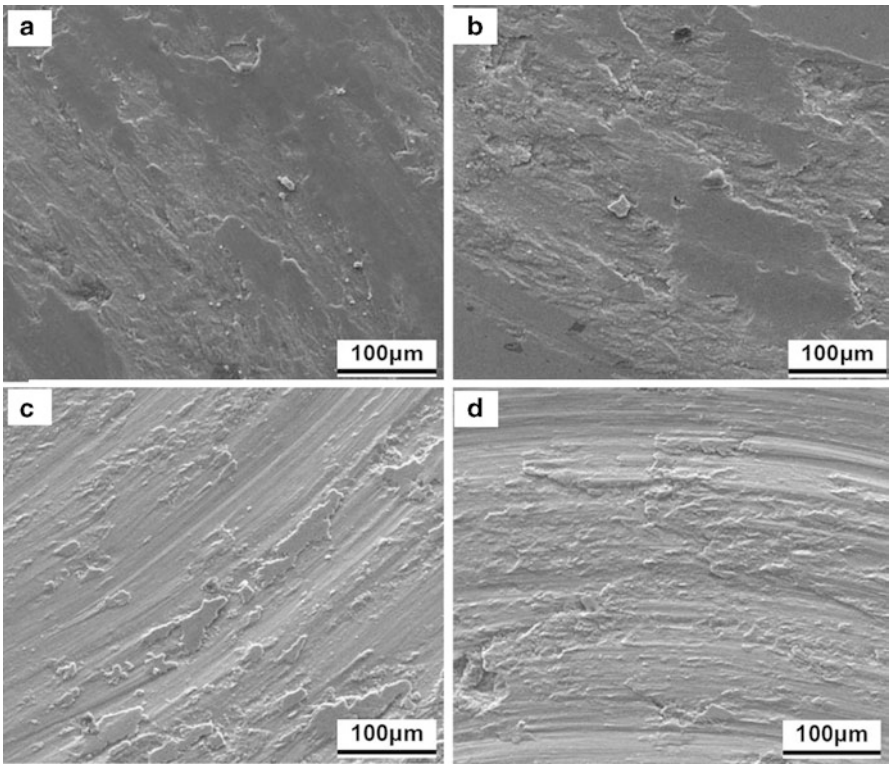


Fig. 3.22 SEM images showing typical morphologies of worn surfaces of TiC/Ti nanocomposite parts using 7.5 wt.% (a), 12.5 wt.% (b), 17.5 wt.% (c), and 22.5 wt.% (d) TiC reinforcement

during sliding, resulting in the spalling and delamination of worn surface. It was accordingly reasonable to conclude that only when the TiC reinforcement maintained the favorable nanostructure after SLM (Fig. 3.19a and b) could its reinforcing effect on microhardness and wear resistance be maximized.

3.7 The Role of Nanopowder in SLM Processing of TiC/Ti Nanocomposite Parts

In this section, SLM was applied to process TiC/Ti nanocomposite powder prepared using two different methods, i.e., the 1st kind of ball milling method and the 2nd kind of directly mechanical mixing method. The evolutions of nanostructures of SLM-processed TiC/Ti nanocomposite parts at different laser processing conditions (i.e., linear laser energy density, LED) were studied and the attendant densification level and tribological property were assessed. The predominant role of the starting nanopowder characteristics and corresponding SLM parameters on the variations in microstructural and mechanical properties was clarified.

3.7.1 The Role of Nanopowder in Densification Behavior

Figure 3.23 depicts the influence of powder preparation method and laser processing parameters on densification rates of SLM-processed TiC/Ti nanocomposite powder. A close comparison revealed that for a given linear laser energy density (LED), the SLM densification level of the ball-milled TiC/Ti nanocomposite powder was generally larger than that of the directly mixed nano-TiC/Ti powder, typically show-

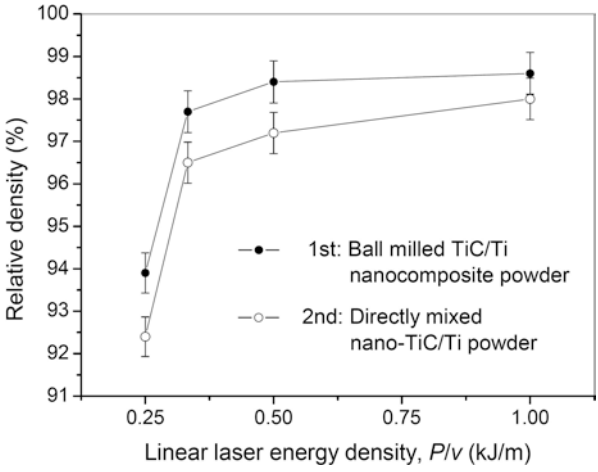


Fig. 3.23 Variations of SLM densities of TiC/Ti nanocomposite parts with powder categorie and SLM processing parameters

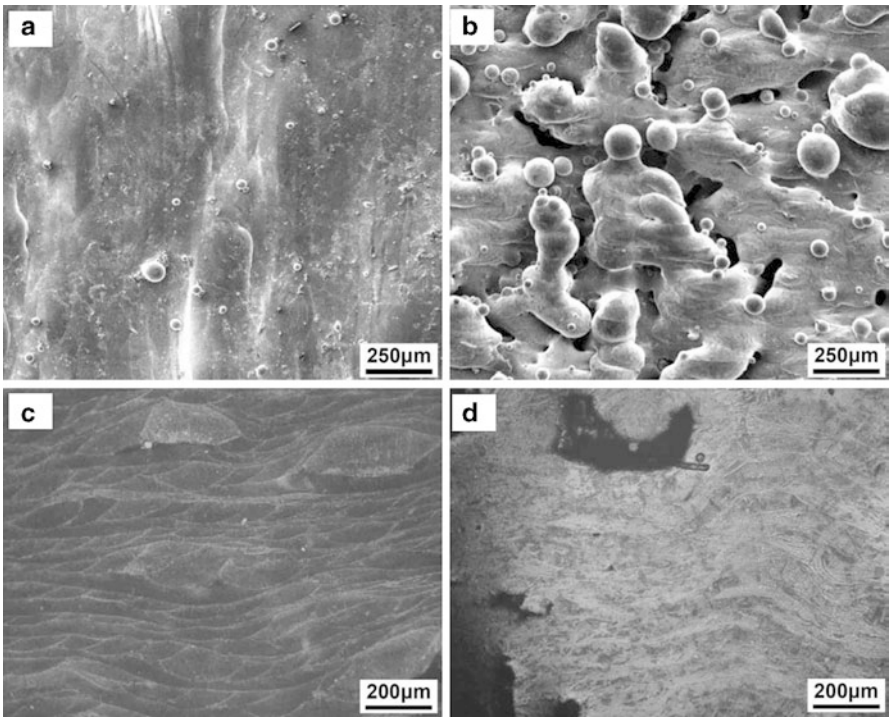


Fig. 3.24 Typical surface morphologies (SEM) and cross-section microstructures (OM) of SLM-processed parts using 1st kind of ball-milled TiC/Ti nanocomposite powder: LED = 1.0 kJ/m, v = 0.1 m/s (**a** and **c**); LED = 0.25 kJ/m, v = 0.4 m/s (**b** and **d**)

ing an improvement of 0.6−1.5 % theoretical density (TD). For the two powder systems, the SLM densification rate increased sharply from ~93 % TD to ~97 % TD as LED increased from 0.25 to 0.33 kJ/m. A further elevation of the applied LED led to a slight increase in the obtained SLM density. As a sufficiently high LED of 1 kJ/m was used, the near fully dense (> 98 % TD) TiC/Ti nanocomposite parts were generally produced after SLM.

Figures 3.24 and 3.25 show respectively the characteristic microstructures on the untreated top surfaces and polished/etched cross-sections of SLM-processed parts using ball-milled and directly mixed TiC/Ti nanocomposite powders. At a relatively high linear laser energy density (LED) of 1.0 kJ/m, the top surface of SLM-processed part using ball-milled TiC/Ti nanocomposite powder was fully dense and smooth, free of any apparent pores (Fig. 3.24a). The corresponding cross-section of the part typically showed a layered microstructure, due to the additive manufacturing nature of SLM. The layers were coherently bonded, without the formation of interlayer pores or cracks (Fig. 3.24c). As a low LED of 0.25 kJ/m was applied, the SLM-processed surface consisted of interrupted, large-sized agglomerates, between which the open pore channels were visible. Furthermore, a number of metallic balls with an average diameter of ~70 μm were present on the porous surface

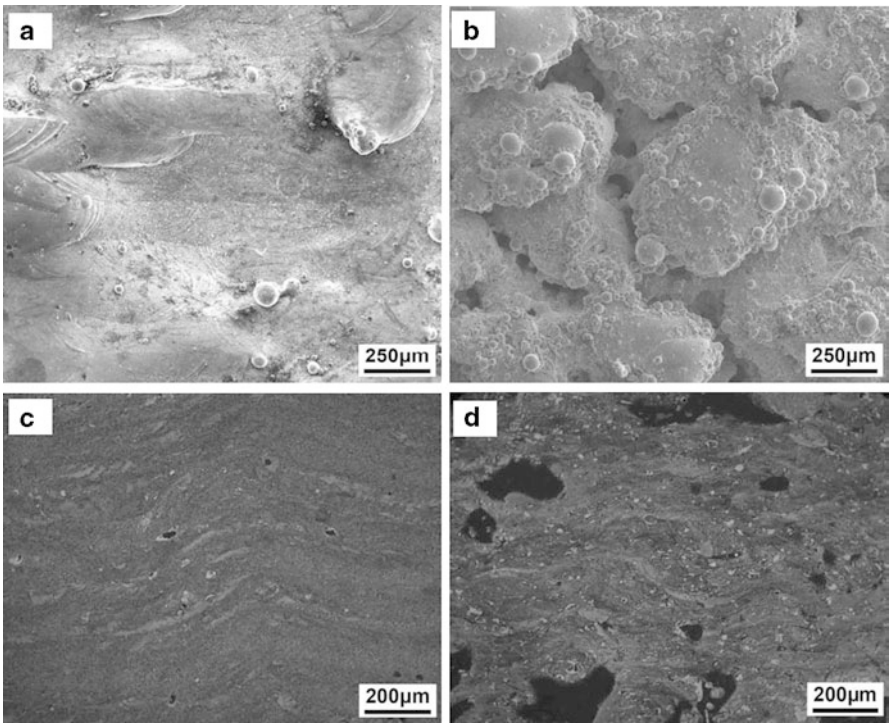


Fig. 3.25 Typical surface morphologies (SEM) and cross-section microstructures (OM) of SLM-processed parts using second kind of directly mixed TiC/Ti nanocomposite powder: LED = 1.0 kJ/m, v = 0.1 m/s (**a** and **c**); LED = 0.25 kJ/m, v = 0.4 m/s (**b** and **d**)

(Fig. 3.24b). It was accordingly concluded that the "balling" effect, which was regarded as a typical metallurgical defect with SLM process, occurred in this instance. As a consequence, the cross-section consisted of irregular shaped interlayer pores on a scale of ~300 μm (Fig. 3.24d), which resulted in a significant decrease in the obtained densification rate (Fig. 3.23).

Basically, the changes of densification behavior and microstructural features of the 2nd kind of directly mixed TiC/Ti nanocomposite powder with SLM processing parameters showed a similar tendency as that of the 1st kind of powder. A close examination of microstructures, however, disclosed some distinct differences due to the change in the starting nanopowder. At a relatively high LED of1.0 kJ/m, although the top surface of SLM-processed part remained dense (Fig. 3.25a), a small amount of micropores were present on the cross-section (Fig. 3.25c). As LED decreased to 0.25 kJ/m, the balling effect on SLM-processed surface became worsened. Two categories of balling phenomena occurred in this case: (i) large-sized, spherical shaped agglomerates with an average size of ~500 μm; and (ii) a large amount of relatively small, micrometer-scaled balls formed around these large agglomerates (Fig. 3.25b). The aggravation of balling effect resulted in the formation of the interconnected interball pore channels on the top surface (Fig. 3.25b) and the

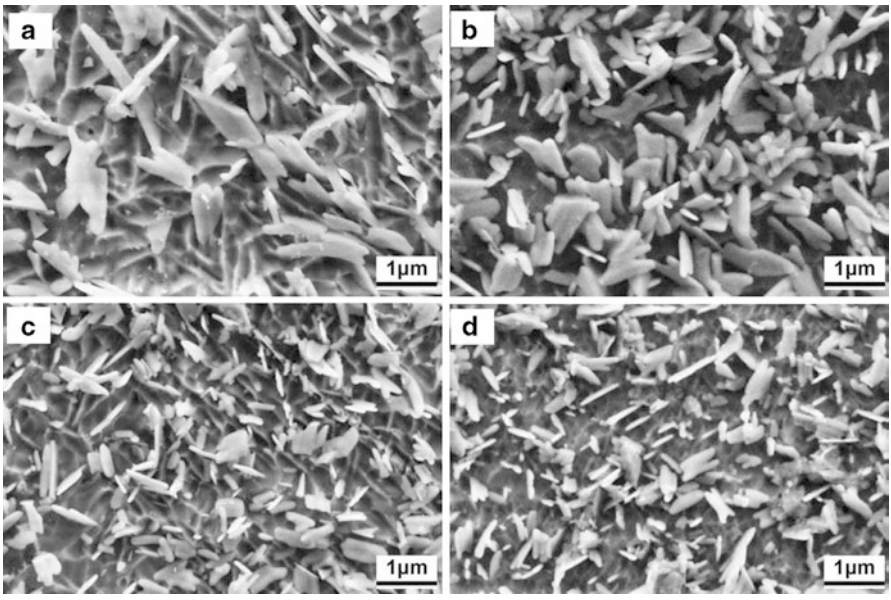


Fig. 3.26 FE-SEM micrographs showing the influence of SLM parameters on microstructural characteristics of nanoscale TiC reinforcing phase in SLM-processed parts using 1st kind of ball-milled TiC/Ti nanocomposite powder: **a** LED = 1.0 kJ/m, v = 0.1 m/s; **b** LED = 0.5 kJ/m, v = 0.2 m/s; **c** LED = 0.33 kJ/m, v = 0.3 m/s; **d** LED = 0.25 kJ/m, v = 0.4 m/s

heterogeneous cross-sectional microstructure consisting of uneven SLM layers and large-sized, irregular-shaped interlayer pores (Fig. 3.25d).

3.7.2 The Role of Nanopowder in Microstructure Development

The characteristic microstructures of the first kind of ball-milled TiC/Ti nanocomposite powder under different SLM conditions are shown in Fig. 3.26. It revealed that the TiC reinforcing phase typically had a lamellar microstructure which was completely different from the starting particulate morphology before SLM (Fig. 3.3d). A quantitative measurement during FE-SEM analysis showed that the thickness of such lamellar TiC reinforcement was generally below 100 nm, while the values of length were distributed from 500 nm to 1.2 μm (Fig. 3.26). According to the definition of nanomaterials [16], it was confirmed that the TiC reinforcement in SLM-processed TiC/Ti nanocomposites under these four different SLM processing conditions generally had a standard nanostructure. Additionally, the ultrafine nanoscale TiC reinforcing phase was dispersed homogeneously throughout the Ti matrix. Except for these common microstructural features, a close examination of microstructures revealed that the TiC reinforcement also demonstrated its individual unique characteristics with variation of linear laser energy density (LED). The

nanostructure of TiC reinforcing phase at the relatively high LED (Fig. 3.26a and b) showed a slight coarsening and aggregation as relative to the TiC reinforcement formed at lower LED (Fig. 3.26c and d). Nevertheless, the lamellar nanostructure and dispersion homogeneity of TiC reinforcing phase in SLM-processed ball-milled TiC/Ti nanocomposites did not show a substantial change with the applied SLM processing parameters.

The changes of the microstructural features of the second kind of directly mixed TiC/Ti nanocomposite powder at various SLM processing parameters are provided in Fig. 3.27. It revealed that the microstructures of the present TiC reinforcement showed a distinct variation with the applied linear laser energy density (LED). As a reasonable LED of 0.33 kJ/m was settled, the ultrafine lamellar nanostructured TiC reinforcement was dispersed uniformly in SLM-processed part (Fig. 3.27c). Such a microstructure was similar as that formed in the SLM-processed ball-milled TiC/Ti nanocomposite powder (Fig. 3.26). As the applied LED increased to 0.5 kJ/m, the TiC reinforcing phase became apparently coarsened and, meanwhile, aggregated into clusters (Fig. 3.27b). At an even higher LED of 1.0 kJ/m, the TiC reinforcement typically exhibited a dendritic growth morphology and a network distribution. The average length of dendrite trunks and primary dendrite arms reached 2.8 μm and 0.8 μm, respectively, typically showing a micrometer-scaled feature (Fig. 3.27a). In this situation, the TiC reinforcement lost its nanostructure after SLM process. It was

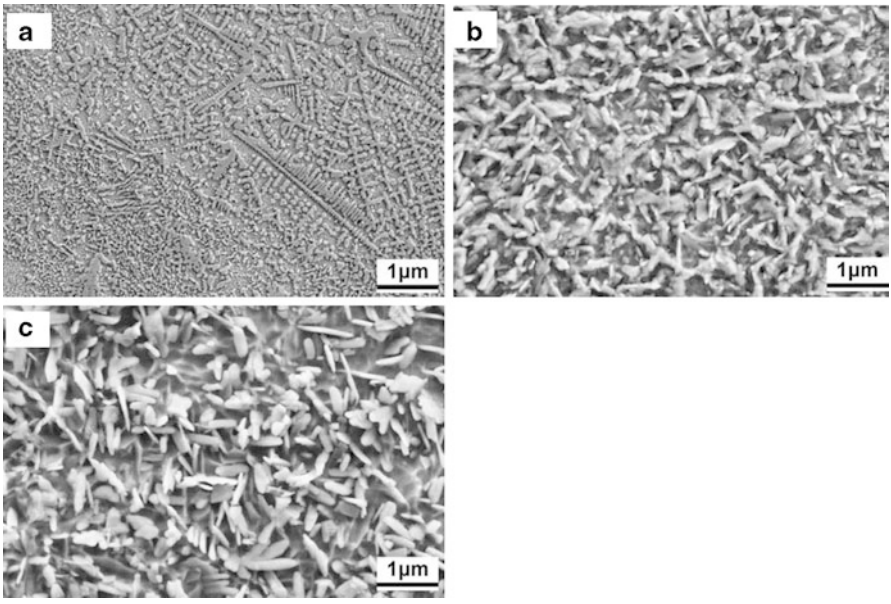


Fig. 3.27 FE-SEM micrographs showing the effect of SLM parameters on microstructural developments of TiC reinforcing phase in SLM-processed parts using second kind of directly mixed TiC/Ti nanocomposite powder: **a** LED = 1.0 kJ/m, *v*LED = 1.0 k**b** LED = 0.5 kJ/m, *v*LED = 0.5 k**c** LED = 0.33 kJ/m, *v*LED = 0.3

accordingly concluded that the microstructural development of the directly mixed TiC/Ti nanocomposite powder during SLM was more sensitive to the applied laser processing parameters.

3.7.3 The Role of Nanopowder in Wear and Tribological Property

The effects of the category of nanopowder and corresponding SLM parameters on the tribological property of SLM-processed parts are depicted in Fig. 3.28 For the SLM part condensed from the 1st kind of ball-milled TiC/Ti nanocomposite powder, the coefficient of friction (COF) was considerably high as a relatively low LED of 0.25 kJ/m was applied, with the average value reached 0.52. For the higher LED

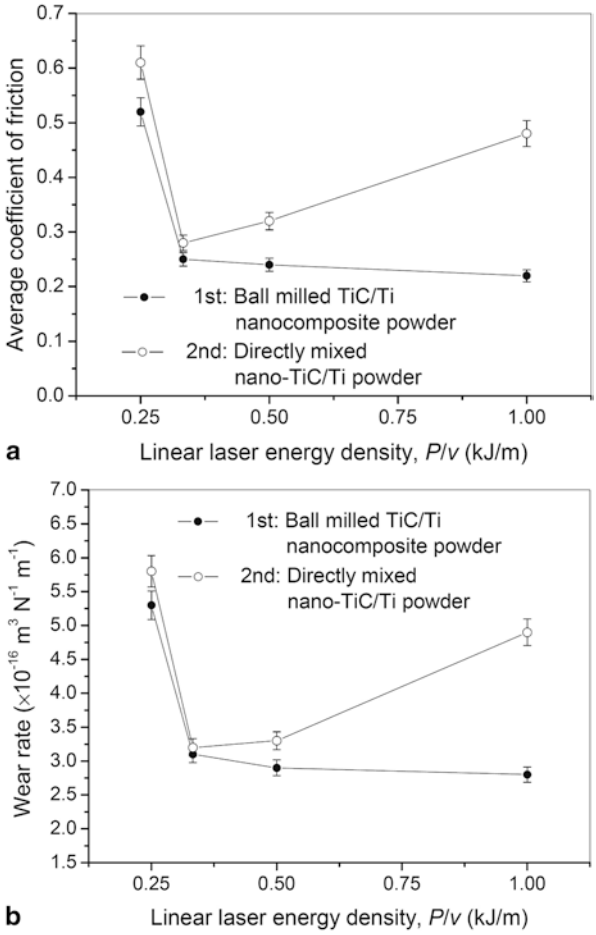


Fig. 3.28 Changes of average COF (a) and wear rate (b) of SLM-processed TiC/Ti nanocomposite parts with powder categories and SLM parameters

from 0.33 to 1.0 kJ/m, the mean COF decreased at least by half, which changed slightly from 0.25 to 0.22 (Fig. 3.28a). The resultant wear rates of SLM parts demonstrated a similar variation tendency as the COF. An insufficient LED of 0.25 kJ/m resulted in a high wear rate of $5.3 \times 10{-}16$ m^3/(Nm). An increase in LED above 0.33 kJ/m lowered the wear rate significantly, and the values were within the range of 2.8×10^{-16}–3.1×10^{-16} m^3/(Nm) (Fig. 3.28b).

As to the second category of nanopowder, the average COFs and attendant wear rates of SLM-processed parts were generally higher than that of the SLM parts using the ball-milled TiC/Ti nanocomposite powder (Fig. 3.28), which implied the relatively low tribological property and antiwear performance of the parts consolidated from the directly mixed TiC/Ti nanocomposite powder. The influence of LED on the COF and wear rate showed its unique characteristics in this instance. At a relatively low LED of 0.25 kJ/m, the average COF of 0.61 and resultant wear rate of 5.8×10^{-16} m^3/(N m) were highest, which was similar as the SLM-consolidated ball-milled TiC/Ti nanocomposite powder. Differently, as the applied LED increased from 0.33 to 1.0 kJ/m, the average COF increased markedly from 0.28 to 0.48 (Fig. 3.28a), resulting in a significant elevation of wear rate from 3.2×10^{-16} to 4.9×10^{-16} m^3/(Nm) (Fig. 3.28b). Furthermore, it was noted that for the given powder system and LED, the wear rate of the SLM-processed TiC/Ti nanocomposite generally showed a decrease as the obtained COF decreased (Fig. 3.28).

The high-magnification FE-SEM characterization was performed to study the morphologies of worn surfaces, in order to disclose the underlying microstructures responsible for the variation of tribological property. For the directly mixed TiC/Ti nanocomposite powder, the worn surface of SLM-processed part at a relatively high LED of 1.0 kJ/m was porous and consisted of loose and coarsened grains with a mean size of 450 nm (Fig. 3.29a). The formation of the coarsened dendritic microstructure and resultant disappearance of nanostructured TiC reinforcement in this case (Fig. 3.27a) were regarded as the direct factor in producing the coarse-grained worn surface (Fig. 3.29a) with a limited anti-wear performance (Fig. 3.28). As the applied LED decreased to 0.5 kJ/m, the worn surface became dense on a microscopic scale and the average grain size decreased to 250 nm (Fig. 3.29b). Interestingly, at an even lower LED of 0.33 kJ/m, the worn surface consisted of significantly refined grains with the sizes generally less than 200 nm (Fig. 3.29c). In this situation, the favorable nanostructured TiC reinforcement was produced after SLM (Fig. 3.27c), which in turn favored the grain refinement within the worn surface (Fig. 3.29c) and the enhancement of tribological property (Fig. 3.28).

3.7.4 Influence of Nanopowder Characteristics on Densification Behavior and Microstructural Development

The study in this section reveals that the preparation and characteristics of nanopowder have some significant effects on the mechanisms of SLM densification and microstructural development. As schematically depicted in Fig. 3.30, the as-used

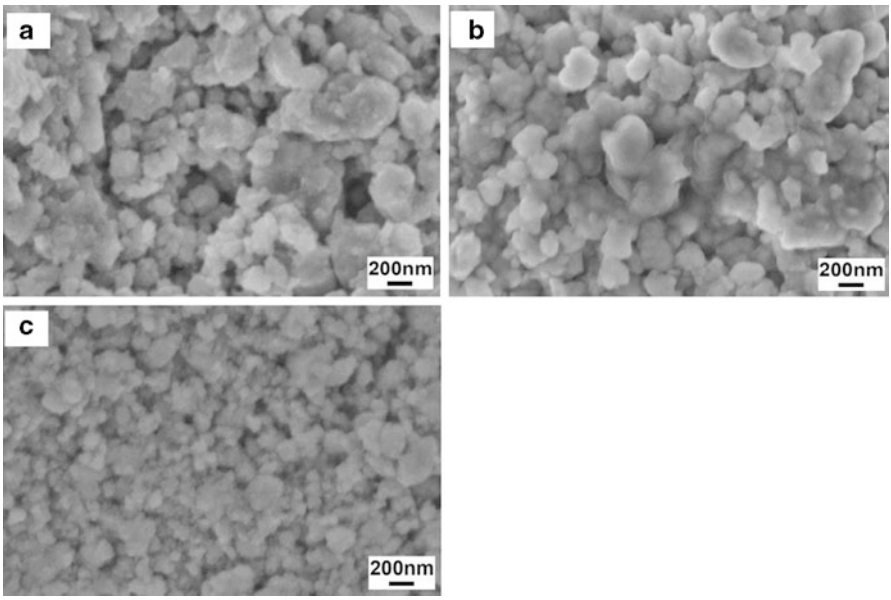


Fig. 3.29 FE-SEM images showing typical microstructures on worn surfaces of SLM-processed parts using the directly mixed TiC/Ti nanocomposite powder and various SLM parameters: **a** LED = 1.0 kJ/m, v = 0.1 m/s; **b** LED = 0.5 kJ/m, v = 0.2 m/s; **c** LED = 0.33 kJ/m, v = 0.3 m/s

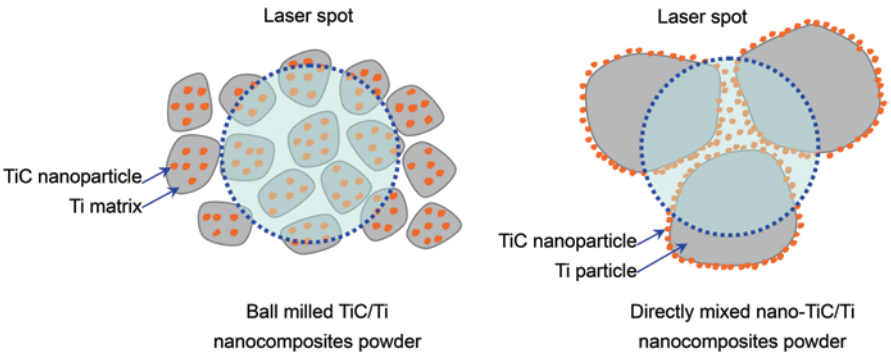


Fig. 3.30 Schematic of interaction mechanisms of laser beam with the two kinds of TiC/Ti nanocomposite powder

two kinds of TiC nanoparticles experience the different laser irradiation mechanisms during laser–powder interaction. For the ball-milled TiC/Ti nanocomposite powder, the TiC nanoparticles are dispersed uniformly in the interior of Ti matrix (Fig. 3.1d). Therefore, in the initial stage of laser melting, the TiC nanoparticles do not expose directly to laser irradiation (Fig. 3.30a). The dissolution of the TiC lags

behind the melting of Ti. With the sufficient wetting of the surrounding Ti liquid, the TiC nanoparticles become melted in laser-irradiated molten pool, followed by a reprecipitation process to form the desired nanostructure. As the melting and crystallization of TiC nanophase are free from the direct interaction of laser beam, the influence of SLM parameters on the microstructural development is not significant. The lamellar nanostructure of the TiC reinforcement in the SLM-processed nanocomposite can be maintained within a wide range of SLM parameters (Fig. 3.26).

Differently, for the directly mixed nano-TiC/Ti nanocomposite powder, the TiC nanoparticles are distributed around the Ti powder surface (Fig. 3.2c) and, accordingly, the laser beam acts on the TiC nanoparticles directly (Fig. 3.30b). The TiC nanoparticles undergo a simultaneous melting as the Ti powder. In the area exposed to the laser beam, the effect of evaporative recoil on the melt is significant and the resultant dynamic recoil pressure tends to exert an effective disturbance on SLM behavior of TiC nanophase. The balling effect, which is essentially caused by the melt instability [29], is more serious in this instance (Fig. 3.25b), thereby decreasing the obtainable densification level (Fig. 3.23). Also, the precipitated TiC nuclei tend to receive a more significant kinetic instability and turbulence on a microscopic scale. Consequently, the microstructures of SLM-processed directly mixed TiC/Ti nanocomposite powder are sensitive to the applied SLM parameters, and the TiC reinforcement experiences a successive variation from the nanoscale lamellar structure to the relatively coarsened dendritic microstructure as the linear laser energy density increases (Fig. 3.27).

Furthermore, the different powder morphology (size and shape) of as-prepared two kinds of powders also influences the final SLM microstructures. As relative to the directly mixed nano-TiC/Ti powder system, the homogeneity of particle structure and size distribution of the ball-milled TiC/Ti composite powder shows a significant enhancement (Fig. 3.1c vs. 3.2c). The interaction of the laser beam with the milled powder, accordingly, becomes much smoother, leading to a steadier laser melting process and fewer disturbances in the crystallization and development of TiC nanostructures (Fig. 3.26 vs. 3.27).

3.7.5 Relationship of Densification, Microstructure, and Wear and Tribological Performance

The study in this chapter reveals that the densification level, microstructural features, and wear and tribological performance of SLM-processed TiC/Ti nanocomposite parts are controlled by the preparation method of nanocomposite powder, the content of nanoparticles, and the corresponding SLM processing parameters. Under the optimal component contents and processing conditions, the SLM-processed bulk-form TiC/Ti nanocomposites have near full density and superior wear and tribological performance. As relative to the pure Ti parts produced using SLM [31], the COF of TiC/Ti nanocomposites decreased at least by 50 %, and the resultant wear rate lowered at least by 75 %. In order to disclose the underlying mecha-

nisms contributed to the performance enhancement, a comprehensive relationship of as-used nanopowder, SLM process, microstructures, and mechanical properties is determined.

Firstly, the densification rate of SLM parts plays a basic role in determining the tribological property. At the relatively low-laser energy input, although the TiC reinforcement exhibits the favorable nanostructure, the SLM densification response is limited due to the pores formation caused by balling effect, resulting in a significant increase in the COF and wear rate. Secondly, only when the nanostructure of the TiC reinforcement is maintained after SLM, can the tribological performance of SLM parts be maximized. For the ball-milled TiC/Ti nanocomposite powder, the nanoscale lamellar TiC reinforcement is formed within a wide range of laser energy densities. During sliding wear tests, the homogeneously dispersed ultrafine TiC nanophase is not easy to be split, but has a high tendency to stick to each other, due to the considerably small interfacial stresses of nanoscale reinforcing phase with the matrix. As the counterface ball slides against the surface, the worn surface experiences a sufficient plastic deformation at a temperature below its recrystallization temperature. A hardened sliding-treated layer consisting of significantly refined grains is thus produced on the wear surface, which favors the enhancement of wear resistance. In contrast, for the directly mixed nano-TiC/Ti powder, the nanostructured TiC reinforcement is not maintained in SLM part using a high-energy density, but showing micron-scale dendritic growth morphology. Although the SLM densification level is sufficiently high in this instance, the present relatively coarsened dendritic TiC reinforcement is easy to be fragmented during sliding, thereby producing a porous wear surface having coarsened grains and limited tribological property.

3.8 Conclusions

In this chapter regarding SLM additive manufacturing of bulk-form TiC/Ti nanocomposite parts, the main conclusions were summarized as follows.

1. The densification behavior of TiC/Ti nanocomposite parts was controlled by laser processing conditions, powder preparation method, and powder characteristics. Using an insufficient laser energy density lowered the SLM densification rate, due to the occurrence of balling effect. An increase in laser energy density produced near fully dense SLM parts. The SLM densification level of the ball-milled TiC/Ti nanocomposite powder showed an improvement of 0.6−1.5 % TD as relative to that of the directly mixed nano-TiC/Ti nanocomposite powder.
2. With the suitable SLM parameters determined, the TiC reinforcing phase in SLM-processed TiC/Ti nanocomposite parts typically had a lamellar nanostructure with a nanoscale thickness, which was completely different from the starting nanoparticle morphology before SLM. The lamellar nanostructure of the TiC reinforcement in SLM-processed ball-milled TiC/Ti nanocomposite parts could

be maintained within a wide range of laser energy densities. The microstructures of SLM-processed directly mixed nano-TiC/Ti nanocomposite powder were sensitive to SLM parameters, and the TiC reinforcement experienced a successive change from the nanoscale lamellar structure to the relatively coarsened dendritic microstructure as the laser energy density increased.

3. The sufficiently high densification rate of SLM-processed TiC/Ti nanocomposite parts played a fundamental role in improving wear and tribological property. In combination with the formation of the nanostructured TiC reinforcement, the considerably low COF and wear rate were obtained. The disappearance of nanoscale reinforcement due to the presence of coarsened dendritic TiC in the SLM-processed directly mixed nano-TiC/Ti powder at a high-laser energy density lowered the wear performance considerably.
4. The microstructural and mechanical properties of SLM-processed TiC/Ti nanocomposite parts were sensitive to the content of starting TiC nanoparticles. A reasonable increase in TiC nanoparticles content favored the formation of the homogeneously dispersed TiC reinforcement having a nanoscale lamellar structure, leading to the elevated microhardness and reduced COF and wear rate. The insufficient densification and disappearance of nanostructured TiC reinforcement at a high-TiC content above 17.5 wt.% decreased the hardness and wear performance.

References

1. Das M, Balla VK, Basu D et al (2010) Laser processing of SiC–particle–reinforced coating on titanium. Scripta Mater 63(4):438–441
2. da Silva AAM, dos Santos JF, Strohaecker TR (2005) Microstructural and mechanical characterisation of a Ti6Al4V/TiC/10p composite processed by the BE–CHIP method. Compos Sci Technol 65(11–12):1749–1755
3. Das M, Balla VK, Basu D et al (2012) Laser processing of in situ synthesized TiB–TiN–reinforced Ti6Al4V alloy coatings. Scripta Mater 66(8):578–581
4. Pei YT, Ocelik V, De Hosson JTM et al (2002) SiC_p/Ti6Al4V functionally graded materials produced by laser melt injection. Acta Mater 50(8):2035–2051
5. Majumdar JD, Li L (2010) Development of titanium boride (TiB) dispersed titanium (Ti) matrix composite by direct laser cladding. Mater Lett 64(9):1010–1012
6. Pang W, Man HC, Yue TM (2005) Laser surface coating of Mo–WC metal matrix composite on Ti6Al4V alloy. Mater Sci Eng A 390(1–2):144–153
7. Kondoh K, Threrujirapapong T, Imai H et al (2009) Characteristics of powder metallurgy pure titanium matrix composite reinforced with multi–wall carbon nanotubes. Compos Sci Technol 69(7–8):1077–1081
8. Lu WJ, Xiao L, Geng K et al (2008) Growth mechanism of in situ synthesized TiB_w in titanium matrix composites prepared by common casting technique. Mater Charact 59(7):912–919
9. Poletti C, Balog M, Schubert T et al (2008) Production of titanium matrix composites reinforced with SiC particles. Compos Sci Technol 68(9):2171–2177
10. Vreeling JA, Ocelík V, De Hosson JTM (2002) Ti–6Al–4 V strengthened by laser melt injection of WC_p particles. Acta Mater 50(19):4913–4924

11. Llorca J (2002) Fatigue of particle– and whisker–reinforced metal–matrix composites. Prog Mater Sci 47(3):283–353
12. Tjong SC (2007) Novel nanoparticle–reinforced metal matrix composites with enhanced mechanical properties. Adv Eng Mater 9(8):639–652
13. Mortensen A, Llorca J (2010) Metal matrix composites. Annu Rev Mater Res 40:243–270
14. Kumar SK, Krishnamoorti R (2010) Nanocomposites: structure, phase behavior, and properties. Annu Rev Chem Biomol Eng 1:37–58
15. Moya JS, Lopez–Esteban S, Pecharromán C (2007) The challenge of ceramic/metal microcomposites and nanocomposites. Prog Mater Sci 52(7):1017–1090
16. Ajayan PM, Schadler LS, Braun PV (eds) (2003) Nanocomposite science and technology. Wiley–VCH, Weinheim
17. Simchi A (2006) Direct laser sintering of metal powders: mechanism, kinetics and microstructural features. Mater Sci Eng A 428(1–2):148–158
18. Gu DD, Hagedorn YC, Meiners W et al (2011) Nanocrystalline TiC reinforced Ti matrix bulk-form nanocomposites by selective laser melting (SLM): densification, growth mechanism and wear behavior. Compos Sci Technol 71(13):1612–1620
19. von Walter M, Hollander DA, Wirtz T et al (2006) Structural, mechanical and in vitro characterization of individually structured Ti-6Al-4 V produced by direct laser forming. Biomaterials 27(7):955–963
20. Oliver Seely Jr (2000) Density and Archimedes' Principle. http://www.csudh.edu/oliver/satcoll/archmede.htm. Accessed 10 Mar 2015
21. Oliver WC, Pharr GM (1992) An improved technique for determining hardness and elastic modulus using load and displacement sensing indentation experiments. J Mater Res 7(6):1564–1583
22. Takamichi I, Roderick ILG (eds) (1993) The physical properties of liquid metals. Clarendon Press, Oxford
23. Simchi A, Pohl H (2003) Effects of laser sintering processing parameters on the microstructure and densification of iron powder. Mater Sci Eng A 359(1–2):119–128
24. Semak VV, Knorovsky GA, MacCallum DO et al (2006) Effect of surface tension on melt pool dynamics during laser pulse interaction. J Phys D 39(3):590–595
25. Zhang W, Sui ML, Zhou YH et al (2003) Electropulsing–induced evolution of microstructures in materials. Acta Metall Sin 39(10):1009–1018
26. Arafune K, Hirata A (1999) Thermal and solutal Marangoni convection in In–Ga–Sb system. J Cryst Growth 197(4):811–817
27. Chan YT, Choi SK (1992) Numerical simulations of inductive–heated float–zone growth. J Appl Phys 72(8):3741–3749
28. Tille J, Kelly JC (1963) The surface tension of liquid titanium. Br J Appl Phys 14(10):717–719
29. Niu HJ, Chang ITH (1999) Instability of scan tracks of selective laser sintering of high speed steel powder. Scripta Mater 41(11):1229–1234
30. Kruth JP, Levy G, Klocke F et al (2007) Consolidation phenomena in laser and powder–bed based layered manufacturing. CIRP Ann Manuf Technol 56(2):730–759
31. Gu DD, Hagedorn YC, Meiners W et al (2012) Densification behavior, microstructure evolution, and wear performance of selective laser melting processed commercially pure titanium. Acta Mater 60(9):3849–3860

Chapter 4
In Situ Ti–Si Intermetallic-Based Composites by Selective Laser Melting (SLM) Additive Manufacturing (AM): Designed Materials and Laser-Tailored *In Situ* Formation

Abstract Based on an integrated processing method of "Designed materials," "Laser-induced *in situ* reaction," and "Tailored mechanical performance," theTiC/Ti_5Si_3 and TiN/Ti_5Si_3 composite parts were produced by selective laser melting (SLM) additive manufacturing (AM) process, starting from the high-energy ball-milled SiC/Ti and Si_3N_4/Ti powder systems. The influence of the applied laser energy density on the densification behavior, microstructural features, microhardness, and wear property of *in situ* Ti_5Si_3-based composites was studied. The occurrence of balling phenomenon at a low-laser energy density combined with a high-scan speed and the formation of thermal cracks at an excessive laser energy input generally decreased densification rate. The *in situ* formed TiC and TiN reinforcing phases experienced a successive morphological change as the SLM processing conditions varied. The underlying metallurgical mechanisms accounted for the different growth mechanisms of TiC and TiN reinforcement during SLM process were disclosed. The *in situ* TiC/Ti_5Si_3 and TiN/Ti_5Si_3 composite parts prepared under the optimal SLM conditions had a near-full density, a significantly elevated microhardness (>980 HV), a considerably low coefficient of friction (<0.2), and a reduced wear rate. The enhanced wear resistance was attributed to the formation of adherent strain-hardened tribolayer covered on the worn surface.

4.1 Introduction

The titanium silicide (Ti_5Si_3)-intermetallic compound has recently been considered as a promising candidate material for high-temperature structural applications, because of its high melting temperature (2403 K), relatively low density (4.32 g/cm^3), capacity to retain high strength up to 1473 K, and excellent oxidation and creep resistance [1, 2]. Nevertheless, due to its complex hexagonal crystal structure with a low symmetry ($D8_8$), the monolithic Ti_5Si_3 has a considerably low fracture toughness at ambient temperature [3]. Therefore, a major challenge for a successful application of Ti_5Si_3 material is to reduce its room temperature brittleness. In this respect, the previous work by Wang et al. [4], Shon et al. [5], and Li et al. [6] has ascertained that the preparation of ceramic-reinforced Ti_5Si_3-based composites by incorporating

© Springer-Verlag Berlin Heidelberg 2015

D. Gu, *Laser Additive Manufacturing of High-Performance Materials,*
DOI 10.1007/978-3-662-46089-4_4

the stiffer ceramic phase within Ti_5Si_3 matrix is an important method to improve the integrated mechanical properties including fracture toughness. In particular, the development of the novel *in situ* composites, in which the ceramic reinforcements are synthesized in the metallic matrix by chemical reactions between elements, exhibits more significant advantages, e.g., the refined microstructural scale of *in situ* formed reinforcements, the clean reinforcement/matrix interfaces with stronger interfacial bonding, and the elevated thermodynamic stability and mechanical properties of the composites [7]. On the other hand, a reasonable selection of the ceramic reinforcement which is feasible for Ti_5Si_3 matrix is required. It is known that the coefficient of thermal expansion (CTE) and the elastic modulus are two most important material properties that determine the level of residual stress in composites [8]. The TiC has been demonstrated to be a suitable candidate material used as the reinforcement for Ti_5Si_3-based composites, due to the similar CTEs (Ti_5Si_3 9.7×10^{-7}/K vs. TiC 7.7×10^{-7}/K) [1, 2]. The TiN, which has an almost same CTE (9.4×10^{-7}/K) as that of Ti_5Si_3, matches even better with Ti_5Si_3 matrix. Furthermore, the elastic modulus of TiN (250.37 GPa) is lower than that of TiC (439.43 GPa) [9] and, normally, the stress of composites can be controlled by using material with a low elastic modulus [8]. Therefore, the TiN is regarded as another more promising ceramic reinforcement for Ti_5Si_3.

Bulk-form composites containing the *in situ* formed reinforcements are normally prepared by conventional methods including powder metallurgy (PM) [10, 11], self-propagating high-temperature synthesis (SHS) [12, 13], and casting [14, 15]. However, the production of composites by these conventional processes is prone to generate large agglomerates of reinforcing phases, thereby decreasing the microstructural homogeneity and resultant mechanical properties. Furthermore, the high-temperature ceramic reinforcing phases are typically remained in particle morphology in the conventional composites, since the workable processing temperature normally cannot elevate above the melting points of ceramics. The incorporation of the solid ceramic particles within the matrix, however, tends to induce the formation of interfacial microcracks, due to the limited wetting characteristics between ceramics and metals. Furthermore, the conventional processes, which generally need expensive and dedicated tools such as moulds or dies, are not suitable for small volume production and complex shapes. The complicated pre- and postprocessing steps necessary in conventional routes make them a time-consuming process. The probability of the formation of process defects also elevates during the long cycle time. Therefore, novel processing methods are highly required for the direct net-shape fabrication of complex-shaped ceramic reinforced composite components having favorable microstructural and mechanical properties.

Selective laser melting (SLM), as mentioned in Chap. 2, has the capability to fabricate three-dimensional parts with any complex configurations directly from powder materials. SLM creates fully dense parts in a layer-by-layer manner by selectively fusing and consolidation of thin layers of loose powder using a high-energy laser beam, without any postprocessing requirements. Recently, the author has focused on the preparation of *in situ* composite parts using SLM process, considering its flexibility in feedstock and shapes. Nevertheless, due to the complex

metallurgical nature of an *in situ* SLM system, which involves both chemical reactions and multiple modes of heat, mass, and momentum transfer, SLM-processed composites may suffer from processing problems, such as gas entrapment, aggregation of reinforcements, residual stresses, and interfacial microcracks. Furthermore, SLM is performed based on a complete melting/solidification mechanism and, accordingly, the high melting point *in situ* ceramic reinforcing phases are formed through a dissolution/precipitation mechanism. Different to the particle morphology before melting, the *in situ* formed ceramic crystals may have versatile growth morphologies in the finally solidified structures. Therefore, the unpredictability and/or uncontrollability of the formation of *in situ* phases and microstructures in an SLM route are still a major challenge. As the microstructural features of SLM-processed powder may significantly influence the attendant mechanical properties, a detailed understanding of the crystallization mechanism and microstructural development of the *in situ* phases during SLM process is required.

In the present Chapter, SLM of the high-energy ball-milled SiC/Ti and Si_3N_4/Ti powder systems was performed to prepare bulk-form TiC/Ti_5Si_3 and TiN/Ti_5Si_3 *in situ* composites. The evolutions of phases and microstructures of SLM-processed composites under different SLM processing parameters were studied and the mechanical properties such as densification rate, microhardness, and wear property were assessed. The predominant metallurgical mechanisms responsible for the variations in microstructural and mechanical properties were disclosed, in order to establish a material–microstructure–property relationship that enables the successful additive manufacturing of novel *in situ* composite parts.

4.2 Selective Laser Melting (SLM) of *In Situ* TiC/Ti_5Si_3 Composite Parts with Novel Reinforcement Architecture and Elevated Performance

4.2.1 Ball Milling of SiC/Ti Powder System for SLM Process

The starting powder materials were 99.0% pure, irregular-shaped SiC powder with an average particle size of 13 μm and 99.9% purity, poly-angular Ti powder with a mean particle size of 45 μm. The original SiC and Ti components were mixed according to a weight ratio of 23.8:76.2, i.e., an equivalent molar ration of 3:8. The two powder components were milled in a Fritsch Pulverisette 6 high-energy planetary mono-mill at a rotation speed of 300 rpm for 15 h, with a ball-to-powder weight ratio of 10:1. For the SLM process using a powder bed method, a thin powder layer with a thickness $\leq$50 μm is normally used, which further requires a refined particle size. The particle size distribution of the ball-milled composite powder was determined using a laser particle size analyzer. The as-milled powder had a considerably refined particle size with an average value D_{50} = 3.16 μm. Furthermore, a high

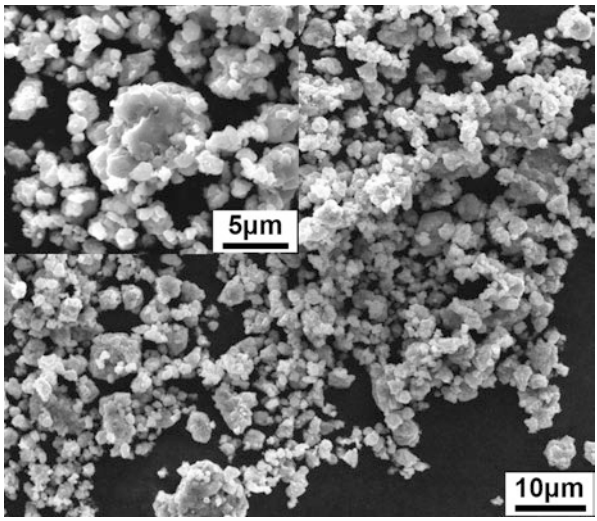


Fig. 4.1 Scanning electron microscope (SEM) image showing typical microstructure of ball-milled SiC/Ti powder system

flowability of the powder system is necessary for a smooth spreading of powder during SLM process. The as-milled composite powder consisted of the equiaxed-shaped fine particles (Fig. 4.1), exhibiting a homogeneous particle size distribution (D_{10} = 1.04 μm, D_{25} = 2.19 μm, D_{75} = 4.01 μm, D_{90} = 5.22 μm). The spreading property of the as-prepared composite powder on the powder bed was sufficiently favorable for SLM. The energy dispersive X-ray spectroscope (EDX) method was applied to determine the chemical compositions of the total powder particles as investigated and the detected elements were 20.7 at.% C, 22.2 at.% Si, and 57.1 at.% Ti (i.e., 6.9 wt.% C, 17.3 wt.% Si, and 75.8 wt.% Ti). As relative to the compositions of the initial powder mixture (i.e., 7.1 wt.% C, 16.8 wt.% Si, and 76.1 wt.% Ti), the change of compositions of the milled powder was considerably slight.

4.2.2 Formation Mechanism and Microstructural Development of In Situ TiC Reinforcement during SLM Processing of SiC/Ti Powder System

4.2.2.1 Formation Mechanism of *In Situ* TiC Reinforcement During SLM

SLM processing of the ball-milled SiC/Ti powder system was performed based on the procedures presented in Sect. 3.3 of Chap. 3. The as-defined fiber laser was applied as the energy source and the following suitable parameters were fixed: the focused spot size of 70 μm, the scan line hatching spacing of 50 μm, and the powder layer thickness of 50 μm. The laser powers (P) of 70–120 W and scan speeds (v) of 0.1–0.5 m/s were settled by SLM control program. The "linear laser energy density"

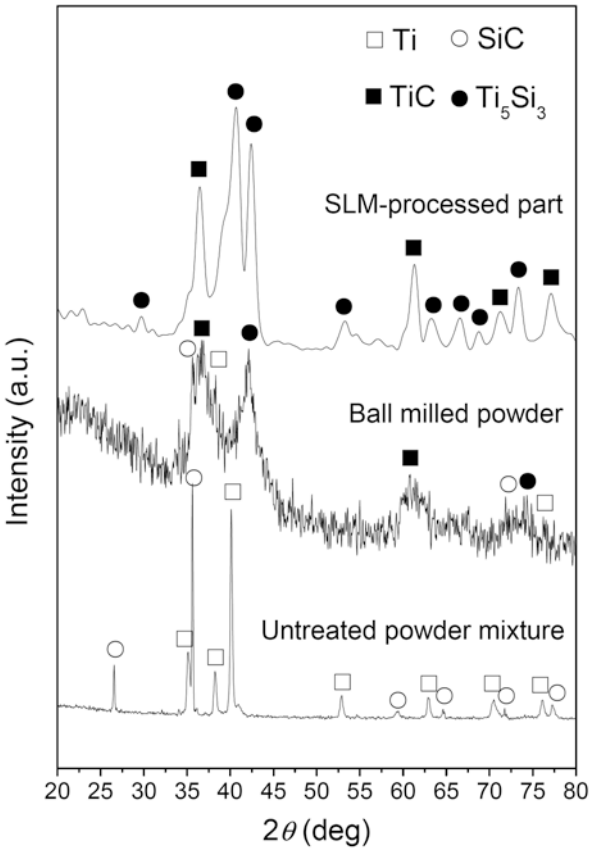


Fig. 4.2 Typical XRD spectra of staring untreated powder, ball-milled powder for SLM, and SLM-processed composite parts

(LED) was defined to assess the combined effect of P and v during individual line scanning.

Figure 4.2 depicts the typical X-ray diffractometer (XRD) spectra of the starting powder mixture, the ball-milled composite powder for SLM, and the SLM-processed part. The diffraction peaks corresponding to SiC and Ti were identified in the initial powder mixture. After ball milling, the diffraction peaks of powder became significantly broadened and, meanwhile, their intensity was weakened, implying the formation of refined crystallites in as-milled powder. Besides the diffraction peaks for the initial SiC and Ti constituents, the peaks corresponding to TiC (based on JCPDS Card No. 05-0693) and Ti_5Si_3 (based on JCPDS Card No. 29-1362) new phases were also detected. As an *in situ* chemical reaction was designed in the present SiC/Ti powder system, the ball milling process led to a partial occurrence of the designed reaction $8Ti + 3SiC = 3TiC + Ti_5Si_3$, due to the continuous microscopic action of the mechanical force by the repeated ball-powder-ball collisions [16]. The detected diffraction peaks in SLM-processed specimen corresponded exactly to TiC

and Ti_5Si_3 phases. It was accordingly concluded preliminarily that the SLM of as-milled powder favored the *in situ* formation of TiC/Ti_5Si_3 composites.

In order to further investigate the crystal structures and constitution phases of SLM-processed composites, the transmission electron microscope (TEM) characterization was performed, with the results illustrated in Fig. 4.3. The chemical compositions of the selected grain were determined by EDX accessory in TEM, as revealed in Table 4.1. The atomic ratio of the detected C and Ti elements was very close to 1:1, whereas the elemental content of Si was negligible. EDX identifica-

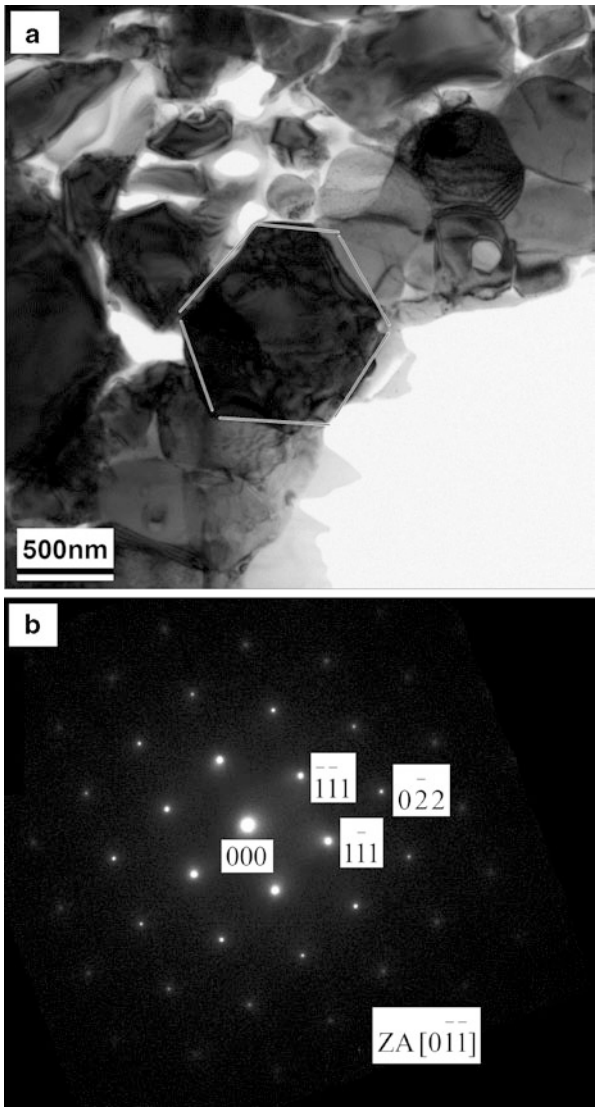


Fig. 4.3 Bright field TEM micrograph showing crystalline microstructure in SLM-processed part (**a**), SADP of TiC phase (**b**)

Table 4.1 Chemical compositions of the selected grain in Fig. 4.3a determined by energy dispersive X-ray spectroscope (EDX)

Element	Weight fraction (wt. %)	Atomic fraction (at. %)	Uncertainty (%)
C (K)	19.48	49.04	0.30
Si (K)	0.28	0.30	0.02
Ti (K)	80.23	50.64	0.31

tion accordingly ascertained the *in situ* formation of TiC grains. Furthermore, the selected area diffraction pattern (SADP) of the corresponding grain in Fig. 4.3a is exhibited in Fig. 4.3b. By calculating, the lattice constant was approximately 4.32 Å, which further confirmed that the grain was TiC. It was accordingly reasonable to conclude that the *in situ* TiC reinforcement was produced after SLM due to the occurrence of the designed *in situ* reaction.

The possibility for the *in situ* formation of TiC/Ti_5Si_3 composites can be proved by the Ti–Si–C ternary phase diagram, as referred in Fig. 4.4. Although the direct measurement of SLM temperature is presently unrealized in this study, it is reasonable to consider that the operative SLM temperature, at least, is higher than the melting temperate of Ti. On the one hand, the laser energy density during SLM is sufficiently high to melt the Ti component, due to the application of high-energy fiber laser with a considerably small focused spot size. On the other hand, the author's previous study on microstructures of SLM-processed pure Ti parts using the similar laser processing conditions has suggested the full melting and re-solidification behavior of Ti [18]. As indicated in Fig. 4.4, the content of Ti component in the present Ti–Si–C system for SLM is lower than the Ti content in the eutectic composition point. The high temperature Ti tends to exhaust during the eutectic reaction, leading to the formation of TiC and Ti_5Si_3 phases. A similar chemical reaction was

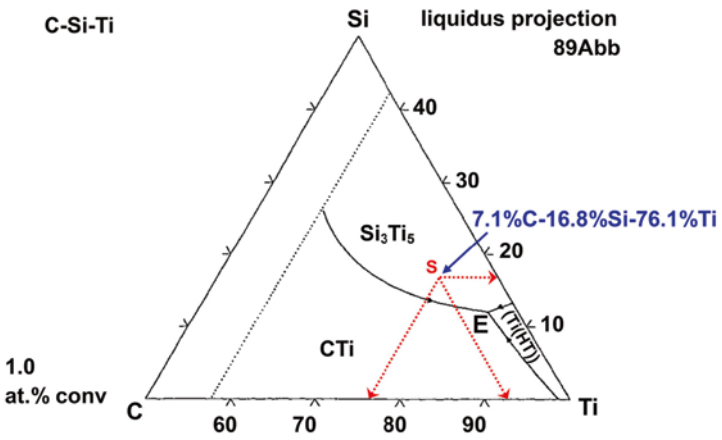


Fig. 4.4 Ti–Si–C ternary phase diagram, see Ref. [17]

also detected in Das et al.'s work [19] on laser engineered net shaping (LENS) cladding of the SiC particle reinforced coating on Ti, using the SiC powder with a large particle size of 50–150 µm. These relatively large SiC particles remained their particle cores after LENS. The SiC particle surface dissolved in the molten pool, leading to the formation of TiC reaction layer around SiC particles. Meanwhile, the Si that was released during the reaction combined with Ti to form Ti_5Si_3. Both the author's present work and the previous research on LENS of SiC/Ti material system revealed that the *in situ* phase reaction in SiC/Ti system to form TiC and Ti_5Si_3 phases was possible during SLM process.

4.2.2.2 Influence of Laser Scan Speed on Microstructural Evolution of *In Situ* TiC Reinforcement During SLM

Figure 4.5 shows the influence of the applied laser scan speed on the characteristic microstructures of the reinforcing phase in SLM-processed composites. The laser power of 90 W was fixed. Generally, the reinforcing phase exhibited the dendritic growth morphologies. Again, the quantitative elemental determination by EDX accessory in SEM revealed that these dendritic reinforcements were generally composed of Ti and C elements with 1:1 atomic ratio. The combination of XRD, TEM, and EDX analyses, accordingly, confirmed the formation of *in situ* TiC reinforcing phase in SLM-processed composites. Different from the above mentioned

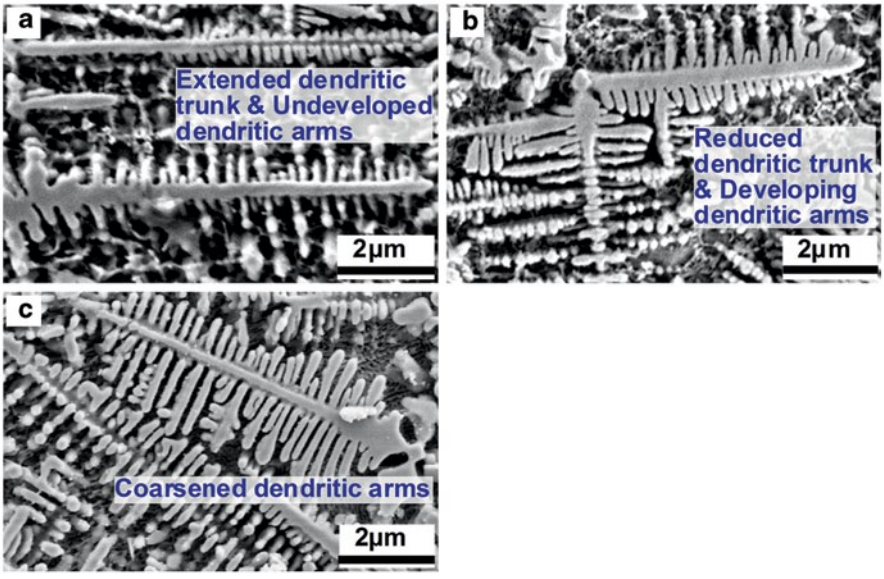


Fig. 4.5 Field emission scanning electron microscope (FE-SEM) images showing characteristic growth morphologies of TiC reinforcing phase in SLM-proceeded TiC/Ti_5Si_3 composites at different scan speeds: **a** 0.5 m/s, **b** 0.3 m/s, **c** 0.1 m/s

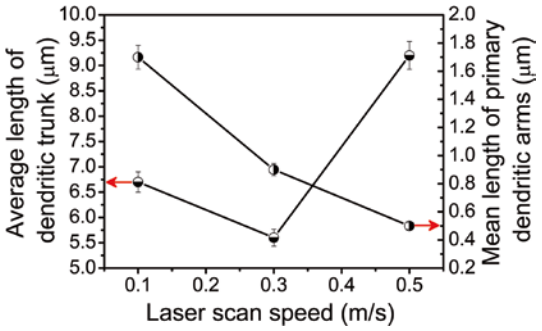


Fig. 4.6 Influence of laser scan speed on the size of dendritic TiC crystals in SLM-proceeded TiC/Ti_5Si_3 composites

Bandyopadhyay et al.'s work [19], in the author's work on SLM of SiC/Ti powder system, the *in situ* reaction was sufficiently processed to form the TiC/Ti_5Si_3 composites. As a main feature, there were no residual SiC particles that were detected after SLM. Since the ball milling process was applied to treat the starting SiC/Ti powder mixture, the SiC component became considerably refined after milling and, meanwhile, a fraction of SiC even decomposed under the long-term action of the mechanical force during milling (Fig. 4.2). In combination with the considerably high laser energy input caused by the small focus fiber laser, the *in situ* reaction was expected to perform fully after SLM. As the second difference in the present study, the *in situ* formed TiC reinforcing phase had unique dendritic growth morphology, differing from the particle morphology of the reinforcement in the LENS or conventional powder metallurgy processing of *in situ* composites containing TiC reinforcing phase. Accordingly, SLM of the ball-milled SiC/Ti *in situ* powder system exhibited an interesting microstructural development.

Nevertheless, a careful comparison of the microscopic features of these dendrites revealed some distinct variations with the applied laser scan speeds. At a relatively higher scan speed of 0.5 m/s, the TiC dendrites typically had the significantly extended dendritic trunks (Fig. 4.5a) and their average length reached 9.2 μm (Fig. 4.6). The primary dendritic arms, however, were not efficiently developed in this instance and a portion of trunks were even bare of the arms (Fig. 4.5a), resulting in a considerably low average arm length of 0.5 μm (Fig. 4.6). As the applied scan speed decreased to 0.3 m/s, the TiC dendritic trunks became shortened and their mean length decreased sharply to 5.6 μm. The primary dendritic arms experienced an apparent growth and the average length increased to 0.9 μm (Figs. 4.5b and 4.6). At an even lower scan speed of 0.1 m/s, the microstructures of TiC dendrites became considerably coarsened. The average length of dendritic trunks increased slightly to 6.7 μm, but the change of the mean length of primary dendritic arms was significant, showing ~twofold increase to 1.7 μm (Figs. 4.5c and 4.6). The growth mechanisms of the *in situ* TiC dendrites at different laser scan speeds were, accordingly, concluded as follows:

- The dendritic trunks became elongated on increasing laser scan speed.
- The primary dendritic arms experienced a more significant development as laser scan speed decreases.

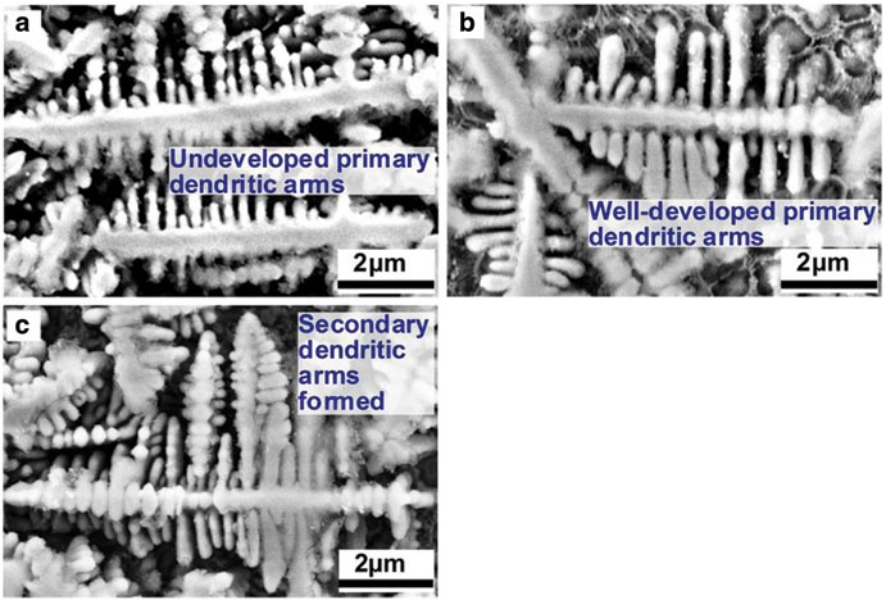


Fig. 4.7 FE-SEM images showing typical microstructures of the dendritic TiC reinforcing phase in SLM-proceeded TiC/Ti_5Si_3 composites using various laser powers: **a** 75 W, **b** 100 W, **c** 120 W

4.2.2.3 Influence of Laser Power on Microstructural Evolution of *In Situ* TiC Reinforcement During SLM

The changes of microstructural features of TiC dendrites in SLM-processed TiC/Ti_5Si_3 composites with the applied laser powers are illustrated in Fig. 4.7. Laser scan speed of 0.3 m/s was constant. It showed that the average length of dendritic trunks (7.6–8.0 μm) remained almost unchanged for the various laser powders (Fig. 4.8), whereas the size and microstructure of dendritic arms were significantly influenced by the applied laser power (Fig. 4.7). For a relatively low laser power of 75 W, the thin, sparse, and short primary dendritic arms with a considerably low average length of 0.7 μm were present (Figs. 4.7a and 4.8), implying an insufficient development of dendritic arms in this institution. As the laser power increased to 100 W, the primary arms of TiC dendrites were well-developed, producing the relatively coarsened arms with an increased average length of 1.3 μm (Figs. 4.7b and 4.8). As an even higher laser power of 120 W was applied, the mean length of the primary dendritic arms further increased to 2.2 μm (Fig. 4.8) and, meanwhile, the formation of the secondary dendritic arms was clearly observed (Fig. 4.7c), which implied that the TiC dendrites underwent a more significant crystal growth and development in this instance. A close look at the microstructural variations of TiC dendrites at diffefrent laser powers revealed that:

- Laser power exerts a significant influence upon the growth morphology of dendritic arms, but a negligible effect on the development of dendritic trunks.

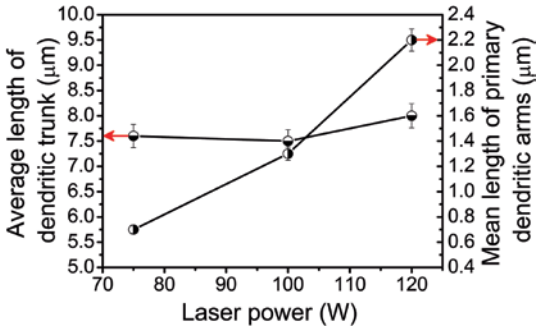


Fig. 4.8 Effect of laser power on the size of TiC dendrites in SLM-proceeded TiC/Ti_5Si_3 composites

- An increase in laser power enhanced the growth activity of primary and even secondary dendritic arms.

Figure 4.9 depicts schematically the crystallization and growth mechanisms of dendritic TiC crystal under different SLM conditions. The applied laser scan speed controls the growth of both dendritic trunks and arms (Figs. 4.5 and 4.6), whereas the laser power mainly influences the development of dendritic arms (Figs. 4.7 and

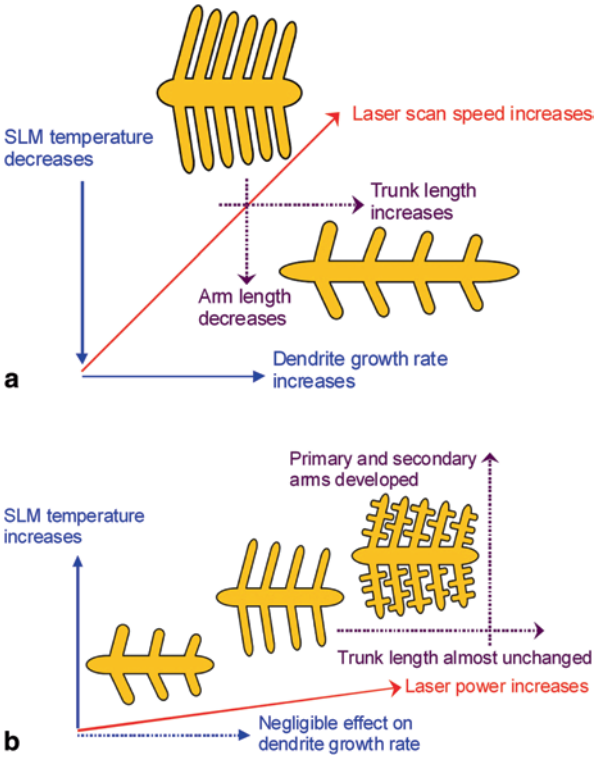


Fig. 4.9 Schematic of the influence of scan speed (**a**) and laser power (**b**) on the development mechanisms of TiC dendritic trunks and arms during SLM

Fig. 4.8). During laser rapid solidification, the local growth velocity (v_s) of dendritic trunk is controlled by laser scan speed (v) and can be calculated by [20]:

$$v_s = v\cos\theta \tag{4.1}$$

where θ is the angle between the vectors v_s and v. A higher scan speed v, accordingly, leads to a more significant growth and elongation of dendritic trunks (Figs. 4.5 and 4.9a), due to the enhanced v_s in this situation. Therefore, it is reasonable to conclude that the growth of TiC dendritic trunks during SLM is kinetically dependent on laser scan speed. On the other hand, both scan speed (v) and laser power (P) influence the linear laser energy density (LED) input to the powder layer being melted, as defined by Eq. 3.1 in Chap. 3. The maximum temperature rise for the melt within the molten pool under laser irradiation can be estimated by [21]:

$$\Delta T_{max} = \frac{2A \times LED}{k}\sqrt{\frac{\kappa_{th}\tau_p}{\pi}} \tag{4.2}$$

where A is the absorptivity, k the thermal conductivity, κ_{th} the heat diffusivity, and τ_p is the laser irradiation duration. A decrease in v or an increase in P generally results in a higher LED and the resultant elevated thermalization of the energy, which further produces a higher operative temperature. Therefore, a larger amount of heat tends to accumulate around the tips of the dendritic arms being developed, which in turn provides a considerable internal energy for the sufficient growth of primary dendritic arms and even secondary arms (Fig. 4.9). It is accordingly concluded that the development of TiC dendritic arms is temperature-dependent, which is further controlled by increasing laser power or decreasing scan speed.

4.2.3 *Influence of SLM Processing Conditions on Densification, Microstructure, and Wear Behavior of In Situ TiC/Ti_5Si_3 Composite Parts*

4.2.3.1 Effect of SLM Parameters on Constitutional Phases

Typical XRD patterns of the SLM-processed specimens using different linear laser energy density (LED) are depicted in Fig. 4.10. The strong diffraction peaks corresponding to Ti_5Si_3 (JCPDS Card No. 29-1362) and TiC (JCPDS Card No. 05-0693) phases were generally identified in SLM-processed specimens using various LED (Figs. 4.10a, b, c, d). Meanwhile, the diffraction peaks for the initial Ti and SiC phases of the powder were not detected after SLM. Thus, it was reasonable to conclude that SLM of the Ti/SiC system led to the *in situ* formation of TiC/Ti_5Si_3 composites free of any residual impurity phases, due to the spontaneous, complete occurrence of the designed reaction $8Ti+3SiC=3TiC+Ti_5Si_3$ during SLM process.

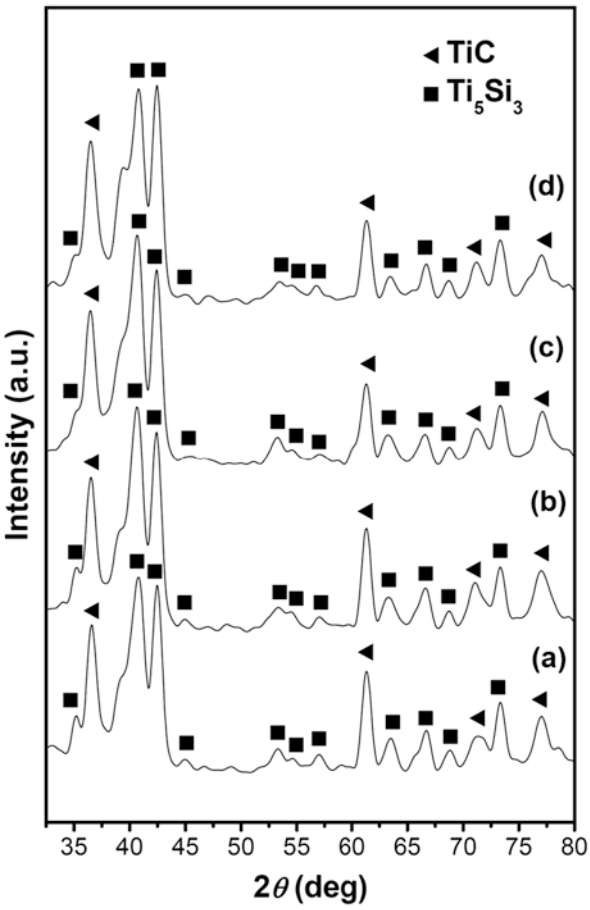


Fig. 4.10 XRD spectra of SLM-processed composite parts at various linear laser energy densities (LED): **a** LED = 0.2 kJ/m, **b** LED = 0.267 kJ/m, **c** LED = 0.4 kJ/m, **d** LED = 0.8 kJ/m

4.2.3.2 Effect of SLM Parameters on Compositions and Microstructures

Figure 4.11 illustrates the influence of linear laser energy density (LED) on microstructures of SLM-processed specimens. The quantitative elemental determination by EDX indicated that the dendrite-shaped constituents were typically composed of Ti and C elements with the atomic ratio very close to 1:1. The Ti and Si elements were detected within the underlying matrix and the Ti:Si atomic ratio was ~5:3. A combination of XRD and EDX results, accordingly, confirmed the *in situ* formation of TiC/Ti_5Si_3 composites after SLM. Nevertheless, the microstructural features of the formed TiC reinforcing phase exhibited distinct variations with the applied SLM processing conditions. At the relatively high scan speeds ($v \geq 0.3$ m/s) and attendant low LED, the TiC phase generally had a considerably slender dendritic structure and dispersed uniformly throughout the Ti_5Si_3 matrix (Figs. 4.11a and c). The length of dendritic trunk and primary dendritic arms reached 8.5–10.0 μm and 0.8–0.9 μm, respectively, and the primary arm spacing, 0.15 μm, was well within

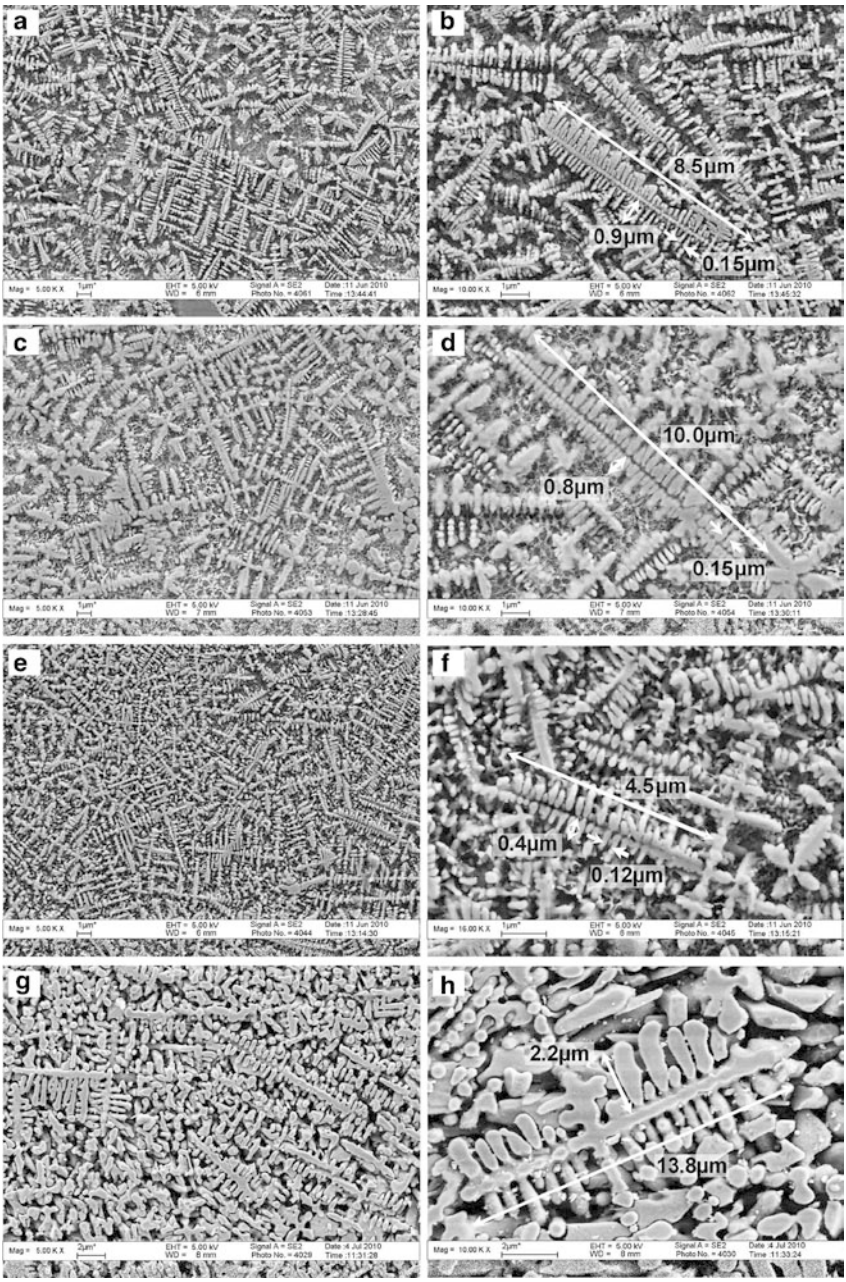


Fig. 4.11 FE-SEM images showing characteristic microstructures of SLM-processed *in situ* TiC/Ti_5Si_3 composite parts at various linear laser energy densities (LED) and scan speeds (v): **a** LED = 0.2 kJ/m, v = 0.4 m/s; **c** LED = 0.267 kJ/m, v = 0.3 m/s; **e** LED = 0.4 kJ/m, v = 0.2 m/s; **g** LED = 0.8 kJ/m, v = 0.1 m/s. **b**, **d**, **f**, and **h** are local magnifications of **a**, **c**, **e**, and **g**, respectively. The length and arm spacing of the dendrites are measured automatically by the image analysis software in SEM system

a submicron scale (Figs. 4.11b and d). As the LED increased by lowering the scan speed to 0.2 m/s, a continuous, homogeneous network of the significantly refined TiC dendrites was formed (Fig. 4.11e). The average length of dendritic trunk and primary dendritic arms decreased below 4.5 μm and 0.4 μm, respectively, and the primary arm spacing was further refined to 0.12 μm (Fig. 4.11f). However, at a low scan speed of 0.1 m/s and resultant high LED of 0.8 kJ/m, although the composite structure was almost uniform, the dendrites showed a large degree of coarsening (Fig. 4.11g). The mean length of dendritic trunk and primary dendritic arms showed three to fivefold increase, reaching 12.8 and 2.2 μm, respectively (Fig. 4.11h).

Previous work on the conventional powder metallurgy (PM) processing of Ti–Si based *in situ* composites reveals that the ceramic reinforcement was typically in the particle morphology [4–6], due to a solid-state sintering (SSS) or a partially melted liquid phase sintering (LPS) mechanism used. Different from these existent results, the TiC reinforcing phase in SLM-processed TiC/Ti_5Si_3 composites is developed into a unique dendritic structure. Normally, SLM is preformed based on a complete melting/solidification manner and the TiC phase is formed through a dissolution/precipitation mechanism by means of the heterogeneous nucleation of TiC nuclei and subsequent grain growth. The local temperature gradient and chemical concentration gradient in the molten pool give rise to surface tension gradient and associated Marangoni convection, producing a significant turbulence in the pool [22]. The TiC precipitates, thus, tend to experience a dendrite growth, due to the instability of the solid–liquid interface caused by the perturbation. According to the Gibbs–Thomson temperature equation, the dendrite tip temperature T_t is expressed as [23]:

$$T_t = T_M + mC_{Li}^* - \frac{RT_M^2}{\Delta H_f} \cdot \frac{V_t}{V_0} \tag{4.3}$$

where T_M is the melting point of the pure component, m the liquidus slope, C_{Li}^* the liquid solute concentration at the solid–liquid interface, ΔH_f the latent heat of the material, V_t the growth rate of dendrite tip, and V_0 is the kinetic constant. As revealed in Eq. 4.1, V_t, which is controlled by laser scan speed v, is proportional to v. Using a higher scan speed, accordingly, leads to a faster development rate of dendrites. Therefore, the length of both dendritic trunk and primary dendritic arms obtained at 0.3 and 0.4 m/s (Figs. 4.11b and d) shows an increase upon that developed at 0.2 m/s (Fig. 4.11f). On the other hand, since laser-induced cooling rate can reach a high value of 10^6 K/s [24], the TiC dendrites generally have insufficient time for crystal growth, thereby retaining the ultrafine submicron scale (Figs. 4.11b, d and f). Based on Eq. 4.3, however, it reveals that at a considerably low v of 0.1 m/s, a significant decrease in the operative V_t tends to markedly elevate T_t. A large amount of heat is thus accumulated around the growing dendrite tips, which provides significant internal energy and thermodynamic potentials for the coarsening of the finally developed TiC dendrites (Fig. 4.11h).

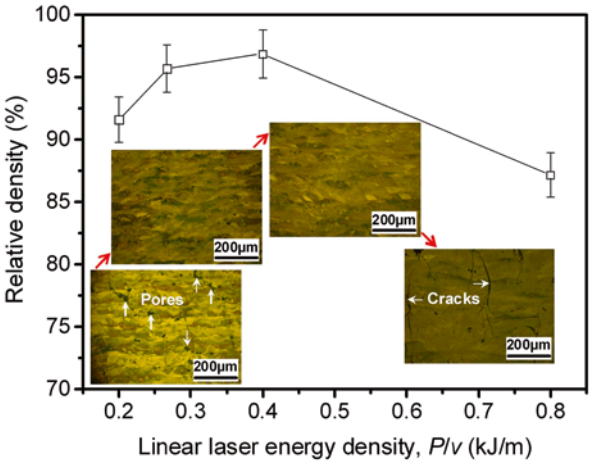


Fig. 4.12 Influence of linear laser energy density (LED) on densification rate and cross-sectional microstructure of SLM-processed TiC/Ti_5Si_3 composite parts

4.2.3.3 Effect of SLM Parameters on Densification Behavior

Figure 4.12 depicts the influence of linear laser energy density (LED) on densification of SLM-processed TiC/Ti_5Si_3 parts. On increasing the applied LED from 0.2 to 0.267 kJ/m, the densification level increased from 91.6 to 95.7%, which was further elevated to a maximum value of 96.9% at a higher LED of 0.4 kJ/m. However, as a considerably high LED of 0.8 kJ/m was used, the densification rate decreased sharply to 87.2%. The corresponding cross-sectional microstructures showed that a number of small-sized interlayer pores with an average size of ~20 μm were formed at a relatively low LED of 0.2 kJ/m. The considerably dense SLM layers without any apparent pores or cracks were produced as the applied LED increased ≥0.267 kJ/m. A significant decrease in the obtained density at 0.8 kJ/m was due to the formation of interconnected cracks vertical to SLM layers, with the length in the order of millimeter.

The success of SLM densification is determined by the wettability of the primarily precipitated TiC phase by the residual Ti–Si liquid in SLM system. According to De Hosson et al.'s results [25], for a reactive wetting system of liquid metals on ceramic phase, the wettability is predominated by the formation of ceramic phase during processing. The equilibrium contact angle θ_{eq} can be approximately written as:

$$\cos\theta_{eq} = (\gamma_{sv} - \gamma_{ls}) / \gamma_{lv} \tag{4.4}$$

where γ_{lv}, γ_{sv}, and γ_{ls} are the interface tensions of liquid metal-vapor, reacted ceramic-vapor, and liquid metal-reacted ceramic, respectively. γ_{lv} may vary during reaction as the reaction product may diffuse into the liquid [25].

For Ti–Si liquid system, γ_{ls} is dependent with the operating temperature T, with the relationship defined by [26]:

$$\gamma_{ls} = 1656 - 0.375T \tag{4.5}$$

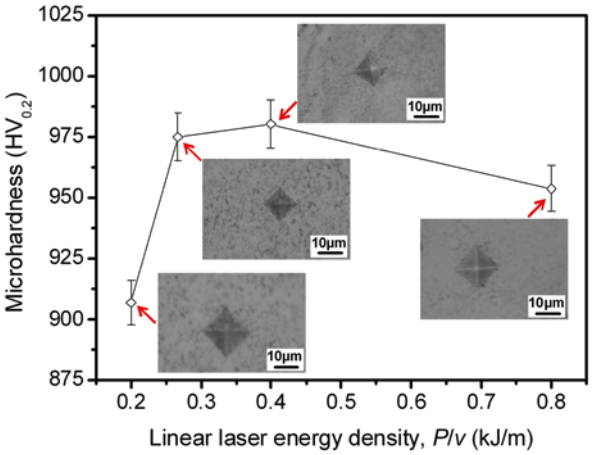


Fig. 4.13 Effect of linear laser energy density (LED) on microhardness and indentation morphology of SLM-processed TiC/Ti_5Si_3 composite parts

An increase in the applied LED to 0.4 kJ/m tends to elevate the workable T, which in turn lowers γ_{ls}. Therefore, a lower contact angle θ_{eq} (Eq. 4.4) and, accordingly, an improved liquid–solid wettability are achieved, favoring a sufficient consolidation of the composite system during SLM (Fig. 4.12). On the other hand, the shrinkage rate $\mathrm{d}(\Delta L/L_0)/\mathrm{d}t$ during solidification can be estimated by [27]:

$$\frac{\mathrm{d}(\Delta L / L_0)}{\mathrm{d}t} = \frac{\Delta P W}{2R\mu} \tag{4.6}$$

where ΔP is the capillary pressure, R the grain radius, W the liquid thickness, and μ is the liquid viscosity. Based on Eq. 3.7 in Chap. 3, μ is directly proportional to γ_{ls}, but inversely proportional to T. As a considerably high LED of 0.8 kJ/m is applied for SLM, the resultant higher T and lower γ_{ls} (Eq. 4.5) both result in a decrease in μ, hence increasing the shrinkage rate during solidification (Eq. 4.6). A large amount of thermal stresses tend to generate in the solidified parts [28], resulting in the formation of thermal cracks and the decrease in densification (Fig. 4.12).

4.2.3.4 Effect of SLM Parameters on Hardness and Wear Performance

The average microhardness measured on the cross-sections of SLM-processed TiC/Ti_5Si_3 composite parts, as shown in Fig. 4.13, exhibited a similar trend as the relative density with respect to the linear laser energy density (LED) (Fig. 4.12). A maximum microhardness value of 980.3 $HV_{0.2}$ was obtained at LED of 0.4 kJ/m. In this situation, a small-sized indentation with a clear configuration was observed, indicating a small degree of deformation during indentation and an elevated hardness performance. For comparison, the pure Ti parts without the addition of SiC were prepared under the same SLM processing conditions and the average microhardness was 281.0 $HV_{0.2}$. The microhardness of *in situ* TiC/Ti_5Si_3 composites prepared by

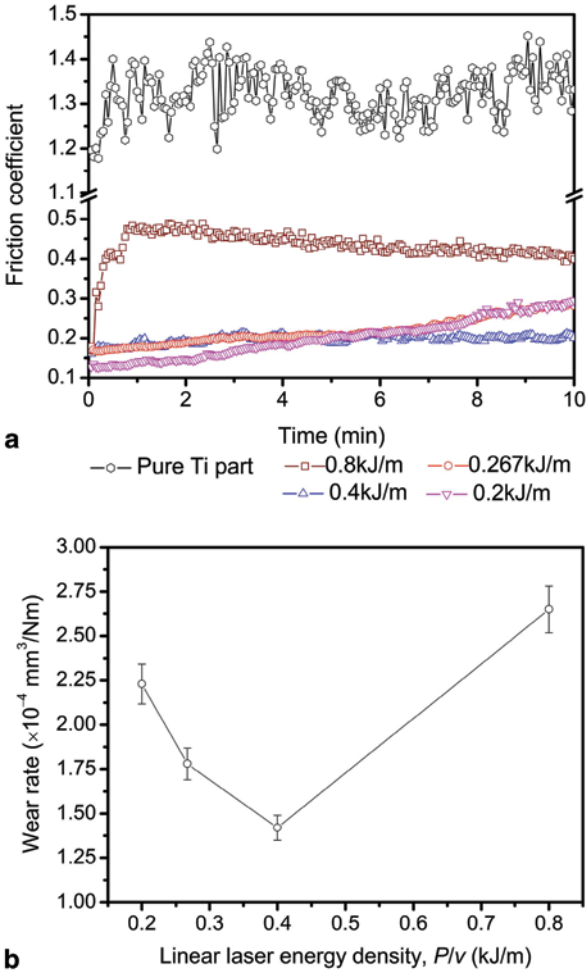


Fig. 4.14 Variations of friction coefficients (**a**) and wear rates (**b**) of SLM-processed TiC/Ti_5Si_3 composite parts with the applied linear laser energy density (LED)

SLM of SiC/Ti system showed more than threefold increase upon that of the unreinforced Ti part.

The variations of friction coefficients and wear rates of SLM-processed parts are provided in Fig. 4.14. The TiC/Ti_5Si_3 composite parts generally had much lower friction coefficients (the average value <0.5) as relative to the pure Ti part (the average value ~ 1.3). Also, the local fluctuation of the friction coefficients of the TiC/Ti_5Si_3 composites was considerably slighter than that of pure Ti part (Fig. 4.14a). A significantly improved wear performance of the TiC/Ti_5Si_3 parts was thus proved. On the other hand, the applied LED played an important role in influencing the wear performance of TiC/Ti_5Si_3 composites. The mean friction coefficient and wear rate of the TiC/Ti_5Si_3 part prepared at a high LED of 0.8 kJ/m increased sharply to 0.45 and 2.65×10^{-4} mm^3/Nm, respectively (Fig. 4.14), due to the formation of signifi-

cantly coarsened dendrites of TiC reinforcing phase (Fig. 4.11g and h) and the relatively low densification rate caused by thermal cracks (Fig. 4.12). By comparison, the TiC/Ti_5Si_3 part prepared using a suitable LED of 0.4 kJ/m demonstrated the superior wear performance. A uniform distribution of friction coefficient with a considerably low average value of 0.2 was obtained and the wear rate, 1.42×10^{-4} mm^3/Nm, was lowest (Fig. 4.14). This was essentially due to the homogeneous dispersion of ultrafine submicron-scale TiC dendrites as the reinforcement (Figs. 4.11e and f) and the sufficiently high densification level in this instance (Fig. 4.12).

Characteristic morphologies of the corresponding worn surfaces are revealed in Fig. 4.15. At a relatively low LED of 0.2 kJ/m, the worn surface of SLM-processed TiC/Ti_5Si_3 part primarily showed parallel grooves representing the abrasion wear (Fig. 4.15a). In this situation, the local severe plowing of the surface during

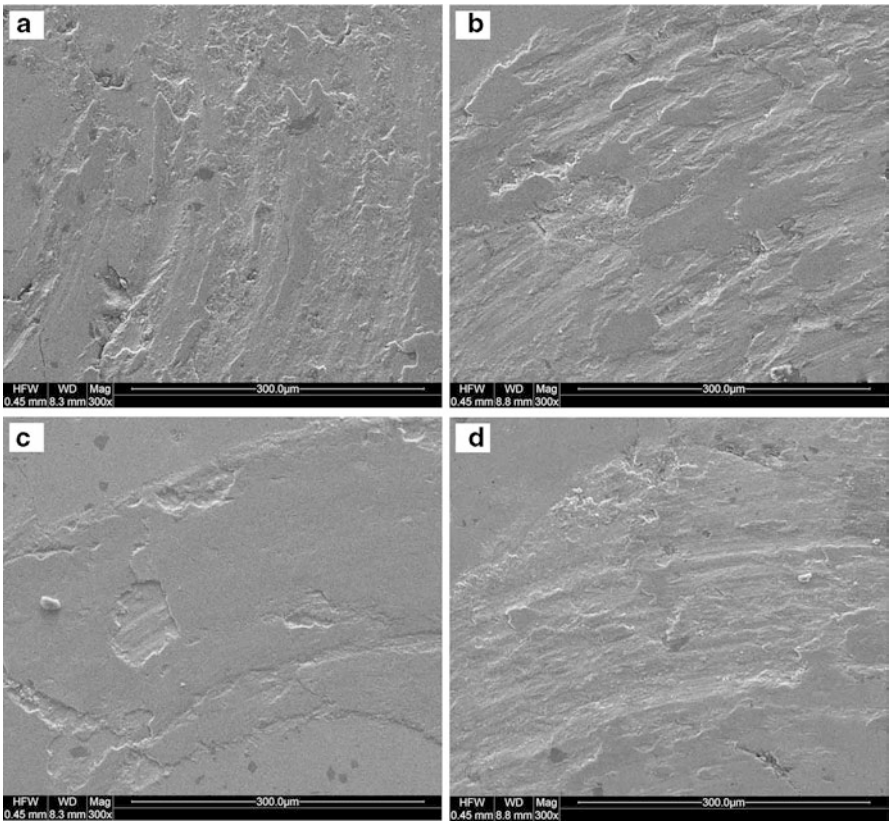


Fig. 4.15 SEM images showing the morphologies of worn surfaces of SLM-processed TiC/Ti_5Si_3 composite parts at different linear laser energy densities (LED): **a** LED = 0.2 kJ/m, showing the occurrence of abrasion and plowing of the surface; **b** LED = 0.267 kJ/m, showing the localized formation of the tribolayer; **c** LED = 0.4 kJ/m, showing the continuous coating of the tribolayer; **d** LED = 0.8 kJ/m, showing the severe fragmentation of the tribolayer and the wear debris

sliding test resulted in a relatively high wear rate (Fig. 4.14b). As LED increased to 0.267 kJ/m, a majority of the worn surface was covered with adhesion tribolayer (Fig. 4.15b). On increasing LED to 0.4 kJ/m, the worn surface of SLM-processed part became rather smooth. A continuously adherent, strain-hardened tribolayer without any significant fracture was formed on the worn surface (Fig. 4.15c). It was reasonable to consider that as the applied LED increased, the mechanism of material removal during sliding changed from the abrasion to the adhesion of tribolayer. Such a transition is expected to stabilize the friction coefficient and reduce the wear rate of SLM-processed parts, as demonstrated in Fig. 4.14. The worn surface of SLM-processed part at an even higher LED of 0.8 kJ/m consisted of severely fragmented tribolayer and also entrapped debris (Fig. 4.15d). The wear rate in this case is nearly two times higher than that of the part processed at the LED of 0.4 kJ/m (Fig. 4.14). A close look at the fine-grained (Fig. 4.11e) and coarse-grained (Fig. 4.11g) TiC/Ti_5Si_3 composites at 0.4 and 0.8 kJ/m revealed that the significant grain coarsening of the TiC reinforcing phase at a higher LED might account for the spalling of tribolayer and the resultant increase in wear rate.

4.3 Selective Laser Melting (SLM) of *In Situ* TiN/Ti_5Si_3 Composite Parts: Densification Mechanism, Microstructural Development, and Wear Property

4.3.1 Ball Milling of Si_3N_4/Ti Powder System for SLM Process

The 99.9% purity Ti powder having a poly-angular structure and an average particle size of 30 μm and the 99.5% purity Si_3N_4 powder having an irregular shape and a mean particle size of 4 μm were used as the starting materials. According to Si_3N_4:Ti weight ratio of 24.55:75.45 (i.e., the equivalent mol ratio of 1:9), the two components were milled using a Fritsch Pulverisette 6 high-energy planetary monomill. Stainless steel grinding balls and powder mixture to be treated were charged into the grinding bowl, with the ball-to-powder weight ratio of 10:1. High purity argon was used as the protective gas. The milling time and the rotation speed of the main disc were settled at 8 h and 250 rpm, respectively. In order to avoid the excessive temperature rise within the grinding bowl, ball milling duration of 20 min was followed by an interval of 10 min. The as-milled Si_3N_4/Ti powder system had a near spherical shape and a refined average particle size of 8 μm, showing the considerably homogeneous particle morphology (Fig. 4.16).

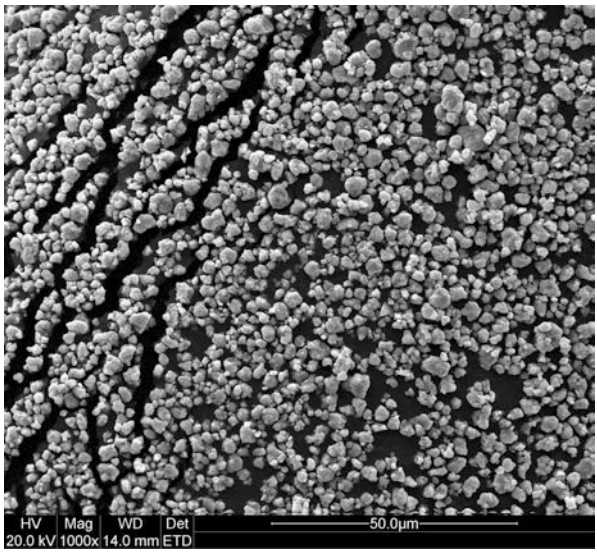


Fig. 4.16 SEM image showing microstructure of ball milled Si_3N_4/Ti powder system

4.3.2 *Influence of SLM Parameters on Constitutional Phases of In Situ TiN/Ti_5Si_3 Composite Parts*

Based on the procedures presented in Sect. 3.2 of Chap. 3, SLM processing of the ball milled Si_3N_4/Ti powder system was performed, using the as-defined CO_2 laser as the energy source. Through a series of preliminary SLM experiments, the following parameters were optimized: the focused spot size at the substrate surface of 0.3 mm, the laser power of 1 kW, the scan line hatching spacing of 0.15 mm, and the powder layer thickness of 100 μm. Meanwhile, the laser scan speeds (v) were settled periodically at 0.1, 0.2, 0.3, and 0.4 m/s by SLM control program. Four different "linear laser energy densities" (LED) of 10, 5, 3.33, and 2.5 kJ/m were accordingly defined to estimate the laser energy input to the powder layer being treated in this study.

Figure 4.17 depicts the typical XRD patterns of SLM-processed composite parts using various linear laser energy densities (LED). The strong diffraction peaks corresponding to TiN (based on JCPDS Card No. 87-0632) and Ti_5Si_3 (based on JCPDS Card No. 29-1362) phases were generally identified in SLM-processed parts at different LED. In order to further reveal the reaction behaviors of the Si_3N_4 and Ti constituents in the starting powder system, a more accurate XRD scan at a relatively low rate was performed in the vicinity of the strongest diffraction peaks of Si_3N_4 ($2\theta = 35.344°$) and Ti ($2\theta = 40.161°$), as illustrated in Fig. 4.18. It was observed that the initial Si_3N_4 and Ti diffraction peaks disappeared completely in all SLM-processed parts. Therefore, it was reasonable to conclude that for the given LED of 2.5–10 kJ/m, SLM processing of the Si_3N_4/Ti powder system generally led to the *in situ* formation of TiN/Ti_5Si_3 composites free of any residual impurity phases.

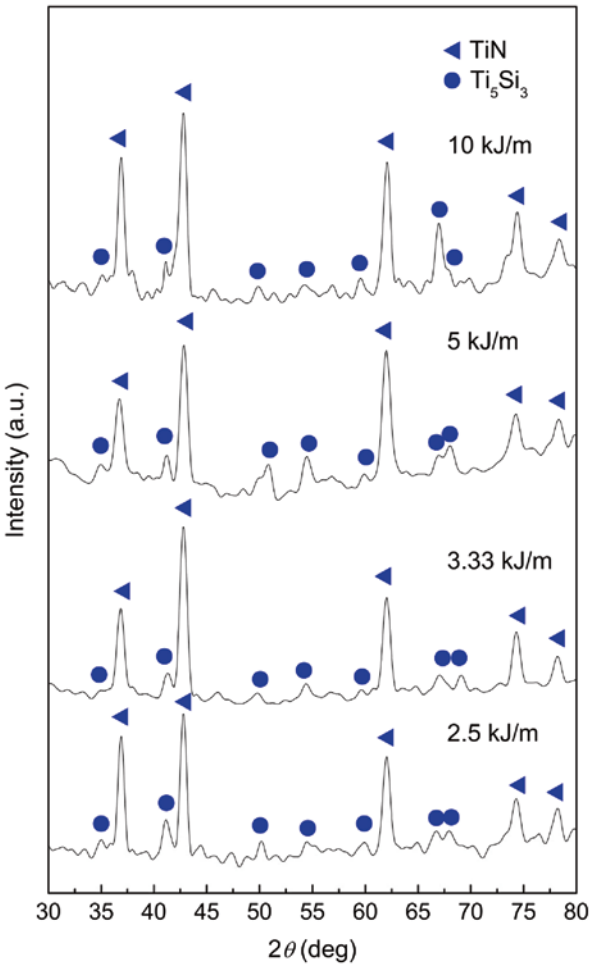


Fig. 4.17 XRD spectra of SLM-processed composite parts at different linear laser energy densities (LED)

When the high-energy laser beam scans over the powder layer, the energy is directly absorbed by the powder through both bulk coupling and powder coupling mechanisms [21], thereby realizing the thermalization of the absorbed laser energy. The Si_3N_4/Ti powder particles are heated up speedily, typically within a considerably short timescale below 4×10^{-3} s [22], leading to the complete melting of Ti constituent as the operative temperature reaches its melting point (~1943 K). Due to a considerably high thermalization caused by the high-energy laser irradiation, coupled with the sufficient wetting of Ti liquid in the molten pool, the Si_3N_4 constituent having a slightly higher decomposition point of ~2173 K tends to decompose to releases atomic Si and N. An *in situ* reaction system consisting of a ternary Ti–Si–N melt is, thus, generated. It is known that there are several possible chemical reactions for the Si_3N_4/Ti system during high-temperature processing, depending on the

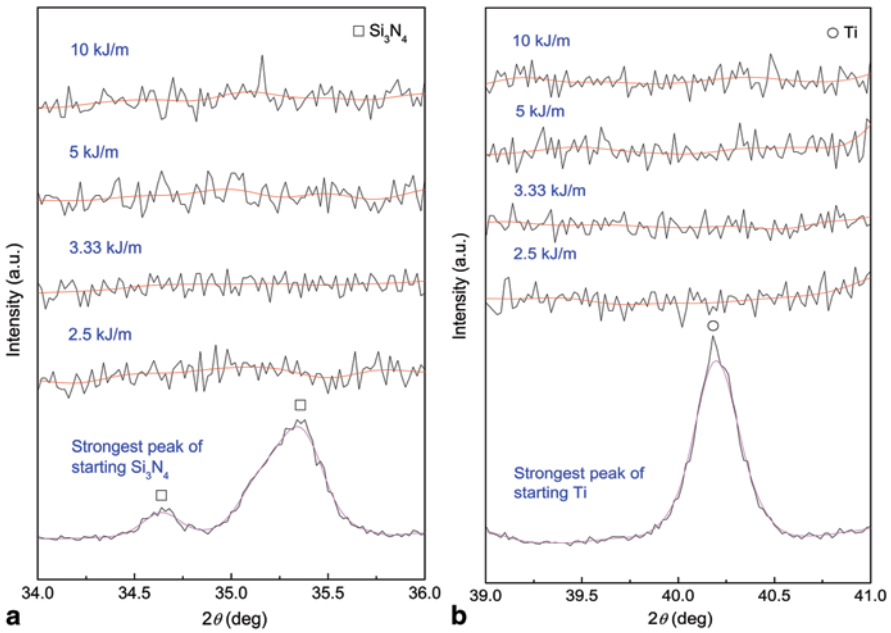


Fig. 4.18 XRD spectra in the vicinity of the strongest diffraction peaks of the starting Si_3N_4 (**a**) and Ti (**b**) phases showing the complete exhaustion of constituents after SLM. The underlying relatively smooth spectra are obtained by XRD scan at a faster rate

initial component ratios. The dependence of the standard Gibbs free energy (ΔG^0, kJ/mol) of these reactions on the temperature (T, K) is as follows [29]:

$$\begin{cases} 5\mathrm{Ti} + \mathrm{Si_3N_4} = \mathrm{Ti_5Si_3} + 2\mathrm{N_2(g)} \\ \Delta G^0 = 25.07 - 0.06T \ \ (T \le 1685\mathrm{K}) \\ \Delta G^0 = -5.07 - 0.042T \ \ (T > 1685\mathrm{K}) \end{cases} \tag{4.7}$$

$$\begin{cases} 3\mathrm{Ti} + \mathrm{Si_3N_4} = 3\mathrm{TiSi} + 2\mathrm{N_2(g)} \\ \Delta G^0 = 160.25 - 0.1298T \ \ (T \le 1685\mathrm{K}) \\ \Delta G^0 = 110.02 - 0.0998T \ \ (T > 1685\mathrm{K}) \end{cases} \tag{4.8}$$

$$\begin{cases} 7\mathrm{Ti} + \mathrm{Si_3N_4} = 4\mathrm{TiN} + 3\mathrm{TiSi} \\ \Delta G^0 = -123.21 - 0.0025T \ \ (T \le 1685\mathrm{K}) \\ \Delta G^0 = -144.74 + 0.0104T \ \ (T > 1685\mathrm{K}) \end{cases} \tag{4.9}$$

$$\begin{cases} 9\mathrm{Ti} + \mathrm{Si_3N_4} = 4\mathrm{TiN} + \mathrm{Ti_5Si_3} \\ \Delta G^0 = -135.31 + 0.008T \ \ (T \le 1685\mathrm{K}) \\ \Delta G^0 = -152.31 + 0.0087T \ \ (T > 1685\mathrm{K}) \end{cases} \tag{4.10}$$

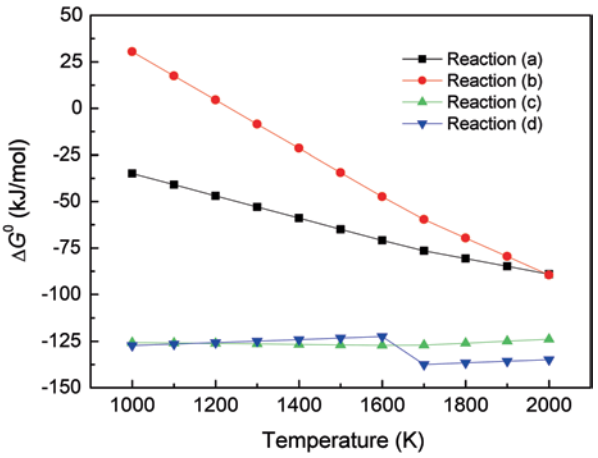


Fig. 4.19 Relation between standard Gibbs free energy and temperature for various reactions of Si_3N_4/Ti system

Thermodynamic analysis, as presented in Fig. 4.19, reveals that when temperature reaches above 1700 K, reaction (4.10) is much easier to proceed than others, since the ΔG^0 of this reaction is in a minimal negative value. SLM of the Si_3N_4/Ti powder system implies that a complete melting mechanism is involved. The operative temperature, thus, approaches or even exceeds 2173 K, favoring the initiation of *in situ* reaction (4.10) as the starting Si_3N_4/Ti molar ratio of 1:9 is settled. Furthermore, according to Ref. [30], the change in the enthalpy (ΔH) of reaction (4.10) is −912.912 kJ/mol. A very small, negative ΔH implies an exothermic nature of the system, which can further act as the driving force for the *in situ* reaction.

4.3.3 *Influence of SLM Parameters on Microstructures and Compositions of In Situ TiN/Ti_5Si_3 Composite Parts*

The characteristic microstructures on the etched cross-sections of SLM-processed TiN/Ti_5Si_3 composite parts are provided in Fig. 4.20. EDX point scans were performed respectively on the reinforcement and the matrix to determine the elemental distributions. The reinforcing phase (Point A) was composed of the Ti and N elements with a near-equal atomic proportion (Fig. 4.21a). The Ti and Si elements were detected within the matrix (Point B), with the Ti:Si atomic ratio being very close to 5:3 (Fig. 4.21b). Combined with XRD (Fig. 4.17) and EDX (Fig. 4.21) results, it was confirmed that the *in situ* TiN reinforced Ti_5Si_3 matrix composites were successfully prepared by SLM of Si_3N_4/Ti powder system. Nevertheless, the microstructural features of the *in situ* presented TiN reinforcing phase (e.g., shape, size, and dispersion state) exhibited distinct changes with the applied laser processing parameters. At a relatively low linear laser energy density (LED) of 2.5 kJ/m, the TiN reinforcing phase exhibited a nonuniform poly-angular structure and a certain degree of agglomeration (Fig. 4.20a), having a relatively large average particle size

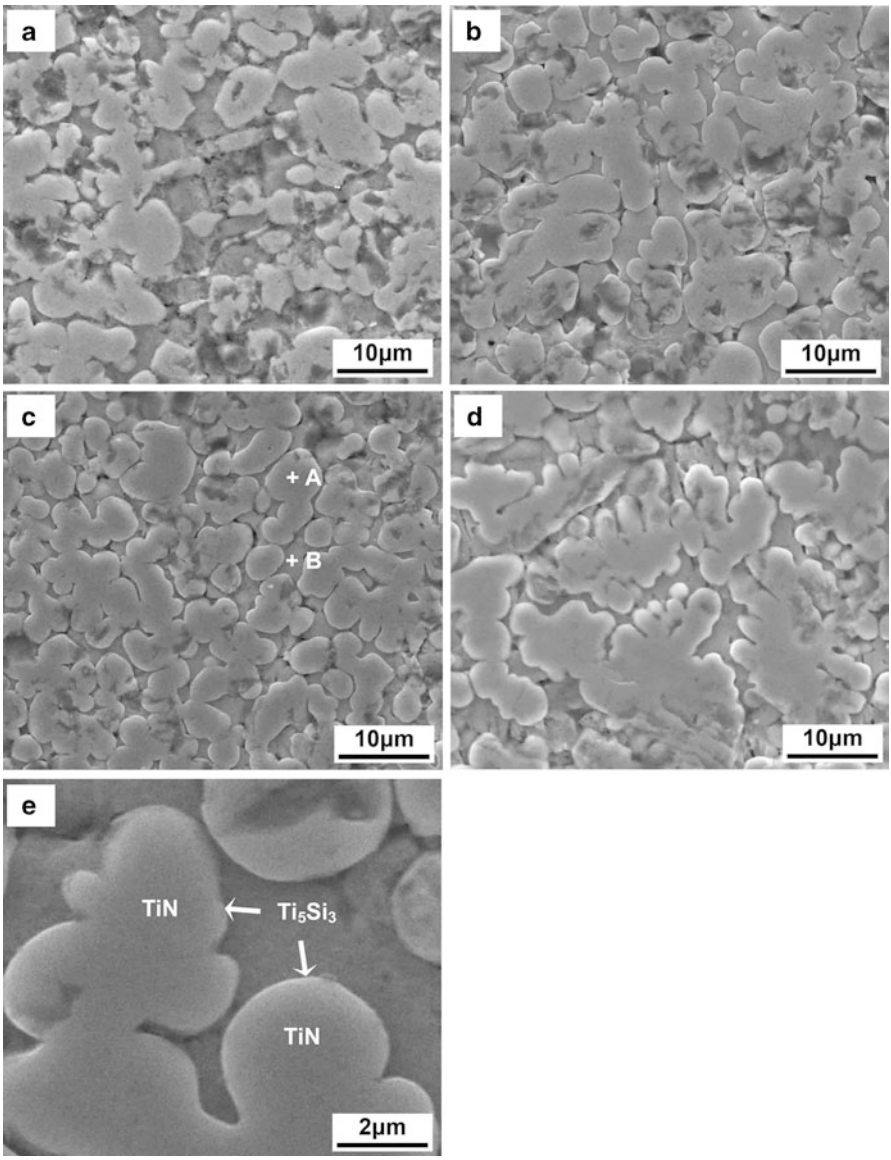


Fig. 4.20 SEM images showing characteristic microstructures of SLM-processed *in situ* TiN/Ti_5Si_3 composite parts at various scan speeds (v) and linear laser energy densities (LED): **a** $v=0.4$ m/s, LED = 2.5 kJ/m; **b** $v=0.3$ m/s, LED = 3.33 kJ/m; **c** $v=0.2$ m/s, LED = 5 kJ/m; **d** $v=0.1$ m/s, LED = 10 kJ/m. High-magnification micrograph showing interfacial microstructure of TiN/Ti_5Si_3 composites prepared at LED = 5 kJ/m (**e**)

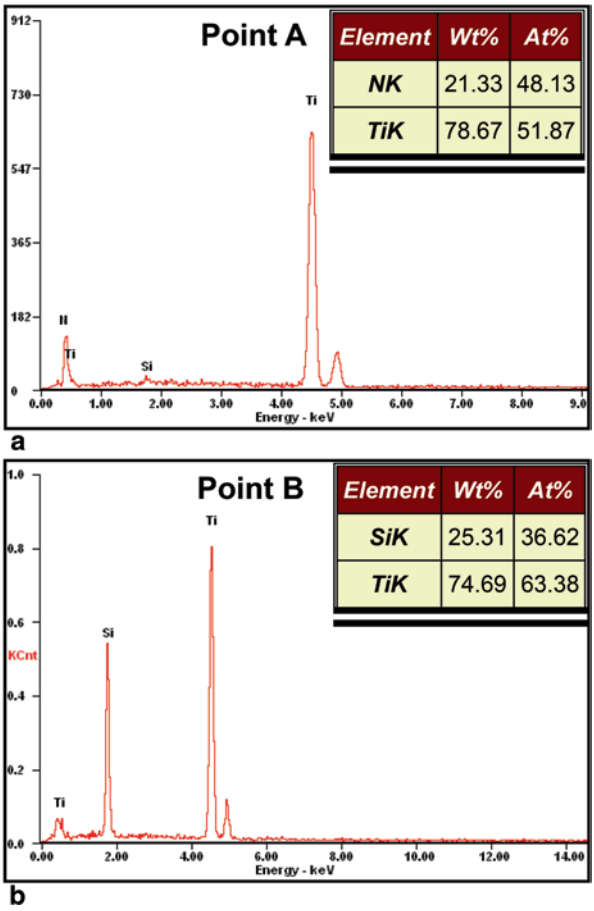


Fig. 4.21 EDX analyses showing chemical compositions collected in Point A (**a**) and Point B (**b**) in Fig. 4.20c

of 11.7 μm (Fig. 4.22). As LED increased to 3.33 kJ/m, the surface of TiN reinforcing phase showed an apparent smoothening (Fig. 4.20b), although the mean particle size remained almost unchanged at 11.0 μm (Fig. 4.22). Interestingly, at a higher LED of 5 kJ/m, the TiN reinforcement had a refined granular morphology with a significantly reduced size of 6.5 μm (Fig. 4.22) and, meanwhile, distributed homogeneously throughout the matrix (Fig. 4.20c). In this instance, the TiN particles exhibited a smooth and near-round shape, having a clear and coherent reinforcement/matrix interface free of any interfacial microcracks (Fig. 4.20e). On further enhancing the applied LED to 10 kJ/m, the growth morphology of TiN reinforcement changed considerably; it developed into an entirely different dendritic structure (Fig. 4.20d). However, the TiN dendrites showed a large degree of coarsening, reaching a considerably large particle size of 18.3 μm (Fig. 4.22).

As stated above, SLM is preformed based on a complete melting/solidification mechanism and, accordingly, the TiN reinforcing phase is formed through a dissolution/precipitation mechanism by means of the heterogeneous nucleation of TiN

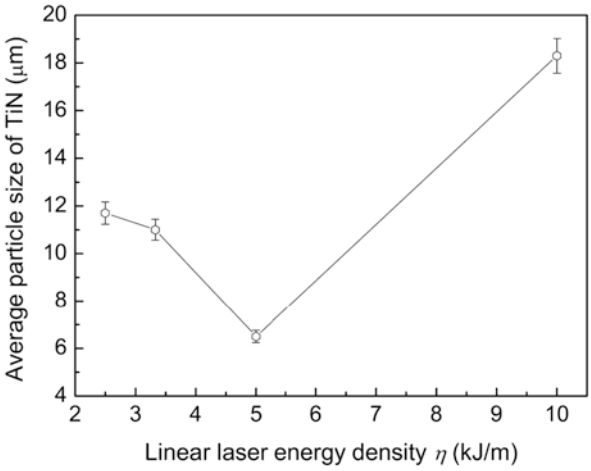


Fig. 4.22 Change of the mean particle size of TiN reinforcing phase with the applied linear laser energy densities (LED)

nuclei from the ternary Ti–Si–N melt and subsequent grain growth. The *in situ* TiN reinforcing phase in SLM-processed TiN/Ti_5Si_3 composites experiences an interesting change in its morphologies from an irregular polyangular shape to a refined near-round shape and, finally, to a coarsened dendritic shape, on increasing the applied linear LED (Figs. 4.20a, b, c and d). During SLM, the local temperature gradient and chemical concentration gradient in the molten pool give rise to surface tension gradient and associated Marangoni convection. The formation of convective stream within the pool induces liquid capillary force, which subsequently exerts on the precipitated solid-state TiN nuclei by the wetting liquid around. The intensity of Marangoni flow can be estimated using the dimensionless Marangoni number (M_a), as defined by Eq. 3.7 in Chap. 3. The wetting property of the *in situ* precipitated reinforcing phase by the liquid is crucial in determining its final morphology and dispersion state. For a reactive wetting system of liquid metal on ceramic phase, the wettability is predominated by the formation of ceramic phase during processing and the equilibrium contact angle can be approximately assessed using Eq. 4.4. A proper increase in the applied LED from 2.5 to 5 kJ/m tends to elevate the workable temperature T, which in turn lowers the interface tension of liquid metal-reacted ceramic γ_{ls} (Eq. 4.5). Therefore, a lower contact angle and the resultant elevated liquid–solid wetting property can be obtained. The *in situ* synthesized TiN reinforcing phase, therefore, tends to undergo a sufficient wetting by the surrounding liquid, leading to a pronounced smoothening and refinement of the initial poly-angular TiN precipitates (Figs. 4.20a, c and 4.23). On the other hand, as a considerably high LED of 10 kJ/m is used for SLM, the resultant higher T and lower γ_{ls} both result in a significant decrease in the dynamic viscosity μ (Eq. 3.3), hence intensifying the Marangoni flow and attendant turbulence within the molten pool (Eq. 3.7). Due to the instability of the solid–liquid interface caused by the perturbation, the *in situ* TiN precipitates tend to experience a dendrite growth (Fig. 4.23). Furthermore, owing to a markedly elevated thermalization of laser energy in this instance, a large

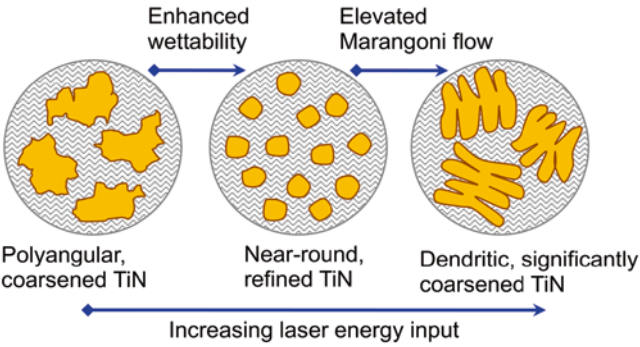


Fig. 4.23 Schematic of growth mechanisms and morphologies of *in situ* TiN reinforcing phase from the liquid under laser beam irradiation

amount of heat is accumulated around the growing dendrite tips, thereby offering significant internal energy and thermodynamic potentials for the coarsening of the finally developed TiN dendrites (Fig. 4.20d).

It is worth noting that in the present study, there is no apparent change in the microstructures along the layer-by-layer deposition direction inside the SLM-processed composite parts. Unlike the additive manufacturing method based on a semi-solid mechanism, e.g., direct metal laser sintering (DMLS) [21, 22], the SLM process is performed based on a complete melting metallurgical mechanism. In other words, each layer is consolidated through the complete melting/solidification manner. Although, to some extent, the surface of the previously processed layer will remelt as the subsequent layer is processed, such a remelting has not resulted in a substantial change of the previously melted/solidified microstructures.

4.3.4 *Influence of SLM Parameters on Densification Behavior of In Situ TiN/Ti_5Si_3 Composite Parts*

Figure 4.24 shows the typical surface morphologies of SLM-processed *in situ* TiN/Ti_5Si_3 composite parts under various processing conditions. The obtained relative densities of the corresponding parts are depicted in Fig. 4.25. At a relatively high scan speed (v) combined with a low linear laser energy density (LED), a considerably rough surface consisting of a large amount of small-sized spherical balls with an average diameter of ~20 μm was formed (Fig. 4.24a). Also, narrow microcracks, as selectively indicated in Fig. 4.24a, were observed on laser-processed surface. The combined influence of these two defects resulted in a limited densification level of 86.3% theoretical density (TD) (Fig. 4.25). On increasing LED by lowering the applied v, the balling phenomenon was alleviated, though the residual open porosity was still present on the surface (Fig. 4.24b). In this situation, the SLM densification response, 89.5% TD, still remained insufficient (Fig. 4.25). As an LED of

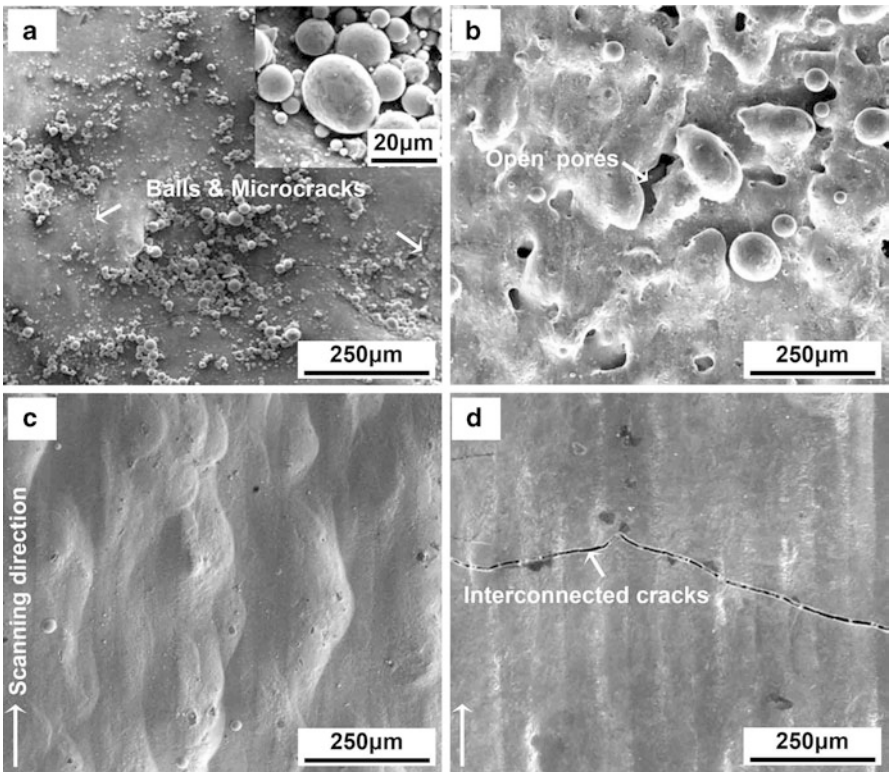


Fig. 4.24 SEM images showing typical surface morphologies of SLM-processed *in situ* TiN/Ti_5Si_3 composite parts at different scan speeds (v) and linear laser energy densities (LED): **a** v = 0.4 m/s, LED = 2.5 kJ/m; **b** v = 0.3 m/s, LED = 3.33 kJ/m; **c** v = 0.2 m/s, LED = 5 kJ/m; **d** v = 0.1 m/s, LED = 10 kJ/m

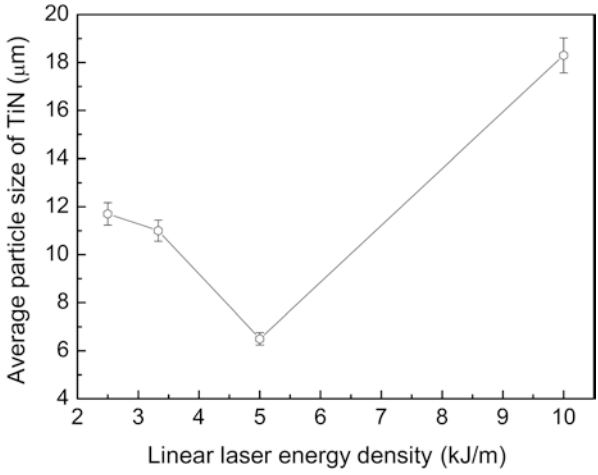


Fig. 4.25 Effect of linear laser energy density on densification rate of SLM-processed TiN/Ti_5Si_3 composite parts

5 kJ/m was properly settled, a pretty dense surface consisting of coherently bonded scan tracks was yielded, free of any balling effect and crack formation (Fig. 4.24c), achieving a near-full 97.7% TD (Fig. 4.25). As a considerably low v and attendant high LED of 10 kJ/m were used, the surface became even smoother. However, interconnected deep cracks were elongated on SLM-processed surface, almost perpendicular to the building direction. The length of cracks was in the order of millimeter and the width was ~15 μm (Fig.4.24d), hence decreasing the densification rate to 92.4% TD (Fig. 4.25).

From the parameter-dependent surface morphologies (Fig. 4.24), one can conclude that the relatively poor densification activity at a lower or a higher LED is due to the occurrence of balling effect (Fig. 4.24a) and thermal cracking (Fig. 4.24d), respectively. As a complete liquid system is generated during SLM, a rapid laser scanning tends to primarily shape the melt into a continuous cylindrical molten track, due to a considerably short dwelling time of laser spot on each irradiating region. However, the present molten track is in a highly unstable state. The surface energy of the liquid track will keep decreasing, in order to obtain a final equilibrium state. According to Niu and Chang's results [31], the applied laser scan speed has a significant influence on the capillary instability of the liquid track. A higher scan speed and the resultant lower LED may result in a rapid decrease of the radius R of the scan track at a constant laser wavelength λ, and thus an increase of λ/R. The increase of the λ/R ratio tends to cause melt instability and, accordingly, enhances the tendency for balling initiation. Under this condition, a number of small-sized liquid droplets tend to splash from the surface of the molten track, due to the reduction in the surface energy of liquid at short length scales (Fig. 4.26). After solidification, a large amount of micrometer-scaled spherical splashes are formed around laser-processed surface (Fig. 4.24a). Balling effect, as a typical defect associated with SLM, tends to produce a high amount of interball residual porosity, severely degrading densification rate of SLM-processed parts.

On the other hand, as analyzed above in Eq. 4.6, using an excessive LED of 10 kJ/m tends to increase the shrinkage rate during solidification considerably. Consequently, a large amount of thermal stresses tend to generate in the solidified parts.

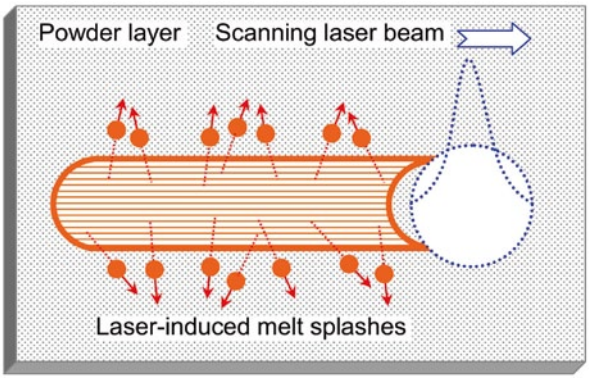


Fig. 4.26 Schematic of balling effect during SLM of composite powder using a high scan speed

Theoretical and experimental studies by Mercelis and Kruth [32] reveal that, in general, the residual stress profile in a SLM part consists of two zones of large tensile stresses at the top and bottom of the part, and a large zone of intermediate compressive stress in between. The residual of such complicated tensile stresses on the surface results in the formation of thermal cracks and the decrease in densification response of SLM parts (Figs. 4.24d and 4.25). The TiN/Ti_5Si_3 composites, as the intermetallic-based material, have a hard, brittle nature. Therefore, the densification response of TiN/Ti_5Si_3 composites during SLM process was very sensitive to the formation of thermal cracks. The SLM processing conditions, both the individual parameters (e.g., laser power and scan speed) and the integrated parameters (e.g., LED), are required to be carefully controlled to yield a full densification rate free of any pores or cracks formation.

4.3.5 *Influence of SLM Parameters on Microhardness and Wear Property of In Situ TiN/Ti_5Si_3 Composite Parts*

Figure 4.27a depicts the microhardness and its distribution measured on the cross-sections of SLM-processed *in situ* TiN/Ti_5Si_3 composite parts. On increasing the applied linear laser energy density (LED) from 2.5 kJ/m to 3.33 kJ/m, the mean microhardness elevated from 1083.5 $HV_{0.3}$ to 1161.7 $HV_{0.3}$. Nevertheless, the microhardness distribution remained a large degree of fluctuation. Differently, a uniform distribution of the microhardness with a considerably high average value of 1358.0 $HV_{0.3}$ was achieved using a suitable LED of 5 kJ/m, due to the formation of the homogeneously dispersed and significantly refined TiN reinforcement (Fig. 4.20c). A further increase in the applied LED to 10 kJ/m, however, lowered the obtained microhardness to 1264.2 $HV_{0.3}$ and, meanwhile, intensified the fluctuation of hardness values. The coarsening of TiN dendrites and the resultant decrease in microstructural homogeneity (Fig. 4.20d) were responsible for this phenomenon. The microhardness of the *in situ* TiN/Ti_5Si_3 composites prepared by SLM of Si_3N_4/Ti system showed at least a fourfold increase upon that of the unreinforced Ti parts prepared using the same SLM parameters. Furthermore, based on Tsukuma et al. [33] and Wani et al.'s [34] work on hot pressing of pure Si_3N_4, the obtained microhardness was generally around 1500 HV. The maximum microhardness of SLM-processed *in situ* TiN/Ti_5Si_3 composites, accordingly, was very close to that of Si_3N_4.

The changes of friction coefficients and wear rates of SLM-processed *in situ* TiN/Ti_5Si_3 composite parts are illustrated in Figs. 4.27b and c, respectively. A comparative study revealed that the *in situ* TiN/Ti_5Si_3 composite parts generally demonstrated much lower friction coefficients than that of the unreinforced Ti part with an average value of ~1.3. Furthermore, the friction coefficients of TiN/Ti_5Si_3 parts exhibited a considerably slight local fluctuation as relative to Ti part. A significantly enhanced wear performance of TiN/Ti_5Si_3 parts was thus ascertained. On the other hand, the applied LED exerted a significant influence on the wear performance of TiN/Ti_5Si_3 parts. An increase in the LED from 2.5 to 3.33 kJ/m led to a decrease in

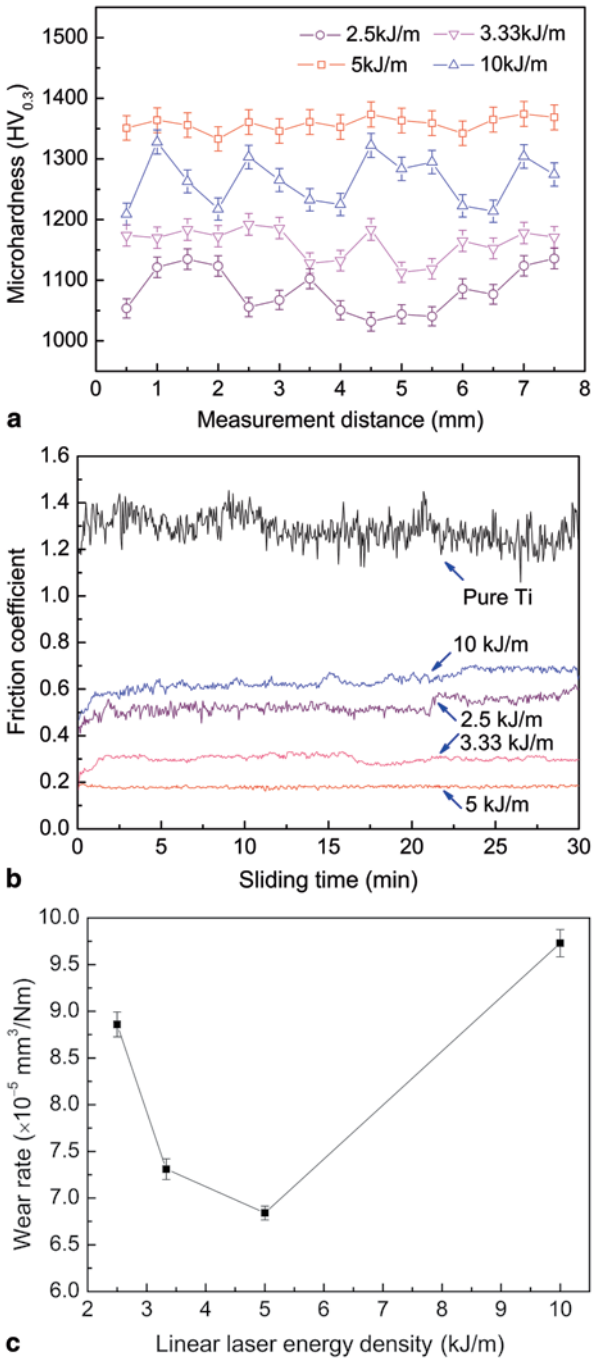


Fig. 4.27 Effect of linear laser energy density on microhardness and its distribution (**a**), friction coefficient (**b**), and wear rate (**c**) of SLM-processed *in situ* TiN/Ti_5Si_3 composite parts

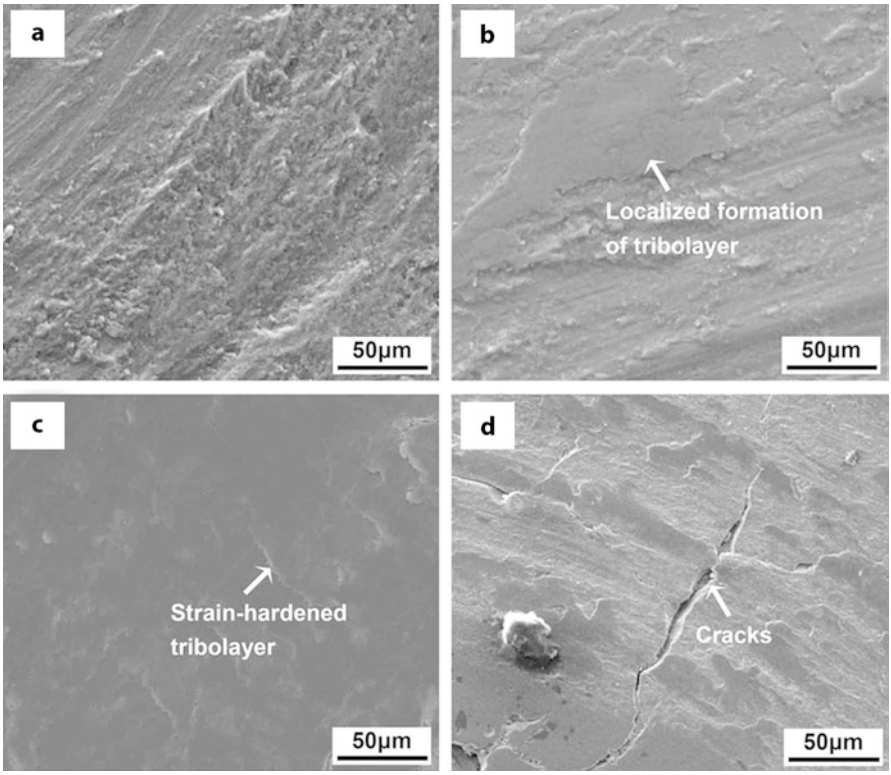


Fig. 4.28 SEM images showing characteristic morphologies of worn surfaces of SLM-processed *in situ* TiN/Ti_5Si_3 composite parts at various linear laser energy densities (LED): **a** LED = 2.5 kJ/m, **b** LED = 3.33 kJ/m, **c** LED = 5 kJ/m, **d** LED = 10 kJ/m

the average friction coefficient from 0.50 to 0.30 and the attendant wear rate from 8.86×10^{-5} mm^3/Nm to 7.31×10^{-5} mm^3/Nm. The TiN/Ti_5Si_3 part prepared at the LED of 5 kJ/m exhibited the superior wear property. A uniform distribution of friction coefficient with a considerably low mean value of 0.19 was obtained, leading to a lowest wear rate of 6.84×10^{-5} mm^3/Nm. However, at an even higher LED of 10 kJ/m, the average friction coefficient and wear rate of TiN/Ti_5Si_3 part increased markedly to 0.65 and 9.73×10^{-5} mm^3/Nm, respectively.

In order to disclose the microstructural features accounting for the wear properties, the morphologies of worn surfaces were characterized in Fig. 4.28. At a relatively low LED of 2.5 kJ/m, the worn surface was considerably rough and loose, consisting of parallel grooves and granular wear debris (Fig. 4.28a). Such a microstructure illustrated that the specimen suffered a severe abrasive wear, which in turn resulted in a relatively high wear rate (Fig. 4.27c). As LED increased to 3.33 kJ/m, a large portion of the worn surface was covered with the smooth adhesion tribolayer (Fig. 4.28b). When an elevated LED of 5 kJ/m was properly settled, a smooth strain-hardened tribolayer was continuously sticking to the worn surface,

showing no local plowing or fracturing of the surface (Fig. 4.28c). During wear tests, the counterface ball continuously slid against the surface. The worn surface experienced the sufficient plastic deformation at a temperature below its recrystallization temperature. The material strengthening, thus, occurred because of the dislocation movements within the crystal structure of the material, typically in the sliding-treated layer, which was known as strain-hardened tribolayer [35]. It was believed that the *in situ* homogeneous and refined TiN reinforcement (Fig. 4.20c) was not easy to split during sliding, but had a high tendency to adhere to each other and get strain-hardened, favoring the complete formation of tribolayer to enhance wear resistance. However, the severely fragmented tribolayer, deep cracks, and large debris were observed on the worn surface of SLM-processed TiN/Ti_5Si_3 part at the LED of 10 kJ/m (Fig. 4.28d). The resultant wear rate showed about 1.5-fold increase upon that of the TiN/Ti_5Si_3 part prepared at the LED of 5 kJ/m (Fig. 4.27c). The poor densification caused by thermal cracking (Fig. 4.24d) and the significant coarsening of the dendritic TiN reinforcement (Fig. 4.20d) might account for the spalling of tribolayer and, accordingly, the decrease in the obtainable wear property.

4.4 Conclusions

In this Chapter regarding SLM additive manufacturing of novel *in situ* Ti–Si intermetallic-based TiC/Ti_5Si_3 and TiN/Ti_5Si_3 composite parts, the main conclusions were summarized as follows.

1. The densification response of *in situ* TiC/Ti_5Si_3 and TiN/Ti_5Si_3 composite parts was controlled by the applied laser energy density. A combination of a low laser energy density and a high scan speed initiated the balling effect, whereas an excessive laser energy input resulted in the thermal cracking. Both defects that were caused by an improper laser process control lowered the densification rate. A near full density was achieved as an optimal laser energy density was properly settled.
2. For the optimally prepared *in situ* TiC/Ti_5Si_3 composites, the uniformly dispersed TiC reinforcing phase had a unique network distribution and a submicron-scale dendritic morphology. The growth of TiC dendritic trunks was kinetically dependent on laser scan speed. Using a higher scan speed resulted in the elongated dendritic trunks. The laser power had a negligible effect on the development of dendritic trunks. The growth of TiC dendritic arms was dependent on thermal energy and temperature. An increase in laser energy density enhanced the growth activity of primary and even secondary dendritic arms.
3. For the *in situ* TiN/Ti_5Si_3 composites, the TiN reinforcing phase experienced a successive change in its morphologies: an irregular poly-angular shape—a refined near-round shape—a coarsened dendritic shape, on increasing the applied laser energy density. The variations in the liquid–solid wettability and the intensity of Marangoni flow within the molten pool were responsible for the different growth mechanisms and morphologies of *in situ* TiN phase.

4. The *in situ* TiC/Ti_5Si_3 and TiN/Ti_5Si_3 composite parts prepared under the optimal SLM conditions had a significantly elevated microhardness (>980 HV), a considerably low coefficient of friction (<0.2), and a reduced wear rate, showing a considerable increase in the microhardness and wear performance as relative to the unreinforced Ti. The enhanced wear resistance was attributed to the formation of adherent strain-hardened tribolayer covered on the worn surface.
5. The microhardness and wear resistance decreased at an excessive laser energy input, due to the formation of thermal cracks and the significant coarsening of TiC and TiN dendritic reinforcements.

References

1. Mitra R (1998) Microstructure and mechanical behavior of reaction hot-pressed titanium silicide and titanium silicide-based alloys and composites. Metall Mater Trans A 29(6):1629–1641
2. Mitra R, Rao VVR (1998) Elevated–temperature oxidation behavior of titanium silicide and titanium silicide based alloy and composite. Metall Mater Trans A 29(6):1665–1675
3. Shim JH, Byun JS, Cho YW (2004) In situ synthesis of TiN particulate/titanium silicide matrix composite powder by mechanochemical process. J Am Ceram Soc 87(10):1853–1858
4. Wang LJ, Jiang W, Qin C et al (2006) In-situ synthesized Ti_5Si_3/TiC composites by spark plasma sintering technology. J Mater Sci 41(12):3831–3835
5. Shon IJ, Kim HC, Rho DH et al (1999) Simultaneous synthesis and densification of Ti_5Si_3 and Ti_5Si_3–20 vol% ZrO_2 composites by field-activated and pressure-assisted combustion. Mater Sci Eng A 269 (1–2): 129–135
6. Li JL, Jiang DL, Tan SH (2002) Microstructure and mechanical properties of in situ produced Ti_5Si_3/TiC nanocomposites. J Eur Ceram Soc 22(4):551–558
7. Tjong SC (2007) Novel nanoparticle-reinforced metal matrix composites with enhanced mechanical properties. Adv Eng Mater 9(8):639–652
8. Gaard A, Krakhmalev P, Bergström J (2006) Microstructural characterization and wear behavior of (Fe, Ni)–TiC MMC prepared by DMLS. J Alloys Compd 421 (1–2): 166–171
9. Shackelford JF, Alexander W (eds) (2000) CRC materials science and engineering handbook 3rd edn. CRC Press, Florida
10. Thein MA, Lu L, Lai MO (2010) Effects of strain rate on tensile properties of pure Mg and in situ AlN reinforced Mg–5Al composite. Mater Sci Eng A 528(1):239–246
11. Chianeh VA, Hosseini HRM, Nofar M (2009) Micro structural features and mechanical properties of Al–Al_3Ti composite fabricated by in–situ powder metallurgy route. J Alloys Compd 473(1–2):127–132
12. Yeh CL, Teng GS (2007) Use of Si_3N_4 as a reactant in preparation of TiN–Ti_5Si_3 composites by solid–state SHS reactions. J Alloys Compd 429(1–2):126–132
13. Yang YF, Wang HY, Zhang J et al (2008) Lattice parameter and stoichiometry of TiCx produced in the Ti–C and Ni–Ti–C systems by self-propagating high-temperature synthesis. J Am Ceram Soc 91(8):2736–2739
14. Kumar S, Sarma VS, Murty BS (2010) Functionally graded Al alloy matrix in-situ composites. Metall Mater Trans A 41 A(1):242–254
15. Hadian R, Emamy M, Campbell J (2009) Modification of cast Al–Mg_2Si metal matrix composite by Li. Metall Mater Trans B 40(6):822–832
16. Suryanarayana C (2001) Mechanical alloying and milling. Prog Mater Sci 46 (1–2): 1–184
17. Villars P, Prince A, Okamoto H (1995) Handbook of ternary alloy phase diagrams. ASM International

18. Gu DD, Hagedorn YC, Meiners W et al (2012) Densification behavior, microstructure evolution, and wear performance of selective laser melting processed commercially pure titanium. Acta Mater 60(9):3849–3860
19. Das M, Balla VK, Basu D et al (2010) Laser processing of SiC–particle-reinforced coating on titanium. Scr Mater 63(4):438–441
20. Liu YC, Han YJ, Yang GC et al (2005) Primary cellular/dendritic spacing selection in rapidly solidified peritectic alloy. Mater Lett 59(23):2915–2919
21. Fischer P, Romano V, Weber HP et al (2003) Sintering of commercially pure titanium powder with a Nd:YAG laser source. Acta Mater 51(6):1651–1662
22. Simchi A, Pohl H (2003) Effects of laser sintering processing parameters on the microstructure and densification of iron powder. Mater Sci Eng A 359 (1–2): 119–128
23. Pan QY, Lin X, Huang WD et al (1998) Microstructure evolution of Cu–Mn alloy under laser rapid solidification condition-banded structure and planar front growth. Prog Nat Sci 8(1):79–86
24. Boccalini M, Goldenstein H (2001) Solidification of high speed steels. Int Mater Rev 46(2):92–115
25. Zhou XB, De Hosson JTM (1996) Reactive wetting of liquid metals on ceramic substrates. Acta Mater 44(2):421–426
26. Yuan ZF, Ke JJ, Li J et al (2006) Surface tension of metals and alloys. Science Press, Beijing
27. Zhu HH, Lu L, Fuh JYH (2004) Influence of binder's liquid volume fraction on direct laser sintering of metallic powder. Mater Sci Eng A 371(1–2):170–177
28. Das S (2003) Physical aspects of process control in selective laser sintering of metals. Adv Eng Mater 5(10):701–711
29. Huang QL, Cai J, Pan W et al (1997) In situ processing of TiN/Si_3N_4 composites by Ti–Si_3N_4 solid state reaction. Mater Lett 31(3–6):221–225
30. Barin I (eds) (1993) Thermochemical data of pure substances. VCH, New York
31. Niu HJ, Chang ITH (1999) Instability of scan tracks of selective laser sintering of high speed steel powder. Scr Mater 41(11):1229–1234
32. Mercelis P, Kruth JP (2006) Residual stresses in selective laser sintering and selective laser melting. Rapid Prototyping J 12(5):254–256
33. Tsukuma K, Shimada M, Koizumi M (1981) Thermal conductivity and microhardness of Si_3N_4 with and without additives. Am Ceram Soc Bull 60(9):910–912
34. Wani MF, Khan ZA, Hadfield M (2010) Effect of sintering additives and reinforcement on microhardness values of Si_3N_4 ceramics and composites. J Adv Res Mech Eng. 1(1):52–59
35. Jain A, Basu B, Kumar BVM et al (2010) Grain size-wear rate relationship for titanium in liquid nitrogen environment. Acta Mater 58(7):2313–2323

Chapter 5
In Situ WC-Cemented Carbide-Based Hardmetals by Selective Laser Melting (SLM) Additive Manufacturing (AM): Microstructure Characteristics and Formation Mechanisms

Abstract Selective Laser Melting (SLM) of a W–Ni–graphite powder mixture was performed to prepare *in situ* WC-cemented carbide-based hardmetals parts, using two different types of CO_2 laser and fiber laser. The WC phase was developed via a multi-laminated growth mechanism and it experienced block-shaped triangular—elliptical morphological change on decreasing the linear laser energy density of the applied CO_2 laser. As the fiber laser was used, the *in situ* formed WC crystals generally had a triangular microstructure. An increase in the applied linear laser energy density, which was realized by increasing laser power or decreasing scan speed, resulted in the coarsening of *in situ* WC crystals in both side length and thickness. The SLM additive manufactured cemented carbide based hardmetals parts possessed a sufficiently high densification level of 96.3 % and a maximum microhardness of 1870.9 $HV_{0.1}$. The dominant metallurgical mechanisms responsible for the variations of microstructural and mechanical properties of SLM-processed hardmetals parts were proposed.

5.1 Introduction

Cemented carbide-based hardmetals hold a leading position in metal machining, moulds, and mineral applications due to their excellent properties in terms of high hardness, low coefficient of thermal expansion, and high wear/corrosion resistance [1]. In particular, tungsten (WC) carbide-based hardmetals have been intensively studied, since WC possesses some unique properties such as a certain amount of plasticity and a sound wettability by molten metals [2]. Normally, cobalt (Co) acts as the traditional binder element for WC-based hardmetals and some other transition metals such as nickel (Ni) and iron (Fe) are used as alternatives [3, 4]. The presence of a binder metal element in the boundaries of WC grains to form WC-based composites leads to the strain energy dissipation and, accordingly, increases toughness.

Recently, the development of novel *in situ* hardmetals, in which the constitutions are synthesized by chemical reactions between elements during processing, exhibits more significant advantages and, thus, attracts more interest. *In situ* hardmetals are thermodynamically stable, leading to less degradation in elevated temperature

© Springer-Verlag Berlin Heidelberg 2015

D. Gu, *Laser Additive Manufacturing of High-Performance Materials,*
DOI 10.1007/978-3-662-46089-4_5

applications. Furthermore, the present ceramic/metal interfaces within *in situ* hardmetals are generally cleaner and more compatible, yielding stronger interfacial bonding and elevated mechanical properties of the final products [5]. *In situ* hardmetals are usually produced following a powder metallurgy (PM) route, which involves mixing of elemental powder, pressing, and sintering [6, 7]. Almost all the current production lines of hardmetals are based on high-temperature pressure sintering except a few that use spark plasma sintering (SPS). Therefore, high temperature, high pressure, and long reaction time are normally required. However, the conventional PM-processed hardmetals are usually of limited shape, high brittleness, and poor machinability, which inevitably restrict their practical applications.

As mentioned previously, Selective Laser Melting (SLM) Additive Manufacturing (AM) technology enables the quick production of three-dimensional parts with any complex configurations directly from metals, alloys, or ceramics powders, without postprocessing requirements such as furnace densification and secondary infiltration [8]. So far, a majority of the researches on SLM have been focused on metallic materials. Recent research efforts have demonstrated that SLM, due to its flexibility in feedstock and shapes, possesses a promising potential for the net-shape production of complex-shaped, high-performance composite parts. The composite systems that have previously been processed and studied using laser AM methods are reviewed in Sect. 2.2.4 of Chap. 2. Nevertheless, due to the complex metallurgical nature of SLM, which involves multiple modes of heat, mass, and momentum transfer induced by localized high-energy laser scanning [9], the processing problems such as gas entrapment, pores formation, aggregation of constitution phases, and interfacial microcracks are most likely to be produced in SLM-processed composite parts. Furthermore, as to the composites synthesized in an *in situ* manner, the dynamic nonequilibrium SLM process makes it rather difficult to control the growth morphology of the *in situ* formed phases. As the phase constitution and crystal structure may significantly influence the final properties of composites, it is highly necessary to be able to understand and control them during SLM.

In the present chapter, SLM processing of a W–Ni–graphite elemental powder mixture was performed to prepare bulk-form *in situ* WC-based hardmetals, using two different types of CO_2 laser and fiber laser. The microstructural characteristics and mechanical properties of SLM-processed composites were assessed and the laser-induced formation mechanisms of *in situ* structures were elucidated.

5.2 Preparation of W–Ni–Graphite Powder System for SLM Process

The starting powder materials were: 99.9% purity Ni powder with an irregular shape and a mean particle size of 45 μm, 99.9% purity W powder with a polyangular structure and an average particle size of 2.5 μm, and pure graphite powder with a sheet-like structure and a mean particle size of 30 μm. The three components were uniformly mixed according to the Ni:W:C weight ratio of 10:85:5 in a Fritsch

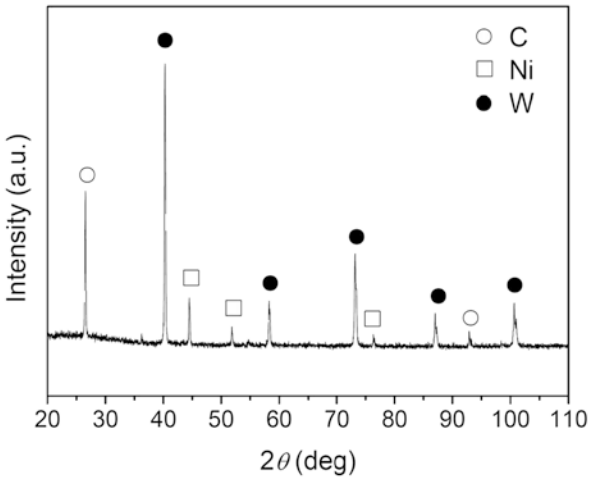


Fig. 5.1 XRD spectrum of the starting W–Ni–graphite powder mixture for SLM process

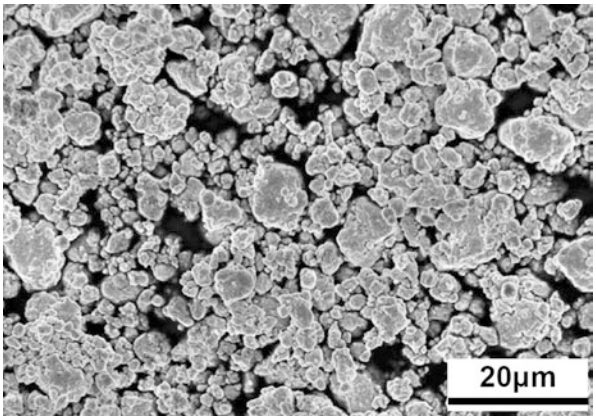


Fig. 5.2 SEM micrograph showing characteristic microstructure of the mixed W–Ni–graphite powder system

Pulverisette 6 planetary monomill at a rotation velocity of 250 rpm for 30 min, using a relatively low ball-to-powder ratio of 5:1. The X-ray diffractometer (XRD) spectrum of the mixed powder system is provided in Fig. 5.1, showing clearly the strong diffraction peaks corresponding to the W, Ni, and C (graphite) phases. The scanning electron microscope (SEM) micrograph of the mixed W–Ni–graphite powder system was shown in Fig. 5.2. The design strategies for the present powder system were addressed as follows. First, the powder system was mixed by the coarse Ni powder and the fine W powder. Such a bimodal mixture with a broad particle size distribution (Fig. 5.2) could lead to an increase in loose packing density. Generally, a powder system with higher loose packing density is preferred in the

powder bed-based SLM process [8]. Second, the W powder having a high melting point was designed as the considerably fine particle morphology in the powder mixture, providing larger surface area to absorb more laser energy and, accordingly, increasing the particle temperature and attendant SLM kinetics. Third, the moderate powder treatment conditions were applied to avoid the large deformation of powder particles and yield a sufficiently high flowability of the powder mixture. Powder flowability is of critical importance to prevent powder agglomeration and facilitate the uniform powder spreading during the layer-by-layer additive manufacturing.

5.3 Effect of SLM Processing Parameters on Phase Evolution of WC-Based Hardmetals Parts Using CO_2 Laser

According to the procedures specified in Sect. 3.3 of Chap. 3, SLM processing of the W–Ni–graphite powder mixture was carried out using the mentioned CO_2 laser as the energy source. Through a series of preliminary SLM experiments, the processing parameters were optimized as follows: the focused spot size at the substrate surface of 0.3 mm, the laser power (P) of 1.2 kW, the scan line hatching spacing (l) of 0.15 mm, and the powder layer thickness (d) of 100 μm. Meanwhile, the laser scan speeds (v) were changed periodically within 0.8–1.2 m/s by SLM control program, in order to vary the laser energy input to the powder layer being melted during SLM process.

Typical XRD patterns of SLM-processed W–Ni–graphite powder at different laser scan speeds are depicted in Fig. 5.3. Generally, the strong diffraction peaks corresponding to WC with a hexagonal structure and Ni_2W_4C (Abbreviated as M_6C, where M were metal atoms) with a cubic structure were identified. According to [10], the $Ni_2W_4C(M_6C)$ was identified as a η-carbide phase. The diffraction peaks for Ni, although the intensity was relatively lower, were also well detected (Fig. 5.3). Furthermore, the existence of the weak diffraction peaks for W suggested the residual of a small amount of W after SLM process, especially for the sample processed at a higher laser scan speed (Fig. 5.3c). Thus, it was reasonable to conclude that SLM of the W–Ni–graphite powder mixture generally led to the *in situ* formation of WC/M_6C (major phase) cemented carbide based hardmetals composed of Ni and W (minor phase) as the binder.

Nevertheless, XRD results revealed that the intensity of WC and M_6C diffraction peaks and the resultant volumetric ratio of WC and M_6C phases were significantly influenced by the applied laser scan speed. For the hardmetals processed at 0.8, 1.0, and 1.2 m/s, the ratio of the intensity of the strongest diffraction peaks of WC(100) (standard $2\theta = 35.722°$) and $M_6C(511)$ (standard $2\theta = 41.643°$), $\frac{I_{WC}}{I_{M_6C}}$, was 2.7, 1.4, and 0.8, respectively. According to [11], the volumetric ratio of WC and M_6C phases can be estimated by:

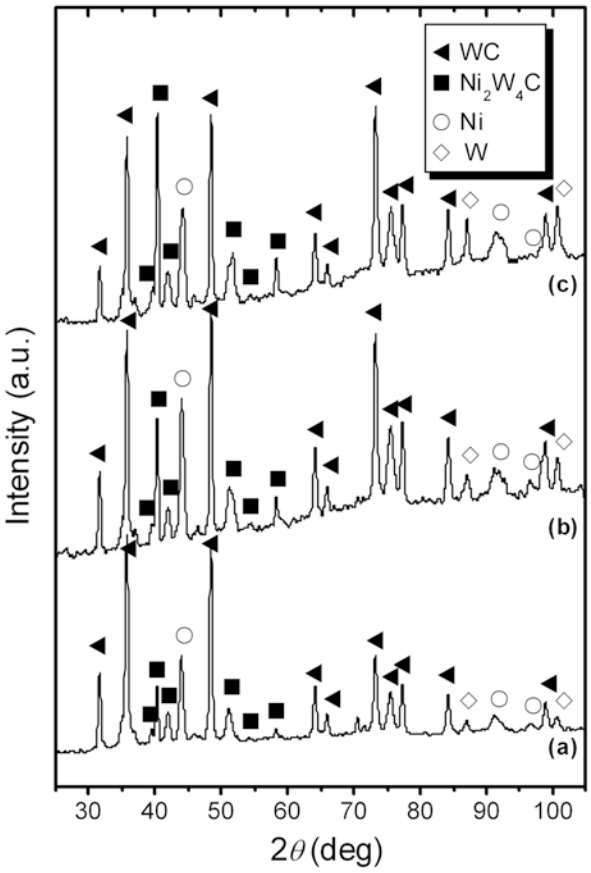


Fig. 5.3 XRD spectra of SLM-processed WC-based hardmetals parts using different laser scan speeds: **a** 0.8 m/s; **b** 1.0 m/s; **c** 1.2 m/s. Fixed processing parameters are laser power $P=1.2$ kW, scan line hatching spacing $l=0.15$ mm, and powder layer thickness $d=0.1$ mm

$$\frac{V_{\mathrm{WC}}}{V_{\mathrm{M_6C}}}=\frac{I_{\mathrm{WC}}}{I_{\mathrm{M_6C}}}\times\frac{R_{\mathrm{M_6C}}}{R_{\mathrm{WC}}}=\frac{I_{\mathrm{WC}}}{I_{\mathrm{M_6C}}}\times\frac{\left[P\left|F_{\mathrm{hkl}}\right|^2\left(\frac{1+\cos 2\theta}{\sin^2\theta\cos\theta}\right)\right]_{\mathrm{M_6C(511)}}}{\left[P\left|F_{\mathrm{hkl}}\right|^2\left(\frac{1+\cos 2\theta}{\sin^2\theta\cos\theta}\right)\right]_{\mathrm{WC(100)}}} \tag{5.1}$$

Here, P is the multiplicity factor; $P=6$ for the hexagonal WC and $P=24$ for the complex fcc M_6C [11]. $\frac{1+\cos 2\theta}{\sin^2\theta\cos\theta}$ is the angle factor and $\left|F_{\mathrm{hkl}}\right|^2$ is the structure

factor and is related to the atomic scattering factor $f(\lambda^{-1}\sin\theta)$. For $M_6C(511)$ and WC(100), $|F_{511}|^2 = 16f^2$ and $|F_{100}|^2 = 3f^2$. For a given material, the values of f vs. different values of $\lambda^{-1}\sin\theta$ are indexed in [11]. The WC/M_6C volumetric ratio in SLM-processed *in situ* structures at 0.8, 1.0, and 1.2 m/s can accordingly be calculated to be 52.5, 27.2, and 15.6, respectively, i.e., the corresponding volumetric fraction of M_6C phase within the WC/M_6C matrix is 1.9, 3.5, and 6.0 %.

5.4 Effect of SLM Processing Parameters on Microstructure and Composition Development of WC-Based Hardmetals Parts Using CO_2 Laser

The typical microstructures on the polished cross-sections of SLM-processed *in situ* WC-based hardmetals parts are provided in Fig. 5.4. As a relatively high laser scan speed of 1.2 m/s was applied, the obtainable linear laser energy density (LED), which was defined as the ratio of laser power (P) and scan speed (v) (Eq. 3.1), was comparatively low. A large amount of small-sized pores were formed throughout the cross-section and, also, the elongated pores were present between the neighboring layers, due to the insufficient bonding of SLM-processed layers (Fig. 5.4a), resulting in a considerably low density of 81.7 % theoretical density (TD). The insufficient densification behavior of the powder during SLM was ascribed to the limited laser energy input in this instance. At a lower scan speed of 1.0 m/s, the densification level of SLM-processed powder, 94.2 % TD, was improved significantly, showing a small amount of narrow microcracks on the polished cross-section (Fig. 5.4b). As the applied laser scan speed was further decreased to 0.8 m/s, a sufficiently high LED was expected to be realized in this situation. The powder system accordingly demonstrated an efficient densification behavior, reaching 96.3 % TD. The polished cross-section of SLM part was smooth and dense and consisted of a very small amount of small-sized pores (Fig. 5.4c), implying a sufficient consolidation of each SLM layer and a sound metallurgical bonding between the neighboring layers.

Figure 5.5 illustrates the influence of laser scan speed on microstructural features of SLM-processed *in situ* hardmetals parts. The quantitative analysis of the chemical compositions of the representative structures was performed by energy dispersive X-ray spectroscope (EDX) small-area scan method, as listed in Table 5.1. SLM-processed part at a relatively low scan speed of 0.8 m/s consisted of a large amount of elongated block-shaped constituent (Fig. 5.5a) and the detected atomic ratio of W and C elements was close to 1:1 (M_1, Table 5.1). Combined with XRD results (Fig. 5.3), the *in situ* formation of WC during SLM was confirmed. The mean grain size of WC was determined to be 17.5 μm and the standard deviation (SD) of the grain size measurement was 2.14. The constituent around WC phase was composed of Ni and W elements (B_1, Table 5.1), which acted as the binder phase. The M_6C, due to a considerably small volumetric fraction of 1.9 % in this case, was not well observed. Interestingly, high-magnification SEM characterization at the edge

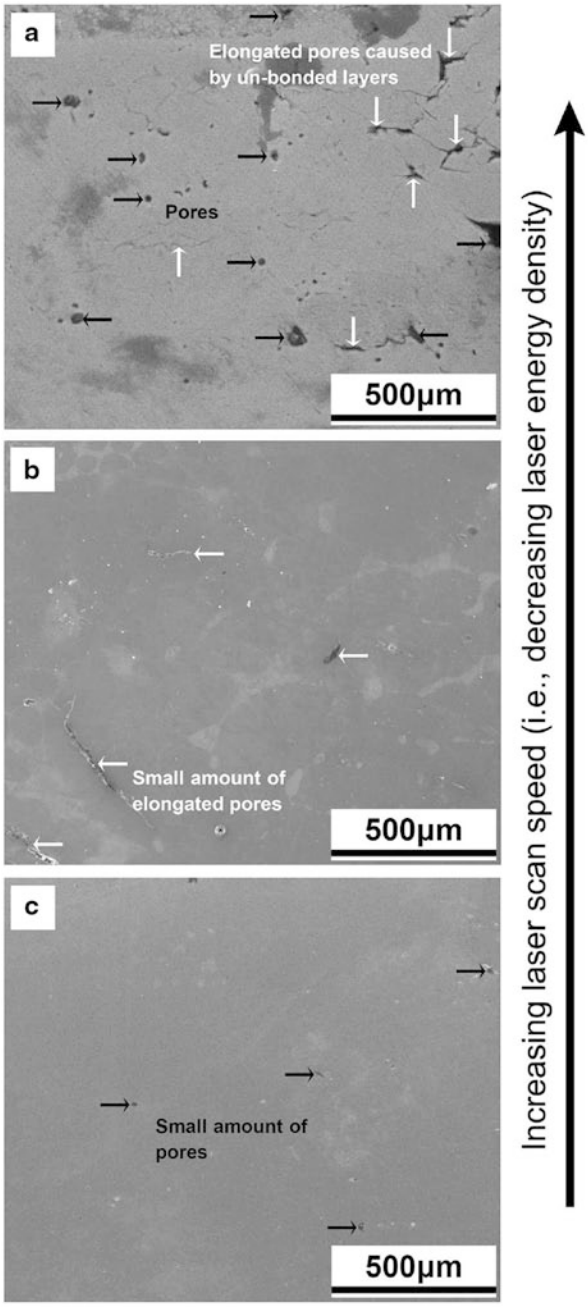


Fig. 5.4 Low-magnification SEM images showing microstructures on the polished cross-sections of SLM-processed *in situ* WC-based hardmetals parts at laser scan speeds of 1.2 m/s (**a**), 1.0 m/s (**b**), and 0.8 m/s (**c**). Laser power $P = 1.2$ kW, scan line hatching spacing $l = 0.15$ mm, and powder layer thickness $d = 0.1$ mm are kept constant

of WC phase showed that the block-shaped WC was developed in a layer-by-layer, multilaminated growth manner (Fig. 5.5b, c). On increasing the laser scan speed to 1.0 m/s, the *in situ* formed WC phase (M_2, Table 5.1) generally changed into a triangle shape and the average grain size slightly increased to 19.6 μm, with the

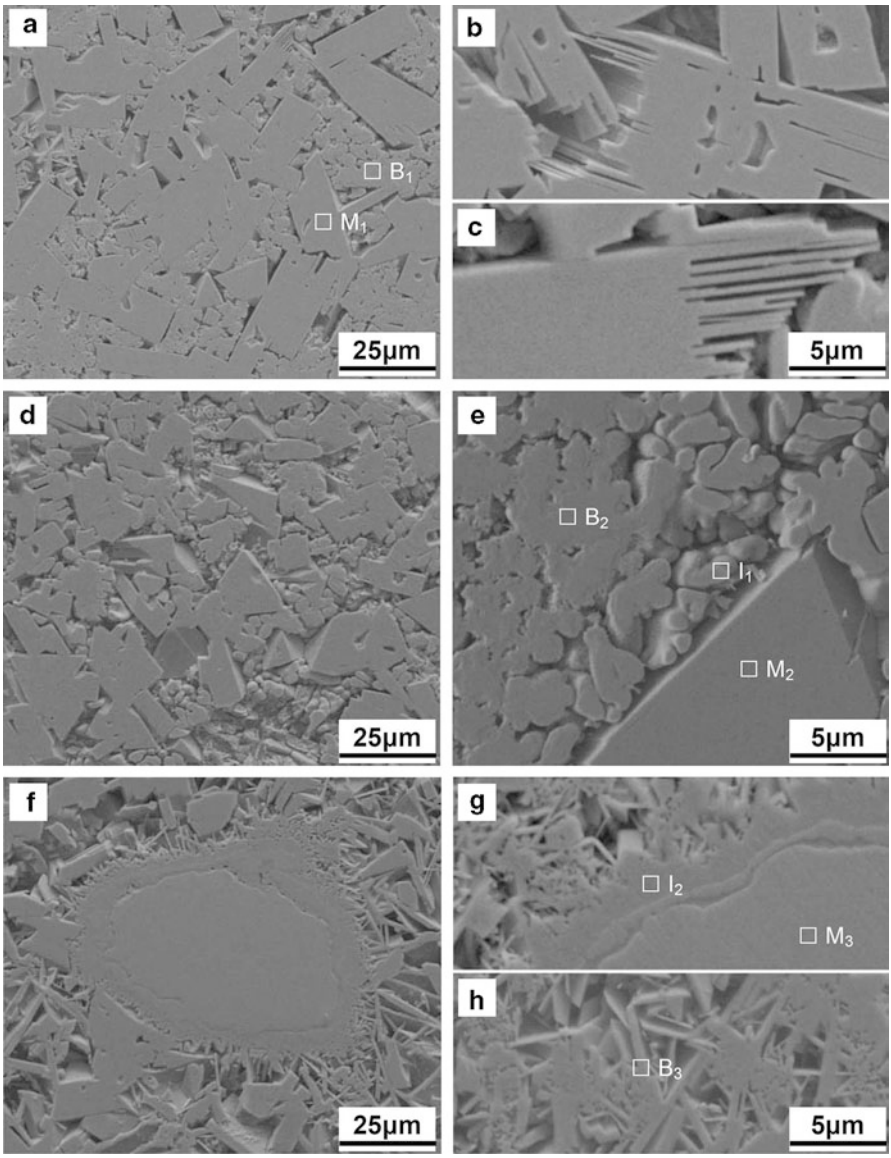


Fig. 5.5 High-magnification SEM images showing characteristic microstructures of SLM-processed *in situ* WC-based hardmetal parts at various laser scan speeds: **a**–**c** 0.8 m/s; **d** and **e** 1.0 m/s; **f**–**h** 1.2 m/s. Laser power $P = 1.2$ kW, scan line hatching spacing $l = 0.15$ mm, and powder layer thickness $d = 0.1$ mm are fixed

SD of the grain size measurement being 2.78 (Fig. 5.5d). Similar as B_1 (Fig. 5.5a), the binder phase was also composed of Ni and W elements (B_2, Table 5.1). Differently, SEM micrograph at a higher magnification revealed the formation of granular

Table 5.1 Chemical compositions measured by EDX small-area scans at different positions in SLM-processed structures shown in Fig. 5.4

Figure	Label	Position	Chemical compositions (at.%)		
			Ni	W	C
5.4a	M_1	Ceramic matrix	–	43.8	56.2
	B_1	Metallic binder	35.9	64.1	–
5.4e	M_2	Ceramic matrix	–	46.5	53.5
	I_1	Granular precipitates at interface	26.3	58.4	15.3
	B_2	Metallic binder	31.3	68.7	–
5.4g and h	M_3	Ceramic matrix	–	55.3	44.7
	I_2	Ring-shaped interfacial layer	27.8	52.5	19.7
	B_3	Metallic binder	29.9	70.1	–

constituent with a mean particle size of 1.7 μm at the interface between WC and binder. The identified elements in such microstructure consisted of Ni, W, and C (I_1, Table 5.1). A combination of XRD and EDX results, thus, confirmed the presence of $Ni_2W_4C(M_6C)$ after SLM. Microstructural features changed significantly in SLM-processed part at an even higher laser scan speed of 1.2 m/s. A ~3 μm thick ring-shaped interfacial layer was observed, which was identified as M_6C by XRD and EDX (I_2, Table 5.1). The M_6C changed from a granular morphology (Fig. 5.5e) to a ring structure (Fig. 5.5f) as the applied laser scan speed increased. The elliptical-shaped constituent inside the M_6C interfacial layer was found to be WC phase (M_3, Table 5.1). The WC phase had an average grain size of 40.8 μm and the SD of the size measurement was 2.26, showing a certain degree of coarsening (Fig. 5.5f). The (Ni, W) binder (B_3, Table 5.1) were developed into a slender dendritic structure in this instance (Fig. 5.5h).

In order to further determine the exact constitutions of the SLM-processed *in situ* WC-based hardmetals at various processing conditions, the X-ray photoelectron spectra were identified by an X-ray photoelectron spectroscopy (XPS) system, with the results depicted in Figs. 5.6, 5.7 and 5.8. The acquisition parameters were: source type AlK Alpha, spot size 500 μm, pass energy 20.0 eV, energy step size 0.100 eV, and number of energy steps 461. Peak identification was performed by reference to the standard XPS database [12]. Figures 5.6a, 5.7a, and 5.8a depict the wide energy-range surveys of the SLM-processed *in situ* parts at various laser scan speeds of 0.8, 1.0, and 1.2 m/s, respectively, in which the XPS peaks of Ni, W, C, and O elements can be detected. Based on this, data were further acquired for the W4f (26–51 eV), C1s (278–296 eV), and Ni2p (846–893 eV) regions. Generally, the W4f spectra consisted of four peaks at 31.50, 33.70, 35.70, and 38.07 eV, which were identified as WC 7/2, WC 5/2, WO3 7/2, and WOx 5/2 (Figs. 5.6b, 5.7b, and 5.8b). The detected peaks in the C1s spectra were 282.70, 285.16, and 286.60 eV, which corresponded to C1s WC, C1s C–CH, and C1s C–OH (Figs. 5.6c, 5.7c, and

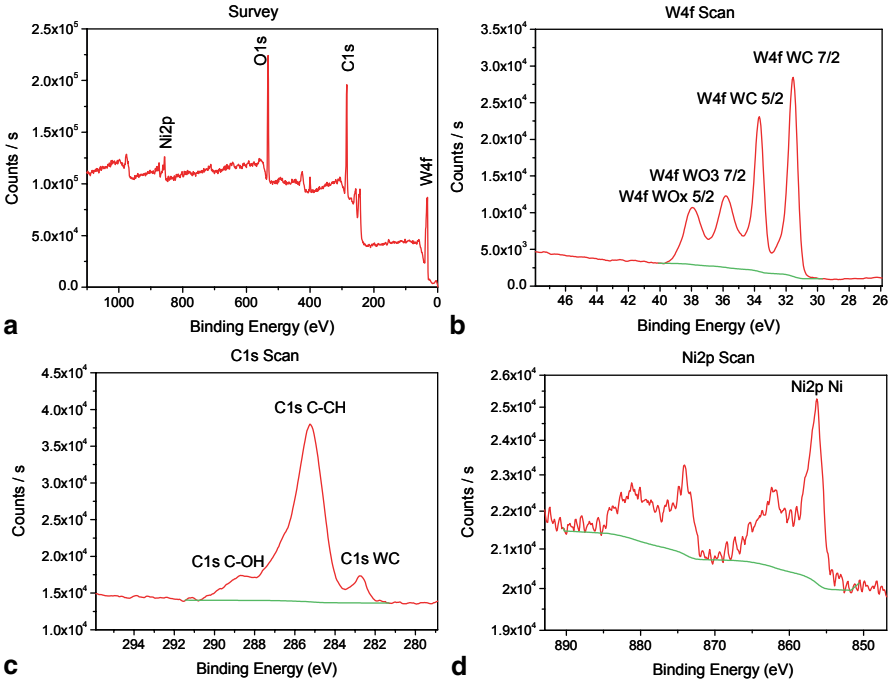


Fig. 5.6 XPS wide energy range survey and high-resolution XPS spectra of W4f, C1s, and Ni2p scans in SLM-processed Ni–W–C powder system at a laser scan speed of 0.8 m/s

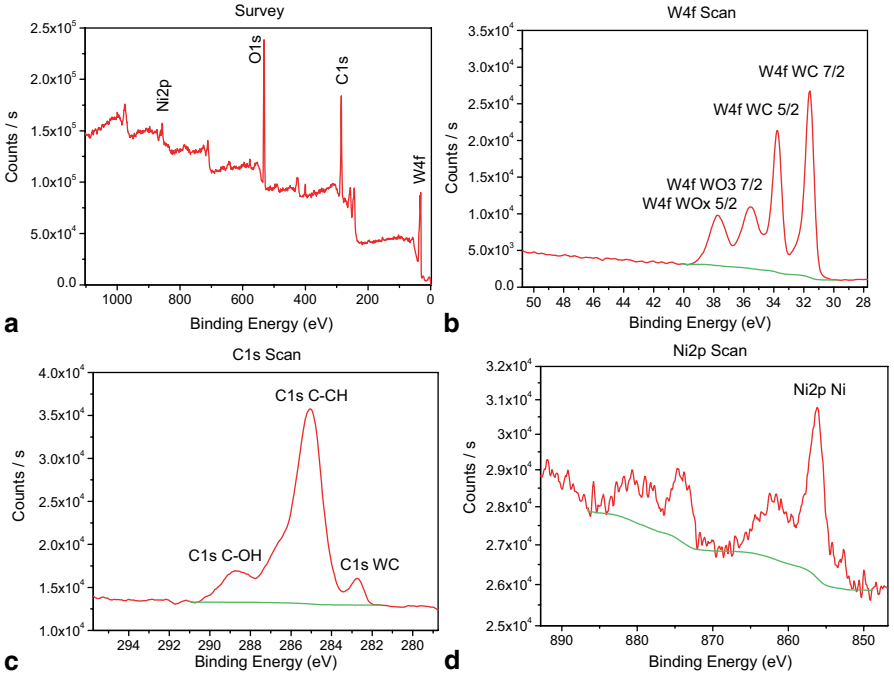


Fig. 5.7 XPS wide energy range survey and high-resolution XPS spectra of W4f, C1s, and Ni2p scans in SLM-processed Ni–W–C powder system at a laser scan speed of 1.0 m/s

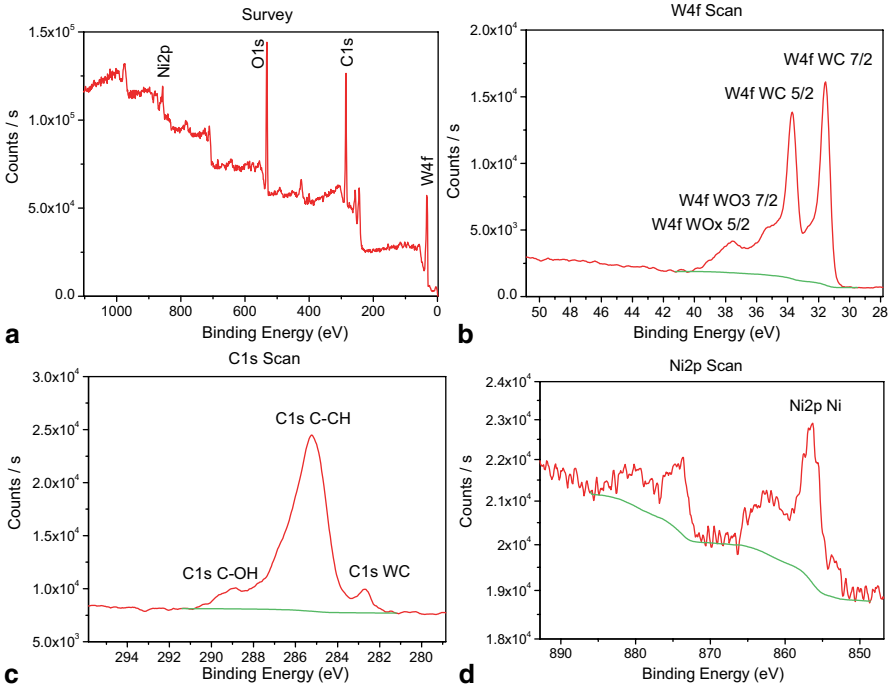


Fig. 5.8 XPS wide energy range survey and high-resolution XPS spectra of W4f, C1s, and Ni2p scans in SLM-processed Ni–W–C powder system at a laser scan speed of 1.2 m/s

5.8c). In the present study, the surfaces of the samples have not been simultaneously sputtered during XPS analysis. The presence of C1s C–CH and C1s C–OH peaks in the C1s spectra might be due to the contamination of the organic compounds introduced from the surfaces of the samples and the analytical instrument. Thus, it was reasonable to conclude that the carbon element was present in the form of WC compound in SLM-processed *in situ* WC-based hardmetals, which was in accordance with the XRD results (Fig. 5.3). The peak for the free carbon was not identified in the C1s spectra. Also, it was noted that the characteristics of the peaks of free carbon were not detected in the XRD patterns. Both XPS and XRD results revealed the nonresidual of free carbon after SLM processing. The atomic percentage of the elements concerned was determined based on the experimentally determined sensitivity factors (F) and the intensity (I) of a photoelectron peak, which was taken as the integrated area under the peak following the subtraction of a linear background [13]. The quantification of compositions based on XPS method showed that the atomic fractions of WC compound in SLM-processed parts at laser scan speeds of 0.8, 1.0, and 1.2 m/s were 7.34, 6.86, and 5.97 at.%, respectively. Accordingly, it reveals that a decrease in the applied laser scan speed (i.e., an increase in the resultant linear laser energy density) leads to a larger amount of formation of

WC compound, due to a relatively longer dwell time of laser beam on the irradiation region and the attendant higher operating temperature. The concentration of the binder phase Ni in the corresponding hardmetals was 3.27, 2.86, and 3.55 at.%, respectively (Figs. 5.6d, 5.7d, and 5.8d), showing a very slight change with the applied laser processing conditions.

5.5 Formation Mechanisms and Conditions of *In Situ* WC Phase during SLM Process Using CO_2 Laser

As previously addressed, when laser beam scans over powder bed, the energy is absorbed by powder particles through both bulk-coupling and powder-coupling mechanisms [14]. In an initial step, the energy is absorbed in a narrow layer of individual particles determined by the bulk properties of the materials, leading to a high temperature of particle surfaces during the interaction. After thermalization of the energy, heat flows mainly toward the centre of particles until a local steady state of the temperature within the powder is obtained. A further thermal development tends to melt the powder completely, producing a molten pool consisting of W–Ni–C melts. Based on the C–Ni–W ternary alloy phase diagram (Fig. 5.9), the point S denotes the starting component ratio used in the present study, i.e., the C:Ni:W weight ratio of 5:10:85. During the subsequent solidification process after

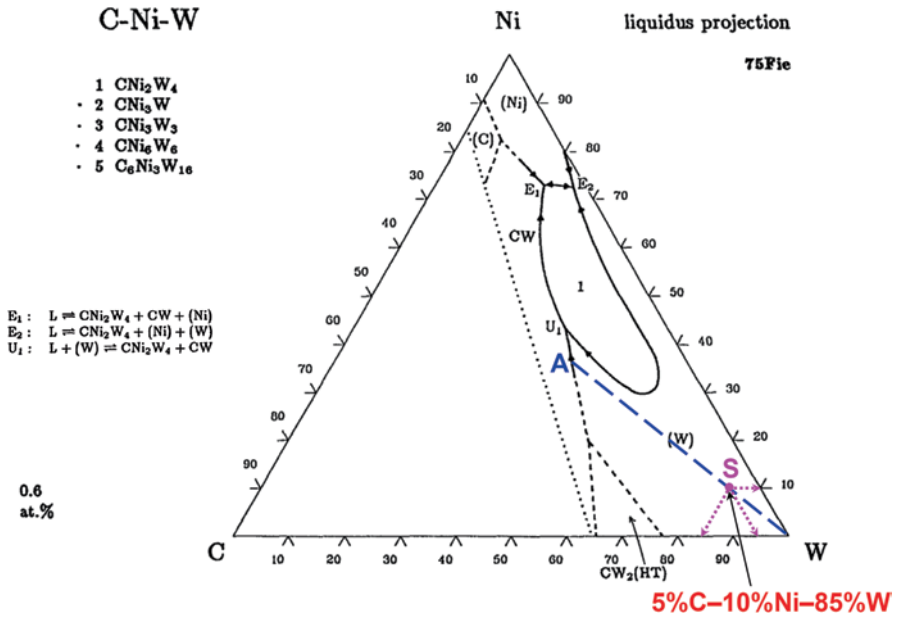


Fig. 5.9 W–Ni–C ternary alloy phase diagram, liquidus projection, see Ref. [15]

laser beam moving away, the ternary solidification system experiences the following reaction scheme:

- Starting from the initial liquid component point S, the liquid system begins to cool down and, accordingly, enters the L+W two-phase region. The (W) phase is solidified and the residual liquid component point locates at point A.
- The solidification system at point A enters a three-phase region L+CW+(W).
- A further decrease in the working temperature produces a quaternary phase equilibrium, i.e., L+(W)+CW+1, within the solidification system. The reaction L+(W)↔CW+1 takes place as the temperature decreases, leading to the formation of WC and Ni_2W_4C phases below U_1 temperature.

Generally, WC and M_6C are formed through a dissolution–precipitation mechanism by means of the heterogeneous nucleation and subsequent nucleus growth. Nevertheless, experimental results reveal that the amount and microstructure of the formed WC and M_6C vary distinctly under different laser processing conditions (Figs. 5.3 and 5.5). It is known that WC has a hexagonal unit cell (P-6m2) with W atoms at (0,0,0) and C atoms at (1/3,2/3,1/2) positions (a=0.2906 and c=0.2837 nm). Since WC has no symmetry centre, the $\{10\bar{1}0\}$ and $\{01\bar{1}0\}$ facets are not equivalent. Interface energy calculations performed by Christensen et al. [16] reveal that one set of prismatic facets develops more significantly than the other one. In this situation, the truncation factor r is introduced to quantify the ratio of development rates of these two sets of prismatic facets. Normally, when WC crystals are observed along <0001>, the corresponding projection is a truncated triangle, as schematically shown in Fig. 5.10a. The truncation factor is defined as the ratio of the length of two types of facets:

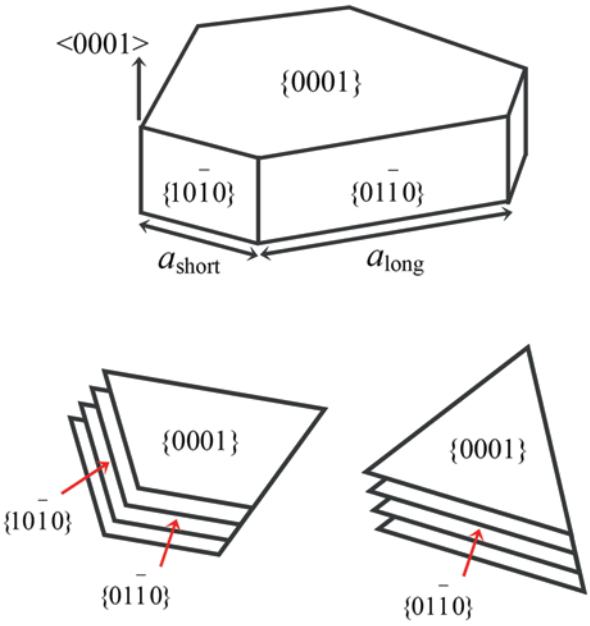


Fig. 5.10 Structure of WC grains showing (0001) basal and two kinds of {10–10} prismatic facets (a); Multi-laminated growth of block- and triangle-shaped WC via different truncation mechanisms of prismatic facets (b)

$$r = \sum a_{\text{short}} / \sum a_{\text{long}} \tag{5.2}$$

The factor r depends on the energy of the two types of facets. The broadest facet is termed as F_{long} and the shortest F_{short}. The broadest facets are related to the smallest energy $\gamma_{F_{\text{long}}}$ and the shortest ones to the highest energy $\gamma_{F_{\text{short}}}$. The factor r can be further defined by [17]:

$$r = \left(\frac{2\gamma_{F_{\text{long}}}}{\gamma_{F_{\text{short}}}} - 1 \right) \Bigg/ \left(2 - \frac{\gamma_{F_{\text{long}}}}{\gamma_{F_{\text{short}}}} \right) \tag{5.3}$$

The formation of the block-shaped WC at a lower scan speed indicates that $r > 1$ (Figs. 5.5a and 5.10b); that is, $\gamma_{F_{\text{long}}} > \gamma_{F_{\text{short}}}$. As $r = 0$, i.e., $\gamma_{F_{\text{long}}} = \frac{1}{2}\gamma_{F_{\text{short}}}$, the WC crystals tend to develop into a triangular shape at a higher laser scan speed (Figs. 5.5e and 5.10b). Thus, it is reasonable to conclude that the various morphologies of the formed *in situ* WC in SLM-processed hardmetals at different laser scan speeds are related to the change in the interfacial energies of $\{10\bar{1}0\}$ and $\{01\bar{1}0\}$ facets and the resultant variation of truncation factor. As a specific configuration determines, the WC crystals tend to grow in a layer-by-layer fashion by means of multi-layered stacking of (0001) basal along <0001> orientation to form a three-dimensional form (Fig. 5.5b and c).

Furthermore, according to Eq. 4.3 in Chap. 4, the working temperature at the tips of WC grains (T_t) is related to the growth rate of tips (V_t); the T_t increases as the V_t decreases. The v_t is further controlled by the applied laser beam scan speed (v); v_t increases in direct proportion to v, as revealed by Eq. 4.1. Combined Eqs. 4.1 and 4.3, it reveals that a decrease in the applied scan speed v leads to a higher working temperature T_t at the tips of WC grains. A larger amount of heat is accordingly accumulated at the tips, which are regarded as the most instable areas of the grains, thereby providing significant internal energy and thermodynamic potentials for the development of tips. The formation of the block-shaped WC grains, which have a larger quantity of tips than the triangle-shaped grains (Fig. 5.5a vs. 5.5d), implies an elevated development degree of the tips of WC grains at a lower scan speed.

On the other hand, on increasing the laser scan speed, the amount of the formed M_6C increases (Fig. 5.3) and its shape changes from an individual granular form (Fig. 5.5e) to a continuous ring structure (Fig. 5.5f). Also, an increase in laser scan speed results in the coarsening of WC grains into an elliptical shape (Fig. 5.5f). A variation of the activity of carbon in W–Ni–C melts under different SLM conditions may account for the above phenomena. According to Kikuchi et al.'s results [18], the carbon activity a_C in a W–Ni–C ternary system is controlled by the operating temperature T and can be expressed as:

$$\ln a_C = \ln\left[Y_C/(1-Y_C)\right] + (-1.07 + 6806/T) + (13.51 + 9554/T)Y_C + (1.21 + 9010/T)Y_W \quad (5.4)$$

where $Y_i = X_i/(1-X_C)$, X_i denotes the atom fraction, and the subscript i stands for either one of W, Ni, and C. It reveals that at a constant chemical concentration, a_C is inversely proportional to T. The working temperature during line-by-line laser scanning is related to the energy gain of the powder and is controlled by the linear laser energy density (LED), which is defined by LED = P/v. Increasing the applied scan speed v lowers the obtainable LED, which in turn decreases the SLM temperature T. The activity of carbon within the melts, consequently, is enhanced, as revealed from Eq. 5.4. In this situation, the solubility of C in (Ni, W) melts increases, leading to a larger amount of M_6C precipitation. Also, as the carbon activity elevates, the M_6C and WC precipitates generally undergo a morphological change, showing a tendency for grain coarsening. Furthermore, it is noted that with the varying operating temperature, the standard Gibbs free energy of formation ($\Delta_f G°$) of compounds changes significantly. According to the thermochemical data in[19], the $\Delta_f G°$ of WC decreased from −32.098 to −33.367 kJ/mol as the temperature decreased from 2500 to 2000 K. Therefore, a reasonable decrease in the working temperature, which can be realized by increasing laser scan speed, results in a decrease in the obtainable $\Delta_f G°$, which in turn leads to a more spontaneous formation of WC constituent.

5.6 Relationship of Processing Conditions, Microstructures, and Microhardness of SLM-Processed WC-Based Hardmetals Parts Using CO_2 Laser

The microhardness of various constitutional phases within SLM-processed *in situ* WC-based hardmetals parts was determined by applying the indentations on the WC matrix, (Ni, W) metal binder, and ceramic/metal interface, respectively. Microhardness measurement on each kind of constitutional phases was repeated in ten different positions and the results of microhardness were expressed using the mean values, as shown in Fig. 5.11. The microhardness of the block-shaped WC phase formed at a laser scan speed of 0.8 m/s was 1619.7 $HV_{0.1}$, which increased to a maximum value of 1870.9 $HV_{0.1}$ for the triangle-shaped WC phase in the hardmetals processed at 1.0 m/s, showing a small-sized indentation with a clear contour and a small degree of deformation (Fig. 5.12b). The elliptical-structured WC phase presented at a higher scan speed of 1.2 m/s possessed a relatively

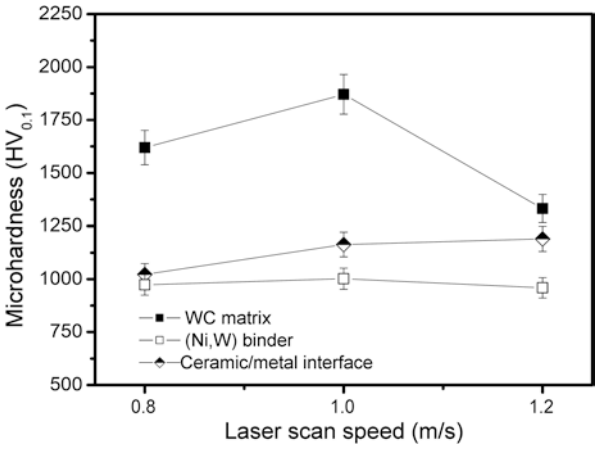


Fig. 5.11 Effect of the applied laser scan speeds on microhardness of SLM-processed *in situ* WC-based hardmetals parts. Constant parameters are: laser power $P = 1.2$ kW, scan line hatching spacing $l = 0.15$ mm, and powder layer thickness $d = 0.1$ mm

low microhardness of 1331.8 $HV_{0.1}$. A comparison of microstructural features of the indentations revealed that the WC matrix experienced a largest degree of deformation in this instance (Fig. 5.12c). The microhardness of the ceramic/metal interface increased from 1022.6 to 1164.4 $HV_{0.1}$ as the laser scan speed changed from 0.8 to 1.0 m/s, due to the presence of M_6C precipitates at the interface in the latter case (Fig. 5.5e). The interfacial microhardness further increased to 1190.8 $HV_{0.1}$, as the M_6C interfacial layer changed into a continuous ring structure in SLM-processed hardmetals at the scan speed of 1.2 m/s (Fig. 5.5f). The microhardness of the (Ni, W) metal binder, which acted as a minor phase within SLM-processed materials, was generally close to 1000 $HV_{0.1}$ and showed no apparent variation for all the applied scan speeds. Compared with the WC–Co hardmetals produced by Laser Engineered Net Shaping (LENS) additive manufacturing process (Maximum microhardness of 1437 HV [20]), the nanocrystalline WC–Co hardmetals prepared by spark plasma sintering (SPS) powder metallurgy method (Microhardness of 700–1500 $HV_{0.1}$ [21]) and the laser clad WC/Ni layers on H13 tool steel substrates (Average surface microhardness of 650 HV [22]), the SLM-processed *in situ* WC/M_6C based hardmetals in the present study possessed a superior microhardness of a maximum value of 1870.9 $HV_{0.1}$. Besides the physical nature of as-prepared WC-based hardmetals, the high hardness obtained was also a consequence of residual stresses inherited in SLM process. On the premise of a sufficiently high densification level without the formation of microcracks, the remainder of the stresses in laser-processed materials favors a further enhancement of the hardness.

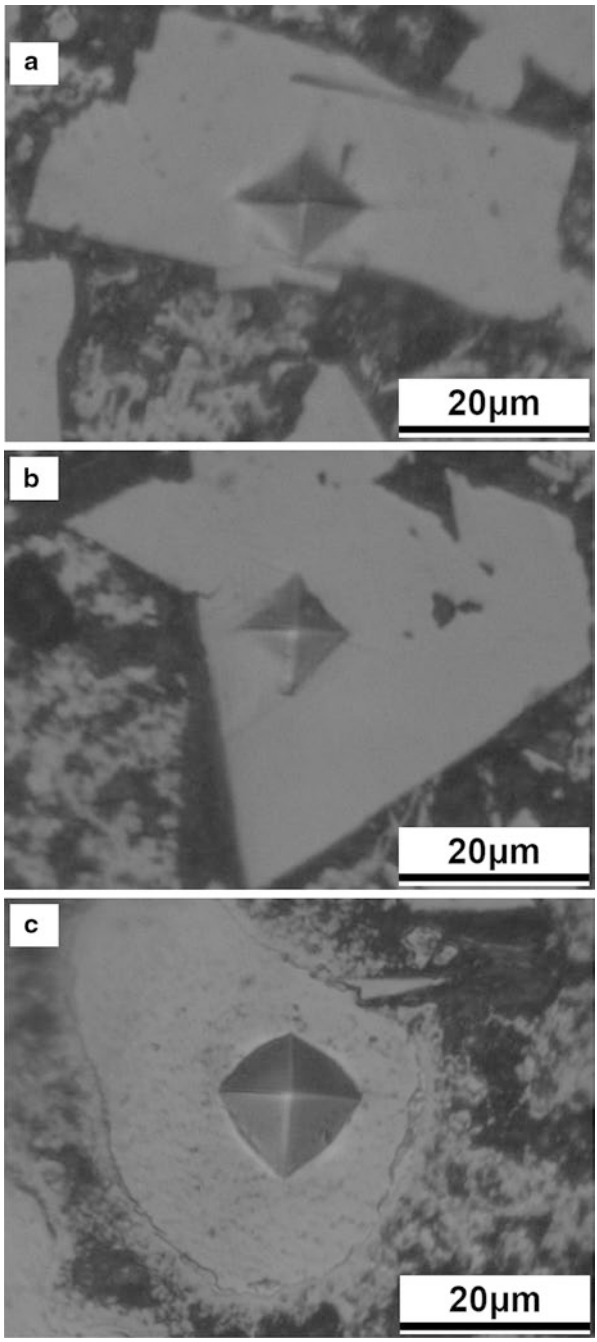


Fig. 5.12 Typical microstructures of indentations during microhardness tests on WC matrixes in SLM-processed *in situ* WC-based hardmetals parts at different laser scan speeds: **a** 0.8 m/s; **b** 1.0 m/s; **c** 1.2 m/s

5.7 Crystal Growth Mechanisms of *In Situ* WC in Selective Laser Melted W–C–Ni Ternary System Using Fiber Laser

In order to study the influence of laser type on the microstructural development of the *in situ* WC phase, SLM processing of the W–Ni–graphite powder mixture with the W:C:Ni weight ratio of 84.7:5.3:10 was performed, using the fiber laser as the energy source, as defined in Sect. 3.2 of Chap. 3. The following SLM parameters were applied: laser power 120–160 W, scan speed 0.2–0.6 m/s, scan line hatch spacing 50 μm, and powder layer thickness 30 μm.

Figure 5.13 depicts the typical XRD patterns of the starting W–Ni–C powder and SLM-processed cermets using the fiber laser. The strong diffraction peaks corresponding to the individual C, W, and Ni phases were identified in the starting powder. After SLM, the apparent diffraction peaks for WC and Ni phases were observed and the intensity of WC peaks was apparently stronger than that of Ni

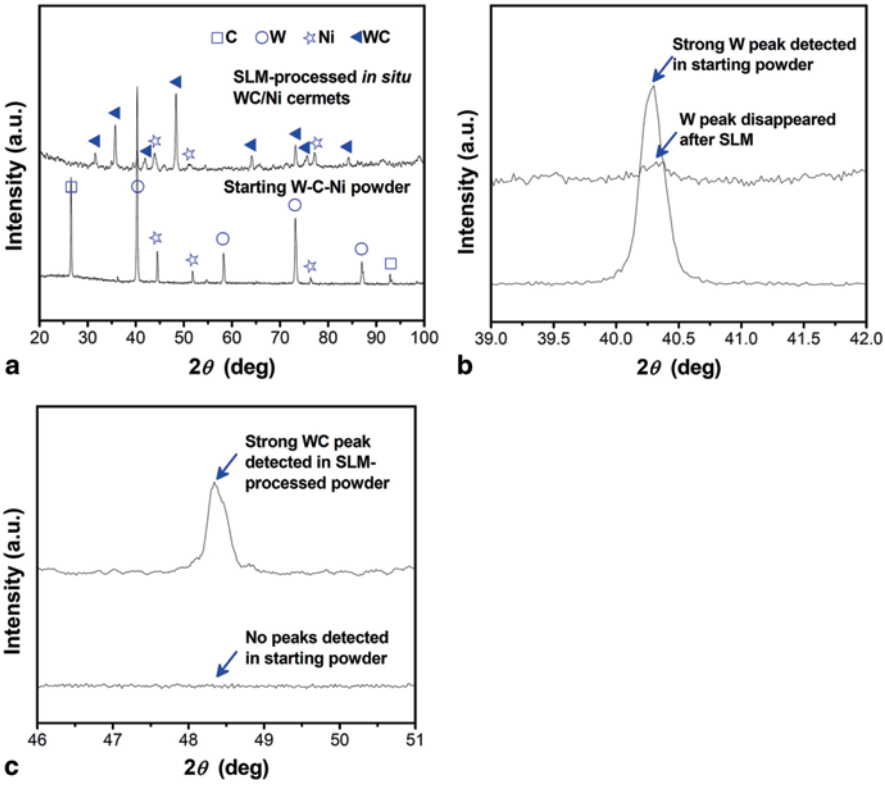


Fig. 5.13 XRD spectra of the starting powder system and SLM-processed *in situ* cermets (**a**); XRD spectra within $2\theta = 39–42°$ (**b**) and $2\theta = 46–51°$ (**c**) showing the changes of the strongest W and WC diffraction peaks

peaks (Fig. 5.13a). In order to further reveal the behaviors of W and C constituents in this synthesis system, XRD characterization in the vicinity of the strongest lines of W (standard $2\theta = 40.264°$) and WC (standard $2\theta = 48.296°$) was performed. The initial strong W peak in the powder disappeared completely after SLM (Fig. 5.13b) and, meanwhile, the strong WC peak was present in SLM-processed cermets (Fig. 5.13c), implying the complete exhausting of W and attendant *in situ* formation of WC during SLM.

XPS surveys were further performed to acquire the peaks within W4f (30–35 eV) and C1s (281–286 eV) regions. The W4f spectra consisted of two peaks at 31.50 and 33.70 eV, which were identified as WC 7/2 and WC 5/2, respectively (Fig. 5.14a). The detected peak in the C1s spectrum at 282.70 eV corresponded to C1s WC (Fig. 5.14b). The XPS characterization further proved the presence of *in situ* WC phase after SLM.

The characteristic crystal microstructures in SLM-processed cermets using different parameters are shown in Fig. 5.15. EDX analysis revealed that the W and C elemental ratio in these crystals was generally close to 1:1, which further testified the *in situ* formation of WC crystals. Generally, the *in situ* WC crystals exhibited a unique triangular microstructure after SLM process using the fiber laser (Fig. 5.15a). A close look at the edges of WC crystals showed that they were developed via a layer-by-layer, multilayered growth mechanism (Fig. 5.15b–d). Meanwhile, the SLM parameters played a critical role in determining the WC crystal structure and size. Here, an integrated parameter "laser energy density" (LED), which was defined by $\mathrm{LED} = P/v$, was applied to estimate the combined influence of laser power (P) and scan speed (v). For each LED, the mean physical dimensions of WC crystals were measured during SEM analysis. At a relatively low LED of 200 J/m, the considerably refined triangular WC crystals were formed, with the average length of the side being 3.9 μm and with a thickness of 0.9 μm (Fig. 5.15b and f). As LED was increased to 300 J/m, the WC crystals exhibited a slight, insignificant coarsening (Fig. 5.15c and f). However, at an even higher LED of 400 J/m, the mean

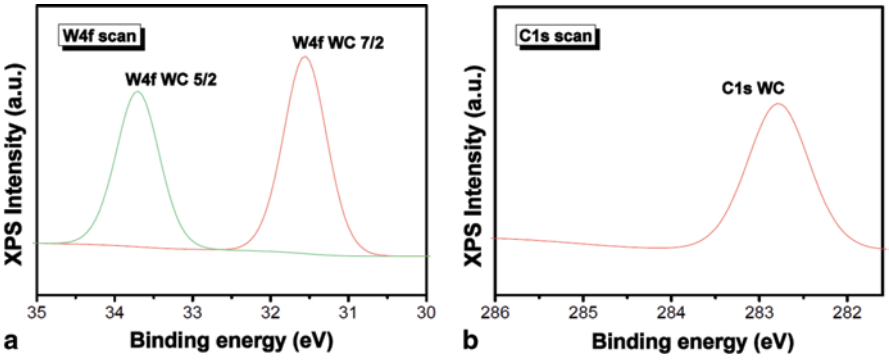


Fig. 5.14 High-resolution XPS spectra of W4f (**a**) and C1s (**b**) scans in SLM-processed cermets showing the *in situ* formation of WC phase

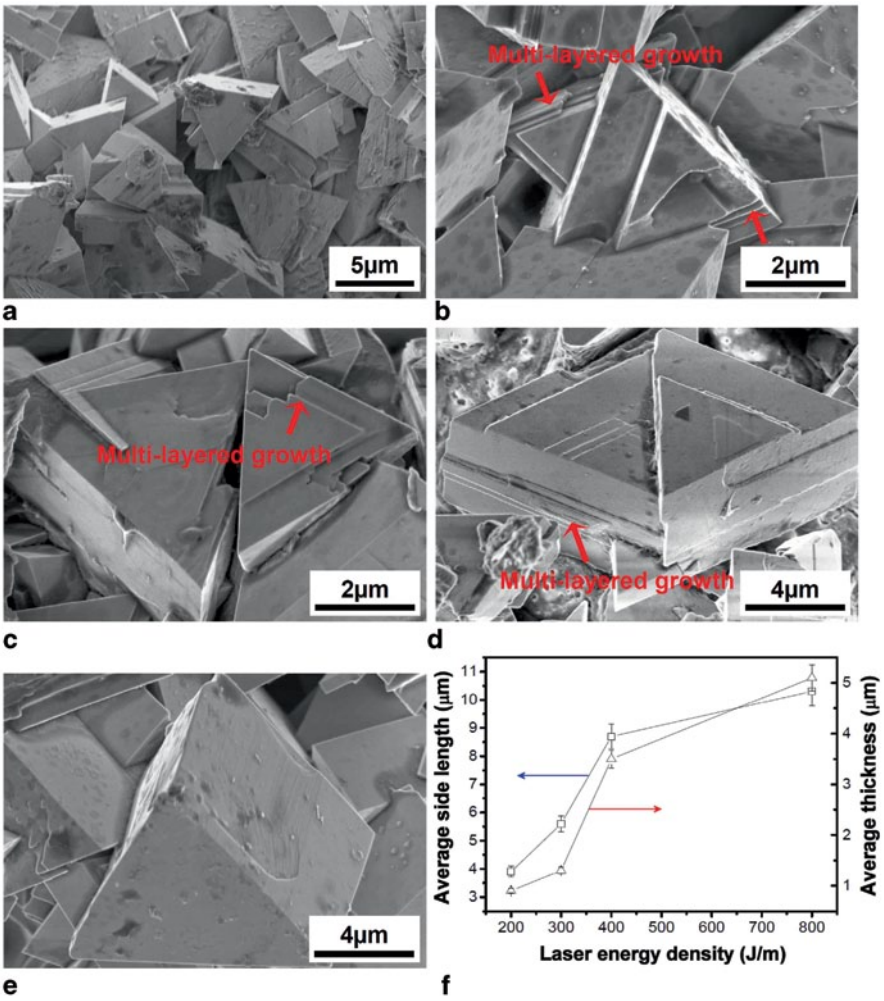


Fig. 5.15 Low-magnification FE-SEM image showing WC crystals in a relatively large observation area in SLM-processed WC/Ni cermets (**a**). FE-SEM images showing characteristic growth morphologies of *in situ* WC crystals using different SLM parameters: (**b**) $P=120$ W, $v=0.6$ m/s, LED = 200 J/m; (**c**) $P=120$ W, $v=0.4$ m/s, LED = 300 J/m; (**d**) $P=160$ W, $v=0.4$ m/s, LED = 400 J/m; (**e**) $P=160$ W, $v=0.2$ m/s, LED = 800 J/m. Influence of the applied LED on physical dimensions of triangular *in situ* WC crystals (**f**)

side length and thickness of triangular WC crystals showed about twice and fourfold increase upon that obtained at 200 J/m, reaching 8.7 and 3.5 μm, respectively (Fig. 5.15d and f). As LED was further elevated to 800 J/m, the triangular WC crystals were coarsened significantly, especially in their thickness, with the average value reached 5.1 μm (Fig. 5.15e and f).

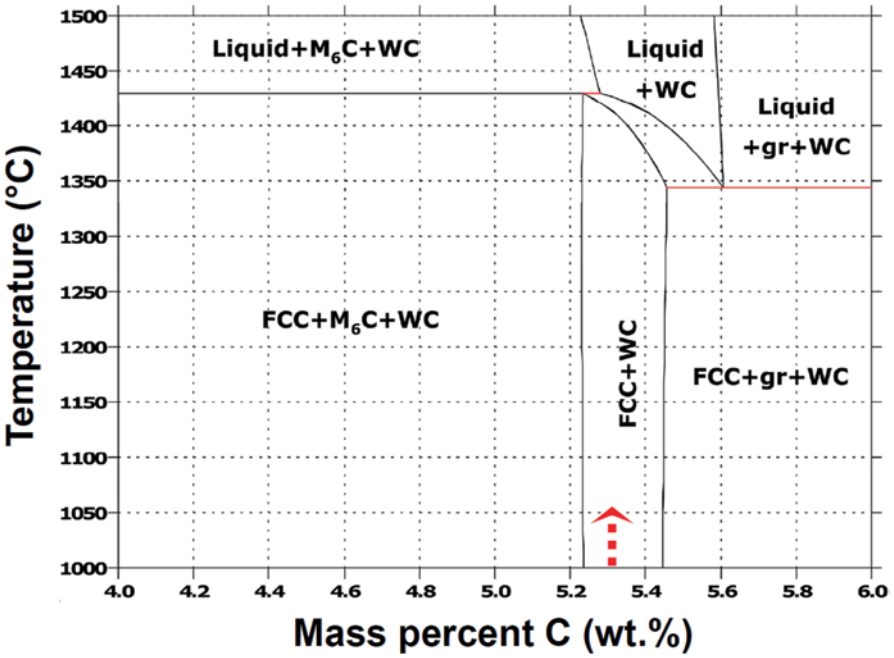


Fig. 5.16 Vertical section of the W–C–Ni phase diagram calculated at 10 wt.% Ni, see Ref. [23]

SLM of the present powder system yields a molten pool consisting of the ternary W–C–Ni melts. Due to the liquid formation in the pool caused by the fiber laser with a high-energy density, the operative temperature, at least, is higher than the melting temperate of Ni (1455 °C). According to W–C–Ni phase diagram (Fig. 5.16), the SLM system with 84.7W–5.3C–10Ni (wt.%) enters the two-phase field WC + liquid above 1455 °C. On cooling, the stoichiometric compositions, i.e., WC + FCC, tend to precipitate. As WC has no symmetry centre, the $\{10\bar{1}0\}$ and $\{01\bar{1}0\}$ facets are not equivalent (Fig. 5.10a) and, normally, one set of prismatic facets develops more speedily than the other one. The truncation factor r is accordingly introduced to quantify the development rates of these facets, as revealed by Eqs. 5.2 and 5.3. As $r = 0$, i.e., $\gamma_{\text{Long}} = \frac{1}{2}\gamma_{\text{Short}}$, the WC crystals develop into a triangular structure during SLM. With the specific crystal structure determined, the WC crystals grow in a layer-by-layer mechanism via the multi-layered stacking of (0001) basal along <0001> orientation to form a three-dimensional triangular form (Fig. 5.15b–d). When a higher LED is applied, a larger amount of heat is accumulated at the tips of WC crystals, providing the thermodynamic potential for the significant elongation of the side length of triangular WC crystals. Also, with the heat input enhanced, more atoms gather and deposit on (0001) basal plane and the triangular layers stack together consecutively, resulting in a significant coarsening of the thickness of WC crystals (Fig. 5.15e).

5.8 Conclusions

In this chapter regarding SLM additive manufacturing of *in situ* WC-based hardmetals parts using two different types of lasers, the main conclusions were summarized as follows.

1. *In situ* WC/Ni_2W_4C(M_6C) cemented carbide based hardmetals parts were prepared by SLM processing of W–Ni–graphite elemental powder mixture using CO_2 laser. A sound densification level of 96.3 % was obtained at a relatively high-laser-energy input.
2. The *in situ* WC phase in SLM-processed WC-based hardmetals using CO_2 laser was developed through a multilaminated growth mechanism and its structure experienced a successive change, i.e., block-shaped triangular—elliptical, on decreasing the applied linear laser energy density. The amount of the formed M_6C phase in SLM-processed WC-based hardmetals increased and its structure changed from a granular form to a ring shape at a lower laser energy input.
3. A maximum microhardness value of 1870.9 $HV_{0.1}$ was obtained in SLM-processed *in situ* WC-based hardmetals parts using CO_2 laser, showing an elevated hardness performance as relative to the conventional WC–Co hardmetals prepared by laser process or powder metallurgy method.
4. The *in situ* WC crystals formed in laser melted W–C–Ni ternary system using fiber laser generally had a triangular microstructure which was also developed via a layer-by-layer growth mechanism by the multi-layered stacking of (0001) basal planes of WC phase. An increase in the applied laser energy density, which was realized by increasing laser power or decreasing scan speed, resulted in the coarsening of *in situ* WC crystals in both side length and thickness, due to the significant increase in the heat accumulation at the tips of triangular WC crystals.

References

1. Upadhyaya GS (ed) (1998) Cemented tungsten carbides: production, properties and testing. Noyes Publications, Westwood
2. Lou D, Hellman J, Luhulima D et al (2003) Interactions between tungsten carbide (WC) particulates and metal matrix in WC–reinforced composites. Mater Sci Eng A 340(1–2):155–162
3. Trindade B, Vieira MT, Bauer-Grosse E (1994) Structural stability and crystallization studies of metastable sputtered W–Ni–C films. Thin Solid Films 252(2):82–88
4. Taheri-Nassaj E, Mirhosseini SH (2003) An *in situ* WC–Ni composite fabricated by the SHS method. J Mater Process Technol 142(2):422–426
5. Tjong SC (2007) Novel nanoparticle-reinforced metal matrix composites with enhanced mechanical properties. Adv Eng Mater 9(8):639–652
6. Veinthal R, Kulu P, Pirso J et al (2009) Characterization and prediction of abrasive wear of powder composite materials. Wear 267(11):2216–2222
7. Matsuura K, Obara Y, Kojima K (2009) Combustion synthesis of boride particle dispersed hard metal from elemental powders. Int J Refract Met Hard Mater 27(2):376–381

8. Kruth JP, Levy G, Klocke F et al (2007) Consolidation phenomena in laser and powder-bed based layered manufacturing. CIRP Ann Manuf Technol 56(2):730–759
9. Simchi A (2006) Direct laser sintering of metal powders: mechanism, kinetics and microstructural features. Mater Sci Eng A 428(1–2):148–158
10. Fiedler ML, Stadelmaier HH (1975) The ternary system nickel-tungsten-carbon. Z Metallkd 66(7):402–404
11. ZhouY WGH (ed) (2007) Analysis methods in materials science-X-ray diffraction and electron microscopy in materials science. Harbin Institute of Technology Press, Harbin
12. National Institute of Standards and Technology (NIST) (2003) X-ray Photoelectron spectroscopy database. Version 3.5, Gaithersburg, http://srdata.nist.gov/xps/ Accessed 10 Mar 2015
13. Watts JF, Wolstenholme J (eds) (2003) An introduction to surface analysis by XPS and AES. Wiley, Chichester
14. Fischer P, Romano V, Weber HP et al (2003) Sintering of commercially pure titanium powder with a Nd:YAG laser source. Acta Mater 51(6):1651–1662
15. Villars P, Prince A, Okamoto H (1995) Handbook of ternary alloy phase diagrams. ASM International, Materials Park, OH
16. Christensen M, Wahnström G, Lay S et al (2007) Morphology of WC grains in WC–Co alloys: theoretical determination of grain shape. Acta Mater 55(5):1515–1521
17. Delanoë A, Lay S (2009) Evolution of the WC grain shape in WC-Co alloys during sintering: effect of C content. Int J Refract Met Hard Mater 27(1):140–148
18. Kikuchi M, Takeda S, Kajihara M et al (1988) Activity of carbon in nickel-rich Ni–Mo and Ni–W alloys. Metal Trans A 19(3):645–650
19. BarinI (ed) (1993) Thermochemical data of pure substances. VCH, New York
20. Xiong Y, Smugeresky JE, Ajdelsztajn L et al (2008) Fabrication of WC–Co cermets by laser engineered net shaping. Mater Sci Eng A 493(1–2):261–266
21. Cha SI, Hong SH, Kim BK et al (2003) Spark plasma sintering behavior of nanocrystalline WC–10Co cemented carbide powders. Mater Sci Eng A 351(1–2):31–38
22. Huang SW, Samandi M, Brandt M (2004) Abrasive wear performance and microstructure of laser clad WC/Ni layers. Wear 256(11–12):1095–1105
23. Fernandes CM, Senos AMR (2011) Cemented carbide phase diagrams: a review. Int J Refract Met Hard Mater 29(4):405–418

Chapter 6
Nanoscale TiC Particle-Reinforced AlSi10Mg Bulk-Form Nanocomposites by Selective Laser Melting (SLM) Additive Manufacturing (AM): Tailored Microstructures and Enhanced Properties

Abstract The nanoscale TiC particle-reinforced AlSi10Mg nanocomposite parts were produced by SLM process. The influence of the SLM processing parameters, especially the "linear laser energy density" (LED), on densification behavior, microstructural evolution, and mechanical properties of SLM-processed nanocomposites were studied. Using an insufficient LED lowered the SLM densification due to the balling effect and the formation of residual pores. The nanostructured TiC reinforcement in SLM-processed parts experienced the significant microstructural variation as the applied LED changed. The sufficiently high densification rate combined with the homogeneous incorporation of nanoscale TiC reinforcement throughout the matrix led to the considerably low coefficient of friction (COF) and resultant wear rate. The obtained microhardness and tensile strength were apparently higher than the unreinforced SLM-processed AlSi10Mg part while maintaining the sufficient ductility. Both the insufficient SLM densification response at a relatively low LED and the disappearance of nanoscale reinforcement at a high LED lowered the hardness and wear performance of SLM-processed TiC/AlSi10Mg nanocomposite parts.

6.1 Introduction

In the past few years, there is an increasing demand for the lightweight materials with high strength and stiffness in modern industries [1]. Particle-reinforced aluminum matrix composites (AMCs), because of their low density, high strength, low coefficient of thermal expansion, and outstanding abrasion resistance, can well meet these requirements and, accordingly, have been widely used in the industries and fields of aerospace, automotive, microelectronics, etc [2–4]. As the potentially feasible reinforcement for AMCs, TiC exhibits a number of favorable characteristics, such as high elastic modulus, high hardness, and especially its good wettability and thermodynamic stability within the molten aluminum [5]. Normally, the large-sized reinforcing particles are used in the conventional processing of particle-reinforced AMCs, ranging from several tens of micrometers to hundreds of micrometers. However, due to the limited interfacial wettability and bonding coherence between ceramics and metals, the large ceramic particles are prone to cracking during mechanical loading, resulting in the poor ductility and

© Springer-Verlag Berlin Heidelberg 2015

D. Gu, *Laser Additive Manufacturing of High-Performance Materials,*
DOI 10.1007/978-3-662-46089-4_6

premature failure of AMCs [6]. It has been revealed that the strength and ductility of AMCs are significantly affected by the particle size of reinforcement; both tensile strength and ductility increase with lowering the particle size [7]. Therefore, the application of the refined reinforcing particles can efficiently favor the improvement of mechanical properties of AMCs, e.g., the reduced particle cracking and the enhanced strengthening. Previous studies have confirmed that the mechanical properties of AMCs can be further enhanced by decreasing the size of ceramic reinforcing particles from micrometer to nanometer levels [8]. Such materials are known as nanocomposites [9]. The production of nanocomposites with unique microstructural and mechanical properties has inspired considerably research interest.

Selective laser melting (SLM) has been treated as one of the most effective powder-based additive manufacturing (AM) methods for metallic parts [10–12]. Due to the unique processing mechanisms of SLM, e.g., a full melting of powder materials followed by a rapid solidification at the rate of 10^6–10^8 K/s [13], the melt tends to experience a particular nonequilibrium metallurgical process during SLM process, thereby providing a capacity to produce unique aluminum-based nanocomposite parts. However, the previous studies have shown that the feasibility of processing aluminum alloy parts by SLM is considerably lower than that of titanium alloys, nickel alloys, or steels [14]. This is mainly attributed to the unique physical properties of the aluminum powder including (i) the considerably low absorptivity (only 9%) of the aluminum powder to the laser beam [14], (ii) the high heat conductivity of 237 W/(mK) that is 11-fold compared to Ti and fivefold compared to Fe [15]; and (iii) the high affinity to oxygen and elevated oxidation kinetics. The rapid dissipation of heat away from the molten pool through the previously solidified material and the formation of oxide layer on the top of the pool in the deposited tracks hinder the diffusion of melt and accordingly reduce the wettability and laser processability. Nevertheless, the parts with densities exceeding 97% can be acquired successfully via SLM process, typically using the casting alloy AlSi10Mg as the starting powder [16, 17]. The AlSi10Mg is selected for SLM because of its favorable weldability, sufficient hardenability, and excellent corrosion resistance. The sound weldability is attributed to the near-eutectic composition of Al and Si, which leads to a narrow solidification range. The addition of small amount of Mg (0.3–0.5 wt%) gives rise to Mg_2Si precipitates by natural or artificial ageing treatments, inducing the hardening of aluminum alloys.

In this chapter, the material as investigated was broadened from the conventional AlSi10Mg alloy to the novel AlSi10Mg-based nanocomposites. The bulk-form TiC/AlSi10Mg nanocomposites with the unique nanoscale reinforcement were successfully prepared by SLM process. The microstructural evolution of nanoscale reinforcement in SLM-processed parts at different SLM processing parameters was studied and the attendant densification level and mechanical properties were assessed. A material–microstructure–property relationship was established to enable the successful production of AMCs parts with nanoscale reinforcement architecture and elevated mechanical performance.

6.2 Powder Preparation and SLM Process of TiC/AlSi10Mg Nanocomposites

The 99.0% purity TiC nanopowder with a near spherical shape and a mean particle size of 50 nm (Fig. 6.1a) and the 99.7% purity AlSi10Mg powder with a spherical shape and an average particle diameter of 30 μm (Fig. 6.1b) were used. The TiC/AlSi10Mg powder system consisting of 2–5 wt.% TiC were mechanically mixed in a Pulverisette 4 vario-planetary mill (Fritsch GmbH, Germany), using a ball-to-powder weight ratio of 1:1, a rotation speed of main disk of 200 rpm, and a mixing duration of 4 h.

Based on the procedures addressed in Sect. 3.3 of Chap. 3, SLM processing of the TiC/AlSi10Mg nanocomposite powder was performed using the as-defined fiber laser as the energy source. Through a series of preliminary SLM experiments, the following processing parameters were chosen for SLM fabrication of rectangular specimens with dimensions of 40 mm × 20 mm × 5 mm: the focused spot size at the substrate surface of 70 μm, the laser power (P) of 80–140 W, the laser scan speeds (v) 100–600 mm/s, the scan line hatching spacing (l) of 50 μm, and the powder layer thickness (d) of 30–50 μm. According to the same strategy for process control as stated previously, the "linear laser energy density" (LED), which is defined by $\mathrm{LED} = \frac{P}{v}$, was used to estimate the laser energy input to the powder layer being melted.

6.3 Phases Identification SLM-processed TiC/AlSi10Mg Nanocomposite Parts

Typical X-ray diffractometer (XRD) spectra of SLM-processed TiC/AlSi10Mg nanocomposite parts obtained within a wide range of 2θ degrees (20–90°) are depicted in Fig. 6.2. The strong diffraction peaks corresponding to Al_9Si (JCPDS Card No. 65-8554) and stoichiometric TiC (JCPDS Card No. 65-8805) were identified, revealing the general formation of TiC-reinforced AMCs at all given LED. Furthermore, the Mg_2Si (JCPDS Card No. 35-0773) precipitates were formed by natural ageing and the detected diffraction peaks were relatively weak. Although the SLM process was performed in an inert argon atmosphere, the atmosphere may still contain 0.1–0.3% residual oxygen [18, 19]. Consequently, the XRD spectra showed that the Al_2O_3 oxide was still formed at the lowest LED of 250 J/m. Nevertheless, the Al_2O_3 diffraction peaks disappeared gradually when the applied LED increased from 500 to 1000 J/m. Based on Louvis et al.'s research on the oxidation phenomenon of aluminum parts during SLM process [14], it revealed that the oxide films tended to be formed both on the top of the molten pool and on the surface of the solidified region of the track. Normally, the temperature of the upper molten surface under the laser beam was high enough to vaporize the oxide film on the top of the molten pool. However, the oxide films on the surface of the solidified region in

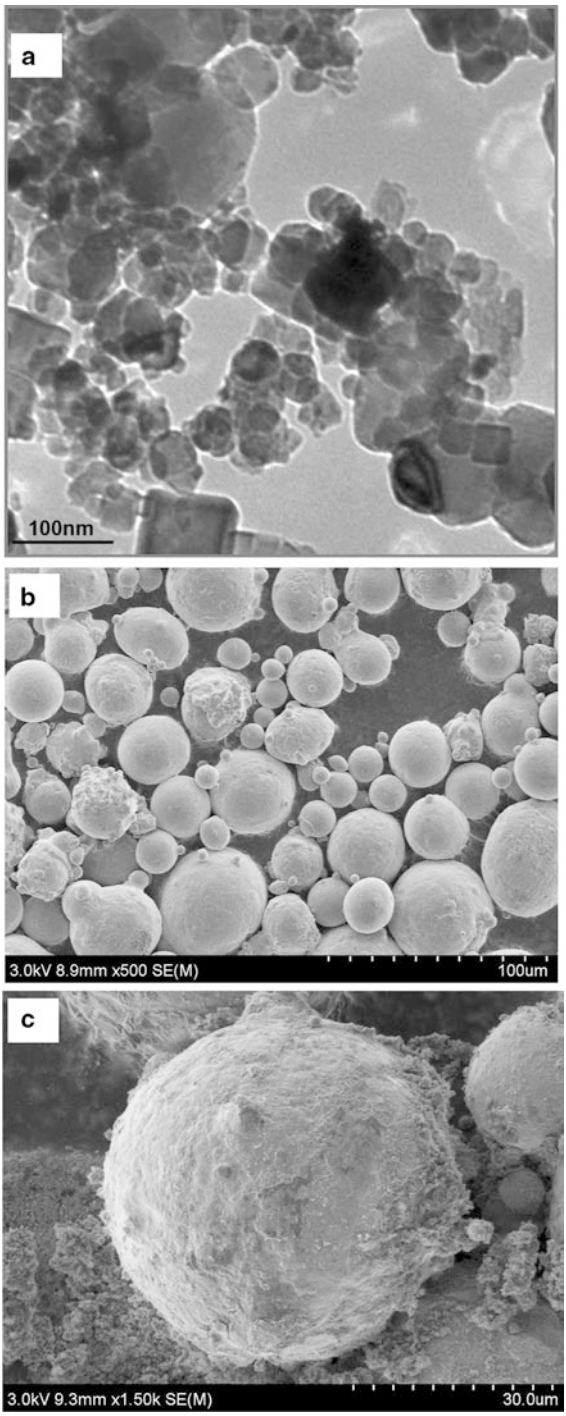


Fig. 6.1 Microstructures of the starting nanoscale TiC powder (**a**), micron-sized AlSi10Mg powder (**b**) and homogeneously mixed TiC/AlSi10Mg nanocomposite powder (**c**)

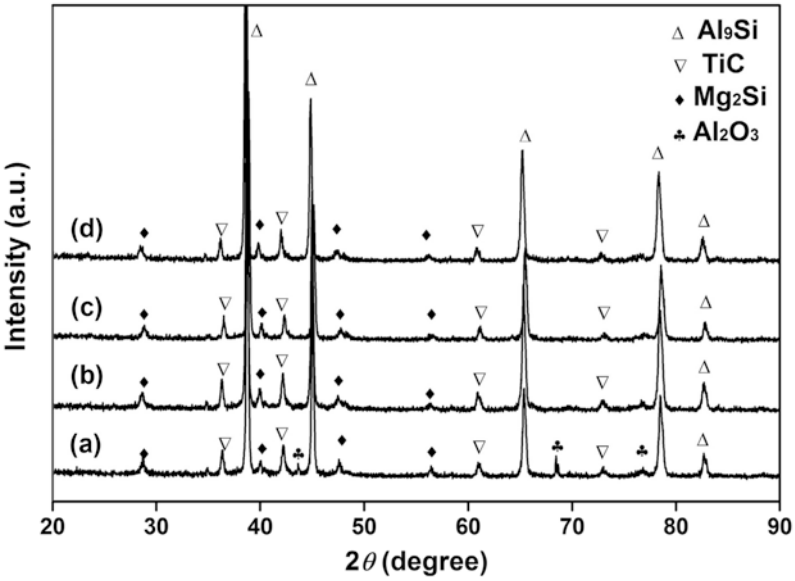


Fig. 6.2 XRD spectra of SLM-processed TiC/AlSi10Mg nanocomposite parts at different laser processing parameters: **a** $P=100$ W, $v=400$ mm/s, LED=250 J/m; **b** $P=100$ W, $v=200$ mm/s, LED=500 J/m; **c** $P=100$ W, $v=143$ mm/s, LED=700 J/m; **d** $P=100$ W, $v=100$ mm/s, LED=1000 J/m

the deposited track could not be easily broken if the insufficient laser power was applied. In the present study, the XRD characterization results revealed that as the applied LED was higher than 500 J/m, the input laser energy was high enough to disrupt the oxide films efficiently, since the Al_2O_3 diffraction peaks vanished from the XRD spectra.

6.4 Effect of SLM Processing Parameters on Densification Behavior of TiC/AlSi10Mg Nanocomposite Parts

The influence of laser energy input on the cross-sectional microstructures and densification behavior of SLM-processed TiC/AlSi10Mg nanocomposite parts is given in Fig. 6.3. Upon etching, the layerwise microstructure features became visible, due to the additive manufacturing nature of SLM. At a relatively low LED of 250 J/m, the cross-section of SLM part showed a relatively heterogeneous layerwise microstructure with the formation of the irregular shaped interlayer pores on a scale of several tens of micrometers (Fig. 6.3a). The corresponding densification rate was about 92.5 % theoretical density (TD) (Fig. 6.4). FE-SEM characterization revealed that there were a large amount of metallic balls with the diameters of several tens

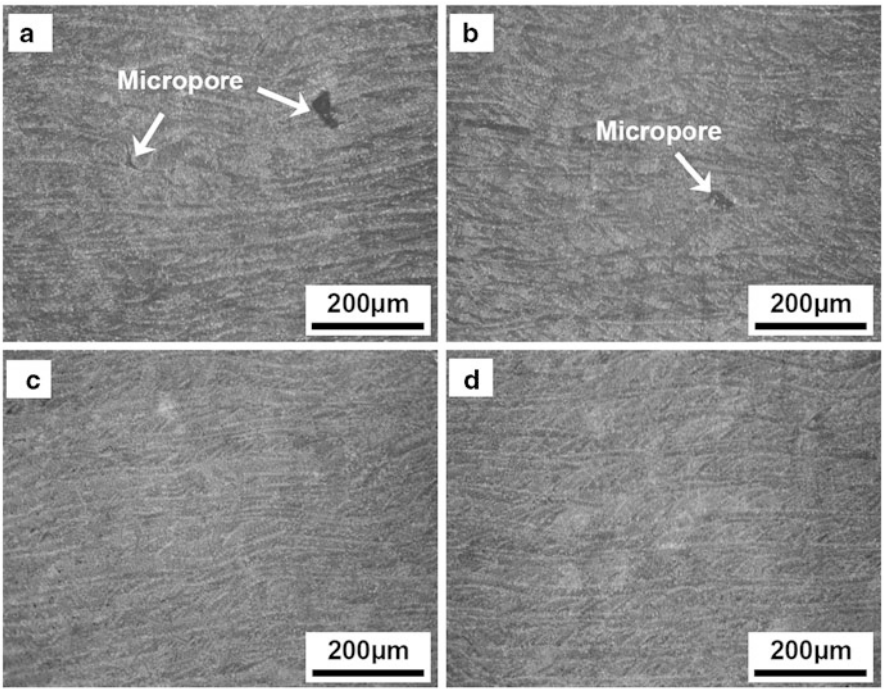


Fig. 6.3 Optical microscope (*OM*) images showing characteristic microstructures on cross-sections of SLM-processed TiC/AlSi10Mg nanocomposite parts at different laser processing parameters: **a** $P = 100$ W, $v = 400$ mm/s, LED = 250 J/m; **b** $P = 100$ W, $v = 200$ mm/s, LED = 500 J/m; **c** $P = 100$ W, $v = 143$ mm/s, LED = 700 J/m; **d** $P = 100$ W, $v = 100$ mm/s, LED = 1000 J/m

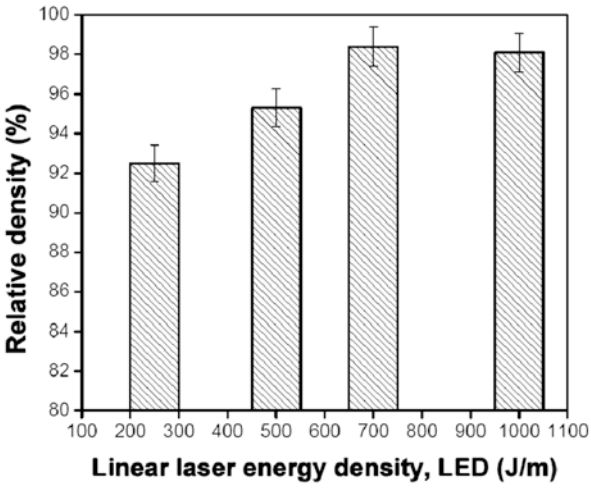


Fig. 6.4 Variation of densification rates of SLM-processed TiC/AlSi10Mg parts with the applied LED

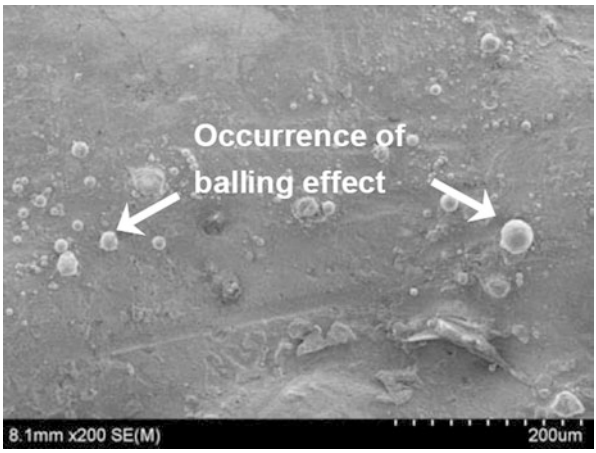


Fig. 6.5 Surface morphology of SLM-processed TiC/AlSi10Mg part at a low LED of 250 J/m (P = 100 W, v = 400 mm/s) showing the occurrence of balling effect

of micrometers formed on the SLM-processed surface (Fig. 6.5). It was accordingly concluded that the balling effect, which was a typical metallurgical defect associated with powder bed-based SLM process [25], initiated in this instance. As the LED increased to 500 J/m, although a small amount of interlayer pores were still present on the cross-section, the size of residual pores became considerably small (Fig. 6.3b), leading to an apparent increase of the relative density to 95.3 % TD (Fig. 6.4). When the LED further increased above 700 J/m, the cross-section showed a homogeneous microstructure with the evenly distributed layers, showing the coherent interlayer bonding ability free of any residual pores (Fig. 6.3c and d). In these situations, the near fully dense (> 98 % TD) TiC/AlSi10Mg parts were generally produced after SLM (Fig. 6.4).

During SLM, the TiC/AlSi10Mg nanocomposite powder is melted line-by-line by the laser beam, forming a mobile molten pool with a continuous liquid front. The amount of the liquid formed in the molten pool influences the densification and the resultant microstructure of the SLM-processed parts by changing the thermokinetic and thermocapillary characteristics, such as viscosity, wettability, and liquid–solid rheological properties. The dynamic viscosity (μ) of the melt in the pool consisting of the Al–Si–Mg liquid and the TiC reinforcing particles can be defined by Eq. 2.3 in Chap. 2. In SLM process, the densification activity of the melt is controlled by the base viscosity (μ_0), which is a strong temperature-dependent viscosity. This viscosity decreases with increasing the operative SLM temperature [20], thereby leading to the better wetting characteristics and improved densification response.

For the TiC/AlSi10Mg system being investigated, the presence of TiC reinforcing particles in aluminum alloy liquid tends to increase the viscosity of the melt significantly, hence handicapping the sufficient flow of the melt and decreasing the overall rheological performance of the composite melt. Meanwhile, using a lower LED results in a limited SLM temperature and, accordingly, elevates the base viscosity (μ_0) of the melt. The combined influence of the material nature and the insufficient laser energy input below 500 J/m tends to reduce the wettability of the melt

within the pool, hence decreasing the densification response after solidification of the melt. Furthermore, during high-energy laser scanning, a steep temperature gradient is developed between the center and edge of the pool across the surface. The temperature gradients in the pool give rise to surface tension gradients and resultant Marangoni convention [21]. Due to the combined effect of Marangoni flow and the poor flowability of the melt caused by the high viscosity, the melt tends to flow radially inward toward the melt pool center, instead of spreading outward on the underlying surface [22]. Consequently, the instable melt track breaks up into several spherical agglomerates to achieve the equilibrium state, which is termed as "balling" effect. During layer-by-layer SLM process, balling effect is detrimental to the uniform deposition of the fresh powder on the previously processed layer. As the laser beam scans over such an uneven powder layer, especially at a high scan speed (i.e., a low LED), the melting/solidification front of the moving molten pool undergoes a significant disturbance and even interruption, causing the residual pores between the uneven SLM layers and the limited densification response after solidification (Fig. 6.3a and b). It is accordingly reasonable to conclude that the high melt viscosity and limited wetting characteristics caused by an insufficient laser energy input are the key factors in producing balling effect and interlayer pores, hence weakening the densification activity of SLM-processed TiC/AlSi10Mg nanocomposite parts.

6.5 Effect of SLM Processing Parameters on Microstructural Evolution of TiC/AlSi10Mg Nanocomposite Parts

Figures 6.6 and 6.7 illustrate the typical microstructures of SLM-processed TiC/AlSi10Mg nanocomposite parts at the fixed laser power of 100 W and the various laser scan speeds. The quantitative determination of the corresponding average particle size of reinforcement is depicted in Fig. 6.8. The quantitative EDX elemental analysis elucidated that the chemical compositions of reinforcement formed at various LED were Ti and C elements with the atomic ratio very close to 1:1. Combined with XRD results (Fig. 6.2), it was reasonable to consider that the reinforcement in SLM-processed nanocomposites was stoichiometric TiC. Although the TiC reinforcement had similar microstructure to the starting particulate morphology before SLM, its dispersion state and particle size were significantly influenced by the applied SLM parameters. At a relatively low LED of 250 J/m (P = 100 W, v = 400 mm/s), the ultrafine TiC reinforcing particles with a mean size of 75 nm were formed (Figs. 6.7a and 6.8). However, the nanostructured TiC reinforcement showed a high tendency to aggregate into clusters, resulting in the formation of micron-sized agglomerates which consisted of several nanoparticles, as selectively indicated in Fig. 6.6a. As the applied LED increased to 500 J/m (P = 100 W, v = 200 mm/s), the low-magnification FE-SEM characterization revealed that the distribution state of TiC reinforcing particles was improved (Fig. 6.6b). Nevertheless, the high-magnification analysis

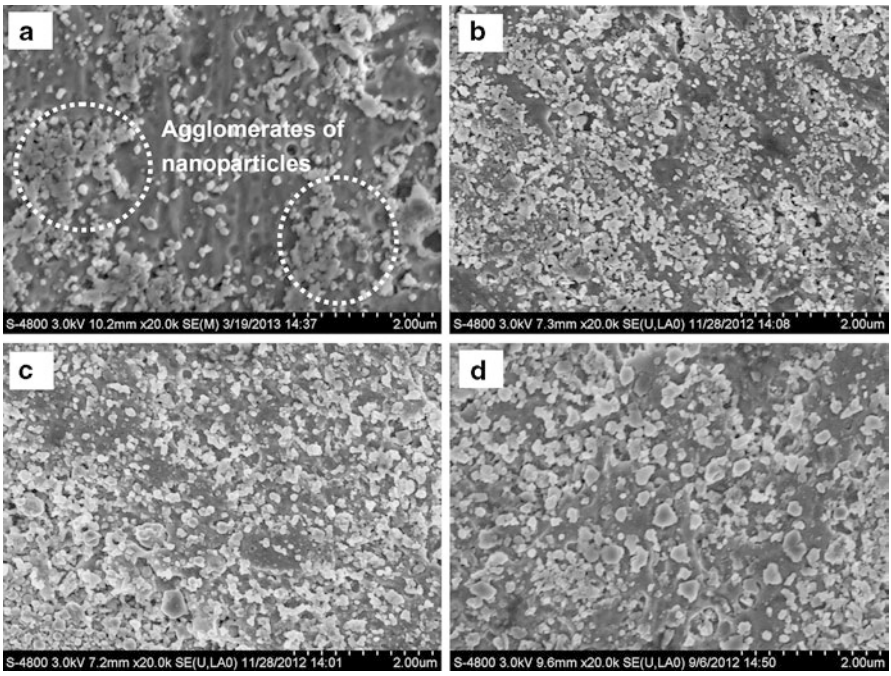


Fig. 6.6 Field emission scanning electron microscope (*FE-SEM*) micrographs showing dispersion states of TiC reinforcement in SLM-processed TiC/AlSi10Mg parts at various processing parameters: **a** $P = 100$ W, $v = 400$ mm/s, LED = 250 J/m; **b** $P = 100$ W, $v = 200$ mm/s, LED = 500 J/m; **c** $P = 100$ W, $v = 143$ mm/s, LED = 700 J/m; **d** $P = 100$ W, $v = 100$ mm/s, LED = 1000 J/m

showed the presence of some inhomogeneous agglomerates of the nanoscale TiC reinforcement in the matrix (Fig. 6.7b). The average particle size of TiC reinforcement slightly increased to 78 nm in this instance (Fig. 6.8). With a further increase in LED to 700 J/m ($P = 100$ W, $v = 143$ mm/s), a uniform distribution of the TiC reinforcement throughout the matrix was obtained (Fig. 6.6c). Even observed in a high magnification, there was no apparent aggregation of TiC nanoparticles in a microscopic scale within SLM-processed structure (Fig. 6.7c). The average size of TiC reinforcing particles, 92 nm, was well within the nanometer scale (Fig. 6.8). At an even higher LED of 1000 J/m ($P = 100$ W, $v = 100$ mm/s), although the uniform distribution state of TiC reinforcement was still maintained (Fig. 6.6d), the mean particle size of TiC reinforcement increased markedly to 161 nm (Figs. 6.7d and 6.8), which indicated that the TiC reinforcement lost its favorable nanostructure after SLM process. It was accordingly concluded that the microstructural development of the nanoscale TiC reinforcement during SLM was sensitive to the laser energy input.

Typically, laser melting offers a high heating/cooling rate, contributing to the development of the nanostructured TiC reinforcement by shortening growth time for TiC grains. In the present study, it is found that as the laser power of 100 W is constant, a reasonable increase in the applied LED from 250 to 700 J/m can

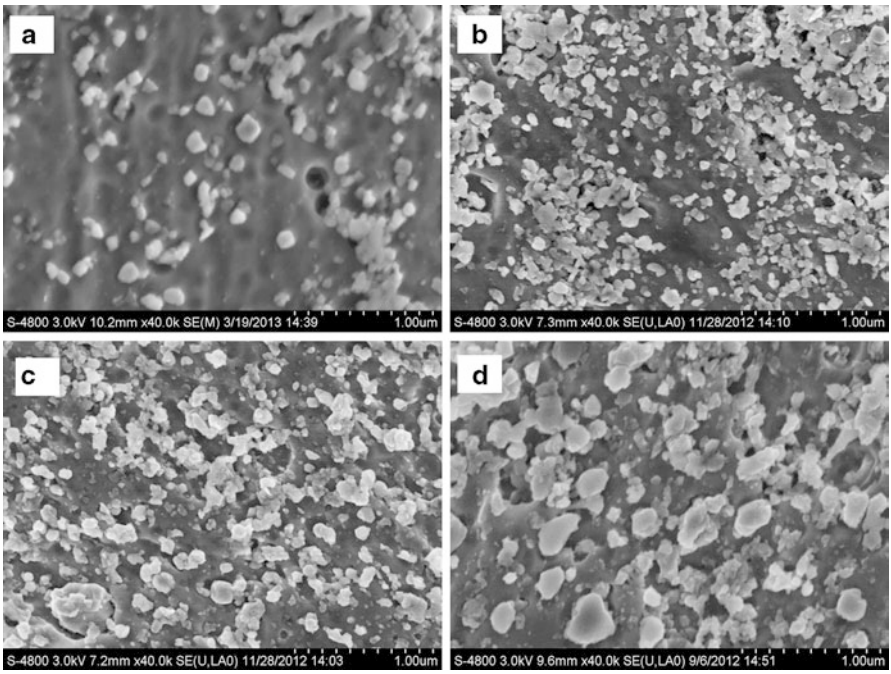


Fig. 6.7 High-magnification FE-SEM micrographs showing characteristic morphologies of TiC reinforcement in SLM-processed TiC/AlSi10Mg parts under different processing conditions: **a** $P = 100$ W, $v = 400$ mm/s, LED = 250 J/m; **b** $P = 100$ W, $v = 200$ mm/s, LED = 500 J/m; **c** $P = 100$ W, $v = 143$ mm/s, LED = 700 J/m; **d** $P = 100$ W, $v = 100$ mm/s, LED = 1000 J/m

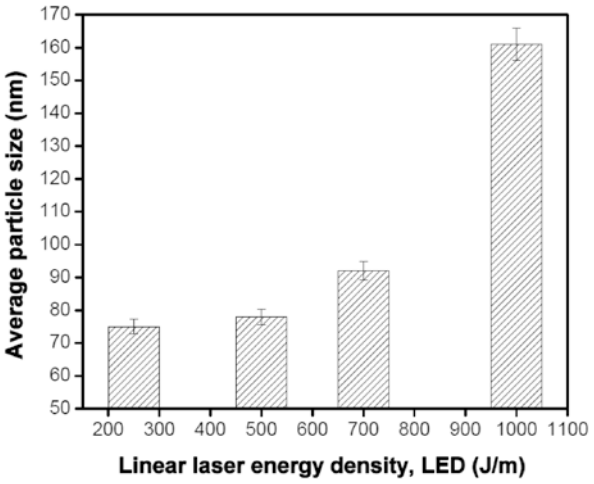


Fig. 6.8 Change of the average particle size of TiC reinforcement with the applied LED. The laser power of 100 W is fixed. The mean sizes of TiC reinforcing particles were measured and calculated during FE-SEM analysis

homogenize the dispersion state of the nanoscale TiC reinforcing particles; however, an excessive laser energy input at 1000 J/m resulted in the significant coarsening of TiC grains and attendant disappearance of the nanostructure of the reinforcement. On the one hand, the formation of the Marangoni convention within the molten pool tends to induce the liquid capillary force, which in turn acts on the TiC reinforcing particles and promotes its rearrangement in the pool. As a relatively high LED is applied, the significantly enhanced SLM temperature causes a considerable decrease in the dynamic viscosity of the melt, thereby intensifying the Marangoni flow in the molten pool and the attendant magnitude of capillary force. Consequently, the rearrangement rate of the nanoscale TiC reinforcing particles in the melt is elevated, thereby avoiding the aggregation of TiC nanoparticles and homogenizing their dispersion state throughout the finally solidified matrix (Figs. 6.6c and 6.7c). On the other hand, the laser energy input influences the microstructural evolution of the nanoscale TiC reinforcement by changing the operative undercooling degree and attendant solidification rate. At a relatively high scan speed and resultant low LED, the solidification rate of the liquid front within the molten pool increases, thereby enhancing the temperature gradients within the pool and the attendant undercooling degree of the melt. The grain growth of nanoscale TiC reinforcement is inhibited effectively, due to the insufficient time supplied for grain coarsening, hence retaining the favorable nanostructured TiC reinforcement after SLM. With the increase of the applied LED by lowering the laser scan speed, the thermalization of laser energy is elevated, resulting in a significant thermal accumulation and a higher SLM temperature within the molten pool. In this situation, the effect of quenching that occurs by conduction of heat through the substrate is not significant. The activity of the grains within the nanoscale TiC reinforcing particles becomes significantly elevated in the molten pool having a slower cooling rate and, accordingly, the TiC grains tend to experience a rapid growth. As a result, the TiC grains become coarsened continuously as the applied LED increases above 1000 J/m and eventually the TiC reinforcing particles lose the initial standard nanostructure after SLM (Figs. 6.7d and 6.8).

Figures 6.9 and 6.10 illustrate the typical microstructures of SLM-processed TiC/AlSi10Mg nanocomposite parts at the relatively low laser power of 80 W and the different laser scan speeds. Apparently, the microstructures of the nanocomposites changed significantly with the variation of SLM conditions. From the relatively low-magnification FE-SEM images, it was observed that the almost similar distribution state of the TiC reinforcing particles on the matrix was obtained when the laser scan speeds were settled at 400 and 200 mm/s (i.e., the resultant LED$\leq$400 J/m) (Fig. 6.9a and b). Nevertheless, the high-magnification FE-SEM analysis showed the presence of some inhomogeneous agglomerates of the TiC reinforcement in the matrix at the relatively high scan speed of 400 mm/s (i.e., a low LED of 200 J/m) (Fig. 6.10a). When the applied scan speed decreased to 200 mm/s and the attendant LED increased to 400 J/m, the distribution state of the TiC reinforcing particles was improved greatly and there was almost no apparent aggregation of TiC particles in a microscopic scale (Fig. 6.10b). As the laser powder was fixed at 80 W and the scan speed further decreased to 133 mm/s, it was interesting to note that a series of regular rings were formed in the matrix in a rather homogenous state (Fig. 6.9c), which

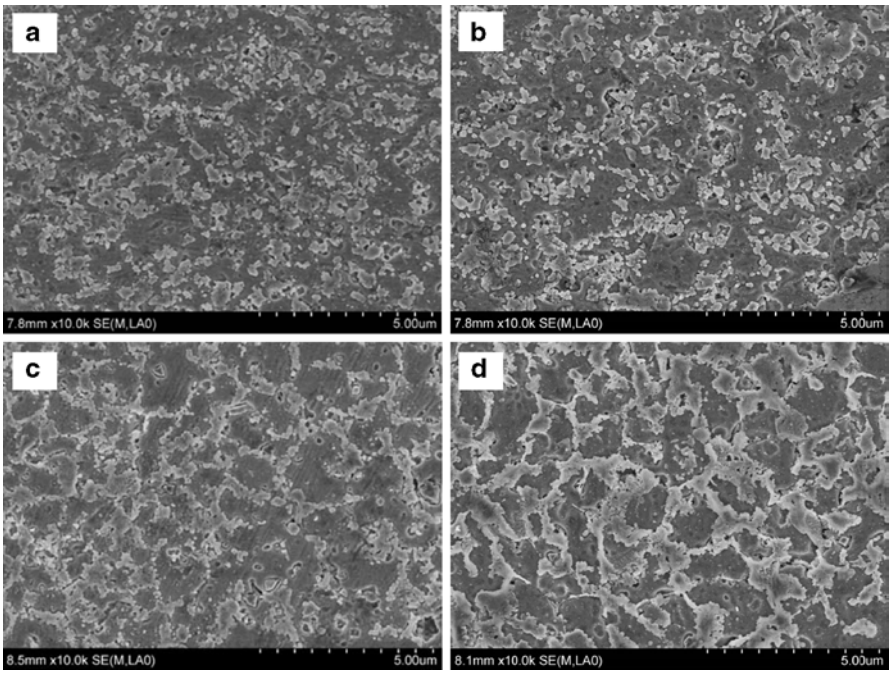


Fig. 6.9 FE-SEM micrographs showing typical microstructures of SLM-processed TiC/AlSi10Mg nanocomposite parts under various SLM processing conditions: **a** $P=80$ W, $v=400$ mm/s; **b** $P=80$ W, $v=200$ mm/s; **c** $P=80$ W, $v=133$ mm/s; **d** $P=80$ W, $v=100$ mm/s

was completely different compared with the microstructures formed in the previous SLM processing situations (Fig. 6.9a and b). When observed in a higher magnification, it was clear that the ring structures with the scale of several hundred nanometers were composed of a number of small nanoscale particles (Fig. 6.10c). With a further decrease in the applied laser scan speed to 100 mm/s, the configuration of ring structures became more regular due to the formation of the highly coherent and distinct reinforcement/matrix boundaries (Fig. 6.9d). The high-magnification FE-SEM characterization revealed that the nanoparticles in the ring structures were bonded with each other completely and it was difficult to distinguish the individual particles (Fig. 6.10d).

In order to quantitative identify the chemical compositions of the microstructures formed at various SLM processing parameters, the EDX spot scans were performed on the reinforcing particle (crisscross 1) and the metal matrix (crisscross 2) in Fig. 6.10b and the EDX line scan was performed on the regularly shaped ring structures along the arrowhead in Fig. 6.10d, with the detailed scan results depicted in Fig. 6.11. It was clear that the reinforcing particle (crisscross 1) was mainly composed of Ti and C elements with the atomic ratio very close to 1:1, while the surrounding metal matrix (crisscross 2) was rich in Al element (Fig. 6.11a and b). EDX line scan results indicated that the elemental distributions of the Al, Si, Ti, and C

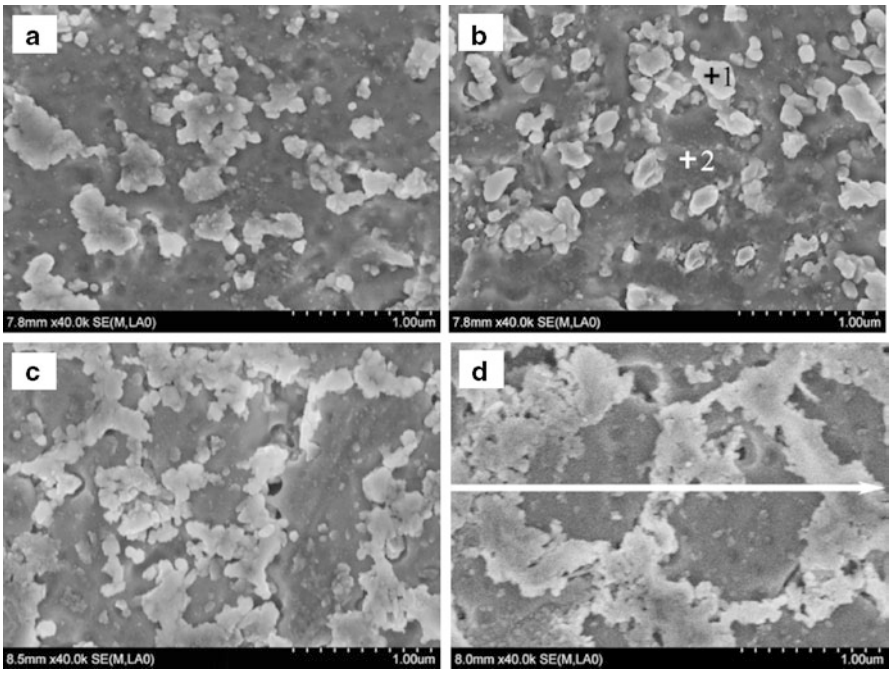


Fig. 6.10 High-magnification FE-SEM images showing characteristic morphologies and dispersion features of TiC reinforcement in SLM-processed TiC/AlSi10Mg nanocomposite parts at different processing parameters: **a** $P = 80$ W, $v = 400$ mm/s; **b** $P = 80$ W, $v = 200$ mm/s; **c** $P = 80$ W, $v = 133$ mm/s; **d** $P = 80$ W, $v = 100$ mm/s

generally exhibited a significant fluctuation; the Ti and C elements showed a higher concentration with the same intensity in the ring structures, while the Al and Si had a higher elemental distribution inside the rings (Fig. 6.11c). It was reasonable to consider that the reinforcement with granular or ring structures in SLM-processed nanocomposite parts were generally stoichiometric TiC and the TiC nanoparticles were present in the novel ring structures at the laser power of 80 W and the scan speed of 200 and 100 mm/s (Figs. 6.9c and d, 6.10c and d, and 6.11c).

Figure 6.12 depicts the reasonable mechanisms for the variation of distribution states of TiC reinforcement with the change of laser scan speeds while at a constant laser power of 80 W. In particular, the formation mechanism of the novel ring structure of TiC reinforcing nanoparticles during SLM is proposed. As stated above, during SLM both thermal gradient and chemical concentration at solid/liquid surface will result in the formation of Marangoni flow on the free surface. Some meaningful research results concerning the Marangoni flow during laser melting of metals have been obtained by Yin et al. [23]. According to their experimental results, the thermal component of the Marangoni flow will lead to a clockwise flow pattern (defined as source flow), whereas the solutal one does the opposite (defined as converging flow); the counterclockwise solutal Marangoni flow is considerably stronger than the clockwise thermal component one, so the overall flow pattern of the molten pool

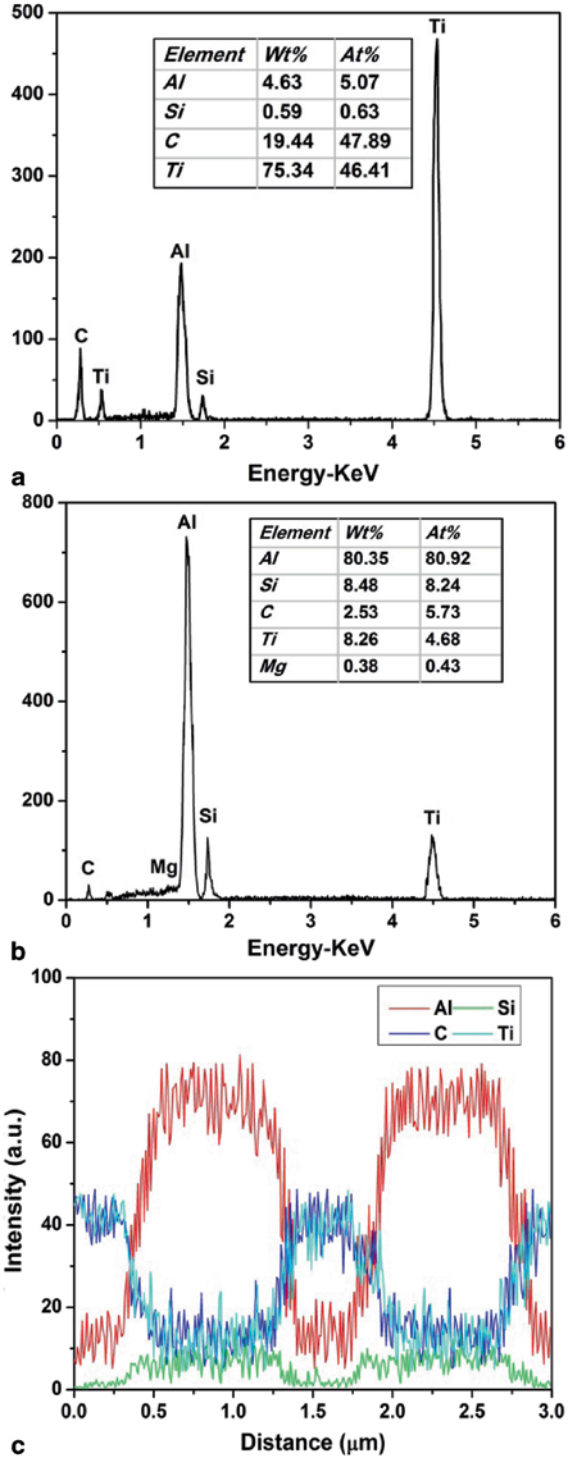


Fig. 6.11 Energy-dispersive X-ray spectroscopy (*EDX*) spot scan analysis showing the elemental concentrations of different phases in Fig. 6.10b: **a** the reinforcing particle and **b** the metal matrix. EDX line scan analysis showing the distribution of elements along arrowhead in Fig. 6.10d (**c**)

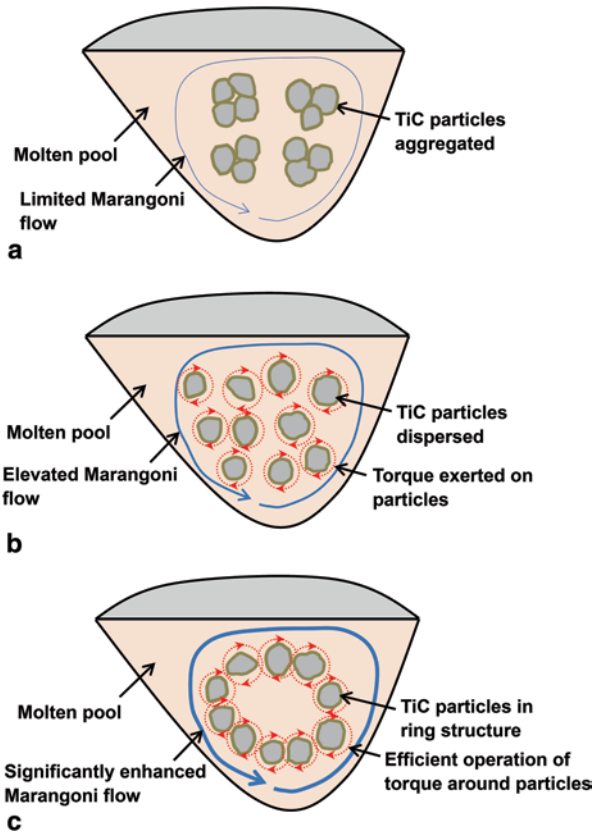


Fig. 6.12 Schematic of the movement mechanisms of TiC reinforcing particles in the melt pool under various SLM processing conditions: **a** $P=80$ W, $v=400$ mm/s; **b** $P=80$ W, $v=200$ mm/s; **c** $P=80$ W, $v=133$ mm/s

is counterclockwise. In the case of SLM processing of nonspherical TiC particles, there exists a torque around the particle, due to (i) the misalignment of the particle center and (ii) the action of the thermal Marangoni flow (i.e., source flow). The present torque tends to rotate the TiC nanoparticles in the molten pool, providing a possibility to redistribute the nanoparticles. It is known that the intensity of thermal Marangoni flow is determined by temperature gradient [24]. The insufficient LED at a high scan speed lowers SLM temperature and accordingly decreases the temperature gradient, thereby weakening the thermal Marangoni flow. Meanwhile, at a relatively high scan speed and resultant low LED, the solidification rate of the liquid front within the molten pool increases, thus leaving considerably short time for the thermal Marangoni flow to rearrange the TiC nanoparticles. Consequently, the distribution state of TiC reinforcement is quite inhomogeneous with the formation of some clusters of reinforcing particles at relatively high scan speed of 400 mm/s (Figs. 6.10a, 6.12a). When the laser scan speed decreased and the resultant LED

increased, the rearrangement rate of the TiC reinforcing nanoparticles in the melt is elevated by intensifying the thermal Marangoni flow and increasing the maintaining time of melt pool, thereby homogenizing the dispersion state of TiC reinforcing nanoparticles (Fig. 6.10b). On the other hand, these homogenized TiC nanoparticles are continually driven by the comparatively stronger solutal Marangoni flow (i.e., converging flow) to form the TiC ring by pushing and gathering the particles around the center of the Marangoni flow pattern. Meanwhile, according to the research of Anestiev et al. [25], the repulsion forces will arise between particles when a sufficient amount of liquid forms. The combined effect of repulsion force and source flow contributes to the remaining of the metal matrix core, even though the converging flow pushes the TiC nanoparticles toward the center. Therefore, a typical ring structure is formed after solidification when sufficiently high LED is applied (i.e., $P=80$ W, $v=133$ mm/s and $P=80$ W, $v=100$ mm/s) (Figs. 6.10c, d, and 6.12c).

6.6 Mechanical Performance of SLM-processed TiC/AlSi10Mg Nanocomposite Parts

6.6.1 Dimensional Accuracy of SLM-processed TiC/AlSi10Mg Nanocomposite Parts

In the practical engineering application of AMCs parts, the mechanical properties such as the dimensional accuracy, microhardness, wear performance, and tensile property are the main concerns. The dimensional accuracy of SLM-fabricated parts is mainly determined by shrinkage behavior which is in general required to be less than 2% in order to ensure the proper functional requirements [26]. In the present study, SLM production of the TiC/AlSi10Mg nanocomposite parts with dimensions of 8 mm × 8 mm × 8 mm were performed and the specific variation of shrinkage along X (scanning direction), Y (transverse direction), and Z (building direction) dimensions with change of SLM processing parameters is provided in Fig. 6.13. It was obvious that there was a significant reduction in shrinkage in all three directions as the applied LED increased from 200 J/m ($P=80$ W, $v=400$ mm/s) to 600 J/m ($P=80$ W, $v=133$ mm/s). With a further increase in LED to 800 J/m ($P=80$ W, $v=100$ mm/s), a very slight reduction in shrinkage was observed, indicating that the dimensional accuracy tended to be stable as the sufficient LED was applied. Nevertheless, the shrinkage measured in the Z direction was much higher than that in X and Y directions at all given SLM parameters. When a relatively low LED of 200 J/m was used ($P=80$ W, $v=400$ mm/s), the values of shrinkage were 1.82, 2.05, and 2.8% in X, Y, and Z directions, respectively, demonstrating a relatively poor dimensional accuracy response. When the LED increased to 600 J/m ($P=80$ W, $v=133$ mm/s), the dimensional accuracy well matched the demand of the industrial applications, with the shrinkage values of 1.26, 1.53 and 1.73% in X, Y, and Z directions, respectively. With a further increase of LED to

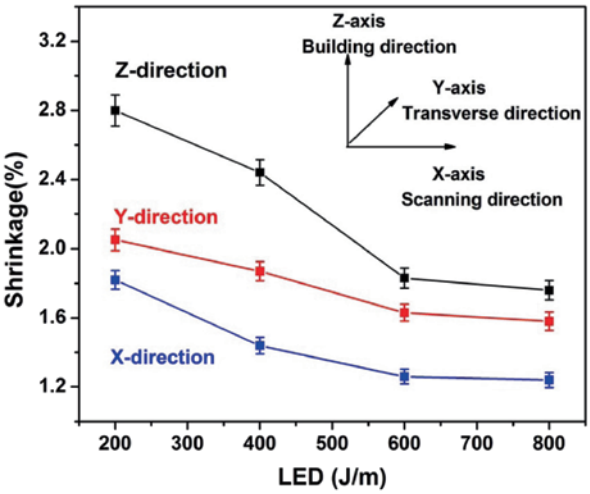


Fig. 6.13 Effect of laser processing parameters on dimensional accuracy of SLM-processed TiC/AlSi10Mg nanocomposite parts

800 J/m (P = 80 W, v = 100 mm/s), the measured shrinkage values of 1.24, 1.50, and 1.72 % in X, Y, and Z directions, respectively, showing no apparent variation in the three dimensions.

6.6.2 Hardness and Wear Performance of SLM-processed TiC/AlSi10Mg Nanocomposite Parts

Figure 6.14 depicts the microhardness and its distribution measured on the cross-sections of SLM-processed TiC/AlSi10Mg nanocomposite parts. With the increase of the applied LED from 250 J/m (P = 100 W, v = 400 mm/s) to 700 J/m (P = 100 W, v = 143 mm/s), the average microhardness experienced a continuous increase from 157.3 $HV_{0.2}$ to 177.6 $HV_{0.2}$; however, as the LED further increased to 1000 J/m (P = 100 W, v = 100 mm/s), the mean microharness decreased to 166.7 $HV_{0.2}$. Furthermore, the microhardness of the part processed at a low LED of 250 J/m fluctuated significantly with the change of the measurement positions. This was mainly contributed to the inhomogeneous distribution of TiC reinforcement throughout the matrix at a low laser energy input (Fig. 6.6a). This situation was considerably improved by increasing the LED to 700 J/m, due to the homogeneous incorporation of nanoscale TiC reinforcing particles throughout the matrix (Fig. 6.6c). However, a further enhancement of the applied LED to 1000 J/m did not lead to a further elevation of the obtainable microhardness, which indicated that the significant grain coarsening and the resultant disappearance of nanostructured TiC reinforcement (Figs. 6.7d and 6.8) tended to lower the hardness performance. Nevertheless, a close comparison revealed that the SLM-processed AlSi10Mg parts reinforced with nanoscale TiC particles, for all the given SLM parameters, demonstrated the superior

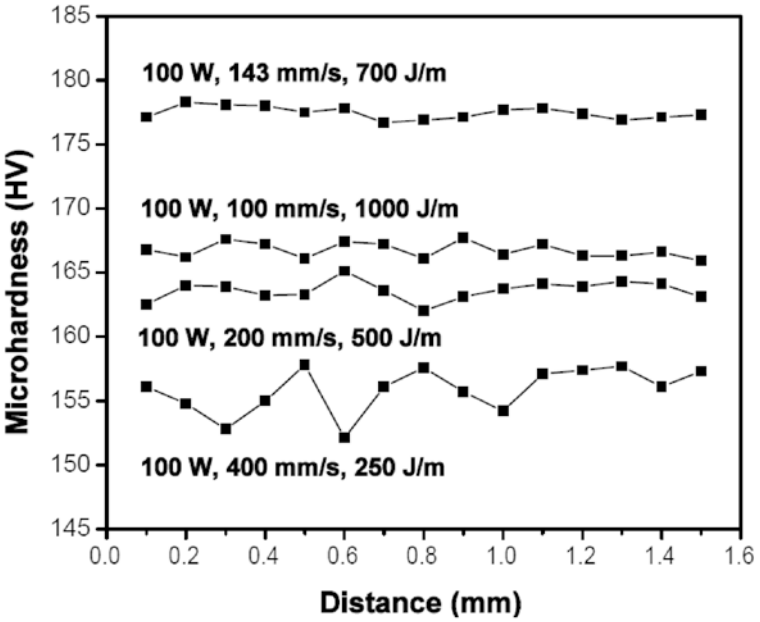


Fig. 6.14 Microhardness and its distribution of SLM-processed TiC/AlSi10Mg nanocomposite parts using different laser processing parameters

hardness compared to the unreinforced AlSi10Mg parts fabricated with the same SLM conditions (maximum at approx. 145 $HV_{0.1}$) [17].

Figure 6.15 shows the influence of SLM processing parameters on COFs and wear rates of SLM-processed TiC/AlSi10Mg nanocomposite parts. The FE-SEM studies of the corresponding worn surfaces are provided in Fig. 6.16. At the initial stage of the wear tests, due to the existence of hard oxide film on the surface of samples, the COF values were relatively high and also showed an apparent fluctuation. The oxide film could be broken easily and shifted by the direct sliding with the counterface, after that the COF values decreased significantly and reached a relatively steady-state with little local fluctuation (Fig. 6.15a). Nevertheless, the large differences in COF values and attendant wear rates among various parts indicated that the wear performance of SLM-processed TiC/AlSi10Mg nanocomposite parts was significantly influenced by the applied laser processing conditions. At a relatively low LED of 250 J/m ($P = 100$ W, $v = 400$ mm/s), the average COF reached a high value of 0.63 (Fig. 6.15a), resulting in a considerably elevated wear rate of 7.46×10^{-5} $mm^3N^{-1}m^{-1}$ (Fig. 6.15b). The wear surface was disruptive and consisted of large-sized agglomerates which contained some ultrafine nanoscale particles (Fig. 6.16a). The presence of irregular shaped fragments revealed the local severe deformation and delamination of the worn surface occurred. On increasing the LED to 500 J/m ($P = 100$ W, $v = 200$ mm/s), although the abrasive fragments still existed on the worn surface, there were no apparent agglomerates of reinforcing nanoparticles in the worn matrix (Fig. 6.16b),

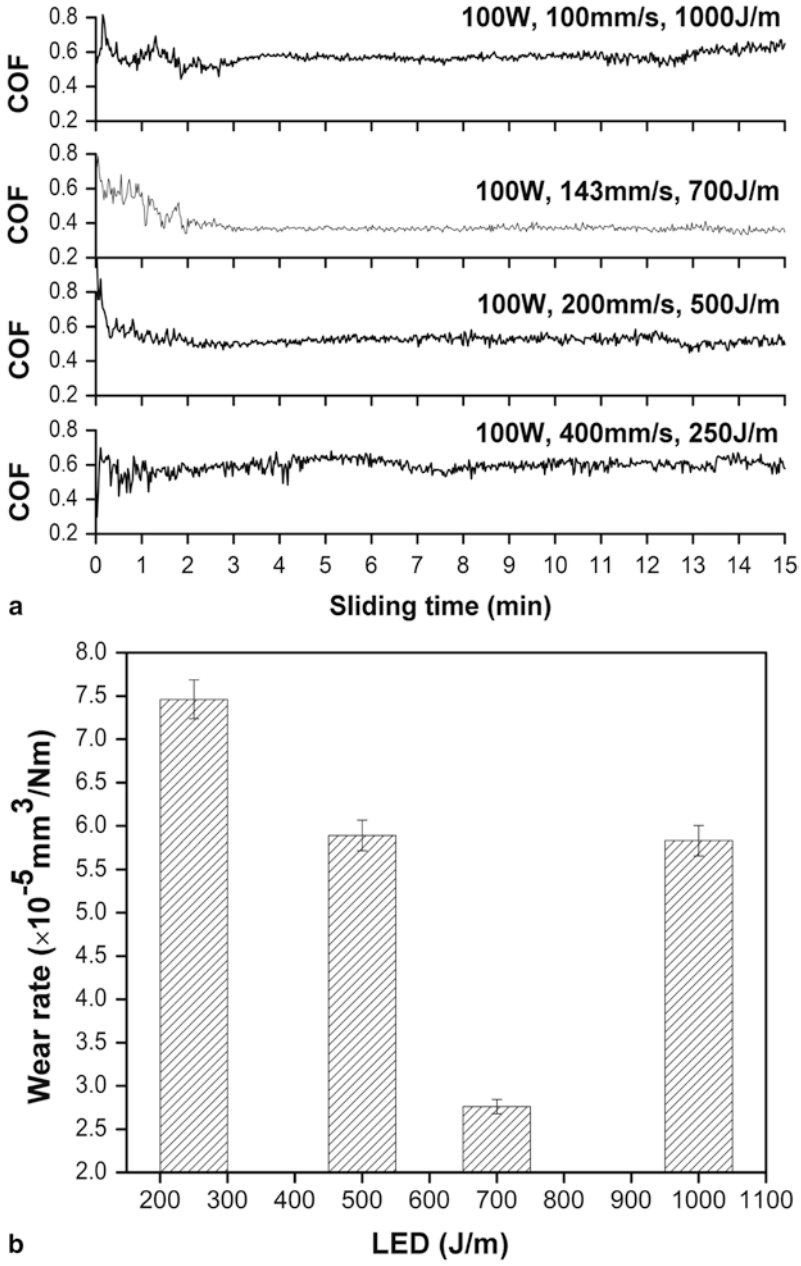


Fig. 6.15 Coefficient of friction (*COF*) values **a** and wear rates **b** of SLM-processed TiC/AlSi10Mg nanocomposite parts with variation of laser processing parameters

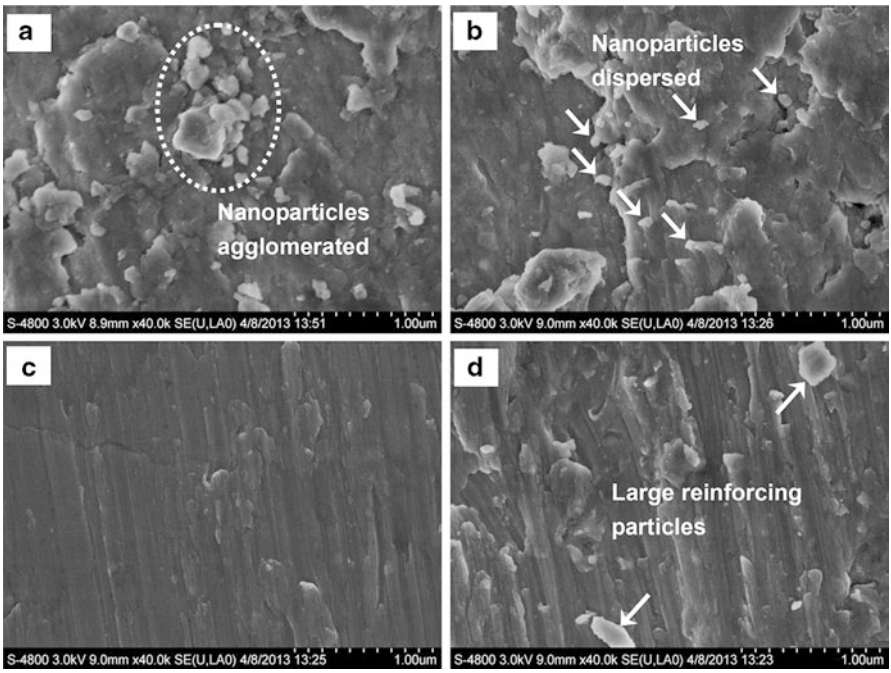


Fig. 6.16 FE-SEM images showing characteristic morphologies of worn surfaces of SLM-processed TiC/AlSi10Mg nanocomposite parts using various laser processing conditions: **a** $P = 100$ W, $v = 400$ mm/s, LED = 250 J/m; **b** $P = 100$ W, $v = 200$ mm/s, LED = 500 J/m; **c** $P = 100$ W, $v = 143$ mm/s, LED = 700 J/m; **d** $P = 100$ W, $v = 100$ mm/s, LED = 1000 J/m

thereby decreasing the mean COF and attendant wear rate to 0.57 (Fig. 6.15a) and 5.89×10^{-5} $mm^3N^{-1}m^{-1}$ (Fig. 6.15b), respectively. Interestingly, at a reasonable LED of 700 J/m ($P = 100$ W, $v = 143$ mm/s), the worn surface of SLM-processed sample became rather smooth and the reinforcing nanoparticles were found to be inserted within the adhesive tribolayer (Fig. 6.16c). The lowest COF of 0.38 (Fig. 6.15a) and wear rate of 2.76×10^{-5} $mm^3N^{-1}m^{-1}$ (Fig. 6.15b) were obtained in this instance. It was accordingly reasonable to consider that as the nanostructured TiC reinforcement with a homogenous dispersion state was formed in SLM-processed parts, the mechanism of material removal during sliding was changed from the abrasion to adhesion of the tribolayer. Such a transition was expected to homogenize the COF values and reduce the wear rate after sliding tests. However, at an even higher LED of 1000 J/m ($P = 100$ W, $v = 100$ mm/s), the parallel, deep grooves were observed on the worn surface (Fig. 6.16d), which revealed the severe deformation and plowing of the surface during siding. In this situation, the wear mechanism was micro-plowing rather than the adhesive wear. Some relatively large-sized reinforcing particles were also observed at the edges of grooves on the worn surface. The obtained average COF value of 0.54 (Fig. 6.15a) and wear rate of 5.83×10^{-5} $mm^3N^{-1}m^{-1}$ (Fig. 6.15b) showed a significant increase in this case.

In order to disclose the underlying mechanisms contributed to the wear performance enhancement, a comprehensive relationship of SLM process, microstructures, and mechanical properties is determined. At the relatively low laser energy input, the SLM densification response is limited due to the occurrence of balling effect (Fig. 6.5) and the formation of residual pores (Figs. 6.3a and 6.4) and, meanwhile, the TiC nanoparticles aggregate into clusters within the laser processed matrix, resulting in a poor microstructural homogeneity (Fig. 6.6a). The pores and nanoparticle aggregates are prone to crack because of the concentration of stress during sliding. The debris is thus formed and split from the wear surface when the expanded cracks are connected to each other (Fig. 6.16a), resulting in a significant increase in the COF and wear rate. When the proper LED is applied, the nanostructured TiC reinforcement with a uniform distribution is formed throughout the matrix (Figs. 6.6c and 6.7c). During sliding tests, the homogeneously dispersed ultrafine TiC nanophase has a high tendency to stick to each other, due to considerably small interfacial stresses of nanoscale reinforcement with the matrix [27]. As the sliding friction acts on the surface, the worn surface experiences a sufficient plastic deformation and, therefore, a strain-hardened sliding-treated layer consisting of the significantly refined TiC reinforcing nanoparticles is produced on the wear surface (Fig. 6.16c), which favors the improvement in wear property. However, at a relatively high LED, although the sufficient densification level is maintained (Figs. 6.3d and 6.4), the TiC reinforcement loses its nanostructure after SLM process (Figs. 6.7d and 6.8). The coarsened TiC reinforcing particles are prone to spall and split from the matrix during sliding. The plowing between the segregated TiC reinforcement and the matrix tends to occur with the action of the tangential force, thereby producing the deep grooves on the worn surface with a limited wear performance (Figs. 6.15 and 6.16d).

6.6.3 Tensile Properties of SLM-processed TiC/AlSi10Mg Nanocomposite Parts

The tensile properties including tensile strength and elongation of the TiC/AlSi10Mg nanocomposite part processed at the optimized SLM parameter ($P = 80$ W, $v = 133$ mm/s) are depicted in Fig. 6.17. As a reference, the tensile properties of the unreinforced AlSi10Mg part processed using the same SLM parameters are also included. It was clear that the tensile strength of SLM-processed TiC/AlSi10Mg nanocomposite part reached a high level of 486 MPa, which increased by 21.5 % in comparison to the unreinforced SLM-processed AlSi10Mg part (400 MPa). It was also worth noting that the elongation of the SLM-processed TiC/AlSi10Mg nanocomposite part did not show any decrease as relative to the unreinforced AlSi10Mg part, although the hard TiC reinforcing particles were incorporated in the AlSi10Mg matrix. Figure 6.18 shows the characteristic microstructures of fracture surfaces of the SLM-processed TiC/AlSi10Mg nanocomposite part. A number of considerably fine dimples having the size of 1–3 μm were observed on the fracture surface,

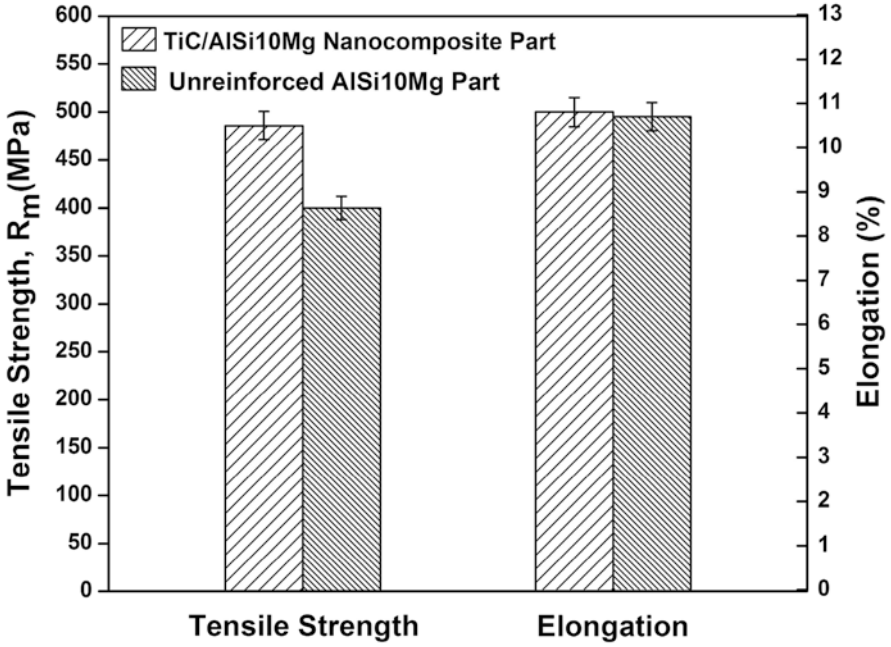


Fig. 6.17 Tensile properties (tensile strength and elongation) of SLM-processed unreinforced AlSi10Mg and TiC/AlSi10Mg nanocomposite parts at $P = 80$ W and $v = 133$ mm/s

exhibiting a typical ductile type of fracture (Fig. 6.18a). FE-SEM characterization at a higher magnification revealed that the ultra-fine TiC reinforcing particles were uniformly inserted in the dimples, showing a sufficiently strong interfacial bonding (Fig. 6.18b). It is accordingly reasonable to consider that the formation of the unique ring structured TiC reinforcement in the SLM-processed TiC/AlSi10Mg nanocomposites (Fig. 6.9c) contributes to the improvement of tensile strength, while maintaining the sufficiently high ductility of the nanocomposites. The significant improvement of tensile strength while maintaining sound ductility can be attributed to [28]:

i. The formation of the ring structured TiC nanoparticles increases the contiguity of the reinforcement, which further increases the strengthening effect of the nanoscale reinforcement;
ii. When the TiC/AlSi10Mg nanocomposite part bears the load, the unique TiC ring structures which contain a number of nanoparticles act as a barrier to the movement of dislocations, leading to the enhancement of the strength.
iii. During the plastic deformation, the uniform distribution of ring structured reinforcement can effectively constrain the crack propagation, which is beneficial to the ductility of the nanocomposites.

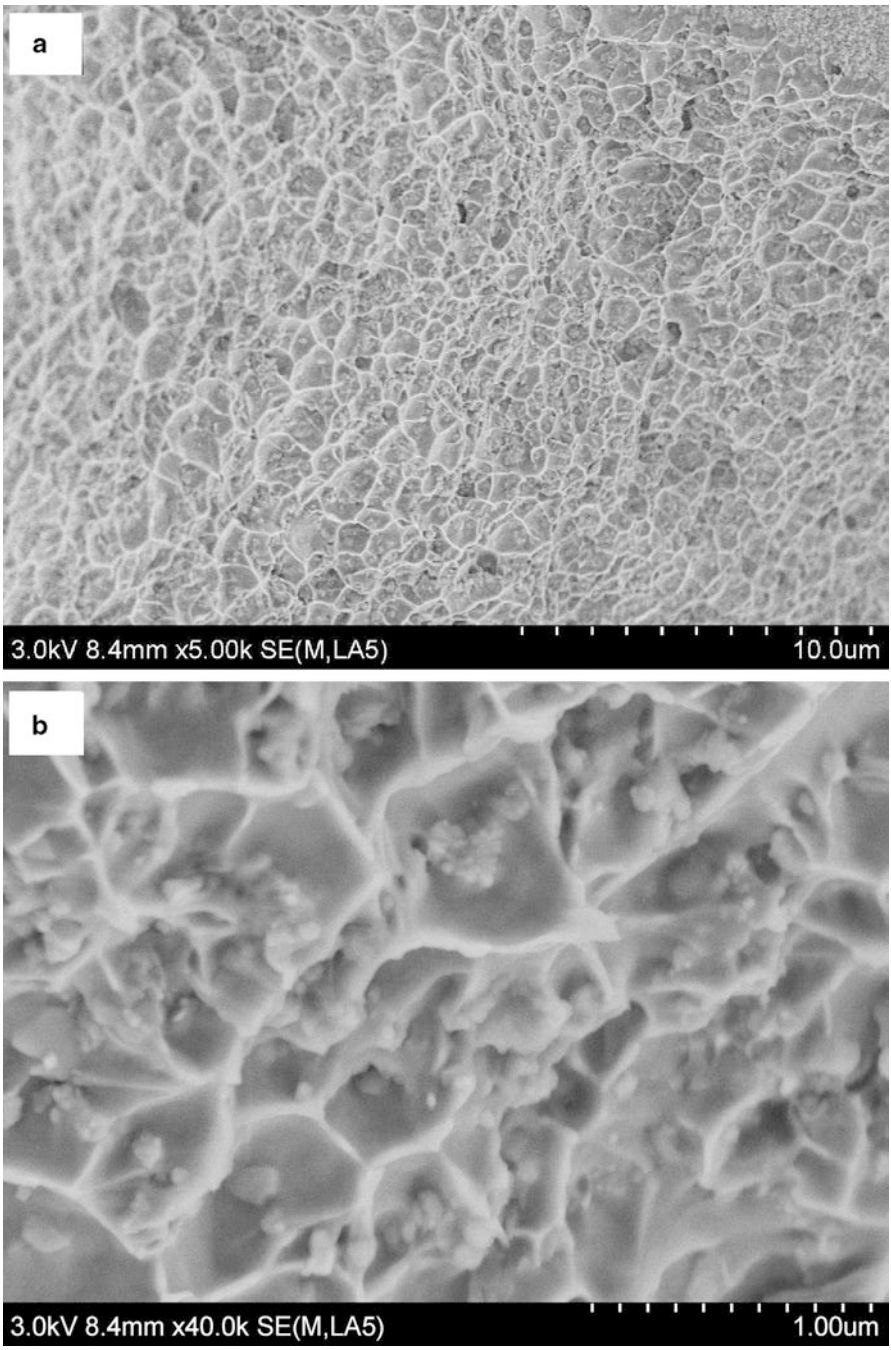


Fig. 6.18 FE-SEM images showing morphologies of fracture surfaces of SLM-processed TiC/AlSi10Mg nanocomposite part produced at $P = 80$ W and $v = 133$ mm/s

6.7 Conclusions

In this Chapter concerning SLM additive manufacturing of nanoscale TiC particle reinforced AlSi10Mg nanocomposite parts, the main conclusions were summarized as follows.

1. The densification behavior of TiC/AlSi10Mg nanocomposite parts was significantly affected by the laser energy input during SLM. Using an insufficient LED lowered the SLM densification rate due to the occurrence of balling effect and the formation of residual pores. The sufficiently high densification level (>98% theoretical density) was achieved for SLM-processed nanocomposite parts processed at optimized parameters.
2. The nanoscale TiC reinforcement in SLM-processed TiC/AlSi10Mg nanocomposite parts experienced a significant structural change with the variation of SLM parameters, especially the applied LED. The dispersion state of nanoscale TiC reinforcement was homogenized from the apparent agglomerates to the uniform distribution with the increase of LED. A unique ring structure of TiC reinforcing nanoparticles was present after SLM processing using reasonable conditions.
3. The densification rate of SLM-processed TiC/AlSi10Mg nanocomposite parts and the particle morphology and dispersion characteristics of TiC reinforcement in the matrix played the key roles in determining the mechanical performance. The sufficiently high densification rate combined with the homogeneous incorporation of nanoscale TiC reinforcement throughout the matrix led to the considerably low COF and resultant wear rate. The obtained microhardness and tensile strength were apparently higher than the unreinforced SLM-processed AlSi10Mg part while maintaining the sufficient ductility. Both the insufficient SLM densification response at a relatively low LED and the disappearance of nanoscale reinforcement at a high LED lowered the hardness and wear performance of SLM-processed TiC/AlSi10Mg nanocomposite parts.

References

1. Buchbinder D, Meiners W, Pirch N et al (2014) Investigation on reducing distortion by preheating during manufacture of aluminum components using selective laser melting. J Laser Appl 26(1):012004
2. Rajmohan T, Palanikumar K, Arumugam S (2014) Synthesis and characterization of sintered hybrid aluminium matrix composites reinforced with nanocopper oxide particles and microsilicon carbide particles. Compos Part B Eng 59:43–49
3. Umasankar V, Xavior MA, Karthikeyan S (2014) Experimental evaluation of the influence of processing parameters on the mechanical properties of SiC particle reinforced AA6061 aluminium alloy matrix composite by powder processing. J Alloys Compd 582(5):380–386
4. Ozden S, Ekici R, Nair F (2007) Investigation of impact behaviour of aluminium based SiC particle reinforced metal-matrix composites. Compos Part A Appl Sci Manuf 38(2):484–494
5. Albiter A, Contreras A, Bedolla E et al (2003) Structural and chemical characterization of precipitates in Al-2024/TiC composites. Compos Part A Appl Sci Manuf 34(1):17–24

6. Moya JS, Lopez-Esteban S, Pecharromán C (2007) The challenge of ceramic/metal microcomposites and nanocomposites. Prog Mater Sci 52(7):1017–1090
7. Tjong SC (2007) Novel nanoparticle-reinforced metal matrix composites with enhanced mechanical properties. Adv Eng Mater 9(8):639–652
8. Gu DD, Hagedorn YC, Meiners W et al (2011) Nanocrystalline TiC reinforced Ti matrix bulk-form nanocomposites by Selective Laser Melting (SLM): densification, growth mechanism and wear behavior. Compos Sci Technol 71(13):1612–1620
9. Gu DD, Wang HQ, Zhang GQ (2014) Selective laser melting additive manufacturing of Ti-Based nanocomposites: the role of nanopowder. Metall Mater Trans A 45(1):464–476
10. Kelbassa I, Wohlers T, Caffrey T (2012) Quo vadis, laser additive manufacturing? J Laser Appl 24(5):050101
11. Yadroitsev I, Bertrand P, Antonenkova G et al (2013) Use of track/layer morphology to develop functional parts by selective laser melting. J Laser Appl 25(5):052003
12. Morsbach C, Höges S, Meiners W (2011) Modeling the selective laser melting of polylactide composite materials. J Laser Appl 23(1):012005
13. Das M, Balla VK, Basu D et al (2010) Laser processing of SiC-particle-reinforced coating on titanium. Scr Mater 63(4):438–441
14. Louvis E, Fox P, Sutcliffe CJ (2011) Selective laser melting of aluminium components. J Mater Process Technol 211(2):275–284
15. Wei XW, Chen CY (2012) Influence of oxidation heat on hard anodic film of aluminum alloy. Trans Nonferrous Met Soc China 22(11):2707–2712
16. Brandl E, Heckenberger U, Holzinger V et al (2012) Additive manufactured AlSi10Mg samples using Selective Laser Melting (SLM): Microstructure, high cycle fatigue, and fracture behavior. Mater Des 34:159–169
17. Buchbinder D, Schleifenbaum H, Heidrich S et al (2011) High Power Selective Laser Melting (HP SLM) of aluminum parts. Phys Procedia 12:271–278
18. Thijs L, Kempen K, Kruth JP et al (2013) Fine-structured aluminium products with controllable texture by selective laser melting of pre-alloyed AlSi10Mg powder. Acta Mater 61(5):1809–1819
19. Das S (2003) Physical aspects of process control in selective laser sintering of metals. Adv Eng Mater 5(10):701–711
20. Gu DD, Shen YF (2007) Effects of dispersion technique and component ratio on densification and microstructure of multi-component Cu-based metal powder in direct laser sintering. J Mater Process Technol 182(1–3):564–573
21. Simchi A (2006) Direct laser sintering of metal powders: mechanism, kinetics and microstructural features. Mater Sci Eng A 428(1–2):148–158
22. Niu HJ, Chang ITH (1999) Instability of scan tracks of selective laser sintering of high speed steel powder. Scr Mater 41(11):1229–1234
23. Yin HB, Emi T (2003) Marangoni flow at the gas/melt interface of steel. Metall Mater Trans B 34(5):483–493
24. Fuhrich T, Berger P, Hügel H (2001) Marangoni effect in laser deep penetration welding of steel. J Laser Appl 13(5):178–186
25. Anestiev LA, Froyen L (1999) Model of the primary rearrangement processes at liquid phase sintering and selective laser sintering due to biparticle interactions. J Appl Phys 86(7):4008–4017
26. Zhu HH, Lu L, Fuh JYH (2006) Study on shrinkage behaviour of direct laser sintering metallic powder. Proc Inst Mech Eng B 220(2):183–190
27. Xu LR, Sengupta S (2005) Interfacial stress transfer and property mismatch in discontinuous nanofiber/nanotube composite materials. J Nanosci Nanotechnol 5(4):620–626
28. Lu K (2010) The future of metals. Science 328:319–320

Chapter 7
Novel Aluminum Based Composites by Selective Laser Melting (SLM) Additive Manufacturing (AM): Tailored Formation of Multiple Reinforcing Phases and its Mechanisms

Abstract Selective laser melting (SLM) of the SiC/AlSi10Mg composites was performed to prepare the Al-based composites with the multiple reinforcing phases. The influence of the SLM processing parameters on the constitutional phases, microstructural features, and mechanical performance of the SLM-processed Al-based composites was studied. The reinforcing phases in the SLM-processed Al-based composites included the unmelted micron-sized SiC particles, the *in situ* formed micron-sized Al_4SiC_4 strips, and the *in situ* produced submicron Al_4SiC_4 particles. As the input "linear laser energy density" (LED) increased, the extent of the *in situ* reaction between the SiC particles and the Al matrix increased, resulting in a larger degree of formation of Al_4SiC_4 reinforcement. The densification rate of the SLM-processed Al-based composite parts increased as the applied LED increased. A sufficiently high density (~96 % theoretical density) was achieved for LED larger than 1000 J/m. Due to the generation of the multiple reinforcing phases, elevated mechanical properties were obtained for the SLM-processed Al-based composites, showing a high microhardness of 214 $HV_{0.1}$, a considerably low coefficient of friction (COF) of 0.39, and a reduced wear rate of $1.56 \times 10^{-5} mm^3 N^{-1} m^{-1}$. At an excessive laser energy input, the grain size of the *in situ* formed Al_4SiC_4 reinforcing phase, both the strip- and particle-structured Al_4SiC_4, increased markedly. The significant grain coarsening and formation of the interfacial microscopic shrinkage porosity lowered the mechanical properties of the SLM-processed Al-based composites.

7.1 Introduction

Selective laser melting (SLM) is a newly developed additive manufacturing (AM) technology [1–5], which enables the quick production of the three-dimensional parts with nearly full density without postprocessing treatments [6–10]. SLM and direct metal laser sintering (DMLS) are the typical powder-bed-based laser AM processes. Generally, DMLS is processed based on a liquid phase sintering (LPS) mechanism involving a partial melting of the metallic powder, i.e., a semi-solid consolidation mechanism [11]. In contrast, SLM of metallic powder is through a complete melting/solidification mechanism. The idea of full melting is supported

© Springer-Verlag Berlin Heidelberg 2015

D. Gu, *Laser Additive Manufacturing of High-Performance Materials,*
DOI 10.1007/978-3-662-46089-4_7

by the availability of fine metal powder specially designed for SLM and the significantly elevated laser processing conditions in recent years, e.g., higher laser power, smaller focused spot size, thinner layer thickness, etc. [12]. The SLM technology can be used to manufacture the complicated parts with any geometry by layer-by-layer melting and consolidating of powder materials, based on the computer-aided design (CAD) data of the objects to be built [13–16]. The SLM process includes scattering and absorption of laser radiation in the powder, heat conduction, melting and coalescence of powder particles, formation of the melt pool, and its solidification [17, 18]. During the SLM process, the interaction time between the laser beam and the powder particles is extremely short (typically between 0.5 and 25 ms) [19], resulting in a considerably high heating and cooling speed [20]. During the laser-induced rapid solidification process, a number of nonequilibrium metallurgical phenomena may occur, such as the microstructural refinement, the solid solution hardening, and the formation of metastable phases, favoring the improvement of the properties of laser-processed materials [21–23]. Due to a laser beam with high energy density applied during the SLM process, the working temperature is high and the powder materials tend to melt completely [6, 24, 25]. The melted materials undergo a typical melting/solidification metallurgical process, leading to sufficiently high densification behavior and attendant mechanical performance of the SLM-processed materials. The SLM technology offers a remarkable degree of processing freedom over traditional processing methods, thereby improving the process ability of components with complex shapes that are hard to process using conventional methods [15, 26–28]. Currently, a number of powder materials such as stainless steel and titanium are being successfully utilized in the SLM process [29].

For the past few decades, aluminum alloys have been widely used in many industrial fields such as aerospace, architectural construction, and automotive because they are lightweight and have high-corrosion resistance, high-thermal conductivity, etc. [13–15]. In order to meet the demands of more comprehensive mechanical properties (e.g., enhanced tensile strength and wear/tribological performance), the development of the particle reinforced aluminum matrix composites (AMCs), especially the SiC particle reinforced AMCs, attracts the considerable attention, exhibiting the inspiring prospects for development [30]. The SiC particle reinforced AMCs have the significant potential for the applications in the aircraft and automotive industries because they are lightweight and have high strength, high elastic modulus, good wear resistance, and low coefficient of thermal expansion [31–33]. Currently, the parts manufactured from the SiC particle reinforced AMCs have been successfully applied in both military and civilian fields, such as aircraft ventral fin [34], wing panels [31], pistons, and engine blocks [35]. Powder metallurgy (PM) and casting are the common conventional processing methods used to produce the SiC particle reinforced AMC parts; the obtainable mechanical performance can basically meet the requirements for the practical applications [32, 36]. However, there are some significant drawbacks that severely hinder the further development of AMCs by conventional methods, such as the expensive PM/casting molds and the complex preprocessing and postprocessing treatments [15]. Furthermore, due to the limited wettability between the ceramic reinforcing phase and the aluminum matrix, the

limited particle/matrix interfacial bonding ability that results from the low working temperature during the conventional process may further decrease the mechanical performance of the final products. Therefore, the development of the new processing method to produce SiC particle reinforced AMC parts is driven by the desire to shorten the processing cycle and to manufacture parts with excellent performance. Thanks to the advances in the AM technology, the application of the SLM process in the production of SiC particle reinforced AMCs is a promising choice. Nevertheless, the intrinsic nature of the aluminum, e.g., the high laser reflectivity, the high heat conductivity, and the elevated affinity to oxygen is the detrimental factor that may lower the properties of AMCs manufactured by the SLM process [37, 38]. Some previous researches have already been carried out regarding laser processing of AMCs. Simchi et al. prepared the SiC/Al-7Si-0.3Mg composite parts [37] and the SiC/Al356 composite parts [38] using the DMLS AM technology. Anandkumar et al. produced the SiC/Al-Si composite coatings on the casting aluminum substrate by laser cladding technology [39]. According to the previous studies, during laser processing, the aluminum tends to react with the SiC and the temperature is regarded as the key factor influencing the reaction procedure. In the temperature range from 940 to 1620 K, the SiC reacts with aluminum to form Al_4C_3 and the reaction procedure is as follows [39]:

$$4Al_{(l)} + 3SiC_{(s)} \rightarrow Al_4C_{3(s)} + 3Si \tag{7.1}$$

When the temperature reaches above 1670 K, the reaction product is Al_4SiC_4 and the reaction procedure is as follows [37, 39]:

$$4Al_{(l)} + 4SiC_{(s)} \rightarrow Al_4SiC_{4(s)} + 3Si \tag{7.2}$$

It is noted that Al_4SiC_4 (1200 HV) is much harder than Al_4C_3 (250 HV), which is regarded as the favorable reinforcing phase for the aluminum matrix. Al_4C_3 is brittle and has a tendency to react with H_2O in wet environments to form amorphous aluminum hydroxide. Hydration of aluminum carbide is accompanied by an increase in volume, which even causes deformation of the surrounding aluminum matrix [40]. Therefore, it is important to avoid the generation of Al_4C_3 in the final materials. From this point of view, setting the elevated manufacturing temperature above 1670 K may be a useful method to achieve proper reinforcement in laser-processed AMCs.

In the present work, the novel AMCs with multiple reinforcing phases were prepared by SLM processing of the SiC/AlSi10Mg composite. The microstructure characteristics and phase development were studied for SLM-processed AMCs using different processing parameters. The SLM densification mechanism of AMCs was analyzed and the mechanical properties, e.g., microhardness and wear resistance, were investigated with a major target to develop new Al-based composite materials and to optimize the SLM process and resultant mechanical performance. The SLM-processed Al-based composites reinforced by *in situ* Al_4SiC_4 exhibited novel reinforcing structures and resultant elevated hardness/wear performance, which, to the best of our knowledge, have not been reported previously in conventionally processed or laser additive manufactured Al-based composites.

7.2 Preparation and SLM Processing of SiC/AlSi10Mg Composite Powder

The raw powder materials applied in this study consisted of 99.7 % pure AlSi10Mg powders with a spherical shape and a mean particle size of 30 μm (Fig. 7.1a), and 99.5 % pure SiC powder with a polyangular structure and an average particle size of 7 μm (Fig. 7.1b). The SiC and AlSi10Mg powder components, according to the weight ratio of 20:80, were mechanically mixed in a Fritsch Pulverisette 4 vario-planetary mill, using a ball-to-powder weight ratio of 1:1, a rotation speed of the main disk of 200 rpm, and a mixing time of 4 h. Since a high flowability of the powder is necessary for its smooth spreading during the SLM process, the ball milling parameters in this work have been carefully determined to maintain the initial spherical structure of the AlSi10Mg matrix powder and, meanwhile, to realize the uniform dispersion of the SiC reinforcing particles in the powder mixture. The morphology and dispersion state of the mixed powder is revealed in Fig. 7.1c. The spreading property of the mixed powder on the powder bed was sufficiently favorable during the SLM process.

According to the procedures referred to in Sect. 3.3 of Chap. 3, SLM processing of the present SiC/AlSi10Mg composite powder was carried out using the as-defined fiber laser as the energy source. As the specimens were to be built, an aluminum substrate was fixed on the building platform and leveled. The building chamber was then sealed and argon gas was fed inside, thereby decreasing the O_2content below 20 ppm. Afterward, the SiC/AlSi10Mg composite powder was deposited on the substrate by the layering mechanism, with a powder layer thickness of 50 μm. The laser beam was then controlled by the CAD data to scan the powder bed surface selectively, thereby producing a two-dimensional profile. The hatch spacing between the neighboring scan lines was 50 μm. A series of SLM experiments using a wide range of processing parameters, i.e., laser powers of 70–190 W and scan speeds of 50–600 mm/s, were performed to testify the SLM processability. Among these parameters, we chose a fixed laser scan speed (v) of 100 mm/s and four various laser powers (P) of 80, 90, 100, and 110 W in the present study, in order to vary the SLM processing conditions. The "linear laser energy density" (LED), which was defined by [41, 42]:

$$\mathrm{LED} = \frac{P}{v} \tag{7.3}$$

was used to describe the laser energy delivered into the powder layer in the unit length along the laser scanning direction. Four different LED of 800, 900, 1000, and 1100 J/m were accordingly changed for SLM experimentation. The cubic specimens with dimensions of 6 mm × 6 mm × 6 mm were fabricated in a layer-by-layer manner until completion.

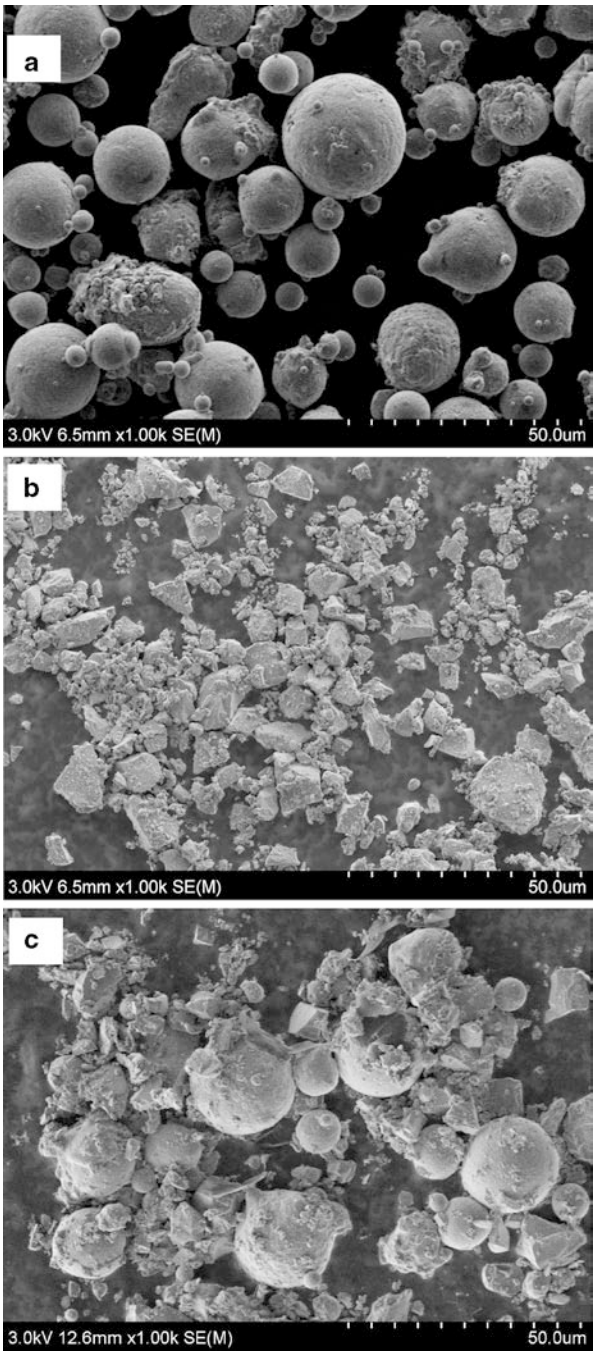


Fig. 7.1 Field emission scanning electron microscope (*FE-SEM*) images showing the typical morphologies of the starting AlSi10Mg powder (**a**) and SiC powder (**b**) and the mixed SiC/AlSi10Mg composite powder (**c**)

7.3 Phases Identification SLM-Processed Al-based Composite Parts from SiC/AlSi10Mg Powder System

Figure 7.2 depicts the typical X-ray diffractometer (XRD) spectra of the SLM-processed Al-based composite parts at the different "linear laser energy density" (LED). The strong diffraction peaks corresponding to α-Al were identified. The newly formed phase Al_4SiC_4 was also determined, which implied that the *in situ* reaction between aluminum melt and silicon carbide occurred at a temperature higher than 1670 K, as disclosed in Eq. 7.2. The characteristic peaks of the residual SiC phase and the new Mg_2Si phase were also detected. Due to the relatively high mass

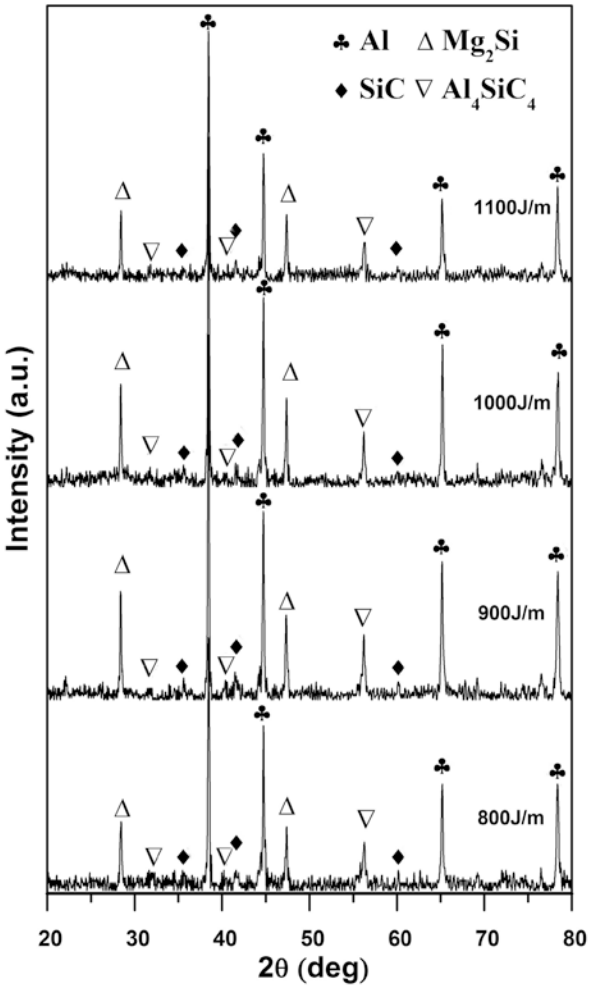


Fig. 7.2 Typical XRD spectra of the SLM-processed Al-based composite parts at the different linear laser energy density (*LED*)

friction of the SiC (20 wt.%) in the starting powder system, the existence of the SiC phase after SLM was reasonable, because of the incomplete *in situ* reaction during the laser-induced rapid melting/solidification process. The presence of the Mg_2Si phase indicated the formation of magnesium silicide by means of the solid solution of silicon atoms into the magnesium lattice. It was worth noting that although the aluminum had a high affinity to oxygen, the XRD results showed that the characteristic peaks of aluminum oxide were not detected in the SLM-processed Al-based composites, due to the efficient protection of the argon atmosphere during SLM.

7.4 Microstructures and Compositions of Al-based Composite Parts Processed by SLM of SiC/AlSi10Mg Powder

Figures 7.3 and 7.4 illustrate the microstructural characteristics of the SLM-processed Al-based composite parts at various linear laser energy densities (LED), using the different FE-SEM magnifications. Typically, three different reinforcing structures existed in the SLM-processed composites under various SLM conditions,

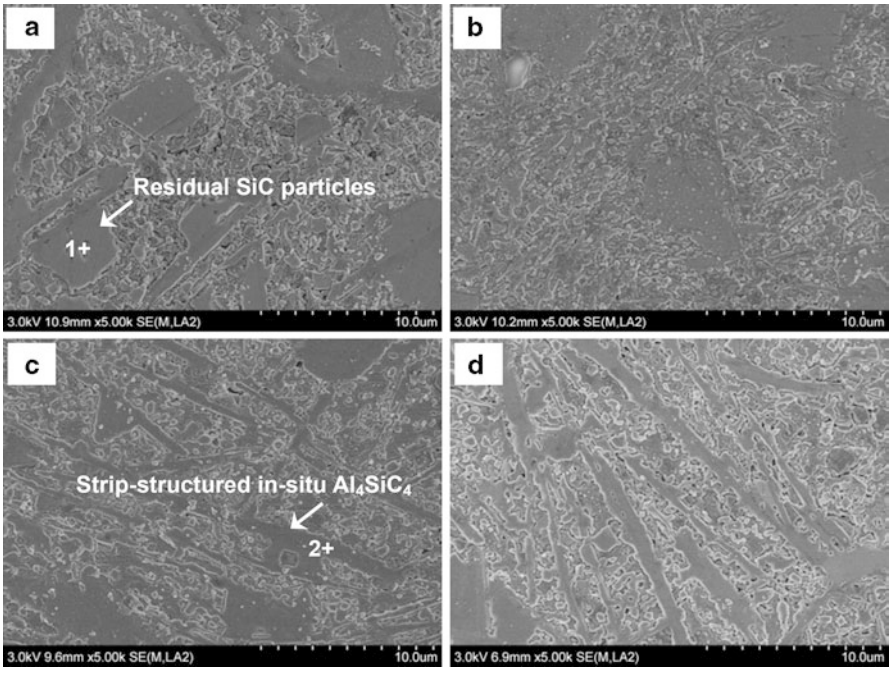


Fig. 7.3 FE-SEM images showing the microstructural characteristics of the SLM-processed Al-based composite parts at the different linear laser energy densities (*LED*): **a** LED = 800 J/m; **b** LED = 900 J/m; **c** LED = 1000 J/m; **d** LED = 1100 J/m

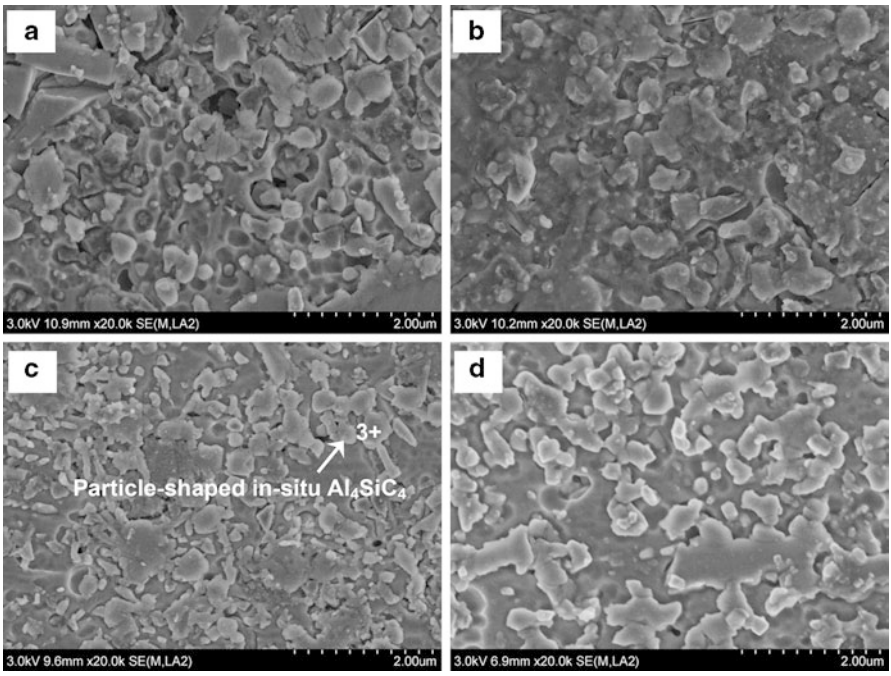


Fig. 7.4 High-magnification FE-SEM images showing the morphologies and distribution states of the reinforcing particles in the SLM-processed Al-based composite parts at the various linear laser energy densities (*LED*): **a** LED = 800 J/m; **b** LED = 900 J/m; **c** LED = 1000 J/m; **d** LED = 1100 J/m

i.e., relatively large-sized reinforcing particles, strip-structured reinforcement, and relatively small-sized reinforcing particles. In order to investigate the chemical compositions of these three kinds of reinforcements in the SLM-processed composites, energy dispersive X-ray spectroscope (EDX) characterization within the different structures, as indicated in Figs. 7.3a, c and 7.4c, was performed, with the results provided in Fig. 7.5. As shown in Fig. 7.5a, an EDX point scan within the large-sized reinforcing particles (point 1, Fig. 7.3a) revealed that C and Si had a near equal atomic proportion. In this instance, the presence of a small amount of Al element (12.51 at.%) was caused by the attachment of the matrix element on the reinforcement during the grinding process of the metallographic samples. It was accordingly reasonable to consider that the first kind of reinforcement was the residual SiC particles, which typically exhibited relatively large particle morphology. Furthermore, as revealed in Fig. 7.5b and c, the presence of Al, Si, and C with an approximate Al:Si:C atom ratio of 4:1:4 was detected within both the strip-structured reinforcement (point 2, Fig. 7.3c) and the small-sized reinforcing particles (point 3, Fig. 7.4c). Combined with the XRD results (Fig. 7.2), it was concluded that the Al_4SiC_4 reinforcing phase was formed *in situ* during SLM via the reaction between aluminum and SiC. The *in situ* presented Al_4SiC_4 typically had two different morphologies, i.e., a relatively large-scale strip-structure and an ultra-fine particle morphology. Generally speaking, the SLM processing of the present SiC/AlSi10Mg composite system led to the formation of three different reinforcements, i.e., the

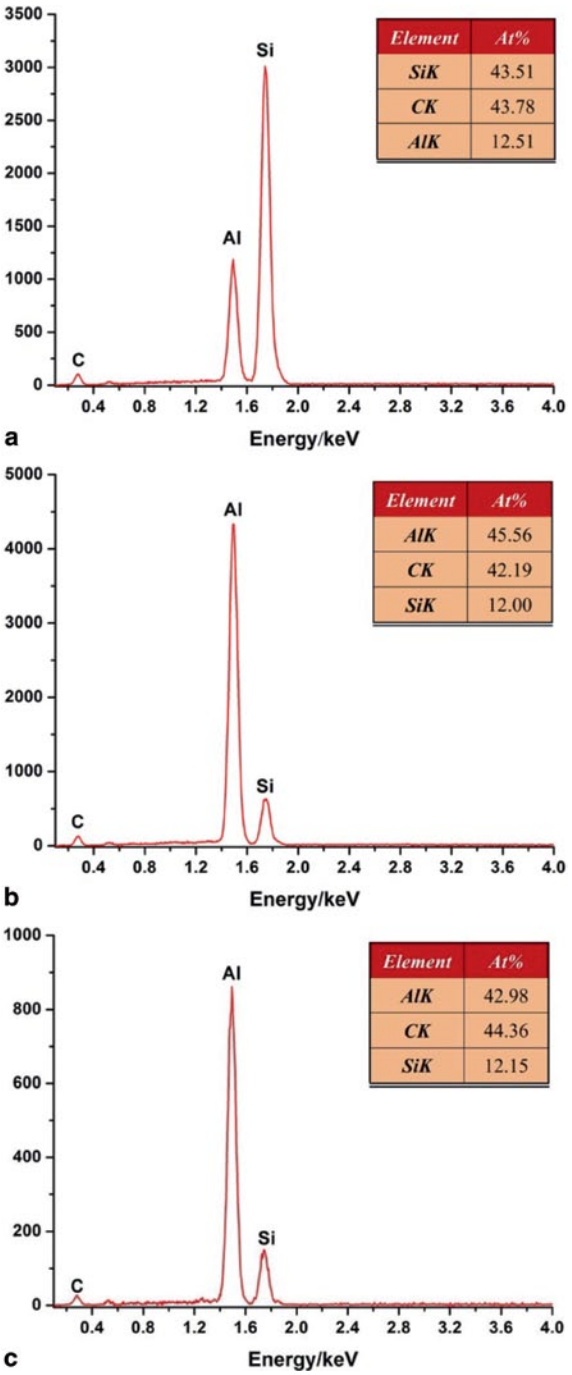


Fig. 7.5 EDX results showing the chemical compositions collected in the different structures in the SLM-processed composites: **a** Large-sized particle-shaped reinforcement (point 1 in Fig. 7.3a); **b** Strip-structured reinforcement (point 2 in Fig. 7.3c); **c** Small-sized particle-structured reinforcement (point 3 in Fig. 7.4c)

unmelted micron-sized SiC particles, the *in situ* formed strip-structured Al_4SiC_4, and the *in situ* produced ultrafine Al_4SiC_4 particles.

It was clear that the microstructures and growth mechanisms of the reinforcements were significantly influenced by the applied linear LED. At a relatively low LED of 800 J/m, irregularly shaped SiC reinforcing particles with an average size of 4 μm remained in the SLM-processed composites and there was no apparent formation of the strip-structured Al_4SiC_4 reinforcing phase (Fig. 7.3a). In this instance, the *in situ* formed Al_4SiC_4 reinforcement was present in the near spherical structure within the Al matrix, with a considerably refined particle size of ~350 nm (Fig. 7.4a). As the applied LED increased to 900 J/m, the volume fraction of the residual SiC reinforcing particles decreased and the particle shape became more regular and smooth. Furthermore, a small amount of the strip-structured Al_4SiC_4 reinforcing phase with a narrow width started to appear around the SiC particles (Fig. 7.3b). A majority of the *in situ* formed Al_4SiC_4 reinforcement was still present in the particle morphology with a slightly lower average size of ~340 nm, which dispersed uniformly throughout the Al matrix (Fig. 7.4b). When the applied LED reached 1000 J/m, the FE-SEM microstructural characterization revealed that the residual SiC particles had a reduced particle size (Fig. 7.3c), which implied a more significant decomposition of SiC particles in the melt. Therefore, the occurrence of the *in situ* reaction between the SiC particles and the Al matrix tended to be enhanced. The strip-structured *in situ* Al_4SiC_4 reinforcement typically had an average length of ~8 μm and a narrow width of ~0.6 μm (Fig. 7.3c). Furthermore, the ultra-fine Al_4SiC_4 reinforcing particles were distributed homogeneously between the strip-structured Al_4SiC_4 in the matrix (Fig. 7.3c), showing the smooth particle surface and the further refined particle size of ~300 nm (Fig. 7.4c). With a further increase in the applied LED to 1100 J/m, the strip-structured *in situ* Al_4SiC_4 reinforcing phase exhibited an apparent coarsening in its crystalline structure and the average length and width of the reinforcing structure increased markedly to ~15 and ~1.6 μm, respectively (Fig. 7.3d). It was also noted that there was a large amount of microscopic shrinkage porosity between the strip-structured reinforcement and the matrix (Fig. 7.3d). Meanwhile, the *in situ* Al_4SiC_4 reinforcing particles also became coarsened, with a considerably elevated average size of ~850 nm. The Al_4SiC_4 particles had a polyangular rough surface, exhibiting a trend to connect with other particles to form coarsened ones (Fig. 7.4d).

During the SLM process, laser energy is delivered into the powder layer via the interaction between the laser beam and the powder materials, within an extremely short duration of action. The laser energy is absorbed by the particles through both bulk coupling and powder coupling mechanisms [43]. Although the intrinsic absorptivity of aluminum to the laser is considerably low, the addition of 20 wt.% SiC with high laser absorptivity is favorable to offset this disadvantage. When the high-energy laser beam irradiates and heats up the powder particles, the temperature of the powder material enhances in an extremely short time. The aluminum with a low melting point of 933 K melts rapidly and the SiC particles having a significantly high melting point remain unmelted. Then, a molten pool consisting of the melted aluminum and the unmelted SiC particles is formed. The aluminum melt surrounds

and wets the unmelted SiC particles due to the flow of the melt under the action of the Marangoni convection in the molten pool and resultant capillary forces of the liquid [44]. With sufficient wetting of the liquid at the elevated temperature, the SiC particles tend to be melted partially, starting from the melting of the particle surface. Because of the *in situ* formation of the Al_4SiC_4 phase, the maximum SLM temperature in the molten pool exceeds 1670 K, as revealed in Eq. 7.2. At the elevated temperature, the Si and C atoms have strong thermal motion ability and consequently, they can easily escape from the equilibrium position of the lattice or be replaced by the Al atoms. Thus, the *in situ* reaction occurs by means of the diffusion of the Al, Si, and C atoms typically on the melted interface between the SiC and Al melt, hence generating the *in situ* Al_4SiC_4 reinforcing phase [40]. The Al_4SiC_4 initially forms as faceted platelets on the interface between the solid and liquid [37], whereas the Si further dissolves into the liquid and forms the Mg_2Si phase (Fig. 7.2). As revealed in Fig. 7.3, the linear laser energy density (LED) has an important influence on the mechanism of the *in situ* formation of the Al_4SiC_4 reinforcing phase and the attendant microstructural features of the SLM-processed Al-based composites. At a relatively low LED of 800 J/m, the energy absorbed by the powder is relatively low. In this situation, only a small amount of fine SiC particles or edges of the irregular large-sized SiC particles tend to melt. The *in situ* reaction only performs partially around the surface of the melted SiC particles, leading to the formation of the particle structured Al_4SiC_4 reinforcement between the residual SiC particles (Fig. 7.4a). Because of the existence of a large amount of unmelted SiC particles in the molten pool, the viscosity of the melt is considerably high, resulting in a relatively low flowability of the melt [45, 46]. Under this condition, the microstructural homogeneity of the SLM-processed Al-based composites, which consist of both large-scale SiC reinforcing particles and *in situ* formed Al_4SiC_4 reinforcing particles, is limited (Fig. 7.3a). When the applied LED increases to 900 J/m, the laser energy that the molten pool receives increases, thereby enhancing the temperature of the pool. A larger degree of the melting of the SiC particles occurs and the activity of the *in situ* reaction between SiC and Al increases, leading to the formation of both the strip-structured (Fig. 7.3b) and the particle-shaped (Fig. 7.4b) *in situ* Al_4SiC_4 reinforcement. The orientated Al_4SiC_4 strips are present on the melted surface of the SiC particles under the effect of the elevated SLM temperature and the significant liquid flow, by means of the heterogeneous nucleation of the Al_4SiC_4 nuclei and the subsequent grain growth. At a relatively higher LED of 1000 J/m, the temperature of the molten pool increases significantly and a large fraction of the SiC particles decompose and react with the aluminum melt, producing a larger amount of the Al_4SiC_4 reinforcing phase. As the *in situ* reaction proceeds, the strip-structured Al_4SiC_4 phase grows continuously and, conversely, the SiC phase is exhausted gradually until it vanishes in the *in situ* reaction system. The *in situ* system accordingly enters a stable state and the *in situ* present Al_4SiC_4 strips become larger in its width and thickness gradually (Fig. 7.3c). Meanwhile, due to the super-high heating and cooling rate during the SLM process, both the strip- and particle-structured *in situ* Al_4SiC_4 reinforcing phase has considerably fine microstructures after solidification (Figs. 7.3c and 7.4c). Furthermore, the efficient action of the Marangoni convection

in the molten pool induces the capillary force of the liquid, which further acts on the *in situ* formed Al_4SiC_4 particles and rearranges their distribution in the pool, leading to a homogeneous dispersion of the fine Al_4SiC_4 particles in the finally solidified composites (Fig. 7.4c). With the excessive enhancement of LED to 1100 J/m, a large amount of heat is accordingly accumulated around the growing edges of the i*n situ* Al_4SiC_4 crystals, which provides sufficient internal thermodynamic potential for the coarsening of the finally developed Al_4SiC_4 strips and particles in the SLM-processed composites (Figs. 7.3d and 7.4d). Furthermore, the significant thermal kinetics during SLM and the attendant thermal stress in the solidified materials result in the formation of a large amount of microscale shrinkage porosity between the strip-structured Al_4SiC_4 and the Al matrix (Fig. 7.4d) and the resultant limited interfacial bonding ability.

It is known that for the fabrication of the AMCs, interfacial bonding strength is regarded as the key factor that influences the performance of the parts. However, the poor wettability between the aluminum and SiC makes it difficult to prepare the SiC particle reinforced AMCs with sufficiently high interfacial bonding strength via conventional manufacturing methods. In the present study, the application of the high energy laser beam makes it possible to process the AMCs at elevated temperatures, which is favorable to enhance the wettability between the ceramic and metal [47]. The ternary carbide Al_4SiC_4 reinforcing phase forms as a result of the *in situ* reaction between the SiC and aluminum. The reaction itself also has a positive influence on the reduction of the contact angle, due to the reduction of the interface energy and the formation of a new reaction product [48]. A fraction of the Al_4SiC_4 phase that grows on the surface of the SiC particles acts as the transition zone, avoiding the direct contact of the two different crystal structures of SiC and aluminum. Furthermore, the other kind of *in situ* Al_4SiC_4 phase, which is in the ultra-fine particle morphology, can further behave as the reinforcement throughout the Al matrix to improve the mechanical properties of the SLM-processed composites.

7.5 Densification Behavior of Al-based Composite Parts Processed by SLM of SiC/AlSi10Mg Powder

The different relative densities and the cross-sectional microstructures of the SLM-processed specimens at the various linear LED are provided in Fig. 7.6. It showed that the relative density of the SLM-processed composite specimens had the trend of increasing as the applied LED increased. At a relatively low LED of 800 J/m, the density of the specimen was only 89.2 % of the theoretical density (TD) of the material, and some voids with a relatively large average size of ~30 μm were observed on the cross-section of the specimen. As the LED increased to 900 J/m, the relative density of the sample increased to 93.4 % and the amount of pores decreased, showing a reduction in the pore size. The SLM-processed Al-based composites with a considerably high relative density of 95.5 % were produced at a high LED of 1000 J/m, exhibiting a cross-section with a small amount of voids of a very small

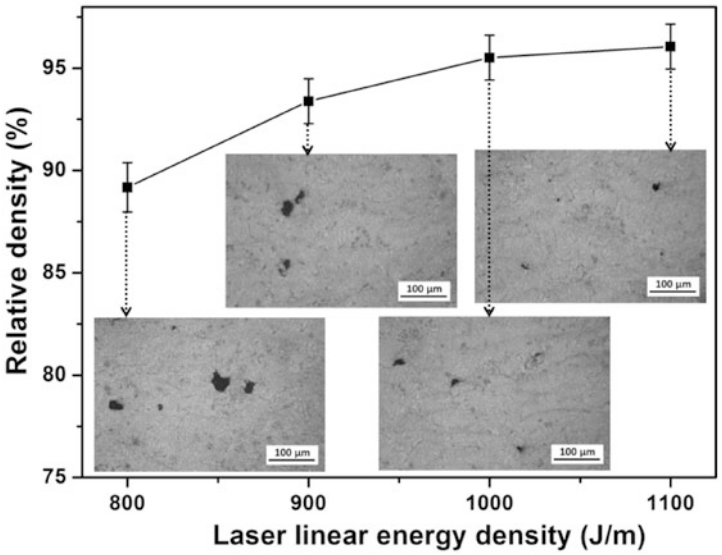


Fig. 7.6 Influence of the linear laser energy density (*LED*) on the relative densities and cross-sectional microstructures of the SLM-processed Al-based composite parts

size. On increasing the LED to 1100 J/m, the relative density exhibited a slight increase to 96.1 % and only a few small pores existed on the cross-section after SLM.

It is known that during the SLM process, the laser energy input has a significant impact on the viscosity of the melt, which further influences the melt flow within the pool. When the applied LED is low, the laser energy input is limited and a large fraction of the unmelted SiC particles remain in the molten pool, hence increasing the viscosity of the melt and lowering the fluidity of the liquid in the molten pool. In this situation, the melt cannot efficiently wet the underlying previously processed layer and the surrounding solidified material in the currently processed layer, thereby producing the residual porosity between the neighboring scan tracks/layers and lowering the densification activity of the SLM-processed parts. At a relatively high LED of 1000 J/m, the higher laser energy input significantly reduces the melt viscosity in the molten pool, due to the elevated SLM working temperature obtained, hence enhancing the wetting characteristics of the melt in the molten pool. Furthermore, according to De Hosson et al.'s work [48], the reaction between the metal matrix and the ceramic particles favors the improvement of their mutual wetting ability. As revealed in Figs. 7.3c and 7.4c, a large amount of SiC particles are consumed and turned into the Al_4SiC_4 phase with the refined microstructures. As relative to the direct interfacial contact of the SiC and aluminum, the *in situ* chemical reaction tends to decrease the interfacial energy significantly and the change of the lattice structures on the interface becomes much tempered [48]. Therefore, the wetting properties, both the microscopic interfacial wetting and the macroscopic layer/layer wetting, tend to be improved, leading to an elevated densification response for the SLM-processed composite parts. As the applied LED continues to increase to

1100 J/m, the relative density of the SLM-processed sample does not show any apparent decrease. Nevertheless, the apparent microscale shrinkage porosity is present between the coarsened strip-structured *in situ* Al_4SiC_4 reinforcing phase and the Al matrix, which may be ascribed to the superheating of the molten pool and resultant significant shrinkage and stress formation during liquid/solid transformation. It is accordingly reasonable to consider that the densification rate of the SLM-processed composites is influenced by the residual large-sized pores, as revealed in Fig. 7.6. The formation of the shrinkage porosity between the coarsened phases/crystals, which is on a considerably microscopic scale, may not have a direct influence on the densification level. Nevertheless, it may exert some detrimental effects on other mechanical properties such as hardness and wear performance, which will be studied and presented in the following sections.

7.6 Hardness and Wear Performance of Al-Based Composite Parts Processed by SLM of SiC/AlSi10Mg Powder

Figure 7.7 depicts variations of microhardness of SLM-processed Al-based composite specimens at different processing parameters. It was clear that the microhardness and its distribution were influenced by the applied linear LED. With the increase of LED from 800 to 900 J/m, the mean microhardness values displayed an

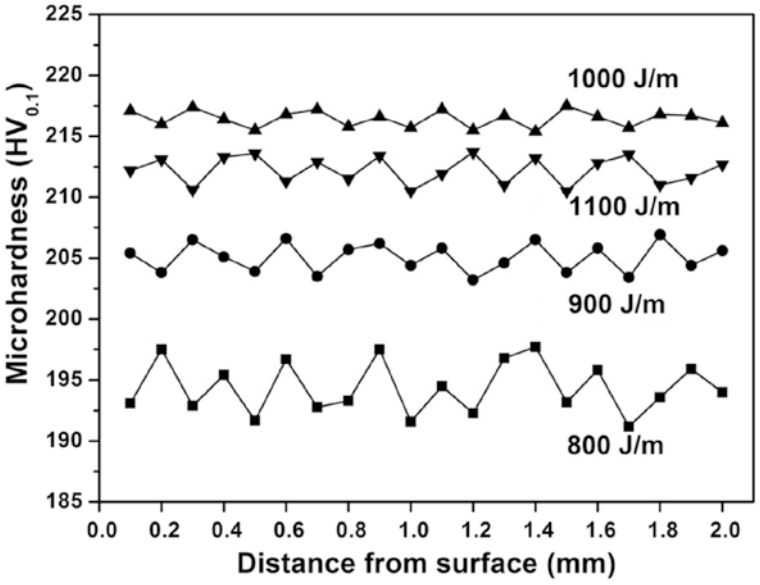


Fig. 7.7 Variations of the microhardness of the SLM-processed Al-based composite parts at the various linear laser energy densities (*LED*)

enhancement from 196 to 203 $HV_{0.1}$, accompanied by a decrease in the fluctuation of the values. At a higher LED of 1000 J/m, the average microhardness value further increased to 214 $HV_{0.1}$ and the fluctuation of the values was further weakened. However, when the applied LED further increased to 1100 J/m, the microhardness suffered a reduction in the average value to 212 $HV_{0.1}$ and the fluctuation of the microhardness values became apparent. A close comparison revealed that for all the given SLM processing parameters, the SLM-processed Al-based composites reinforced with the multiple reinforcements demonstrated superior hardness compared to the unreinforced AlSi10Mg parts fabricated using the same SLM conditions (the maximum microhardness of ~145 $HV_{0.1}$) [49], showing 26–32% enhancement upon the unreinforced AlSi10Mg alloy.

In general, due to the effect of the grain refinement strengthening in laser-processed materials, the SLM-processed parts typically exhibit higher hardness than parts manufactured by conventional methods. Figure 7.7 reveals that the linear laser energy density (LED) of 1000 J/m is a critical value corresponding to the different hardness performance. When the applied LED is below 1000 J/m, the density of the SLM-processed Al-based composites is relatively low due to the presence of residual interlayer pores, which decreases the obtainable microhardness values. Also, due to the insufficient *in situ* reaction between the SiC and aluminum, the microstructural homogeneity of the reinforcement in SLM-processed composites is limited, hence enhancing the fluctuation of microhardness distribution. The highest microhardness is obtained at the LED of 1000 J/m, with the minimum fluctuation of hardness values. In this case, the densification level of the SLM-processed composites is sufficiently high (~96%), which acts as the underlying basis for the improvement of hardness. Furthermore, multiple reinforcing structures are produced due to the *in situ* reaction during the SLM process, having a positive influence on the hardness performance. The strip-structured Al_4SiC_4 reinforcing phase has a stronger ability to withstand the load than the matrix. Meanwhile, the ultrafine particle-shaped Al_4SiC_4phase embeds throughout the Al matrix and plays an important role in hindering dislocation movement, exhibiting the effect of dispersion strengthening. Furthermore, during the laser-induced rapid solidification process, a large amount of Si atoms tend to diffuse into the lattice of the matrix metals, thereby working as the solid solution strengthening effect to further improve microhardness [12]. However, the excessive increase of the applied LED above 1000 J/m results in the decrease of hardness, which is caused by the formation of coarsened grains resulting from significant grain growth (Figs. 7.3d and 7.4d).

Figure 7.8 depicts the variations of the COF values and resultant wear rates of the SLM-processed Al-based composite parts under the different SLM processing conditions. As the applied linear LED increased from 800 to 900 J/m, the mean COF values changed slightly from 0.45 to 0.47 and the attendant wear rates decreased from 4.27×10^{-5} $mm^3N^{-1}m^{-1}$ to 3.38×10^{-5} $mm^3N^{-1}m^{-1}$. As the applied LED increased to 1000 J/m, the average COF value and the wear rate decreased markedly to 0.39 and 1.56×10^{-5} $mm^3N^{-1}m^{-1}$, respectively, and the fluctuation of the COF values became insignificant, implying the excellent wear resistance of the SLM-processed Al-based composites in this instance. However, the wear performance

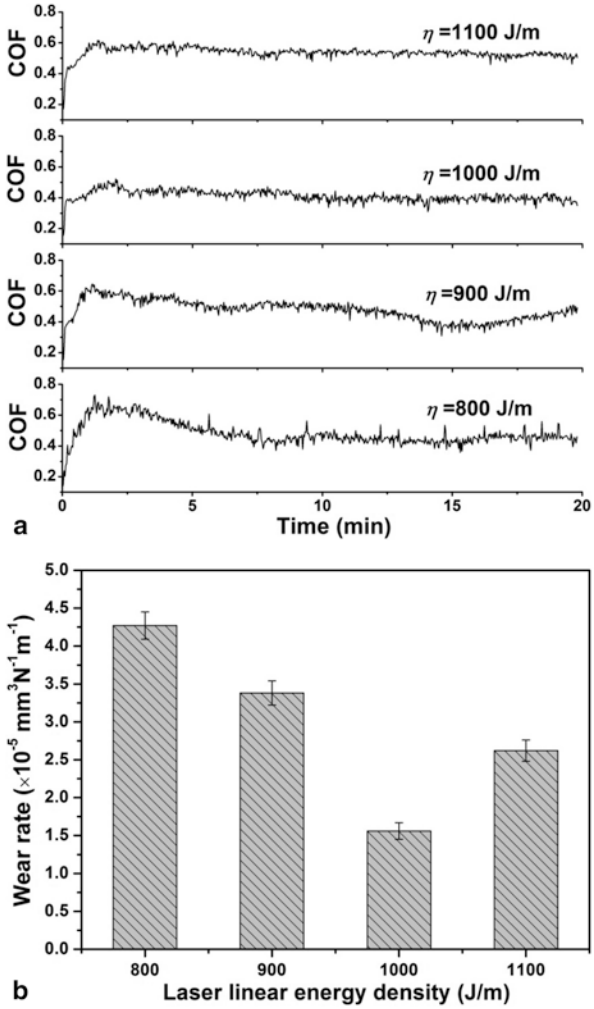


Fig. 7.8 The coefficient of friction (*COF*) **a** and the resultant wear rate **b** of the SLM-processed Al-based composite parts using the different linear laser energy densities (*LED*)

of the SLM-processed Al-based composites at an even higher LED of 1100 J/m showed a decreasing tendency; the average COF value increased to 0.52 with an elevated wear rate of 2.62×10^{-5} $mm^3N^{-1}m^{-1}$.

In order to further study the wear mechanism at different SLM processing parameters, the detailed FE-SEM studies of the corresponding worn surfaces are shown in Figs. 7.9 and 7.10, using the various magnifications for SEM images. At a relatively low LED of 800 J/m, a rough, heterogeneous worn surface consisting of parallel grooves and aggregated, protruding particles was observed (Fig. 7.9a). A high-magnification FE-SEM image showed the presence of particle-shaped fragments with an average size of ~500 nm at the edges of the grooves (Fig. 7.10a), which revealed

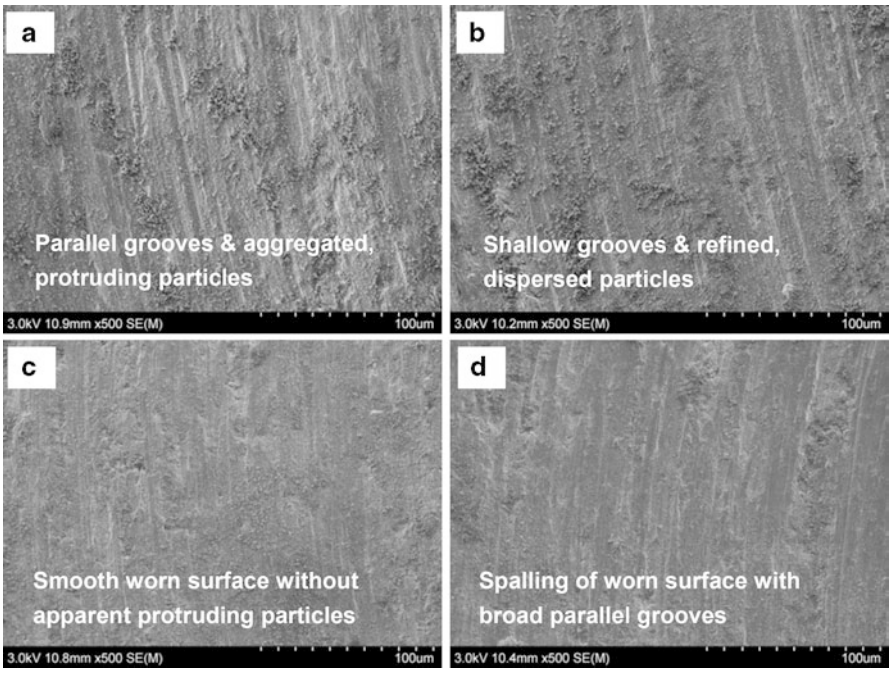


Fig. 7.9 FE-SEM images showing morphologies of worn surfaces of SLM-processed Al-based composite parts at different linear laser energy densities (*LED*): **a** LED = 800 J/m; **b** LED = 900 J/m; **c** LED = 1000 J/m; **d** LED = 1100 J/m

severe deformation and plowing of the surface during sliding. As the applied LED increased to 900 J/m, the grooves on the worn surface became shallower (Fig. 7.9b) and the protruding particles became dispersed on the surface, showing an apparently decreased size of ~300 nm (Fig. 7.10b). The relatively smooth and dense worn surface was formed at an LED of 1000 J/m, without the presence of apparent protruding particles (Figs. 7.9c and 7.10c). At an excessive LED of 1100 J/m, the worn surface suffered apparent spalling, showing broader parallel grooves on the surface (Fig. 7.9d). In this situation, the debris in the morphology of the aggregated small-sized particles appeared again on the worn surface (Fig. 7.10d).

During the wear tests, the counterface ball slides against the surface continuously and the wear performance is primarily influenced by the microstructural features and hardness of the corresponding specimens [50, 51]. When the applied LED is low, some SiC particles with a high hardness remain unmelted due to the low SLM working temperature. During sliding, under the action of the strong compression effect from the load, the aluminum matrix with a relatively lower hardness performs a large deformation and, meanwhile, the residual SiC particles in the matrix tend to protrude from the worn surface under the shearing stress. Since these protruded SiC particles exist between the specimen surface and the sliding ball, the hard ceramic particles severely plow the specimen surface and, consequently, some deep

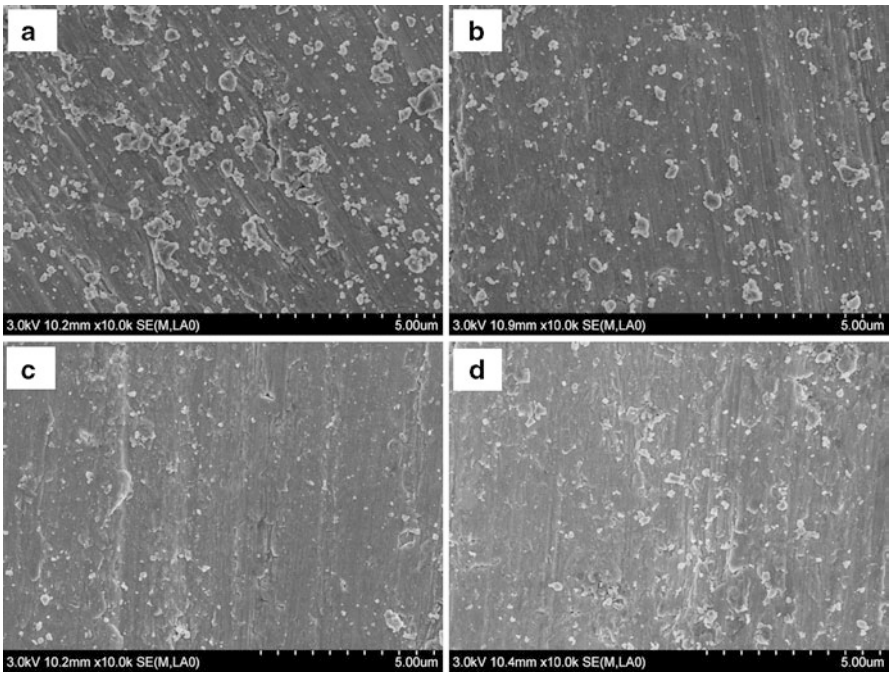


Fig. 7.10 High-magnification FE-SEM images showing the typical morphologies of reinforcement on worn surfaces of SLM-processed Al-based composite parts at various linear laser energy densities (*LED*): **a** LED = 800 J/m; **b** LED = 900 J/m; **c** LED = 1000 J/m; **d** LED = 1100 J/m

grooves are formed on the worn surface (Figs. 7.9a and 7.10a). The mechanism of the abrasive wear is represented in this situation, resulting in low wear resistance with a significantly high wear rate (Fig. 7.8). With the increase of the applied LED, the *in situ* reaction in the molten pool occurs more efficiently and the SiC particles are exhausted in this reaction system. Therefore, the plowing effect of the SiC particles on the testing surface decreases and the worn surface shows the shallower grooves with few protruding particles (Figs. 7.9b and 7.10b). Meanwhile, the *in situ* formed strip-structured and particle-shaped Al_4SiC_4 with considerably refined microstructures are generated in the SLM-processed composites, which have excellent bonding strength with the matrix (Figs. 7.3c and 7.4c). As the worn surface experiences sufficient plastic deformation at a temperature below its recrystallization temperature, the material strengthening occurs because of the dislocation movements within the crystal structure of the material, typically in the sliding-treated layer, which is known as the strain-hardened tribolayer [52]. It is believed that the *in situ* formed homogenous and refined Al_4SiC_4 reinforcements are not easy to split during sliding but have a high tendency to adhere to each other and get strain-hardened, favoring the complete formation of tribolayer to enhance wear resistance (Figs. 7.8, 7.9c and 7.10c). The sufficiently high densification activity (Fig. 7.6) and the enhancement of hardness (Fig. 7.7) also contribute to the improvement of the wear

performance of the SLM-processed composites in this case. It is thus reasonable to consider that the mechanism of material removal during sliding changes from the abrasion (Figs. 7.9a and 7.10a) to the adhesion of the tribolayer (Figs. 7.9c and 7.10c), thereby favoring the stabilization of COF values and the reduction in wear rate after sliding (Fig. 7.8). However, for the composites produced at an even higher LED, because the energy input and resultant SLM temperatures are too high, the grains of the *in situ* strip- and particle-structured Al_4SiC_4 are coarsened significantly (Figs. 7.3d and 7.4d), hence decreasing their strengthening effect upon the Al matrix. Moreover, the formation of a large amount of microscopic shrinkage porosity between the coarsened strip-structured Al_4SiC_4 reinforcement and the matrix is also detrimental to the hardness and wear performance of the SLM-processed Al-based composites.

A close comparison of the phase constitutions (Fig. 7.2), microstructural characteristics (Figs. 7.3 and 7.4), and densification activity (Fig. 7.6) of the SLM-processed Al-based composites reveals that the limited hardness and wear performance of parts processed at a low linear laser energy density (LED) is ascribed to: (i) the insufficient densification rate due to the formation of residual pores (Fig. 7.6); and (ii) the inhomogenous reinforcing structure caused by the insufficient *in situ* chemical reaction and the residual SiC particles (Fig. 7.3a). For the SLM-processed composites at a high LED, although the sufficiently high densification level (Fig. 7.6) should favor improvement in mechanical performance, the significant coarsening of the *in situ* Al_4SiC_4 reinforcements and the formation of interfacial microscopic shrinkage porosity (Figs. 7.3d and 7.4d) weakens the hardness and wear property.

7.7 Conclusions

In this chapter, SLM additive manufacturing of the SiC/AlSi10Mg composite powder was performed to prepare Al-based composites with multiple reinforcing phases. The main conclusions were summarized as follows:

1. The reinforcing phases in the SLM-processed Al-based composites included unmelted micron-sized SiC particles, *in situ* formed micron-sized Al_4SiC_4 strips, and *in situ* produced submicron Al_4SiC_4 particles. As the input laser energy density increased, the extent of the *in situ* reaction between the SiC particles and the Al matrix increased, resulting in a larger degree of the formation of Al_4SiC_4 reinforcement with more homogenous microstructures.
2. The densification rate of SLM-processed Al-based composite parts increased as the applied laser energy density increased. A sufficiently high densification response of ~96% theoretical density was achieved for the linear laser energy density larger than 1000 J/m.
3. Due to the generation of multiple reinforcements after SLM, elevated mechanical properties were obtained for SLM-processed Al-based composites having a high microhardness of 214 $HV_{0.1}$, a considerably low COF of 0.39, and a reduced wear rate of 1.56×10^{-5} $mm^3N^{-1}m^{-1}$.

4. The grain size of the *in situ* formed Al_4SiC_4 reinforcing phase, both the strip- and particle-structured Al_4SiC_4, increased considerably using an excessive laser energy input. The significant grain coarsening of the reinforcement and the formation of interfacial microscopic shrinkage porosity between the reinforcement and the matrix lowered the mechanical performance of the SLM-processed Al-based composites.

References

1. Tang L, Landers RG (2011) Layer-to-layer height control for laser metal deposition process. ASME J Manuf Sci Eng 133(2):021009
2. Kamara AM, Marimuthu S, Li L (2011) A numerical investigation into residual stress characteristics in laser deposited multiple layer waspaloy parts. ASME J Manuf Sci Eng 133(3):031013
3. Mahamood RM, Akinlabi ET, Shukla M, Pityana S (2013) Characterizing the effect of laser power density on microstructure, microhardness, and surface finish of laser deposited titanium alloy. ASME J Manuf Sci Eng 135(6):064502
4. Edwards P, O'Conner A, Ramulu M (2013) Electron beam additive manufacturing of titanium components: properties and performance. ASME J Manuf Sci Eng 135(6):061016
5. Sammons PM, Bristow DA, Landers RG (2013) Height dependent laser metal deposition process modeling. ASME J Manuf Sci Eng 135(5):054501
6. Tsopanos S, Mines RAW, McKown S et al (2010) The influence of processing parameters on the mechanical properties of selectively laser melted stainless steel microlattice structures. ASME J Manuf Sci Eng 132(4):041011
7. Chen TB, Zhang YW (2007) Three-dimensional modeling of laser sintering of a two-component metal powder layer on top of sintered layers. ASME J Manuf Sci Eng 129(3):575–582
8. Chen TB, Zhang YW (2006) Three-dimensional modeling of selective laser sintering of two-component metal powder layers. ASME J Manuf Sci Eng 128(1):299–306
9. Xiao B, Zhang YW (2008) Numerical simulation of direct metal laser sintering of single-component powder on top of sintered layers. ASME J Manuf Sci Eng 130(4):041002
10. Gu DD, Meiners W, Wissenbach K et al (2012) Laser additive manufacturing of metallic components: materials, processes and mechanisms. Int Mater Rev 57(3):133–164
11. Kruth JP, Levy G, Klocke F et al (2007) Consolidation phenomena in laser and powder-bed based layered manufacturing. CIRP Ann Manuf Technol 56(2):730–759
12. Gu DD, Hagedorn YC, Meiners W et al (2012) Densification behavior, microstructure evolution, and wear performance of selective laser melting processed commercially pure titanium. Acta Mater 60(9):3849–3860
13. Louvis E, Fox P, Sutcliffe CJ (2011) Selective laser melting of aluminium components. J Mater Process Technol 211(2):275–284
14. Brandl E, Heckenberger U, Holzinger V et al (2012) Additive manufactured AlSi10Mg samples using Selective Laser Melting (SLM): microstructure, high cycle fatigue, and fracture behavior. Mater Des 34:159–169
15. Sercombe TB, Schaffer GB (2003) Rapid manufacturing of aluminum components. Science 301(5637):1225–1227
16. Gu DD, Dai DH, Zhang GQ et al (2012) Growth mechanisms of in situ TiC in laser melted Ti-Si-C ternary system. App Phys Lett 101(17):171603
17. Gusarov AV, Yadroitsev I, Bertrand Ph et al (2009) Model of radiation and heat transfer in laser-powder interaction zone at selective laser melting. ASME J Heat Transfer 131(7):072101
18. Li YL, Gu DD (2014) Parametric analysis of thermal behavior during selective laser melting additive manufacturing of aluminum alloy powder. Mater Des 63:856–867

19. Agarwala M, Bourell D, Beaman J et al (1995) Direct selective laser sintering of metals. Rapid Prototyp J 1(1):26–36
20. Das M, Balla VK, Basu D et al (2010) Laser processing of SiC-particle-reinforced coating on titanium. Scr Mater 63(4):438–441
21. Lavernia EJ, Srivatsan TS (2010) The rapid solidification processing of materials: science, principles, technology, advances, and applications. J Mater Sci 45(2):287–325
22. Bartkowiak K, Ullrich S, Frick T et al (2011) New developments of laser processing aluminium alloys via additive manufacturing technique. Phys Procedia 12:393–401
23. Dadbakhsh S, Hao L (2012) Effect of Al alloys on selective laser melting behaviour and microstructure of in situ formed particle reinforced composites. J Alloy Compd 541:328–334
24. Tang L, Landers RG (2010) Melt pool temperature control for laser metal deposition processes-part I: online temperature control. ASME J Manuf Sci Eng 132(1):011010
25. Tang L, Landers RG (2010) Melt pool temperature control for laser metal deposition processes-part II: layer-to-layer temperature control. ASME J Manuf Sci Eng 132(1):011011
26. Prashanth KG, Scudino S, Klauss HJ et al (2014) Microstructure and mechanical properties of Al-12Si produced by selective laser melting: Effect of heat treatment. Mater Sci Eng A 590:153–160
27. Zhang BC, Liao HL, Coddet C (2012) Effects of processing parameters on properties of selective laser melting Mg-9%Al powder mixture. Mater Des 34:753–758
28. Santos EC, Shiomi M, Osakada K et al (2006) Rapid manufacturing of metal components by laser forming. Int J Mach Tools Manuf 46(12–13):1459–1468
29. Kruth JP, Wang X, Laoui T et al (2003) Lasers and materials in selective laser sintering. Assem Autom 23(4):357–371
30. Bassani P, Capello E, Colombo D et al (2007) Effect of process parameters on bead properties of A359/SiC MMCs welded by laser. Compos Part A 38(4):1089–1098
31. Eliasson J, Sandström R (1995) Applications of aluminuium matrix composites. Key Eng Mater 104–107:3–36
32. Su H, Gao WL, Zhang H et al (2010) Optimization of stirring parameters through numerical simulation for the preparation of aluminum matrix composite by stir casting process. ASME J Manuf Sci Eng 132(6):061007
33. Yang Y, Li XC (2007) Ultrasonic cavitation-based nanomanufacturing of bulk aluminum matrix nanocomposites. ASME J Manuf Sci Eng 129(2):252–255
34. Maruyama B (1999) Discontinuously reinforced aluminum: current status and future direction. JOM 51(11):59–61
35. Prasada SV, Asthana R (2004) Aluminum metal-matrix composites for automotive applications: tribological considerations. Tribol Lett 17(3):445–453
36. Asgharzadeh H, Simchi A (2009) Supersolidus liquid phase sintering of Al6061/SiC metal matrix composites. Powder Metall 52(1):28–35
37. Simchi A, Godlinski D (2008) Effect of SiC particles on the laser sintering of Al-7Si-0.3Mg alloy. Scr Mater 59(2):199–202
38. Simchi A, Godlinski D (2011) Densification and microstructural evolution during laser sintering of A356/SiC composite powders. J Mater Sci 46(5):1446–1454
39. Anandkumar R, Almeida A, Colaço R et al (2007) Microstructure and wear studies of laser clad Al-Si/$SiC_{(p)}$ composite coatings. Surf Coat Technol 201(24):9497–9505
40. Ureña A, Rodrigo P, Gil L et al (2001) Interfacial reactions in an Al-Cu-Mg (2009)/SiCw composite during liquid processing Part II Arc welding. J Mater Sci 36(2):429–439
41. Gu DD, Shen YF (2009) Effects of processing parameters on consolidation and microstructure of W-Cu components by DMLS. J Alloys Compd 473(1–2):107–115
42. Gu DD, Shen YF, Yang JL et al (2006) Effects of processing parameters on direct laser sintering of multicomponent Cu based metal powder. Mater Sci Technol 22(12):1449–1455
43. Fischer P, Romano V, Weber HP et al (2003) Sintering of commercially pure titanium powder with a Nd: YAG laser source. Acta Mater 51(6):1651–1662
44. Xu G, Schultz WW, Kannatey-Asibu E (2004) Application of a front tracking method in gas metal arc welding (GMAW) simulation. ASME J Manuf Sci Eng 127(3):590–597

45. Wu YF, Kim GY, Anderson IE et al (2010) Experimental study on viscosity and phase segregation of Al-Si powders in microsemisolid powder forming. ASME J Manuf Sci Eng 132(1):011003
46. Jeswani AJ, Roux JA (2007) Manufacturing modeling of three-dimensional resin injection pultrusion process control parameters for polyester/glass rovings composites. ASME J Manuf Sci Eng 129(1):143–156
47. Gu DD, Shen YF (2006) Processing and microstructure of submicron WC-Co particulate reinforced Cu matrix composites prepared by direct laser sintering. Mater Sci Eng A 435–436:54–61
48. Zhou XB, De Hosson JThM (1996) Reactive wetting of liquid metals on ceramic substrates. Acta Mater 44(2):421–426
49. Buchbinder D, Schleifenbaum H, Heidrich S (2011) High Power Selective Laser Melting (HP SLM) of aluminum parts. Phys Procedia 12:271–278
50. Schrock DJ, Kang D, Bieler TR et al (2014) Phase dependent tool wear in turning Ti-6Al-4V using polycrystalline diamond and carbide inserts. ASME J Manuf Sci Eng 136(4):041018
51. Bassoli E, Atzeni E, Iuliano L (2011) Grinding micromechanisms of a sintered friction material. ASME J Manuf Sci Eng 133(1):014501
52. Jain A, Basu B, Kumar BVM et al (2010) Grain size-wear rate relationship for titanium in liquid nitrogen environment. Acta Mater 58(7):2313–2323

Chapter 8
Particle-Reinforced Cu Matrix Composites by Direct Metal Laser Sintering (DMLS) Additive Manufacturing (AM): Interface Design, Material Optimization, and Process Control

Abstract The interface design, material optimization, and process control during direct metal laser sintering (DMLS) additive manufacturing of $(WC–Co)_p$/Cu composite parts were performed. By means of the addition of WC reinforcing particles in the form of WC–Co composite powder, the design strategy and formation mechanism of the graded interface during DMLS were investigated to improve the interfacial bonding and material integrity between the WC reinforcement and the Cu matrix. The effects of both laser processing parameters (e.g., laser power, scan speed, and powder layer thickness) and WC–Co reinforcement content on densification behavior, microstructural features (e.g., the particle dispersion homogeneity and the interfacial bonding ability), and mechanical properties (e.g., microhardness and its distribution, tensile strength, and fracture surface morphology) of DMLS-processed (WC–Co)/Cu composite parts were studied comprehensively, in order to propose the effective process control and material optimization methods to improve microstructural and mechanical performance of DMLS-processed metal matrix composites (MMCs). A detailed investigation of the influence of rare earth (RE) La_2O_3 addition on densification and microstructures of DMLS-processed (WC–Co)/Cu composite was performed, thereby proposing a key additive material for the improvement of the laser processing ability of MMCs.

8.1 Introduction

Particle-reinforced metal matrix composites (MMCs) exhibit an optimal combination of metallic matrix and stiffer and stronger reinforcements [1]. A proper selection and compatibility of matrix and reinforcement is critical in obtaining the desired properties of the final MMCs products [2]. Hard metals, such as WC–Co, have favorable properties such as high strength, high hardness, wear resistance, and reasonable fracture toughness [3]. Copper is characterized by excellent electrical and thermal conductivities and outstanding resistances to fatigue and corrosion [4]. In order to combine their superior properties, the development of WC–Co particle-reinforced Cu matrix composites is of significance. Generally, such MMCs are produced by conventional casting or powder metallurgy (PM) methods, which are productive and can obtain pretty dense parts [5]. However, conventional techniques,

© Springer-Verlag Berlin Heidelberg 2015

D. Gu, *Laser Additive Manufacturing of High-Performance Materials,*
DOI 10.1007/978-3-662-46089-4_8

which need expensive and dedicated tools such as moulds or dies, are not suitable for small volume production and complex shapes [6]. Therefore, novel processing methods should be innovatively applied for the fabrication of the complex shaped MMCs parts with favorable microstructural and mechanical properties.

As stated in Chap. 2, direct metal laser sintering (DMLS) is a typical additive manufacturing (AM) technique that enables the quick production of complex shaped three-dimensional parts directly from metallic powder. The DMLS process creates parts in a layer-by-layer fashion by selectively fusing thin layers of loose powder with a scanning laser beam. This technique competes effectively with other conventional manufacturing processes when the part geometry is complex and the production run is not large. The advances in DMLS have demonstrated that this technique gives a great promise for the net shape fabrication of functional prototypes and the small volume production of tooling for injection molding and die casting [7–9]. Therefore, it is reasonable to conclude that the DMLS process, due to its flexibility in materials and shapes, exhibits a great potential for creating complex shaped MMCs parts that cannot be easily developed by other conventional methods.

Generally, the DMLS process uses a mixture consisting of high melting point metal/ceramic powder, acting as structural particles, and low melting point metal powder, as a binder. Laser radiation selectively melts the binder and, subsequently, the liquid metal is driven by capillary forces into the voids between the structural particles. Consolidation of the solid–liquid mixture is attained by solidification of the liquid metal on cooling. So far, considerable metal powder systems have been investigated for DMLS process, as reviewed in Chap. 2. However, a review of existing literature reveals that not much previous work has been reported on the basic principles for the fabrication of ceramic particle-reinforced MMCs using DMLS, including the strategies for interface design and material optimization, the process control methods, the microstructural and mechanical properties, and the underlying metallurgical mechanisms.

In the present chapter, DMLS additive manufacturing process was applied to produce $(WC–Co)_p$/Cu MMC parts and the following issues were studied and included:

i. Interfacial design in ceramic particle-reinforced MMCs and its formation mechanism during DMLS
   Normally, the strength and stability of the interfacial region between the reinforcing particles and the metal matrix govern the mechanical properties of MMCs. Nevertheless, since the wettability between ceramics and metals is usually poor, the limited particle–matrix interfacial bonding may cause several problems. The most serious problem is that the ceramic particles are prone to separating from the matrix during mechanical loading, resulting in the premature failure and low performance of MMCs [10–12]. To circumvent this problem, a novel strategy to design and modify the interfacial structure has been successfully implemented in the present study. A graded interfacial layer between the reinforcing particles and the matrix is formed and tailored during DMLS processing, which improves the wettability and resultant interfacial bonding ability.

ii. Control and optimization of process conditions to improve microstructural and mechanical properties of MMCs
As is evident from previous work [13, 14], the aggregation of the reinforcing particles and the resultant crack formation between the reinforcement and the matrix occur frequently in the laser-processed MMCs, due to the complex metallurgical nature of DMLS involving multiple modes of heat, mass, and momentum transfer. Therefore, in order to obtain high-quality MMCs parts by DMLS, it is important to establish the processing conditions under which laser fabrication is able to generate a uniform distribution of particles in the composites. The capability of defining the suitable process window in improving the particle dispersion homogeneity is becoming an important consideration. The effects of laser power, scan speed, and powder layer thickness on microstructural features of DMLS-processed MMCs, especially the dispersion states of the reinforcing particles (e.g., the dispersion uniformity, particle shape, and particle size) should be investigated, in order to obtain high-performance MMCs with controllable microstructures.
iii. Material design and optimization to improve microstructural and mechanical properties of MMCs
Besides the determination of suitable DMLS processing conditions, the powder materials characteristics (e.g., particle shape, particle size and its distribution, weight fraction of reinforcing particles) also play a key role in determining the final densification, microstructures, and mechanical properties of DMLS-processed MMCs parts. However, not much previous work has been reported on the basic principles of the material optimization for laser fabrication of MMCs parts using DMLS. Common problems associated with DMLS of MMCs such as balling effect, insufficient densification, and particle agglomeration are still difficult to completely overcome. The strategies for materials design and optimization are accordingly required to be proposed to process complex, net-shaped MMCs parts meeting the performance and cost requirements for industrial standards.

8.2 Preparation of $(WC–Co)_p$/Cu Composite Powder System for DMLS Process

8.2.1 Preparation of Submicron WC–Co Composite Powder

In the present study, the WC reinforcing particles were added in the form of the WC–10 %Co composite powder to the Cu matrix. The WC–Co composite powder was synthesized using a novel “spray drying and fixed bed” technique, which involved spray drying a precursor solution containing ammonium metatungstate (AMT) and $Co(NO_3)_2$, followed by calcination, ball milling, reduction,

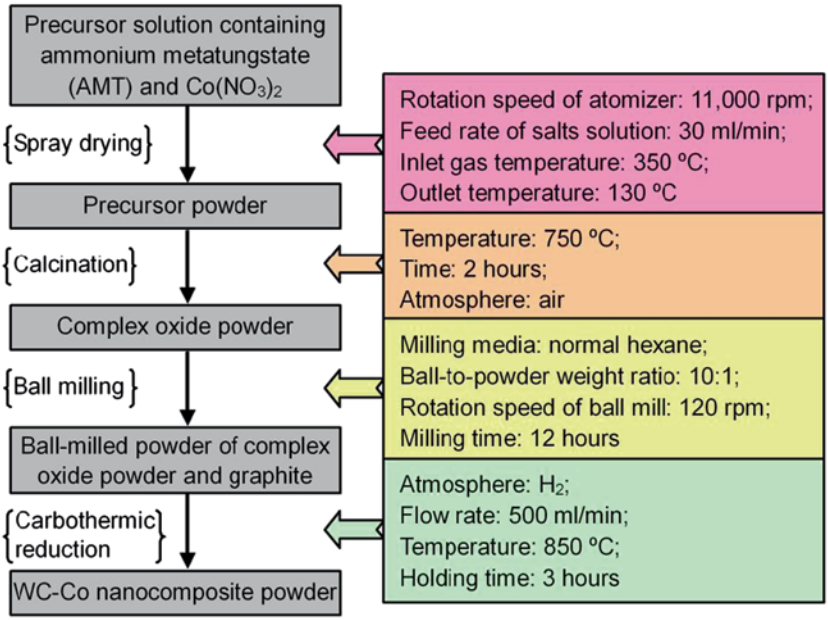


Fig. 8.1 Flowchart and processing parameters for preparation of WC–Co nanocomposite powder

and carbonization [15]. The flowchart and processing parameters for each step of powder preparation are shown in Fig. 8.1.

8.2.2 Preparation of $(WC–Co)_p$/Cu Composite Powder System

The electrolytic 99% purity Cu powder with a round dendrite shape and a mean particle size of 15 µm (Fig. 8.2a) and the as-prepared submicron WC–10%Co composite powder with an irregular shape and a mean equivalent spherical diameter of 0.6 µm (Fig. 8.2b) were used in this study. It was clear that the Co was present as a binder in between the WC particles and the average size of the WC grains was about 50 nm (Fig. 8.2c). The two powder components were mixed according to Cu: (WC–Co) weight ratios of 80:20, 70:30, and 60:40. Powder dispersion was performed in a horizontal ball mill with a vacuum-pumping system at a rotation speed of 150 rpm for 60 min, with a ball-to-powder weight ratio of 5:1. The typical morphology of the mixed powder, as shown in Fig. 8.2d, revealed that the fine WC–Co particles were dispersed around the comparatively coarse Cu particles in a homogeneous state.

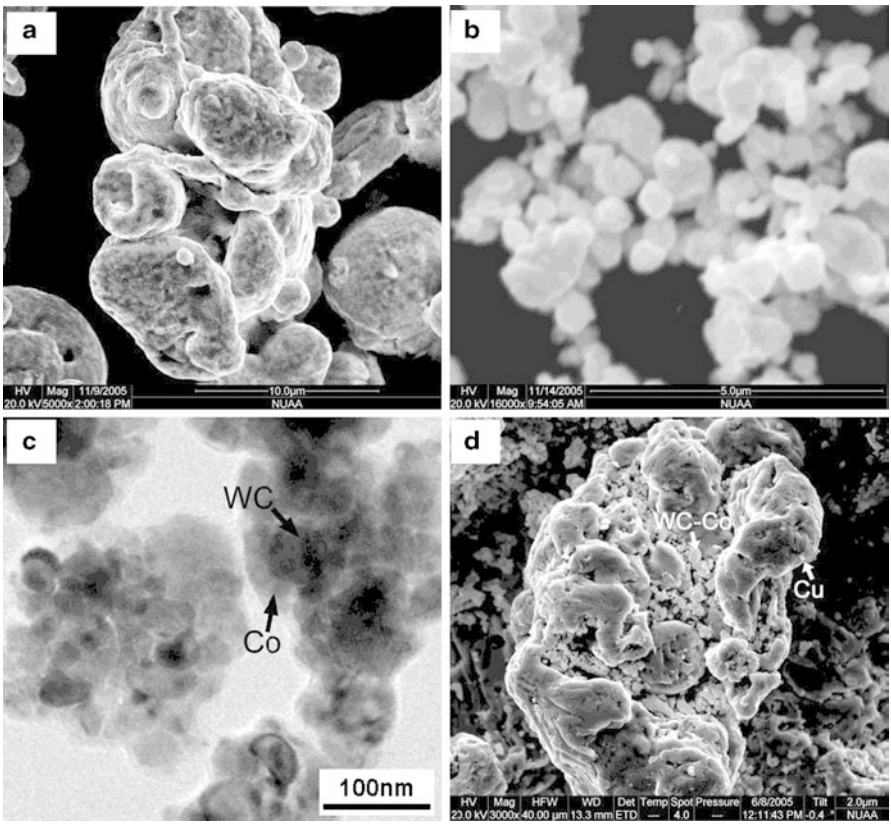


Fig. 8.2 Scanning electron microscope (SEM) images showing morphologies of the starting Cu powder (**a**), WC–Co composite powder (**b**), and the homogeneously mixed (WC–Co)/Cu powder mixture (**d**); Transmission electron microscope (TEM) image showing interior microstructure of WC–Co composite powder (**c**)

8.3 Interface Design and Processing Conditions of Submicron WC–Co Particle-Reinforced Cu Matrix Composite Prepared by Direct Metal Laser Sintering (DMLS)

8.3.1 Interface Design and Formation Mechanism of $(WC–Co)_p$/Cu Composite System during DMLS

8.3.1.1 Microstructures and Compositions

Following the procedures specified in Sect. 3.3 of Chap. 3, DMLS processing of the (WC–Co)/Cu powder mixture was performed using the as-defined CO_2 laser as the

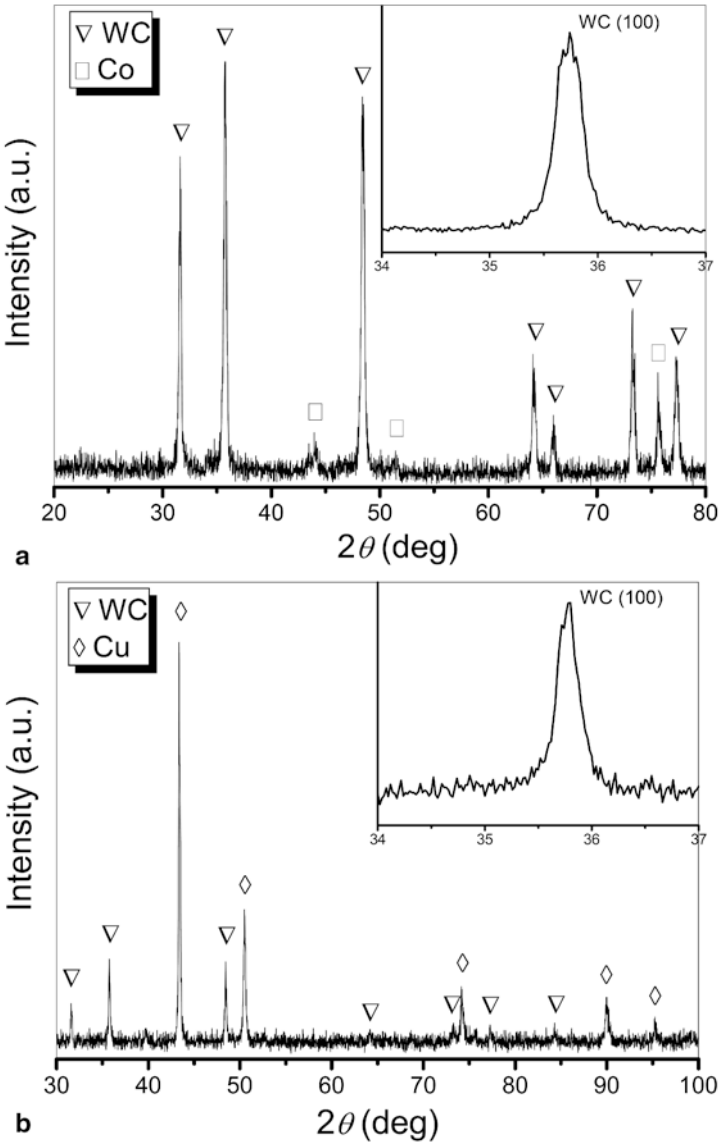


Fig. 8.3 XRD spectra of the starting WC–Co composite powder (**a**) and the DMLS-processed part (**b**)

energy source. The processing conditions as investigated were as follows: spot size of 0.30 mm, laser power (P) of 500–800 W, scan speed (v) of 0.01–0.07 m/s, scan line hatch spacing (l) of 0.15 mm, and powder layer thickness (d) of 0.10–0.50 mm.

Figure 8.3a depicts the typical X-ray diffractometer (XRD) spectrum of the starting WC–Co composite powder, showing the diffraction peaks corresponding to WC

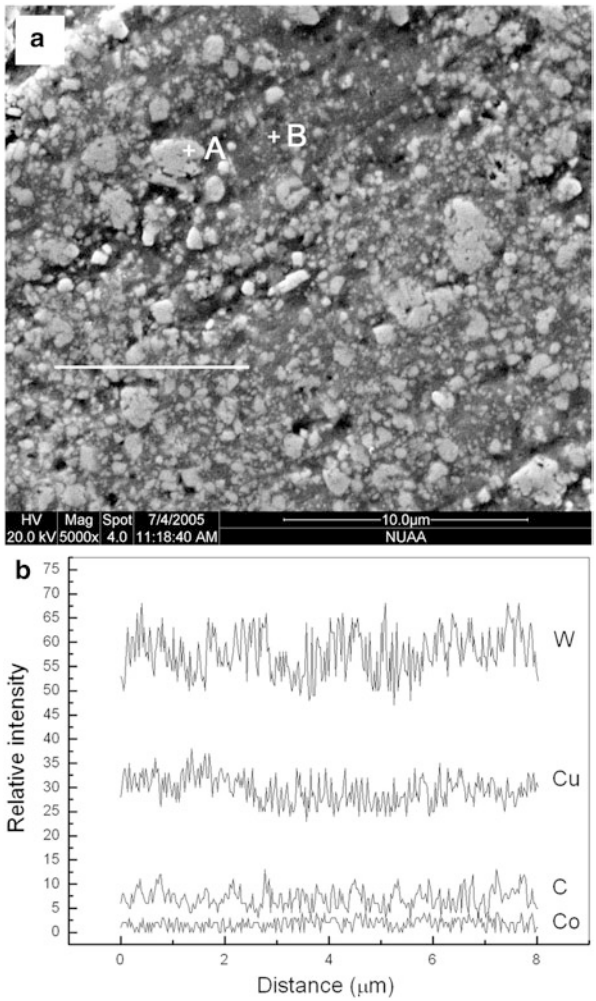


Fig. 8.4 SEM image showing the characteristic microstructure of DMLS-processed part (**a**); Energy dispersive X-ray spectroscope (EDX) line-scan pattern showing the distributions of various elements (**b**)

and Co phases. The typical XRD spectrum of the DMLS-processed part is shown in Fig. 8.3b. The strong diffraction peaks of Cu (fcc structure) and WC (hexagonal structure) were clearly observed. The Co peaks, however, were not well detected, due to its comparatively small content in the starting powder system. Thus, it was preliminarily considered that the Cu and WC phases acted as the main constitutional phases of laser-processed composites.

Figure 8.4a shows the characteristic microstructure on the polished section of the laser-processed part. It was clear that the sintered structure was pretty dense and free of apparent cracks and pores. The reinforcing particles, which exhibited a fine and smooth shape, were dispersed uniformly in the matrix. The interfaces

Table 8.1 Chemical compositions at different regions in the laser processed structure by EDX point scan analyses

Label	Position	Chemical compositions (wt. %)			
		W	C	Co	Cu
A, Fig. 8.4a	The particle	54.42	35.26	4.09	6.13
B, Fig. 8.4a	The matrix	7.06	5.14	6.73	81.07

between the reinforcing particles and the matrix were continuous and compatible, showing a homogeneous metallurgical bonding feature. The chemical compositions of the dispersed particles and the matrix are listed in Table 8.1. The reinforcing particles (position A) mainly contained W and C elements, while the matrix (position B) was found to be Cu dissolved with W, C, and Co elements. Combined with the XRD results (Fig. 8.3), it was confirmed that the WC particle-reinforced Cu matrix composites were successfully prepared. An energy-dispersive X-ray (EDX) line scan was performed in Fig. 8.4a, with the elemental distributions of W, Cu, C, and Co shown in Fig. 8.4b. It was observed that the distributions of W and C elements showed a relatively pronounced fluctuation, while the Cu and Co elements distributed homogenously in the DMLS-processed structure.

The atomic force microscope (AFM) method was applied to further study the characteristic microstructures of the polished sample, as shown in Fig. 8.5. It can be seen that the fine WC particles dispersed uniformly in the Cu matrix (Fig. 8.5a). This is mainly attributed to the homogeneous distribution of WC–Co and Cu powder obtained by mechanical milling prior to laser processing (Fig. 8.2d) and the optimal laser processing parameters, which will be addressed in detail in Sect. 8.3.2. Analyses have confirmed that there exists a critical laser scan speed, which determines the trapping or pushing of reinforcing particles by the advancing solid–liquid interface. Trapping might bring about a uniform distribution of particles, whereas pushing results in the segregation at regions finally solidified. Local magnification of Fig. 8.5a showed the excellent interfacial integrity between the reinforcement and the matrix (Fig. 8.5b). Further enlargement of zones A and B in Fig. 8.5b revealed the diversity of the morphologies of reinforcing particles (Fig. 8.5c and d). Figure 8.5c showed the first kind of particles, which had smooth and round shape with mean particle size of ~0.3 μm. Compared with the original particle characteristics (Fig. 8.2b), it is reasonable to conclude that the larger WC particles are dissolved partially with the wetting liquid. This might be followed by the rapid rearrangement of solid particles under the influence of capillary forces exerted on them by the liquid. Interestingly, the second kind of particles, shown in Fig. 8.5d, had a completely different morphology from the above. Ultrafine particles with a mean size of ~40 nm were dispersed uniformly in the matrix. In this instance, it is possible that the smaller WC particles are completely dissolved in the liquid. Due to the rapid cooling induced by the laser beam, the molten WC might precipitate again in the form of refined and dispersed particles. Another possibility is that there already exist some ultra-fine nanometer-scaled WC particulates in the raw materi-

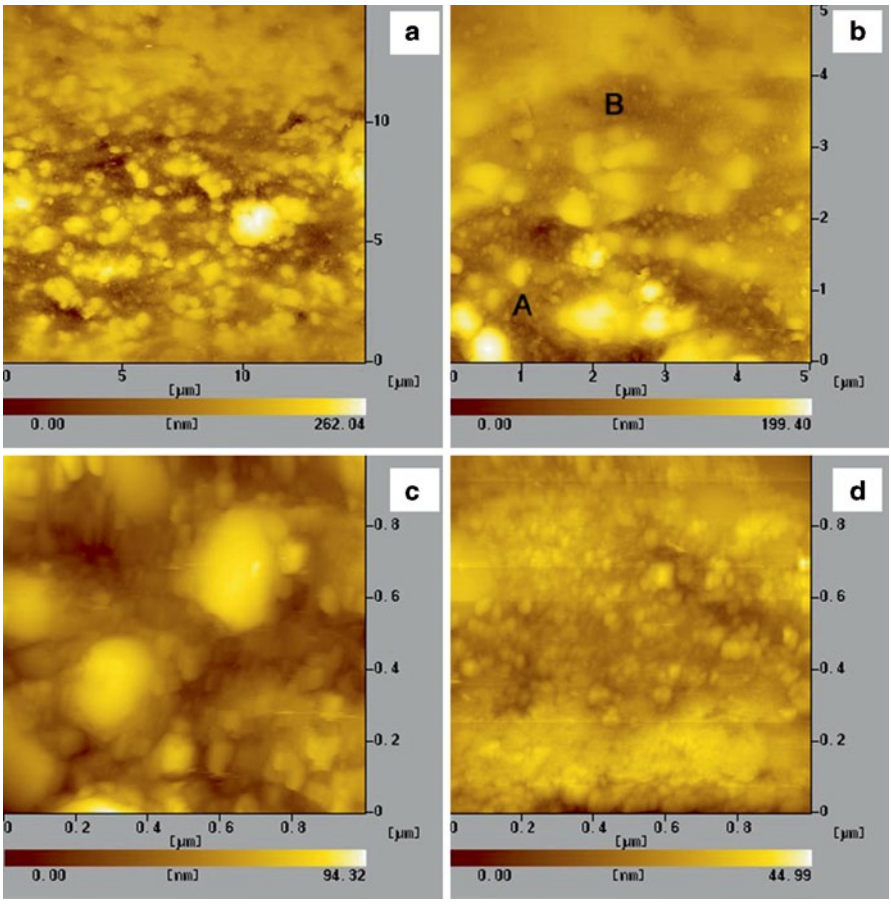


Fig. 8.5 Atomic force microscope (AFM) images showing the characteristic microstructures of DMLS-processed (WC–Co)/Cu composites: **a** 15 × 15 μm scan area; **b** 5 × 5 μm scan area; **c** 1 × 1 μm scan area on zone A in **b**; **d** 1 × 1 μm scan area on zone B in **b**

als of WC–Co composite powder, and the highly nonequilibrium nature of laser processing retains such nanophase in the laser-processed composites.

8.3.1.2 Interface Design and Formation Mechanism during DMLS

In order to further characterize the distributions of various elements in the interfacial areas in DMLS-processed composites, an EDX elemental mapping was performed, as revealed in Fig. 8.6. Interestingly, it was found that the Co element (Fig. 8.6d) showed a high concentration around the WC particles (Fig. 8.6b and c). It was reasonable to consider that the Co graded interfacial layer was formed between the WC reinforcing particles and the Cu matrix.

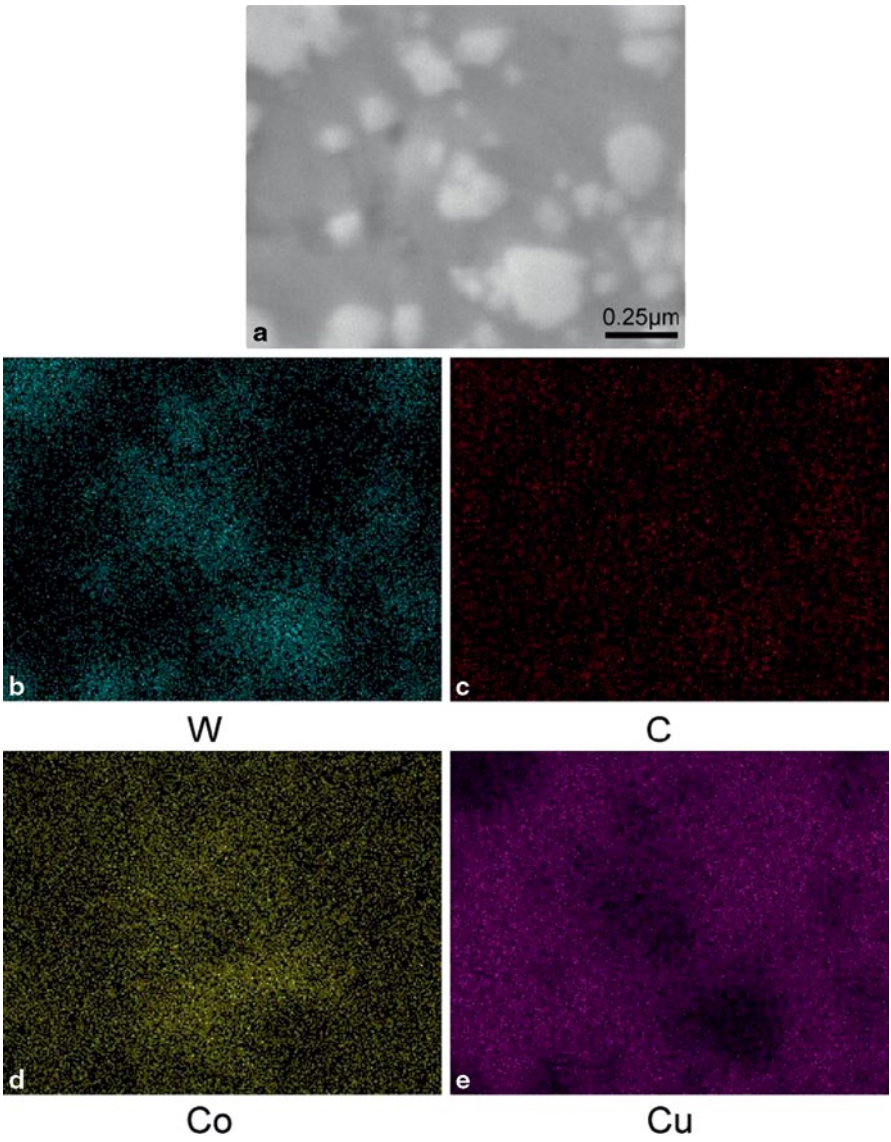


Fig. 8.6 EDX elemental mapping showing distributions of W (**b**), C (**c**), Co (**d**), and Cu (**e**) elements in DMLS-processed (WC–Co)/Cu composite structure (**a**)

Figure 8.7 illustrates the interface design strategy and the attendant formation mechanisms involved in laser sintering of such a (WC–Co)/Cu composite system. During DMLS, the laser energy is directly absorbed by the solid particles through both bulk coupling and powder coupling mechanisms [16], hence heating up the powder particles speedily. For the as-used fine-grained WC–Co composite powder

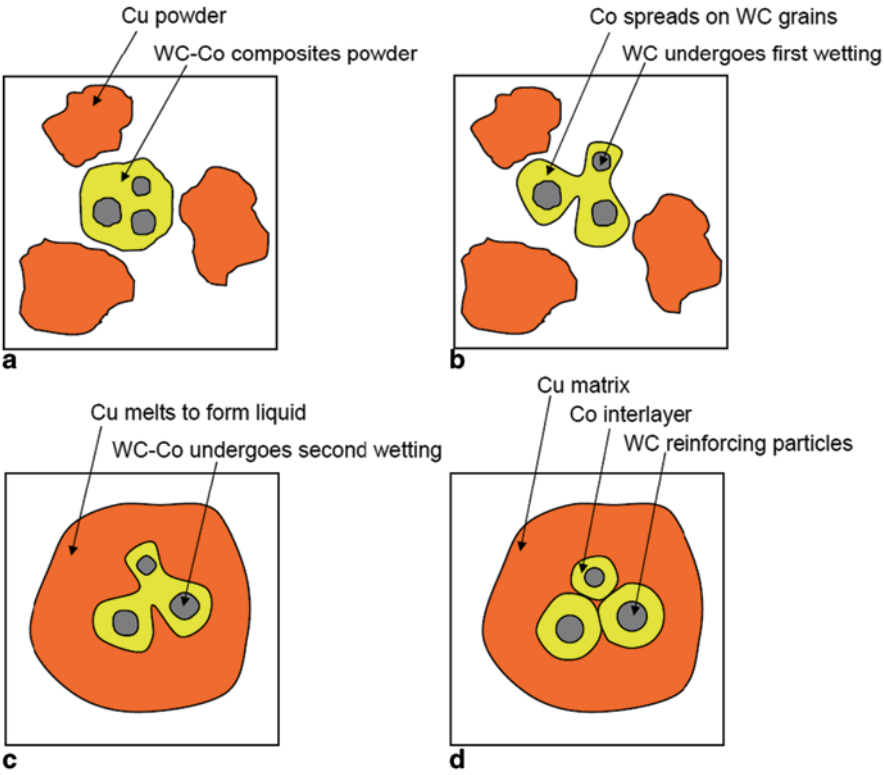


Fig. 8.7 Schematic of interface design and double stages of wetting during DMLS of (WC–Co)/Cu composite system

(Fig. 8.2c), the binder phase Co tends to spread on the WC grains after the sintering temperature reaches ~1000 °C [3], thereby wetting the WC particles primarily (we termed it "first stage of wetting," Fig. 8.7a and b). Here, it is noted that the initially formed Co-coated WC structure in the starting WC–Co composite powder (Fig. 8.2c) also favors the occurrence of the first stage of wetting. A further increase in the working temperature above the melting point of the matrix metal Cu (~1083 °C) leads to a larger degree of melting, forming a molten pool containing both liquid (Cu) and solid (WC) phases in the laser irradiating region. The Co phase in a mushy state is expected to dissolve in the Cu liquid. Since a Gaussian laser beam is used in the sintering, a large temperature gradient tends to form between the center and edge of the molten pool, giving rise to the surface tension gradient and the resultant Marangoni convection [17]. The formation of a significant Marangoni convection induces capillary forces for liquid flow, leading to a further wetting of the WC–Co system by the Cu liquid (we termed it "second stage of wetting," Fig. 8.7c and d). With the action of such double stages of wetting, the WC reinforcing particles experience a favorable wetting and a subsequent sufficient particle

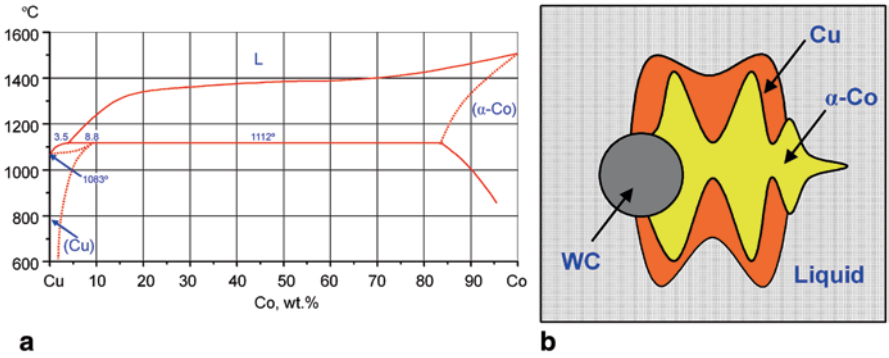


Fig. 8.8 Binary phase diagram of Co–Cu system, see Ref. [18] (**a**); Schematic of microstructural development during Co–Cu peritectic reaction (**b**)

rearrangement, thereby limiting the neighboring WC grains from aggregating and coarsening. Under this condition, a homogenous dispersion of WC nanoparticles in the metal matrix can be easily obtained (Fig. 8.5).

According to the Co/Cu phase diagram (Fig. 8.8a), for the two matrix metals (Cu and Co) in the solidifying system, the high-temperature phase (α-Co) precipitates primarily in some favorable sites around the WC particle surface. Afterward, the Cu phase presents and surrounds the primary phase (α-Co) by means of the peritectic reaction. However, due to the laser-induced nonequilibrium rapid solidification process, the solute has insufficient time to transfer and penetrate the newly developed second-phase (Cu), handicapping a further proceeding of peritectic reaction and, accordingly, retaining the α-Co phase between the WC and Cu phases (Fig. 8.8b). When the operating temperature decreases below the peritectic temperature, the residual liquid phase crystallizes to form Cu phase. Thus, it is reasonable to conclude that the constitutional phases of the matrix metals after DMLS are α-Co and Cu.

In the present study, both the preparation method of the (WC–Co)/Cu composite powder (i.e., the addition of WC reinforcing particles in the form of WC–Co composite powder) and the double stages of wetting and attendant phase development during DMLS favored the formation of the graded interfaces between the WC reinforcing particles and the Cu matrix. It is known that the wetting property of the liquid to the reinforcing phase is essential for formation of a dense laser-processed structure [13]. Since the molten Co has been homogenously spread around the WC reinforcing particles in the first stage of sintering (Fig. 8.7b), the liquid Cu directly contacts the metallic phase Co, rather than the ceramic phase WC. For a metal–metal system, the wetting characteristics are generally better than a metal/ceramic system because of the lower surface energy [19]. Consequently, such a Cu/Co (metal–metal) interface can efficiently improve wettability between the liquid and the reinforcing phases as relative to the Cu/WC (metal–ceramic) interface. In other words, the Cu/Co interface acts as a graded wetting intermedium, through which a

sound metallurgical bonding between the WC particles and the Cu matrix can be obtained. The above presented interfacial design and formation strategy proves to be effective in improving the interfacial bonding and material integrity between the reinforcement and the matrix in DMLS-processed (WC–Co)/Cu composite part.

8.3.2 Influence of DMLS Processing Parameters on Microstructural and Mechanical Properties of $(WC–Co)_p$/Cu Composite Parts

8.3.2.1 Mechanical Properties of (WC–Co)/Cu Parts at Different DMLS Processing Parameters

Figure 8.9 shows the effects of laser power and scan speed on the relative density of the laser sintered (WC–Co)/Cu composite parts. For a given scan speed, there existed a critical laser power of ~700 W, below which the sintered density generally increased with increasing the laser power. For laser powers above the critical value, the sintered density was found to decrease with increasing the laser power, at a constant scan speed. The effect was more pronounced at a lower scan speed.

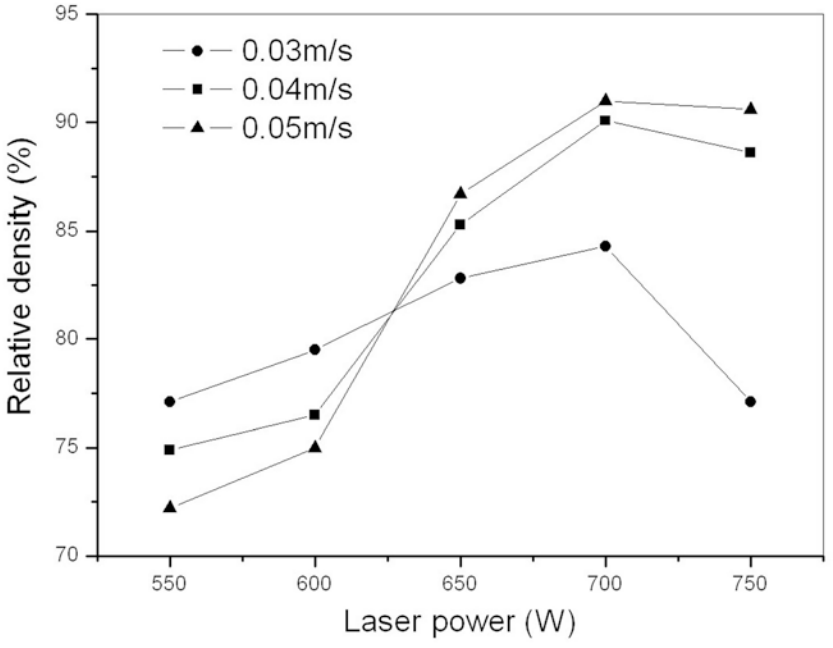


Fig. 8.9 Effects of laser power and scan speed on the relative density of DMLS-processed (WC–Co)/Cu samples. Fixed processing parameter: layer thickness of 0.20 mm

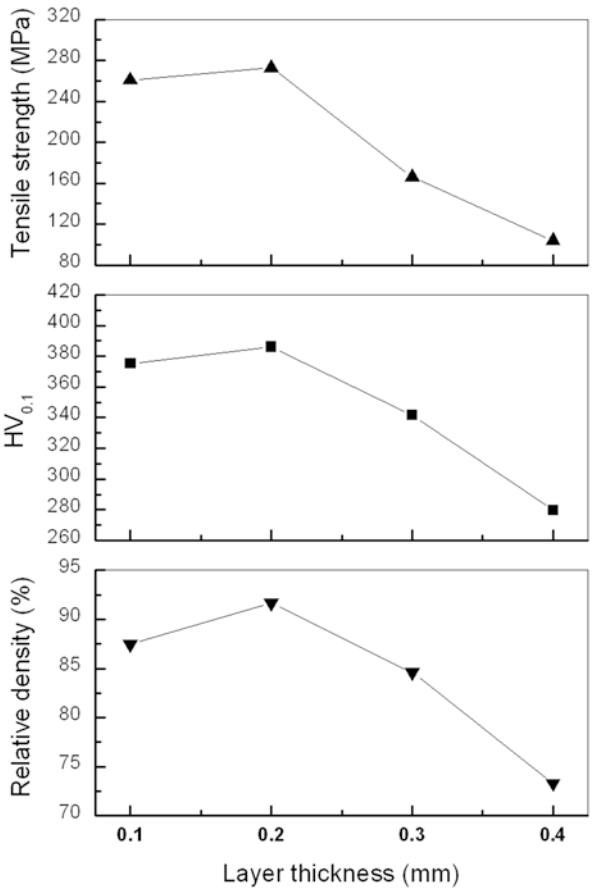


Fig. 8.10 Variations of the relative density, microhardness, and tensile strength of DMLS-processed (WC–Co)/Cu parts with powder layer thickness. Fixed processing parameters: laser power of 700 W; scan speed of 0.05 m/s

Furthermore, a laser power of ~625 W was found to be another critical value, below which the attainable density increased with lowering the scan speed, at a fixed laser power; whereas above which, an opposite trend was exhibited, i.e., lowering the scan speed resulted in a decrease in densification, for a given laser power.

Figure 8.10 depicts the effect of powder layer thickness on the relative density and the resultant mechanical properties of DMLS-processed (WC–Co)/Cu composite parts. The 18.4% theoretical density was improved if lowering the layer thickness from 0.40 to 0.20 mm. However, further lowering the layer thickness below the critical value, 0.20 mm, resulted in a decrease in the obtainable density. The microhardness and tensile strength of DMLS-processed samples, which were equivalent to or superior than conventional powder metallurgy processed Cu and its alloys (microhardness of $HV_{0.1}$120–180 and tensile strength of 200–360 MPa [20]), exhibited a similar trend as density with respect to the powder layer thickness.

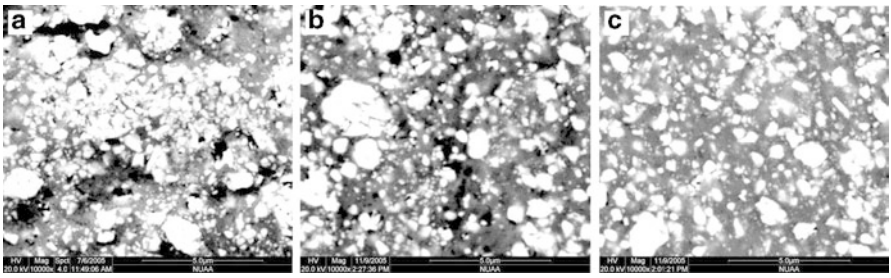


Fig. 8.11 SEM images in back-scattered electron (BSE) mode showing characteristic microstructures of DMLS-processed (WC–Co)/Cu composites at different laser powers: **a** 600 W, **b** 650 W, **c** 700 W. Fixed processing parameters: scan speed of 0.04 m/s; powder layer thickness of 0.20 mm

8.3.2.2 Microstructural Characteristics of (WC–Co)/Cu Parts at Different DMLS Processing Parameters

Figure 8.11 shows the characteristic microstructures of DMLS-processed (WC–Co)/Cu composites prepared at different laser powers. It was clear that the densification and attendant microstructural features such as the shape, amount, and connectivity of pores and the distribution homogeneity of the reinforcing particles depended on the variation of laser powers. At a low laser power of 600 W, the laser-sintered structure was heterogeneous and consisted of large and irregularly shaped pores and significantly aggregated WC particles (Fig. 8.11a). At a higher laser power of 650 W, the less aggregation of WC particles occurred; however, small and interconnected pores were still in visible (Fig. 8.11b). DMLS processing at an even higher laser power of 700 W led to a higher densification with a homogeneous distribution of WC reinforcing particles, showing a coherent bonding ability between the reinforcement and the matrix (Fig. 8.11c).

Figure 8.12 illustrates the typical microstructures of DMLS-processed (WC–Co)/Cu composites using various scan speeds. It was noted that the distribution homogeneity of the WC reinforcing particles was strongly affected by scan speed. The results revealed that there was a critical scan speed of ~0.04 m/s, below which the reinforcing particles generally exhibited a serious aggregation (Fig. 8.12a and b), whereas increasing the scan speed above the critical value led to an improvement in the distribution homogeneity of reinforcing particles (Fig. 8.12c and d).

The tensile fracture surfaces of the laser processed (WC–Co)/Cu composite samples at different layer thicknesses are shown in Fig. 8.13. At a high powder layer thickness of 0.40 mm, a loose fracture surface consisting of large and interconnected pores was observed. The aggregates of the WC reinforcing particles were segregated in local regions and, consequently, the particle–matrix interface debonding would occur easily (Fig. 8.13a). On decreasing the powder layer thickness to 0.30 mm, the fracture surface was smooth and free of apparent cracks, showing characteristics of intercrystalline fracture (Fig. 8.13b). At a low powder layer thickness of 0.20 mm, a number of dimples were visible on the fracture surface, exhibiting a ductile type of fracture of DMLS-processed composite part (Fig. 8.13c).

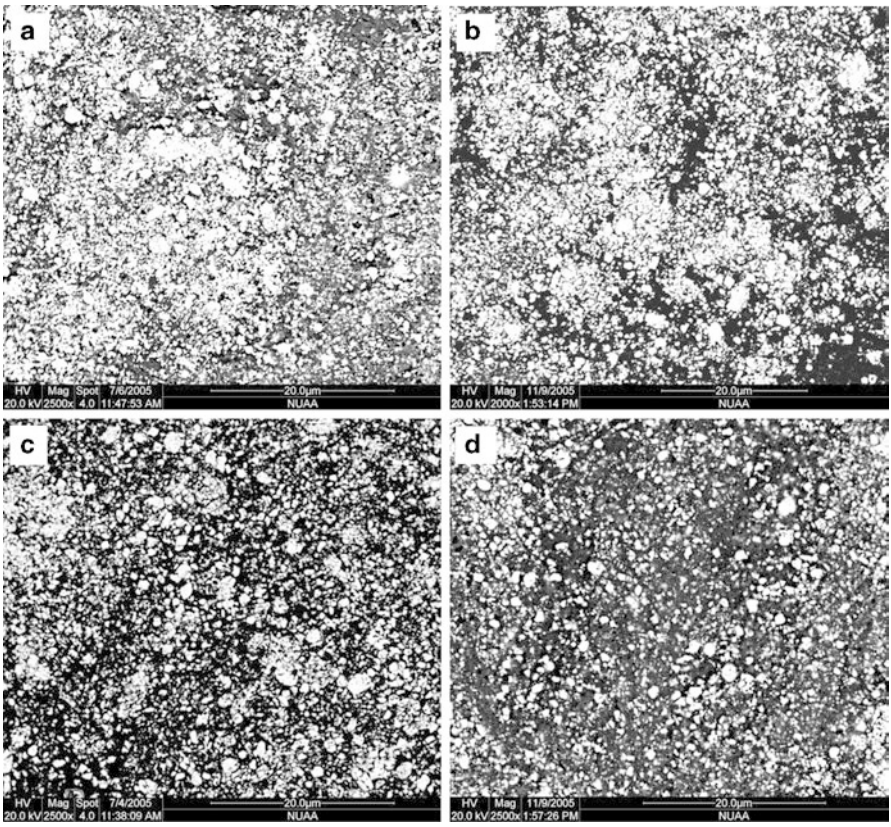


Fig. 8.12 SEM images in BSE mode showing microstructures of DMLS-processed (WC–Co)/Cu composites with variation of scan speeds: **a** 0.02 m/s; **b** 0.03 m/s; **c** 0.05m/s; **d** 0.06 m/s. Fixed processing parameters: laser power of 700 W; layer thickness of 0.20 mm

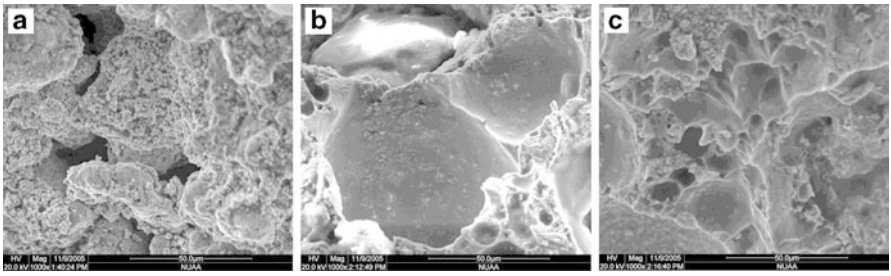


Fig. 8.13 SEM images showing fracture surfaces of DMLS-processed (WC–Co)/Cu composite samples at different layer thicknesses: **a** 0.40 mm; **b** 0.30 mm; **c** 0.20 mm. Fixed processing parameters: laser power of 700 W; scan speed of 0.05 m/s

8.3.2.3 Processing Conditions and Optimization Mechanisms for DMLS of (WC–Co)/Cu Composites

During DMLS, the incident energy of a scanning laser beam causes a selective melting of the matrix metal Cu, forming a molten pool containing both liquid and solid phases. The formation of Marangoni convection in the pool induces capillary forces for liquid flow, facilitating an efficient densification of the reinforcing particles with the wetting liquid. The obtained results, shown in Figs. 8.9 and 8.11, reveal that for a given scan speed, a proper increase in the laser power can leads to a high densification with a homogeneous distribution of the reinforcing particles. Increasing the laser power at a constant scan speed will result in a higher DMLS temperature and, consequently, a larger amount of liquid formation. Therefore, the liquid viscosity and surface tension decreases, and, accordingly, the flow of molten liquid and the rearrangement of reinforcing particles become easier, hence handicapping the reinforcing particles from aggregation (Fig. 8.11c). Also, an increase in the temperature lowers the wetting angle between the liquid and solid phases [21], thereby permitting a better wetting property and thus an improved densification with a coherent interface bonding ability between the reinforcement and the matrix (Fig. 8.11c). However, it is noted that an excessive increase in the laser power (>700 W) at a given scan speed generally lowers the densification (Fig. 8.9). This is mainly caused by the balling effect, a typical process defect involved in DMLS [22]. The occurrence of balling phenomenon implies an excess amount of liquid formation and a local overheating of the DMLS system under the applied processing conditions, which ultimately results in the formation of metallic spheres as a consequence of the surface energy reduction.

On the other hand, the obtained results reveal two different situations concerning the effect of scan speed on the DMLS densification with variation of laser powers. For a relatively low laser power (<625 W), lowering the scan speed leads to a higher densification (Fig. 8.9). Under this condition, the applied laser power is too low to generate sufficient liquid phase. As the scan speed decreases, the amount of energy absorbed by the powder under the laser beam increases, hence causing a larger degree of melting. It is known that the wetting characteristics and the attendant rearrangement force of solid reinforcing particles in the liquid phase increase as the amount of liquid increases [4]. Thus, using a lower scan speed can improve solid–liquid wettability, so as to rearrange the reinforcing particles efficiently in the liquid and achieve a higher DMLS density. Whereas, for a relatively high laser power (>625 W), lowering the scan speed results in a decrease in densification (Fig. 8.9). In this instance, the applied laser power is high enough to form a sufficient amount of the liquid. A decrease in the scan speed, however, results in a significant increase in liquid formation and its lifetime, favoring balling effects and track interruption. Furthermore, the decrease in the obtainable DMLS density is ascribed to the significant aggregation of the reinforcing particles occurred at lower scan speeds (Fig. 8.12a and b). The microdistribution of the reinforcing particles mainly depends on the interactions between the particles and the advancing solid–liquid interface (pushing versus trapping) [23]. The pushing of the reinforcing particles

by the solid–liquid interface results in pile-ups and local segregation of particles at regions finally solidified, while the trapping brings about a uniform distribution of the reinforcing particles in the matrix. Based on the results shown in Fig. 8.12, it is reasonable to consider that the scan speed plays a pronounced effect on the distribution state of the reinforcing particles and there exists a critical speed, ~0.04 m/s, corresponding to the transition of pushing to trapping of the reinforcing particles by the advancing solid–liquid interface. Furthermore, it is noted that increasing the scan speed above the critical value favors the trapping effect (Fig. 8.12c and d). Using a higher scan speed promises a rapid infiltration rate of the liquid into the powder bed, hence facilitating the feeding of fresh melts to the interparticle regions and, accordingly, forming a continuous infiltration front to fill the voids between the reinforcing particles [13]. Thus, the reinforcing particles cease to be pushed by the interface, but are wetted and incorporated in the matrix (i.e., trapped), so as to obtain a homogenous distribution of the reinforcing particles without the apparent segregation.

The fabrication of MMC parts using DMLS requires a proper powder layer thickness to be determined. Large and interconnected pores will be formed in the DMLS-processed structure (Fig. 8.13a) if the powder layer has not been completely melted down because of the insufficient energy penetration of the laser beam. The obtained results reveal that the upper limit of layer thickness is ~0.30 mm for the formation of dense sintered layers. Below the critical value, the interlayer densification can be improved by decreasing the thickness (Fig. 8.13b and c). Under this condition, the partial laser energy is used to remelt the top of the previous layer to obtain a good bonding. It has been shown that the remelting of solidified materials does not contribute to balling effect, while melting of the powder may result in the formation of balls due to the high surface tension effect [24]. For a given laser energy, the thinner the powder layer is, the greater extent to which the previously processed layer remelts, thereby obtaining coherently bonded layers with less balling phenomena. On the other hand, a large amount of air exists in the pores between the particles, and will be trapped as bubbles in the melting powder during DMLS. For a thinner layer, most of air bubbles, even at the bottom of the powder layer, are able to move up to the layer's surface, and collapse when the molten liquid solidifies rapidly, leading to less DMLS porosity. Consequently, the better mechanical properties can be easily obtained using a thinner layer (Fig. 8.10). However, the minimum layer thickness that can be successfully used should be well determined; otherwise the obtainable densification and mechanical properties show a decrease (Fig. 8.10). The useable minimum layer thickness is mainly controlled by the maximum particle size in the powder system. In the present study, lowering the layer thickness to 0.10 mm will result in the difficulty in spreading the homogenous layers of the fresh powder without disturbing previously sintered layers, thus weakening the ultimate DMLS quality.

8.4 Influence of Reinforcement Weight Fraction on Microstructure and Properties of $(WC–Co)_p$/Cu Composite Parts Prepared by DMLS

8.4.1 Effect of Reinforcement Content on Particle Dispersion State and Microhardness and its Distribution

Figure 8.14 shows the characteristic microstructures on the polished sections of DMLS-processed (WC–Co)/Cu composite parts with variation of WC–Co contents. It revealed that the microstructural characteristics of the WC reinforcing particles, in terms of particle shape, particle size, and dispersion homogeneity, were found to be depending on the initial contents of WC–Co. At a low WC–Co content of 20 wt.%, the WC particulates exhibited a slight aggregation, although some dispersed particles were visible in the matrix, thereby resulting in the formation of some small pores in the sintered structure (Fig. 8.14a). As the WC–Co content increased to 30 wt.%, the ultrafine WC reinforcing particles were uniformly dispersed in the matrix without any aggregation, showing a pretty dense and homogeneous microstructure (Fig. 8.14b). However, DMLS processing of a powder system with 40 wt.% WC–Co resulted in a poor sinterability with a serious agglomeration of WC particles and a large amount of porosity (Fig. 8.14c).

Figure 8.15 depicts the profiles of microhardness measured on the corresponding sections of the polished (WC–Co)/Cu parts. The microhardness, which is generally higher than conventional powder metallurgy copper and copper alloys ($HV_{0.1}$120–180) [20], is also associated with the variation of WC–Co contents. A uniform microhardness distribution with a high average value of $HV_{0.1}$391.9 was obtained using 30 wt.% WC–Co (Fig. 8.15b). However, at the WC–Co contents of 20 and 40 wt.%, the microhardness, with the average value being $HV_{0.1}$286.0 and $HV_{0.1}$320.0, respectively, fluctuates considerably (Fig. 8.15a and c).

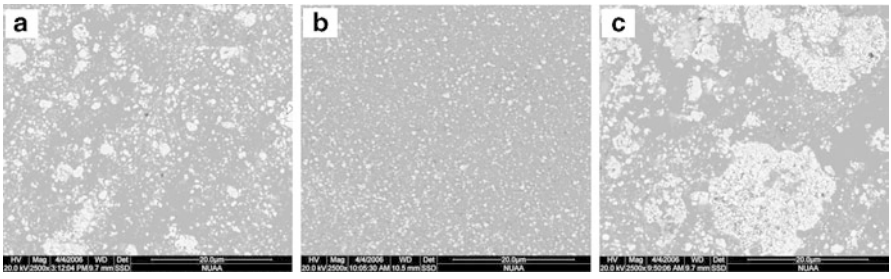


Fig. 8.14 SEM images in BSE mode showing characteristic microstructures on polished sections of DMLS-processed (WC–Co)/Cu composite parts using different contents of WC–Co: **a** 20 wt.%, **b** 30 wt.%, **c** 40 wt.%

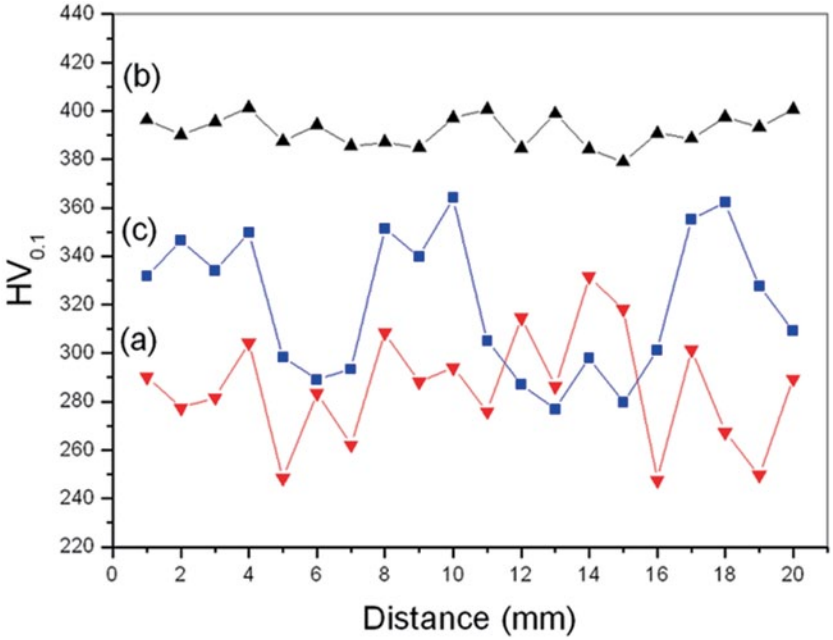


Fig. 8.15 Variations of microhardness on polished sections of DMLS-processed (WC–Co)/Cu composite parts with WC–Co contents: **a** 20 wt.%; **b** 30 wt.%; **c** 40 wt.%

8.4.2 Effect of Reinforcement Content on Particle–Matrix Interfacial Microstructure

Figure 8.16 shows the characteristic particle/matrix interfacial microstructures of DMLS-processed (WC–Co)/Cu composites with variation of WC–Co contents. At a low WC–Co level of 20 wt.%, the reinforcing particulates exhibited a round and smooth shape; however, some deleterious microcracks were visible between the reinforcement and the matrix (Fig. 8.16a). At a high WC–Co content of 40 wt.%, the particle–matrix interface was discontinuous and incompatible, showing a relatively weak interfacial bonding (Fig. 8.16b). Interestingly, the interfacial microstructures of DMLS-processed composites with 30 wt.% WC–Co, as shown in Fig. 8.16c–f, were generally clear and compatible, and free from apparent microcracks. The reinforcing particles, furthermore, were well dispersed and refined, exhibiting a stronger metallurgical bonding with the matrix (Fig. 8.16c–f).

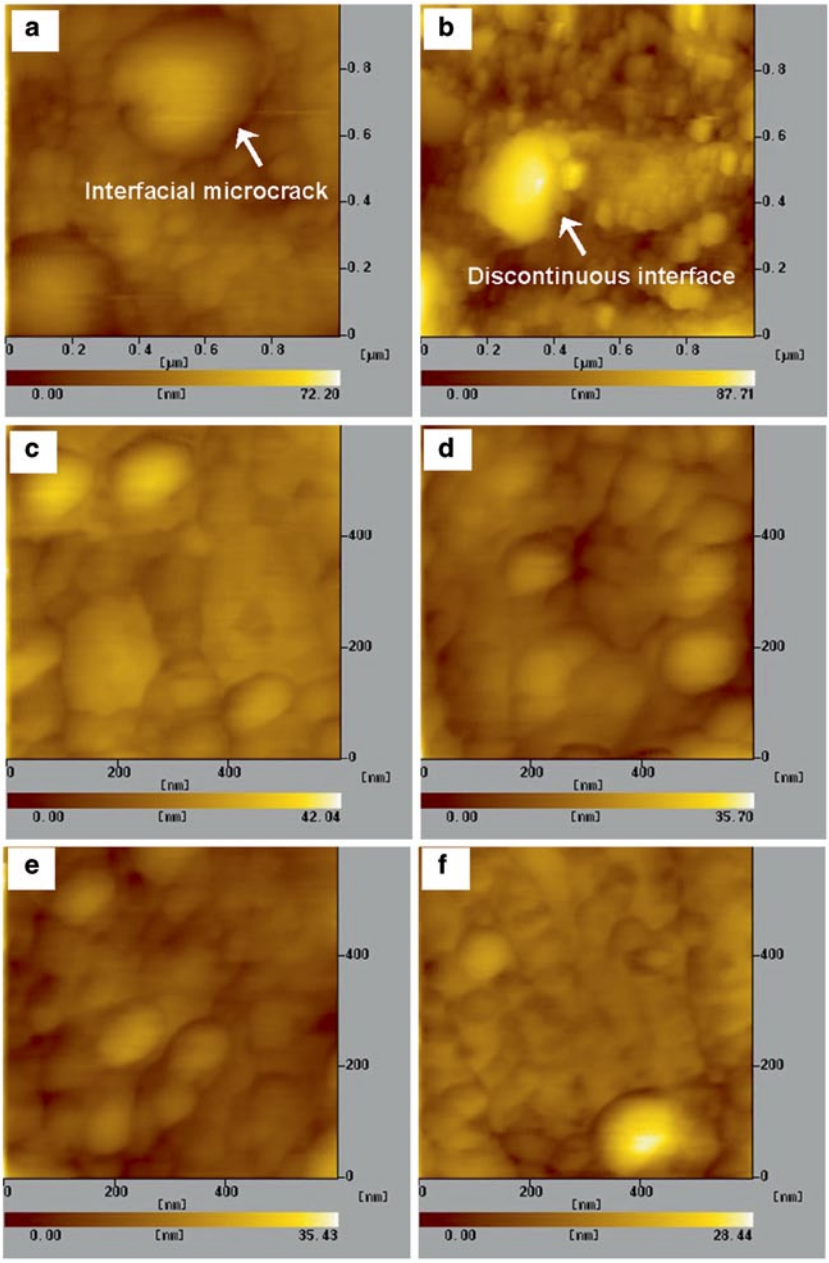


Fig. 8.16 AFM images showing characteristic interfacial microstructures at different WC–Co contents: **a** 20 wt.%; **b** 40 wt.%; **c**–**f** 30 wt.%

8.4.3 *Effect of Reinforcement Content on Tensile Property and Fracture Surface Morphology*

Figure 8.17 depicts the effect of WC–Co content on the relative density and the fracture strength of DMLS-processed (WC–Co)/Cu composite parts. It was clear that increasing the WC–Co content from 20 to 30 wt.% led to an enhancement of the sintered density from 76.4 to 90.3 % theoretical density and the fracture strength from 158 to 256 MPa. Further increasing the WC–Co content to 40 wt.%, however, decreased the obtainable density to 81.6 % theoretical density and the fracture strength to 203 MPa.

Figure 8.18 shows the characteristic microstructures of fracture surfaces of DMLS-processed (WC–Co)/Cu composite parts at different WC–Co contents. At a low WC–Co content of 20 wt.%, the fracture surface consisted of significantly coarsened spherical particles and open and large cracks, showing a porous and heterogeneous structure (Fig. 8.18a). Metallographic study at higher magnification shows the serious aggregation and segregation of the WC reinforcing particles, thereby resulting in an easy debonding of particle–matrix interface (Fig. 8.18b). When 30-wt.% WC–Co was used, a number of dimples were observed in the fracture surface, exhibiting a ductile type of fracture (Fig. 8.18c). In this instance, the WC reinforcing particles were uniformly inserted in the matrix, showing a stronger interfacial bonding (Fig. 8.18d). At a high WC–Co content of 40 wt.%, the fracture surface was mainly characterized by a brittle fracture, although some small dimples were visible (Fig. 8.18e). The WC reinforcing particles, although the distribution state was almost uniform, slightly segregated in local areas of the matrix (Fig. 8.18f).

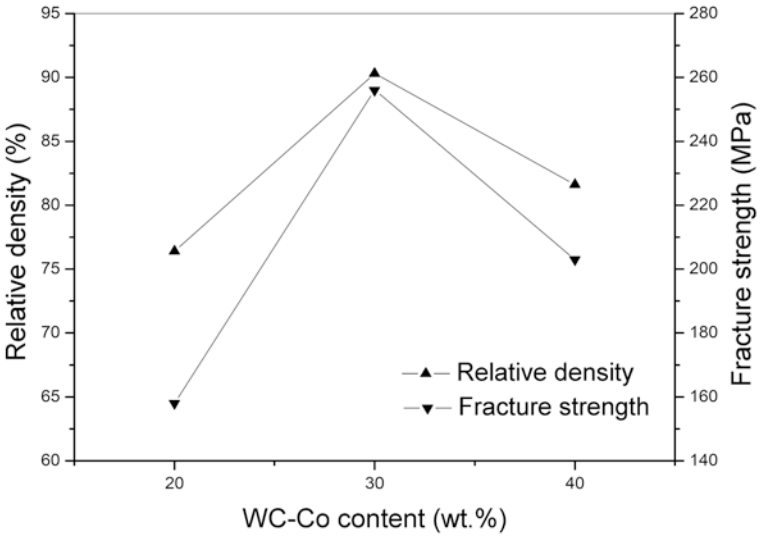


Fig. 8.17 Variations of the relative density and fracture strength of DMLS-processed (WC–Co)/Cu composite parts with WC–Co contents

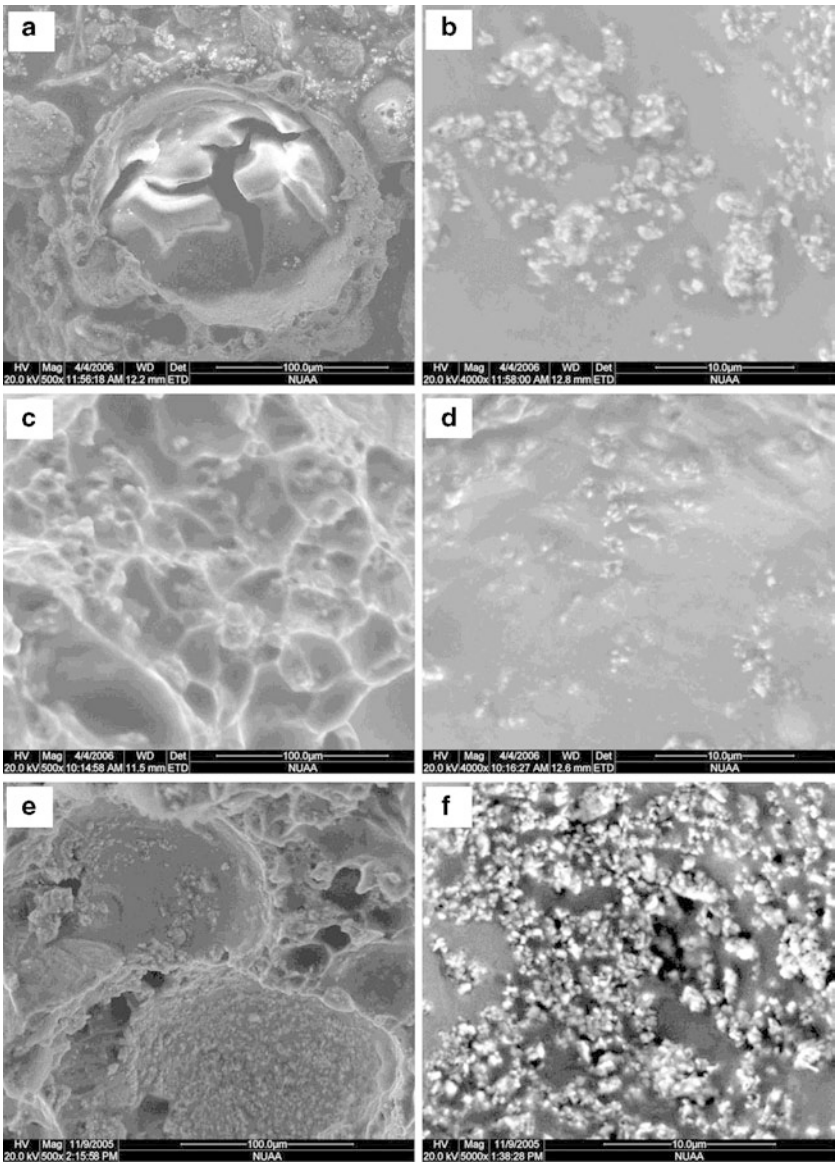


Fig. 8.18 SEM images of fracture surfaces of DMLS-processed (WC–Co)/Cu composite parts at different WC–Co contents: (**a** and **b**) 20 wt.%; (**c** and **d**) 30 wt.%; (**e** and **f**) 40 wt.%

8.4.4 Influencing Mechanisms of Reinforcement Content on Microstructural and Mechanical Properties

It is known that the DMLS is a complex metallurgical process which involves multiple modes of mass, heat, and momentum transfer [7, 17]. The densification level,

microstructural features, and resultant mechanical properties of the laser-processed parts are influenced by both processing parameters (e.g., laser power, scan speed, scan line hatch spacing, powder layer thickness) and materials characteristics (e.g., component ratio, particle shape, particle size and its distribution). Therefore, in order to fabricate the laser-sintered parts with desirable microstructures and properties, both processing conditions and materials characteristics should be optimized. In the present study, the optimization of the weight fraction of reinforcement in the $(WC–Co)_p$/Cu composite system is emphasized. Therefore, the DMLS-processed samples with the three different material combinations (20, 30, and 40 wt.% WC–Co) are prepared. The processing conditions, however, are kept fixed for the three powder systems, since the laser processing parameters, as mentioned above, will also influence the final properties of the laser processed samples. The obtained experimental results reveal some pronounced variations in the laser processed microstructures and properties with the starting component ratios. These differences are mainly ascribed to the variation in the weight fractions of the reinforcement, since the same processing conditions are used for all the prepared samples. The significant influence of reinforcement content can be highlighted as follows.

i. Influence on particle dispersion homogeneity
   It has been shown that the microdistribution of the reinforcing particles mainly depends on the interaction between the solid particles and the advancing liquid flow. This interaction may lead to trapping or pushing of particles by solid–liquid interface. Trapping leads to a uniform distribution of the reinforcing particles, whereas pushing results in segregation of particles at regions finally solidified. At a low WC–Co content, the pushing effect will prevail since the significant Marangoni flow, which is induced by the excessive liquid formation, tends to push the reinforcing particles towards the center of the laser scan track, thereby resulting in the pile-ups and local segregation of particles (Fig. 8.14a). On increasing the reinforcement content, the presence of a larger amount of WC reinforcing particles in the molten pool will influence the Marangoni effect and, thus, the material flow will be restricted. Consequently, the reinforcing particles cease to be pushed by Marangoni flow, but are trapped in the matrix, hence obtaining a homogenous particulate distribution (Fig. 8.14b). However, using even higher reinforcement content (i.e., a relatively low content of matrix metal) will result in a considerably small amount of liquid formation, thereby enhancing the liquid viscosity and surface tension. The Marangoni flow, consequently, is significantly suppressed, hence decreasing the penetration rate of the liquid into the voids between the reinforcing particles and, accordingly, leading to porosity in DMLS-processed structure. Furthermore, the wetting properties between solid and liquid phases will decrease and, accordingly, the rate of particle rearrangement will slow down, resulting in a pronounced aggregation of reinforcing particles and the resultant microhardness fluctuation (Figs. 8.14b and 8.15).
ii. Influence on interfacial characteristics
   During DMLS, the thermodynamic and kinetic characteristics of the reinforcing particles and the matrix metal, such as the coefficient of thermal expansion

(CTE), surface energy, viscosity, and wettability, have an important influence upon the interface bonding characteristics. In the present study, the as-designed Cu/Co (metal–metal) graded interface, due to its lower surface energy, can efficiently improve solid–liquid wettability as compared with the Cu/WC (ceramic–metal) interface. It is noted that at the WC–Co contents of 20 and 30 wt.%, the reinforcing particles generally exhibit round and smooth shape (Fig. 8.16a, c–f). As compared with the starting irregular shaped powder (Fig. 8.2b), it is reasonable to consider that the WC reinforcing particles are well wetted by the liquid. However, the interfacial features between the reinforcing particles and the matrix are found to be depending on the starting WC–Co contents in the powder systems (Fig. 8.16). The obtained results, as shown in Fig. 8.16a, reveal that the interface bonding coherence shows a decrease when a low WC–Co content of 20 wt.% is used. It has been shown that the main strengthening mechanism for particle-reinforced MMCs is transfer of stress from the matrix to the reinforcement through a shear mechanism [23], and a smooth transfer of stresses leads to a compatible interface bonding without microcracks. Gåård et al.'s work [13] confirms that the stress in composites is developed as a consequence of internal constraints caused by different CTE of various phases. According to the Turner model [25], the average CTE, α_t, of multiphase materials can be calculated by the following equation:

$$\alpha_t = \sum_{i=1}^{n} \alpha_i V_i K_i \Big/ \sum_{i=1}^{n} V_i K_i \tag{8.1}$$

where α is the CTE, V the volume fraction, and K the bulk modulus. For the (WC–Co)/Cu composite system as investigated, lowering the reinforcement content (i.e., using a larger amount of matrix metal) leads to a higher average CTE, due to higher CTE of Cu relative to WC (Table 8.2), thereby resulting in thermal microcracks between the reinforcement and the matrix (Fig. 8.16a). Increasing the WC–Co content, whereas, leads to a reduction in average CTE values, which can be attributed to the presence of a larger amount of submicron WC reinforcement possessing a lower CTE value and the excellent ability of the ultra-fine reinforcing particles to effectively constrain the expansion of the matrix. Therefore, a pretty coherent interfacial integrity between the submicron reinforcing particles and the metal matrix is obtained at the WC–Co content of 30 wt.% (Fig. 8.16c–f).

However, it reveals that an increase in WC–Co content to 40 wt.%, although an even lower composite CTE is obtained, cannot lead to a further improvement in the interface bonding properties (Fig. 8.16b). In this instance, it is reasonable to

Table 8.2 Material properties of various components in the powder system

Material	CTE ($\times 10^{-6}$/K)	Absorptance to CO_2 laser
Cu	17.0	0.26
Co	12.5	No available data
WC	6.0	0.48

consider that the influence of the average CTE on the interfacial characteristics is less significant, while the possible causes are as follows. At higher reinforcement content, more WC particles are expected to dissolve in the molten pool due to the higher absorptance to CO_2 laser (Table 8.2) and the ultrafine submicron nature, increasing the viscosity and surface tension of the liquid metal. The significant recrystallization of WC at the front of the advancing liquid–solid interface may decrease the penetration rate of the liquid into the powder bed. Consequently, it is difficult to form a continuous infiltration front to spread and coat the reinforcing particles, decreasing the solid–liquid wetting properties and, accordingly, resulting in a poor densification with an incompatible interfacial integrity (Fig. 8.16b).

iii. Influence on densification and properties
In DMLS process, laser scanning is performed line by line and the laser energy causes melting along a row of powder particles, forming a continuous liquid scan track in shape of cylinder. The diminishing in the surface energy of the cylindrical track is going on until the final equilibrium state of the cylinders through the breaking up of the cylinder into several metallic agglomerates in spherical shape, which is called a balling effect [26]. Since DMLS is a layer-by-layer additive manufacturing process, balling phenomenon occurred in the laser processed materials is a serious impediment to interlayer bonding and causes defects such as curling deformation, delamination, and poor densification [27]. Balling, which is one of the complex problems involved in DMLS process, is significantly influenced by the amount and the viscosity of the melt. Based on Agarwala et al. and Tolochko et al.'s results [21, 28], the viscosity of a solid–liquid mixture, μ, during DMLS can be defined as:

$$\mu = \mu_0 \left(1 - \frac{1-\varphi_L}{\varphi_M}\right)^{-2} \tag{8.2}$$

where μ_0 is a base viscosity that includes temperature terms, φ_L the volume fraction of liquid phase, and φ_M a critical volume fraction of solids above which the mixture has essentially infinite viscosity. During DMLS, particle bonding is controlled by the base viscosity, μ_0, which is a strong temperature-dependent viscosity and decreases with increasing the working temperature. This viscosity should be low enough that liquid completely surrounds the reinforcing particles, so as to obtain a sufficient densification. However, the mixture viscosity, μ, should be high enough to prevent balling phenomena [21], i.e., the excessive molten material with too low melt viscosity tends to cause significant balling. In this study, the presence of balling and thermal cracks at a low reinforcement content of 20 wt.% (Fig. 8.18a) implies an excess amount of liquid phase formation (i.e., an extremely low μ) and a high degree of overheating of the low melting phase. The reinforcing particles severely aggregate during balling process and, accordingly, segregate from the matrix (Fig. 8.18b), resulting in a poor densification and properties (Fig. 8.17). On the other hand, the limited DMLS quality obtained at the reinforcement content of 40 wt.% (Fig. 8.18e and f) is mainly ascribed to an enhanced value of μ_0, which is

caused by a considerably small amount of liquid formation in this instance. The obtained results, as shown in Fig. 8.18c and d, reveal that the combination of controlled μ and low μ_0, which can be realized using 30 wt.% reinforcement, leads to a sound sinterability with little or no balling during DMLS.

8.5 Influence of Processing Parameters on Particle Dispersion in $(WC–Co)_p$/Cu Composite Parts Prepared by DMLS

8.5.1 Process Map for Particle Dispersion in DMLS-processed $(WC–Co)_p$/Cu Composites

In the present study, a series of DMLS-processed samples were prepared under different processing parameters (indicated by different symbols in Fig. 8.19), in order to establish the process window in which laser sintering is able to generate a uniform distribution of particles in the $(WC–Co)_p$/Cu composites. The changes of

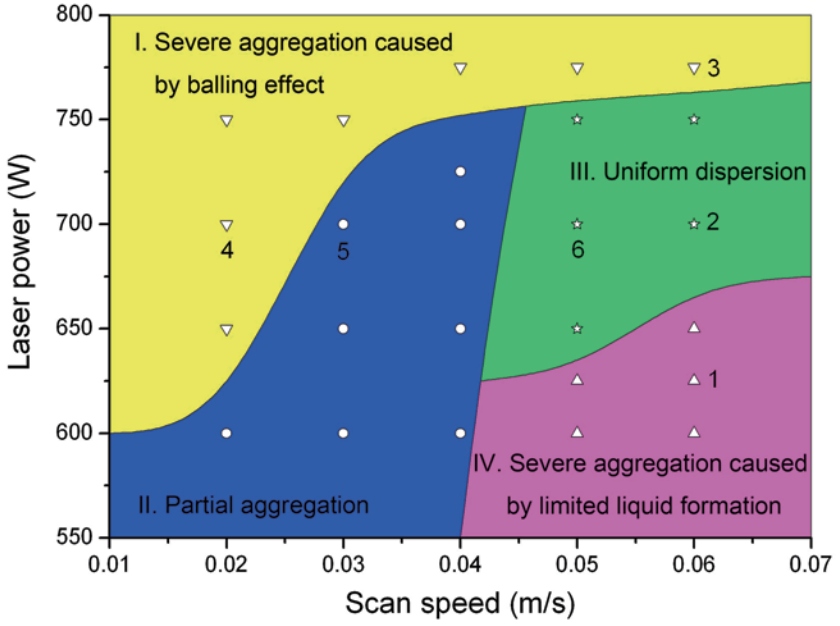


Fig. 8.19 Process windows for dispersion states of reinforcing particles over a wide range of laser powers and scan speeds. Laser sintering using processing parameters denoted by *inverted triangles* results in severe aggregation of particles caused by balling effect; laser sintering using processing parameters denoted by *circles* leads to partial aggregation of particles; laser sintering using processing parameters denoted by *stars* yields uniform dispersion of particles; laser sintering using processing parameters denoted by *upright triangles* results in severe aggregation of particles caused by limited liquid formation

the dispersion states of the reinforcing particles in DMLS-processed samples under different processing conditions are depicted in Fig. 8.19. Over the entire range of laser powers and scan speeds, the following four process windows are defined.

i. Severe aggregation caused by balling effect: At a relatively high laser power for all scan speeds, a considerably high energy input leads to a large amount of liquid formation with a too low melt viscosity, resulting in the interruption of liquid scan tracks into rows of spheres due to significant surface tension effects ("balling" effect). The reinforcing particles aggregate severely during balling process, resulting in a nonuniform dispersion of the reinforcement in the matrix.
ii. Partial aggregation: At a relatively low laser power combined with a lower scan speed, the delivered energy density of the laser beam is moderate, thereby forming a suitable amount of liquid phase to avoid balling effect. However, the used lower scan speed limits the sufficient trapping of the particles by an advancing liquid–solid interface, resulting in a partial aggregation of the reinforcing particles in the finally solidified metal matrix.
iii. Uniform dispersion: Laser sintering at a suitable laser power (~650–~750 W) generates a sufficient amount of liquid phase; and, meanwhile, a higher scan speed (>0.04 m/s) favors the particle trapping effect, leading to a homogeneous distribution of the reinforcement in the matrix.
iv. Severe aggregation caused by limited liquid formation: At a lower laser power combined with a higher scan speed, a significantly low energy input results in an insufficient liquid formation with a high melt viscosity, hence decreasing the capillary forces for particle rearrangement and, ultimately, resulting in a serious aggregation of the reinforcing particles after DMLS.

8.5.2 *Microstructural Development of Particle Dispersion in DMLS-Processed $(WC–Co)_p$/Cu Composites*

Figure 8.20 shows the characteristic microstructures on the polished sections of (WC–Co)/Cu composite parts processed at different laser powers. The typical morphologies of the WC reinforcing particles in the corresponding samples are pro-

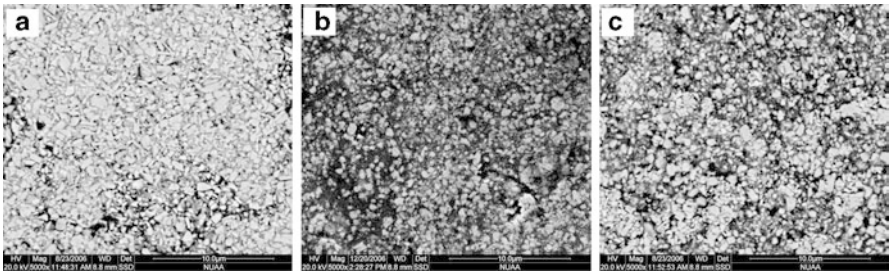


Fig. 8.20 SEM images in BSE mode showing characteristic microstructures of DMLS-processed (WC–Co)/Cu composites at different laser powers: **a** 625 W (point 1 in Fig. 8.19); **b** 700 W (point 2); **c** 775 W (point 3). Fixed processing parameters: scan speed 0.06 m/s and layer thickness 0.20 mm

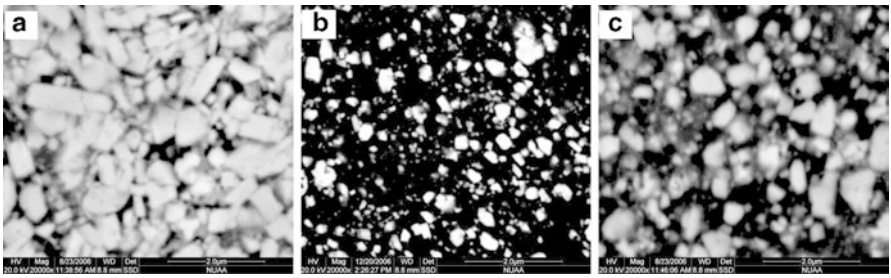


Fig. 8.21 SEM images in BSE mode showing characteristic morphologies of WC reinforcing particles at different laser powers: **a** 625 W (point 1 in Fig. 8.19); **b** 700 W (point 2); **c** 775 W (point 3). Fixed processing parameters: scan speed 0.06 m/s and layer thickness 0.20 mm

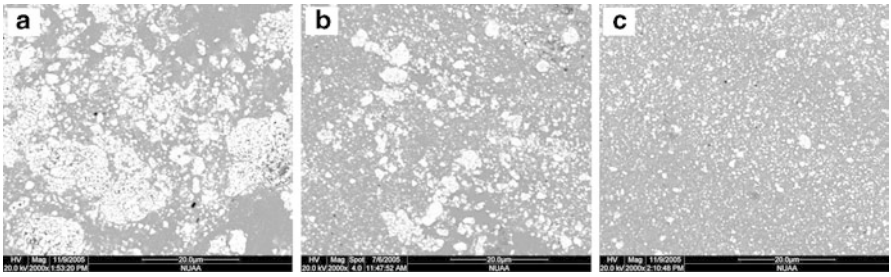


Fig. 8.22 SEM images in BSE mode showing characteristic microstructures of DMLS-processed (WC–Co)/Cu composites with variation of scan speeds: **a** 0.02 m/s (point 4 in Fig. 8.19); **b** 0.03 m/s (point 5); **c** 0.05 m/s (point 6). Fixed processing parameters: laser power 700 W and layer thickness 0.20 mm

vided in Fig. 8.21. It revealed that the dispersion states and microstructural features of the WC reinforcing particles are significantly influenced by the laser power. At a low laser power of 625 W (point 1 in region IV), the WC reinforcing particles exhibited a serious agglomeration (Fig. 8.20a) and had an irregular polygonal shape with a particle size larger than 1 μm (Fig. 8.21a). DMLS processing at a higher laser power of 700 W (point 2 in region III) favored the deagglomeration of clusters of particles, leading to a pretty homogeneous distribution of particles possessing significantly smoothened surfaces (Figs. 8.20b and 8.21b). However, at an even higher laser power of 775 W (point 3 in region I), although the WC reinforcing particles were partially smoothened (Fig. 8.21c), the large clusters of the WC reinforcing particles were visible in the matrix (Fig. 8.20c).

Figure 8.22 shows the characteristic microstructures on the polished sections of DMLS-processed (WC–Co)/Cu composites at different scan speeds. The etched microstructures on the corresponding sections are exhibited in Fig. 8.23. It was clear that the distribution states of the WC reinforcing particles and the dendritic growth morphologies of the matrix metal varied with the applied scan speeds. At a low scan speed of 0.02 m/s (point 4 in region I), the significantly coarsened clusters of the WC reinforcing particles were visible (Fig. 8.22a). Such particle clusters

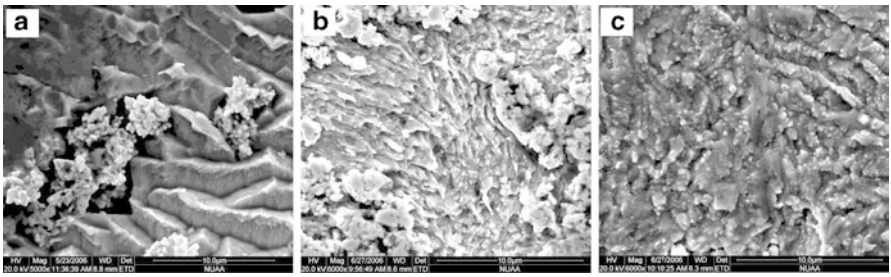


Fig. 8.23 SEM images showing characteristic microstructures of etched samples with variation of scan speeds: **a** 0.02 m/s (point 4 in Fig. 8.19); **b** 0.03 m/s (point 5); **c** 0.05 m/s (point 6). Fixed processing parameters: laser power 700 W and layer thickness 0.20 mm

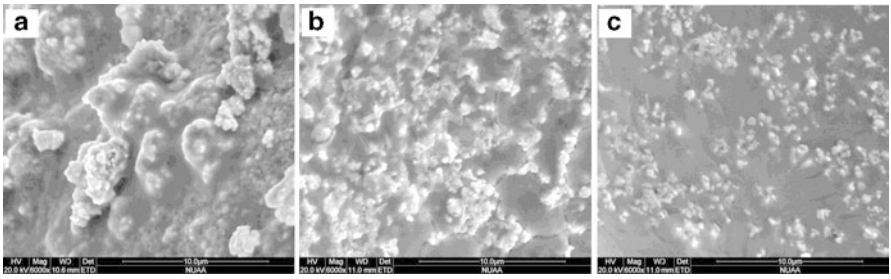


Fig. 8.24 SEM images showing dispersions of WC reinforcing particles on fracture surfaces of DMLS-processed (WC–Co)/Cu composite parts at different powder layer thicknesses: **a** 0.30 mm; **b** 0.25 mm; **c** 0.20 mm. Fixed processing parameters: laser powder 700 W and scan speed 0.06 m/s

were pushed by the growing dendrites and segregated toward the tips of dendrites (Fig. 8.23a). On increasing the scan speed to 0.03 m/s (point 5 in region II), the dispersion homogeneity of the WC reinforcing particles was improved, although some small-scaled aggregates were still visible (Fig. 8.22b). In this case, the WC reinforcing particles ceased to be pushed, but started to be incorporated into the growing dendrites (Fig. 8.23b). Interestingly, the DMLS at a higher scan speed of 0.05 m/s (point 6 in region III) led to an almost uniform dispersion of the fine WC reinforcing particles (Fig. 8.22c). The dendrites of the matrix metal were well developed and the WC reinforcing particles were completely trapped in the dendrites (Fig. 8.23c).

Figure 8.24 illustrates the characteristic dispersion states of the WC reinforcing particles on the fracture surfaces (i.e., cross sections) of DMLS-processed (WC–Co)/Cu composite parts at different powder layer thicknesses. At a relatively high powder layer thickness of 0.30 mm, the fracture surface was consisted of large and coarsened clusters of the reinforcing particles, showing a heterogeneous microstructure (Fig. 8.24a). On decreasing the layer thickness to 0.25 mm, the WC reinforcing particles started to be refined and dispersed (Fig. 8.24b). At a low layer thickness of 0.20 mm, the WC reinforcing particles were uniformly inserted in the matrix, exhibiting a homogenous distribution state (Fig. 8.24c).

8.5.3 *Mechanisms of Particle Dispersion in DMLS-processed $(WC–Co)_p$/Cu Composites at Different Processing Parameters*

The obtained results, as shown in Figs. 8.19, 8.20, 8.21, 8.22, 8.23, and 8.24, reveal that the applied processing parameters, e.g., laser power, scan speed, and layer thickness, significantly influence the particle dispersion in DMLS-processed MMCs. The different microstructures are related to the variation in the thermodynamic and kinetic characteristics, such as solid–liquid wettability, solid-interface interaction, and particle rearrangement, during DMLS. Therefore, it is necessary to rule out the exact reasons why the particles aggregate or disperse under certain processing conditions.

8.5.3.1 Influence of Laser Power on Solid–liquid Wettability

It is known that the excellent wetting characteristics of the solid phase by the liquid phase are crucial in obtaining a uniform dispersion of the reinforcement in the finally solidified matrix. The obtained results, as shown in Figs. 8.19, 8.20, and 8.21, reveal that for a given scan speed, a proper increase in the laser power can homogenize the dispersion of particles. According to Eq. 8.2, increasing the laser power at a constant scan speed leads to a higher DMLS temperature and, accordingly, a lower μ_0. Also, an increase in the operating temperature results in a larger amount of liquid formation, i.e., a higher φ_L. Both a lower μ_0 and a higher φ_L lead to a lower mixture viscosity μ, thereby facilitating a sufficient removal of the molten liquid in conjunction with solid particles. Under this condition, the liquid can successfully surround the reinforcing particles, hence increasing the liquid–solid wettability and the amount of particle rearrangement. The clusters of reinforcing particles, therefore, undergo a significant deagglomeration (Fig. 8.20a and b), hence changing from the severe aggregation to the uniform dispersion in the finally solidified metal matrix (Fig. 8.19). Meanwhile, the edges of irregularly shaped reinforcing particles are expected to dissolve in the wetting liquid, leading to the smoothening of particle surfaces (Fig. 8.21a and b).

On the other hand, since laser scanning is carried out line by line, the laser energy causes melting along a row of powder particles, hence forming a continuous liquid scan track in a cylindrical shape. The liquid track is likely to break up into a row of spheres in order to diminish the surface tension ("balling" effect). According to Agarwala et al.'s results [21], the balling effect is controlled by the mixture viscosity μ. This viscosity should be high enough to prevent balling during DMLS. However, using an even higher laser power at a fixed scan speed tends to induce an excessive amount of liquid formation, since there is an effect of remelting that may take place on previously processed layer when a higher energy input is used. In this instance, although the particle surfaces become smooth due to the favorable wetting behavior of reinforcing particles (Fig. 8.21c), the mixture viscosity μ decreases

overmuch, hence causing the significant balling. The reinforcing particles tend to aggregate severely during balling process, resulting in a heterogeneous distribution of the reinforcing particles in the matrix (Fig. 8.20c).

8.5.3.2 Influence of Scan Speed on Particle–Interface Interaction

In general, the laser-induced melting of such a composite system is followed by a non-unidirectional solidification process which is characterized by the rapid growth of dendrites [29]. This is because (i) a local destabilization of an initially planar solid–liquid interface caused by the different thermal conductivities and specific heats of the solidifying matrix and the particle material is inherent to the solidification process of a composite system; (ii) the laser generated turbulence (i.e., Marangoni flow) in the melt pool will easily destroy such a planar solidification interface. The dendritic interface morphology during solidification introduces a new mode of particle–interface interaction in the melt pool, i.e., the interaction between the particles and the growing dendrites. It is known that during unidirectional solidification process, the particle–interface interaction proceeds with a planar solidification front, since the particles have only one degree of freedom [30]. In this instance, the particles are either pushed or trapped by the advancing solidification front, due to the negligible settling velocity of small particles [31]. It is obvious that the pushing results in pile-ups and local aggregation of particles at regions finally solidified, whereas the trapping brings about a uniform dispersion of the particles in the matrix. In the case of dendritic solidification, however, the mechanisms of particle–interface interaction change significantly, because the lateral migration of the particles into the inter-dendritic regions becomes possible. Therefore, the velocity of the dendrite tip and the lateral growth velocity of the dendrite trunk should be taken into account in the analysis of the particle-interface interaction during dendritic solidification.

During laser-induced solidification process, the local growth rate of dendrite tip is directly proportional to laser beam scan speed and can be expressed by Eq. 4.1. A close look at the obtained experimental results, as shown in Figs. 8.19, 8.22 and 8.23, reveals that the scan speed plays a significant role in determining the growth velocity of dendrites and, thus, the crystalline morphologies of dendrites and attendant particle dispersion states. The mechanisms of the particle–dendrite interaction at different scan speeds can be classified into the following three categories, as schematically shown in Fig. 8.25.

i. Pushing: At a low laser scan speed, i.e., a small dendritic growth velocity, the reinforcing particles are rejected by a moving dendritic interface; that is, they are pushed ahead into the liquid, traveling along with the interface as it advances. These particles inevitably impinge upon other particles in the liquid, resulting in pile-ups which extend a number of particles in the direction normal to the dendritic interface (Fig. 8.23a). Consequently, the significantly coarsened particle aggregates are segregated along grain boundaries after solidification (Figs. 8.22a and 8.25a).

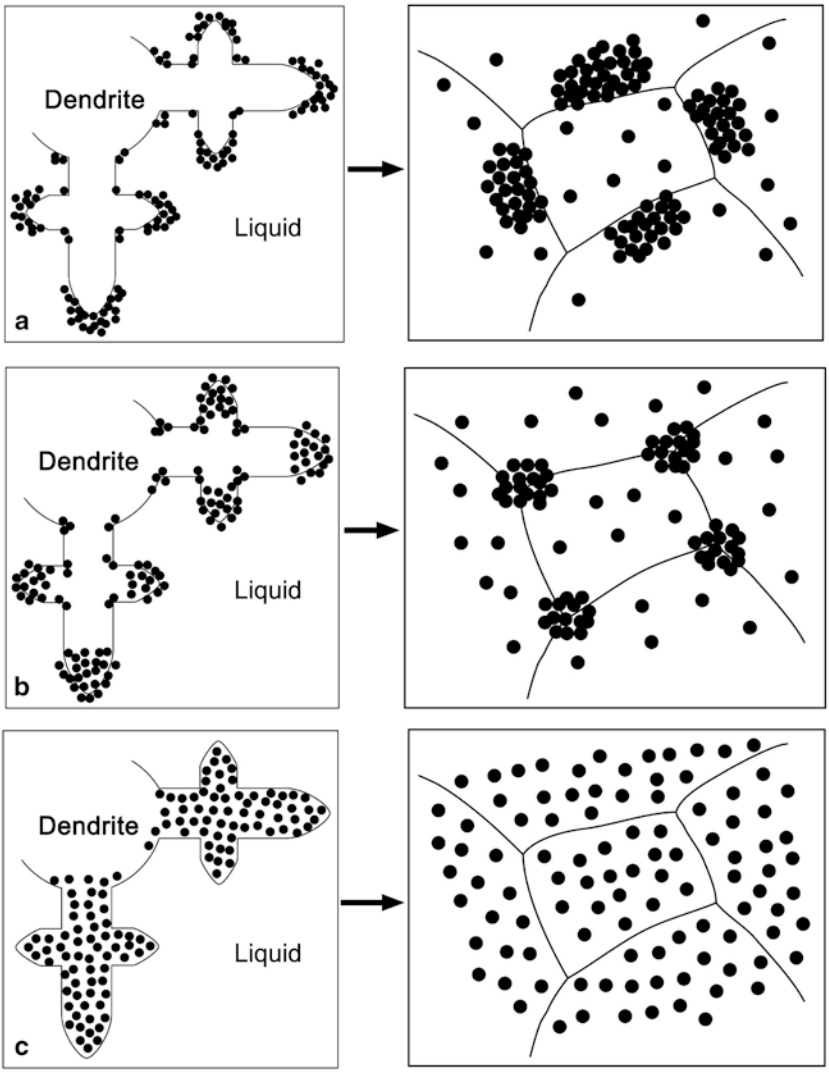


Fig. 8.25 Mechanisms of particle–dendrite interactions and the resultant dispersion states of reinforcing particles: **a** pushing, aggregated; **b** semiengulfment, partially aggregated; **c** trapping, dispersed

ii. Semiengulfment: On increasing the scan speed, some reinforcing particles start to be entrapped by the tip of the dendrite trunk and the first side branches near the trunk (Fig. 8.23b), because of a larger degree of dendrite thickening and side branch coarsening caused by a higher dendritic growth velocity. Such entrapped particles can eventually get incorporated in the metal matrix, whereas other particles that are pushed by the advancing dendritic interface dwell near the interior of grains after complete solidification (Figs. 8.22b and 8.25b).

iii. Trapping: As the scan speed increases above a critical one of ~0.04 m/s (Fig. 8.19), the reinforcing particles cease to be pushed by the advancing dendritic interface, but are well incorporated in the growing dendrite trunk and the side branches (Fig. 8.23c), thereby leading to a uniform dispersion of the reinforcing particles in the solidified metal matrix on cooling (Figs. 8.22c and 8.25c).

Therefore, it is reasonable to conclude that a successive transition from pushing to semi-engulfment and, subsequently, to trapping of the particles by the dendritic solidification front occurs on increasing the scan speed, leading to a change of the particle dispersion states from the severe aggregation to the partial aggregation and, afterwards, to the uniform dispersion. For a given laser power between ~650 and ~750 W, there exists a critical scan speed, ~0.04 m/s, above which the particles are much easy to be trapped by the mobile dendritic interface (Figs. 8.19, 8.22c, and 8.23c).

8.5.3.3 Influence of Powder Layer Thickness on Metallurgical Behavior of Melt Pool

As addressed in Sect. 8.3.2, in order to obtain a high DMLS densification with a coherent inter-layer bonding ability, a suitable powder layer thickness (<0.40 mm), which is less than the thermal penetration depth of the laser beam, is required to allow the input laser energy reaching the bottom of the powder layer. In the present study, although the applied powder layer thicknesses are generally less than 0.40 mm, i.e., within the thermal penetration depth of the laser beam, the particle dispersion states in the DMLS-processed structures vary considerably with the used powder layer thickness (Fig. 8.24). Here, it should be pointed out that although the shape and size of the melt pools cannot be observed directly in the solidified structures, the characteristic morphologies of the reinforcing particles (Fig. 8.24) can well reflect the metallurgical behaviors of the reinforcing particles in the different melt pools during DMLS.

Since the delivered laser energy can well penetrate and melt the powder layer, the depth of the formed melt pool increases with increasing the powder layer thickness. Meanwhile, the energy density of the laser beam is constant, because of the same laser power and scan speed applied. For a given energy input, an increase in the depth of the melt pool weakens the laser induced Marangoni convection and the attendant liquid capillary forces, thereby slowing down liquid flow and particle arrangement. Consequently, the reinforcing particles are much likely to settle to the bottom of the melt pool under the action of the gravity force, resulting in a severe aggregation and a local segregation of the reinforcing particles (Fig. 8.26). In other words, a proper decrease in the powder layer thickness facilitates an improvement in the thermodynamic and kinetic characteristics of both molten liquid and solid reinforcing particles in the melt pool during DMLS, so as to obtain a more homogeneous dispersion of the reinforcing particles in the matrix metal on cooling (Fig. 8.24).

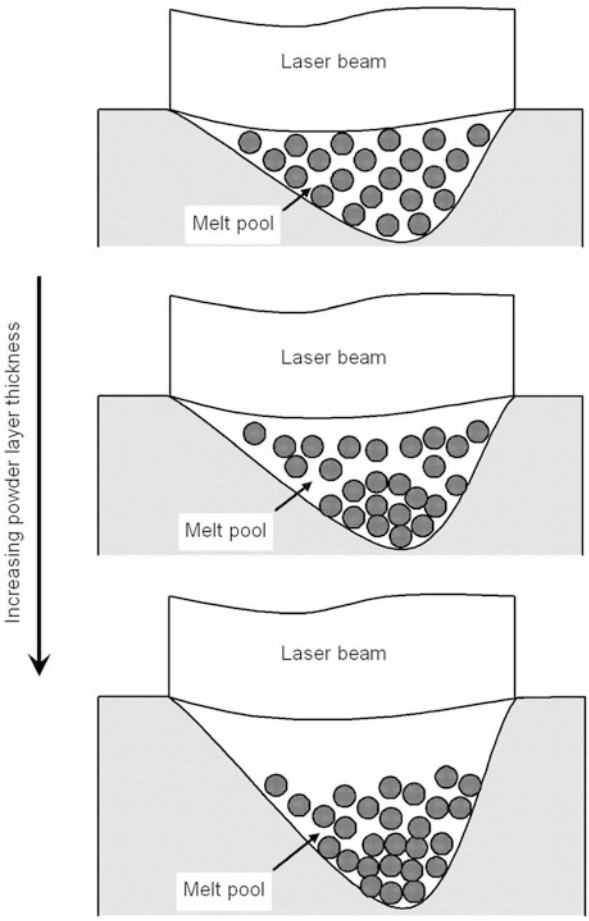


Fig. 8.26 Schematic of DMLS behaviors of reinforcing particles in melt pools at different powder layer thicknesses

8.6 The Role of Rear Earth (RE) La_2O_3 Addition in DMLS Processing of Submicron $(WC–Co)_p$/Cu Composite Parts

8.6.1 Phase Identification of DMLS-processed $(WC–Co)_p$/Cu Composites Containing Various Contents of La_2O_3

Rare earth (RE) elements, due to their unique physical and chemical properties, have been called the "vitamins" of metals, which means that a small number of RE elements can greatly enhance the properties of metals such as processability, mechanical property, and high-temperature behavior [32]. The introduction of RE elements in laser processing of particle-reinforced MMCs is a new direction in broadening their application fields. Also, the process problems associated with

DMLS-processed MMCs, such as the insufficient densification response, the severe particle aggregation, and resultant crack formation between the reinforcement and the matrix, are expected to be resolved by using RE elements. This section presents a detailed investigation of the influence of RE element in the form of La_2O_3 on densification, microstructure and mechanical properties of direct laser sintered (WC–Co)/Cu MMCs parts, with the aim of evaluating the exact metallurgical mechanisms of RE elements in changing the DMLS behavior of particle-reinforced MMCs.

DMLS processing of the (WC–Co)/Cu composites consisting of four different contents of La_2O_3 (0, 0.5, 1.0, and 1.5 wt.%) was performed. Figure 8.27 depicts the typical XRD spectra of DMLS-processed samples with variation of La_2O_3 contents. In general, the strong diffraction peaks of WC (hexagonal structure) and Cu (fcc structure) were clearly observed. Thus, it could be preliminarily considered that the laser sintered MMCs were mainly composed of WC and Cu phases. The diffraction peaks for Co were not detected in laser-sintered samples, due to its relatively small amount in the starting powder systems. Furthermore, Fig. 8.27b–d revealed that the La element was retained in the initial form of La_2O_3 after DMLS. On increasing the

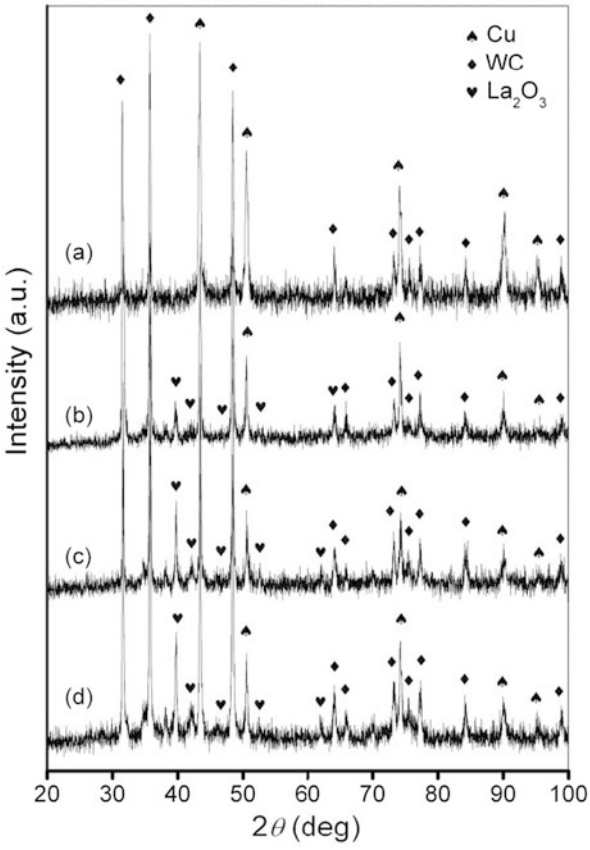


Fig. 8.27 XRD spectra of DMLS-processed (WC–Co)/Cu composites containing different contents of La_2O_3 addition: **a** 0 wt.%, **b** 0.5 wt.%, **c** 1.0 wt.%, **d** 1.5 wt.%

starting La_2O_3 additions, the intensity of La_2O_3 diffraction peaks in laser sintered samples showed a significant increase.

8.6.2 *Densification Response of DMLS-processed $(WC–Co)_p$/Cu Composites Containing Various Contents of La_2O_3*

The typical low-magnification microstructures of the polished samples at different La_2O_3 contents are provided in Fig. 8.28. Figure 8.29 depicts the influence of La_2O_3 contents on DMLS densification levels. DMLS processing of the powder system without La_2O_3 produced a large amount of interconnected pore channels (Fig. 8.28a), resulting in a considerably low sintered density of 79.8% theoretical density (Fig. 8.29). When 0.5 wt.% La_2O_3 was added, the DMLS density improved markedly to 87.6% theoretical density, although some small-sized pores were still visible in the laser-processed structure (Fig. 8.28b). As the La_2O_3 content increased to 1.0 wt.%, the sintered structure was pretty dense and free of any apparent pores (Fig. 8.28c), leading to a high densification of 92.3% theoretical density. However,

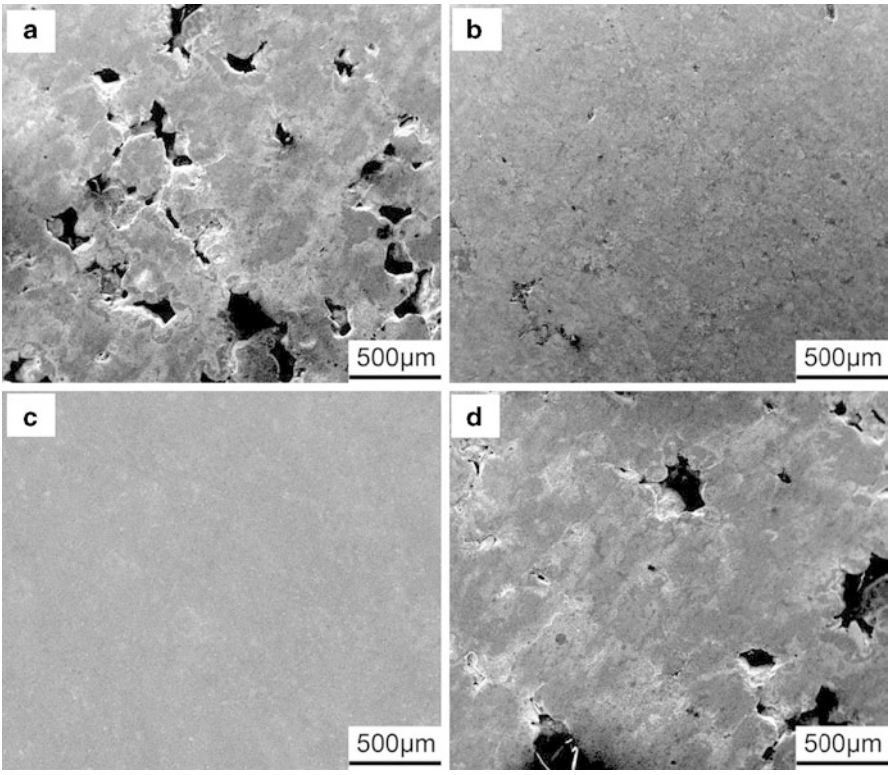


Fig. 8.28 Low-magnification SEM images showing microstructures of polished samples with different additions of La_2O_3: **a** 0 wt.%; **b** 0.5 wt.%; **c** 1.0 wt.%; **d** 1.5 wt.%

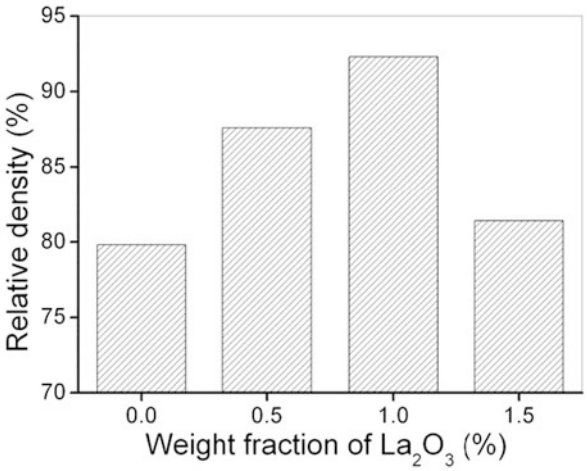


Fig. 8.29 Change of relative density of DMLS-processed (WC–Co)/Cu composites with La_2O_3 contents

at an even higher La_2O_3 content of 1.5 wt.%, the significantly coarsened pores were formed (Fig. 8.28d), resulting in a sharp decrease of the DMLS density to 81.4% theoretical density (Fig. 8.29).

8.6.3 Particle Dispersion and Particle Morphology of DMLS-processed $(WC–Co)_p$/Cu Composites Containing Various Contents of La_2O_3

Figure 8.30 shows the characteristic high-magnification microstructures on polished sections of DMLS-processed (WC–Co)/Cu samples with various La_2O_3 contents. Figure 8.31 depicts the profiles of microhardness measured on the corresponding sections. The EDX spot analyses revealed that the dispersed white particles were composed of W and C elements with a near isoatomic proportion, while the surrounding gray matrix was rich in Cu and Co elements. Combined with XRD results (Fig. 8.27), it was reasonable to conclude that the WC particle-reinforced MMCs could generally be prepared. However, the dispersion states of the WC reinforcing particles and resultant microhardness distributions were significantly influenced by La_2O_3 additions. When no La_2O_3 was added, the WC reinforcing particles agglomerated severely in the matrix (Fig. 8.30a), resulting in a significant fluctuation of microhardness with a considerably low average value of $HV_{0.1}$246.8 (Fig. 8.31a). By adding 0.5 wt.% La_2O_3, the particle dispersion became more uniform, although a fraction of WC reinforcing particles were still aggregated (Fig. 8.30b). With 1.0 wt.% La_2O_3 added, the highly fine WC reinforcing particles were homogeneously dispersed in the matrix, showing very little aggregation (Fig. 8.30c). On increasing the La_2O_3 content from 0.5 to 1.0 wt.%, the microhardness distribution became more homogeneous and, moreover, the average value increased from $HV_{0.1}$349.8 to $HV_{0.1}$403.5 (Fig. 8.31b and c). However, a further addition of 1.5 wt.% La_2O_3 could

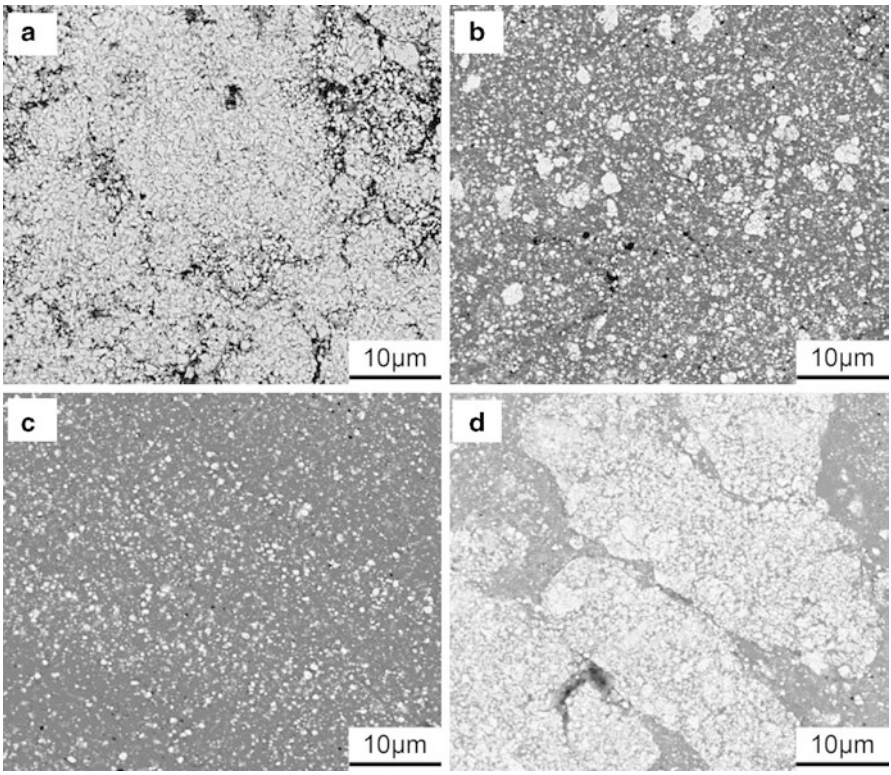


Fig. 8.30 High-magnification SEM images in BSE mode showing particle dispersion states in polished samples prepared with different contents of La_2O_3 addition: **a** 0 wt.%, **b** 0.5 wt.%, **c** 1.0 wt.%, **d** 1.5 wt.%

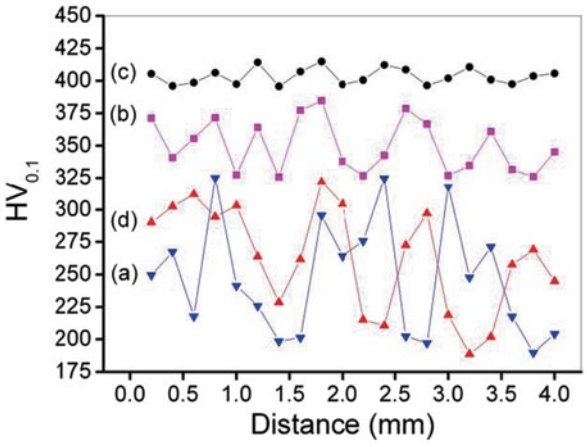


Fig. 8.31 Variation of micro-hardness on polished sections of DMLS-processed (WC–Co)/Cu composites with La_2O_3 contents: **a** 0 wt.%, **b** 0.5 wt.%, **c** 1.0 wt.%, **d** 1.5 wt.%

not further homogenize the particle dispersion; instead, the WC reinforcing particles accumulated significantly to form coarsened aggregations with an ellipsoidal shape (Fig. 8.30d). In this case, the microhardness fluctuated considerably and the average value decreased sharply to $HV_{0.1}$262.9 (Fig. 8.31d).

In order to study the influence of La_2O_3 addition on chemical compositions of DMLS-processed samples, the EDX analyses in selected areas (Fig. 8.30b–d) were performed, as illustrated in Fig. 8.32. It was clear that with variation of La_2O_3 additions, the contents of oxygen element in DMLS-processed structures changed markedly, whereas the contents of other elements generally exhibited a relatively slight change. In more details, on increasing the La_2O_3 content from 0.5 to 1.0 wt.%, the oxygen content increased slightly (Fig. 8.32a and b); however, a further increase of La_2O_3 addition to 1.5 wt.% significantly enhanced the oxygen content in DMLS-processed powders (Fig. 8.32c), implying a serious oxidation of the DMLS system in this instance.

The characteristic morphologies of the WC reinforcing particles in DMLS-processed structures are provided in Fig. 8.33. It was clear that the microstructural features of particles (e.g., particle shape, particle size, and dispersion state) were significantly influenced by La_2O_3 contents. With La_2O_3 lacking, the WC particles exhibited an irregular polygonal shape and were about 1 μm in size (Fig. 8.33a).

With 0.5 wt.% La_2O_3 added, a majority of WC reinforcing particles started to be separated, although a small amount of coarsened particles were still visible (Fig. 8.33b). Interestingly, with an addition of 1.0 wt.% La_2O_3, the WC reinforcing particles were present in a fine and dispersed morphology (Fig. 8.33c). In this case, the 3D morphologies of the reinforcing particles were further characterized by AFM, as shown in Fig. 8.34. It was observed that the ultrafine reinforcing particles generally had a round and smooth surface without any apparent edges. The interfaces between the particles and the matrix were continuous and compatible and free of microcracks. However, at an even higher La_2O_3 addition of 1.5 wt.%, the WC reinforcing particles were again accumulated and coarsened, although the particle surfaces were partially smoothened (Fig. 8.33d).

8.6.4 Etched Microstructure of Metal Matrix of DMLS-processed $(WC–Co)_p$/Cu Composites Containing Various Contents of La_2O_3

Figure 8.35 illustrates the characteristic microstructures of etched samples with various La_2O_3 additions. It was clear that the growing morphologies of dendrites in laser-sintered structures and resultant particle dispersion states were significantly affected by La_2O_3 contents. When no La_2O_3 was added, highly coarsened aggregates of WC particles were formed and dendritic structures of the matrix metal were not developed (Fig. 8.35a). With 0.5 wt.% La_2O_3 added, the matrix metal started to grow in a dendritic morphology, although some small-scaled aggregates of particles were still visible (Fig. 8.35b). At a La_2O_3 content of 1.0 wt.%, the well-developed and refined dendrites were visible and the reinforcing particles were completely trapped

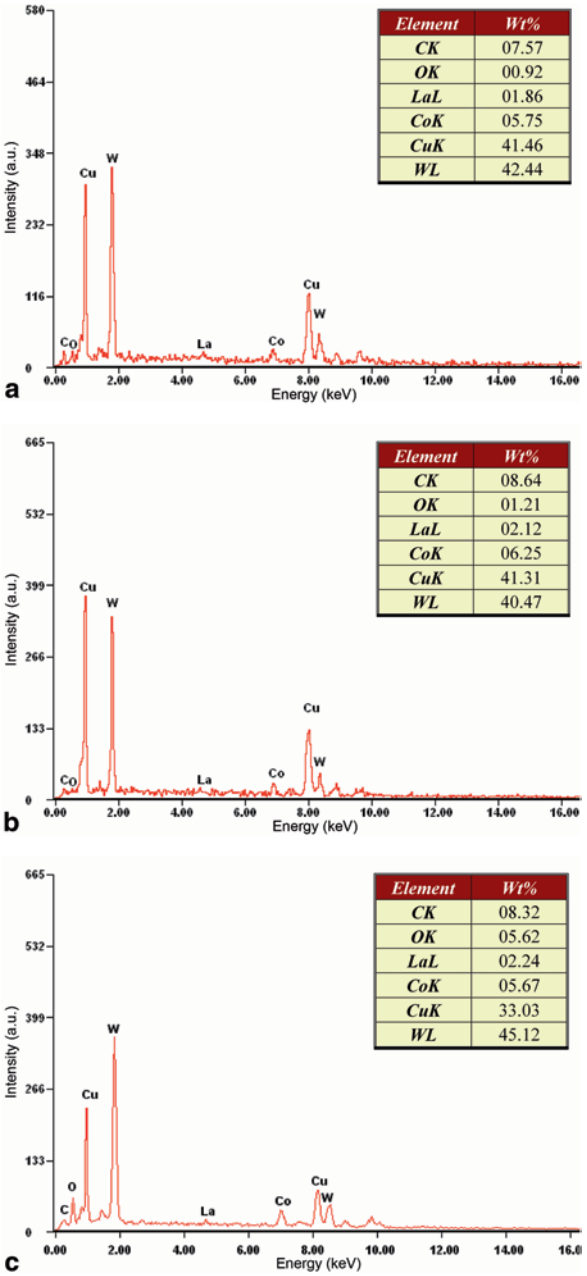


Fig. 8.32 EDX results showing chemical compositions measured in **a** Fig. 8.30b, **b** Fig. 8.30c, and **c** Fig. 8.30d

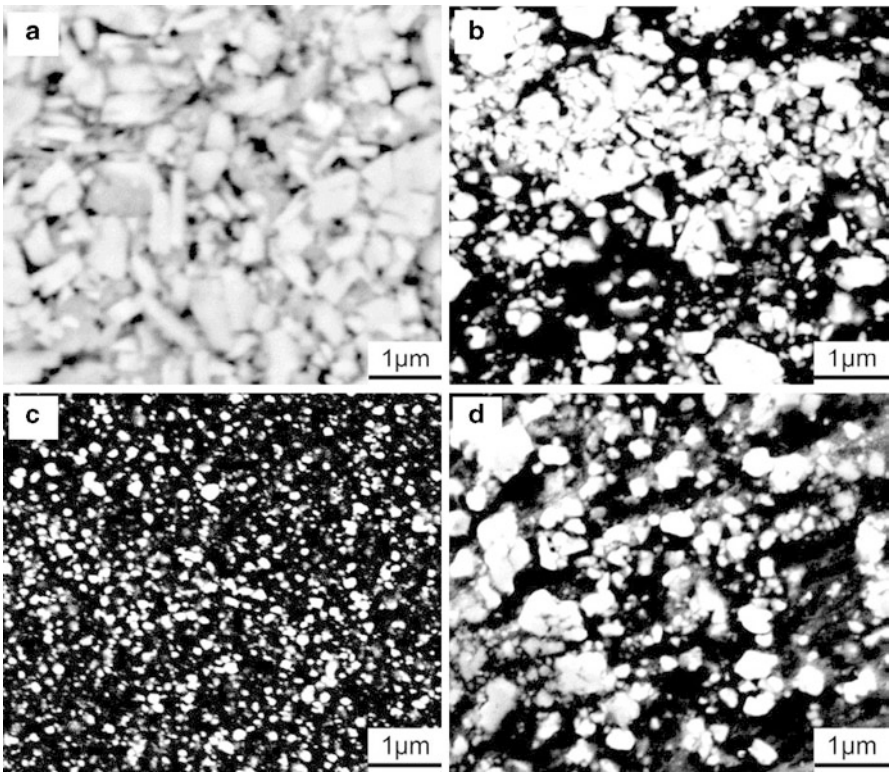


Fig. 8.33 SEM images in BSE mode showing characteristic morphologies of reinforcing particles in DMLS-processed (WC–Co)/Cu composites containing different contents of La_2O_3: **a** 0 wt.%; **b** 0.5 wt.%; **c** 1.0 wt.%; **d** 1.5 wt.%

in such dendrites (Fig. 8.35c). However, at a higher La_2O_3 content of 1.5 wt.%, the grains in the laser-sintered structure were significantly coarsened, between which a large amount of microcracks were continuously distributed (Fig. 8.35d).

8.6.5 Functions of RE Element in DMLS of Particle-Reinforced MMCs

In order to alleviate the particle aggregation and the formation of deleterious microcracks between the reinforcement and the matrix in DMLS-processed (WC–Co)/Cu composites, the design of graded interface (Sect. 8.3) and the optimization of materials components ratio (Sect. 8.4) and laser processing conditions (Sect. 8.5) prove to be effective. Furthermore, the present study reveals that a proper addition of La_2O_3 (1.0 wt.%) to the (WC–Co)/Cu powder system can improve the sintered density, homogenize the particle dispersion, and improve the particle–matrix in-

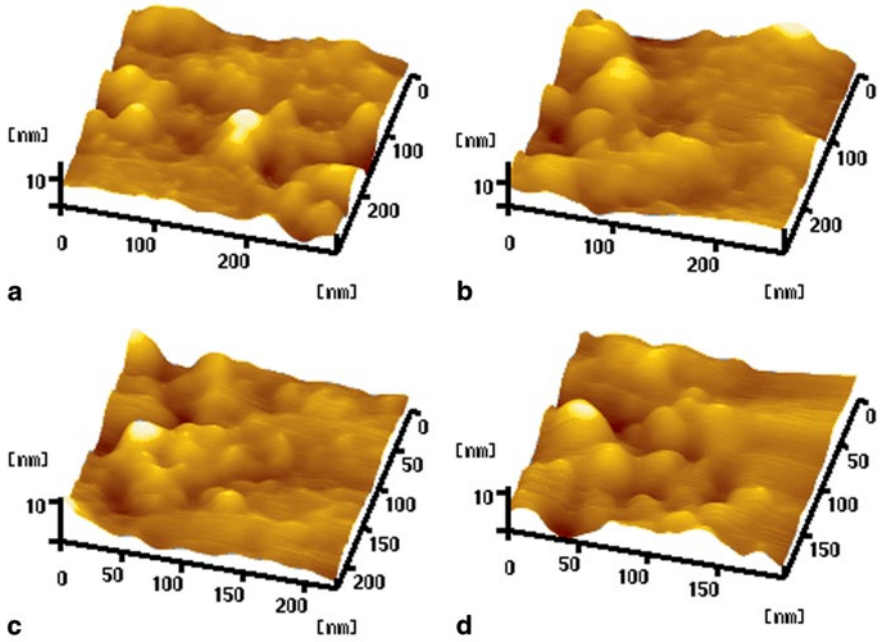


Fig. 8.34 a–d AFM images of four different positions showing 3D morphologies of reinforcing particles in DMLS-processed (WC–Co)/Cu composites with 1.0 wt.% La_2O_3 addition

terfacial compatibility. However, the amount of La_2O_3 addition should be reasonably determined; otherwise, some detrimental effects on laser forming ability will be produced. The significant functions of La_2O_3 addition in DMLS processing of particle-reinforced MMCs are highlighted in the following.

i. Influence on surface tension of liquid
As stated above, laser sintering of the (WC–Co)/Cu composite system yields a molten pool consisting of a mixture of solid (WC) and liquid (Cu, Co) phases. The viscosity of a solid–liquid mixture (μ) is related to the volume fraction of liquid phase (φ_L) and the base viscosity (μ_0), and can be defined by Eq. 8.2. In the case of powder without RE element, a high weight fraction of the reinforcement (i.e., a relatively low content of matrix metal) results in a considerably small amount of liquid formation (i.e., a limited φ_L), thereby enhancing the solid–liquid viscosity μ. The Marangoni convection within the pool, consequently, is significantly suppressed, hence decreasing the flowability of the liquid into the voids between reinforcing particles. The solid–liquid wetting characteristics, thus, are reduced, handicapping the rearrangement of solid particles. The reinforcing particles are inevitably aggregated in the finally solidified matrix (Figs. 8.30a, and 8.33a), thereby decreasing densification level and microstructural homogeneity of laser processed materials (Fig. 8.28a).

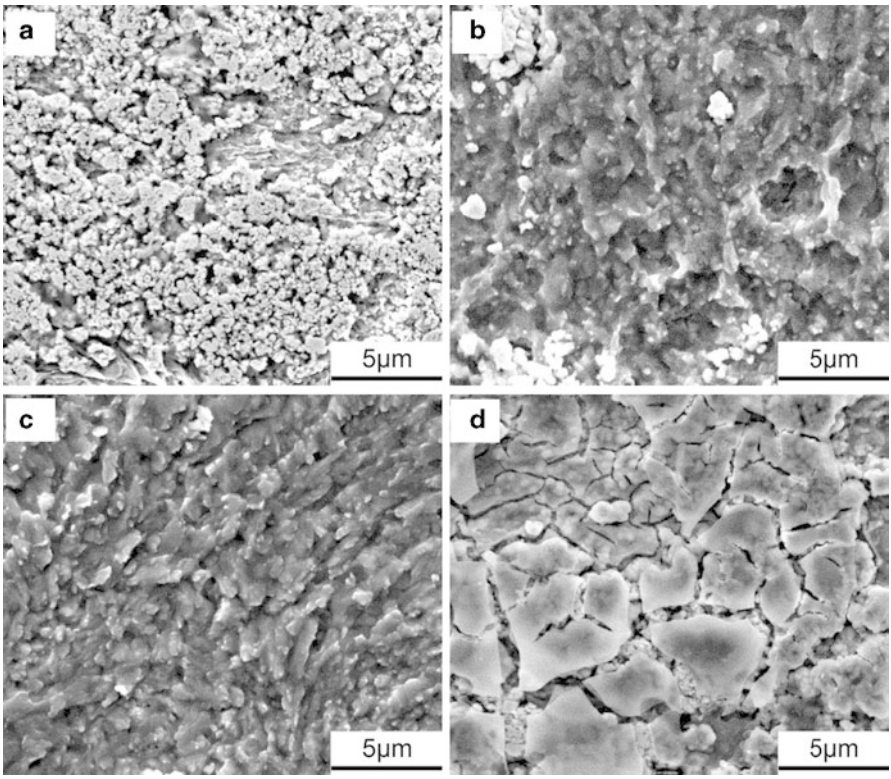


Fig. 8.35 SEM images showing characteristic microstructures of etched samples containing different contents of La_2O_3: **a** 0 wt.%; **b** 0.5 wt.%; **c** 1.0 wt.%; **d** 1.5 wt.%

It is known that the wetting of a solid by a liquid is controlled by the surface tension of solid–liquid (γ_{sl}), solid–vapor (γ_{sv}), and liquid–vapor (γ_{lv}) interfaces. The solid–liquid wettability can be defined by the contact angle (θ) using Eq. 2.1. When the La_2O_3 is added, with the sufficient wetting of the molten liquid, the La atoms tend to be mobile in the melt, since the La is a very reactive element [33]. The atomic La, as a typical surface active element, has a considerably lower surface tension than that of the molten Cu and Co (Table 8.3). Therefore, with a reasonable increase in the amount of La element, the γ_{sl} decreases significantly, thereby improving solid–liquid wettability by lowering the contact angle θ. The

Table 8.3 Thermophysical data of La, Cu, and Co [35]

Substance	Temperature, T (°C)	Surface tension, γ (mN/m)	Surface tension temperature coefficient, $d\gamma/dT$ (mN/(m K))
La	920	729	−0.098
Cu	1083	1349	−0.24
Co	1500	1981	−0.44

reinforcing particles, thus, undergo a more sufficient wetting by the liquid, leading to a more significant smoothening and refinement of the starting irregularly shaped particles (Fig. 8.30b and c, Fig. 8.33b and c) and, accordingly, a more coherent particle/matrix bonding (Fig. 8.34). On the other hand, Table 8.3 reveals that the surface tension temperature coefficient (STTC) of La is much larger than that of Cu and Co. Thus, an increase in the La element addition yields a higher STTC of the DMLS system. According to Niu and Chang's results [34], increasing the STTC across the surface tends to enhance the magnitude of the thermocapillary force, favoring the flow of the melt. The liquid, consequently, is much easy to penetrate into the voids between reinforcing particles, so as to obtain a higher sintered density (Fig. 8.28b and c, Fig. 8.29). Also, an increase in the thermocapillary force improves the rearrangement rate of solid particles in the wetting liquid, preventing the aggregation of particles and, accordingly, improving the dispersion homogeneity of particles in the solidified matrix (Fig. 8.30b and c).

However, the obtained results also reveal that at a high La_2O_3 addition of 1.5 wt.%, the oxygen content in the sintered structure enhances sharply (Fig. 8.32) and, furthermore, the densification level and microstructural homogeneity of laser-sintered materials decrease significantly (Figs. 8.28d, 8.30d, and 8.33d). The atomic La RE element, due to its considerably strong chemical activity, is much easy to react with the oxygen element in the DMLS system [36], forming high melting point RE oxide La_2O_3 (Fig. 8.27). The decomposition of RE oxide under high energy density laser beam and the subsequent recombination of RE element with oxygen have also been confirmed by Tian et al. [33]. With a suitable amount of RE oxide present, such compounds tend to float on the surface of the molten pool under the action of localized mass transfer and material convection within the pool. After solidification, slag may occur on the surface of the sintered layer, forming a "protective film" between the sintered powders and the ambient atmosphere. Such a protective film prevents the sintered layer from oxidization, since it isolates the sintered materials from the oxygen. Thus, the inclusions within the sintered layers are reduced, thereby purifying the DMLS system. However, with an even higher addition of La element, a larger amount of RE oxide slag will be formed. Under this condition, the viscosity of the melt within the pool increases markedly, thereby decreasing the rheological properties of the liquid in conjunction with solid particles. Due to the resultant limited solid–liquid wettability, the obtainable sintered density shows a decrease (Fig. 8.28d). On the other hand, the addition of 1.5 wt.% La_2O_3 increases the tendency for balling initiation, which is known as a typical defect associated with DMLS. It is noted that an excessive addition of La element results in a highly elevated oxygen content in the DMLS system (Fig. 8.32c). This, in turn, results in an overmuch increase of the STTC across the liquid surface and a change of its sign from a negative to a positive value, thereby changing the direction of fluid flow from a radially outward to an inward flow [34]. The radially inward flow, thus, tends to cause a radial contraction and breakage of the cylindrical shaped molten track and increase the tendency of balling, leaving a large amount of porosity in laser-sintered structure (Fig. 8.28d). Also, the reinforcing particles tend to aggregate heavily during balling process (Fig. 8.30d) and, thus, become highly coarsened (Fig. 8.33d).

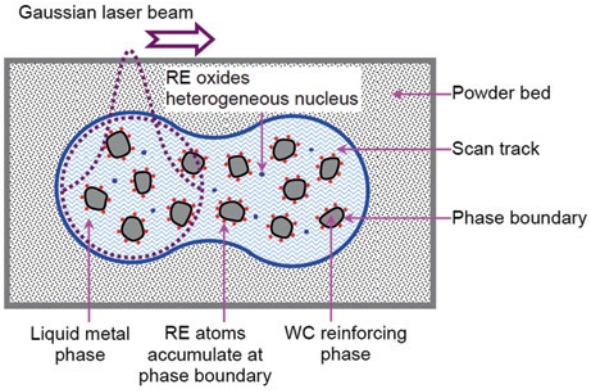


Fig. 8.36 Schematic of metallurgical mechanisms of RE element during DMLS of (WC–Co)/Cu composite system

ii. Influence on migration of grain/phase boundaries
Within the molten pool, there exist a large amount of solid (WC)–liquid (Cu, Co) interfaces. It is known that such a solid–liquid interface cannot be simplified as a geometric plane; instead, it represents a 3D region with the thickness of several atomic diameters, in which there exist a large amount of crystal defects such as dislocation and vacancy [37]. Because the La is a surface-active element and its atomic radius (0.274 nm) is considerably larger than that of Cu (0.157 nm) and Co (0.167 nm), it can be easily captured by these defects and, thus, accumulates along these interfaces, where the atomic arrangement is irregular, which is called "adsorption effect" [32], as illustrated in Fig. 8.36. The obtained results, as shown in Figs. 8.30, 8.33 and 8.35, reveal that the adsorption phenomenon of RE element significantly influences the solidification process of the matrix metal and, accordingly, the microstructural features of the reinforcing particles. It is known that the adsorption of surface-active RE element at various crystal planes is different. In general, the plane with maximum surface tension grows the fastest, whilst the amount of RE element adsorbed is maximized. The amount of surface-active materials adsorbed at a plane K (Γ^K) can be estimated by [32]:

$$\Gamma^K = -\frac{C}{RT}\frac{\mathrm{d}\gamma^K}{\mathrm{d}C} \tag{8.3}$$

where C is the concentration of surface-active materials, R the Planck constant, T the absolute temperature, and γ^K is the surface tension of plane K. After the plane K adsorbs a layer of active materials, the surface tension can be deduced from the integral of Eq. 8.3:

$$\gamma_C^K = \gamma_0^K - RT\int_0^C \frac{\Gamma^K}{C}dC \tag{8.4}$$

where γ_0^K and γ_C^K are the surface tensions of plane K before and after the adsorption of active materials. Thus, the surface free energy of the whole crystal can be expressed by:

$$\sum_K \gamma_C^K A_K = \sum_K \left(\gamma_0^K - RT \int_0^C \frac{\Gamma^K}{C} dC \right) A_K \tag{8.5}$$

where A_K is the area of plane K. Therefore, in order to minimize the surface free energy, it requires that:

$$\sum_K A_K \int \frac{\Gamma^K}{C} dC \to \max \tag{8.6}$$

Equation 8.6 indicates that the plane with the largest Γ^K value plays the most important role in minimizing the free energy of the entire interface. Therefore, the adsorption of RE element on such planes not only decreases the difference of surface energy of the crystal, but also prevents the plane with the maximum surface energy from further growth. In other words, this adsorption induces a dragging (or pinning) effect on the movement of grain and phase boundaries. With a reasonable increase in the addition of La element, a larger amount of La atoms are expected to be segregated to grain/phase boundaries, thereby intensifying the dragging (or pinning) effect. Therefore, for the liquid phase in the DMLS system, the impetus for grain growth is weakened and, accordingly, the nucleation rate is enhanced, favoring the formation of well-developed dendrites of the matrix metal (Fig. 8.35b and c). As to the solid reinforcing phase in the DMLS system, the migration of phase boundaries will also be pinned, preventing the neighboring particles from accumulating. This favors the trapping of particles by the advancing dendritic solidification front, leading to a uniform dispersion of the fine particles in finally solidified matrix (Fig. 8.30b and c, Fig. 8.33b and c). Therefore, by adding a suitable amount of La_2O_3 (1.0 wt.%), the combined effect of the above-stated two factors enhances densification level and attendant mechanical properties of laser-processed composites (Figs. 8.29, 8.31).

However, with an excessive addition of La_2O_3 (1.5 wt.%), a heterogeneous microstructure consisting of significantly accumulated particles (Fig. 8.30d) and coarsened grains (Fig. 8.35d) is formed in the DMLS-processed structure. According to Ji's work [38], due to the considerably low first ionization energy of RE element, the valence electrons of RE atoms at grain–phase boundaries are easy to shift or, even, partially disengage from the bound of atomic nucleus, leading to the polarization of RE atoms and the resultant decrease in atomic radius. These polarized atoms, thus, are much easy to enter the interior of crystals through the vacancy diffusion mechanism, resulting in the additional distortion of crystal lattice. At these sites, so-called "polarized balls" which are consisted of several thousands of polarized atoms will be formed [39]. The polarization among these atoms increases the atomic binding forces considerably, forming local stress fields. With an excessive addition of RE element, the interaction between polarized balls enhances, thereby intensifying the action of stress fields and, thus, forming atomic diffusion barriers. Consequently, a further atomic diffusion is suppressed, decreasing

the activity of RE atoms. In other words, only when a suitable concentration of RE element is obtained in the DMLS system can the RE atomic activity be maximized, through which a maximum improvement in the laser forming ability is achieved (Figs. 8.28c, 8.30c and 8.35c).

8.7 Conclusions

In this chapter regarding DMLS additive manufacturing of $(WC–Co)_p$/Cu composites, the main conclusions are summarized as follows.

1. The WC reinforcing particles were added to the Cu matrix in the form of WC–Co composite powder, favoring the presence of the double stages of wetting during DMLS process and, accordingly, the formation of the graded interfaces between the WC reinforcing particles and the Cu matrix. The graded interfacial design and formation strategy proves to be effective in improving the interfacial bonding and material integrity between the reinforcement and the matrix in DMLS-processed (WC–Co)/Cu composites.
2. The effects of laser processing parameters such as laser power, scan speed, and powder layer thickness on microstructures and properties of DMLS-processed (WC–Co)/Cu composites were investigated. It was found that below 700 W, increasing the laser power led to a higher densification with an improved interfacial bonding ability between the reinforcement and the matrix. An increase in the scan speed above a critical value 0.04 m/s led to a more homogeneous distribution of reinforcing particles. A proper decrease in the powder layer thickness below 0.30 mm permitted higher DMLS densification and attendant mechanical properties.
3. The influence of reinforcement content on the DMLS densification and the attendant microstructures, e.g., the dispersion homogeneity of the reinforcing particles and the interfacial bonding ability, was investigated. It showed that using a low reinforcement content of 20 wt.% resulted in a poor densification with severe balling phenomena, due to a higher average composite coefficient of thermal expansion (CTE) and a superheating of the melt. A heterogeneous microstructure with a significant particle aggregation was obtained at a high reinforcement content of 40 wt.%, because of a limited liquid formation and the resultant high liquid viscosity and reduced Marangoni effect. Using an optimal reinforcement content of 30 wt.% led to a favorable DMLS densification response, a uniform distribution of the reinforcing particles and a compatible interfacial microstructure.
4. The effects of processing parameters in terms of laser power, scan speed, and powder layer thickness on the particle dispersion behavior in DMLS-processed (WC–Co)/Cu composites were studied. It showed that for a given scan speed larger than 0.04 m/s, a proper increase in the laser power between ~650 and ~750 W led to a uniform dispersion of smooth and fine WC particles, due to a sufficient liquid formation and an improved wettability. However, an excessive

increase in the laser power resulted in a severe particle aggregation, because of the balling effect. There existed a critical scan speed of 0.04 m/s, above which the particles could be well trapped by the advancing dendritic front, thereby homogenizing the particulate dispersion in the matrix. A proper decrease in the powder layer thickness to 0.20 mm can alleviate the particle aggregation, due to the elevated Marangoni convection and liquid capillary forces.

5. A detailed investigation of the influence of rare earth (RE) oxide (La_2O_3) addition on densification and microstructure of DMLS-processed (WC–Co)/Cu composites was performed. It was found that on increasing La_2O_3 addition to a suitable amount (1.0 wt.%), the particle dispersion was homogenized and the particle/matrix interfacial bonding was improved. However, with an excessive addition of La_2O_3 (1.5 wt.%), a heterogeneous microstructure consisting of highly accumulated particulates was present. The exact metallurgical roles of RE element in DMLS of particle-reinforced MMCs were addressed. It showed that a proper addition of RE element (i) decreased surface tension of the melt and enhanced solid–liquid wettability; (ii) dragged and/or pinned grain/phase boundaries and resisted grain coarsening and particulate aggregating. However, the balling phenomenon occurred and the activity of RE atoms decreased at an even higher La_2O_3 content, thereby producing detrimental effects on laser-forming ability.

References

1. Jiang QC, Wang HY, Ma BX et al (2005) Fabrication of B4C particulate reinforced magnesium matrix composite by powder metallurgy. J Alloys Compd 386(1–2):177–181
2. Mortensen A, Llorca J (2010) Metal matrix composites. Annu Rev Mater Res 40:243–270
3. Breval E, Cheng JP, Agrawal DK et al (2005) Comparison between microwave and conventional sintering of WC/Co composites. Mater Sci Eng A 391(1–2):285–295
4. Zhu HH, Lu L, Fuh JYH (2004) Influence of binder's liquid volume fraction on direct laser sintering of metallic powder. Mater Sci Eng A 371(1–2):170–177
5. Miracle DB (2005) Metal matrix composites—From science to technological significance. Compos Sci Technol 65(15–16):2526–2540
6. Maeda K, Childs THC (2004) Laser sintering (SLS) of hard metal powders for abrasion resistant coatings. J Mater Process Technol 149(1–3):609–615
7. Simchi A, Petzoldt F, Pohl H (2003) On the development of direct metal laser sintering for rapid tooling. J Mater Process Technol 141(3):319–328
8. Tang Y, Loh HT, Wong YS et al (2003) Direct laser sintering of a copper–based alloy for creating three–dimensional metal parts. J Mater Process Technol 140:368–372
9. Das S, Wohlert M, Beaman JJ et al (1998) Producing metal parts with selective laser sintering/hot isostatic pressing. JOM 50(12):17–20
10. Tjong SC (2007) Novel nanoparticle–reinforced metal matrix composites with enhanced mechanical properties. Adv Eng Mater 9(8):639–652
11. Moya JS, Lopez–Esteban S, Pecharromán C (2007) The challenge of ceramic/metal microcomposites and nanocomposites. Prog Mater Sci 52(7):1017–1090
12. Llorca J (2002) Fatigue of particle–and whisker–reinforced metal–matrix composites. Prog Mater Sci 47(3):283–353

13. Gåård A, Krakhmalev P, Bergström J (2006) Microstructural characterization and wear behavior of (Fe, Ni)–TiC MMC prepared by DMLS. J Alloys Compd 421(1–2):166–171
14. Ghosh SK, Saha P, Kishore S (2010) Influence of size and volume fraction of SiC particulates on properties of ex situ reinforced Al–4.5Cu–3Mg metal matrix composite prepared by direct metal laser sintering process. Mater Sci Eng A 527(18–19):4694–4701
15. Yang MC, Xu J, Hu ZQ (2004) Synthesis of WC–TiC35–Co10 nanocomposite powder by a novel method. Int J Refract Met Hard Mater 22(1):1–7
16. Fischer P, Romano V, Weber HP et al (2003) Sintering of commercially pure titanium powder with a Nd:YAG laser source. Acta Mater 51(6):1651–1662
17. Simchi A, Pohl H (2004) Direct laser sintering of iron–graphite powder mixture. Mater Sci Eng A 383(2):191–200
18. Yu JQ, Yi WZ, Chen BD et al (1987) Binary alloy phase diagrams. Shanghai Scientific & Technical Publishers, Shanghai
19. Gu DD, Shen YF (2006) Influence of phosphorus element on direct laser sintering of multi-component Cu-based metal powder. Metall Mater Trans B 37(6):967–977
20. Matucha KH (1996) Structure and properties of nonferrous alloys. VCH, Weinheim
21. Agarwala M, Bourell D, Beaman J et al (1995) Direct selective laser sintering of metals. Rapid Prototyp J 1(1):26–36
22. Niu HJ, Chang ITH (1999) Selective laser sintering of gas and water atomized high speed steel powders. Scr Mater 41(1):25–30
23. Wu XL, Chen GN (1999) Microstructure and wear resistance of in situ TiCp composite coating by laser cladding. J Mater Sci Technol 15(3):233–238
24. Chatterjee AN, Kumar S, Saha P et al (2003) An experimental design approach to selective laser sintering of low carbon steel. J Mater Process Technol 136(1–3):151–157
25. Wong WLE, Karthik S, Gupta M (2005) Development of high performance Mg–Al2O3 composites containing Al2O3 in submicron length scale using microwave assisted rapid sintering. Mater Sci Technol 21(9):1063–1070
26. Gu DD, Shen YF (2009) Balling phenomena in direct laser sintering of stainless steel powder: metallurgical mechanisms and control methods. Mater Des 30(8):2903–2910
27. Das S (2003) Physical aspects of process control in selective laser sintering of metals. Adv Eng Mater 5(10):701–711
28. Tolochko N, Mozzharov S, Laoui T et al (2003) Selective laser sintering of single- and two-component metal powders. Rapid Prototyping J 9(2):68–78
29. Wilde G, Perepezko JH (2000) Experimental study of particle incorporation during dendritic solidification. Mater Sci Eng A 283(1–2):25–37
30. Han Q, Hunt JD (1995) Redistribution of particles during solidification. ISIJ Int 35:693–699
31. Youssef YM, Dashwood RJ, Lee PD (2005) Effect of clustering on particle pushing and solidification behaviour in TiB2 reinforced aluminium PMMCs. Compos Part A 36(6):747–763
32. Wu CML, Yu DQ, Law CMT et al (2004) Properties of lead–free solder alloys with rare earth element additions. Mater Sci Eng R 44(1):1–44
33. Chen CZ, Tian YS, Chen LX et al (2006) Effect of RE oxides on the microstructure of the coatings fabricated on titanium alloys by laser alloying technique. Scr Mater 54(5):847–852
34. Niu HJ, Chang ITH (1999) Instability of scan tracks of selective laser sintering of high speed steel powder. Scr Mater 41(11):1229–1234
35. Yuan ZF, Ke JJ, Li J (2006) Surface tension of metals and alloys. Science Press, Beijing
36. Wang KL, Zhang QB, Sun ML et al (2003) Microstructural characteristics of laser clad coatings with rare earth metal elements. J Mater Process Technol 139(1–3):448–452
37. Zhai QJ, Guan SK, Shang QY (1999) Alloy thermo–mechanism: theory and application. Metallurgy Industry Press, Beijing
38. Ji ZS (2000) Effect of RE–B–Al on composition of permeation layer. J Chin Rare Earth Soc 18: 27–30
39. Zhong HR (1998) Chemical heat treatment of steels with rare earth. National Defence Industry Press, Beijing

Chapter 9
Nano/Micron W–Cu Composites by Direct Metal Laser Sintering (DMLS) Additive Manufacturing (AM): Unique Laser-Induced Metallurgical Behavior of Insoluble System

Abstract The densification behavior and attendant microstructural characteristics of the direct metal laser sintering (DMLS)-processed nano/micron W–Cu composites under different processing conditions were investigated. The methods for improving the controllability of laser processing were elucidated. A "linear energy density (LED)" parameter, which was defined by the ratio of laser power to scan speed, was used to tailor the powder melting mechanisms. It showed that using a suitable LED between ~13 and ~19 kJ/m combined with a scan speed less than 0.06 m/s led to a continuous melting of the Cu component, yielding a sound densification rate without any balling phenomenon. A "volumetric energy density (VED)" parameter was defined to facilitate the integrated process control by considering the combined effect of various processing parameters. It was found that setting the VED within ~0.6 and ~0.8 kJ/mm^3 favored a better yield of high-density DMLS parts. The influence of Cu-liquid content on densification and microstructures of DMLS-processed nano/micron W–Cu was also studied. It showed that at a suitable Cu elemental content of 60 wt.%, a series of regularly shaped W-rim/Cu-core structures were formed after DMLS processing. The metallurgical mechanisms for the formation of such a novel structure were proposed.

9.1 Introduction

W–Cu composites offer the opportunity to combine a refractory W-phase possessing a high strength and a low coefficient of thermal expansion (CTE) with a Cu-phase having a high thermal and electrical conductivity [1, 2]. These materials are promising candidates for electrical and thermal applications. In general, W–Cu composites with 10–20 wt.% Cu are used as heat sinks to match the adjacent silicon or ceramics substrates in electronic packages, so that the thermal stress induced by different CTEs can be avoided and the heat generated by power devices in circuits can be dissipated speedily [3, 4]. The W–Cu composites with Cu contents above 20 wt.% are used as heavy duty electrical contact materials, which need a combination of good wear resistance and thermal conductivity to alleviate erosions and arcing problems incurred during power switching [5, 6].

© Springer-Verlag Berlin Heidelberg 2015

D. Gu, *Laser Additive Manufacturing of High-Performance Materials,*
DOI 10.1007/978-3-662-46089-4_9

One of the common processes used in producing W–Cu composites is to infiltrate a porous sintered W skeleton by liquid Cu. This technique, however, is limited in its feasibility because it is much easy to produce defects in structures (e.g., pores, copper lakes, and tungsten agglomerates) and, more important, the processing quality is susceptible to these defects [4, 6]. Another method, the most widely applied one, is to mix the elemental W and Cu powder and, subsequently, to press and sinter the powder mixture through liquid phase sintering (LPS) mechanism. However, W–Cu composites are difficult for full-densification by LPS, due to the mutual insolubility of W and Cu and the considerably high contact angle of liquid Cu on W [7, 8]. Currently, the ultrafine submicron and even nanocrystalline W–Cu composites and advanced preparation methods, e.g., high-energy mechanical alloying [9], co-reduction of oxides [10], and mechanochemical process [11], are generally applied to improve sinterability of these W–Cu composites through LPS. Additionally, the pieces must be preworked in a mould to give the right shape before sintering. However, due to the limitation of currently available moulds, some complex shapes, which are necessary for W–Cu components (e.g., heat sinks) [4], are always difficult to be created. Therefore, novel processing methods should be innovatively designed to obtain highly dense complex shaped W–Cu pieces.

To overcome the above mentioned shortcomings, a new fabrication technique, i.e., direct metal laser sintering (DMLS) additive manufacturing, has been introduced for the production of W–Cu components. DMLS, due to its flexibility in materials and shapes, allows complex three-dimensional W–Cu objects to be produced without any tools. The following issues are included in the present chapter regarding DMLS processing of W–Cu composites:

i. Effects of processing parameters on consolidation and microstructure of nano/micron W–Cu components processed by DMLS

A review of existing literature reveals that little previous work has focused on the basic principles of the fabrication of W–Cu components using laser-based additive manufacturing process. Actually, due to the complex metallurgy nature of DMLS, process defects associated with DMLS such as balling, curling, and delamination are still difficult to be eliminated completely. The laser processing parameters (e.g., laser power, scan speed, scan line hatch spacing, and powder layer thickness) influence the densification level and the attendant microstructures of DMLS-processed materials significantly. The possibility of controlling processing parameters in improving the microstructural and mechanical properties of DMLS-processed W–Cu components is becoming an important consideration. This chapter presents the DMLS mechanisms, surface morphologies, and microstructural features of DMLS-processed W–Cu composites using a wide range of processing parameters, with an aim to elucidate the optimal processing conditions and the relevant control methods.

ii. Influence of Cu-liquid content on densification and microstructure of nano/micron W–Cu composites prepared by DMLS

Generally, DMLS process uses a bed of loose powder. The useable particle sizes for DMLS are in the 10–100 μm range [12]. The ultrafine nanocrystalline powder, although it possesses enhanced sinterability during conventional sintering process, exhibits poor flow and spreading properties in powder bed, thereby decreasing the densification response during layer-by-layer DMLS process. Fortunately, the preparation of a nano/micron W–Cu composite powder system would be a solution to this problem. By using this method, not only the flowability of the whole powder system is increased but also the enhanced sinterability of ultrafine powder component is still available. In the present chapter, the DMLS processing of a composite system consisting of nanocrystalline W–Cu powder and micron Cu powder was performed. The influence of Cu-liquid content on densification level and microstructural features of DMLS-processed W–Cu components was highlighted, in order to propose the materials design and optimization methods to improve the laser processing ability of W–Cu composites.

iii. Formation mechanism of a novel W-rim/Cu-core structure during DMLS of W–Cu composite system

The W–Cu is a unique system having the mutual insolubility of W and Cu, and meanwhile, the laser processing has a nonequilibrium physical nature featured by the considerably high undercooling degree and attendant rapid solidification process. The combined effects of the unique material and process may lead to the formation of novel microstructures and properties that are absent in the conventionally processed W–Cu composites. This chapter also presents an interesting characterization of a novel W-rim/Cu-core structure formed in DMLS-processed W–Cu composites, with an aim to evaluate the exact metallurgical mechanism of its formation.

9.2 Preparation of Nano/Micron W–Cu Composite Powder System for DMLS Process

9.2.1 Preparation of Nanocrystalline W–Cu Composite Powder

The nanocrystalline W–20 wt.% Cu powder was synthesized by means of combining spray drying and hydrogen reduction process [13]. The precursor materials were AMT: $(NH_4)_6(H_2W_{12}O_{40})\cdot H_2O$ (molecular weight 3029.132) and $[Co(NO_3)_2]\cdot 3H_2O$ (molecular weight 241.55). Powder preparation involved the following steps: (1) spray drying the precursor solution (feed rate of solution 20 ml/min; rotation speed of atomizer 21000 rpm); (2) burning out the precursor powder to obtain the oxide powder (temperature 500 °C; time 2 h); (3) ball milling of the oxide powder (ball-to-powder weight ratio 5:1; milling time 12 h); (4) reduction of the ball-milled

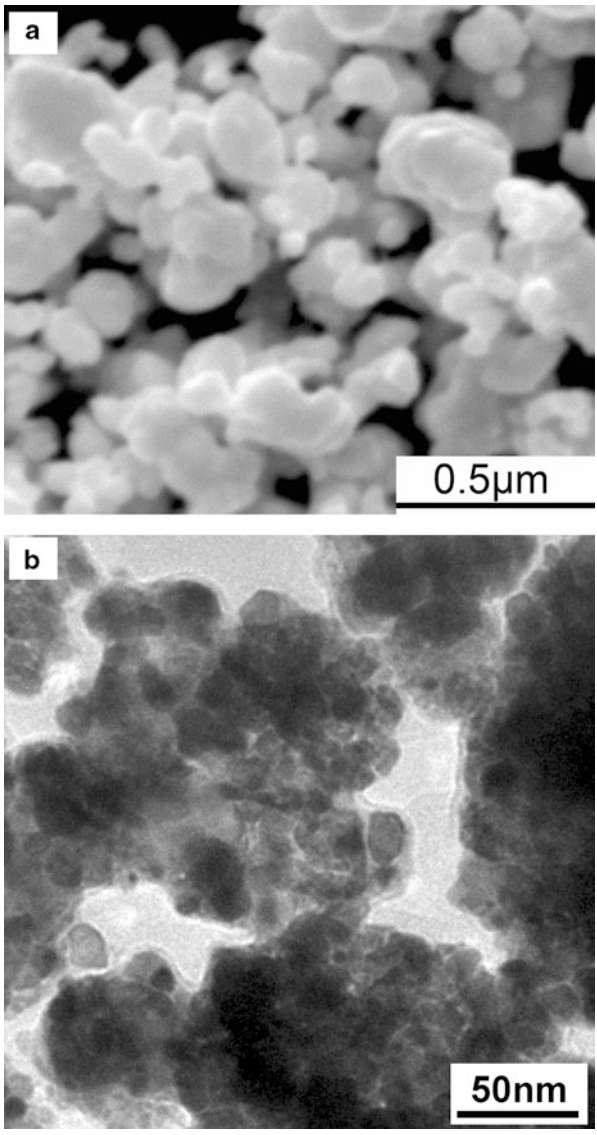


Fig. 9.1 Scanning electron microscope (*SEM*) image showing characteristic morphology of submicron W–Cu powder (**a**); Transmission electron microscope (*TEM*) micrograph showing interior nanostructure of W–Cu composite powder (**b**)

powder in H_2 atmosphere (temperature 750 °C; holding time 2 h). The as-prepared W–20 wt.% Cu composite powder had an irregular shape and an average particle size of 0.24 μm (Fig. 9.1a). The considerably refined nanoscale crystallites were formed in the interior of the W–Cu composite powder, with the crystalline size of W phase of 20–30 nm (Fig. 9.1b).

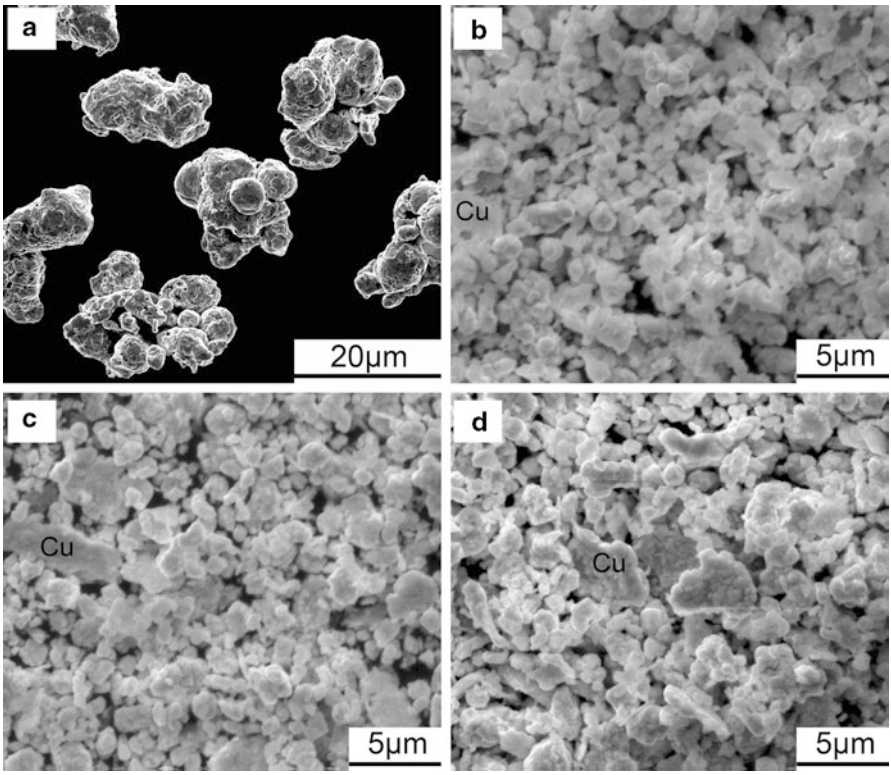


Fig. 9.2 SEM images showing characteristic morphologies of starting micron Cu powder **a** and the powder systems with various contents of micron Cu powder after mechanical milling: **b** 35 wt.% Cu powder; **c** 50 wt.% Cu powder; **d** 65 wt.% Cu powder

9.2.2 Preparation of Nano/Micron (W–Cu)/Cu Composite Powder System

The electrolytic 99% purity Cu powder with an irregular structure and a mean particle size of 15 μm (Fig. 9.2a) and the as-prepared submicron W–20 wt.% Cu composite powder (Fig. 9.1) were used in this study. Three powder systems with different component ratios, as listed in Table 9.1, were prepared by mixing the two powder components in a Fritsch Pulverisette 6 planetary mono-mill at a rotation speed of 350 rpm for 60 min, using a ball-to-powder weight ratio of 10:1. The typical morphologies of the three powder systems after ball milling are shown in Fig. 9.2b–d. It was clear that the starting irregularly shaped coarse Cu powder particles underwent a significant flattening and refinement during milling, as selectively indicated in Fig. 9.2b–d. A homogeneous W–Cu mixture was generally obtainable. Using such a homogeneously mixed bimodal-sized powder bed is expected to improve the flowability of the whole powder mixture while keeping fine structures of nanocrystalline W in the system.

Table 9.1 Compositions of three powder systems with variation of component ratios (wt.%)

Powder system	Powder component fraction		Equivalent elemental fraction	
	Cu powder	W–20 wt.% Cu powder	Cu element	W element
A	35	65	48	52
B	50	50	60	40
C	65	35	72	28

9.3 Effects of Processing Parameters on Consolidation and Microstructure of Nano/Micron W–Cu Components Processed by DMLS

9.3.1 Mechanisms of Powder Melting and Densification during DMLS of Nano/Micron W–Cu Composite Powder

Following the procedures specified in Sect. 3.3 of Chap. 3, DMLS processing of the as-prepared nano/micron W–Cu powder systems was performed using the as-defined CO_2 laser. Single layer DMLS tests were performed primarily by repeated scanning a powder layer (0.15 mm in thickness) on a Q235 steel substrate using a simple linear raster scan pattern. From these experiments, a series of typical processing parameters were chosen for the further preparation of three-dimensional samples with dimensions. The applied processing parameters were: spot size 0.30 mm, laser power 300–1200 W, scan speed 0.02–0.08 m/s, scan line hatch spacing 0.15–0.30 mm, and powder layer thickness 0.10–0.30 mm.

Figure 9.3 depicts the process map regarding the change of mechanisms of single layer melting of W–Cu composites. Over the entire range of laser powers and scan speeds, the following four process windows can be defined.

I. Slight melting: The incident laser energy was great enough to exert an effect on the powder bed, but was insufficient to induce any significant melting of the powder.
II. Continuous melting: The delivered energy produced continuous molten tracks by means of the complete melting of the Cu component, leading to coherent laser-sintered tracks after solidification.
III. Melting with balling: Using a high laser power and a high scan speed (> 0.06 m/s) resulted in the formation of liquid scan tracks of a long thin cylindrical shape, which then broke up into a series of metallic spheres as a consequence of surface tension reduction.
IV. Melting with breakage: At a high laser power combined with a low scan speed (< 0.06 m/s), the localized heat input and the attendant heat affected zone around the molten pool were enhanced considerably. The molten scan tracks broke up at longer intervals due to the excessive shrinkage during liquid–solid transition, forming the interrupted laser-sintered tracks on cooling.

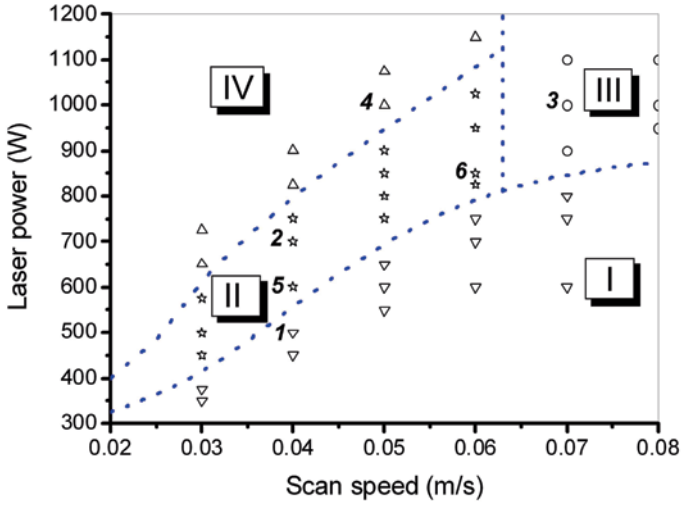


Fig. 9.3 Mechanisms of single layer melting processed over a wide range of laser powers and scan speeds for the W–Cu composite system. Laser sintering using "▽"-denoted parameters results in slight melting; Laser sintering using "☆"-denoted parameters leads to continuous melting; Laser sintering using "○"-denoted parameters results in melting with balling; Laser sintering using "△"-denoted parameters results in melting with breakage

It should be noted that the process map is defined based on a series of points which are indicated by different symbols in Fig. 9.3. In each process window, DMLS processing using the processing parameters within it yielded a similar mechanism of melting. With these key pointes determined, the boundaries between the four different windows were drawn approximately. The boundary locations were not absolutely strict, due to the span of parameters choice (typically 50 W for the laser power and 0.01 m/s for the scan speed). In spite of that, the four process windows can be used to choose the suitable processing conditions under which laser sintering will generate a feasible mechanism of melting.

The characteristic surface morphologies of DMLS-processed multilayer W–Cu samples obtained in the described windows are provided in Fig. 9.4. Table 9.2 depicts the statistics for the sintered densities using different sintering mechanisms. Laser sintering using parameters within zone I (point 1) produced a porous sintered surface containing some residual unsintered powder particles (denoted by circles, Fig. 9.4a), resulting in a considerably low sintered density (Table 9.2). For point 2 within zone II, a relatively smooth and fully dense sintered surface was obtainable (Fig. 9.4b). The densification level of DMLS-processed samples using parameters within zone II was generally higher than 92 % theoretical density (TD). In the case of point 3 within zone III, the laser-sintered surface consisted of rows of coarsened balls and interconnected interball pore channels (Fig. 9.4c), leaving a high residual porosity (Table 9.2). More severely, balling effect, in most cases, handicapped the completion of a desired multilayer sample, because balling phenomena made the

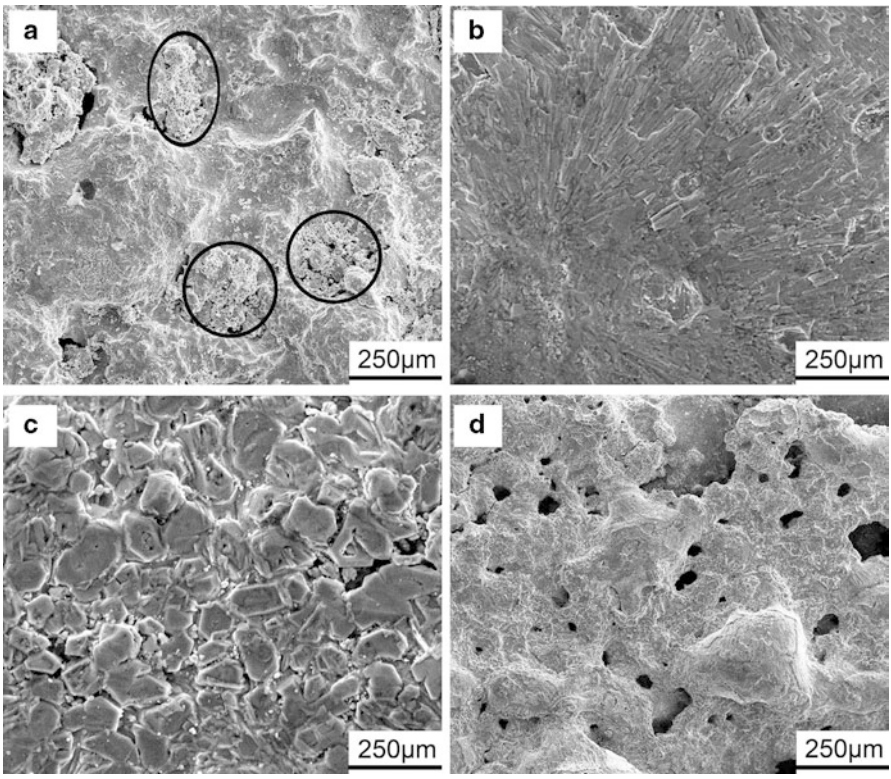


Fig. 9.4 SEM images showing typical surface morphologies of laser-sintered W–Cu samples prepared with selected parameters in different windows in Fig. 9.3: **a** 500 W, 0.04 m/s (point 1, zone I); **b** 700 W, 0.04 m/s (point 2, zone II); **c** 1000 W, 0.07 m/s (point 3, zone III); **d** 1000 W, 0.05 m/s (point 4, zone IV). Fixed parameters: scan line hatch spacing 0.15 mm; powder layer thickness 0.15 mm

Table 9.2 Average densification level of laser-sintered multilayer W–Cu samples with various mechanisms of melting

Melting mechanism	Slight melting	Continuous melting	Melting with balling	Melting with breakage
Process window	Zone I	Zone II	Zone III	Zone IV
Densification level	<70% TD	>92% TD	<75% TD	~80% TD

smooth spreading of fresh powder on the previously processed layer impossible, especially at the latter stage of DMLS process. As to point 4 within zone IV, a highly rippled surface consisting of large-sized pores was found (Fig. 9.4d). Besides the limited densification (Table 9.2), the laser-sintered samples generally exhibited significant geometric distortion (curling or delamination).

9.3.2 Microstructural Characteristics of Nano/Micron W–Cu Components Processed by DMLS

Although DMLS processing using the various parameters within zone II (Fig. 9.3) generally yielded a favorable densification (Table 9.2), the microstructural features on the internal sections of laser-sintered W–Cu samples showed some pronounced differences, as revealed in Fig. 9.5. In general, the energy dispersive X-ray spectroscope (EDX) analyses showed that the white phase was W, while the surrounding grey matrix was Cu. At a laser power of 600 W and a scan speed of 0.04 m/s (point 5), a heterogeneous microstructure consisting of the clusters of W solids and irregular Cu-rich regions was visible (Fig. 9.5a). A high-magnification SEM image revealed that the fine W solids aggregated severely in the matrix (Fig. 9.5b). At a higher laser power of 700 W and the same scan speed (point 2), the regular-shaped chainlike structures were present after DMLS processing, showing a more homogeneous structure (Fig. 9.5c). More interestingly, the W solids were well arranged into a novel W-rim/Cu-core structure (Fig. 9.5d). However, at a higher scan speed of 0.06 m/s (point 6), the W solids again showed some aggregation in laser-sintered matrix, thereby destroying the previously formed W-rim/Cu-core structure (Fig. 9.5e and f).

Figure 9.6 discloses that the surface morphologies of laser-sintered W–Cu samples (e.g., size and shape of sintered agglomerates, amount of porosity) are strongly affected by scan line hatch spacing. At a high scan line hatch spacing of 0.30 mm (i.e., no overlap between scan lines), the narrow columnar agglomerates parallel to the scan direction (arrowheaded) were formed, which were separated by large and interconnected gaps (Fig. 9.6a). As the hatch spacing decreased to 0.25 mm (i.e., the overlap between scan lines of 8.3 %), the gaps between sintered agglomerates became shallow, although the surface was still rippled and rough (Fig. 9.6b). Interestingly, at an even lower hatch spacing of 0.15 mm (i.e., the overlap between scan lines of 25 %), an almost fully dense and comparatively smooth surface was obtained (Fig. 9.6c).

In order to study the influence of powder layer thickness on the DMLS processing activity and densification response of the W–Cu powder system, the powder beds with various layer thicknesses were scanned at a fixed laser energy input, with the real-time DMLS process illustrated in Fig. 9.7. The interlayer bonding properties of the finished multilayer W–Cu samples are shown in Fig. 9.8. At a high powder layer thickness of 0.30 mm, a considerably large sparkle was observed in the laser irradiating region during DMLS, resulting in a severe splash of the heated powder (Fig. 9.7a). In this situation, the interconnected pore channels were present between DMLS-processed layers, resulting in a poor densification of 78.3 % TD (Fig. 9.8a). Differently, on decreasing the powder layer thickness to 0.15 mm, the powder was smoothly sintered without any apparent splash during DMLS, exhibiting a small spark during powder-beam interaction (Fig. 9.7b). As a consequence, a sufficient densification (94.1 % TD) combined with a favorable interlayer bonding ability was obtained, showing no apparent pores or cracks between layers (Fig. 9.8b). However,

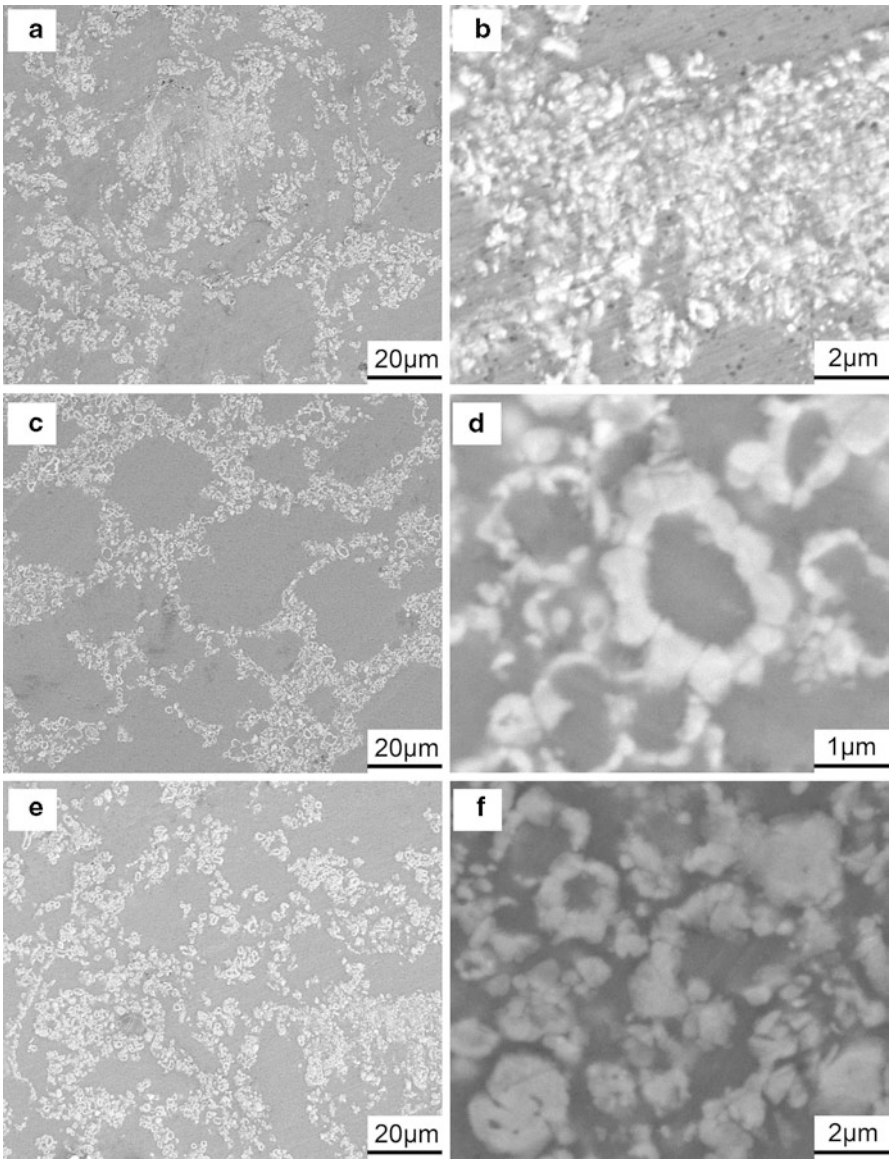


Fig. 9.5 SEM images showing characteristic microstructures on polished sections of laser-sintered W–Cu samples at different laser powers and scan speeds: **a** 600 W, 0.04 m/s (point 5, Fig. 9.3); **c** 700 W, 0.04 m/s (point 2); **e** 850 W, 0.06 m/s (point 6). Fixed parameters: scan line hatch spacing 0.15 mm and powder layer thickness 0.15 mm. (**b**), (**d**), and (**f**) are local magnifications of (**a**), (**c**), and (**e**), respectively

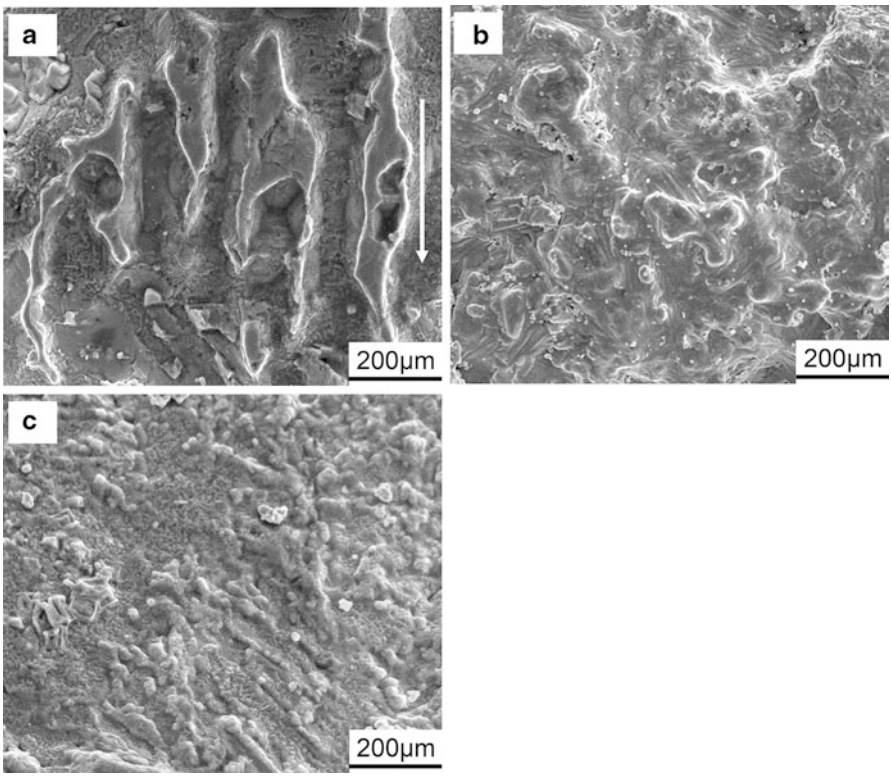


Fig. 9.6 SEM images showing typical surface morphologies of laser-sintered W–Cu samples with various scan line hatch spacings: **a** 0.30 mm; **b** 0.25 mm; **c** 0.15 mm. Fixed parameters: laser power 850 W, scan speed 0.05 m/s, and powder layer thickness 0.15 mm

it was noted that a further decrease in the layer thickness to 0.10 mm reduced the level of interlayer microstructural homogeneity (Fig. 9.8c). The obtainable DMLS-processed densification level, 82.6 % TD, also showed a decrease.

9.3.3 Process Control and its Mechanisms for DMLS of W–Cu Components

9.3.3.1 Control of Melting Mechanisms by "Linear Energy Density" (LED)

During DMLS process, laser scanning is performed line-by-line over the powder bed at a constant speed. The dwelling time of the laser spot at any irradiating region is extremely short, typically less than 4 ms [14]. Due to such a localized nature of the rapid DMLS process, the particle bonding must occur speedily, in the order of seconds [15]. Therefore, a sintering mechanism involving the formation of liquid

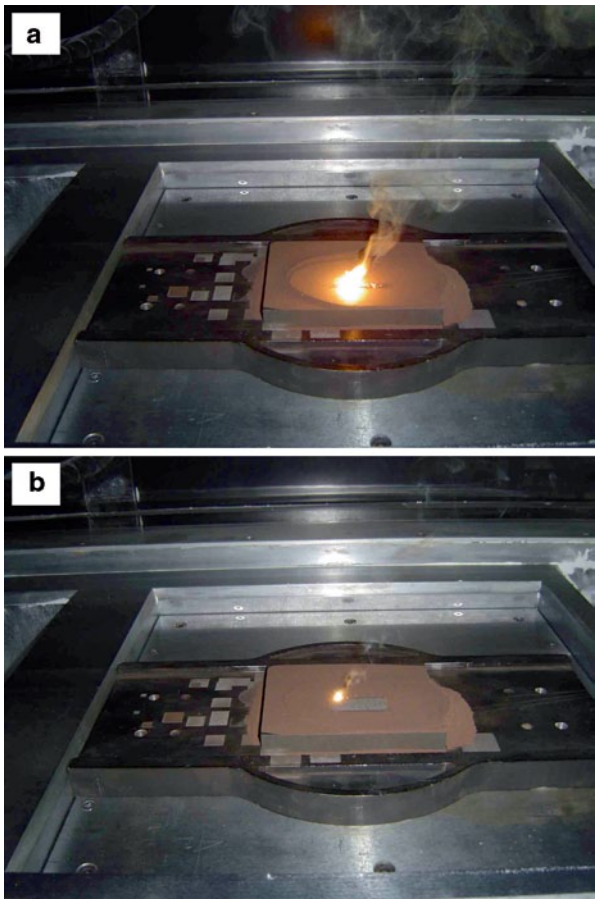


Fig. 9.7 Photographs of the real-time DMLS process of W–Cu components using different powder layer thicknesses: **a** 0.30 mm; **b** 0.15 mm

Cu phase is more reasonable for DMLS. Laser sintering of W–Cu composite powder starts by means of the selective melting of Cu component, due to a significant difference in the melting temperatures of Cu and W (~1083 °C vs. ~3410 °C). A close look at the process map (Fig. 9.3) reveals that processing parameters are required to be carefully tailored, in order to achieve a favorable mechanism of melting. It is worth noting that the laser power (P) and scan speed (v) are the two main parameters involved in the individual line scanning. In order to assess their combined effect, a new parameter, i.e., "linear energy density (LED)," is defined by:

$$\text{LED} = \frac{P}{v} \tag{9.1}$$

After converting Fig. 9.3 into Fig. 9.9 using the defined LED, it is easy to find that the powder melting mechanisms show a distinct change with the incident LED. For a given LED below ~13 kJ/m, laser sintering at all scan speeds induces a considerably low degree of liquid formation due to an insufficient melting of the low melting

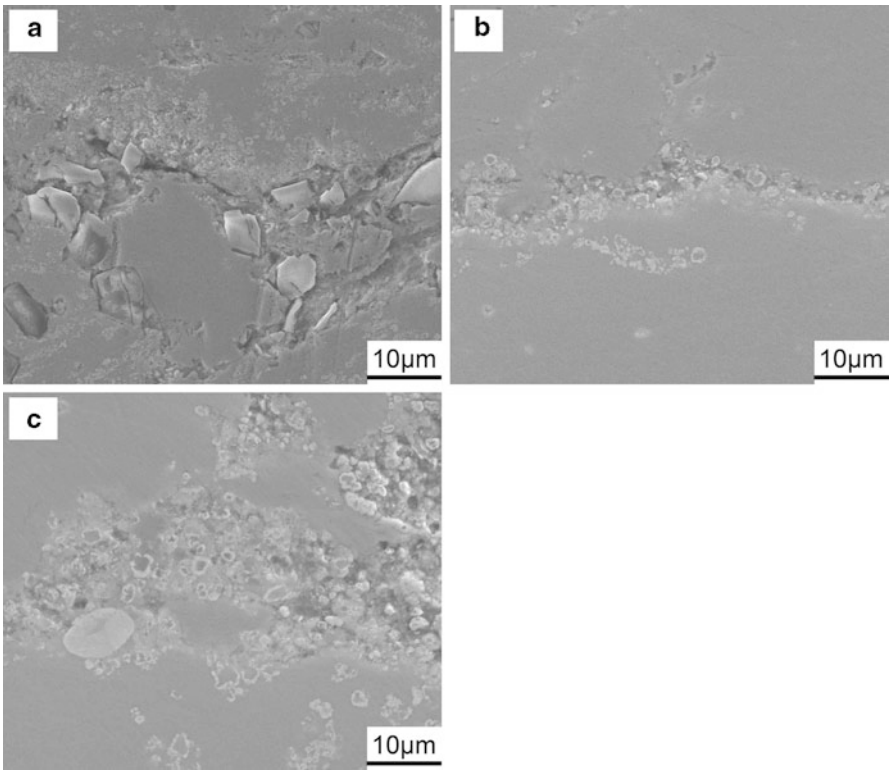


Fig. 9.8 SEM images on cross-sections of laser-sintered W–Cu samples showing interlayer bonding at different powder layer thicknesses: **a** 0.30 mm; **b** 0.15 mm; **c** 0.10 mm. Fixed parameters: laser power 850 W, scan speed 0.05 m/s, and scan line hatch spacing 0.15 mm

point Cu component, which inevitably results in a large amount of residual porosity after DMLS process (Fig. 9.4a). Using a LED between ~13 and ~19 kJ/m proves to be feasible in realizing a continuous melting of the Cu component, thereby producing a sufficient amount of liquid phase. More molten liquid is thus likely to flow and infiltrate into the voids between the W solids, yielding a denser microstructure (Fig. 9.4b). However, using a high scan speed larger than 0.06 m/s incurs detrimental effects due to the occurrence of balling, even though the obtained LED falls within this favorable range (Fig. 9.4c). In this situation, the Cu liquid is able to spread around the W solid particles into a continuous film of a cylindrical shape in the initial stage of melting, owing to the sufficient energy input. However, due to an enhanced capillary instability effect induced by a higher scan speed, a significant transverse shrinkage distortion tends to initiate in interparticle areas, resulting in the breakage of Cu liquid film along the molten track. Also, a higher scan speed results in a rapid decrease in the diameter of the cylindrical shaped scan track. Thus, the radial contraction of the liquid track occurs, changing the direction of fluid flow from radially outward to radially inward and, eventually, causing the balling effect [16].

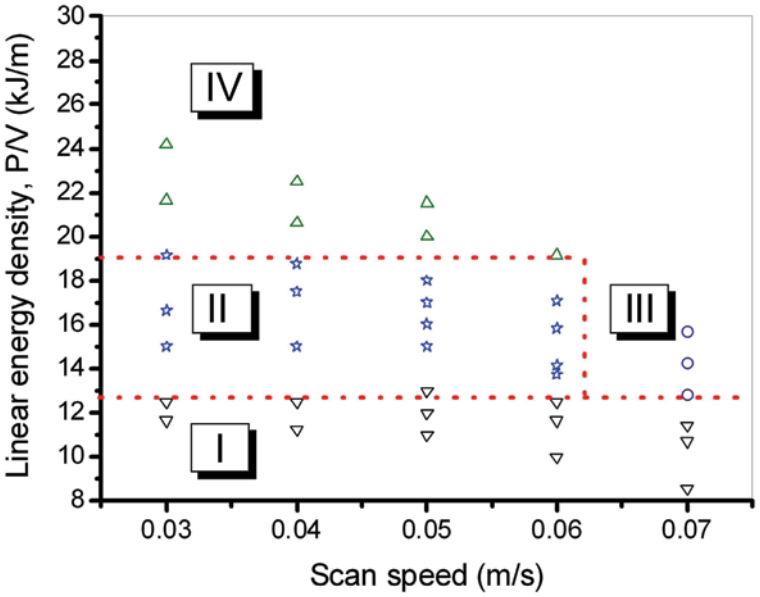


Fig. 9.9 Variation of powder melting mechanisms with linear energy density for DMLS processing of W–Cu composite powder system

At an even higher LED above ~19 kJ/m, an excessive energy input enhances the operating temperature significantly, resulting in a high degree of superheating of the low melting phase Cu. The viscosity of liquid–solid mixture, thus, decreases markedly, which in turn elevates the Marangoni effect considerably. As a consequence, a significant shrinkage occurs during liquid–solid transition, thus decreasing the attainable density due to the formation of interrupted scan tracks and large-sized pores (Fig. 9.4d). Also, the overheating of the sintering system causes a large degree of warping of the DMLS-processed parts owing to the high thermal gradients which induce residual stresses relieved by shape change.

9.3.3.2 Influence of Processing Parameters on Microstructural Development

It is well known that the conventional LPS process consists of three overlapping stages: particle rearrangement, solution reprecipitation, and solid state sintering [17]. The W–Cu as investigated is a unique material combination because of the good wettability yet mutual insolubility of W in Cu, which makes the contribution of solution reprecipitation negligible [7, 8]. Therefore, only the first stage, i.e., particle rearrangement, plays a main role in realizing a successful DMLS due to the short interaction duration between the laser and the powder. In general, laser sintering using different LEDs within zone II of Fig. 9.9 yields a sound density (Table 9.2), which is mainly ascribed to the sufficient amount of liquid formation

(Fig. 9.3). However, the microstructural homogeneity of DMLS-processed W–Cu composites varies with the LED (Fig. 9.5). In detail, the LEDs corresponding to Fig. 9.5a, b, and c are 15, 17.5, and 14.2 kJ/m, respectively. Thus, it can be assumed that using a higher LED leads to a more homogeneous microstructure (Fig. 9.5c) combined with an interesting W-rim/Cu-core structure (Fig. 9.5d). A comparative study reveals that increasing laser power (Fig. 9.5a vs. 9.5c) or decreasing scan speed (Fig. 9.5e vs. 9.5c) can generally enhance the LED. A higher LED, thus, favors a higher DMLS temperature, due to a larger energy gain of the powder. It is known that the surface tension (σ, mN/m) of Cu liquid has a linear relationship with the temperature (T, °C), and can be estimated by [18]:

$$\sigma = 1330 - 0.23(T - 1085) \tag{9.2}$$

Therefore, a higher LED leads to a higher T and, accordingly, a lower σ. On the other hand, based on Takamichi and Roderick's results [19], the dynamic viscosity of the liquid (η, Pa·s) is dependent on the surface tension (σ) and the temperature (T); either a higher T or a lower σ leads to a smaller η. During DMLS of W–Cu composites, the main forces acting on W solids are: the capillary force for the rearrangement of W particles and the friction force due to the flow of Cu liquid around W particles. Anestiev and Froyen's work [20] reveals that the capillary force is in inverse proportion to the σ, while the friction force is proportional to the η. Therefore, a decrease in σ and η, which can be realized by increasing LED, enhances the capillary force and, meanwhile, lowers the friction force. The combined effect of these two factors favors the sufficient rearrangement of W particles, thus producing a homogeneous sintered structure free of the apparent aggregation of W solids (Fig. 9.5c). Additionally, an interesting W-rim/Cu-core structure is present in this situation (Fig. 9.5d). Its formation mechanism and underlying influencing factors will be proposed in detail in Sect. 9.5.

On the other hand, the DMLS processing and densification behavior of the W–Cu powder system would be influenced by scan line hatch spacing during line-by-line laser melting (Fig. 9.6). As is evident from Niu and Chang's work [21], there exists a torque around the nonspherical W particles in Cu liquid, due to the misalignment of W solids. In addition, since the spatial intensity profile of the used laser beam follows a Gaussian distribution (Fig. 9.10), a large thermal gradient tends to develop between the center and edge of the melt pool, which further gives rise to surface tension gradient and attendant Marangoni flow [22]. The combined effect of the present torque and Marangoni flow tends to rotate the W solids in the melt pool and, meanwhile, moves them toward the centre of the laser beam, where the temperature is the highest. As a consequence, arrays of agglomerates located at the center of the scanned tracks and the large intertrack gaps are formed (Fig. 9.6a). Decreasing the scan line spacing brings the scan tracks closer to each other until they overlap (Fig. 9.10). The overlapping of the adjacent tracks makes it possible that a large part of the laser spot would scan over the previously scanned track and, accordingly, re-melt the previously processed materials. This favors the flow and spreading of liquid between scan tracks and the escaping of some previously

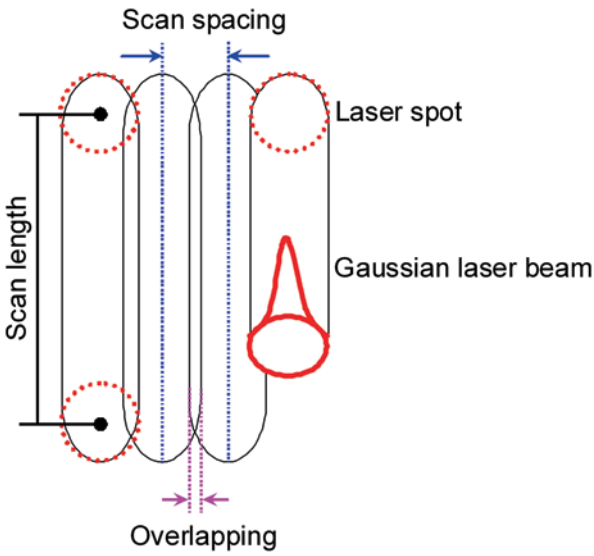


Fig. 9.10 Schematic of multiline laser scanning during DMLS process

trapped air, leading to the enhancement of the intertrack bonding and the reduction in the sintered porosity (Fig. 9.6b and c).

The move to the fabrication of a multilayer sample requires that an appropriate layer thickness to be determined. When the laser beam scans over the powder layer, the laser energy is directly absorbed by the solid particles through both, bulk coupling and powder coupling mechanisms [23]. Primarily, the laser energy is absorbed in a narrow layer of individual powder particles determined by the bulk properties of the materials, inducing a high temperature of the particle surface. The heat flows mainly toward the center of the particles until a uniform temperature within the particles is obtained. Subsequently, the surrounding powder properties are responsible for the further thermal development. It is known that a large volume of gas phase exists in pores between particles. The heat conductivity of a loosely packed powder layer (k_p) can be described as [24]:

$$k_p = k_a \left(\frac{3}{\varphi_p} - 2 \right) \tag{9.3}$$

where k_a is the heat conductivity of the air and φ_p is the porosity of the powder layer. Equation 9.3 reveals that the k_p is directly proportional to the k_a. Thus, at an initial stage of DMLS the k_p is considerably low, since the k_a (0.0259W/(m·K) @ 20°C and 1.01325×10^5 Pa) is negligible. Consequently, the heat generated during laser-powder interaction is difficult to conduct and transfer into the interior of the powder layer, especially for a thicker layer. The heat, thus, tends to accumulate on the surface of the layer, resulting in overheating and severe splashing of the powder (Fig. 9.7a). Also, interconnected pore channels between adjacent layers would be

formed in this instance (Fig. 9.8a), since the powder layer has not been completely melted down due to the insufficient energy penetration. It is known that a certain portion of air in pores between particles tends to be trapped as bubbles during laser melting [25]. If the layer is thin, most bubbles, even at the bottom of the layer, are able to rise up to the surface of the layer and collapse, leading to less porosity. Furthermore, for a thinner layer, the laser energy can not only completely penetrate the current layer, but also re-melt the surface of the previously processed layer, thus obtaining coherently bonded layers (Fig. 9.8b). However, for a given laser energy, a further decrease in layer thickness would result in an excessive liquid formation via overmuch re-melting of the previously processed materials, thus greatly enhancing the Marangoni effect. The elevated Marangoni forces would roughen the sintered surface, producing a considerably heterogeneous interlayer microstructure (Fig. 9.8c).

9.3.3.3 Integrated Process Control Using "Volumetric Energy Density" (VED)

DMLS is a complicated freeform shaping process, which follows a processing routine from a "line" to a "layer" and, subsequently, to a "bulk". DMLS starts with a single line scanning, thus introducing two main parameters, i.e., laser power (P) and scan speed (v). The completion of multiple scan lines leads to the formation of a laser-processed layer. Here, another parameter, i.e., scan line hatch spacing (h), is involved. The layer-by-layer bonding and consolidation yields a bulk component, which requires a suitable powder layer thickness (d) to be determined. In light of the experimental results (Figs. 9.3–9.8), it is clear that the P, v, h, and d all have great influence on the densification and attendant microstructural features of DMLS-processed W–Cu composites. In order to evaluate the combined effect of these parameters and, thus, control the DMLS process integrally, besides the above-proposed LED, another single factor termed "volumetric energy density (VED)" is defined as follows:

$$\mathrm{VED} = \frac{P}{vhd}. \tag{9.4}$$

The unit of VED is kJ/mm^3. Figure 9.11 depicts the relationship between the laser-sintered density and the VED under different processing conditions. It is evident that for a given VED between ~0.6 and ~0.8 kJ/mm^3, the attainable density is generally high (>90 % TD). Either a VED below ~0.6 kJ/mm^3 or a VED above ~0.8 kJ/mm^3 results in a poor densification. For example, the surface morphologies of laser-sintered samples at the VEDs of 0.556, 0.756, and 0.889 kJ/mm^3 are shown in Figs. 9.4a, d, and 9.6c, respectively. Here, it should be noted that although a suitable VED can be obtained by using a high laser power combined with a high scan speed, balling phenomena would initiate under such condition (Figs. 9.3 and 9.9), which ultimately deteriorates the densification level. For instance, the VED corresponding

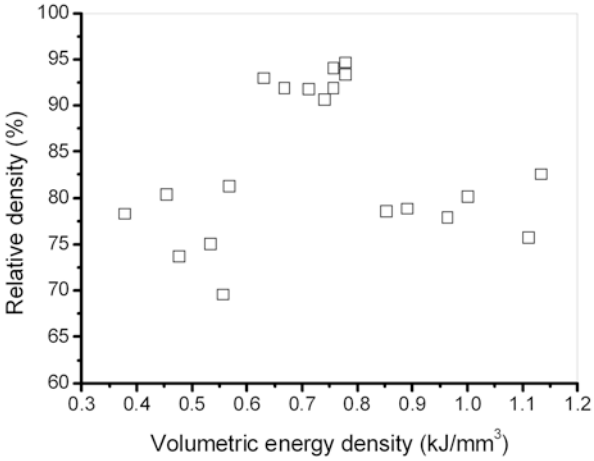


Fig. 9.11 Change of relative density of laser-sintered samples with volumetric energy density for the W–Cu composite system. Only valid between 0.02 and 0.06 m/s scan speeds

to Fig. 9.4c (i.e., 0.635 kJ/mm^3) falls within the above favorable range, but a higher scan speed in this case (i.e., 0.07 m/s) causes the balling and resultant porosity in DMLS-processed W–Cu composites.

9.4 Influence of Cu-Liquid Content on Densification and Microstructure of Nano/Micron W–Cu Composites Prepared by DMLS

9.4.1 Densification and Microstructure of DMLS-Processed W–Cu Composites with Variation of Cu-Liquid Contents

Figure 9.12 shows the characteristic surface morphologies of DMLS-processed W–Cu composites using different contents of micron Cu powder. At a low content of 35 wt.% (powder A, Table 9.1), a rough surface consisting of a large amount of cracks was present. Such surface also contained some remaining unsintered powder particles (Fig. 9.12a). Laser sintering of powder B consisting of 50 wt.% micron Cu powder yielded a pretty dense sintered surface without any apparent pores or cracks (Fig. 9.12b). However, when the content of micron Cu powder increased to 65 wt.% (powder C), the sintered surface consisted of rows of coarsened balls, between which interconnected pore channels were formed (Fig. 9.12c). Thus, it was inferred that "balling" phenomenon, which was regarded as a typical defect associated with DMLS, initiated in this case.

Unlike the conventional press/sintering powder metallurgy route, DMLS is a laser-based additive manufacturing process that builds objects layer-by-layer using

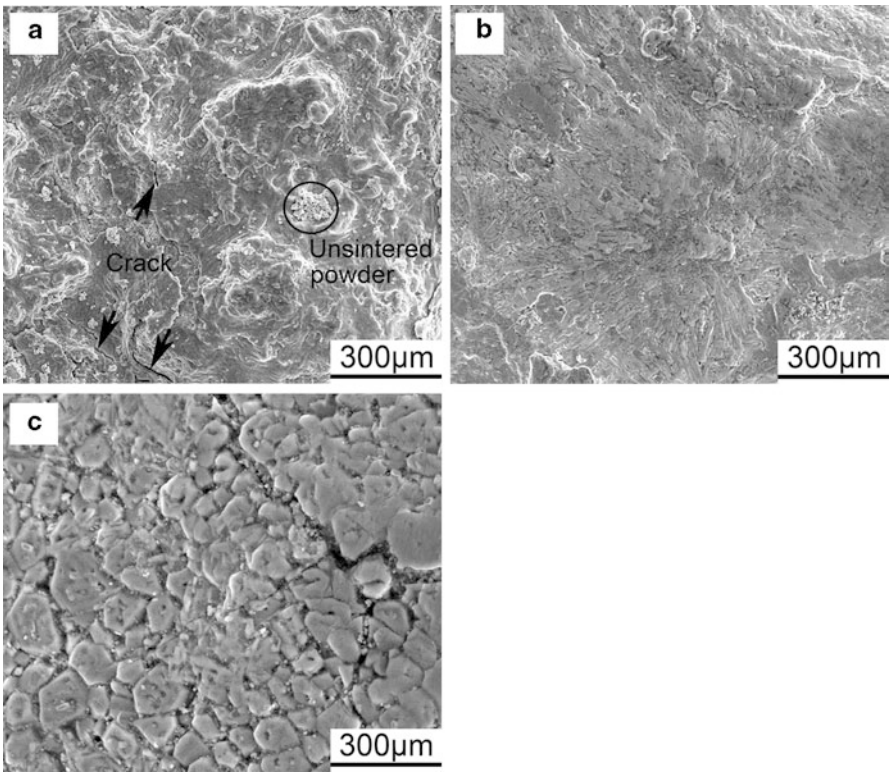


Fig. 9.12 SEM images showing typical surface morphologies of laser-sintered W–Cu samples using different contents of micron Cu powder: **a** 35 wt.% Cu powder; **b** 50 wt.% Cu powder; **c** 65 wt.% Cu powder

a bed of loose powder. Therefore, it is important to study densification behavior of the loose powder during layer-by-layer DMLS process. Figure 9.13 exhibits the cross-sectional microstructures in laser-sintered W–Cu samples at different contents of micron Cu powder. In order to further characterize the interlayer bonding property in each sample, a higher magnification observation was used, as illustrated in Fig. 9.14. Figure 9.15 depicts the laser-sintered density of the corresponding sample. In the case of powder A containing 35 wt.% Cu powder (Table 9.1), the obvious layerwise structure was formed after laser sintering (Fig. 9.13a). SEM micrograph at a higher magnification revealed that deep and interconnected pore channels were visible between sintered layers, resulting in a poor interlayer bonding and, accordingly, a low densification response (81.6% theoretical density) (Figs. 9.14a, 9.15). Interestingly, laser sintering of powder B with 50 wt.% Cu powder led to the formation of a rather dense cross-section without any apparent layerwise structure (Fig. 9.13b). In this instance, no pores or cracks were present between laser-sintered layers, thereby producing a coherent interlayer bonding (Fig. 9.14b). Under this condition, a high sintered density (94.8% theoretical density) was obtained

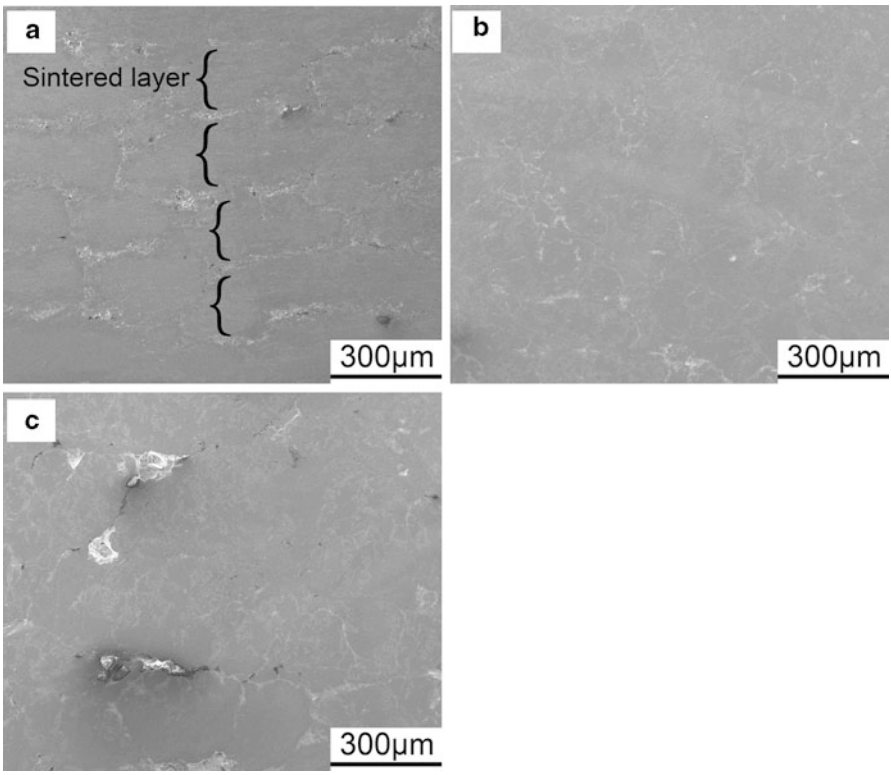


Fig. 9.13 Low-magnification SEM images showing cross-sectional microstructures in laser-sintered W–Cu samples using different contents of micron Cu powder: **a** 35 wt.% Cu powder; **b** 50 wt.% Cu powder; **c** 65 wt.% Cu powder

(Fig. 9.15). Thus, it is reasonable to consider that DMLS holds a high promise to manufacture W–Cu components with densification level equivalent to or superior than conventionally PM-processed materials. However, as to powder C consisting of 65 wt.% Cu powder, large-sized pores were visible in the cross section of laser-sintered sample (Fig. 9.13c), resulting in a low bonding ability between laser-sintered layers (Fig. 9.14c). Consequently, the obtainable densification level of laser-sintered W–Cu composites, i.e., 85.3 % theoretical density, was limited (Fig. 9.15).

The high-magnification microstructures on the polished sections of laser-sintered W–Cu samples are provided in Fig. 9.16. Generally, the EDX results revealed that the white phase was the W, while the surrounding gray matrix was the Cu. The microstructural features of W phase (e.g., shape, size, and dispersion state), however, were varied with the Cu contents in the DMLS processing system. Laser sintering of powder A consisting of 35 wt.% Cu powder produced the clusters of fine W grains (Fig. 9.16a). Interestingly, in laser-sintered structure of powder B containing 50 wt.% Cu powder, a series of white rings were distributed in a rather homogeneous state (Fig. 9.16b). The EDX results, as listed in Table 9.3, revealed

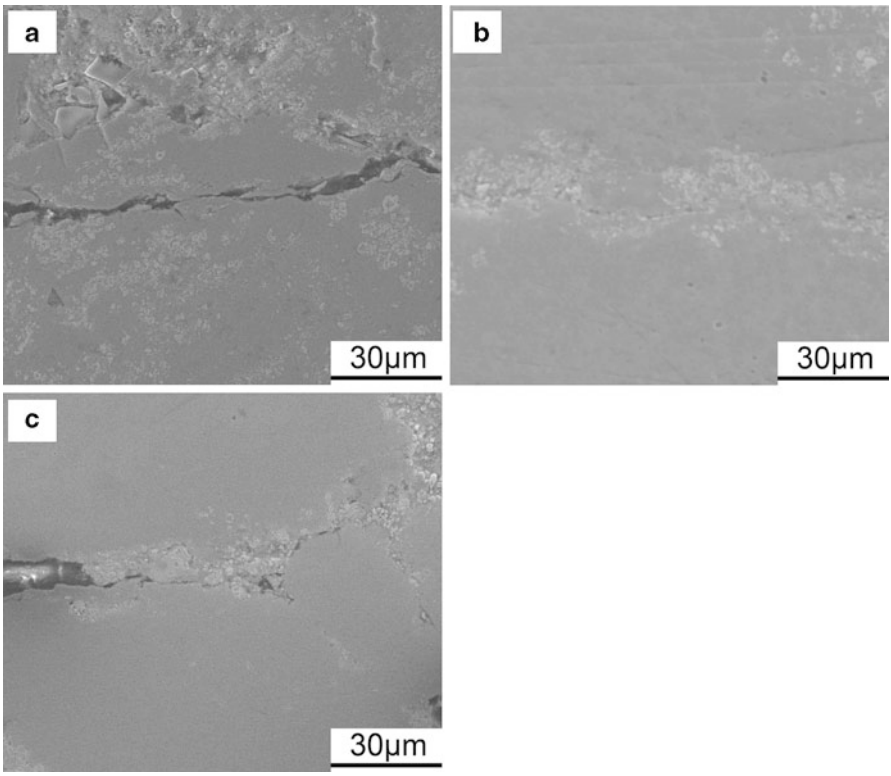


Fig. 9.14 High-magnified SEM images showing interlayer bonding in laser-sintered W–Cu samples using different contents of micron Cu powder: **a** 35 wt.% Cu powder; **b** 50 wt.% Cu powder; **c** 65 wt.% Cu powder

that the white ring (position 1) was mainly composed of the W element, while the surrounding dark matrix (position 2) was rich in the Cu element. Figure 9.17 depicts the typical XRD spectrum of the corresponding W–Cu sample. The strong diffraction peaks for W (bcc structure) and Cu (fcc structure) phases were clearly observed. Thus, it could be considered that the laser-sintered materials were composed of the W and Cu phases. SEM characterization at a higher magnification showed that the white W solids were well arranged and connected into a regularly-shaped ring structure (Fig. 9.18a). In order to further examine the distributions of W and Cu elements in the present structure, an EDX line-scan was performed along the line AB in Fig. 9.18a. It was observed that the W element showed a higher concentration in the ring structures, while the Cu had a higher elemental distribution inside the rings (Fig. 9.18b). Combined with the XRD, SEM and EDX results, it was confirmed that the W–Cu composites with an interesting W-rim/Cu-core structure were successfully prepared by DMLS of powder B. In the case of powder C consisting of 65 wt.% Cu powder, no W rings were formed after DMLS processing; instead, the significantly coarsened aggregates of W solids were visible in the matrix (Fig. 9.16c).

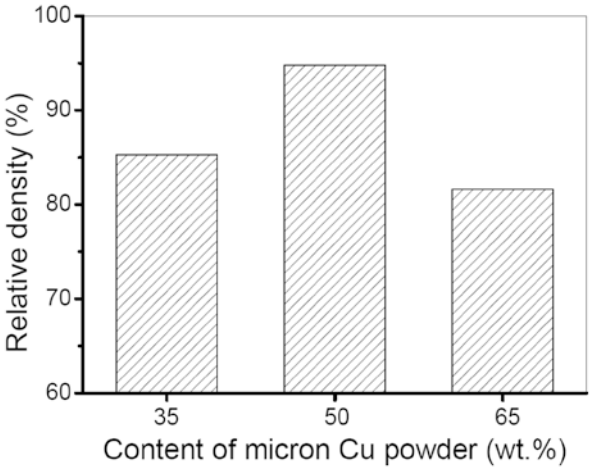


Fig. 9.15 Change of laser-sintered densities of W–Cu samples with contents of micron Cu powder

9.4.2 The Role of Cu-Liquid Content in Densification Behavior and Microstructural Development of DMLS-Processed W–Cu Composites

As mentioned previously, during DMLS the duration of laser beam at any irradiating zone depends on both spot size and scan speed, and is typically less than 4 ms [14]. In such an extremely short heating cycle, sintering must be occurring rather speedily, and, for this reason, a LPS mechanism rather than a solid phase sintering (SPS) one is more feasible to account for DMLS. In general, densification during LPS occurs through a combination of particle rearrangement due to capillary forces, grain-shape accommodation by solution reprecipitation, and sintering of the skeletal structure by solid state diffusion [7]. Exceptionally, for W–Cu system, the insolubility of W in Cu makes the contribution of solution reprecipitation negligible, densification, thus, can be attributed to either rearrangement or SPS [8]. Due to the localized nature of laser scanning, the dwell time of heat resource at any scanning zone is extremely short, so laser-induced melting is followed by a rapid solidification and cooling. In other words, the last SPS stage is generally negligible. Thus, particle rearrangement is a dominant stage in realizing a successful LPS during DMLS processing.

Within the laser-induced molten pool, either concentration differences or temperature gradient at solid–liquid interfaces within the pool may generate surface tension gradients and resultant Marangoni flow [16]. The formation of convective streams within the pool induces liquid capillary forces. Densification, accordingly, occurs as a result of the rearrangement of solid particles under the influence of capillary forces exerted on them by the liquid. The obtained results, as shown in Fig. 9.12a and b, reveal that a proper increase in Cu-liquid content yields a denser sintered surface. According to Tolochko et al.'s results [26], a higher volume

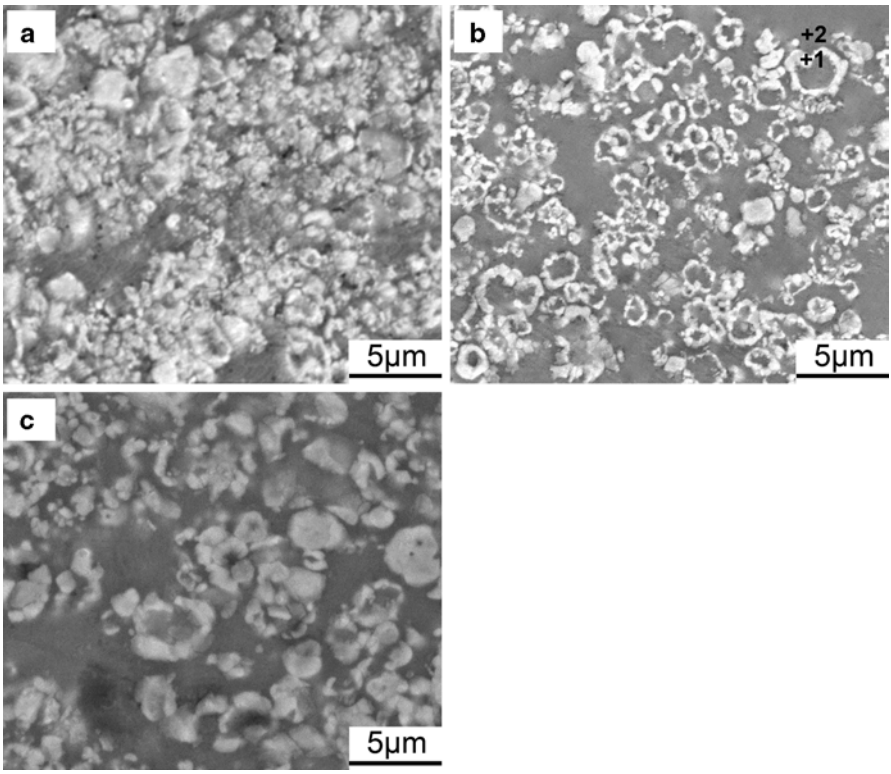


Fig. 9.16 SEM images showing characteristic microstructures on polished sections of laser-sintered W–Cu samples using various contents of micron Cu powder: **a** 35 wt.% Cu powder; **b** 50 wt.% Cu powder; **c** 65 wt.% Cu powder

Table 9.3 Chemical compositions at different regions in laser-sintered structure

Label	Position	Chemical compositions (wt.%)	
		W	Cu
1, Fig. 9.16b	The white rim	82.73	17.27
2, Fig. 9.16b	The dark core	24.58	75.42

fraction of liquid phase in a sintering system leads to a lower viscosity of a solid–liquid mixture. In the present study, on increasing Cu-liquid content, the mixture viscosity within the molten pool decreases, leading to a favorable rheological properties of the molten liquid in conjunction with solid particles. Under this condition, the W solid particles are expected to experience a sufficient rearrangement in the liquid, so as to obtain a high sintering activity and attendant sound densification response (Fig. 9.12b). Furthermore, the previous results [27] have shown that the molten liquid cylinder will be stable against any perturbation if $\lambda < \pi D$, where λ is the wavelength and D is the initial diameter of an unperturbed track. For a given

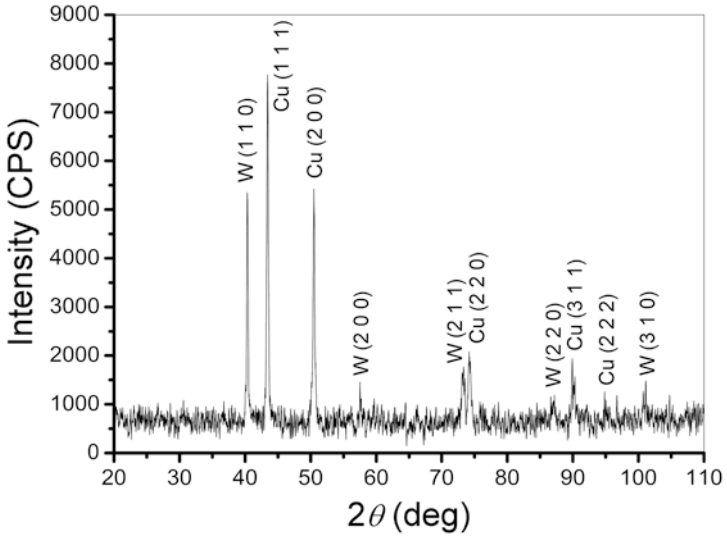


Fig. 9.17 XRD spectrum of laser-sintered W–Cu composites

λ, the molten track becomes more stable with increasing D. Considering the fact that a larger amount of liquid formation can significantly decrease the viscosity of a liquid–solid mixture, the resultant favorable spreadability of the melt leads to an increase in D. Therefore, the liquid tracks are not easy to break up, so as to improve the intertrack binding and reduce the surface roughness of laser-processed layer (Fig. 9.12a and b). On the other hand, the successful consolidation of bulk-form W–Cu components by DMLS requires a coherent bonding between multiple sintered layers. A close comparison of the obtained results (Fig. 9.13a vs. b, Fig. 9.14a vs. b) reveals that a higher densification with a better interlayer bonding is obtainable if using a higher Cu-liquid content. Here, a larger amount of liquid formation induces a lower viscosity of the molten materials, which in turn favors a sufficient removal and flattening of the liquid on the previously processed layer. In this situation, a stronger bonding between the fresh layer and the pretreated layer can be easily obtained (Figs. 9.13b, 9.14b).

However, a further increase in Cu-liquid content cannot lead to an improvement in laser-sintered density (Fig. 9.15), due to the occurrence of balling phenomenon (Fig. 9.12c). Based on Agarwala et al.'s work [15], the solid–liquid mixture viscosity should be high enough to prevent balling during DMLS. In the present study, however, an even higher Cu-liquid content results in an overmuch decrease in mixture viscosity, thereby causing the significant balling. The occurrence of balling phenomenon results in the formation of discontinuous scan tracks and poor interline bonding properties (Fig. 9.12c). Furthermore, balling phenomenon is a severe impediment to the uniform deposition of the fresh powder on the previously sintered layer. As a consequence, for a fixed energy input, the fresh powder layer cannot be smoothly sintered. The regions where the powder layer is thicker undergo an insufficient melting, leaving a large amount of porosity between sintered layers.

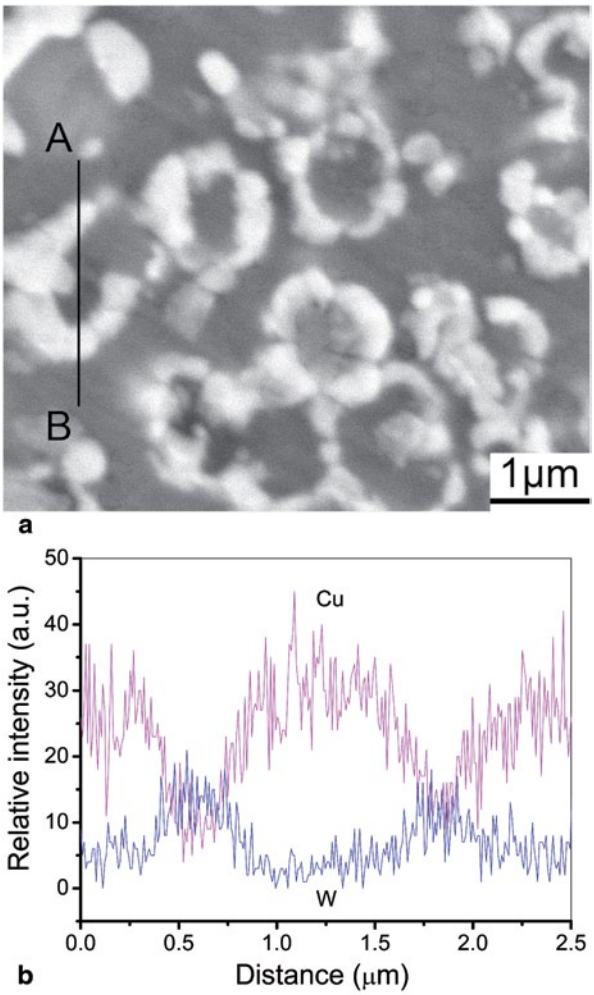


Fig. 9.18 SEM image showing typical W-rim/Cu-core structure (**a**); EDX analysis showing distributions of W and Cu elements (**b**)

Whereas, the regions possessing a thinner powder layer undergo an excessive melting, producing a considerably large thermal stress. The combined influence of the above two factors causes an apparent delamination induced by poor interlayer bonding (Figs. 9.13c, 9.14c), resulting in a significant decrease in densification level (Fig. 9.15).

9.4.3 Formation Mechanism of a Novel W-rim/Cu-Core Structure During DMLS of W–Cu Composite System

The obtained results, as shown in Figs. 9.16b and 9.18, reveal that by using a suitable amount micron Cu powder (50 wt.%), an interesting W-rim/Cu-core struc-

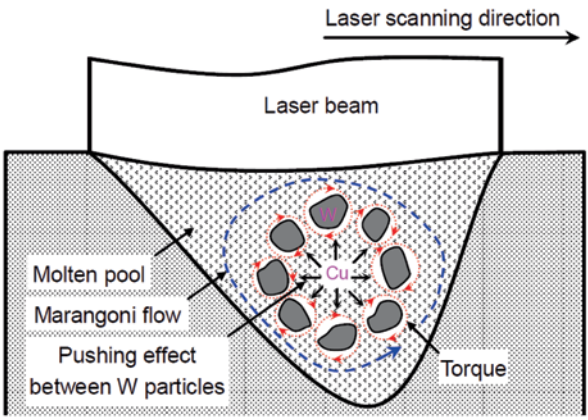


Fig. 9.19 Schematic of the formation mechanism of W-rim/Cu-core structure during laser sintering of W–Cu composites

ture is formed after laser sintering, besides the obtaining of a high sintered density (Figs. 9.13b, 9.14b). The mechanism for the formation of such a novel structure during DMLS is presented, as schematically illustrated in Fig. 9.19. As stated above, either temperature gradient or concentration differences at solid (W)/liquid (Cu) interfaces will lead to surface tension gradients and resultant Marangoni flow. The total Marangoni flow, accordingly, can be divided into two parts: the thermal Marangoni flow and the solutal one [28, 29]. Based on Yin et al.'s experimental results [28], the thermal component of Marangoni flow will lead to a clockwise flow pattern (defined as source flow), whereas the solutal one does the opposite (defined as converging flow); the clockwise thermal component is weaker than the counterclockwise solutal one, so the overall flow pattern observed is counterclockwise. In the case of LPS of nonspherical W particles, there exists a torque around the particle, due to (i) the misalignment of the particle center [21] and (ii) the action of the thermal Marangoni flow (i.e., source flow). The present torque tends to rotate the W particles in the molten pool, favoring a rapid rearrangement of particles. Meanwhile, the comparatively stronger solutal Marangoni flow (i.e., converging flow) continuously drives these W particles, gathering the particles around the center of the Marangoni flow pattern to form the W-rim. On the other hand, the particle pushing effect during rapid solidification of the Cu melt can also be operative, since Anestiev et al.'s work [20] reveals that repulsion forces will arise between particles when a sufficient amount of liquid forms. In this situation, the W particles remain a certain distance from the center of Marangoni flow pattern, even in the presence of the converging flow to drive them toward the center, which well accounts for the remaining of the Cu-core. Thus, a typical W-rim/Cu-core structure is expected to be formed after solidification (Figs. 9.16b, 9.18).

The present results also reveal that only when a suitable amount of liquid is present, the novel W-rim/Cu-core structure can be formed (Fig. 9.16b). A smaller amount of liquid formation produces clusters of W solids (Fig. 9.16a), whereas coarsened W aggregates are formed at a higher liquid content (Fig. 9.16c). The change of microstructural features with Cu-liquid contents is believed to ascribe to

the variation in Marangoni flow within the molten pool. According to Arafune and Hirata's work [29], the dimensionless Marangoni number (M_a) can be defined by Eq. 3.11. The M_a is inversely proportional to the dynamic viscosity μ of the liquid. For a low liquid content, the total intensity of Marangoni flow within the pool is limited, due to a higher μ of the molten materials. In this situation, the simultaneous heat and mass transport, which is primarily governed by Marangoni flow [30–32], is restrained. In other words, the DMLS processing kinetics is too low to accomplish the forming process of the W-rim/Cu-core structure, although it can provide some impetus to fulfill a certain amount of particle rearrangement (Fig. 9.16a). On the other hand, using an even higher Cu content leads to a considerably large amount of liquid formation, resulting in a significantly decrease in μ and, accordingly, a sharp increase in M_a. It has been found that the surface velocity of solutal component of Marangoni flow is about three to five times higher than that of thermal component [29]. In other words, an increase in M_a results in a more significant enhancement of solutal Marangoni flow (i.e., converging flow). Consequently, the fine W solid particles are much easy to converge into a series of coarsened aggregates, showing no residual Cu cores after sintering (Fig. 9.16c).

9.5 Conclusions

In this Chapter regarding DMLS additive manufacturing of nano/micron W–Cu composites, the main conclusions were summarized as follows.

1. The processing conditions and control methods for DMLS of W–Cu composite powder system were investigated. Using a LED between ~13 and ~19 kJ/m combined with a suitable scan speed (<0.06 m/s) led to a continuous melting of the Cu component, yielding a sound densification level (>92% theoretical density) free of any balling phenomena. A proper increase in the LED above ~13 kJ/m, which was realized by increasing laser power or lowering scan speed, improved the microstructural homogeneity of laser-sintered materials. Narrowing the scan line spacing to 0.15 mm was able to enhance the intertrack bonding, and to reduce the roughness of the laser-sintered surface. Decreasing the powder layer thickness to 0.15 mm was a promising approach for improving the bonding ability between sintered layers. A further decrease in the powder layer thickness to 0.10 mm produced a heterogeneous interlayer microstructure. Setting the VED within ~0.6 and ~0.8 kJ/mm^3 facilitated an integrated control of the laser sintering process, which proved to be an efficient method to produce high-density sintered parts.
2. The influence of Cu-liquid content on densification response and microstructural development of direct laser-sintered W–Cu components was investigated. A proper increase of Cu elemental fraction to 60 wt.% yielded a high densification of 94.8% theoretical density, due to a favorable viscosity of liquid–solid mixture and the resultant sufficient rearrangement of W particles. However, a

further increase in Cu-liquid content deteriorated laser-sintered density, due to the occurrence of balling phenomenon. The present Cu-liquid content affects microstructural features of laser-sintered components. A smaller amount of liquid formation produces clusters of W solids, whereas coarsened W aggregates are formed at a higher liquid content. Such microstructural changes are ascribed to the variation in intensities of Marangoni flow within the molten pool.

3. At the suitable Cu elemental content and DMLS processing conditions, a series of regularly shaped W-rim/Cu-core structures were formed after laser sintering. The metallurgical mechanisms for the formation of such a novel structure were proposed. The formation of the W-rim was attributed to the combined action of the clockwise thermal Marangoni flow and the counterclockwise solutal one, which was induced by temperature gradient or chemical concentration at the solid–liquid interface. The repulsion forces between W particles in Cu liquid and the particle pushing effect during rapid solidification of Cu melt prevented the W-rim from merging and, accordingly, remained the Cu-core after solidification.

References

1. Maneshian MH, Simchi A, Hesabi ZR (2007) Structural changes during synthesizing of nanostructured W–20 wt.% Cu composite powder by mechanical alloying. Mater Sci Eng A 445–446:86–93
2. Ozer O, Missiaen JM, Lay S et al (2007) Processing of tungsten/copper materials from W–CuO powder mixtures. Mater Sci Eng A 460–461:525–531
3. Kim DG, Kim GS, Suk MJ et al (2004) Effect of heating rate on microstructural homogeneity of sintered W–15 wt%Cu nanocomposite fabricated from W–CuO powder mixture. Scr Mater 51(7):677–681
4. da Costa FA, da Silva AGP, Gomes UU (2003) The influence of the dispersion technique on the characteristics of the W–Cu powders and on the sintering behavior. Powder Technol 134(1–2):123–132
5. Zhou ZJ, Kwon YS (2005) Fabrication of W–Cu composite by resistance sintering under ultra-high pressure. J Mater Process Technol 168(1):107–111
6. German RM, Hens KF, Johnson JL (1994) Powder metallurgy processing of thermal management materials for microelectronic applications. Int J Powder Metall 30(2):205–215
7. Johnson JL, Brezovsky JJ, German RM (2005) Effect of liquid content on distortion and rearrangement densification of liquid-phase-sintered W–Cu. Metall Mater Trans A 36A(6):1557–1565
8. Johnson JL, Brezovsky JJ, German RM (2005) Effects of tungsten particle size and copper content on densification of liquid-phase-sintered W–Cu. Metall Mater Trans A 36A(10):2807–2814
9. Alam SN (2006) Synthesis and characterization of W–Cu nanocomposites developed by mechanical alloying. Mater Sci Eng A 433(1–2):161–168
10. Yoon ES, Lee JS, Oh ST et al (2002) Microstructure and sintering behavior of W–Cu nanocomposite powder produced by thermo-chemical process. Int J Refract Met Hard Mater 20(3):201–206
11. Kim DG, Lee BH, Oh ST et al (2005) Mechanochemical process for W–15 wt.%Cu nanocomposite powders with WO_3–CuO powder mixture and its sintering characteristics. Mater Sci Eng A 395(1–2):333–337

12. Williams JM, Adewunmi A, Schek RM et al (2005) Bone tissue engineering using polycaprolactone scaffolds fabricated via selective laser sintering. Biomaterials 26(23):4817–4827
13. Yang MC, Song ZZ, Lu K (2004) Synthesis of W–20%Cu nanocomposite powders. Acta Metall Sin 40(6):639–642
14. Simchi A, Pohl H (2003) Effects of laser sintering processing parameters on the microstructure and densification of iron powder. Mater Sci Eng A 359(1–2):119–128
15. Agarwala M, Bourell D, Beaman J et al (1995) Direct selective laser sintering of metals. Rapid Prototyp J 1(1):26–36
16. Niu HJ, Chang ITH (1999) Instability of scan tracks of selective laser sintering of high speed steel powder. Scr Mater 41(11):1229–1234
17. Zhu HH, Lu L, Fuh JYH (2004) Influence of binder's liquid volume fraction on direct laser sintering of metallic powder. Mater Sci Eng A 371(1–2):170–177
18. Yuan ZF, Ke JJ, Li J (2006) Surface tension of metals and alloys. Science Press, Beijing
19. Takamichi I, Roderick ILG (1993) The physical properties of liquid metals. Clarendon Press, Oxford
20. Anestiev LA, Froyen L (1999) Model of the primary rearrangement processes at liquid phase sintering and selective laser sintering due to biparticle interactions. J Appl Phys 86(7):4008–4017
21. Niu HJ, Chang ITH (1999) Selective laser sintering of gas and water atomized high speed steel powders. Scr Mater 41(1):25–30
22. Lampa C, Kaplan AFH, Resch M et al (1998) Fluid flow and resolidification in deep penetration laser welding. Laser Eng 7(3–4):241–252
23. Fischer P, Romano V, Weber HP et al (2003) Sintering of commercially pure titanium powder with a Nd:YAG laser source. Acta Mater 51(6):1651–1662
24. Gu DD, Shen YF, Liu MC et al (2004) Numerical simulations of temperature field in direct metal laser sintering process. Trans Nanjing Univ Aeronaut Astronaut 21(3):225–233
25. Dingal S, Pradhan TR, Sundar JKS et al (2008) The application of Taguchi's method in the experimental investigation of the laser sintering process. Int J Adv Manuf Technol 38(9–10):904–914
26. Tolochko N, Mozzharov S, Laoui T et al (2003) Selective laser sintering of single- and two-component metal powders. Rapid Prototyp J 9(2):68–78
27. Niu HJ, Chang ITH (1998) Liquid phase sintering of M3/2 high speed steel by selective laser sintering. Scr Mater 39(1):67–72
28. Yin HB, Emi T (2003) Marangoni flow at the gas/melt interface of steel. Metall Mater Trans B 34(5):483–493
29. Arafune K, Hirata A (1999) Thermal and solutal Marangoni convection in In-Ga-Sb system. J Cryst Growth 197(4):811–817
30. Gu DD, Shen YF (2006) Influence of phosphorus element on direct laser sintering of multi-component Cu-based metal powder. Metall Mater Trans B 37(6):967–977
31. Wu MH, Ludwig A, Ratke L (2003) Modelling the solidification of hypermonotectic alloys. Model Simul Mater Sci Eng 11(5):755–769
32. Dong WC, Lu SP, Li DZ et al (2008) Numerical simulation of effects of the minor active-element oxygen on the Marangoni convection and the weld shape. Acta Metall Sin 44(2):249–256

Chapter 10
Summary and Prospective View

Abstract Researches on laser-based additive manufacturing (AM) of metallic components are interdisciplinary, integrating laser technology, materials science, mechanical engineering, metallurgical engineering, etc. For the powder bed-based AM processes, i.e., selective laser melting (SLM) and direct metal laser sintering (DMLS), significant research and understanding are still required in the aspects of materials preparation and characterization, process control and optimization, microstructural and mechanical properties evaluation, and theories of physical and chemical metallurgy. This chapter summarizes the main findings of this book concerning SLM and DMLS production of new materials components, including nanostructured material, *in situ* composite material, particle reinforced metal matrix composites (MMCs), etc. The issues that are of particular significance for the future development of laser-based AM technology are also proposed.

10.1 Summary of Main Work and Findings

For the laser-based additive manufacturing (AM) technology, the combination of unique materials incremental manufacturing philosophy and a highly nonequilibrium metallurgical nature of laser process provides a beneficial method to simultaneously develop new materials, complex configurations, and unique microstructural and mechanical properties. The selective laser melting (SLM) and direct metal laser sintering (DMLS) technology, which are based on the powder bed-based processing method, are presently regarded as one of the most versatile AM processes. SLM and DMLS processes have demonstrated a high capability in producing complex-shaped functional metallic components, including metals, alloys, and metal matrix composites (MMCs) that cannot be easily produced by the conventional processing methods. This book chooses a unique angle to present the recent progress in research and development of SLM/DMLS AM technology, focusing on the materials aspects of SLM/DMLS. The development of components of new materials by SLM/DMLS AM process is presented in this book, particularly highlighting the nanostructured material, *in situ* composite material, particle reinforced MMCs, etc. The book covers comprehensively the following aspects of SLM/DMLS AM of new material components, including materials design and preparation, process

© Springer-Verlag Berlin Heidelberg 2015

D. Gu, *Laser Additive Manufacturing of High-Performance Materials,*
DOI 10.1007/978-3-662-46089-4_10

control and optimization, microstructural characterization, mechanical properties and evaluation, and physical and chemical metallurgical theories. A key strategy for the sustainable development in SLM/DMLS AM of high-performance metallic components, i.e., the integration of "designed material," "tailored process," and "controllable property," is emphasized in the present book. The material–process–microstructure–property relationship is proposed for each material system, in order to enable the successful production of new material components with novel microstructural characteristics and elevated mechanical performance. The main work and findings that are presented in this book are summarized as follows.

In Chap. 1, the development history of laser-based AM technology is briefly introduced and the nomenclature principles for naming different types of AM processes are reviewed. The general processing philosophy of AM is addressed and the typical applications of AM technology are presented.

Chapter 2 deals with the general review of three most versatile laser-based AM processes, i.e., laser sintering (LS), laser melting (LM), and laser metal deposition (LMD). The definition of LS/LM/LMD processes and the corresponding operative consolidation mechanisms for metallic components are proposed. Powder materials used for laser-based AM processes, in the categories of pure metal powder, prealloyed powder, and multicomponent metals/alloys/MMCs powder, and the associated densification mechanisms during laser AM are addressed. An in-depth review of material and process aspects of laser AM, including the physical aspects of materials for AM and the microstructural and mechanical properties of AM-processed metallic components, is presented. The main purpose of Chap. 2 is to establish a general relationship of material, process, microstructural and mechanical properties, and metallurgical mechanism for laser-based AM of metallic components.

In Chap. 3, SLM is applied to process the nanocrystalline TiC reinforced Ti matrix nanocomposites through the complete melting mechanism. The unique energy feature, heating manner, and metallurgical mechanism of high-energy laser irradiation are sufficiently considered, in order to realize the controllable growth and dispersion of nanoscale ceramic reinforcement. The microscopic pressure, Marangoni flow, velocity and solute fields within the nonequilibrium laser molten pool and their effects on the growth and dispersion of the nanoscale ceramic reinforcement are theoretically studied, thereby proposing the laser-controlled formation mechanisms of the nanoscale ceramic reinforcing phase. The influence of the contents of reinforcing ceramics and matrix metals, the physical properties of powders, and the laser processing parameters on the growth mechanisms of nanoscale ceramic reinforcement is quantitatively studied, in order to propose the material and process methods to obtain the homogeneous and controllable microstructures of nanoscale reinforcing phases. Chapter 3 accordingly provides the scientific basis for SLM net-shape forming of novel metal matrix nanocomposite parts with unique nanostructured reinforcement and significantly elevated mechanical properties (e.g., microhardness and wear performance).

In Chaps. 4 and 5, according to an integrated processing method of "designed materials", "laser induced *in situ* reaction," and "tailored mechanical performance," the *in situ* TiC/Ti_5Si_3 and TiN/Ti_5Si_3 composites and the *in situ* WC-based

hardmetals were produced by SLM AM process, starting from the high-energy ball milled SiC/Ti, Si_3N_4/Ti, and W–Ni–graphite powder systems. The influence of the applied SLM processing parameters on the microstructural development and formation mechanisms of the *in situ* TiC, TiN, and WC reinforcing phases is disclosed. The relationship of SLM processing conditions, densification behavior of SLM-processed parts, microstructural features of *in situ* reinforcements, and hardness and wear performance of *in situ* composites is proposed. It reveals that the laser induced development of the *in situ* reinforcements having unique microstructure and dispersion features favors the formation of adherent strain-hardened tribolayer covered on the worn surface, thereby enhancing the wear performance of SLM-processed *in situ* composites significantly. A new wear and tribological mechanism for laser processed *in situ* composites is accordingly proposed to get a better understanding of the relevancy of microstructures and performance of laser processed new materials.

Chaps. 6 and 7 focus on the SLM AM of high-performance light-weight composite materials, i.e., aluminum matrix composites reinforced with novel-structured ceramic reinforcements. Chapter 6 presents the SLM processing of the nanoscale TiC particle reinforced AlSi10Mg nanocomposite parts. The microstructural evolution of nanoscale reinforcement in SLM-processed parts at different SLM processing parameters is studied and the attendant densification level and mechanical properties are assessed, in order to enable the successful production of Al-based composites with nanoscale reinforcement architecture and elevated mechanical performance. In Chap. 7, SLM AM of the SiC/AlSi10Mg composite powder having an *in situ* reaction nature was performed to prepare the Al-based composites with the multiple reinforcing phases. The influence of the SLM processing parameters on the constitutional phases, microstructural features, and mechanical performance (e.g., densification, microhardness, and wear property) of the SLM-processed Al-based composites was disclosed, which indicated the promising potential of SLM process in producing novel Al-based composites with unique reinforcing phases/structures and performance.

Chapter 8 presents the research work on DMLS AM of WC particle reinforced Cu matrix composites. A strategy for the design and formation of the graded interfaces between WC reinforcing particles and Cu matrix is proposed. The WC reinforcing particles are added to the Cu matrix in the form of WC–Co composite powder, favoring the formation of the graded interfaces between the WC reinforcing particles and the Cu matrix. The graded interfacial design and formation are effective in improving the interfacial bonding and material integrity and the resultant mechanical properties of DMLS-processed (WC–Co)/Cu composites. The interaction behaviors and pushing/trapping effects of the WC reinforcing particles with the advancing solid–liquid interfaces in the laser induced molten pool are proposed. The effects of DMLS processing parameters in terms of laser power, scan speed, and powder layer thickness on the particle dispersion behavior and interfacial structures in DMLS-processed (WC–Co)/Cu composites are disclosed. To favor the particle trapping effect and improve the particle dispersion homogeneity, a proper increase in laser power and scan speed and a decrease in the powder layer thickness are proved to be feasible. The underlying effect of materials design, e.g., the addition of rare

earth (RE) elements and the optimization of reinforcement content, on densification, microstructure, and mechanical properties of DMLS-processed (WC–Co)/Cu composites is disclosed. The exact metallurgical roles of RE elements in improving the DMLS processing ability of particle reinforced composites are proposed, i.e., (i) decreasing surface tension of the melt and enhancing solid–liquid wettability; (ii) dragging and/or pinning grain/phase boundaries and resisting grain coarsening and particle aggregating.

In Chap. 9, the processing conditions and control methods for DMLS AM of W–Cu composite system with a nature of mutual insolubility are studied. The application of the integrated processing parameters, i.e., the linear laser energy density and the volumetric laser energy density, proves to be efficient in controlling the DMLS processing ability and in improving the densification rate and microstructural homogeneity of DMLS-processed W–Cu composites. The influence of Cu-liquid content on densification response and microstructural development of DMLS-processed W–Cu components is disclosed, thereby proposing the materials optimization method to enhance DMLS-processed quality. With the suitable component content and DMLS processing conditions determined, a series of regularly shaped W-rim/Cu-core structures are found to be formed after DMLS processing. The metallurgical mechanisms for the formation of such a novel structure are proposed, thereby proposing the new metallurgical phenomenon and its mechanisms for DMLS processing of this special material system.

10.2 Prospective View

10.2.1 Fundamental and Scientific Issues for Laser AM

With the prevailing of the interchangeable concept of 3D Printing (3DP) in recent years, additive manufacturing (AM) technology attracts considerable attention and interest from the global industrial and academic communities. AM technology, which has been regarded as one of the most significant innovations in the twentieth century by the Natural Science Foundation of America [1], is becoming one of the significant research highlights in engineering and materials disciplines. AM technology has changed the traditional manufacturing philosophy substantially, renovating the conventional “materials removal” method to the entirely contrary “material incremental manufacturing” method. AM technology provides the promising technical opportunities for the low-cost, short-cycle, and net-shape manufacturing of high-performance components with any complex configurations, thereby accelerating the manufacturing revolution in the aeronautical, astronautical, biomedical, mechanical, automotive, and other industries [2, 3].

In recent years, the researches on laser additive manufacturing/3D printing (AM/3DP) have received the continued attention and support from the governments

of the different countries in the world. Through the government-orientated top-level design, the forward-looking layout and development of key technologies of laser AM have been performed. In particular, the basic researches on laser AM have been promoted significantly, in order to obtain a strategic high ground of this advanced technology. In 2014, laser AM/3DP technology, for the first time, has been incorporated into the "National High-tech R&D Program (863 Program)" and the "National S&T Support Program for Manufacturing" funded by the Ministry of Science and Technology of China. In the "Thirteen Five" (2016–2020) disciplinary strategic planning of the Mechanical Engineering Discipline of the National Natural Science Foundation of China (NSFC), AM/3DP technology will also be managed in the interdiscipline or cross-department area, thereby giving the funding priority [4].

Nevertheless, as a newly developed technology, the development history of AM/3DP is merely over 20 years and, therefore, it still faces a series of technological difficulties and scientific challenges. The relevant scientific issues arise from a number of disciplines including mechanical engineering, material science, control, optics, etc [2]. With the in-depth study and development of AM/3DP technology, especially with the integration of advanced laser technology and new materials technology, a number of significant fundamental problems associated with laser AM/3DP have been produced, mainly in the following three aspects:

i. Scientific and theoretical basis:
   For laser AM/3DP of high-performance materials (e.g., metals, alloys, ceramics, composites, and biomaterials), what are the relevant key scientific issues, theoretical basis, and scientific significance?
ii. Material and technical basis:
   To achieve an integration of "Designed Material," "Tailored Process," and "Controlled performance" for laser AM/3DP of high-performance complex-structured components, what are the technical approach, key methods, basic mechanisms, and relevant scientific basis?
iii. Functionality and application basis:
   Which industrial sectors in the world may act as the specific "foothold" to meet the strategic requirements and development goals of laser AM/3DP technology? What are the industrial requirements, design and manufacturing methods, and application and evaluation methods for laser AM/3DP of components with an integration of designed structures and preferable functions? How to achieve a smooth transfer from the basic research results to the practical engineering applications of laser AM/3DP technology?

In order to give an accurate answer to the three basic questions above, it is necessary to consider carefully the development strategies, future research directions, and cutting-edge scientific issues of laser AM/3DP technology, which not only helps to further enhance the level of AM/3DP research and innovation in the world, but also contributes to the progress and development of AM/3DP technology itself. Corresponding to the above three aspects of questions, the related fundamental research

and development areas and main contents proposed for further consideration and discussion include but are not limited to:

i. Fundamental issues concerning scientific and theoretical basis

- Physics-based process and its simulation for laser AM/3DP, including materials phase transformation mechanisms under nonequilibrium laser interaction, materials metallurgical thermodynamics, and kinetics behaviours in laser-induced molten pool;
- Process and material property modelling and optimization for laser AM, including prediction of temperature field, velocity field, and solute field in laser-induced molten pool, mechanisms of laser rapid solidification, and methods and theories for controlling internal metallurgical defects in laser AM-processed materials;
- Laser AM fabrication process and performance modeling and optimization, including multi-scale prediction of development and evolution mechanisms of multiple types of stresses in a whole process of laser AM, prevention mechanisms of deformation and cracking of laser AM-processed components.

ii. Fundamental issues concerning material and technical basis

- Special metal materials and biomaterials for laser AM/3DP: Design of chemical compositions and physical properties, powder preparation techniques, and characterization methods;
- Multiple and novel materials processed by laser AM/3DP: Nanomaterials, composite materials, porous materials, smart materials, etc;
- Laser AM/3DP equipments and devices: Integration approach and optimization mechanisms of optical systems, closed-loop control systems, processing systems, etc;
- Laser AM/3DP processes and process enhancement: Laser AM/3DP production methods and control mechanisms of high-performance complex-shaped components with “designed structures” and “tailored properties” based on material–process–microstructure–performance integrated control.

iii. Fundamental issues concerning functionality and application basis

- Function-oriented innovative design of optimized configurations for laser AM/3DP: New methods and principles;
- New processes and technologies based on laser AM/3DP: Micro/nano-fabrication systems, principles, and methods;
- Bio-Additive Manufacturing Technology: Tailored materials, process, performance, and innovative applications;
- Novel applications of laser AM/3DP in aerospace and automotive fields: Function requirements, manufacturing processes, and evaluation methods.

10.2.2 Particular Considerations for Future Development and Application of Laser AM Technology

Research and development on laser-based AM of metallic components are interdisciplinary, integrating materials science, metallurgical engineering, mechanical engineering, and laser technology. For the successful development and application of laser AM technology in the future, the significant research and understanding are still required in the aspects of materials preparation and characterization, process control and optimization, microstructural and mechanical properties evaluation, and theories of physical and chemical metallurgy for each AM technology, both the powder bed-based SLM/DMLS process and the LMD process using the powder feeding approach. The following issues are of particular significance for future development and application of AM technology.

i. Extension of AM applicable powders

The basic role of powder material properties in a successful AM production has long been recognized [5–7]. Certain powder materials which have sound processability in conventional PM routes are found inapplicable for AM processes. The unique processing manner of AM brings forward some special requirements of applicable powders. For instance, high flowability is a primary consideration for powders, since AM processing is based on powder spreading (LS/LM) or powder feeding (LMD/DMD). Further studies in terms of chemical and physical properties, preparation technique, and characterization method of powder materials are required to fit a successful AM application. Material researches should be extended to multiple systems and forms, including pre-alloyed/blended/composite Fe^{-}, Ni^{-}, Ti^{-}, Al^{-}, Cu^{-}, and Mg-based powders, in order to realize a diversity of AM-applicable materials.

ii. Development of novel materials and "designed materials"

The application of AM technology to prepare novel-structured high-performance functional components is of unique interest and practical significance for industrial applications. The special material incremental manufacturing processing procedure and highly nonequilibrium nature of AM favor the formation of bulk-form materials with unique microstructures and properties. It provides a beneficial method to develop new materials such as nanophase, amorphous, functionally gradient, and porous materials. On the other hand, the unique integration of homogenization design, heterogeneous modeling, and LMD/DMD process (as reviewed in Chap. 2) offers a revolutionary approach for manufacturing "designed materials" with properties and functions, which do not currently exist.

iii. Establishment of AM process database

Comprehensive knowledge is involved in AM processes, including laser technology, material science, powder metallurgy, and rapid solidification. The suitable AM

processing data for various metallic materials should be accumulated. Combined with the optimization in powder material design and preparation, the corresponding optimal AM processing parameters should be experimentally determined. After a sufficient accumulation, the material-process database can be established, realizing a simplified, precise, and stable control of AM treatment of versatile powder materials for industrial applications.

iv. Microstructure development and metallurgical mechanism

AM processes offer a promising potential for development of novel bulk-form materials of designed compositions, microstructures, and properties. However, due to the significant nonequilibrium nature of laser processing and the complicated mutual influence of material and process parameters, the unpredictability and/or uncontrollability of the formation of phases and microstructures in an AM route still remain as a major challenge. The underlying physical and chemical metallurgical mechanisms responsible for the variation of microstructural and mechanical properties should be determined, in order to give a strong theoretical basis for AM processes.

v. Theoretical modeling and simulation

The existent reports on the theoretical modeling and simulation of AM processes are mostly focused on the relatively macroscopic thermal field [8], stress field [9], and volume shrinkage [10], based on a heat transfer model or heat-stress coupled model with a necessary consideration of melting/solidification phase transformations [11]; but few have incorporated the microscopic fluid flow calculations due to the involved complexity. The theoretical study of the metallurgical thermodynamics and kinetics behaviors of the melt within nonequilibrium molten pool is of particular importance, including the mass transfer and fluid flow, crystal nucleation and growth, and melting and mixing behavior of key alloying/additive elements [12], thereby enabling the microstructure to be tailored according to the local performance requirements of the component.

References

1. Department of Engineering and Materials Sciences, National Natural Science Foundation of China (NSFC) (2010) Mechanical engineering disciplines development strategy report (2011-2020). Science Press, Beijing
2. Wang GB (2011) Photonic manufacturing science & technology: overview and outlook. J Mech Eng 47(21):157–169
3. Li DC, He JK, Tian XY et al (2013) Additive manufacturing: integrated fabrication of macro/microstructures. J Mech Eng 49(6):129–135
4. Young Scholars Forum on Additive Manufacturing Science and Technology, Mechanical Engineering Department of National Natural Science Foundation of China (NSFC), Xi'an, China. http://www.nsfc.gov.cn/publish/portal0/tab110/info45674.htm. Accessed 10 Mar 2015
5. Kruth JP, Wang X, Laoui T et al (2003) Lasers and materials in selective laser sintering. Assem Autom 23(4):357–371

6. King D, Tansey T (2002) Alternative materials for rapid tooling. J Mater Process Technol 121(2–3):313–317
7. Simchi A, Petzoldt F, Pohl H (2001) Direct metal laser sintering: material considerations and mechanisms of particle bonding. Int J Powder Metall 37(2):49–61
8. Dai K, Shaw L (2004) Thermal and mechanical finite element modeling of laser forming from metal and ceramic powders. Acta Mater 52(1):69–80
9. Wang L, Felicelli SD, Pratt P (2008) Residual stresses in LENS-deposited AISI 410 stainless steel plates. Mater Sci Eng A 496(1–2):234–241
10. Dai K, Shaw L (2005) Finite element analysis of the effect of volume shrinkage during laser densification. Acta Mater 53(18):4743–4754
11. Qi H, Mazumder J, Ki H (2006) Numerical simulation of heat transfer and fluid flow in coaxial laser cladding process for direct metal deposition. J Appl Phys 100(2):024903
12. Moat RJ, Pinkerton AJ, Li L et al (2009) Crystallographic texture and microstructure of pulsed diode laser-deposited Waspaloy. Acta Mater 57(4):1220–1229